

# FUNCTIONAL DISCOTIC LIQUID CRYSTALS THROUGH MOLECULAR SELF-ASSEMBLY FOR APPLICATION IN ORGANIC ELECTRONIC DEVICES

**INDU BALA**

*A thesis submitted for the partial fulfillment of  
the degree of Doctor of Philosophy*



Department of Chemical Sciences  
Indian Institute of Science Education and Research Mohali  
Knowledge city, Sector 81, SAS Nagar, Manauli PO, Mohali 140306, Punjab, India.

March 2021





*"When you feel like quitting, remember why you started".*

*-Fearless Motivation*

*Dedicated to*

*My Beloved Parents  
and Family...*



## Declaration

The work presented in this thesis entitled “*Functional Discotic Liquid Crystals through Molecular Self-Assembly for Application in Organic Electronic Devices*” has been carried out by me under the guidance of **Dr. Santanu Kumar Pal** at the Indian Institute of Science Education and Research Mohali. This work has not been submitted in part or in full for a degree, a diploma, or a fellowship to any other university or institute. Whenever contributions of others are involved, every effort is made to indicate this clearly, with due acknowledgements of collaborative research and discussions. This thesis is a bonafide record of original work done by me and all sources listed within have been detailed in the bibliography.

**INDU BALA**

In my capacity as the supervisor of the candidate’s thesis work, I certify that the above statements by the candidate are true to the best of my knowledge.

**Dr. SANTANU KUMAR PAL**

Associate Professor

Department of Chemical Sciences

Indian Institute of Science Education and Research Mohali



# Acknowledgements

The journey towards the completion of my doctoral research filled with lessons, hardships, joys, celebrations and experiences was accompanied by many peoples to whom I would like to convey my heartfelt thanks. First and foremost, with the deep sense of reverence, I would like to express my sincere thanks to my supervisor, *Dr. Santanu Kumar Pal* for his profound guidance, patience, valuable discussions and constant help during my research work. Working with him was a great pleasure and procured me a lot of learning experience. I could not have imagined having a better advisor and mentor for my doctoral research.

I owe my sincere gratitude to *Dr. Sugumar Venkataramani* and *Dr. Ujjal K Gautam*, members of my doctoral committee for their valuable suggestions during the yearly work assessment. I would like to acknowledge our former directors, *Prof. N. Sathyamurthy*, *Prof. Debi P. Sarkar*, our officiating directors, *Prof. Siva Umapathy*, *Prof. Arvind*, and our current director *Prof. J. Gowrishankar* for providing the research and infrastructural facilities. I am thankful to former HOD, Department of Chemical Sciences, *Prof. K. S. Viswanathan* and *Dr. A. S. Arulananda Babu* along with the current HOD *Dr. Sanjay Singh* for permitting the use of various departmental facilities. Besides, I am highly grateful to all the faculty members of IISER Mohali for their motivation and encouragement.

I acknowledge IISER Mohali for central NMR, HRMS and SAXS/WAXS facility. I would like to thank Department of Chemical Sciences for providing various departmental facilities like UV-vis-NIR, FTIR spectrophotometers, TGA, DSC, Fluorimeter etc. I also acknowledge the training received from *Dr. Kavita Dorai* and *Dr. A. S. Arulananda Babu* to operate the NMR and HRMS instrument, respectively.

I express my heartfelt thanks to *Dr. Santosh Prasad Gupta* (Patna University) for helping in X-ray diffraction analysis. With his simple way of explanation, he has enriched my knowledge of X-ray diffraction. I extend my heartiest gratitude to *Dr. Upendra Kumar Pandey* (Shiv Nadar University) for helping in various useful discussions related to SCLC measurements and for his valuable suggestions and encouragements at various stages of the work. I am highly thankful to *Dr. Deepak Kumar Dubey* and *Dr. Rohit Ashok Kumar Yadav* (NTHU, Taiwan) for countless discussions related to OLED device measurements and widening my knowledge in this field. I also thank *Prof. J. H. Jou* (NTHU, Taiwan) for helping in OLED device

fabrication and measurement studies. I would also like to express my sincere gratitude to *Dr. Kamalakannan Kailasam* (INST Mohali) for his insightful comments and encouragement, and his lab members including *Dr. Sunil Kumar*, *Mr. Venugopala Rao Battula* and *Ms. Neha*. I thank *Dr. Dharmendra Pratap Singh* (UDSMM, France) for helping in TOF measurements. I am thankful to *Dr. Sugumar Venkataramani* and his group members, including *Dr. Sudha Devi*, *Mr. Pravesh Kumar* and *Mr. Himanshu* for various useful discussions. I am highly thankful to *Mr. Mrityunjay pandey* and *Dr. Goutam Sheet* for helping in AFM measurements. I express my deep sense of gratitude to my former and current lab-mates *Dr. Sumyra Sidiq*, *Dr. Shilpa Setia*, *Dr. Monika Gupta*, *Dr. Dibyendu Das*, *Dr. Harpreet Singh*, *Dr. Indu Verma*, *Joydip De*, *Nitya Singh*, *Harpreet Kaur*, *Supreet Kaur*, *Vidhika Punjani*, *Varsha Jain*, *Ipsita Pani*, *Madhusudan Maity*, *Shruti Rani*, *Yogendra Nailwal*, *Tarang Gupta*, *Musthafa Iqbal*, *Abdul Haseeb M. M.*, *Ishan Sarkar*, *Ritobrata De*, and *Shallu Dhingra* for making a comfortable working atmosphere in the lab. My special thanks to *Joydip De* for helping me in various possible ways and for making my journey easy and enjoyable. I would like to thank post-doctoral fellows *Dr. Manisha Devi*, *Dr. Golam Mohiuddin*, and *Dr. Rajib Kumar Nandi* for sharing their experiences.

I am thankful to all the staff members of stores, purchase office, administrative office, account section, library, computing facility of IISER Mohali and lab assistants of chemistry teaching lab for their help and co-operation during the course of time.

I am thankful to CSIR for a timely dispersal of research fellowship and IISER Mohali for financial support. I also acknowledge IISER Mohali for providing partial international travel grant to attend 27<sup>th</sup> International Liquid Crystal Conference held in Kyoto, Japan, in 2018.

Finally, my PhD endeavor could not have been completed without the unending support from my family members and relatives. I deeply express my sincere gratitude to my parents, *Sh. Joginder Singh* and *Smt. Urmila* for their constant motivation, patience and belief in me. My *Nana* and *Nani* is a constant source of inspiration for me. I specially thank my uncle (*Sh. Praveen Kumar*) and aunt (*Smt. Veena*) for giving me various useful advices. I thank my sister (*Sadhana*), brother-in-law (*Sunil*) and brother *Tarun* for constantly supporting me. My lovely cousins *Vanisha*, *Viveka*, *Riya*, *Anurag*, *Mayank*, *Pratiksha* and *Vansh* made my journey easy. At last, I thank God for the wisdom he bestowed upon me, good health, the strength and the peace of my mind.

# Contents

## CHAPTER 1: Introduction: Discotic Liquid Crystals for Application in Organic

<b>Electronic Devices</b>	<b>1</b>
1.1 Overview	3
1.2 Liquid Crystals and its discovery	4
1.3 Classification of liquid crystals	7
1.4 Discotic liquid crystals	8
1.5 Characterization of discotic liquid crystals	11
1.6 Alignment in columnar discotic liquid crystals	15
1.7 Discotic liquid crystals as charge transport materials	18
1.8 Techniques used to measure charge transport in discotic liquid crystals	21
1.8.1 Space charge limited current technique	21
1.8.2 Time of flight method	24
1.8.3 Pulse-radiolysis time-resolved microwave conductivity	26
1.9 Molecular order and temperature dependence of mobilities	27
1.10 Application of charge transport DLCs in devices	29
1.10.1 Discotic liquid crystals as optical compensation films	29
1.10.2 Organic Field-effect transistors	30
1.10.3 Organic photovoltaic devices	31
1.10.4 Organic light-emitting diodes	33
1.11 Molecular approaches towards functional columnar liquid crystals	36
1.11.1 Hydrogen-bonded interactions based discotic liquid crystals	36
1.11.2 Charge transfer interactions based discotic liquid crystals	38
1.11.3 Ionic interactions based discotic liquid crystals	39
1.12 Outline of thesis	10
<b>References</b>	<b>43</b>

## CHAPTER 2: Heptazine based Discotic Liquid Crystals for Organic Optoelectronics 51

2.1 Electroluminescence and conductivity measurements in DLCs based on fluorescent and electron-deficient heptazine discotic core	53
---	----

2.1.1	Introduction	53
2.1.2	Objectives	54
2.1.3	Results and discussions	55
2.1.3.1	Synthesis and characterization	55
2.1.3.2	Thermal studies	56
2.1.3.3	X-ray diffraction studies	57
2.1.3.4	Photophysical, electrochemical and theoretical studies	63
2.1.3.5	Electroluminescence properties	68
2.1.3.6	Conductivity measurements	73
2.1.4	Conclusions	74
2.1.5	Experimental section	74
2.1.5.1	Synthesis of cyameluric chloride	74
2.1.5.2	Synthesis of compounds 3a-c	75
2.2	Fluorescent H-bonded columnar liquid crystals based on heptazine core	77
2.2.1	Introduction	77
2.2.2	Objectives	77
2.2.3	Results and discussions	78
2.2.3.1	Synthesis and characterization	78
2.2.3.2	Comparative infrared and NMR study of the complexes	79
2.2.3.3	Thermal behaviour	82
2.2.3.4	X-ray diffraction studies	85
2.2.3.5	Photophysical behaviour	94
2.2.4	Conclusions	96
2.2.5	Experimental section	97
2.2.5.1	Synthesis of heptazine derivatives Hpz-Cm = 6,10	97
2.2.5.2	Synthesis of acids A10, A12, A16	98
2.2.5.3	Synthesis of heptazine complexes	98
2.3	Segregated donor-acceptor columnar assembly based on heptazine-triphenylene H-bonded system	101
2.3.1	Introduction	101
2.3.2	Objectives	102



2.3.3 Results and discussions	103
2.3.3.1 Molecular design and synthesis	103
2.3.3.2 Comparative IR and NMR studies	104
2.3.3.3 Thermal behaviour	107
2.3.3.4 X-ray diffraction studies	109
2.3.3.5 Absorption studies in solution and solid state	116
2.3.3.6 Theoretical and electrochemical studies	116
2.3.3.7 Charge transport measurements	118
2.3.4 Conclusions	122
2.3.5 Experimental section	122
2.3.5.1 Synthesis of triphenylene based benzoic acids	122
2.3.5.2 Synthesis of Hpz-C <sub>n</sub> -TP (n = 6, 8, 9) complexes	123
<b>References</b>	<b>125</b>
<b>Appendix II</b>	<b>133</b>

## **CHAPTER 3: Functional Triphenylene-Pentaalkynylbenzene based Disc-Disc and Truxene-Cyanobiphenyl based Rod-Disc Oligomers**

3.1 Triphenylene-pentaalkynylbenzene discotic liquid crystalline dyads as an emitter in blue OLEDs and their charge transfer complexes with ambipolar charge transport	163
3.1.1 Introduction	163
3.1.2 Objectives	164
3.1.3 Results and discussions	165
3.1.3.1 Synthesis and characterization	165
3.1.3.2 Thermal behaviour of pure PA-TP oligomers	167
3.1.3.3 X-Ray diffraction studies of pure PA-TP oligomers	168
3.1.3.4 Thermal behaviour and X-Ray diffraction studies of PA-TP oligomers/TNF complexes	172
3.1.3.5 Photophysical, electrochemical and theoretical studies	178
3.1.3.6 Electroluminescent properties	182
3.1.3.7 Charge Carrier Mobility for the complex	186
3.1.4 Conclusions	187

3.1.5 Experimental section	188
3.1.5.1 Synthesis of compound 5a	188
3.1.5.2 Synthesis of the compounds 2a-c	188
3.1.5.3 Synthesis of the compounds 3a-c	188
3.1.5.4 Synthesis of the compounds 4a-c	188
3.1.5.5 Synthesis of the compound 7	188
3.1.5.6 Synthesis of the target compounds 8a-c & 9a-c	189
3.1.5.7 Quantum yield calculation	191
3.2 Rod-disc oligomeric liquid crystal based on 4-cyanobiphenyl and truxene core	193
3.2.1 Introduction	193
3.2.2 Objectives	194
3.2.3 Results and discussions	195
3.2.3.1 Synthesis and characterization	195
3.2.3.2 Thermal and photophysical behaviour	196
3.2.3.3 X-ray diffraction	198
3.2.3.4 Surface manometry, BAM and AFM studies	199
3.2.3 Conclusions	201
3.2.4 Experimental section	202
3.2.4.1 Synthesis of compound 7	202
3.2.4.2 Synthesis of compound 8	202
3.2.4.3 Synthesis of compound 4	203
3.2.4.4 Synthesis of target compound 5	203
<b>References</b>	<b>204</b>
<b>Appendix III</b>	<b>209</b>
 <b>CHAPTER 4: Design Strategy Enabling High Charge Transport in Room Temperature</b>	
<b>Columnar Liquid Crystalline Tetrathienoanthracene based Discotics</b>	<b>219</b>
4.1 Introduction	221
4.2 Objectives	222
4.3 Results and discussions	223
4.3.1 Synthesis and characterization	223

4.3.2 Thermal behaviour	224
4.3.3 X-ray diffraction	225
4.3.4 Photophysical, Electrochemical, and Theoretical studies	229
4.3.5 Charge transport studies	231
4.4 Conclusions	236
4.5 Experimental section	236
4.5.1 Synthesis of compound 9	236
4.5.2 Synthesis of compound 10	237
4.5.3 Synthesis of compound 11	237
4.5.4 Synthesis of compound 12a	237
4.5.5 Synthesis of compound 12b	238
4.5.6 Synthesis of compound 13a	238
4.5.7 Synthesis of compound 13b	238
4.5.8 Synthesis of compound 14a	239
4.5.9 Synthesis of compound 14b	239
4.5.10 Synthesis of tetrathienoanthracene derivative, 1	239
4.5.11 Synthesis of tetrathienoanthracene derivative, 2	240
<b>References</b>	<b>241</b>
<b>Appendix IV</b>	<b>245</b>

## **CHAPTER 5: Luminescent Perylene Tetraesters based Columnar Assemblies for Optoelectronic Applications** **257**

5.1 Perylene-triazine based columnar liquid crystals as solid-state fluorescent emitters in solution-processable organic light-emitting diodes	259
5.1.1 Introduction	259
5.1.2 Objectives	260
5.1.3 Results and discussions	261
5.1.3.1 Synthesis and characterization	261
5.1.3.2 Thermal behaviour	262
5.1.3.3 X-Ray diffraction studies	264
5.1.3.4 Photophysical electrochemical and theoretical studies	268

5.1.3.5 Charge carrier mobility measurements	273
5.1.3.6 Electroluminescent behavior	274
5.1.4 Conclusions	281
5.1.5 Experimental section	282
5.1.5.1 Synthesis of precursor 2	282
5.1.5.2 Synthesis of alkyl azides	282
5.1.5.3 Synthesis of final PTE derivatives, 3a-d	283
5.1.5.4 Ultraviolet photoelectron spectroscopy	284
5.2 Perylene-pentaalkynylbenzene based disc tetramers stabilizing columnar nematic and soft crystalline columnar assemblies	285
5.2.1 Introduction	285
5.2.2 Objectives	286
5.2.3 Results and discussions	286
5.2.3.1 Synthesis and characterization	286
5.2.3.2 Thermal behaviour	288
5.2.3.3 X-Ray diffraction studies	290
5.2.3.4 Photophysical and electrochemical properties	297
5.2.3.5 Conductivity measurements	300
5.2.4 Conclusions	301
5.2.5 Experimental section	302
5.2.5.1 Synthesis of compound 5a	302
5.2.5.2 Synthesis of compound 5b	302
5.2.5.3 Synthesis of compound 5c	303
5.2.5.4 Quantum yield calculation	303
5.2.5.5 Energy levels calculation from cyclic voltammetry	304
5.2.5.6 Conductivity measurements by ac impedance spectroscopy	304
<b>References</b>	<b>305</b>
<b>Appendix V</b>	<b>311</b>

<b>CHAPTER 6: Linear and Star-Shaped Donor-Acceptor Bridged Structures for (Opto)-Electronic Applications</b>	<b>327</b>
---	------------

6.1 High performing D- $\pi$ -A- $\pi$ -D benzothiadiazole based hybrid local and charge transfer emitters in solution-processed OLEDs	329
6.1.1 Introduction	329
6.1.2 Objectives	330
6.1.3 Results and discussions	331
6.1.3.1 Synthesis and characterization	331
6.1.3.2 Photophysical studies	332
6.1.3.3 Theoretical and electrochemical studies	335
6.1.3.4 Sensing and bio-imaging studies	339
6.1.3.5 Electroluminescence behaviour	342
6.1.4 Conclusions	348
6.1.5 Experimental section	349
6.1.5.1 Characterization data of Intermediate 4,7-bis[4-(diphenylamino)phenyl]-2,1,3-benzothiadiazole 5	349
6.1.5.2 Characterization data of BTD derivative 1	349
6.1.5.3 Characterization data of BTD derivative 2	349
6.1.5.4 Calculation of dipole moment	350
6.1.5.5 Calculations of quenching constant, detection limit and binding constant	350
6.1.5.6 Theoretical studies	351
6.1.5.7 OLED device fabrication and testing	351
6.2 Electroluminescent and ambipolar charge transport behaviour of AIE-active discotic liquid crystals based on alkoxy cyanostilbenes connected benzenetricarboxamide	353
6.2.1 Introduction	353
6.2.2 Objectives	354
6.2.3 Results and discussions	355
6.2.3.1 Synthesis and Characterization	355
6.2.3.2 Thermal behaviour	356
6.2.3.3 Photophysical, electrochemical and theoretical studies	361
6.2.3.4 Charge transport properties	362

6.2.3.5 Electroluminescent properties	364
6.2.4 Conclusions	367
6.2.5 Experimental section	368
6.2.5.1 Synthesis of target materials 1a-c	368
6.2.5.2. SCLC device fabrication	369
6.2.5.3. OLED device fabrication	370
<b>References</b>	<b>373</b>
<b>Appendix VI</b>	<b>377</b>
 <b>CHAPTER 7: Conclusions</b>	 <b>389</b>
<b>List of publications</b>	<b>399</b>

## General Remarks

Chemicals and solvents were all of AR quality and were used without further purification. Column chromatographic separations were performed on silica gel (60-120, 100-200 & 230-400 mesh). Thin layer chromatography (TLC) was performed on aluminium sheets precoated with silica gel (Merck, Kieselgel 60, F254). Structural characterization of the synthesized compounds was carried out through a combination of infrared spectroscopy (Perkin Elmer Spectrum AX3),  $^1\text{H}$  NMR and  $^{13}\text{C}$  NMR (Bruker Biospin Switzerland Avance-iii 400 MHz spectrometer), UV-vis-NIR spectrophotometers (Perkin Elmer Lambda 900 and Agilent Technologies UV-vis-NIR Spectrophotometer), MALDI (Waters synapt G2-S) and elemental analysis (Carlo-Erba 1106 analyser).  $^1\text{H}$  NMR spectra were recorded using deuterated chloroform ( $\text{CDCl}_3$ ) as solvent and tetramethylsilane (TMS) as an internal standard. The transition temperatures and associated enthalpy values were determined using a differential scanning calorimeter (DSC, Perkin-Elmer, Model Pyris 1D) which was operated at a scanning rate of  $5\text{ }^\circ\text{C min}^{-1}$  both on heating and cooling. The apparatus was calibrated using indium as a standard. Textural observations of the mesophase were performed with Nikon Eclipse LV100POL polarising microscope provided with a Linkam heating stage (LTS 420). All images were captured using a Q-imaging camera. Small-angle/Wide-angle X-ray scattering (SAXS/WAXS) studies were carried out on powder samples using  $\text{Cu-K}\alpha$  ( $\lambda = 1.54\text{ \AA}$ ) radiation from a source (GeniX 3D, Xenocs) operating at 50 kV and 0.6 mA. The diffraction patterns were collected on a two module Pilatus detector. Fluorescence emission spectra and steady state anisotropy experiments were performed on Horiba scientific fluoromax spectrofluorometer 4. Time resolved lifetime measurements were done on time correlated single photon counter from Horiba Jobin Yvon. For time resolved experiments, excitation was done by 375 nm laser diode. Langmuir monolayers were studied using surface manometry, Brewster angle microscopy (BAM) and atomic force microscopy (AFM).

Ultra-thin films were studied using a combination of surface manometry, Brewster angle microscopy (BAM) and atomic force microscopy (AFM). The surface manometry experiments were carried out using an APEX LB-2007 and a NIMA 611M trough. The subphase used was ultrapure deionized water obtained from Millipore Milli-Q system. The stock solutions were prepared using chloroform (HPLC grade, Merck). After spreading it on the air-water interface, the film was left for 20 min, allowing the solvent to evaporate. The  $\pi$ -Am isotherms were

obtained by symmetric compression of the barriers with a constant compression rate of 10 cm<sup>2</sup>/min. The surface pressure ( $\pi$ ) was measured using the standard Wilhelmy plate technique. A Brewster angle microscope (BAM), MiniBAM (NFT, Nanotech, Germany) was employed to observe the films at the air-water interface. LB technique was employed to transfer various layers of the films onto hydrophilic and hydrophobic substrates at target surface pressure ( $\pi_t$ ) with a dipping speed of 1 mm/min. For hydrophilic surfaces, freshly cleaved mica was used. To obtain hydrophobic surfaces, freshly etched silicon wafers were dipped in hexamethyldisilazane (HMDS) for 12 h and then rinsed with HPLC grade chloroform. Silicon wafers were etched by treating polished silicon wafers for about 5 min. in hot acidic piranha solution (3:1 ratio) which were then rinsed in ultrapure deionized water and then dried. The AFM studies on these LB films were performed using Asylum Research MFP 3D. We used silicon tips (radius:  $9 \pm 2$  nm) with spring constant of 42 N/m and resonance frequency of 300 kHz. Non-contact mode was used to obtain the topography of the film. Surface manometry, BAM and depositions were carried out at room temperature ( $25 \pm 0.5$  °C). AFM was carried out at different temperatures. Cyclic Voltammetry (CV) studies were done using setup by Princeton Applied Research VersaSTAT 3. The experimental setup for CV measurements consists of a single compartment cell equipped with Ag/AgNO<sub>3</sub> as reference electrode, platinum wire as counter electrode and glassy carbon as working electrode. 10<sup>-3</sup> M solutions of all the compounds were used for CV measurements. A 0.1 M solution of tetrabutylammoniumhexafluorophosphate was used as a supporting electrolyte. The half-wave potential of the ferrocene/ferrocenium (Fc/Fc<sup>+</sup>) was calculated as  $E_{1/2, \text{Fc/Fc}^+} = (E_{\text{anodic peak potential}} + E_{\text{cathodic peak potential}})/2$ . The LUMO energy levels were obtained by the formula  $E_{\text{LUMO}} = - (4.8 - E_{1/2, \text{Fc/Fc}^+} + E_{\text{red, onset}})$  eV, while the HOMO energy levels by  $E_{\text{HOMO}} = - (4.8 - E_{1/2, \text{Fc/Fc}^+} + E_{\text{ox, onset}})$  eV. DFT calculations were performed with the use of Gaussian 09 suite of packages. A full optimization was carried out using the hybrid functional, Becke's three parameter exchange and the LYP Correlation Functional (B3LYP) at a split valence basis set 6-31G(d,p). The dielectric impedance measurements by ac impedance spectroscopy technique were carried out using a Solartron SI 1260 Impedance/gain-phase analyzer and Solartron dielectric interface 1296 with Mettler Toledo FP82HT temperature controller. The measurements were performed by applying fixed alternate voltage with varying frequency that ranges from megahertz to millihertz. The graphs were interpreted in terms of equivalent circuits consisting of electrical



components as capacitors, resistors and inductors by using a software Nano-electronic Measurement Systems (NeMS), India. The samples were heated to their isotropic temperature and were filled through capillary action in an ITO (Indium-Tin oxide) cell and then allowed to cool slowly until the mesophase temperature reached for measurement. To execute TOF measurement, the materials were filled in a commercially purchased homeotropic anchored ITO cell (from AWAT, Poland) of  $\mu\text{m}$  thickness. The sample was excited by a Nd:YAG pulsed laser with a laser spot of 8 mm in diameter having excitation wavelength of 355 nm and 5 ns pulse width. The measurement was performed in the cooling cycle started from its isotropic temperature with a rate of 2 °C/min. The filling of sample cell was conducted in  $\text{N}_2$  atmosphere in order to avoid the recombination of electrons with the space charges and/or oxygen molecules. To measure the charge mobility, external voltage was applied with the help of Keithley 6487. The induced charge displacement was observed via transient photocurrent curve which was recorded by a digital oscilloscope (Agilent, DSO 1012A) connected to a voltage amplifier. The output transient photocurrent curve was used to calculate the charge carrier mobility by using formula:  $\mu = d^2/T_r.V$ , where  $T_r$  is the transient time obtained by photocurrent curves, V is the applied voltage and d is the ITO cell thickness. For mobility measurement by space charge limited current (SCLC) method, effective cell thickness of SCLC cells were measured by using interferometry (Perkin Elmer lambda 35). Current-Voltage measurement and dielectric constant of the samples were obtained using Keithley 4200 SCS parametric analyzer. For SCLC measurements, cells were prepared using fluorine-doped tin oxide (FTO)/Indium-doped tin oxide (ITO) (Xinyan Technologies, Taiwan,  $7 \Omega/\text{cm}^2$ ) and Gold (Au) Electrodes. FTO substrates were patterned using zinc powder and 2M hydrochloric acid (Sigma Aldrich) solution. Firstly, the FTO substrate was masked using Kapton tape of required dimension (1 to 1.5 mm), then the unmasked area was covered using Zinc Powder. 2M HCl solution was then added drop wise to cover the entire substrate. Once the reaction is finished, HCl and zinc powder was cleaned using clean room cotton buds. Patterned substrates were then sequentially cleaned for 20 min each using 10% soap solution (Hellmanex<sup>TM</sup> III) in distilled water, acetone and isopropyl alcohol in an ultrasonicator at room temperature. Gold electrodes were prepared by sputtering unit (Tecport sputtering unit) using shadow mask during sputtering of 10 nm Ti/Ni followed by 100 nm of Gold. Prior to cell fabrication, 20 min. UV ozone (Nova Scan PSD- Pro Series) was performed on both FTO/ITO

and Au electrodes. Cells for mobility measurement were then fabricated by sandwiching 2.5  $\mu\text{m}$  thick mylar sheet in between two electrodes (FTO/ITO and Au) at corners with the help of UV curable epoxy to get uniform thickness. The thickness of different samples was measured from the interference maxima and minima in visible to NIR region by recording the transmitted light using Perkin Elmer (Lambda 35) UV-vis Spectrophotometer. SCLC cells were filled using capillary technique by melting the compounds above ( $+10\text{ }^{\circ}\text{C}$ ) their isotropic transition temperature. Once filled, samples were allowed to cool down slowly to the room temperature. Current voltage (J-V) characteristics and dielectric constant of materials under study was measured using Keithley 4200 SCS Semiconductor Parameter Analyzer. All the solution-processed OLED devices were fabricated on indium-tin oxide (ITO) coated glass substrates and were employed as anode. Firstly, ITO substrates was sequentially cleaned in ultrasonication bath with the detergent solution, deionized water (10 min), acetone (30 min,  $50\text{ }^{\circ}\text{C}$ ), and isopropanol (30 min,  $60\text{ }^{\circ}\text{C}$ ). Subsequently, the as-cleaned substrates were treated by ultraviolet (UV) ozone for 15 min and then poly(3,4-ethylenedioxythiophene)/polystyrenesulfonate (PEDOT:PSS) was spin-coated (4000 rpm, 20 sec) onto the substrates from aqueous solution, which was then baked at  $120\text{ }^{\circ}\text{C}$  for 15 min inside the nitrogen maintained glove box. Afterward, the emissive layer (CBP: x wt% emitter; x = 1.0, 3.0, 5.0, and 100) was spin-coated onto the PEDOT:PSS layer. Finally, TPBi (35 nm), LiF (0.5 nm), and Al (150 nm) layers were constructively deposited via a thermal evaporation process. PEDOT:PSS acted as the hole transporting material (HTM), 2,2',2''-(1,3,5-benzinetriyl)-tris(1-phenyl-1-H-benzimidazole) (TPBi) was employed as electron transporting material (ETM). The EL spectra were recovered through an optical analyzer, Photo Research PR745. The current-density and luminance versus applied voltage characteristics were measured by Keithley 2400 and Konica Minolta Chromameter CS200, respectively. All the instruments were interfaced with a computer and a suitable computer program written in Lab View was used to control the experiment.

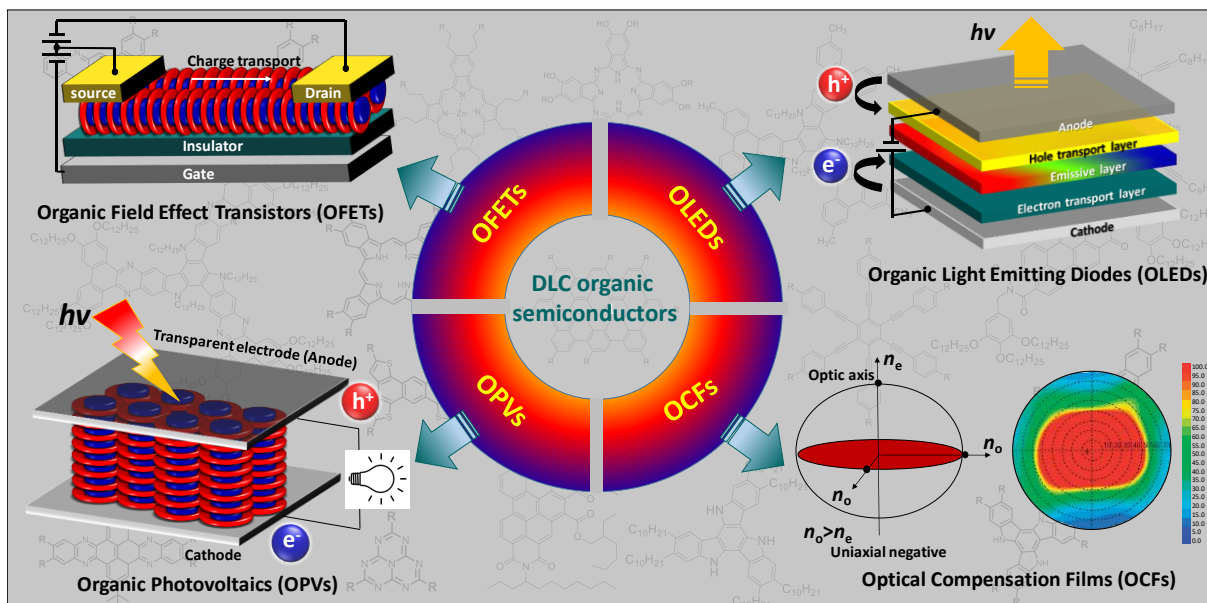




# Chapter 1

## INTRODUCTION: Discotic Liquid Crystals for Application in Organic Electronic Devices

*Discotic liquid crystals (DLCs), discovered about four decades ago by S. Chandrasekhar & co-workers have emerged out as advanced soft functional materials of recent technology. The remarkable interest in DLCs fueled primarily by the possibility of constructing a new generation of organic semiconductors and wide viewing displays. The spontaneous organization of DLCs particularly in columnar architectures exhibiting one-dimensional charge transport property led to their applicability in OFET, OLED and OPV devices. In addition to charge transport property, luminescent nature of many DLCs opens a new pathway towards the generation of emissive materials in OLED devices. The liquid crystalline property of DLC organic semiconductors provides advantage of self-healing of structural defects and increased device durability over their amorphous counterparts while the alkyl chain substitution offers low-cost solution processability and easy purification. Besides the potential of columnar phases in devices, the nematic phase of DLCs has been used as optical compensation films to widen the viewing angle of display devices.*





## 1.1 Overview

Organic electronics and optoelectronics is an interdisciplinary field. For more than a half-century, it has been the attention of the emerging areas of exploration in chemistry and physics, involving the design, synthesis, and characterization of novel organic molecules followed by their utilization as an active component in the fabrication of devices. From the time of the first revelation of thin-film organic light-emitting diode (OLED)<sup>1</sup> operated at low-drive voltage, organic thin films emerged out as a useful form<sup>2,3</sup> to be employed in various devices including organic thin-film transistors (OTFT), organic photovoltaics (OPV), and so forth. However, the transfer of material properties onto the thin films required a careful investigation of appropriate processing techniques. Although the vacuum deposition technique prevails in that sense but not in the agreement of simple manufacturing and low-cost fabrication. From an industrial perspective, fabrication of large ordered areas, easy processing and low fabrication cost is highly warranted for mass production that can be successfully achieved by the solution processing technique. In addition to processing sensitivity to thin film morphology, materials itself ability to grow and nucleate in a constructive manner also play a pivotal role and can be controlled by molecular design. Therefore, the molecular architecture, self-organizing features and lastly the solution processability of the materials are important parameters for their efficacious applicability in electronic devices. In this direction, one class of materials is liquid crystals (LCs), in particular, discotic liquid crystals (DLCs)<sup>4-7</sup> having the ability to self-assemble into columnar architecture due to supramolecular interactions among the central aromatic core. The self-assembly mechanism of LCs is a very striking feature and large monodomain samples can be produced in a way that is otherwise not feasible for crystalline materials, and the liquid-crystalline nature of such films indicates the self-healing of defects by thermal annealing.<sup>4-7</sup> Since in DLCs, intracolumnar  $\pi$ - $\pi$  interactions are much stronger than intercolumnar interactions, thus charge transport is anticipated to be quasi-one-dimensional in these kinds of materials.<sup>4-7</sup> The flexible side groups (usually alkyl chains) surrounded the central rigid core controls the self-assembly behaviour in solution as well as in bulk phase whereas conjugated core governs the electronic properties at molecular-level. Therefore, the overall electronic properties depend on both core and side substituents, hence they can be tuned by modifying either of them. For instance, on one side, the use of highly planar conjugated

cores show significant molecular overlap which can lead to high mobility DLC semiconductors. The energy gap values for DLCs are observed to be as low as 1.1 eV and in the range of that of graphite (1.0–1.4 eV).<sup>8</sup> Also, the high charge carrier mobility of value up to  $8.84 \text{ cm}^2 \text{ V}^{-1} \text{ s}^{-1}$  has been realized in columnar DLCs.<sup>9</sup> On the other side, the use of available luminescent cores and side groups can give rise to DLC that can be used as solid-state emitters in OLEDs. In this manner, DLC materials allow molecular engineering in accordance to the desired property demanded for different device architectures based on OLEDs, organic field-effect transistors (OFETs), OPV solar cells, etc.<sup>4-7</sup> In addition, DLC materials endowed with alkyl chains on their periphery offer the self-healing of defects and damage which can be annealed away, hence can increase the durability of the device. The presence of alkyl chains also provides the ease of device fabrication by solution processing technique.

This thesis deals with the rational design, synthesis and finally the application of room temperature DLCs, in particular, columnar LCs as a (i) solid-state emitter in OLED devices, and (ii) charge transport organic semiconductors. Moreover, this thesis also described the usage of hydrogen-bonded non-covalent strategy to achieve various discotic materials for optoelectronic applications because of its high ease to synthesis the materials and no tedious purification required at the final stage.

## 1.2 Liquid crystal and its discovery

Liquid crystal, a special state of matter intermediate to solid and liquid, thereby also called ‘mesophases’ uniquely combines the property of order and mobility (Figure 1.1).<sup>10,11</sup> In this state of matter, the molecules possess *positional* as well as *orientational* order that is molecules center of mass occupy specific positions and molecular axes direct towards certain directions. Although crystals also exhibit *positional* and *orientational* order but they are not mobile due to the fixed positions occupied by molecules at regular intervals while liquids are mobile but do not exhibit any kind of order. In order to form an LC phase, the molecular design should have a rigid and flexible part, not only that but there should be a subtle balance of interactions between both of these parts to form mesophases. However, other factors such as shape anisotropy, molecular segregation at a macroscopic scale, etc. are responsible for the



occurrence of mesophases. The LCs can show a variety of mesophases such as nematic, smectic, columnar and many more as discussed in the following sections.

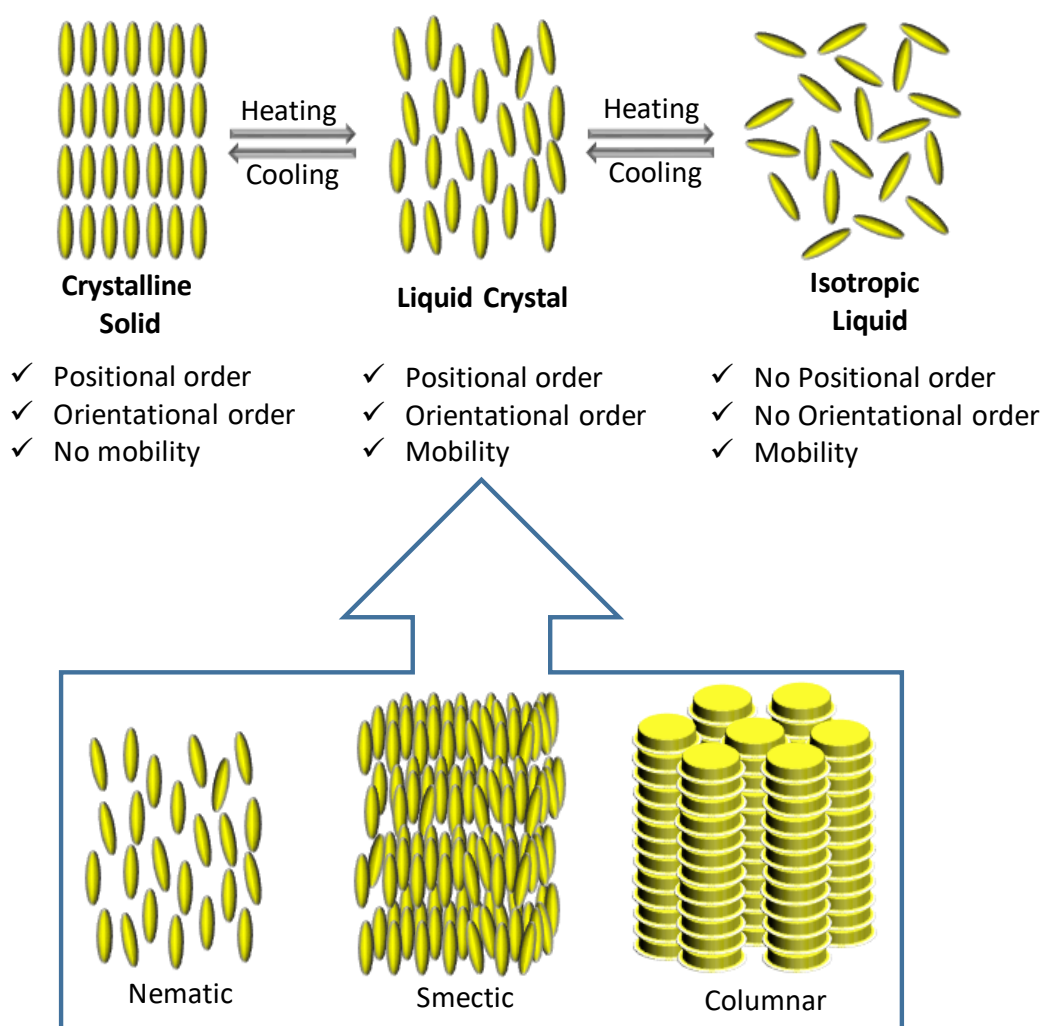


**Figure 1.1** Schematic showing the phase transition and molecular ordering present in various phases i.e. in crystals, LCs, and isotropic liquid. Rod-like molecules form nematic and smectic LC phases while disc-shaped molecules mainly form columnar phases (Redrawn from Ref. 11).

The discovery of LC was itself a multidisciplinary task and epitome of today's broad interest of scientists in different fields. Although the researchers in the late 1850s came across this state of matter but were ignorant of the uniqueness of phenomena.<sup>12</sup> The discovery happens when in 1888, an Austrian botanist found unusual melting of cholesteryl benzoate, **1** (Figure 1.2)

which passes through a cloudy liquid (at 145.5 °C) before becoming a clear liquid (at 178.5 °C).<sup>13</sup> This enigmatic of double melting was solved by German physicist Otto Lehmann who first mentioned them as ‘soft crystals’; then ‘crystalline fluids’ and finally named as “Liquid Crystals” when fully convinced that the opaque phase exhibit property of liquids as well as crystals.<sup>14</sup> After that, Daniel Vorländer and his team had systematically synthesized about 1100 LC compounds to derive structure-property relationships and concluded that all compounds of rod-shaped were only exhibiting mesophases, now known as calamitic molecules.<sup>15</sup> Later on, in 1922, Friedel proposed the classification of calamatics into nematic, smectic and cholesteric solely based on polarized optical microscopy (POM) while first X-ray experiments were conducted in 1923.<sup>16</sup> The actual interest in the LC field aroused when in 1968, Heilmeyer expressed his view for LCs application in display technology. However, in 1973, George Grey pioneered the LC research by inventing the first stable room temperature nematic LC 4'-Pentyl-4-cyanobiphenyl (**2**) (Figure 1.2) that found application in LC display technology.<sup>17</sup>

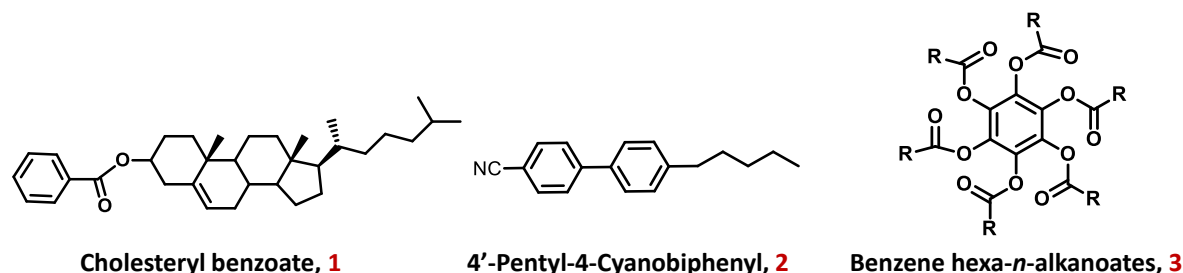


**Figure 1.2** Chemical structures of historically important LC molecules.

While applied scientists and engineers were perfecting LC displays, one more interesting discovery in the LC field revolutionize the world, which was the discovery of DLCs. In 1977 at Raman research institute Bangalore, S. Chandrasekhar with his colleagues reported the benzene-hexa-*n*-alkanoates, **3** (Figure 1.2) and showed that besides rod-like molecules, disc-shaped molecules can also show LC phase.<sup>18</sup> After characterizing the phase through POM and XRD, they proposed a model where the disc-shaped molecules stack on top of each other forming columns-like architecture. Later on, several DLC molecules were reported by scientists all over the world. Then in 1996, different from calamitic and discotic, another class of LC formed by banana or bent shaped molecules was recognized by Niori and coworkers forming achiral smectic phases and showing ferroelectric behaviour.<sup>19</sup> Although Vorlander

reported several bent-core molecules in 1929 and Matsunaga in the early 1990s, however, did not recognize the significance of mesophases. The occurrence of ferroelectricity in achiral banana-shaped molecules excites physics scientists along with chemists to study the novel properties exhibited by these latest additives. Additionally, other applications included flexoelectricity, nonlinear optics, molecular electronics, photoconductivity, and new structural design of the biaxial nematic phase were found for these latest additives.

### 1.3 Classification of LCs

There are many ways by which LCs can be classified (Figure 1.3). For instance, it can be categorized based on:

- Molecular weight into monomeric, oligomeric, and polymeric LCs.
- Method by which it can be achieved such as either by varying temperature (thermotropic LCs) or by addition of solvent (Lyotropic LCs). However, LC phase occurrence in a material by both varying temperatures as well as on adding solvent (amphoteric LCs) are rare.
- Type of constituent components i.e. organic, inorganic or organometallic.

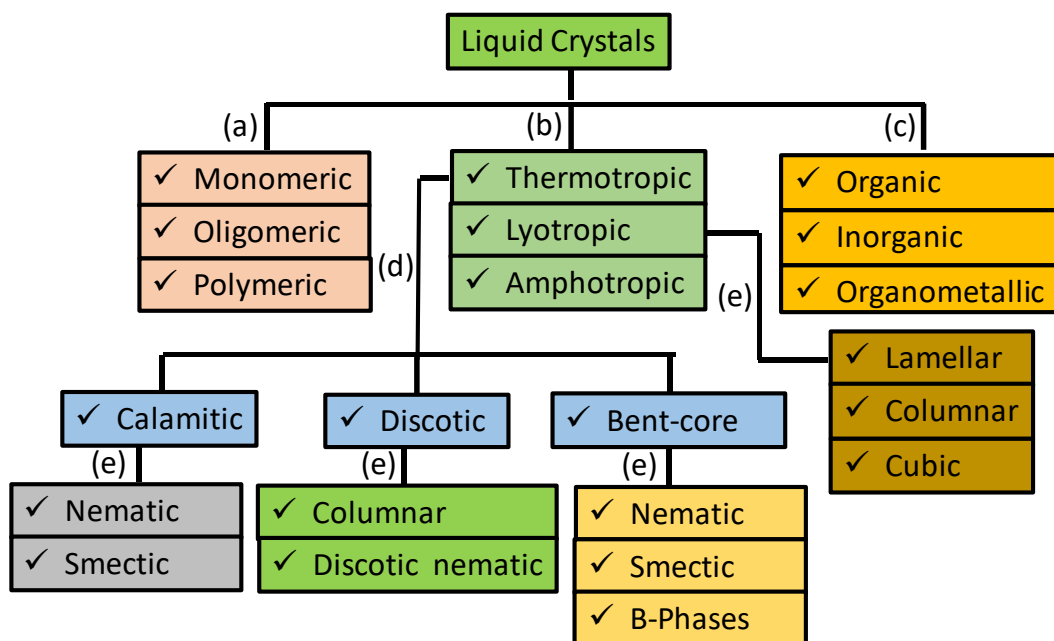


**Figure 1.3** Classification of LCs depending on several factors as illustrated in the text (Redrawn from Ref. 4).

(d) The shape of molecules whether it is rod-like (calamitic LCs), disc-like (DLCs) or banana-shaped (bent-core LCs).

(e) Self-organization of LC molecules in various ways *viz.* nematic, smectic, columnar, cubic, Banana (B)-phases, and so on.

The present thesis deals with the disc-shaped or DLCs, therefore it will be elaborately described in the next section.

### 1.4 Discotic Liquid Crystals

The discovery of DLCs in 1977 by S. Chandrasekhar<sup>18</sup> and his colleagues (discussed in section 1.2) showed that the self-organization of disc-shaped molecules, quite different from the conventional rod-shaped LCs (discovered in 1888 by Reinitzer) can also show mesomorphism.

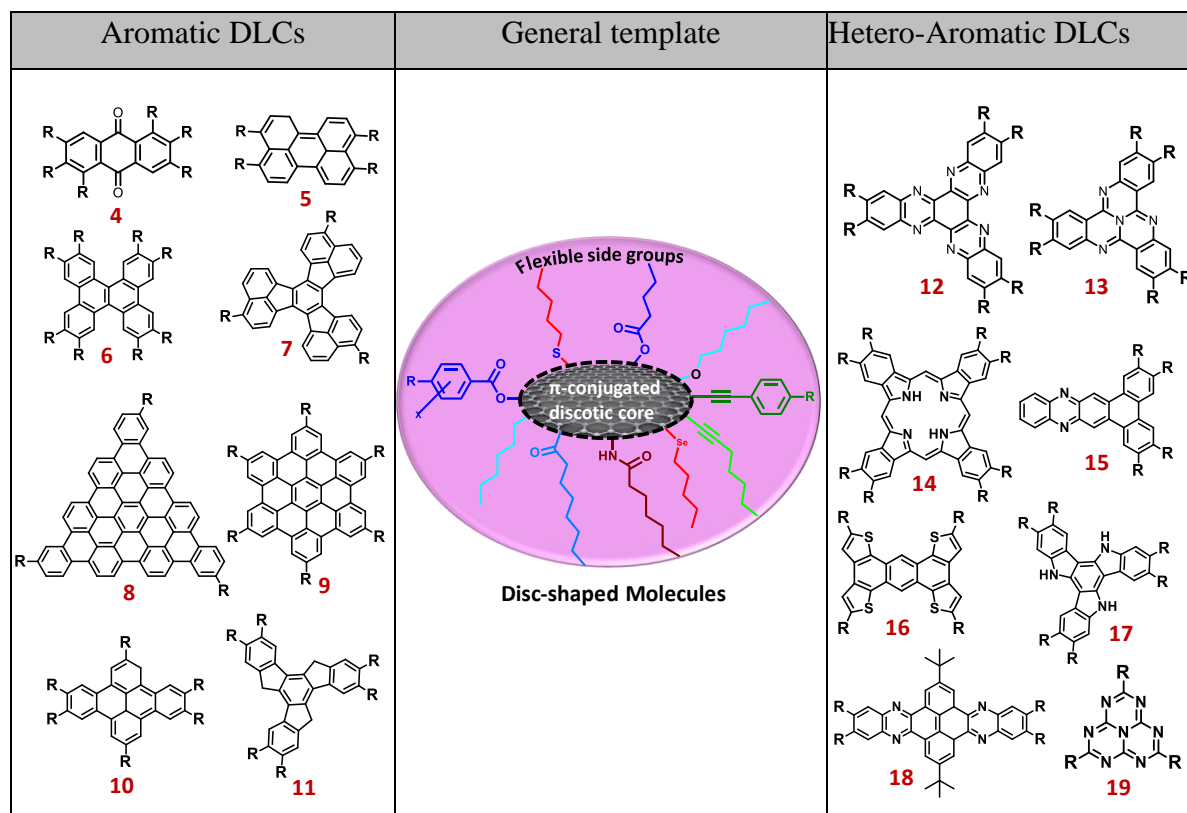


**Figure 1.4** Basic structural template of DLCs (middle) with several examples of various polycyclic aromatic (Left) and hetero-aromatic (Right) DLCs (Redrawn from Ref. 4).

Since then sincere efforts have been aimed to understand the nature of the molecular aspects that can favour the formation of DLCs. It is now well recognized that the disc-shaped molecules composed of rigid and highly planar aromatic ( $\pi$ -conjugated) cores substituted with 3-12 number of saturated side chains usually form DLCs (Figure 1.4).<sup>4</sup> The aromatic cores can

be composed of polycyclic aromatic hydrocarbons and polycyclic hetero-aromatic hydrocarbons and examples of some of them are listed as (Figure 1.4)- *Polycyclic aromatic hydrocarbons based discotic cores*: Anthraquinone (4), perylene (5), chrysene (6), decacycene core (7), graphenes (8), hexabenzocoronene (9), dibenzonaphthacene (10), truxene (11).

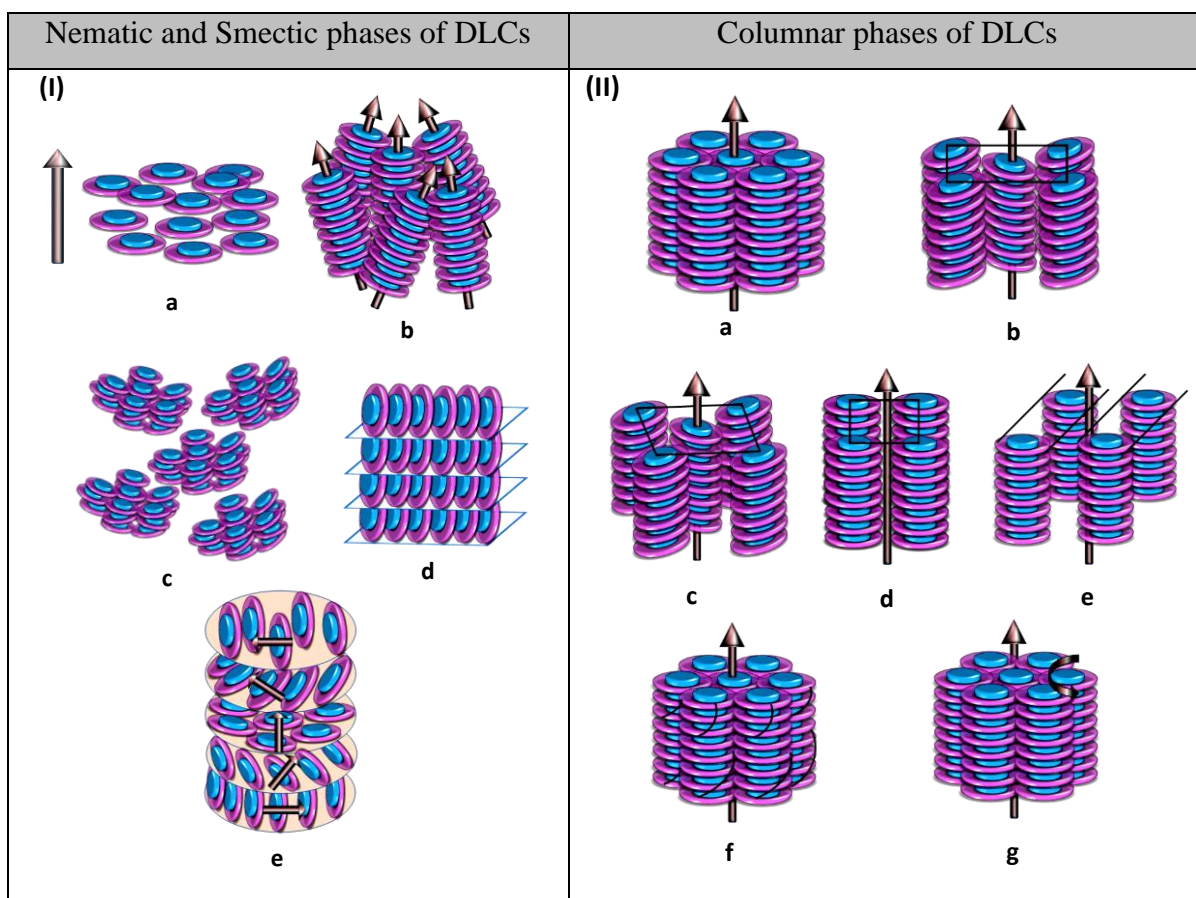


**Figure 1.5** Schematic showing the several phases exhibited by DLC molecules: **I.** (a) Discotic Nematic ( $N_D$ ), (b) Columnar Nematic ( $N_{Col}$ ), (c) Nematic Lateral ( $N_L$ ), (d) Smectic (Discotic Lamellar), (e) Chiral discotic nematic ( $N_D^*$ ); **II.** (a) Columnar hexagonal ( $Col_h$ ), (b) Columnar rectangular ( $Col_r$ ), (c) Columnar oblique ( $Col_{ob}$ ), (d) Columnar tetragonal ( $Col_{tet}$ ), (e) Columnar Lamellar ( $Col_{Lam}$ ), (f) Columnar Helical (H), (g) Columnar Plastic ( $Col_p$ ) (Redrawn from Ref. 4).

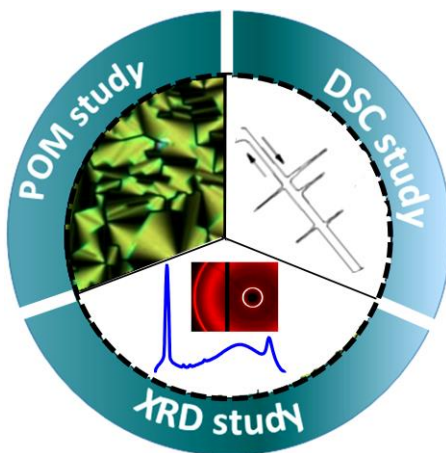
*Polycyclic hetero-aromatic hydrocarbons based discotic cores*: hexaazatrinaphthylene (12), hexaazatriphenylene (13), phthalocyanine (14), dibenzophenazines (15), tetrathienoanthracene (16), triazatruxene (17), bisphenazine (18), and heptazine (19). However, some exceptions

with non-planar<sup>20-23</sup> and non-aromatic<sup>23-25</sup> core with a lesser number of chains are also there. Moreover, a variety of linkers such as ether, ester, thioether, amide, alkanoyloxy, alkynyl, and so on are available that can be utilized to connect the flexible side groups with the central rigid core.<sup>4-7,17-33</sup> The liquid crystallinity in the DLCs mainly results from the nano-segregation between the two parts: crystalline character is stimulated by the interaction among rigid  $\pi$ -conjugated cores while the melting of flexible alkyl chains is responsible for providing the fluidity to the system. Such types of molecules can spontaneously self-assemble into one-dimensional stacks which in turn can laterally be arranged to form two-dimensional columnar superstructures and hence also called columnar LCs. The research of DLCs is mostly governed by changing the size, shape and nature of the central aromatic core as well as flexible side groups with the possibility to obtain different self-organization of the discotic molecules.<sup>4</sup> Today, there are more than 50 discotic cores known in the literature and their size varies from small benzene ring to large extended aromatic cores consists of nearly 132 carbon atoms. The anisotropic nature of the mesogenic molecules results in a variety of molecular packing in their respective mesophases. Discotic molecules, in particular, can self-organize into three types of assemblies in a broader way: columnar, nematic and smectic (Lamellar) where the columnar assemblies are the most common. The nematic phases of the discotic molecules (Figure 1.5) include the discotic-nematic ( $N_D$ ), columnar-nematic ( $N_{col}$ ), nematic lateral ( $N_L$ ) and chiral nematic ( $N_D^*$ ). The discotic nematic phase is the least ordered and less viscous phase among other nematic phases and possesses orientational order but lacking long-range positional order. The discotic nematic phase can also form a chiral phase by either mixing a chiral dopant or in pure chiral discotic molecules. In the columnar nematic, the molecules are stacked in columnar fashion but do not extend into the 2D lattices. In this phase, the columnar rods display long-range orientational order but short-range positional order. Another variety of nematic phases is lateral nematic where disk-shaped molecules form a short array of columnar superstructures which arranges in a nematic fashion due to strong lateral interactions. Besides nematic, another rare in DLCs are the smectic phases which occur when less number of peripheral chains are there in the molecular design. Here, the discotic molecules are organized in a layered manner which is separated by the sublayers of peripheral chains. On the other hand, the most common assemblies in DLCs are the columnar assemblies which in turn can self-organize into various

2D lattices as shown in Figure 1.5. All these phases differ from each other in terms of symmetry, the extent of ordering inside the columns and orientational behaviour of discs with reference to a columnar axis.

### 1.5 Characterization of DLCs

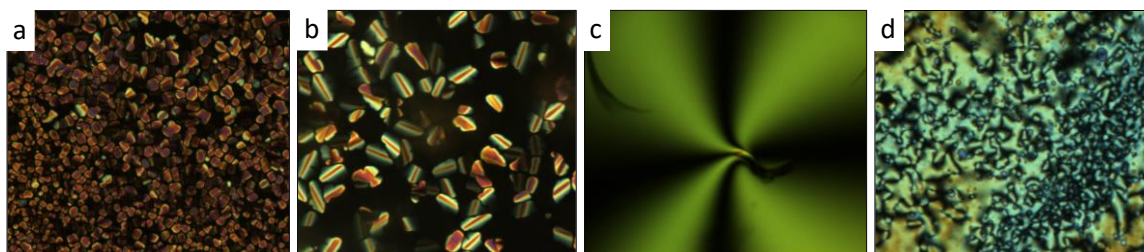
All these LC phases can be characterized by the combination of several experimental techniques such as POM, differential scanning calorimetry (DSC), X-ray diffraction (XRD) study. For instance, POM is used for textural observations of LCs. Beautiful birefringent textures are observed for LCs under POM due to their anisotropic nature as shown below (Figure 1.6). The exact phase transition temperatures can be obtained by DSC (Figure 1.7). The molecular packing in different lattices can be determined with the use of small-angle and wide-angle X-ray scattering (SAXS/WAXS) study (Figure 1.8). Grazing incidence small-angle and wide-angle X-ray scattering (GISAXS/GIWAXS) can also be done to obtain the structural characterization in the thin-film state. The thin film XRD characterization is extremely useful as most of the electronic and optoelectronic devices use these materials in the form of thin-films.



The first step to detect the existence of the LC phase is to observe the compound under POM. The shearable birefringent textures are an indication of the presence of the LC phase. The observation of birefringence is due to the deviation of molecular orientation from its normal axis when placed between the polarizer and analyzer placed at  $90^\circ$  to each other. The birefringence disappears when the compound enters into its isotropic phase. Therefore,

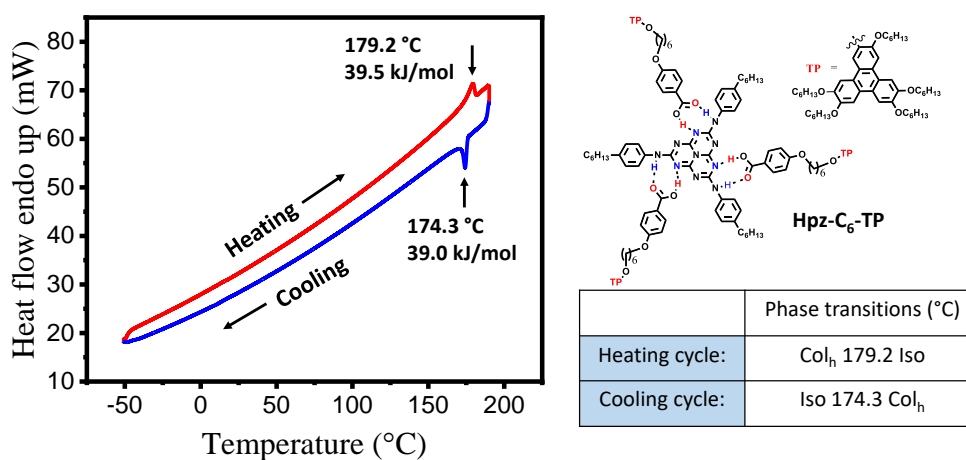


mesophase to isotropic transition can be roughly noted from the POM. Calamitic nematic and discotic nematic show characteristic schlieren textures while the columnar phases displayed by discotic molecules exhibit the various types of textures including mosaic, rectilinear defects, focal-conic, pseudo-focal-conic, dendritic, marble-like, and so on (Figure 1.6).



**Figure 1.6** Polarized optical images of mesophases formed by discotic molecules: (a) mosaic textures and (b) textures of rectilinear defects dispersed in homeotropic region of  $\text{Col}_h$  phase in trinitrofluorenone (TNF) complexes of triphenylene-pentaalkynylbenzene discotic dimer<sup>34</sup>; (c) spherulitic domain of columnar nematic phase of perylene based discotics<sup>35</sup>; (i) schlieren textures of discotic nematic phase of oligomeric rod-disc truxene-cyanobiphenyl<sup>36</sup> derivative.

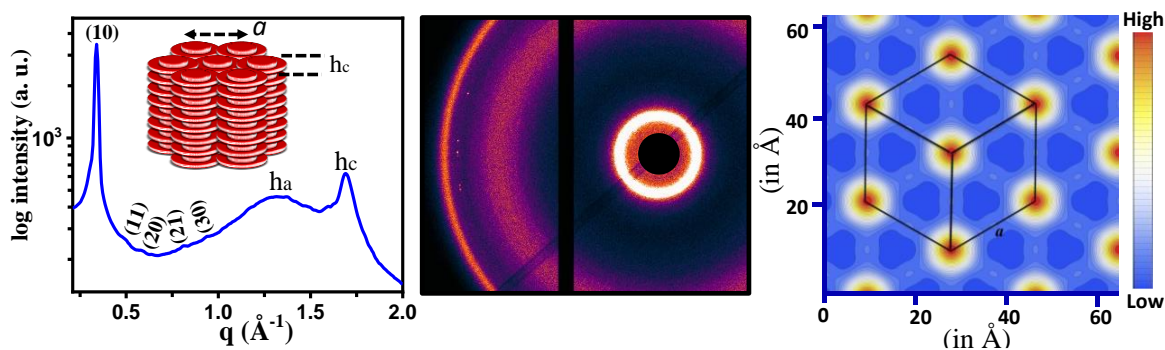
The exact phase transition temperatures and their associated enthalpies are estimated from the corresponding peaks observed in DSC thermogram (Figure 1.7).<sup>37</sup> The enthalpy value is an indication of the order present in the mesophase. Thereby the less ordered nematic phases are



**Figure 1.7** DSC thermogram of heptazine-triphenylene based DLC<sup>37</sup> (**Hpz-C<sub>6</sub>-TP**) showing room temperature mesophase.



usually associated with lower enthalpies than the columnar phases. The information about the presence of different types of mesophases can also be obtained as the corresponding transition peak appears in the thermogram. The distinction between nematic and columnar phases can be preliminarily done by POM as nematic phases show mostly characteristic schlieren textures while columnar phases exhibit focal-conic, rectilinear defects, mosaic textures and so on.<sup>4</sup> However, within the columnar phases, the confirmation of phase-type i.e. hexagonal, rectangular, oblique, etc. can be obtained by XRD technique. The small-angle region gives an indication about the type of columnar lattice while the wide-angle regime provides the intracolumnar information. For example, in the case of Col<sub>h</sub> phase, the diffraction pattern exhibit the peaks in the ratio of  $1:1/\sqrt{3}:1/\sqrt{7}:1/\sqrt{9}...$  indicate the formation of hexagonal lattice while the wide halo peak,  $h_a$  due to molten alkyl chains suggests the occurrence of the LC phase (Figure 1.8).

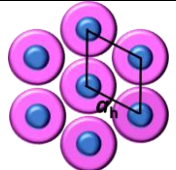
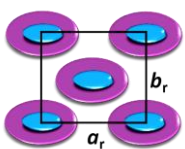
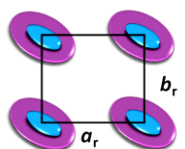
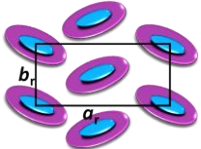


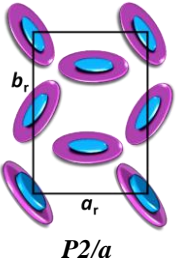
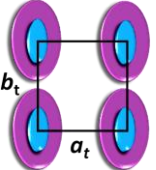
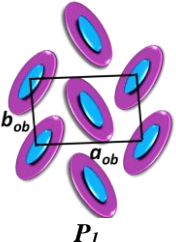
**Figure 1.8** X-ray diffraction pattern (Left) corresponding to Col<sub>h</sub> assembly (inset) of TNF complexes of triphenylene-pentaalkynylbenzene discotic dimer and its corresponding 2D diffraction pattern (middle) and electron density map (EDM) (right) where red color correspond to highest electron density region and blue color represents the lowest.<sup>34</sup>

In addition to  $h_a$  peak, the sharp  $h_c$  peak in the wide-angle represents the core-core stacking and hence confirms the columnar nature of the mesophase. The absence of this peak directs the formation of less ordered columnar assembly. Similarly, the  $d$ -spacing corresponding to peaks in the diffraction pattern can be fitted to various lattices as per the formulas mentioned in **Table 1.1**. The number of columns correlated to the neighboring columns in the 2D columnar lattices determines the degree of order present in the lattice structure which is termed as correlation length and can be calculated by using Scherrer equation  $\xi = [k 2\pi]/[(\Delta q)]$ .<sup>38-40</sup>

Here,  $k$  represents the shape factor with a characteristic value of 0.89,  $\Delta q$  is the broadening of a peak at half the maximum intensity (FWHM) and is obtained by Lorentzian fitting of the XRD pattern. Another useful information about the molecular self-organization in the mesophases can be obtained from the electron density maps (EDM).<sup>38-40</sup> EDM provides the variation of electron density, for instance, high electron density regions correspond to the rigid aromatic cores while the low electron density regimes represent the alkyl chains. The obtained electron density contrast provides a clear visualization of the molecular arrangement in the columnar 2D lattice. The EDM is usually calculated by taking into account the intensity of intense diffraction peaks observed in XRD pattern.<sup>38-40</sup>

**Table 1.1** Two dimensional lattices of columnar LCs with the relation between  $d$ -spacings and miller indices ( $hk$ ) for calculating inter-planar distance.

Columnar lattice type	Unit cell representation	Equation for indexing	Extinction rules	Area
Columnar hexagonal (Col <sub>h</sub> )	 <i>P6/mmm</i>	$\frac{1}{d_{cal}^2} = \left[ \frac{4}{3} \left( \frac{h^2 + hk + k^2}{a_h^2} + \frac{l^2}{c^2} \right) \right]$	-	$S_h = \frac{\sqrt{3}}{2} a_h^2$
Columnar rectangular (Col <sub>r</sub> )	 <i>C2/m</i>	$\frac{1}{d_{cal}^2} = \left[ \frac{h^2}{a_r^2} + \frac{k^2}{b_r^2} \right]$	$\begin{aligned} hk: h+k &= 2n \\ h0: h &= 2n \\ k0: k &= 2n \end{aligned}$	$S_r = a_r b_r$
	 <i>P2m</i>		-	
	 <i>P2<sub>1</sub>/a</i>		$\begin{aligned} hk: &\text{no conditions} \\ h0: h &= 2n \\ 0k: k &= 2n \end{aligned}$	

	 $P2/a$		-	
Columnar tetragonal (Col <sub>t</sub> )	 $a_t$ $b_t$	$\frac{1}{dcal^2} = \frac{h^2 + k^2}{a_t^2}$	-	$S_t = a_t^2$
Columnar tetragonal (Col <sub>ob</sub> )	 $a_{ob}$ $b_{ob}$ $P_1$	$\frac{1}{dcal^2} = \frac{1}{\sin^2 \alpha} \left[ \frac{h^2}{a_{ob}^2} + \frac{k^2}{b_{ob}^2} - \frac{2hk \cos \alpha}{a_{ob} b_{ob}} \right]$	-	$S_{ob} = a_{ob} b_{ob} \sin \gamma$

### 1.6 Alignment in columnar DLCs

The occurrence of columnar phases associated with electronic charge transport has stimulated the fundamental and technological research on DLC-based organic semiconductors. The LCs are highly anisotropic thereby their electronic properties are greatly affected by the type of molecular alignment. For example, in columnar LCs, two types of alignment are largely perceived one is homeotropic and the other is planar (Figure 1.9).<sup>41</sup>

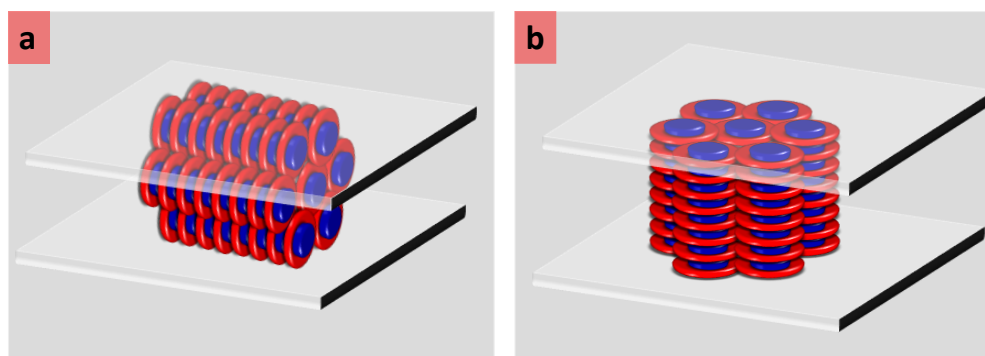


**Figure 1.9** Schematic showing the orientation of columns in (a) planar (or homogeneous) and (b) homeotropic alignment of DLCs.

In homeotropic alignment, the columns (or the discotic molecules) are oriented normal to the substrate surface while in planar alignment the columns are aligned parallel to the substrate surface. Further, in case of planar (or homogeneous) alignment, the two possibilities exist i.e. degenerate planar alignment (Figure 1.10a) in which the columns are randomly aligned and uniaxial planar alignment (Figure 1.10b) where the columns are particularly oriented in a single direction. The uniaxial planar alignment is very useful from a device point of view and is required in OFET devices where the charge flows in the horizontal direction from source to drain electrodes. However, the homeotropic alignment is required in the OLED and OPV solar cells where the semiconducting material is sandwiched between the two electrodes from bottom to top, hence the conducting property is also measured in the same direction. The preliminary identification of both homeotropic and planar alignment can be done by POM study (Figure 1.10). In the case of degenerate planar alignment, birefringent textures with defects (Figure 1.10a) are usually observed while the uniform colored backgrounds with the

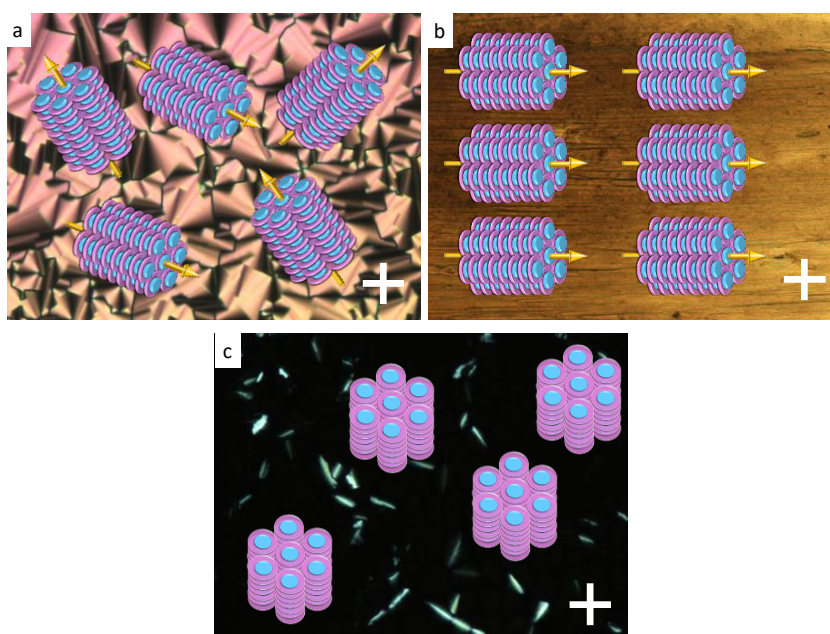


**Figure 1.10** Polarized optical microscopic images and corresponding columnar orientation of (a) degenerate (or random) planar alignment of the columnar phase of heptazine derivatives,<sup>39</sup> (b) uniaxial planar alignment (obtained on shearing in one direction) of triphenylene-pentaalkynylbenzene based discotic dimers,<sup>34</sup> (c) homeotropic alignment in the columnar phase of heptazine based discotic molecules.<sup>39</sup>

absence of defects (Figure 1.10b) characterize the uniaxial planar alignment. For homeotropically aligned samples, black regions are observed under crossed polarizer (Figure 1.10c) due to the coinciding of the columnar axis with the optic axis suggesting the optically isotropic nature of the homeotropic alignment. The type of alignment can be further determined by XRD technique. Specifically, the GISAXS technique offers the characterization of the orientational order of the self-assembled molecules in the thin-film state (Figure 1.11a), thereby employed extensively to determine the self-assembly of wide-variety of materials such as LCs, polymeric materials, and so on. More importantly, as most of the materials are implemented in devices in the form of thin-film state and different devices demand a different type of molecular assembly, thereby film characterization by GISAXS becomes more important for the proper functioning of devices. The GISAXS pattern for homeotropically and planarly aligned samples for the columnar mesogens are shown in Figure 1.11b,c.<sup>34,43</sup> Several alignment strategies are available to control the orientation of discotic molecules in either planar or homeotropic manner which could be then transferred to various devices.<sup>41</sup> For instance, homeotropic alignment can be obtained by thermal annealing which involves the slow

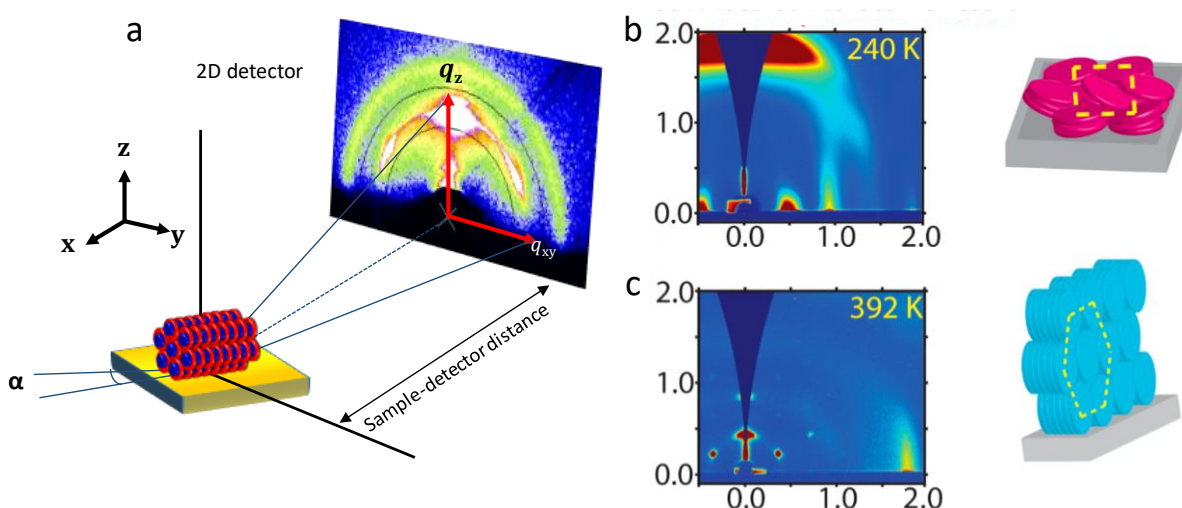


**Figure 1.11** (a) Schematic showing the assembly for GISAXS and pattern obtained for the sheared samples in room temperature Col<sub>h</sub> phase of triphenylene-pentaalkynylbenzene<sup>34</sup> based discotic dimer. (b) GIWAXS pattern for homeotropic orientation of triphenylene-ester<sup>42,43</sup> and (c) planar orientation of phenanthroperylene-ester<sup>42,44</sup> based columnar mesogens (Reproduced with the permission from Ref. 42).

cooling of the sample from its isotropic melt. On the other hand, planar alignment can be achieved by mechanical shearing of the viscous samples in the mesophase. Generally, the solution-processable techniques lead to the planar alignment of discotic molecules. The various other physical and chemical methods such as electric field, magnetic field, optical field, specific surface treatments, alignment by zone casting, Langmuir-Blodgett and chemically modifying the chemical structure, etc. can be used depending on the type of orientation is required for the respective device application.

### 1.7 DLCs as charge transport materials

DLCs are  $\pi$ -conjugated materials involving extensive  $\pi$ -orbitals overlap, hence electrons can be delocalized easily from one orbital to another.<sup>4-7</sup> As such DLCs are insulators, but charges can be generated by chemical doping i.e. by oxidation or reduction, by optical stimulation or by injection from metallic contacts and then charge transport can take place. The self-assembled columns of co-facially stacked aromatic cores in the mesophases of DLCs quite resemble the DNA-base pairs  $\pi$ -stack (Figure 1.12).

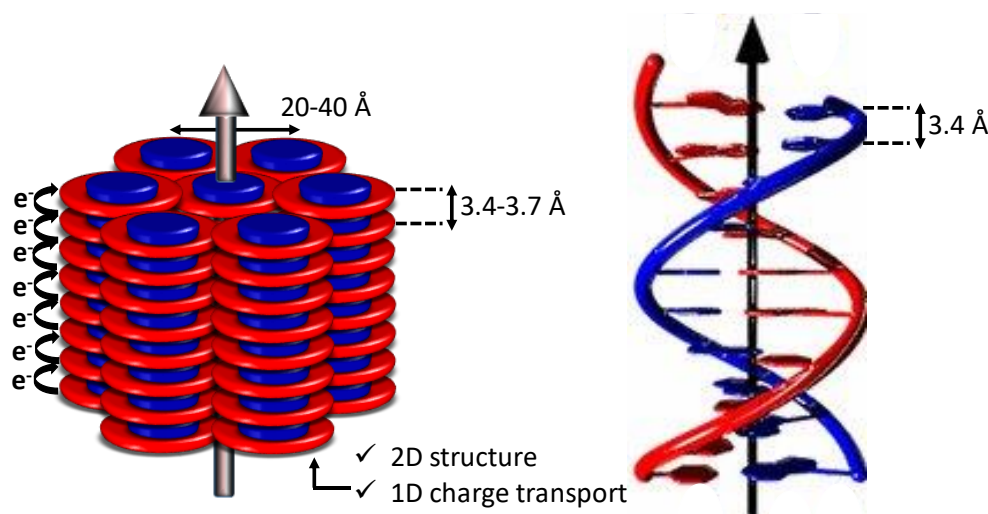


**Figure 1.12** Schematic showing the charge transport model system of DLCs and DNA.

For many years, charge transport in DNA remains the question of on-going debate among scientists from different disciplines as it can help to understand the delineating aspects of carcinogenesis and mutagenesis in DNA.<sup>44-48</sup> Therefore, DLCs can be considered as model compounds to understand the charge transport in the DNA base pairs stacks. In DLCs, the



charge along the vertical direction is more prominent than in lateral directions as the surrounded aliphatic chains are responsible for providing insulation. Therefore, DLC materials are considered as 1D charge carrier transport materials or molecular nanowires. The hopping mechanism is responsible for the charge transfer in these DLC organic semiconductors.<sup>6</sup> As discotic molecules form dynamic molecular aggregated states, thereby the efficient charge transport relies on how constructively the molecules organized in such aggregated states for efficient charge hopping. The time-averaged overlap molecules are primarily important for efficient hopping, hence for high charge transport. Due to the stacking distance of several Å in columnar LCs, charges hop several times before reaching the opposite electrode which lies at a distance of 100 nm to several mm. The charge hopping rate,  $k$ , can be calculated from the semi-classical Marcus theory<sup>49,50</sup>:

$$k = (4\pi/h)t^2 (4\pi\lambda k_B T)^{-0.5} \exp(-\lambda/4k_B T)$$

The above equation suggests that the charge transfer rate depends on two factors: intermolecular transfer integral,  $t$  and reorganization energy,  $\lambda$ . The large value of  $t$  and small value of  $\lambda$  determines the high charge transfer rate and hence high mobility values. The charge carrier mobility of semiconductors is considered as a measuring factor to employ them in electronic devices, as high mobility values can lead to fast switching times in devices.<sup>51-53</sup> From a structural point of view, generally, the electron-rich DLCs result in hole charge transport<sup>54,55</sup> and electron-deficient systems give rise to electron-transport<sup>56,57</sup> in the materials. On the other hand, the presence of electron-rich and deficient moiety in the molecular design can lead to the achievement of ambipolar charge transport.<sup>58-60</sup> Thereby, one can easily tune the charge transport property of the material by interplaying the molecular design system. However, the ambipolar transport behaviour has also been obtained in the DLC systems where no separated electron-rich and deficient moieties are present.<sup>61-63</sup> This also indicates that hole and electron transport is the inherent property of organic semiconductor materials.

The density functional theory (DFT) calculations of the molecular structure provide preliminary insight into the nature of charge transport in the material (Figure 1.13).<sup>9,64</sup> Generally, the HOMO of the material delocalized on the electron-rich moiety while the LUMO distributed on the electron-deficient part. The spatially distributed HOMO and LUMO in the

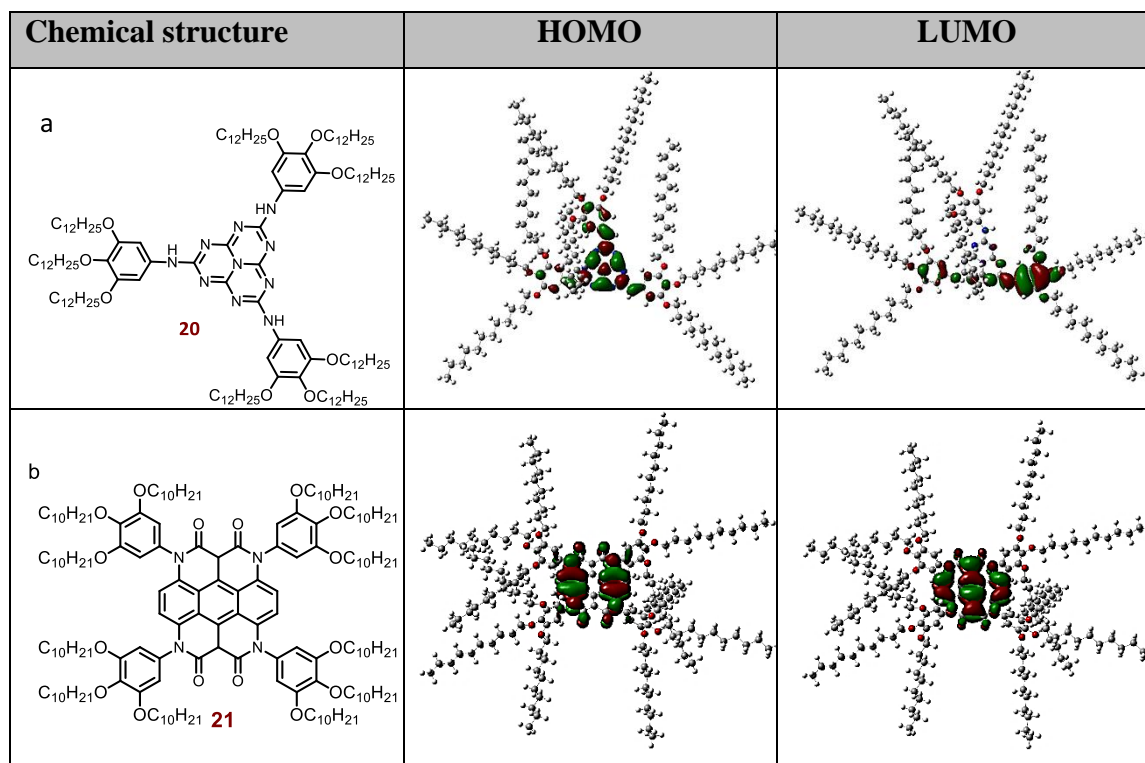


**Figure 1.13** Chemical structure and corresponding HOMO and LUMO of DLCs based on (a) electron-donor heptazine derivative (**20**)<sup>64</sup> and (b) heterocoronene (**21**)<sup>9</sup> based DLC system.

material form donor-acceptor system and impart ambipolar charge transport to the system. For instance, in heptazine-based donor-acceptor derivative (**20**),<sup>64</sup> the LUMO lies on the central electron-deficient heptazine ring while the HOMO is distributed on the electron-donor 3,4,5-trialkoxybenzene moiety. However, the molecular design consists of the single chromophore (i.e. combination of electron-rich and electron-deficient part) and hence lead to ambipolar charge transport behaviour are rare. Such systems are interesting as their molecular orbitals HOMO and LUMO are located on the central part of the aromatic core of DLCs and provide effective time-averaged overlap which is otherwise found to be less in spatially distributed molecular orbitals. For instance, in heterocoronene based DLC system (**21**),<sup>9</sup> both the orbitals majorly located on central heterocoronene moiety. The effective molecular orbital overlap is one of the prerequisites of high charge transport in the DLC systems. The charge transport behaviour of the DLC materials can be studied by using various techniques such as space-charge limited current (SCLC), time-of-flight (TOF) technique and pulse-radiolysis time-resolved microwave conductivity (PR-TRMC) technique. The charge mobility values extracted



from all these techniques will differ from each other due to the different requirements of each of the techniques.<sup>65-67</sup>

## 1.8 Techniques used to measure charge transport in DLCs

### 1.8.1 Space charge limited current (SCLC) technique

Charge transport of DLC materials has been extensively studied by using the SCLC technique.<sup>9,54-56,69-73</sup> In this technique, the organic semiconductor materials of a few micrometer thicknesses are sandwiched between the two electrodes i.e. cathode and anode such that there will be an ohmic contact between the material and the injecting electrode (Figure 1.14). In SCLC method, two separate cells i.e. hole-only and electron-only need to prepare for extracting hole and electron transport behaviour. For efficient hole (or electron) injection, HOMO (or LUMO) of the material should be aligned well with the work-function of an anode (or cathode) while the large energy barrier is maintained between the cathode (or anode) and LUMO (or HOMO) of the material. A characteristic  $J$ - $V$  curve obtained for tetrathienoanthracene based DLC material<sup>74</sup> is shown in Figure 1.14.

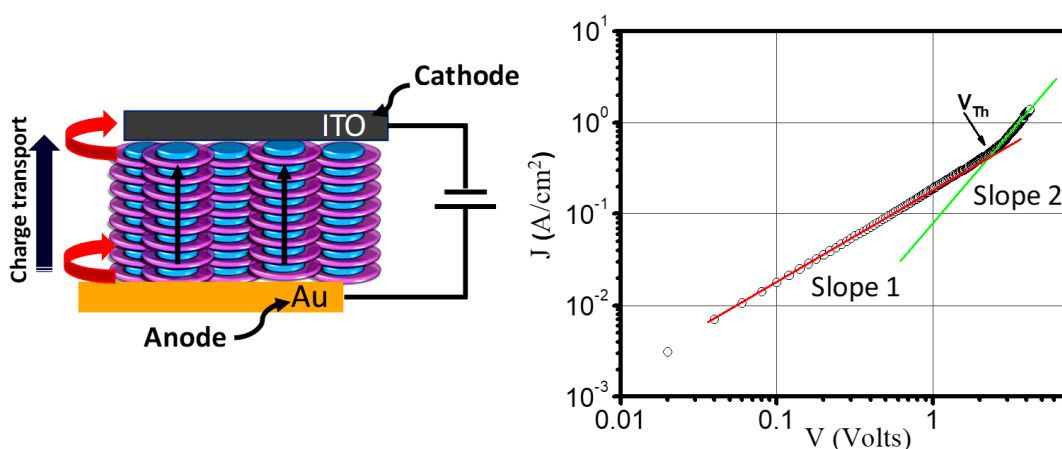


**Figure 1.14** Schematic showing the SCLC device architecture and the  $J$ - $V$  characteristics generally obtained during SCLC measurements ( $J$ - $V$  plot shown here is based on tetrathienoanthracene based DLC<sup>74</sup> exhibiting Col<sub>r</sub> mesophase where Slope 1 represents Ohmic regime and Slope 2 correspond to the SCLC regime).

At lower voltages ( $V$ ), the current ( $J$ ) is ohmic represented by a linear region (slope 1) while the current becomes space charge limited at higher voltages with the quadratic regime (slope

2). The SCLC regime of the  $J$ - $V$  curve is used to extract the mobility of the material by fitting the curve into the Mott-Gurney equation<sup>68</sup>:

$$J = \frac{9}{8} \varepsilon_0 \varepsilon_r \mu \frac{V^2}{L^3} \quad (1)$$

Where  $J$  is the current density measured at applied voltage  $V$ ,  $\varepsilon_0$  is the permittivity of free space,  $\varepsilon_r$  is the dielectric constant of the material,  $\mu$  is the charge mobility of material and  $L$  is the thickness of the sample used for SCLC measurements.

The SCLC method has been extensively used for charge carrier mobility measurements of DLC systems (e.g. **22-27**) and few of them chemical structures are drawn in Figure 1.15.<sup>9,54-56,69-73</sup> Recently, by using SCLC method, our group was able to achieve the high hole and electron mobility of  $8.84 \text{ cm}^2 \text{ V}^{-1} \text{ s}^{-1}$  and  $3.59 \text{ cm}^2 \text{ V}^{-1} \text{ s}^{-1}$  in Col<sub>r</sub> and Col<sub>h</sub> phase, respectively, of heterocoronene based room temperature DLCs.<sup>9</sup> Berta Gómez-Lor reported several Col triindole derivatives (**22-24**) which are shown to exhibit high SCLC mobility values (hole) in the range of  $0.09$ - $2.8 \text{ cm}^2 \text{ V}^{-1} \text{ s}^{-1}$ .<sup>54,55,70,71</sup> Chi and co-workers found high hole mobilities of the order of  $0.14 \text{ cm}^2 \text{ V}^{-1} \text{ s}^{-1}$  and  $0.69 \text{ cm}^2 \text{ V}^{-1} \text{ s}^{-1}$  in a large core-expanded triazatruxene-based DLCs (**25**) when used in SCLC devices.<sup>69</sup> Sierra et al. disclosed hole mobility of value  $1 \times 10^{-2} \text{ cm}^2 \text{ V}^{-1} \text{ s}^{-1}$  in H-bonded donor-acceptor systems by SCLC measurement.<sup>58</sup> Marder reported electron mobility as high as  $1.3 \text{ cm}^2 \text{ V}^{-1} \text{ s}^{-1}$  in perylenebisimide DLC derivative (**26**)<sup>56</sup> at ambient temperature which is higher than that of amorphous silicon whereas, Bechtold showed in his report that how the homeotropic alignment in compound **27** led to 5 orders increase in mobility in comparison to the unaligned sample.<sup>75</sup> Serrano and Golemme's recent work highlights the SCLC hole mobility of  $0.15$  and  $1.1 \text{ cm}^2 \text{ V}^{-1} \text{ s}^{-1}$  in discotic nematic<sup>73</sup> phases of porphyrin DLCs (**28**) while  $0.5 \text{ cm}^2 \text{ V}^{-1} \text{ s}^{-1}$  in Janus-type DLCs dendrimers (**29**)<sup>72</sup> as shown in Figure 1.16. In these reports, DLCs exhibit high in-plane homeotropic alignment in SCLC cells which are highly beneficial as charge transport in the SCLC technique is measured in perpendicular direction. All these reported results of charge carrier mobilities based on DLC systems concluded that in addition to charge injection effectiveness, SCLC mobility is highly dependent on the alignment, morphology and size of the columnar domains. Therefore, the DLC materials exhibiting good alignment ability, tendency to form uniform morphology and

having larger columnar domains are beneficial for achieving astounding charge transport properties.

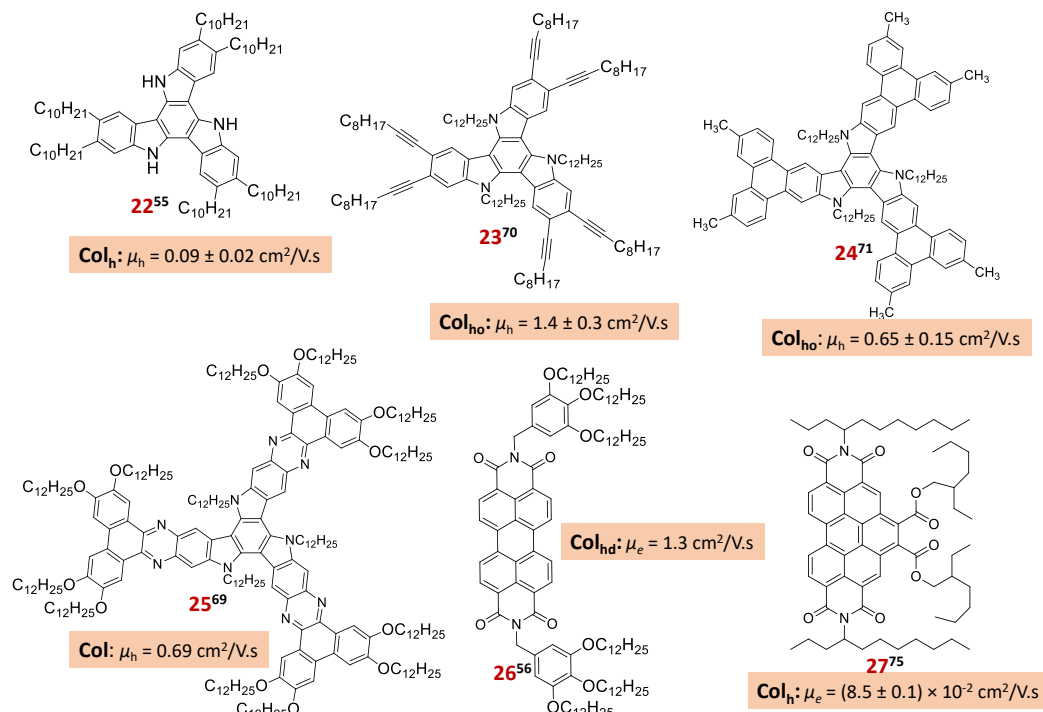


**Figure 1.15** Mobility values obtained in the past in columnar phases of DLCs as measured by SCLC method.

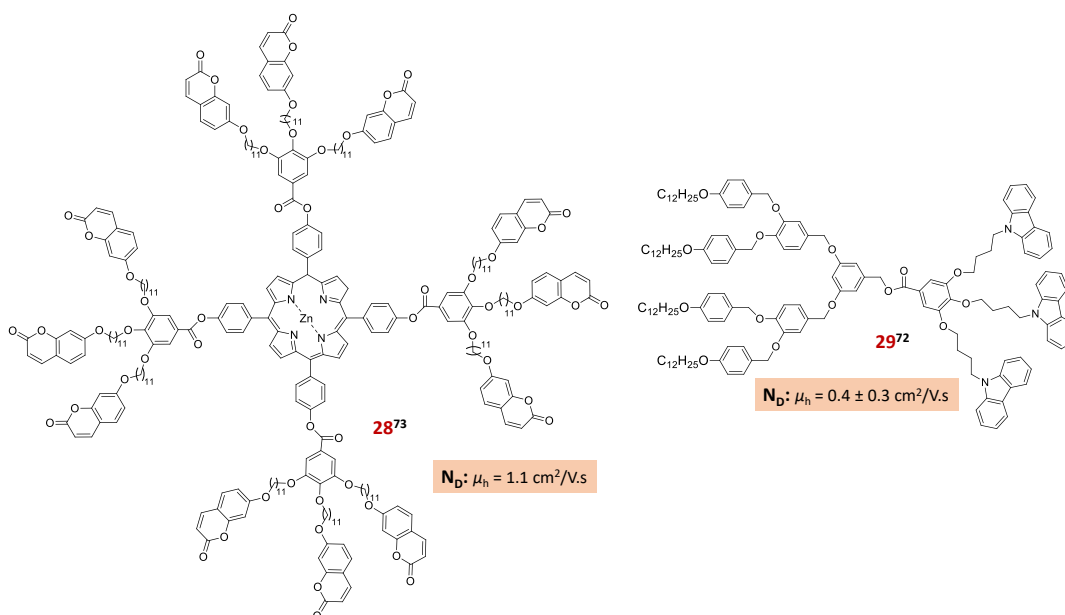


**Figure 1.16** Charge carrier mobilities in discotic nematic phases of DLCs as measured by SCLC method.

### 1.8.2 Time of flight (TOF) method

TOF is another useful technique to determine the charge transport properties of DLC materials. Unlike SCLC, TOF technique does not need to maintain the ohmic contacts rather the materials should have good absorption properties in order to generate the photo charge-carriers by the incident of laser light of appropriate wavelength. In this method, a sample of a few micrometer thickness is crammed between two electrodes separated by certified distance (Figure 1.17). In the case of DLC material, the sample in the cells is filled from its isotropic melt *via* capillary action. A laser pulse of the appropriate wavelength is used to irradiate the sample in the proximity of a transparent electrode where the charge carriers (holes and electrons) get separated and migrate towards the opposite electrodes under the influence of the electric field. Then the current at the electrode surface is measured as a function of time and mobility of the respective charge carriers is calculated by  $\mu = d^2/T_r V$  where  $T_r$  is the transient time,  $V$  is the applied voltage and  $d$  is the ITO cell thickness. The important benefit of the TOF method is that both electron and hole mobility can be measured separately in the same cells by just reversing the polarity of the applied voltage.

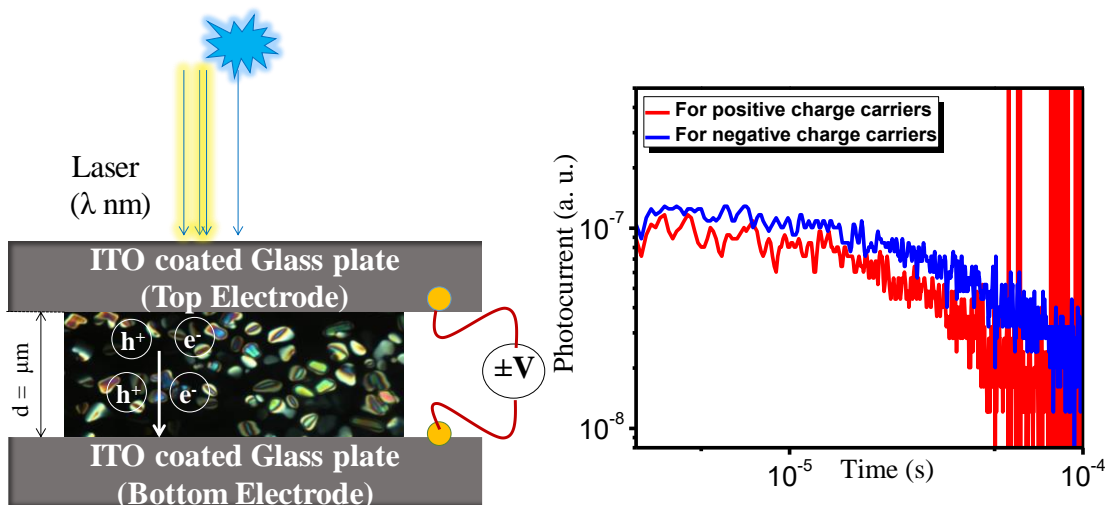


**Figure 1.17** Schematic showing the device structure used for TOF measurements and photocurrent response with time curve obtained during TOF measurements (curve shown here is for triphenylene–pentalkynylbenzene/TNF complexes<sup>34</sup> exhibiting Col<sub>h</sub> phase).

In TOF, the transient photocurrent signal can be non-dispersive and dispersive (Figure 1.18).<sup>76,77</sup> The non-dispersive signals can be characterized by a clear flat region from which the transit time ( $t_{tr}$ ) can be easily obtained. In contrast, the constantly decaying photocurrent signal does not give a clear indication of  $t_{tr}$ .

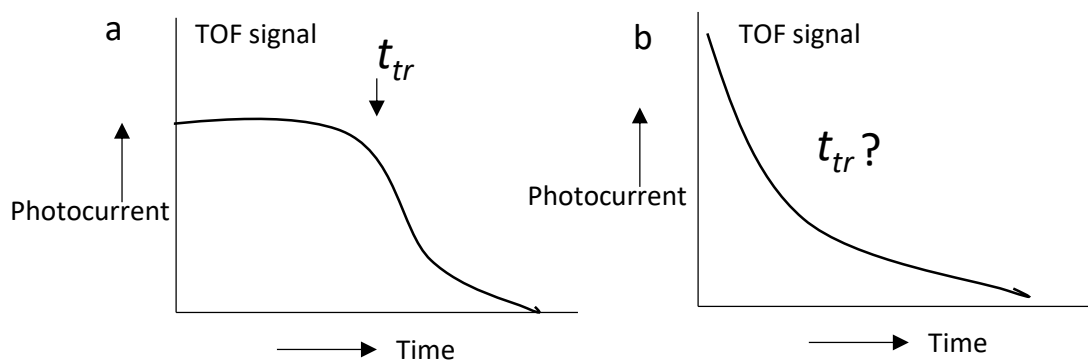


**Figure 1.18** (a) Non-dispersive and (b) dispersive nature of the transient signal.

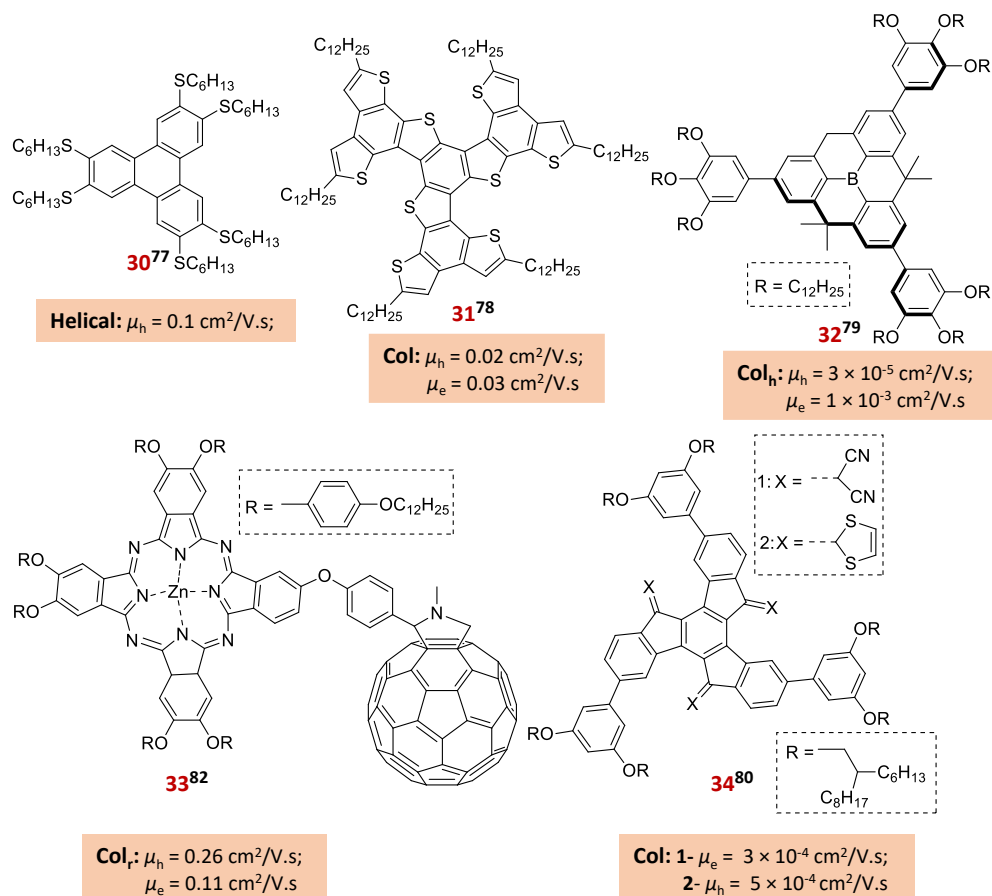


**Figure 1.19** Mobility values reported in the past in DLCs columnar phases as measured by TOF technique.

Similar to the SCLC method, the homeotropic alignment of DLC molecules is favourable for the resistant free diffusion of charge carriers within the anisotropic materials and determined the high charge transport of the materials. The TOF method is also extensively exploited for measuring the charge transport properties of the DLC materials and a few of them are listed here (Figure 1.19).

For instance, in 1994, Ringsdorf and Haarer group reported fast photoconduction of the order of  $0.1 \text{ cm}^2 \text{ V}^{-1} \text{ s}^{-1}$  in the helical Col phase of hexahexylthiotriphenylene (**30**).<sup>77</sup> The high hole mobility and electron mobility of  $0.02 \text{ cm}^2 \text{ V}^{-1} \text{ s}^{-1}$  and  $0.03 \text{ cm}^2 \text{ V}^{-1} \text{ s}^{-1}$ , respectively in propeller-shaped fused oligothiophenes (**31**) based Col mesogens was measured by the TOF method.<sup>78</sup> Kato and group studied various DLC materials by TOF method e.g. planarized triphenylborane (**32**),<sup>79</sup> thiafulvene-appended truxene (**34**)<sup>80</sup> and oligothiophene<sup>81</sup> DLCs. Imahori et al. reported charge mobility of  $0.26 \text{ cm}^2 \text{ V}^{-1} \text{ s}^{-1}$  for a hole and  $0.11 \text{ cm}^2 \text{ V}^{-1} \text{ s}^{-1}$  for electron charge carriers in phthalocyanine and fullerene (**33**) based donor-acceptor columnar LCs.<sup>82</sup> The TOF and SCLC technique has been applied in this thesis to investigate the charge transport properties of columnar DLCs.

### 1.8.3 Pulse-radiolysis time-resolved microwave conductivity (PR-TRMC)

PR-TRMC is a contactless, time-resolved microwave conductivity technique where the bulk material is excited by a short pulse (nanosecond duration) of very energetic electrons from Van de Graff generator that creates free charge carriers. These carriers increase the sample conductivity that can be monitored by the rise in the diminution of the microwave power. The change in conductivity is given by<sup>89</sup>:

$$\Delta\sigma = e\sum\mu N_{e-h}$$

where  $\sum\mu$  = summation of the hole and electron mobilities and  $N_{e-h}$  is the combined density of generated electron-hole pairs and are not able to separate in this PR-TRMC method. This technique is contact-free, hence conductivity values are not affected by the space-charge effects. This technique does not take into account the effect of structural defects and impurities present in the sample and also measured the charge transport in the non-aligned multi-domain samples, therefore, it always gives the larger mobility values when compared to the TOF and

SCLC method.<sup>82,83</sup> The disadvantage of the PR-TRMC method is that this technique does not permit the estimation of individual contributions of the positive and negative charge carriers.

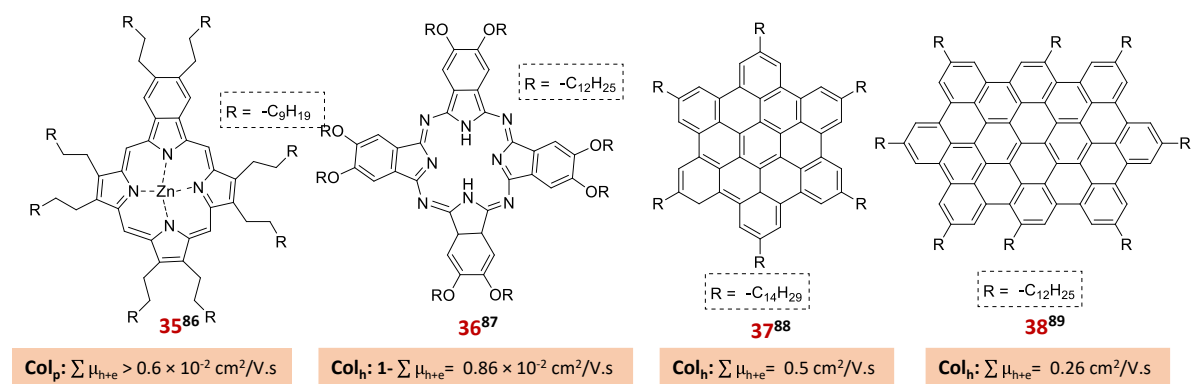


**Figure 1.20** Mobility values obtained in the past in DLC systems by PR-TRMC technique.

The early studies of charge transport in DLC systems were measured by PR-TRMC methods (Figure 1.20) while with the advancement of DLC semiconductors research, scientists preferred other methods such as SCLC, TOF to evaluate their charge transport properties. By using the PR-TRMC technique, the charge transport was firstly studied in porphyrin (**35**) and phthalocyanine (**36**) based DLC systems by Schouten et al.<sup>84-86</sup> Phthalocyanine exhibit structural similarity to that of porphyrin, however, constitute four phenyl group joining to pyrrole units and nitrogen atoms replace the bridging carbon atoms. In the porphyrin systems, the mobility values over  $0.1 \text{ cm}^2 \text{ V}^{-1} \text{ s}^{-1}$  were found and charge transport measurement results showed that columnar architecture is required for fast charge transport as microwave conductivity decreased or almost vanished rapidly in the isotropic liquid where the columnar aggregates are presumed to be absent.<sup>86</sup> Using the microwave conductivity technique, Müllen et al. extensively studied the conductive properties of coronene-based (**37** and **38**) discotics<sup>87,88</sup> and reported high mobility as high as  $0.5 \text{ cm}^2 \text{ V}^{-1} \text{ s}^{-1}$  by PM-TRMC method.

### 1.9 Molecular order and temperature dependence of charge carrier mobilities

As discussed in the above section that one of the factors on which charge carrier mobility depends is the molecular orbital overlap. Generally, the mobility increases with an increased molecular overlap which in turn enhanced with high molecular order. The various phases of DLCs exhibit different molecular order e.g.  $N_D$  phase is the least ordered while the columnar

helical phase exhibit the highest molecular order (Figure 1.21). Therefore, the mobility values can vary from one phase to another for a particular compound.

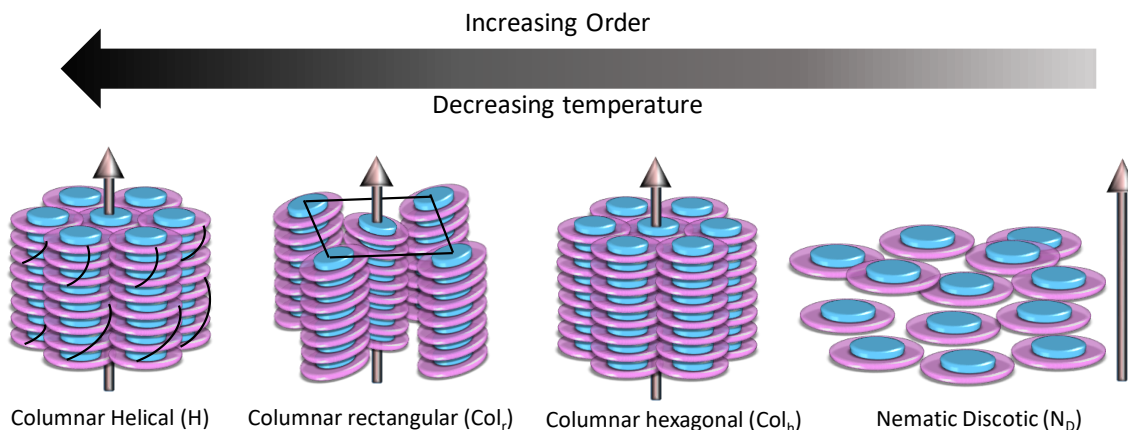


**Figure 1.21** Mesophases formed by discotic molecules can be categorized by degree of positional order and symmetry, and rearrangement from one phase to another can happen upon temperature change.

The DLCs can form more than one phase upon changing the temperature, thereby their mobilities can show temperature dependence from one phase to another while within the same mesophase, the value remains almost constant. For instance, Ringsdorf and group in hexahexylthiotriphenylene (**30**) recorded mobility values in the observed crystalline phase,

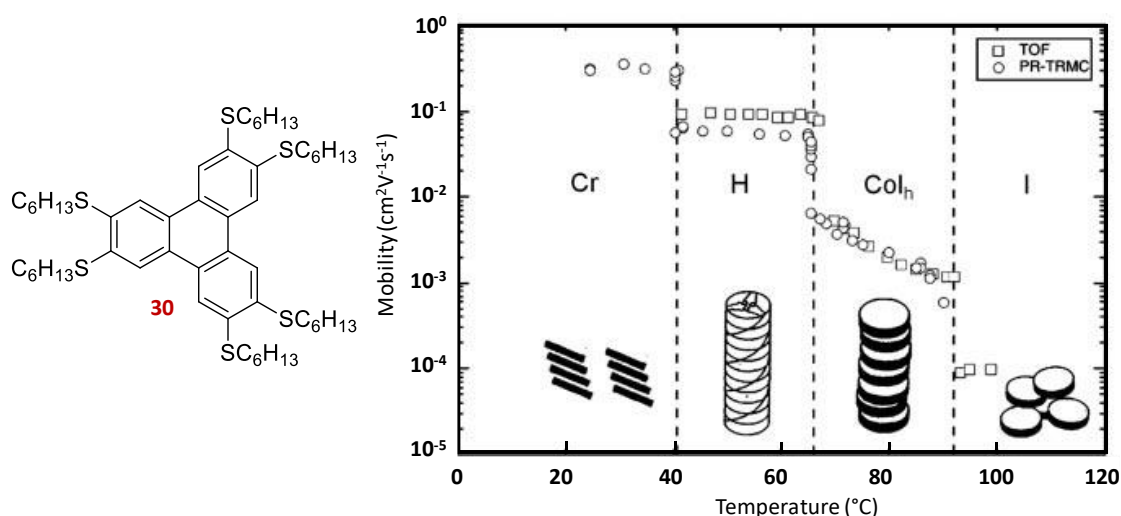


**Figure 1.22** Temperature-dependent charge carrier mobilities measured in various phases of hexahexylthiotriphenylenes DLCs measured by TOF and PR-TRMC technique (Reproduced with the permission from Ref. 89).



helical phase, Col<sub>h</sub> phase and isotropic phase as a function of temperature by TOF and PR-TRMC method (Figure 1.22).<sup>77,83,89</sup> The mobility values follow the trend of the order of mesophase i.e. Cr > H > Col<sub>h</sub> > Iso. This outcome is a general feature that is valid for a variety of DLCs and is attributed to the ordered packing of the molecules.

### **1.10 Application of charge transport DLC semiconductors in devices**

DLCs are predicted to be viable organic semiconductors for low-cost, macroscopic areas and flexible electronics towards their implementation in OFETs, OPVs, OLEDs, and in display devices.<sup>4-7,10</sup> Also, they have several advantages over their inorganic and polymeric counterparts in terms of purity, processability, flexibility and durability. The ability of DLCs to act as organic semiconductors can be utilized in various applications related to electronic and optoelectronic devices as described below. Charge-transporting DLC materials in OFET devices act as an anisotropic medium for the passage of charge carriers from source to drain electrodes. On the other hand, in OPV devices, charge-transporting DLCs play a dual role i.e. as photoinduced charge carriers generation along with charge transport material. Likewise in OLEDs, DLCs can play a double function i.e. as an emitting material and charge transport materials.

#### **1.10.1 DLCs as optical compensation films (OCFs)**

The nematic mesophase of calamitics has found diverse implementation in various electro-optic devices such as mobiles, laptops, calculators, watches, telephones, and so on. Apart from these, the calamitics dominates the different display devices such as twisted nematic (TN) and supertwisted nematic (STN) displays. However, the problem of narrow-viewing-angle due to leakage of light limits their use in fast-moving display devices. To rectify this issue, OCFs were introduced by the Fuji photo film laboratory that has good light transmittance capability and used to increase the contrast ratio with widen viewing angle.<sup>90</sup> The discotic nematic material was being used as OCFs as it exhibits negative optical anisotropy that can compensate for the positive anisotropy of the rod-like molecules oriented in a similar direction as that of discotic nematic material. The compensation film alignments of opposite anisotropies minimize the leakage of light from oblique directions that resulted in the improved viewing angle of displays.

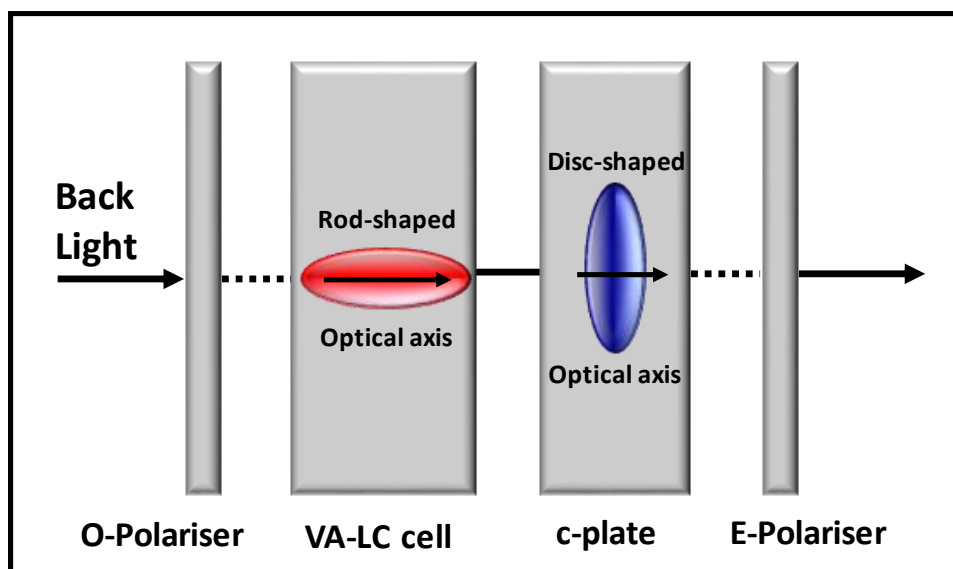


**Figure 1.23** Schematic showing the use of OCF as a negative compensator in vertically aligned (VA) LC display (Redrawn from Ref. 90).

As shown in Figure 1.23, the thin film crystal E-polarizer has been employed in combination with positive anisotropic rod-shaped and negative anisotropic disc-shaped material in vertically aligned displays to improve the contrast ratio and viewing angle property of the displays.<sup>88</sup>

### 1.10.2 Organic Field-effect transistors (OFETs)

In a typical OFET device,<sup>2</sup> source and drain electrodes are connected to the gate electrodes and separated by an insulator material. The DLC material is deposited so that it can act as a bridge between source and drain electrodes (Figure 1.24). Since so-called DLCs are as such insulators, therefore, source electrodes exhibiting ohmic contacts with the DLC semiconductor inject charge carriers into the material. When there is no gate voltage applied, a negligible amount of current flows in the semiconductor material in the direction of source to drain electrode and the device is in its off-state. However, on the application of negative (or positive) gate voltage, the positive (or negative) charge carriers get accumulated on the gate dielectric interface, hence hole (or electron) transport takes place from source to drain and the device is in its on-state. Such types of OFET devices result in *p*-type (or *n*-type) devices. As discussed in earlier sections, the planar columnar alignment of DLC molecules is required in OFET

devices which have been achieved in OFET devices by PTFE alignment, zone-casting, Langmuir-Blodgett technique.

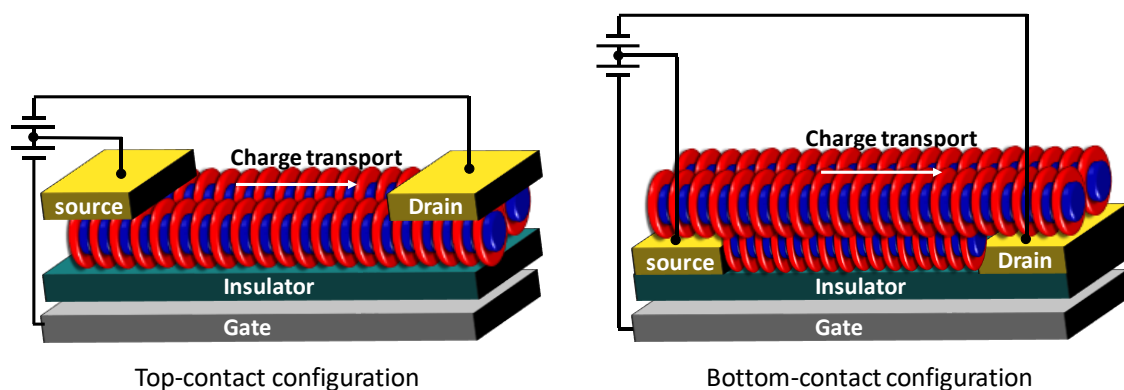


**Figure 1.24** OFET device structures with Top-contact and Bottom-contact device configuration employing columnar DLC as a charge transport material.<sup>2</sup>

Furthermore, OFET devices can be fabricated in two configurations as shown in Figure 1.24. Few reports based on hexabenzocoronenes,<sup>91-93</sup> phthalocyanines<sup>91,96,97</sup>, and perylene<sup>98,99</sup> DLCs are reported where the high electron mobility of  $2.1 \text{ cm}^2 \text{ V}^{-1} \text{ s}^{-1}$  in perylene diimide<sup>99</sup> based OFETs were obtained, although the device was not air-stable under normal conditions. Therefore, rational molecular designs are needed for the usage of DLCs in stable OFET devices. In this thesis, several DLC materials have been studied for charge transport properties by TOF and SCLC methods that can be utilized in OFET devices.

### 1.10.3 Organic photovoltaic devices (OPVs)

OPV materials are a powerful tool to convert solar energy into electrical energy. The construction of OPV devices<sup>2,10,100</sup> involves the organic semiconductor material to be sandwiched between two electrodes i.e. cathode and anode (Figure 1.25). The semiconductor material should have a good absorption ability towards incident photons in order to form excitons (bound electron-hole pair). The photogenerated hole-electron pair have to travel to their respective electrodes under the applied potential (Figure 1.26c). The efficiency of a device is limited by how efficiently these separated charges can reach the electrodes without recombination in the way. Likewise, the energy levels of the semiconductor material are equally significant for the proper charge separation at its interface and hence determines the

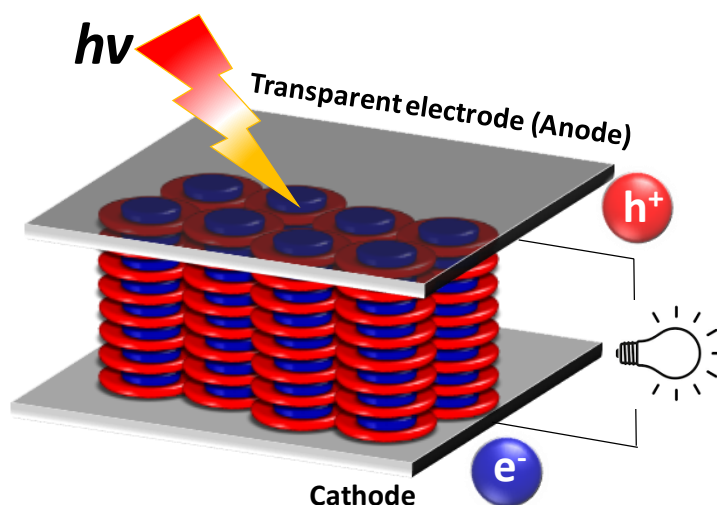


**Figure 1.25** OPV device structures employing columnar DLC as charge transport and charge generating material.<sup>89</sup>

output efficiency of the device. For efficient OPV devices, donor-acceptor materials are most suitable as they can stabilize the generated charge carriers thereby can reinforce their movement in the direction of the corresponding electrodes.

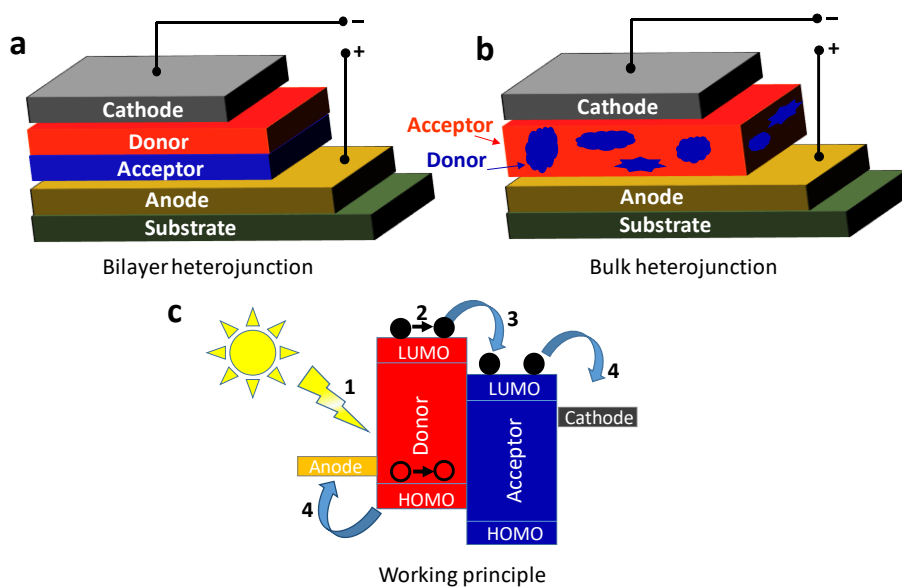


**Figure 1.26** OPV different device structures with bilayer heterojunction and bulk heterojunction device configuration. Device working principle (Redrawn from Ref. 100).

Many DLC materials owing to the  $\pi$ -conjugated aromatic cores exhibit high absorption coefficients over the complete solar spectrum, hence capable to act as efficient materials in OPV devices. Apart from this, DLCs possess high charge transport which triggers the resistant free hopping of photoinduced charge carriers toward their respective electrodes. The homeotropic alignment of the DLCs in the OPV devices further reinforced the journey of charge carriers to electrodes (up to 100 nm) and precluding the probability of charge recombination on halfway. Gregg et al. in 1990 published the first report on DLC-based OPV where he sandwiched the semiconducting layer of porphyrin DLC in between the ITO-coated glass electrodes.<sup>101</sup> After that phthalocyanines, hexabenzocoronenes, perylene, etc. DLCs systems were reported in different device geometries *viz.* single layer, bilayer and bulk heterojunction one after another in order to improve the device efficiency (Figure 1.26).<sup>102,103</sup> At that time, the milestone achievement was obtained in the bulk-heterojunction device based on the blend of *p*-type hexabenzocoronene and *n*-type perylene-based discotic system as a semiconducting layer and able to achieve more than 34% external quantum efficiency and 2 % power conversion efficiency.<sup>103</sup>

#### 1.10.4 Organic light-emitting diodes

OLEDs work exactly in the opposite way as that of OPVs.<sup>2</sup> In an OLED device, the hole (from cathode) and electron (from anode) charge carriers are injecting into the HOMO and LUMO of the respective transporting layers (Figure 1.27). Then the charges migrate under the applied driving voltage and recombination takes place at the interface of the emitter layer which then emits light. Therefore, OLED device structure consists of three sublayers of the hole-transporting layer, the emitting layer and then electron-transporting layer (Figure 1.27). In some cases instead of using the electron-transporting layer and hole-transporting layer separately, a layer of ambipolar material can be used to simplify the device structure to the bilayer. Likewise, a single layer of material having the charge transport property as well as luminescence behaviour further simplifies the device architecture to a single layer. The efficiency of the OLED device depends on the charge injection effectiveness into the respective layers at low driving voltage, proper charge balance, no leakage of charge carriers from the emitter layer to increase the possibility of charge recombination. Apart from that, the materials

forming hole-transporting layers (HTL), electron-transporting layers (ETL) and emitting layers should have the capability to form uniform thin films to avoid the formation of pinholes.

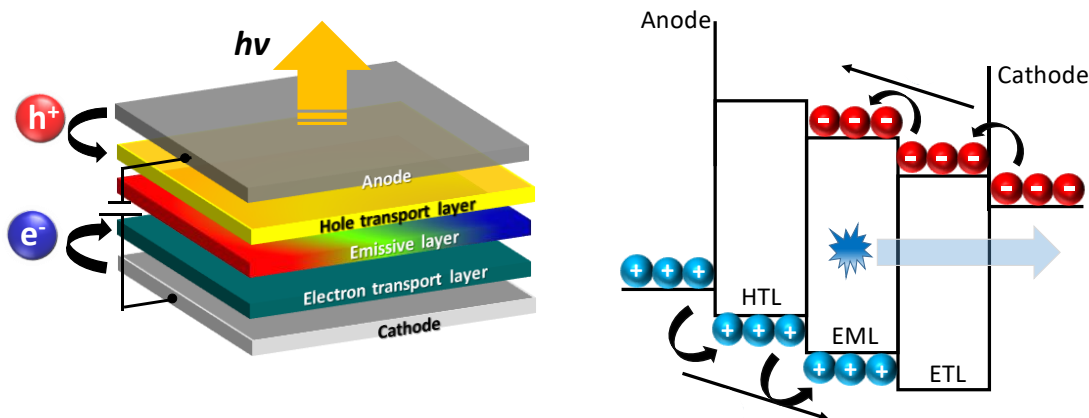


**Figure 1.27** Schematic of OLED device and its working principle.<sup>2</sup>

Also, the different layers have different requirements e.g. transporting layers should have good charge transport properties, the emissive layer should possess high luminescence efficacy and moderate charge transport ability. Based on the molecular architecture of DLC materials, they possess the potential to meet all the spectrum of requirements for OLEDs. For instance, DLC materials can act as charge transport layers due to the existence of 1D columnar structures which ensures the uniaxial charge carrier migration if aligned in one direction. In OLEDs, the homeotropic alignment of columns is required for high charge transport across the layers. Majority of discotic mesogens such as dibenzopyrene, hexabenzocoronene and triphenylene *etc.* are electron-rich systems and found to be good hole transporters (*p*-type), whereas discotics consequent from electron-deficient aromatic systems with electron-accepting character like triazines, perylenediimide, hexaazatriphenylene, quinoxalines and hexaazatrinaphthylene *etc.* can act as good electron transport materials.

Besides charge-transporting layers, DLCs can act as emitter materials as many of the DLC materials are highly conjugated materials and are generally luminescent. DLCs are known to emit light in the red, blue and green wavelength which are the three constituent colors of the OLED device. However, many columnar aromatic systems display good luminescence behaviour in solution state but their emission gets quenched in technologically important solid-state. This makes the domain experts design inherently luminescent discotic mesogens which

can show solid-state luminescent behaviour. As for efficient OLEDs, if the emitter material possesses both solid-state emission behaviour and great charge carrier mobility, the device efficiency improves further. The high charge carrier mobility of emitter moves charge carriers *via* hopping process faster within the emitter layer which leads to better recombination of holes and electrons and hence expected to have better device efficiency.

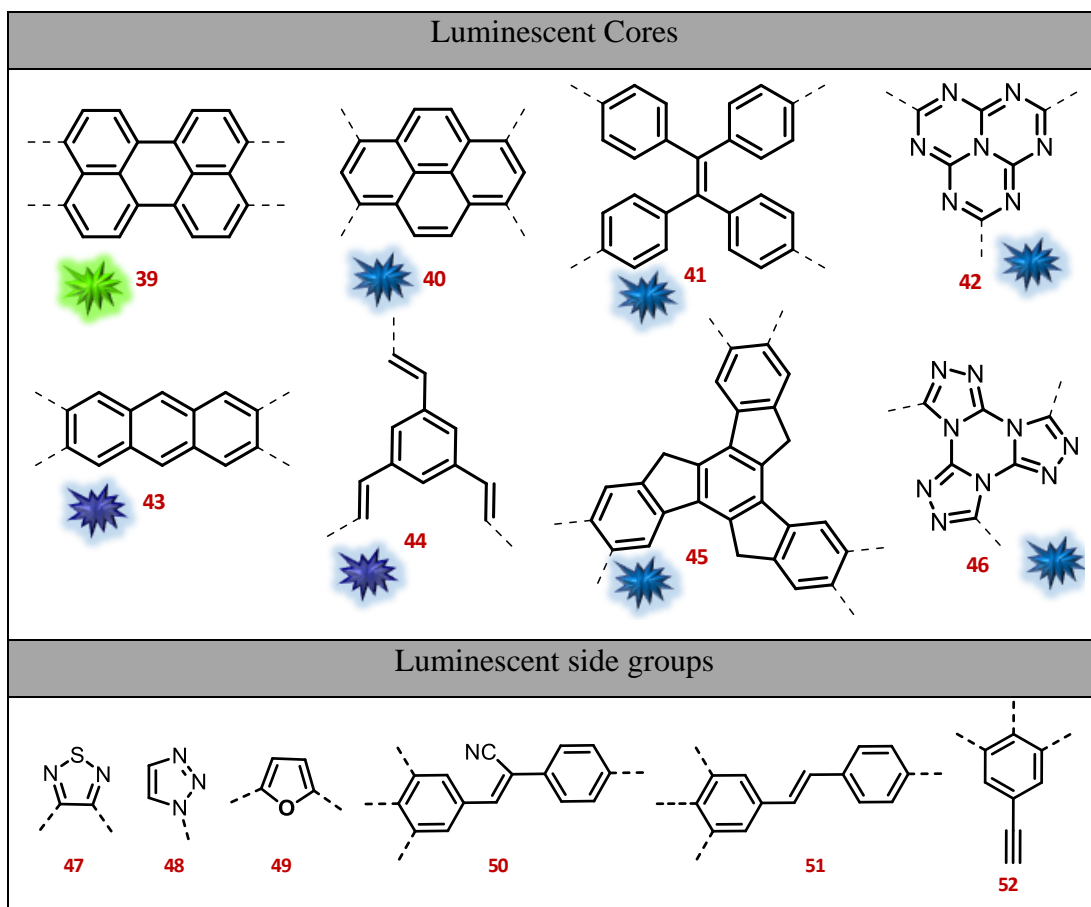


**Figure 1.28** Various luminescent discotic cores and luminescent side groups that can be used to produce DLC-based emitter materials in OLEDs.

Therefore, new DLC materials can be designed which will exhibit luminescence behaviour by either incorporating various luminescent conjugated cores (Figure 1.28) *viz.* perylene (39), pyrene (40), tetraphenylethylene (41), heptazine (42), anthracene (43), oligophenylenevinylene (44), truxene (45), triatriazolotriazine (46) and so on, or small luminophore side groups e.g. benzothiadiazole (47), triazole (48), oxazole (49), cyanostilbenes (50), phenylenevinylene (51), phenylalkynyl (52) etc. along with alkyl chains at the periphery

for their use as emitter materials in OLEDs. There are three possibilities for the design of new luminescent materials. The first possibility based on chromophoric central core connected with flexible alkyl chains can exhibit enhanced photo-luminescence. The second is to combine columnar self-assembly and luminescence, we will choose a molecular design strategy, where the fluorophores are organized around the central core, with a mantle of flexible peripheral tails. The third includes where both the central rigid core and the peripheral substituents are luminescent. Moreover, the additional advantages are that LC materials offer the ease of processability, self-healing of structural defects, charge transporting properties, luminescence ability, thereby, increases the demand for new molecular designs. Nguyen reported the bilayer OLED device based on DLC materials by combining the electron transparent layer and emitter layer into one layer with the implication of *n*-type fluorescent tetraethylperylene-3,4,9,10-tetracarboxylate. On the other hand, *p*-type 2,3,6,7,10,11-hexabutoxytriphenylene was used as a hole-transporting layer. We have developed a few discotics based on heptazine,<sup>64</sup> phenylenevinylenes,<sup>104,105</sup> triphenylene-pentakynylbenzene<sup>42</sup> that act as the blue emitter in OLED devices. One part of this thesis dealt with the synthesis and application of various DLC materials as solid-state emitters in OLED devices.

### **1.11 Molecular approaches towards functional columnar LCs**

The columnar phases of DLCs have great demand in various types of optoelectronic applications as discussed in the above section, thereby, their achievement becomes important for functional devices and some of the approaches in this direction are discussed here. The conventional practice to achieve the columnar LCs involves the use of rigid aromatic core attached to flexible units by covalent interactions. However, the introduction of non-covalent interactions in the molecular design itself is very useful for the accomplishment of dynamic supramolecular columnar LCs.<sup>106-109</sup> Various non-covalent interactions such as hydrogen (H)-bonded interactions, charge-transfer interactions and ionic interactions can be employed to further stabilize the columnar phases as discussed briefly below.

#### **1.11.1 Hydrogen-bonded interactions based DLCs**

Since the discovery of complementary H-bonded liquid crystalline systems by Kato et al., hydrogen-bonded approach has been widely used to achieve stable columnar phases.<sup>107-109</sup> The



advantage of H-bonded LCs involves their easy synthesis and no purification is required in the final synthetic step which otherwise requires the tedious purification in the case of conventional DLCs. Therefore, one can choose the complementary components of different or similar molecules and can unite them by highly directional hydrogen bonds for the realization of supramolecular columnar LCs of particular interest (Figure 1.29).

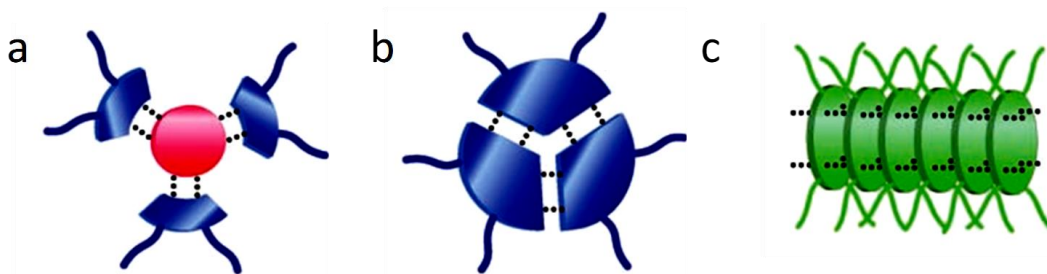


**Figure 1.29** Supramolecular self-assembly of H-bonded molecules: (a) between different molecules, (b) between the same molecules, formation of 1D channels by the association of identical components through H-bonded chains (Reproduced with the permission from Ref. 106).

Interestingly, the non-mesogenic complementary components when hydrogen-bonded together results in the mesogenic molecules. The well-known complementary functionality that is used to form a variety of H-bonded DLCs is the amide ( $\text{-NHCO}$ ) and carboxylic moiety ( $\text{-COOH}$ ).

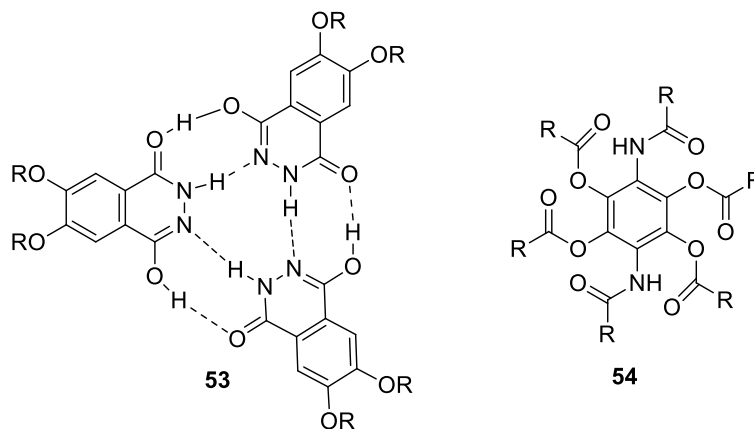


**Figure 1.30** (a) Intermolecular H-bonded columnar assembly forming H-bonded trimers, (b) Intramolecular H-bonded stabilizing columnar phase.<sup>106</sup>

The intermolecular and intramolecular H-bonded systems are known for the formation and stabilization of columnar DLCs. Compound **53** and **54** are representative examples of H-bonded Col LCs (Figure 1.30). In benzene triamide systems,<sup>110-113</sup> the columnar mesomorphism arises due to intramolecular H-bonding. On the other hand, the triazines,<sup>114</sup> melamines<sup>115-116</sup> and recently heptazine derivative<sup>117</sup> are known to form intermolecular H-bonded columnar LCs which consist of H-bond donor and acceptor groups.

### 1.11.2 Charge transfer interactions based DLCs

Generally, the charge transfer interactions induce stable columnar mesomorphism in the DLC molecules.<sup>106</sup> Most of the DLC systems are electron-rich materials, thereby the addition of disc-shaped electron-deficient moiety to them consequent in the realization of charge-transfer complexes.

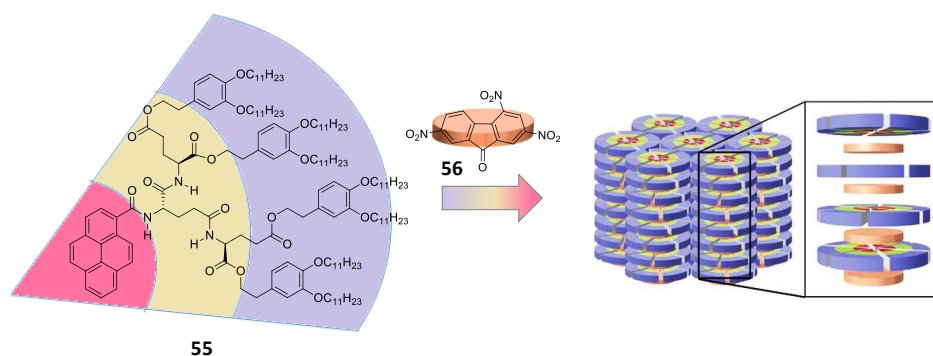


**Figure 1.31** Supramolecular columnar LCs induced columnar mesomorphism by charge transfer donor-acceptor interactions (Reproduced with the permission from Ref. 119).

The charge transfer interactions help in the induction of mesomorphism in the non-mesomorphic materials and can further stabilize the mesophase in case it already exists which can be monitored by an increase in isotropization temperature. For instance, pyrene-containing oligo(glutamic acid) derivative **55** is non-liquid crystalline in its neat state, however, an equimolar mixture of pyrene derivative (electron-rich) with the electron-deficient 2,4,7-trinitrofluorenone (TNF, **56**) reveals a columnar LC phase at ambient temperature (Figure 1.31).<sup>119</sup> In another case, as reported in this thesis, triphenylene and pentalkynylbenzene discotic dimer system exhibit unstable columnar rectangular mesomorphism at room

temperature while doping the dimer in 2:1 ratio with TNF exhibit Col<sub>h</sub> phase with an increased isotropic temperature.<sup>106</sup>

### 1.11.3 Ionic interactions based DLCs

Most of the columnar LCs are neutral molecules, however, the ionic LCs<sup>120</sup> consist of both cations and anions and their properties may vary as that from the conventional LCs. The electrostatic interactions among cationic and anionic parts are the driving force for the formation of highly organized columnar superstructures. The advantage of the ionic LCs is they can be purified by simple recrystallization, extraction or precipitation process.

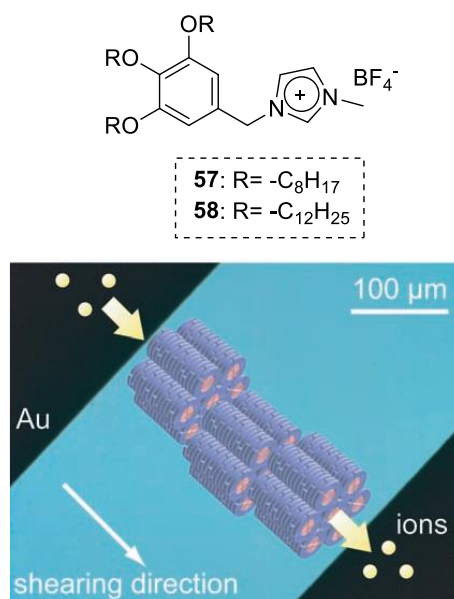


**Figure 1.32** 1D charge conduction in ionic columnar LCs (Reproduced with the permission from Ref. 120).

The step of ionization is usually adopted as the last step because the purification of neutral molecules is simpler than ionic ones by column chromatography. The interest in ILCs based on quaternary ammonium, phosphonium, imidazolium, pyridinium, and viologen ILCs have been aroused more among the plethora of other ionic systems due to their easy preparation by quaternization (or ionization) with alkyl halides.<sup>120</sup> Ionic LCs are studied for their 1D conduction for planarly aligned columnar domains (Figure 1.32).

## 1.12 Outline of thesis

This thesis describes the development of mainly room temperature DLC materials for different device applications. For example, heptazine core-based functional discotic materials synthesized by employing covalent and non-covalent synthetic strategies were utilized as active components in semiconductor devices. The emissive and charge transport application of luminescent perylene tetraesters based DLCs were also explored. The design strategy employing tetrathienoanthracene as discotic core enables the achievement of high charge transport in room temperature DLC materials. Several other design strategies e.g. oligomeric disc-disc and rod-disc design strategies, linear and star-shaped donor-acceptor bridged structures were utilized for the development of functional DLCs. A brief overview of the subsequent chapters is given below.

**Chapter 2** describes the design, synthesis, and characterization of room temperature DLC materials based on electron-deficient as well as luminescent heptazine discotic core. This chapter is subdivided into three parts. The first part presents the conventional synthetic methodology to achieve columnar architectures based on heptazine core which was formerly, unfamiliar to discotic mesomorphic materials before this report. In this work,  $C_3$ -symmetric heptazine core is attached to three tri-alkoxy (Alkyl chain:  $R = -CH_3$ ,  $-C_8H_{17}$  and  $-C_{12}H_{25}$ ) substituted benzene derivatives *via* amino linkage. The derivative with  $Col_h$  self-assembly has been investigated for the conductivity measurements and for OLED devices. The second and third parts demonstrate a non-covalent H-bonded synthetic approach to achieve supramolecular self-assembled columnar structures based on heptazine core. Such systems have self-assembled into columnar mesophases, though both the H-bonded components were not mesogenic on their own.

**Chapter 3** demonstrates the oligomeric disc-disc and rod-disc synthetic approach towards the achievement of novel functional DLC materials that has combined the properties of both the (disc, rod) entities into a single compound. The first part presents the first representatives of triphenylene (TP) and pentaalkynylbenzene (PA) based discotic dimers connected by using the CuI-Et<sub>3</sub>N catalyzed click reaction between terminal TP alkyne and PA azide. The synthesis, thermal behaviour, and the mesomorphic properties of neat compounds and their binary

systems (attained after doping with TNF) are discussed in detail. The doped devices have been fabricated by using neat compounds as emitter materials in OLED devices and the electronic properties of one of the charge transfer complex are investigated *via* TOF method. The second part illustrates a new rod-disc oligomeric DLC system containing six cyanobiphenyl based rod-like moieties attached radially to a central truxene (TX) discotic core *via* flexible alkyl spacers. The ultrathin monolayer of TX derivative was studied at air-water and air-solid interface by Brewster angle microscopy and atomic force microscopy, respectively.

**Chapter 4** illustrates a new design system that showed remarkably high hole mobility at room temperature when used in SCLC devices. Our strategy was to use a new core fragment for DLCs namely, tetrathienoanthracene (TTA) attached to which are four tri-alkoxybenzene units *via* alkynyl spacers. The derivatives result in the formation of room temperature columnar phases. The design was motivated by the following two goals. First, the inclusion of multiple S $\cdots$ S interactions coupled with  $\pi$ - $\pi$  stacking in TTA derivatives provide an effective spatial overlap of the electronic wave functions of the molecules in discs and lead to excellent hole-carrier mobilities. Second, the presence of triple bond spacers provides extended conjugation over the whole molecule and at the same time can reduce the stacking distances, favourable for high charge transport. The materials showed homeotropic columnar ordering at room temperature over a macroscopic area and the effect of alignment on bulk mobility was measured *via* SCLC method. A high hole mobility of  $4.22\text{ cm}^2\text{ V}^{-1}\text{ s}^{-1}$  was observed at ambient temperature in the largely aligned sample.

**Chapter 5** presents the synthesis, characterization, and application of perylene tetraesters (PTE) based luminescent DLCs. The first part explains the design strategy for the achievement of a new series of PTE-based DLCs that exhibit the room temperature columnar mesophase and act as efficient fluorescent emitter materials in OLEDs. All the PTE derivatives exhibited ordered columnar rectangular mesophases at ambient temperatures suitable for various device applications. The electron mobility of triazole modified PTE derivative was measured in the mesophase by time of flight (TOF) technique and a series of devices were fabricated by utilizing PTE derivative as a sole emitter and in the dispersed form. The second part demonstrates the oligomeric DLCs, consisting of PTE core attached to which four bulky pentalkynylbenzene units through flexible methylene spacers  $[-(\text{CH}_2)_n]$ . All compounds

exhibited excellent fluorescence emission properties with a very good quantum yield and large bandgap. Electrical characterization of columnar assemblies showed the potential of the derivatives to act as ion conductors.

**Chapter 6** described the linear and star-shaped  $\pi$ -conjugated luminogens that form donor-acceptor bridged structures which were then utilized in device applications. The first part explained the synthesis of benzothiadiazole (BTD) based donor-acceptor  $\pi$ -conjugated fluorescent molecules for their application in solution-processed green OLED devices that exhibited high EQE as high as 8.1%. Besides the impressive EL properties of the emitters, the material was investigated as a chemosensor that showed the selective sensing of metal cation ( $\text{Fe}^{2+}$ ) and anion ( $\text{I}^-$ ). The second part presents the benzene tricarboxamide based DLC materials where the  $C_3$ -symmetric triamide core is substituted with cyanostilbene based flexible luminophores. Electroluminescence (EL) performance of the materials was studied in solution-processed multilayer doped and non-doped OLED devices. The electronic properties of the triamide-cyanostilbene DLC derivatives were investigated by the SCLC technique in solution-processable thin-films.

This thesis is concluded with **Chapter 7**, which summarizes the significant interpretations derived from all of the above chapters.

At the end of each chapter, the structural analyses ( $^1\text{H}$  and  $^{13}\text{C}$  NMR, IR, UV-vis, DSC etc.) are also provided in the **Appendix**.

## References

1. Tang C. W.; Vanslyke S. A. *Appl. Phys. Lett.* **1987**, *51*, 913-915.
2. Shirota, Y.; Kageyama, H. *Chem. Rev.* **2007**, *107*, 953-1010.
3. Forrest, S. R. *Nature* **2004**, *428*, 911-918.
4. Kumar, S. in *Chemistry of Discotic Liquid Crystals: From Monomers to Polymers*, CRS Press, Taylor & Francis Group: Boca Raton, **2011**.
5. Kumar, S. *Chem. Soc. Rev.* **2006**, *35*, 83-109.
6. Wöhrle, T.; Wurzbach, I.; Kirres, J.; Kostidou, A.; Kapernaum, N.; Litterscheidt, J.; Haenle, J. C.; Staffeld, P.; Baro, A.; Giesselmann, F.; Laschat, S. *Chem. Rev.* **2016**, *116*, 1139-1241.
7. Kaafarani, B. R. *Chem. Mater.* **2010**, *23*, 378-396.
8. Crispin, X.; Cornil, J.; Friedlein, R.; Okudaira, K. K.; Lemaure, V.; Crispin, A.; Kestemont, G.; Lehmann, M.; Fahlman, M.; Lazzaroni, R.; Geerts, Y.; Wendin, G.; Ueno, N.; Bredas, J. L.; Salaneck, W. R. *J. Am. Chem. Soc.* **2004**, *126*, 11889-11899.
9. De, J.; Bala, I.; Gupta, S. P.; Pandey, U. K.; Pal, S. K., *J. Am. Chem. Soc.* **2019**, *141*, 18799-18805.
10. Demus, D.; Goodby, J.; Gray, G. W.; Spiess, H. W.; Vill, V. in *Handbook of Liquid Crystals*, ed., Wiley-VCH, Weinheim, 1998, Vol 1-3.
11. Kato, T.; Hirai, Y.; Nakaso, S.; Moriyama, M. *Chem. Soc. Rev.* **2007**, *36*, 1857-1867.
12. W. Heintz, *J. Prakt. Chem.* **1855**, *66*, 1-51.
13. Reinitzer, F. *Liq. Cryst.* **1989**, *5*, 7-18.
14. Lehmann, O. *J. Phys. Chem.* **1889**, *4*, 462-467.
15. Vorlander, D. *Kristallinisch-flüssige Substanzen*, Enke, Stuttgart, **1905**.
16. Friedel G. *Ann. Phys.* **1922**, *18*, 273-274.
17. Gray, G. W.; Harrison, K. J.; Nash, J. A. *Electron. Lett.* **1973**, *9*, 130-131.
18. Chandrasekhar, S.; Sadashiva, B. K.; Suresh, K. A. *Pramana* **1977**, *9*, 471-480.
19. Niori, T.; Sekine, T.; Watanabe, J.; Furukawa, T.; Takezoe, H. *J. Mater. Chem.* **1996**, *6*, 1231-1233.
20. Sarkar, M.; Spielberg, N.; Praefcke, K.; Zimmermann, H. *Mol. Cryst. Liq. Cryst.* **1991**, *203*, 159-169.

21. Poupko, R.; Luz, Z.; Spielberg, N.; Zimmermann, H. *J. Am. Chem. Soc.* **1989**, *111*, 6094-6105.
22. Zimmermann, H.; Poupko, R.; Luz, Z.; Billard, J. *Liq. Cryst.* **1988**, *3*, 759-770.
23. Percec, V.; Cho, C. G.; Pugh, C. *J. Mater. Chem.* **1991**, *1*, 217-222.
24. Morris, N. L.; Zimmermann, R. G.; Jameson, G. B.; Dalziel, A. W.; Reuss, P. M.; Weiss, R. G. *J. Am. Chem. Soc.* **1988**, *110*, 2177-2185.
25. Lehn, J. M.; Malthete, J.; Levelut, A. M. *J. Chem. Soc. Chem. Commun.* **1985**, 1794-1796.
26. Kato, T.; Yasuda, T.; Kamikawa, Y.; Yoshio, M. *Chem. Commun.* **2009**, 729-739.
27. Laschat, S.; Baro, A.; Steinke, N.; Giesselmann, F.; Hagele, C.; Scalia, G.; Judele, R.; Kapatsina, E.; Sauer, S.; Schreivogel, A.; Tosoni, M. *Angew. Chem. Int. Ed.* **2007**, *46*, 4832-4887.
28. Wu, J.; Pisula, W.; Mullen, K. *Chem. Rev.* **2007**, *107*, 718-747.
29. Boden, N.; Bushby, R. J.; Clements, J.; Movaghar, B. *J. Mater. Chem.* **1999**, *9*, 2081-2086.
30. Bushby, R. J.; Lozman, O. R. *Curr. Opin. Solid State Mater. Sci.* **2002**, *6*, 569-578.
31. Bushby, R. J.; Lozman, O. R. *Curr. Opin. Colloid Interface Sci.* **2002**, *7*, 343-354.
32. Takezoe, H.; Kishikawa, K.; Gorecka, E. *J. Mater. Chem.* **2006**, *16*, 2412-2416.
33. Ohta, K.; Hatsusaka, K.; Sugibayashi, M.; Ariyoshi, M.; Ban, K.; Maeda, F.; Naito, R.; Nishizawa, K.; van de Craats, A. M.; Warman, J. M. *Mol. Cryst. Liq. Cryst.* **2003**, *397*, 25-45.
34. Bala, I.; Yang, W. Y.; Gupta, S. P.; De, J.; Yadav, R. A. K.; Singh, D. P.; Dubey, D. K.; Jou, J. H.; Douali, R.; Pal, S. K. *J. Mat. Chem. C* **2019**, *7*, 5724-5738.
35. Bala, I.; Gupta, S. P.; De, J.; Pal, S. K. *Chem. Eur. J.* **2017**, *23*, 12767-12778.
36. Bala, I.; Pal, S. K. *Liq. Cryst.* **2016**, *43*, 963-971.
37. Bala, I.; De, J.; Gupta, S. P.; Pandey, U. K.; Pal, S. K. *J. Mater. Chem. C* **2021**, DOI: 10.1039/D1TC01898A.
38. Gupta, M.; Gupta, S. P.; Pal, S. K. *J. Phys. Chem. B* **2017**, *121*, 8593-8602.
39. Bala, I.; Singh, H.; Battula, V. R.; Gupta, S. P.; De, J.; Kumar, S.; Kailasam, K.; Pal, S. K. *Chem. Eur. J.* **2017**, *23*, 14718-14722.



40. Gupta, S. P.; Gupta, M.; Pal, S. K. *ChemistrySelect* **2017**, 2, 6070-6077.
41. Bisoyi, H. K.; Li, Q. *Prog. Mater. Sci.* **2019**, 104, 1-52.
42. Gujral, A.; Gomez, J.; Ruan, S.; Toney, M. F.; Bock, H.; Yu, L.; Ediger, M. D. *Chem. Mater.* **2017**, 29, 9110-9119.
43. Gujral, A.; Gomez, J.; Ruan, S.; Toney, M. F.; Bock, H.; Yu, L.; Ediger, M. D. *Chem. Mater.* **2017**, 29, 9110-9119.
44. Holmlin, R. E.; Dandliker, P. J.; Barton, J. K. *Angew Chem. Int. Ed. Eng.* **1997**, 36, 2714-2730.
45. Okahata, Y.; Kobayashi, T.; Tanaka, K.; Shimomura, M. *J. Am. Chem. Soc.* **1998**, 120, 6165-6166.
46. Hall, D. B.; Holmlin, R. E.; Barton, J. K. *Nature* **1996**, 382, 731.
47. Hall, D. B.; Barton, J. K. *J. Am. Chem. Soc.* **1997**, 119, 5045-5046.
48. Arkin, M. R.; Stemp, E. D. A.; Holmlin, R. E.; Barton, J. K.; Hörmann, A.; Olson, E. J. C.; Barbara, P. F. *Science* **1996**, 273, 475-480.
49. Lemaure, V.; da Silva Filho, D. A.; Coropceanu, V.; Lehmann, M.; Geerts, Y.; Piriš, J.; Debije, M. G.; van de Craats, A. M.; Senthilkumar, K.; Siebbeles, L. D. A.; Warman, J. M. *J. Am. Chem. Soc.* **2004**, 126, 3271-3279.
50. Feng, X.; Marcon, V.; Pisula, W.; Hansen, M. R.; Kirkpatrick, J.; Grozema, F.; Andrienko, D.; Kremer, K.; Müllen, K. *Nat. mater.* **2009**, 8, 421.
51. Moreno, C.; Pfattner, R.; Mas-Torrent, M.; Puigdollers, J.; Bromley, S. T.; Rovira, C.; Veciana, J.; Alcubilla, R. *J. Mater. Chem.* **2012**, 22, 345-348.
52. Zaumseil, J.; Sirringhaus, H. *Chem. Rev.* **2007**, 107, 1296-1323.
53. Smits, E. C.; Setayesh, S.; Anthopoulos, T. D.; Buechel, M.; Nijssen, W.; Coehoorn, R.; Blom, P. W.; de Boer, B.; de Leeuw, D. M. *Adv. Mater.* **2007**, 19, 734-738.
54. Benito-Hernández, A.; Pandey, U. K.; Caverio, E.; Termine, R.; García-Frutos, E. M.; Serrano, J. L.; Golemmé, A.; Gómez-Lor, B. *Chem. Mater.* **2013**, 25, 117-121.
55. Talarico, M.; Termine, R.; García-Frutos, E. M.; Omenat, A.; Serrano, J. L.; Gómez-Lor, B.; Golemmé, A. *Chem. Mater.* **2008**, 20, 6589-6591.
56. An, Z.; Yu, J.; Jones, S. C.; Barlow, S.; Yoo, S.; Domercq, B.; Prins, P.; Siebbeles, L. D. A.; Kippelen, B.; Marder, S. R. *Adv. Mater.* **2005**, 17, 2580-2583

57. An, Z.; Yu, J.; Domercq, B.; Jones, S. C.; Barlow, S.; Kippelen, B.; Marder, S. R. *J. Mater. Chem.* **2009**, *19*, 6688-6698.
58. Feringan, B.; Romero, P.; Serrano, J. L.; Folcia, C. L.; Etxebarria, J.; Ortega, J.; Termine, R.; Golemme, A.; Gimenez, R.; Sierra, T. *J. Am. Chem. Soc.* **2016**, *138*, 12511-12518.
59. Yasuda, T.; Shimizu, T.; Liu, F.; Ungar, G.; Kato, T. *J. Am. Chem. Soc.* **2011**, *133*, 13437-13444.
60. Kushida, T.; Shuto, A.; Yoshio, M.; Kato, T.; Yamaguchi, S. A. *Angew. Chem., Int. Ed.* **2015**, *54*, 6922-6925.
61. Liao, Y.-L.; Lin, C.-Y.; Liu, Y.-H.; Wong, K.-T.; Hung, W.-Y.; Chen, W.-J. *Chem. Commun.* **2007**, 1831-1833.
62. Liu, X. Y.; Usui, T.; Hanna, J. *Chem. Mater.* **2014**, *26*, 5437-5440.
63. Iino, H.; Hanna, J.; Haarer, D. *Phys. Rev. B: Condens. Matter Mater. Phys.* **2005**, *72*, 193203.
64. Bala, I.; Ming, L.; Yadav, R. A. K.; De, J.; Dubey, D. K.; Kumar, S.; Singh, H.; Jou, J. H.; Kailasam, K.; Pal, S. K. *ChemistrySelect* **2018**, *3*, 7771-7777.
65. Domercq, B.; Yu, J.; Kaafarani, B. R.; Kondo, T.; Yoo, S.; Haddock, J. N.; Barlow, S.; Marder, S. R.; Kippelen, B. *Mol. Cryst. Liq. Cryst.* **2008**, *481*, 80-93.
66. Xiao, Q.; Sakurai, T.; Fukino, T.; Akaike, K.; Honsho, Y.; Saeki, A.; Seki, S.; Kato, K.; Takata, M.; Aida, T. *J. Am. Chem. Soc.* **2013**, *135*, 18268-18271.
67. Ruiz, C.; Pandey, U. K.; Termine, R.; García-Frutos, E. M.; López-Espejo, G.; Ortiz, R. P.; Huang, W.; Marks, T. J.; Facchetti, A.; Ruiz Delgado, M. C.; Golemme, A. *ACS Appl. Mater. Interfaces* **2016**, *8*, 26964-26971.
68. Mott, N. F.; Gurney, D. *Electronic Processes in Ionic Crystals*; Academic Press: New York, 1970; p 45
69. Ye, Q.; Chang, J.; Shao, J.; Chi, C. *J. Mater. Chem. C* **2012**, *22*, 13180-13186
70. García-Frutos, E. M.; Pandey, U. K.; Termine, R.; Omenat, A.; Barberá, J.; Serrano, J. L.; Golemme, A.; Gómez-Lor, B. *Angew. Chem. Int. Ed.* **2011**, *50*, 7399-7402.
71. García-Frutos, E. M.; Omenat, A.; Barberá, J.; Serrano, J. L.; Gómez-Lor, B. *J. Mater. Chem. C* **2011**, *21*, 6831-6836.

72. Iguarbe, V.; Concellón, A.; Termine, R.; Golemme, A.; Barberá, J.; Serrano, J. L. *ACS Macro Lett.* **2018**, *7*, 1138-1143.
73. Concellón, A.; Marcos, M.; Romero, P.; Serrano, J. L.; Termine, R.; Golemme, A. *Angew. Chem.* **2017**, *129*, 1279-1283.
74. Bala, I.; De, J.; Gupta, S. P.; Singh, H.; Pandey, U. K.; Pal, S. K. *Chem. Commun.* **2020**, *56*, 5629-5632.
75. Eccher, J.; Faria, G. C.; Bock, H.; von Seggern, H.; Bechtold, I. H. *ACS Appl. Mater. Interfaces* **2013**, *5*, 11935-11943.
76. Scher, H.; Montroll, E. W. *Phys. Rev. B* **1975**, *12*, 2455-2477.
77. Adam, D.; Schuhmacher, P.; Simmerer, J.; Haussling, L.; Siemensmeyer, K.; Etzbach, K. H.; Ringsdorf, H.; Haarer, D. *Nature* **1994**, *371*, 141-143.
78. Xiao, Q.; Sakurai, T.; Fukino, T.; Akaike, K.; Honsho, Y.; Saeki, A.; Seki, S.; Kato, K.; Takata, M.; Aida, T. *J. Am. Chem. Soc.* **2013**, *135*, 18268-18271.
79. Kushida, T.; Shuto, A.; Yoshio, M.; Kato, T.; Yamaguchi, S. *Angew. Chem. Int. Ed.* **2015**, *54*, 6922-6925.
80. Isoda, K.; Yasuda, T.; Kato, T. *Chem. Asian J.* **2009**, *4*, 1619-1625.
81. Yasuda, T.; Shimizu, T.; Liu, F.; Ungar, G.; Kato, T. *J. Am. Chem. Soc.* **2011**, *133*, 13437-13444.
82. Hayashi, H.; Nishihashi, W.; Umeyama, T.; Matano, Y.; Seki, S.; Shimizu, Y.; Imahori, H. *J. Am. Chem. Soc.* **2011**, *133*, 10736-10739.
83. van de Craats, A. M.; Warman, J. M.; de Haas, M. P.; Adam, D.; Simmerer, J.; Haarer, D. and Schuhmacher, P. *Adv. Mater.* **1996**, *8*, 823-826.
84. Schouten, P. G.; Warman, J. M.; de Haas, M. P.; van Nostrum, C. F.; Gelinck, G. H.; Nolte, R. J.; Copyn, M. J.; Zwikker, J. W.; Engel, M. K. *J. Am. Chem. Soc.* **1994**, *116*, 6880-6894.
85. Schouten, P. G.; Warman, J. M.; de Haas, M. P.; Fox, M. A.; Pan, H. L. *Nature* **1991**, *353*, 736-737.
86. Warman, J. M.; de Haas, M. P.; van der Pol, J. F.; Drenth, W. *Chem. Phys. Lett.* **1989**, *164*, 581-586.

87. van de Craats, A. M.; Warman, J. M.; Fechtenkötter, A.; Brand, J. D.; Harbison, M. A.; Müllen, K. *Adv. Mater.* **1999**, *11*, 1469-1472.
88. Debije, M. G.; Piris, J.; de Haas, M. P.; Warman, J. M.; Tomović, Ž.; Simpson, C. D.; Watson, M. D.; Müllen, K. *J. Am. Chem. Soc.* **2004**, *126*, 4641-4645.
89. Xue, C.; Li, Q. *Liquid Crystals Beyond Displays: Chemistry, Physics, and Applications* **2012**, p29-82.
90. Bisoyi, H. K.; Kumar, S., *Chem. Soc. Rev.* **2010**, *39*, 264-285.
91. Shimizu, Y.; Oikawa, K.; Nakayama, K.; Guillon, D. *J. Mater. Chem.* **2007**, *17*, 4223-4229.
92. van de Craats, A. M.; Stutzmann, N.; Bunk, O.; Nielsen, M. M.; Watson, M.; Mullen, K.; Chanzy, H. D.; Sirringhaus, H.; Friend, R. H. *Adv. Mater.* **2003**, *15*, 495-499.
93. Pisula, W.; Menon, A.; Stepputat, M.; Lieberwirth, I.; Kolb, U.; Tracz, A.; Sirringhaus, H.; Pakula, T.; Mullen, K. *Adv. Mater.* **2005**, *17*, 684-689.
94. Pisula, W.; Kastler, M.; Wasserfallen, D.; Pakula, T.; Mullen, K. *J. Am. Chem. Soc.* **2004**, *126*, 8074-8075.
95. Shklyarevskiy, I. O.; Jonkheijm, P.; Stutzmann, N.; Wasserberg, D.; Wondergem, H. J.; Christianen, P. C. M.; Schenning, A. P. H. J.; de Leeuw, D. M.; Tomovic, Z.; Wu, J.; Mullen, K.; Maan, J. C. *J. Am. Chem. Soc.* **2005**, *127*, 16233-16237.
96. Shimizu, Y.; Oikawa, K.; Nakayama, K.; Guillon, D. *J. Mater. Chem.* **2007**, *17*, 4223-4229.
97. Cherian, S.; Donley, C.; Mathine, D.; LaRussa, L.; Xia, W.; Armstrong, N. *J. Appl. Phys.* **2004**, *96*, 5638-5643.
98. Tatemichi, S.; Ichikawa, M.; Koyama, T.; Taniguchi, Y. *Appl. Phys. Lett.* **2006**, *89*, 112108.
99. Schmidt, R.; Oh, J. H.; Sun, Y. S.; Deppisch, M.; Krause, A. M.; Radacki, K.; Braunschweig, H.; Konemann, M.; Erk, P.; Bao, Z.; Wurthner, F. *J. Am. Chem. Soc.* **2009**, *131*, 6215-6228.
100. Kumar, M.; Kumar, S. *Polym. J.* **2017**, *49*, 85-111.
101. Gregg, B. A.; Fox, M. A.; Bard, A. J. *J. Phys. Chem.* **1990**, *94*, 1586-1598.

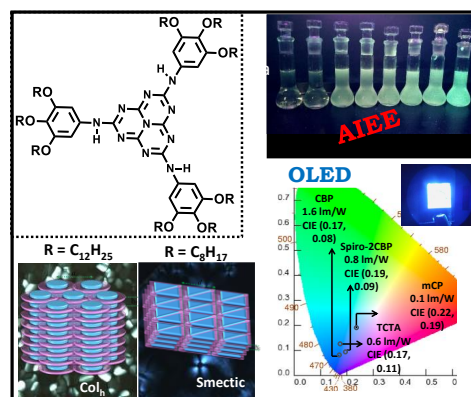
102. Petritsch, K.; Friend, R. H.; Lux, A.; Rozenberg, G.; Moratti, S. C.; Holmes, A. B. *Synth. Met.* **1999**, *102*, 1776-1777.
103. Thiebaut, O.; Bock, H.; Grelet, E. *J. Am. Chem. Soc.* **2010**, *132*, 6886-6887.
104. De, J.; Gupta, S. P.; Swayamprabha, S. S.; Dubey, D. K.; Bala, I.; Sarkar, I.; Dey, G.; Jou, J. H.; Ghosh, S.; Pal, S. K. *J. Phys. Chem. C* **2018**, *122*, 23659-23674.
105. De, J.; Yang, W. Y.; Bala, I.; Gupta, S. P.; Yadav, R. A. K.; Dubey, D. K.; Chowdhury, A.; Jou, J. H.; Pal, S. K. *ACS Appl. Mater. Interfaces* **2019**, *11*, 8291-8300.
106. Kato, T.; Mizoshita, N.; Kishimoto, K. *Angew. Chem. Int. Ed.* **2006**, *45*, 38-68.
107. Kato, T.; J. M. J. Fréchet. *J. Am. Chem. Soc.* **1989**, *111*, 8533-8534.
108. Brienne, M. -J.; Gabard, J.; Lehn, J. -M.; Stibor, I. *J. Chem. Soc., Chem. Commun.* **1989**, 1868-1870.
109. Cheng X. H.; Gao H. F. Hydrogen Bonding for Supramolecular Liquid Crystals. In: Li, Z. T.; Wu, L. Z. (eds), vol 88. Springer, Berlin, Heidelberg, **2015**.
110. Devi, S.; Bala, I.; Gupta, S. P.; Kumar, P.; Pal, S. K.; Venkataramani, S. *Org. biomol. Chem.* **2019**, *17*, 1947-1954.
111. Bushey, M. L.; Nguyen, T. -Q.; Zhang, W.; Horoszewski, D.; Nuckolls, C. *Angew. Chem., Int. Ed.* **2004**, *43*, 5446-5453.
112. Bushey, M. L.; Hwang, A.; Stephens, P. W.; Nuckolls, C. *Angew. Chem. Int. Ed.* **2002**, *41*, 2828-2831.
113. Bushey, M. L.; Hwang, A.; Stephens, P. W.; Nuckolls, C. *J. Am. Chem. Soc.* **2001**, *123*, 8157-8158.
114. Feringán, B.; Romero, P.; Serrano, J. L.; Giménez, R.; Sierra, T. *Chem. Eur. J.* **2015**, *21*, 8859-8866.
115. Barbera', J.; Puig, L.; Romero, P.; Serrano, J. L.; Sierra, T. *J. Am. Chem. Soc.* **2005**, *127*, 458-464.
116. Piermattei, A.; Giesbers, M.; Marcelis, A. T. M.; Mendes, E.; Picken, S. J.; Crego-Calama, M.; Reinhoudt, D. N. *Angew. Chem. Int. Ed.* **2006**, *45*, 7543-7546.
117. Bala, I.; Gupta, S. P.; Kumar, S.; Singh, H.; De, J.; Sharma, N.; Kailasam, K.; Pal, S. K. *Soft matter* **2018**, *14*, 6342-6352.
118. Kamikawa, Y.; Kato, T. *Org. Lett.* **2006**, *8*, 2463-2466.

119. Kato, T.; Yasuda, T.; Kamikawa, Y.; Yoshio, M. *Chem. Commun.* **2002**, 729-739.
120. Yoshio, M.; Mukai, T.; Ohno, H.; Kato, T. *J. Am. Chem. Soc.* **2004**, 126, 994-995.

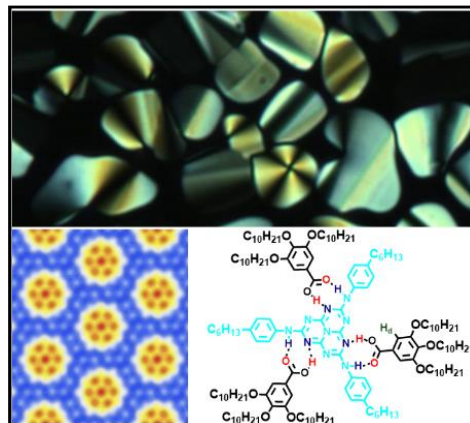
## Chapter 2

### Heptazine based Discotic Liquid Crystals for Organic Optoelectronics

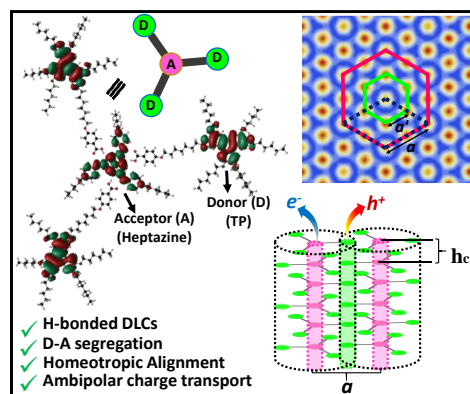
**Part A:** Room temperature discotic liquid crystals (DLCs) based on electron-deficient heptazine core are reported and their interesting mesomorphic behaviour was investigated. The salient feature of the heptazine core is that it exhibits AIE characteristics, while DLCs based on other discotic cores known, exhibit majorly aggregation caused quenching (ACQ) behaviour. The solution-processed OLED has been fabricated by using a host-guest configuration exhibiting deep-blue emission when doped with different hosts.



**Part B:** The tendency of the *s*-heptazine core to form *H*-bonded fluorescent liquid crystals (FLCs) has been explored for the first time. Interestingly, the pure heptazine derivatives (non-mesomorphic) on complexation with tri-alkoxy benzoic acids exhibit enantiotropic columnar mesomorphism over a wide range of temperatures including room temperature. This indicates the strength of the resulting hydrogen (*H*)-bonded complexes. Because of the inherently fluorescent pure heptazine derivative, the resulting complexes exhibit fluorescent behaviour in the solution state as well as in the solid-state.



**Part C:** Heptazine-based *H*-bonded segregated columnar assembly formed by electronically decoupled donor (*D*) (triphenylene) and acceptor (*A*) (heptazine) units are reported in this work. Discrete conduction channels together with highly preorganized homeotropically aligned conduction pathways are observed in the reported complexes, resulting in efficient ambipolar charge transport.







## 2.1 Part A: Electroluminescence and conductivity measurements in DLCs based on fluorescent and electron-deficient heptazine discotic core

### 2.1.1 Introduction

There is a considerable demand of discotic liquid crystals (DLCs) in organic electronics due to their tendency to self-assemble into columnar superstructures with one-dimensional charge carrier migration properties.<sup>1-3</sup> In literature, DLCs with electron-rich cores are numerous, while a few examples of electron-deficient systems are known.<sup>4</sup> Such electron-deficient discotic molecules with low bandgap are potential candidates as excellent organic semiconductors for both positive and negative charge transport materials.<sup>5</sup> Further, the charge transport and luminescent properties in this kind of materials can be enhanced by the inclusion of an *N*-heterocycle core suitable for applications in electro-optical devices.<sup>6</sup> Moreover, nitrogen-containing polycyclic aromatic core is particularly advantageous as their electronic properties can be tuned from *p*-type to *n*-type (on exchanging the  $sp^2$ -carbon atoms by N atoms) without modifying the overall structure. In recent years, there has been ever-increasing interest in the field of *N*-heterocyclic based discotic materials to the realization of new classes of organic semiconductors.<sup>7-10</sup> In particular, heptazine, since its discovery, has been explored widely as a metal-free catalyst<sup>11</sup>, photo-catalyst for H<sub>2</sub> formation from water splitting,<sup>12,13</sup> as smart material for potential applications in OLEDs<sup>14</sup> and so on. In addition, heptazine (C<sub>6</sub>N<sub>7</sub>) possesses a disc-shaped core and although its derivatives have the potential for advanced materials in devices, it has not yet been explored in the field of DLCs. If the intriguing thermal,<sup>15</sup> optical<sup>16-18</sup> and electronic properties<sup>19</sup> of heptazine are combined with the self-organization features of LCs, it will definitely improve their usability in devices. This will also open a new field based on heptazine discotics that might overcome the physical and chemical properties of the equivalent *s*-triazine system due to its larger core.

In addition to the potential semiconducting properties, heptazine core is highly potent to develop emissive DLC materials. Luminescent DLCs can act simultaneously as an emitter and charge carrier transporting layer in OLEDs and hence can reduce the device fabrication cost without compromising device efficiency. Usually, many luminescent DLCs are known, but

majority of them exhibit the luminescent behaviour in the solution state, while in solid-state they show low emission efficiencies due to the aggregation-caused quenching (ACQ) behaviour of the  $\pi$ -conjugated core.<sup>20-26</sup> The luminogens which exhibit enhanced emission in their aggregated state as compared to their solution state, generally, known as aggregation-induced emitting materials. In 2001, Tang and his group presented the first report of such a system in which molecules exhibit no emission behaviour in the solution state while becomes highly luminescent in their aggregated state.<sup>27</sup> And various AIE luminogens show outstanding device performance of the OLEDs.<sup>28,29</sup> W. Zhou recently reported highly efficient blueish-green fluorescent OLEDs based on AIE liquid crystal molecules.<sup>30</sup> As many AIE luminogens are known, but only very few reports of AIE luminogens which exhibit liquid crystalline phases are there.<sup>30-32</sup>

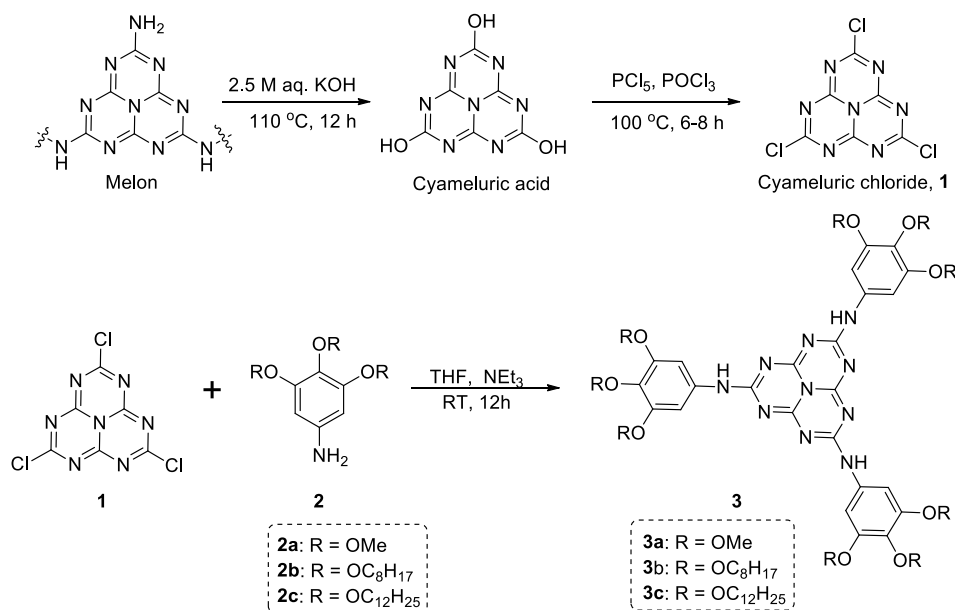
### 2.1.2 Objectives

Various luminescent mesogens formed by peripherally substituting the luminescent  $\pi$ -conjugated core with the alkyl chains are reported.<sup>33-36</sup> This strategy, however, enables to induce liquid crystallinity in the materials but their emission efficiency gets quenched in the solid-state. Therefore, to employ luminescent DLCs in OLEDs, a kind of discotic core is needed which upon substituting with peripheral alkyl chain length induces liquid crystalline behaviour as well as show enhanced luminescent behaviour in solid-state. This approach requires a unique balance of the  $\pi$ - $\pi$  interaction to form DLCs and not to quench luminescence efficiency. In this context, we have synthesized heptazine-based DLCs attached to which are three tri-alkoxy substituted benzene derivatives *via* amino linkage (Scheme 2.1) AIE and electroluminescence behaviour of columnar liquid crystalline material was investigated and deep-blue OLED devices were fabricated by using host-guest configuration. The sky-blue emitter enables to form deep-blue OLEDs when fabricated with different hosts because of host effect as reported previously.<sup>37</sup> The material is doped with four different hosts: carbazolyl)-1,1'-biphenyl (CBP) host, 4',4''-tri(N-carbazolyl)triphenylamine (TCTA), 2,7-Bis(carbazol-9-yl)-9,9-spirobifluorene (Spiro-2CBP), and 3,5-di(9H-carbazol-9-yl) tetraphenylsilane (SimCP2) by varying dopant concentration. The device shows external quantum efficiency (EQE) of 1.6%, 0.8%, 0.6% and 0.1% using CBP host, Spiro-2CBP, TCTA and SimCP2, respectively, with 3% dopant concentration. Additionally, the conductivity measurement was performed for the derivative exhibiting columnar hexagonal mesophase.

## 2.1.3 Results and discussions

### 2.1.3.1 Synthesis and characterization

Firstly, the synthesis of a precursor material heptazine (cyameluric) chloride ( $C_6N_7Cl_3$ ) **1** (Scheme 2.1) was commenced from the polymeric material, melon which in turn synthesized from melamine.<sup>38</sup> When melamine was heated in a closed crucible at 330 °C in the furnace for 2 days, it condensed to form a white-beige colored solid, melem. On further heating the obtained beige-colored solid at 520 °C for 1 day, it formed a light yellow-colored polymeric product called the melon. The basic hydrolysis of polymeric melon with aqueous KOH at 110 °C forms white-colored material, cyameluric acid which then further treated with  $PCl_5$  and  $POCl_3$  at 110 °C under ultra-dried conditions to form cyameluric chloride **1** having a bright yellow color. Finally, the cyameluric chloride **1** was reacted with 3,4,5-trialkoxyphenylamine **2** in presence of  $NEt_3$  as a base in THF solvent at room temperature to get the desired product **3**. Compound **1** is sensitive towards hydrolysis and therefore the reaction was carried out under extremely inert conditions in the glove box.



**Scheme 2.1** Synthesis of cyameluric chloride from melon and 3,4,5-trialkoxyphenylamine substituted heptazine derivatives.

Three heptazine derivatives **3a-c** were synthesized and their thermal behaviour was investigated using a combination of POM and DSC (*vide infra*). Interestingly, compounds **3b** and **3c** with peripheral chain lengths  $R = -C_8H_{17}$  and  $R = -C_{12}H_{25}$ , respectively, were found to

be mesomorphic. Compound **3b** with a shorter alkyl chain length exhibits a smectic (Sm) phase while **3c** with longer chain length exhibits columnar hexagonal mesophase (Col<sub>h</sub>) which is well supported by their POM and X-ray diffraction studies (*vide infra*). The compound **3a** with R = Me was synthesized as a model compound and found to be crystalline. The structures of final materials **3a-c** were characterized using <sup>1</sup>H, <sup>13</sup>C NMR and IR spectra, HRMS (Figure A1-A10, Appendix II, Page 133) and elemental analysis.

### 2.1.3.2 Thermal studies

Under POM, compound **3c** exhibits room temperature mesophase. On heating, it starts clearing at 98 °C ( $\Delta H = 5.8 \text{ kJ mol}^{-1}$ ) to the isotropic phase as observed from DSC (Figure 2.1d). During cooling the phase appears at 96 °C which remains stable down to room temperature. The mesomorphic texture obtained on cooling at 80 °C and 60 °C from the isotropic phase is shown in Figure 2.1a and 2.1b, respectively. However, below 45 °C, it exhibits glassy nature (Figure

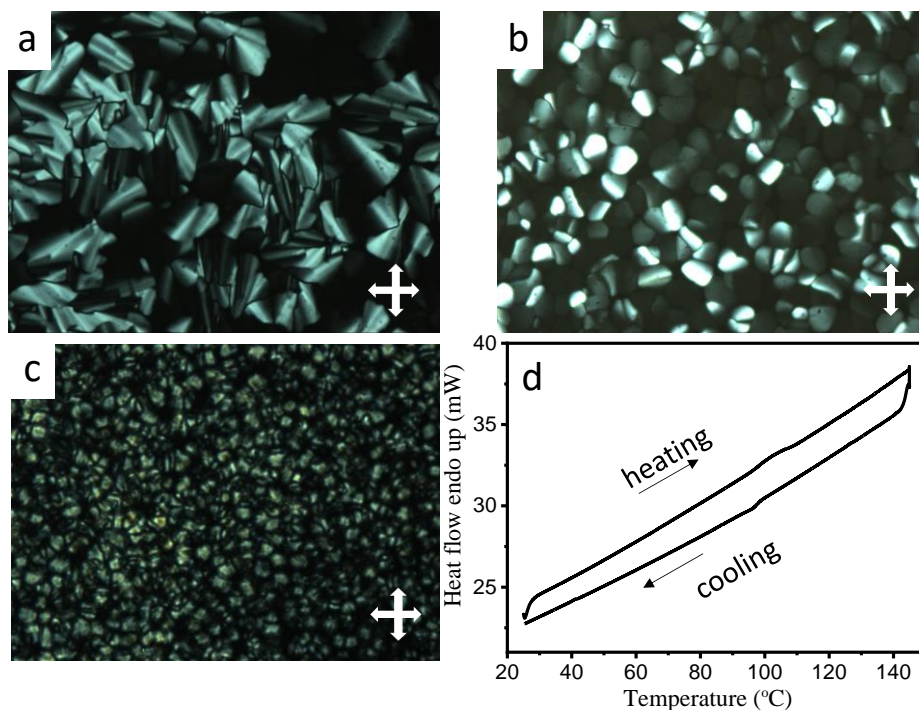


**Figure 2.1** POM images of compound **3c** displaying columnar textures (a) at 80 °C (×500), (b) at 60 °C (×100) and (c) at 38 °C (Col<sub>h</sub> in glassy phase) (×100), observed on cooling from the isotropic liquid. (d) DSC curves of compound **3c** recorded with a scan rate of 5 °C/min.

2.1c). Compound **3b** also exhibits mesophase at room temperature and the phase is mostly homeotropically aligned (Figure 2.2b). The compound goes to isotropic at 149 °C ( $\Delta H = 4.6$

$\text{kJ mol}^{-1}$ ) which on cooling reappears at  $143\text{ }^{\circ}\text{C}$ . The occurrence of orthogonal isogyre textures (observed on pressing the top of the glass slide), as shown in Figure 2.2a, indicate the formation of Sm phase.<sup>39</sup>

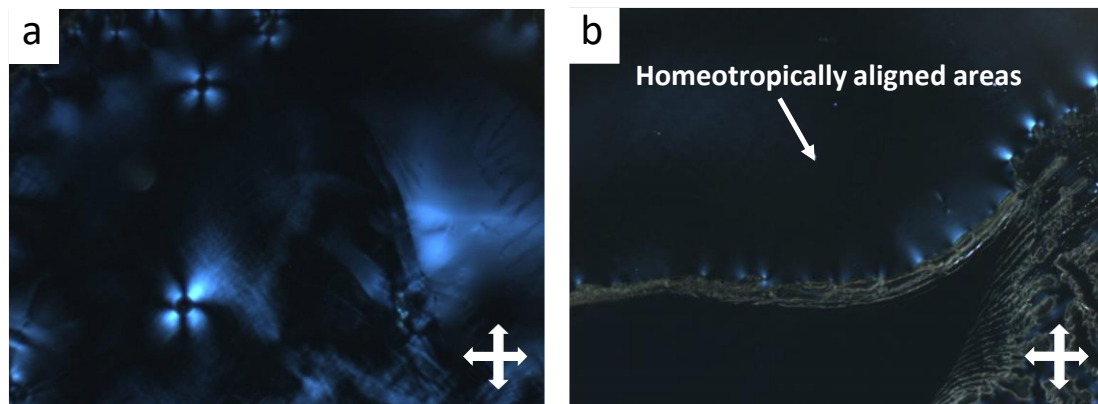


**Figure 2.2** (a) Orthogonal isogyre textures of compound **3b** at  $60\text{ }^{\circ}\text{C}$ , observed on pressing the homeotropically aligned areas develops on the glass slide when cooled from the isotropic liquid, (magnification  $\times 500$ , crossed polariser). (b) Homeotropically aligned areas along with the inclination along the walls of the coverslip of compound **3b** observed on pressing the microscopic glass slides, on cooling from the isotropic liquid (magnification  $\times 50$ , crossed polariser).

### 2.1.3.3 X-ray diffraction studies

Next, small and wide-angle X-ray (SAXS/WAXS) experiments were performed to examine the quantitative details of mesophase behaviour of compounds **3b** and **3c**. The diffraction pattern of compound **3b** at  $60\text{ }^{\circ}\text{C}$  exhibits one sharp peak in the small-angle region of spacing  $28.13\text{ }\text{\AA}$  (Figure 2.3a). However, in the wide-angle regime, one halo peak ( $h_a$ ) of spacing  $4.80\text{ }\text{\AA}$  with one additional weak peak ( $h_c$ ) of spacing  $3.65\text{ }\text{\AA}$  were found which is further confirmed by the de-convolution of the wide-angle peak as shown in the Figure 2.3a (inset (right)). The diffraction pattern also reinforced the formation of Sm phase. The small-angle peak is indexed to be (100) and corresponds to the layer spacing ( $d$ ). Further,  $h_a$  and  $h_c$  peaks of the wide-angle region reflect the fluid alkyl chain-chain and heptazine core-core (side to side) separations, respectively. The correlation length corresponding to the (100) peak is found to be about  $112\text{ }\text{\AA}$  which corresponds to  $\sim 4$  number of correlated layers. The diffraction pattern in the temperature range  $45\text{ }^{\circ}\text{C}$  to  $150\text{ }^{\circ}\text{C}$  is similar to that of at  $60\text{ }^{\circ}\text{C}$  (Figure 2.4).

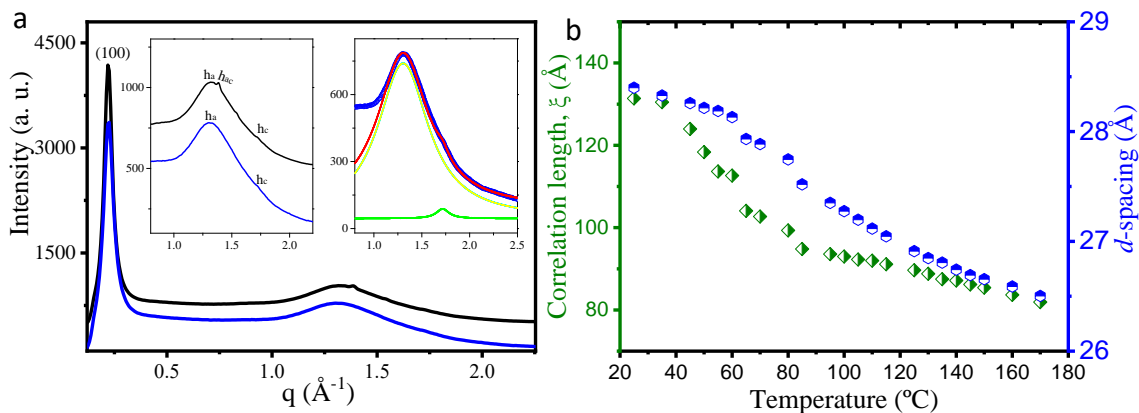


**Figure 2.3** (a) X-ray diffraction pattern of Sm phase of compound **3b** at 25 °C (black colored) and 60 °C (blue colored), Inset (left) shows the zoomed area of wide-angle regime at 25 °C (black colored) and 60 °C (blue colored), Inset (right) shows the deconvolution of the wide-angle peak at 60 °C, the curve with half-filled diamond in blue color represents the wide-angle data. The curves in the cyan and green colors correspond to fluid chain-chain and heptazine core-core (face to face) correlations, respectively. And curve in the red color is the sum of the cyan and green color curve.  $h_a$  - fluid chain-chain separations,  $h_{ac}$  - crystallize chain-chain separation and  $h_c$  – heptazine core-core (face to face wise) separation. (b) Variation of correlation length ( $\xi$ ) and d-spacing corresponding to (100) peak with temperature for compound **3b**.

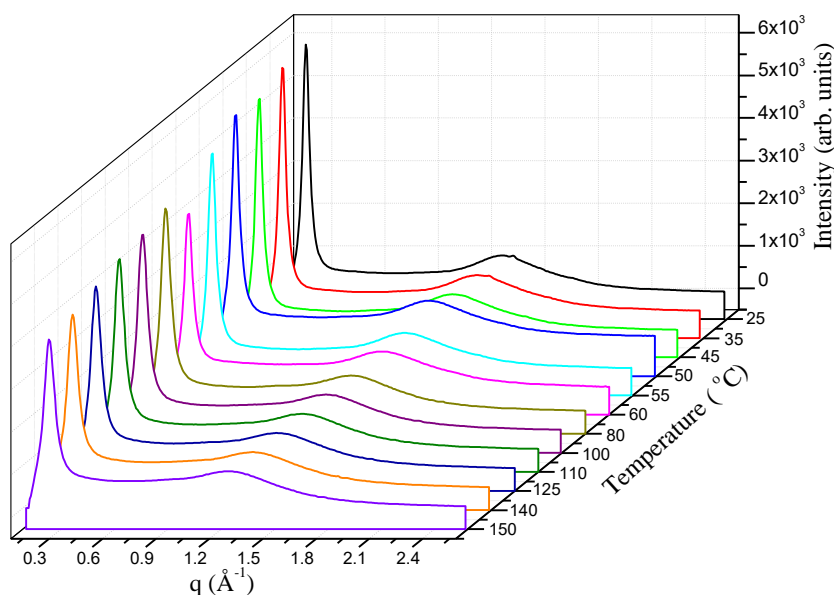


**Figure 2.4** Systematic temperature-dependent X-ray diffraction studies of compound **3b** from room temperature (25 °C) to isotropic phase (150 °C).

However, below 45 °C, the small-angle peak (correspond to (100)) is found to be similar to that of at 60 °C with relatively higher  $d$ -spacings and correlation length value (Figure 2.3b). But the wide-angle region exhibits a narrow peak ( $h_{ac}$ ) of spacing 4.5 Å in addition to  $h_a$  (4.76 Å) and  $h_c$  (3.64 Å) peaks (Figure 2.3a (inset (left))). The  $h_{ac}$  peak appears due to crystallize chain-chain correlation and reflects the less fluid behaviour at a lower temperature. Further, the  $d$ -spacing [(100) peak] value and corresponding correlation length are found to be decreasing with increasing the temperature (Figure 2.3b).

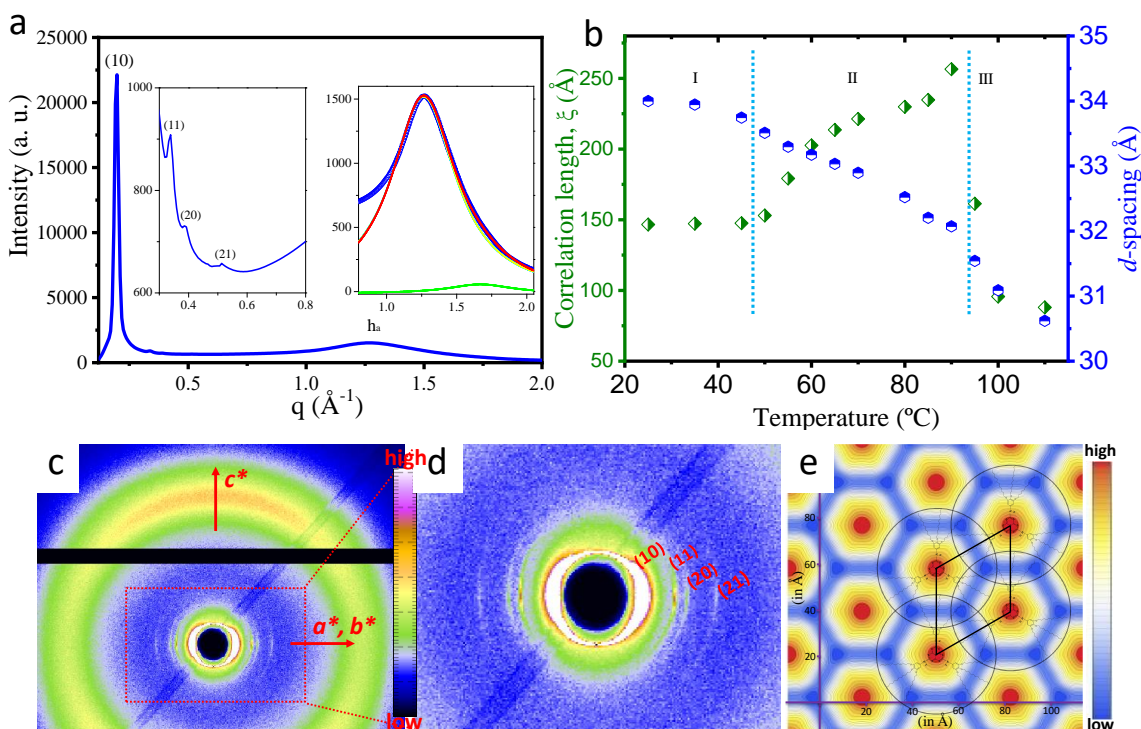


**Figure 2.5** (a) X-ray diffraction pattern of Col<sub>h</sub> phase of compound **3c** at 90 °C, Inset shows (i) zoomed area of small-angle region in Col<sub>h</sub> phase (ii) deconvolution of the wide-angle peak at 90 °C, the curve with a half-filled diamond in blue color represents the wide-angle data. The curves in the cyan and green colors correspond to fluid chain-chain and heptazine core-core (face to face,  $h_c$ ) correlations, respectively. And curve in the red color is the sum of the cyan and green color curve.  $h_a$  - fluid chain-chain correlations and  $h_c$  - heptazine core-core (face to face) correlations (b) Variation of correlation length ( $\xi$ ) and  $d$ -spacing corresponding to (10) peak with temperature for compound **3c** (c) Corresponding 2D aligned X-ray diffraction pattern of **3c** recorded at 90 °C;  $a^*$ ,  $b^*$  and  $c^*$  are the reciprocal lattice vectors (d) Zoomed area of small-angle regime with indexing (b) Reconstructed electron density map of **3c** in Col<sub>h</sub>



phase, showing the arrangement of the column on the 2D hexagonal lattice. Red represents the highest electron density and deep blue is the lowest. Parallelogram in black color on the map shows the respective 2D unit cell.

The X-ray diffraction pattern of compound **3c** at 90 °C showed four peaks in the small-angle region (Figure 2.5a). The corresponding  $d$ -spacing is found to be 32.07 Å, 18.54 Å, 16.02 Å and 12.21 Å and they are in ratios  $\frac{1}{1}:\frac{1}{\sqrt{3}}:\frac{1}{2}:\frac{1}{\sqrt{7}}$ , confirming the occurrence of 2D hexagonal phase (Figure 2.5a (inset (left))). According to the ratios, the observed four peaks were assigned to the reflection of the (10), (11), (20) and (21) planes, respectively (Table 2.1). In-addition, one broad peak is present in the wide-angle region which is found to be the convolution of two peaks corresponding to  $h_a$  and  $h_c$  peaks of spacings 4.97 Å and 3.76 Å, respectively (Figure 2.5a (inset (right))). Based on the results the LC phase is best described as the columnar hexagonal ( $\text{Col}_h$ ) phase. The corresponding 2D X-ray diffractogram reflects the crescent-moon pattern (Figure 2.5c,d). The reciprocal lattice vectors  $a^*$  and  $b^*$  are found to be along the equator and  $c^*$  is along the meridian. The corresponding 2D electron density map is shown in Figure 2.5e.

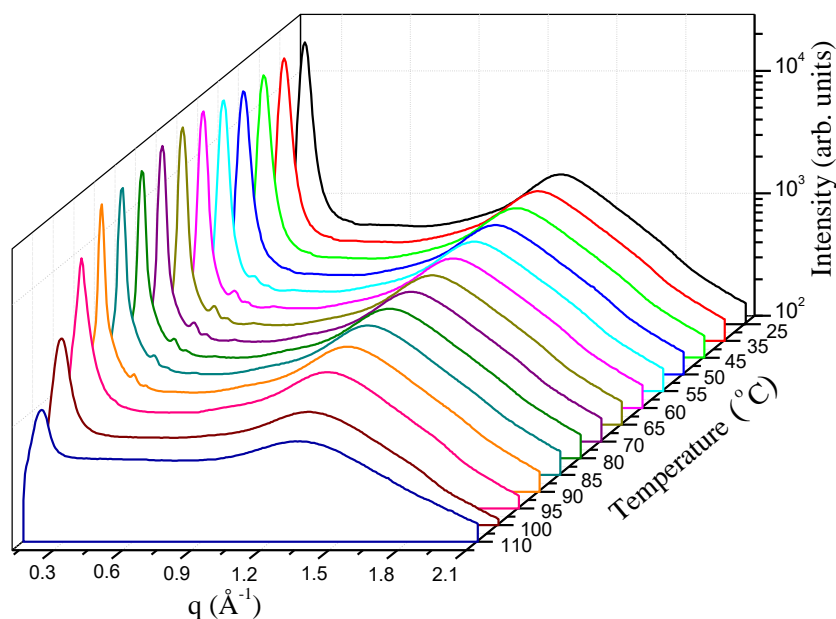


**Figure 2.6** Systematic temperature-dependent X-ray diffraction studies of compound **3c** from room temperature (25 °C) to isotropic phase (110 °C).



The lattice parameter,  $a$ , (column-column separation) is calculated by using the relation:  $a = \frac{2d_{10}}{\sqrt{3}}$ , where  $d_{10}$  is the spacing corresponding to (10) peak. The value of the calculated lattice parameter,  $a$  is found to be 37.04 Å. The  $h_c$  peak set the value of the lattice parameter,  $c$  (distance between heptazine discs within the column) to 3.76 Å representative of  $\pi$ - $\pi$  stacking of disc in the column. The calculated value of  $n$  (number of molecule per unit cell of hexagonal lattice) at 90 °C is found to be 1.28 suggesting the formation of hexagonal phase in a monomeric manner but with a significant volume of inter-digitations of fluid alkyl chains.

Further, the observed diffraction pattern in the temperature range 25 °C to 98 °C is very similar to that of at 90 °C (Figure 2.6). However, in the temperature range 25 °C to 45 °C, the higher-order reflections ((11), (20) and (21)) are very weak and also the (10) peak is broader than that of at 90 °C. Nonetheless, in the temperature range 45 °C to 98 °C, the higher-order reflections are developing and (10) peak gets sharper with increasing the temperature. Moreover, in the temperature range between 98 °C to 110 °C, the peak corresponding to (10) becomes broad and with no signature of hexagonal ( $Col_h$ ) phase, confirming the appearance of isotropic phase. In order to quantify the phase behaviour, correlation length has been calculated. The variation of correlation length ( $\xi$ ) and  $d$ -spacing corresponding to (10) peak (first small-angle peak) with temperature is shown in Figure 2.5b. The  $d$ -spacing is found to be decreased continuously from 34.00 Å at 25 °C to 30.62 Å at 110 °C. However, the variation of correlation length ( $\xi$ ) exhibit three clear regions: (I) 25 °C to 45 °C, (II) 45 °C to 98 °C and (III) 98 °C to 110 °C. The correlation length in the first region is about  $146.6 \pm 3.5$  Å and remains the same within this temperature range. However, in the second regime, it is found to increase rapidly from  $153.0 \pm 3.5$  Å at 50 °C and reaches a maximum to  $256.5 \pm 3.5$  Å at 90 °C and decreases to  $146.2 \pm 3.5$  Å at 98 °C and then dropped quickly in the third region to  $88.0 \pm 3.5$  Å at 110 °C.

These regions, I, II, and III correspond to  $Col_h$  phase with most likely glassy in nature,  $Col_h$  phase and isotropic liquid phase, respectively, which is also consistent with DSC and POM data. The behaviour of  $\xi$  with temperature could be understood as follows. As temperature increases, alkyl chain becomes more fluid which results into better packing in  $Col_h$  phase, and hence  $\xi$  increases as observed in the second region. However, at a very higher temperature, the thermal vibration breaks the lattices and leads to the isotropic liquid phase and thus  $\xi$  decreases as observed in the third region. In order to determine the exact positions of the heptazine

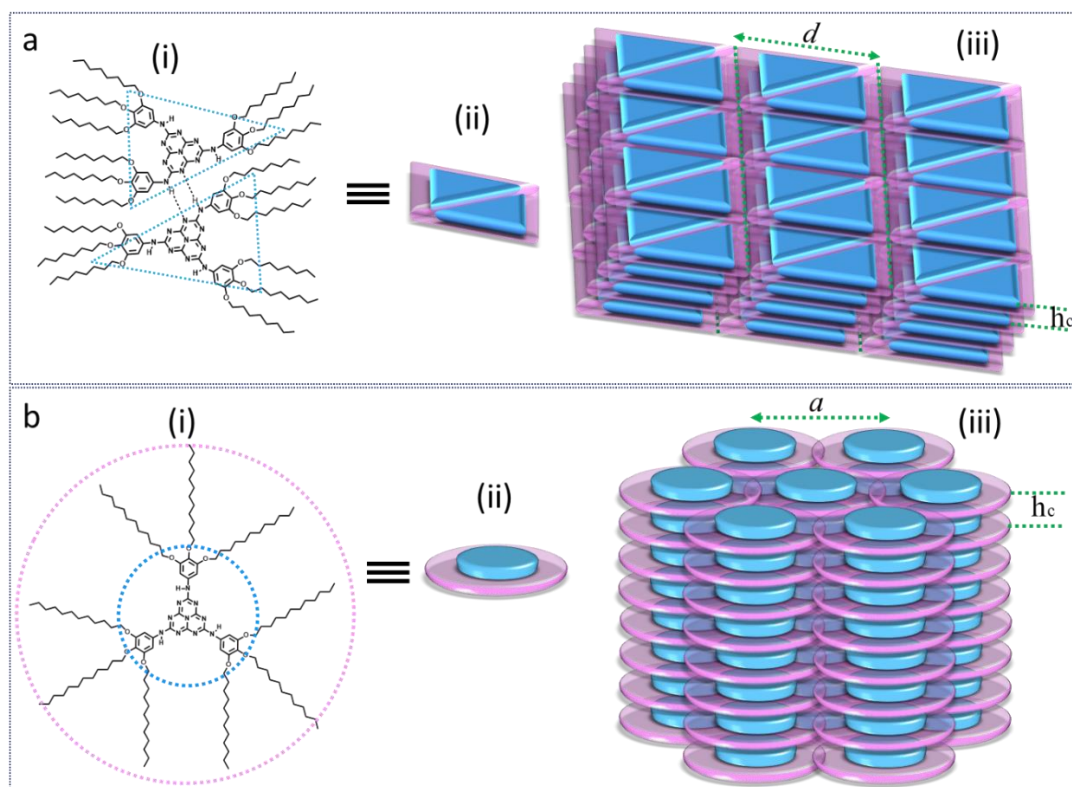


**Figure 2.7** Plausible molecular packing model: (a) compound **3b** in Sm phase, (i and ii) Hydrogen-bonded ribbon-like aggregates of heptazine ring (iii) which assembled to form a layer structure of Sm phase (b) compound **3c** in Col<sub>h</sub> phase (i and ii) molecule modeled as a disc which amassed into a column and (iii) form the columnar hexagonal structure.

molecule in the unit cell of the 2D hexagonal lattice, electron density maps were reconstructed from the diffraction pattern. The electron density map as shown in Figure 2.5e is produced by taking the first four peaks of the small-angle region of the Col<sub>h</sub> phase at 90 °C. Red color represents the highest electron density and dark blue the lowest. Technically, the Miller indices of the peaks and corresponding intensities are used to build-up the map (Table 2.1).

In brief, compound **3b** exhibits Sm structure in the mesophase. The Sm structure most possibly could be induced by the hydrogen-bonded ribbon-like aggregation of the heptazine ring (Figure 2.7a (i)). The schematic of the most plausible layer structure of the Sm phase is shown in Figure 2.7a. In contrast to **3b**, **3c** showed Col<sub>h</sub> phase and further the X-ray diffraction results, electron density map and the calculated value of  $n$  (number of molecule per unit cell) allows the Col<sub>h</sub> phase to be schematically drawn as shown in the Figure 2.7b.

**Table 2.1** Phase behaviour, Miller Indices, lattice constants, and *d*-spacing observed from the X-ray diffraction studies for compound **3c**.

Compound	Mesophase	Lattice constants (Å)	$d_{\text{obs}}^a$ (Å)	$d_{\text{cal}}^b$ (Å)	MI <sup>c</sup> (hk)	RI (Φ)(M) <sup>c</sup>
<b>3c</b>	Col <sub>h</sub> at 90 °C	$a = 37.04$	32.07	32.08	10	22133(0)(6)
			18.54	18.52	11	908(π)(6)
			16.02	16.04	20	728(π)(6)
			12.21	12.12	21	658(0)(12)
			4.97		h <sub>a</sub>	
			3.76		h <sub>c</sub>	

<sup>a</sup> $d_{\text{obs}}$ : experimental *d*-spacing; <sup>b</sup> $d_{\text{cal}}$ : calculated *d*-spacing by using the relation for Col<sub>h</sub>:

$\frac{1}{d_{\text{cal}}^2} = \left[ \frac{4}{3} \left( \frac{h^2 + hk + k^2}{a^2} \right) + \frac{l^2}{c^2} \right]$ ; *h*, *k*: Miller indices of observed reflections; *a*, unit cell parameter, h<sub>a</sub>: alkyl chain-chain correlation; h<sub>c</sub>: core-core correlation. <sup>c</sup>Abbreviations: MI- Miller Indices; RI (Φ)(M)- Relative Intensity (Phase value)(Multiplicity).

The observed Sm to Col<sub>h</sub> phase transformation with an increasing peripheral chain length from **3b** to **3c** could be understood as follows. As peripheral chain length increases, alkyl chains become more flexible and as a result, they cannot better accommodate in the Sm phase. Therefore, the hydrogen bonding breaks and in consequence each molecule behaves as a disc that assembled itself and leads to the formation of hexagonal phase. Hence, the generation of the Sm and Col<sub>h</sub> phase is attributed to the formation of hydrogen-bonded ribbon and disc-like (with no hydrogen bonding) self-assembled structures. Further, this type of lamellar (Sm) to hexagonal transformation is also seen in some lyotropic systems.<sup>40</sup>

#### 2.1.3.4 Photophysical, electrochemical and theoretical studies

The photophysical properties of compounds **3b** and **3c** were carried out both in solution (chloroform as a solvent) (Figure 2.8) as well as in solid-state. In solution state, compounds **3b** and **3c** show well-resolved two peaks at 270 & 330 nm which are likely due to  $\pi$ - $\pi^*$  and  $n$ - $\pi^*$  transitions, respectively.<sup>41</sup> The emission spectra, however, exhibited one peak centred at 446 nm for **3b** and 487 nm for **3c** along with a shoulder peak at 412 nm. On the other hand, in the solid-state, compounds **3b** and **3c** show their respective absorption peaks at 274 & 334 nm while the emission spectra showed maxima centred at 475 nm for both the compounds. It is observed that absorption peaks were red-shifted by 4 nm in solid-state than in the solution

state. However, in the solid-state emission spectra, the peak was red-shifted (446 to 475 nm) for compound **3b** and blue shifted (487 to 475 nm) for compound **3c** with respect to the solution state. The blue shift for compound **3c** is likely due to allowed excitonic transition in aggregates with nearly parallel transition dipoles in the solid-state as reported earlier.<sup>42</sup> These photo-physical behaviours are found to be well-matched with the previously reported monomeric heptazine derivatives.<sup>14</sup> The absorption and emission studies of the compound are done in different solvents *viz.* hexane, carbon tetrachloride, toluene, chloroform, dichloromethane, tetrahydrofuran and ethyl acetate (Figure 2.9). The concentration was kept the same ( $4.75 \times 10^{-5}$  M) for all the solutions of compound **3c**. There were changes in absorption maxima as well as in emission maxima on varying the solvents. The compound was found to be more emissive in non-polar solvents in comparison to polar solvents. The reason is obvious that in non-polar solvents aggregation is more as compared to the polar solvents and this compound is good emissive in the aggregated state. The absorption and emission peaks values of compound **3c** in different solvents are summarized in Table 2.2.

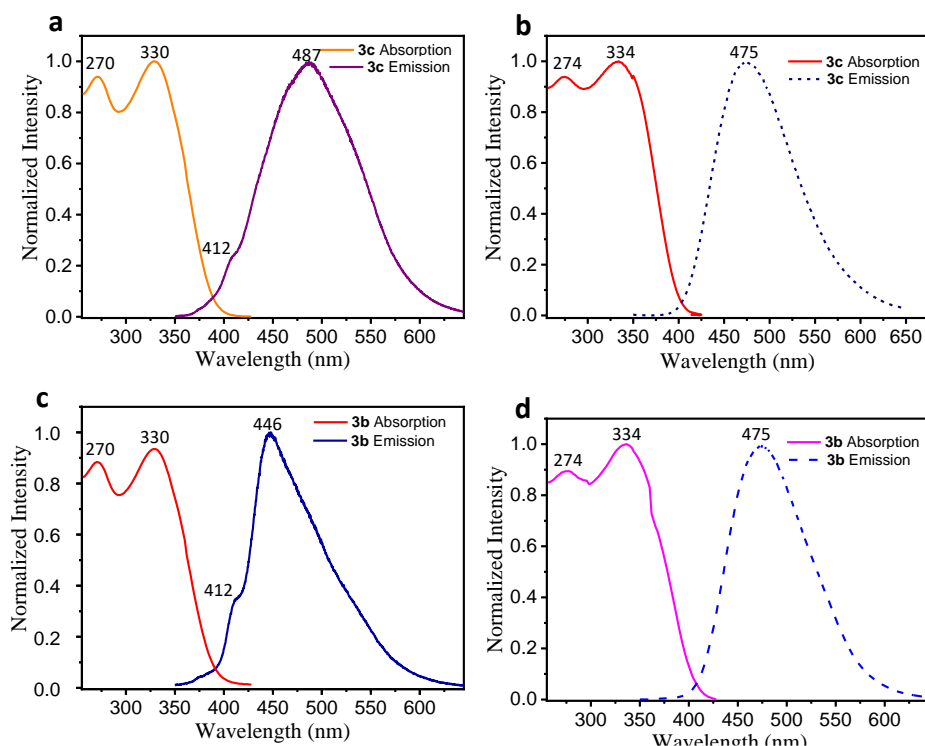


**Figure 2.8** Absorption (left) and Emission spectra (right): (a) in solution state (chloroform,  $1.0 \times 10^{-5}$  M) for compound **3c** (b) in solid state for compound **3c** (c) in solution state of compound **3b** (d) in solid state of compound **3b**.

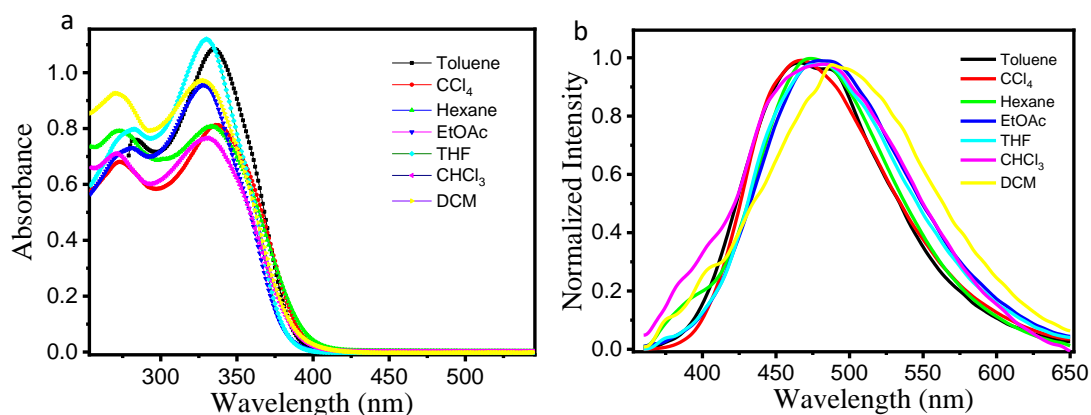


**Figure 2.9** (a) The UV-Vis (left side) and (b) fluorescence (right side) spectra of compound **3c** in various solvents.

**Table 2.2** UV-Vis and fluorescence peaks of compound **3c** in different solvents.

Solvent	Absorption Peaks (nm)	Emission Peaks (nm) <sup>b</sup>
Hexane	272, 333 <sup>a</sup>	475
Carbon tetrachloride	272, 337 <sup>a</sup>	470
Toluene	282, 335 <sup>a</sup>	469
Chloroform	271, 330 <sup>a</sup>	486
Dichloromethane	271, 328 <sup>a</sup>	489
Tetrahydrofuran	282, 330 <sup>a</sup>	481
Ethylacetate	281, 328 <sup>a</sup>	479

<sup>a</sup>absorption maxima ( $\lambda_{\max}$ ). <sup>b</sup>Emission peaks are observed when the molecules are excited at their corresponding  $\lambda_{\max}$ .

Compounds **3b** and **3c** were also found to be highly emissive (the aggregation-induced emission (AIE)) in the solid-state, while, in the solution state the compound becomes non-emissive or weakly emissive (Figure 2.10). The AIE behaviour is also indicated by its increased fluorescence intensity in solid-state when compared to the solution state (shown for compounds **3b** and **3c**). The emission intensity in solution form is very less, almost parallel to the abscissa (Figure 2.10). Similarly, when the compound is visualized under 365 nm UV light,

in solid-state, it shows cyan colored luminescence while in solution it shows almost no color (Figure 2.10 insets). The AIE properties of the heptazine derivative were confirmed by investigating the emission spectra of their dilute solutions in a THF-water solvent mixture with varying water fractions (Figure 2.11). As the compound is soluble in THF and as the amount of water is increasing, the aggregation of the compound goes on increasing. In pure THF and up to 24%, the compound showed almost no emission on illumination under 360 nm UV light as shown by the fluorescence spectra are nearly parallel to the abscissa, while the intensity goes on increasing as the water content increases and the fluorescence intensity abruptly increases above 85%. The emission intensity at 95% water fraction is 690 fold higher than at in pure THF. The compound show sky blue emission in their pristine state (Figure 2.11b inset).

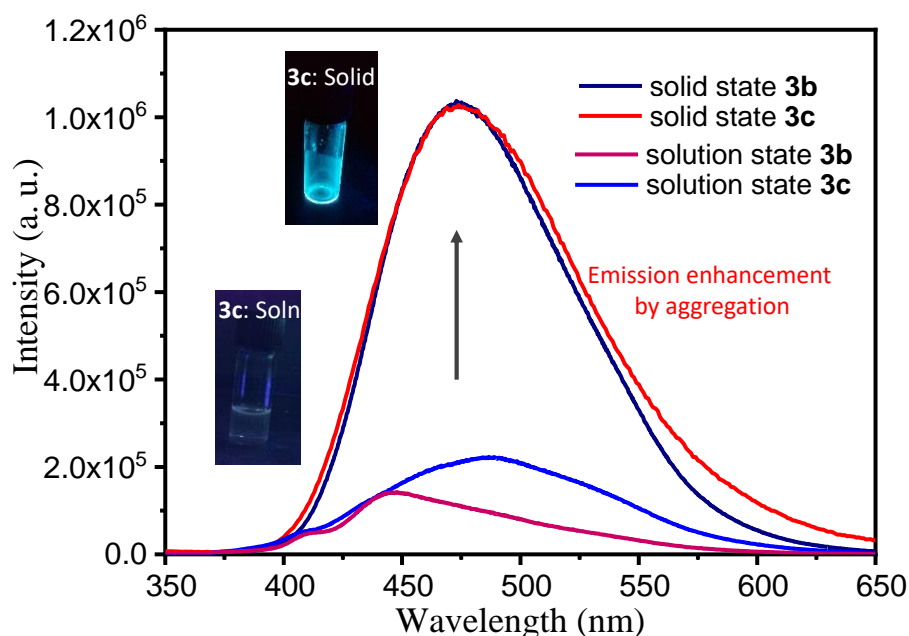


**Figure 2.10** Fluorescence spectra of **3b** and **3c** in the solid-state and solution state (chloroform) with a molar concentration of  $1.0 \times 10^{-5}$  M at their  $\lambda_{\text{max}}$  (abs) excitations

This observation clearly demonstrates the AIE phenomena showed by the compound as further evidenced by the fluorescence intensity plots (Figure 2.11a). Figure 2.11b inset shows the emission images of the compound in different water fractions under UV light illumination. The solution starts to show sky blue emission when the water content exceeding from 24% and the intensity becomes maximum for the water fraction surpassing 95%.

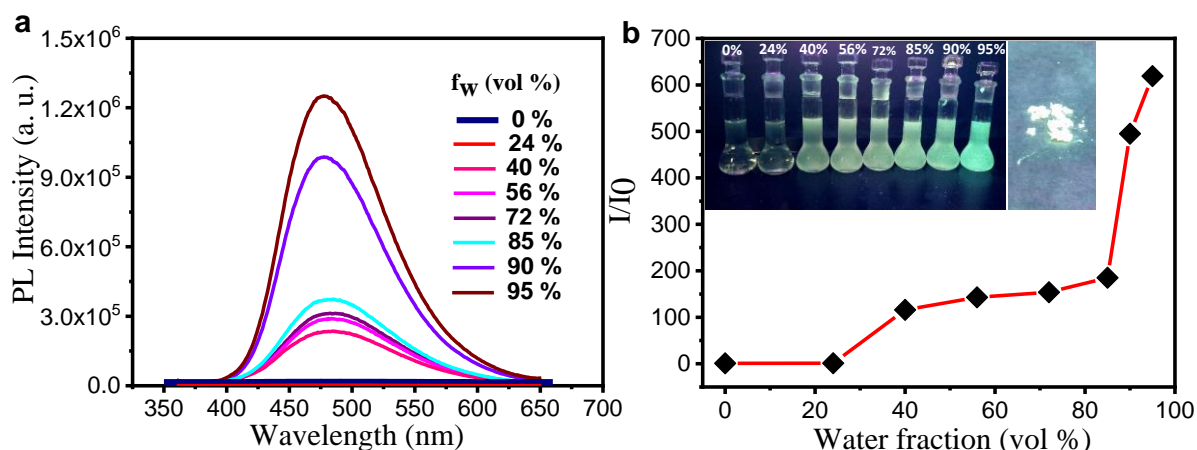


**Figure 2.11** (a) Fluorescence intensity plots of compound **3c** with varying water fractions from 0% to 95% (b) Plot of  $I/I_0$  versus water fractions ( $f_w$ ) where  $I_0$  = emission intensity in pure THF solution. Inset shows the emission images displays bluish-green color under the illumination of 360 nm UV light.

In order to probe the electronic properties of the heptazine derivatives, the electrochemical behaviour of compound **3c** has been studied by cyclic voltammetry study. It is showing reversible oxidation and reduction potential waves (Figure 2.12). Assuming that the oxidation and reduction potentials can typically be correlated with the potentials of its HOMO (valence band) and LUMO (conduction band), respectively, the electrochemical bandgap for compound **3c** is 2.0 eV, lesser than its optical bandgap ( $\Delta E_{UV} = 1240/\lambda_{onset} = 2.91$  eV) calculated from the absorption edge (425 nm) of the UV-vis spectrum.

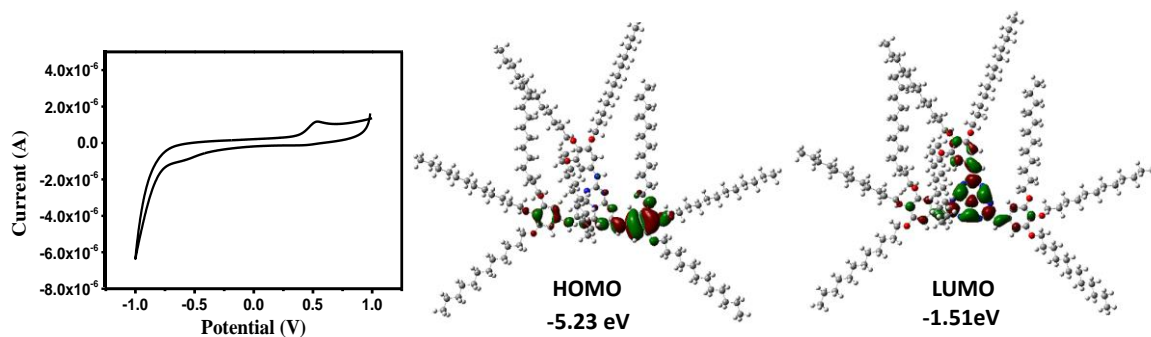


**Figure 2.12** Cyclic Voltammogram of compound **3c** in anhydrous dichloromethane solution of tetrabutylammonium hexafluorophosphate (0.1 M) at a scanning rate of 100 mV/s and its DFT optimized spatial distribution and energy levels of frontier molecular orbitals.

Density functional theory (DFT) calculations were performed by using Gaussian 09 software with a B3LYP/6-31G (d,p) basis set to understand the geometrical and electronic structures of compound **3c**. The frontier molecular orbitals of compound **3c** are shown in Figure 2.12. The HOMO of the compound is predominantly located on the electron-rich tri-alkoxy benzene ring while the LUMO is distributed on the electron-deficient heptazine core. The well-separated HOMO and LUMO on the electron-rich and electron-deficient part, respectively, provide separate transporting channels for holes and electrons and results in better EL performance.

### 2.1.3.5 Electroluminescence properties

Figure 2.13 illustrates the studied solutions processed deep-blue OLED devices with four different hosts and their corresponding energy level diagrams. The device configuration is ITO/PEDOT:PSS/Host:Emitter/TPBi/LiF/Al with different dopant concentrations. The OLED devices were composed of a 125 nm indium tin oxide (ITO) anode layer, a 35 nm poly(3,4-ethylene-dioxythiophene)-poly(styrenesulfonate) (PEDOT:PSS) hole injection layer (HIL), a 20 nm single emissive layer (EML) with different concentrations of 1, 3, 5, and 100 wt% doped in 4,4'-Bis(9-carbazolyl)-1,1'-biphenyl (CBP) host, a 30 nm 1,3,5-tris(N-phenylbenzimidazol-2-yl) benzene (TPBi) electron transporting layer (ETL), a 1 nm lithium fluoride (LiF) electron injection layer (EIL), and a 100 nm aluminum (Al) cathode layer.

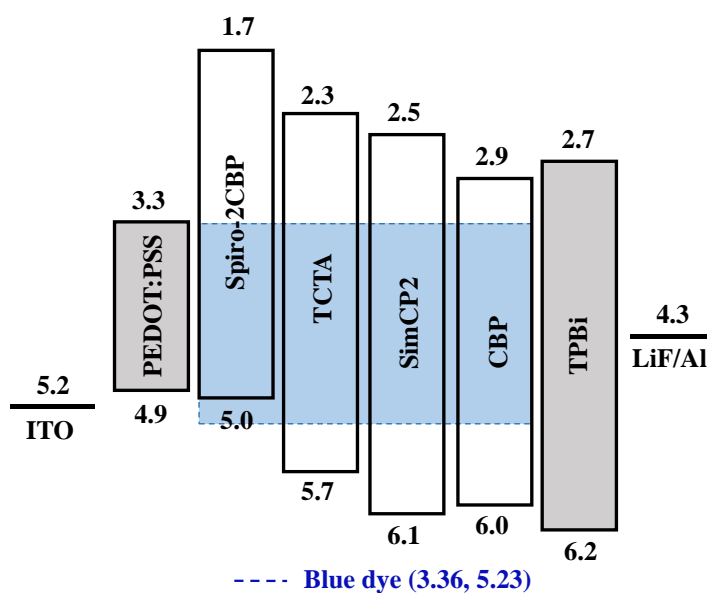


**Figure 2.13** Schematic diagram of the energy levels of the studied solution-processed deep-blue OLED devices composed with four different hosts Spiro-2CBP, TCTA, SimCP2, and CBP.



Besides the CBP host, three other host molecules, 4,4',4''-tri(N-carbazolyl)triphenylamine (TCTA), 2,7-Bis(carbazol-9-yl)-9,9-spirobifluorene (Spiro-2CBP), and 3,5-di(9H-carbazol-9-yl) tetraphenylsilane (SimCP2) were also studied herein. The doping concentration of the fluorescent deep-blue fluorescent emitter strongly influences the device efficiency and EQE. Table 2.3 summarizes the effects of the host material and guest concentration on the electroluminescence (EL) characteristics, including operation voltage (OV), power efficiency (PE), current efficiency (CE), external quantum efficiency (EQE), and CIE coordinates at brightness of 100  $\text{cd m}^{-2}$ , and the maximum luminance. SimCP2 host containing OLED device displayed 0.1% EQE at 100  $\text{cd m}^{-2}$ , which was increased to 0.6%, 0.8% and 1.6% as the host was altered to TCTA, Spiro-2CBP, and CBP, respectively. These were all based on a 3 wt% doping concentration. Moreover, the EQE of the CBP host containing device increased from 1.1 to 1.6% as the doping concentration was increased from 1 to 3 wt%. Furthermore, as the concentration increased to 5 wt%, the EQE of the device dropped to 1.1%, which may be attributed to triplet-triplet annihilation (TTA) and concentration-quenching. In host-guest systems used in OLEDs, the role of triplet diffusion decreases with decreasing emitter concentration.<sup>43,44</sup>

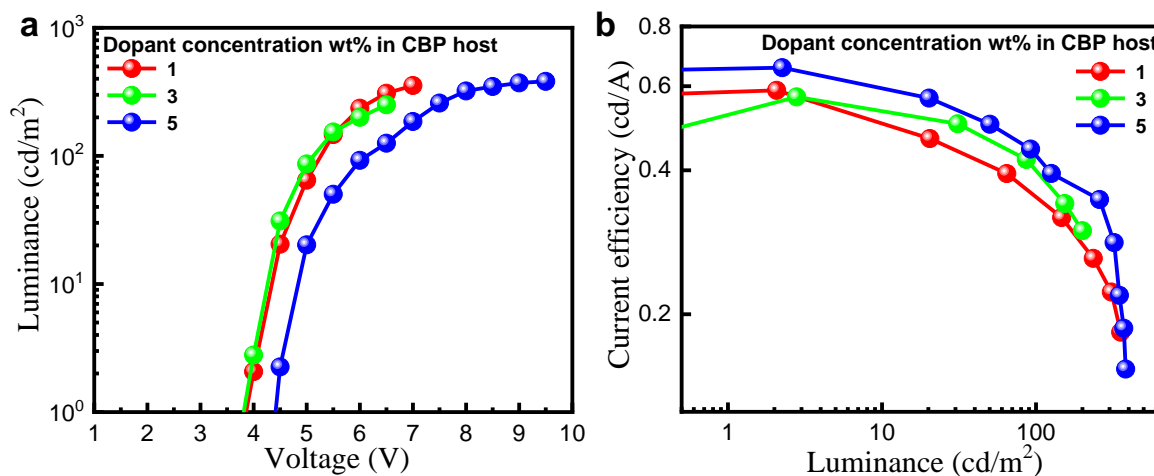


**Figure 2.14** Dopant concentration effect on (a) Luminance-voltage and (b) current efficiency-luminance plots of the solution-processed deep-blue OLED devices using CBP host with 1, 3, and 5 wt% dopant concentrations.

The different employed host materials show different effects on the device efficiency and EQE (Table 2.3). For example, at 3 wt%, the optimized doping concentration, the best performing CBP containing device attained a power efficiency of  $0.3 \text{ lm W}^{-1}$ , a current efficiency of 0.4

$\text{cd A}^{-1}$ , an EQE of 1.6%, and CIE coordinates of (0.17, 0.08) at brightness  $100 \text{ cd m}^{-2}$ , as shown in Figure 2.14 and 2.15a. By changing the host to TCTA, the EQE of the device decreased judiciously to 0.6% and CIE coordinates to (0.17, 0.11) with a maximum luminance of  $889 \text{ cd m}^{-2}$ . Furthermore, as the host changed from CBP to Spiro-2CBP, the power efficiency and EQE dropped to  $0.2 \text{ lm W}^{-1}$  and 0.8%, respectively with CIE coordinates of (0.19, 0.09). The SimCP2 based device exhibited an EQE of 0.1% and CIE coordinates of (0.22, 0.19) with a maximum luminance of  $127 \text{ cd m}^{-2}$ .

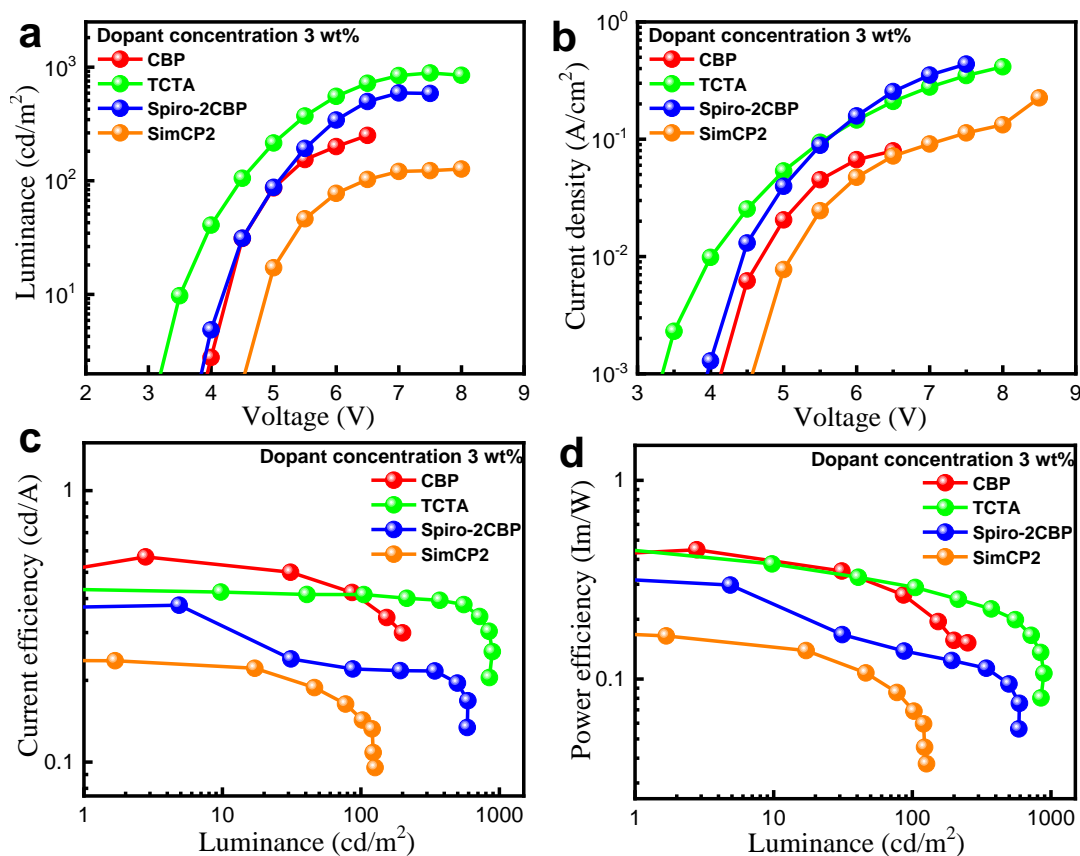


**Figure 2.15** Hosts effect on (a) Luminance-voltage, (b) current density-voltage, (c) current efficiency-luminance, and (d) power efficiency-luminance plots of the solution-processed blue OLED devices using CBP, TCTA, Spiro-2CBP, and SimCP2 hosts with 3 wt% dopant concentration.

The reason why the CBP host containing devices showed the best performance, as revealed in Table 2.3, may be attributed to three important factors in the device architecture. First, the CBP host has a lowest unoccupied molecular orbital (-2.9 eV) lower than that of TPBi (-2.7 eV), due to which the resulting device architecture possesses a most favourable electron injection

pathway, i.e. -0.2 eV electron trap, whereas the other three hosts have an electron injection barrier from 0.2 to 1.05 eV. This architecture would facilitate the injection of electrons into the desired emissive layer to counterbalance the hole injection, leading to high device efficiency. Second, Figure 2.13 shows that the overlapping area for the host CBP is much greater than that of the other employed hosts TCTA, Spiro-2CBP or SimCP2. This reveals that the CBP host would mostly effectively transfer energy to the guest, enabling an effective host-to-guest energy transfer mechanism, resulting in a higher EQE as compared to the other counterparts. Third, the CBP host has a comparatively higher hole and electron mobilities than the other hosts. The high mobility of CBP would lead to more effective carrier recombination and hence a higher EQE and device efficiency.

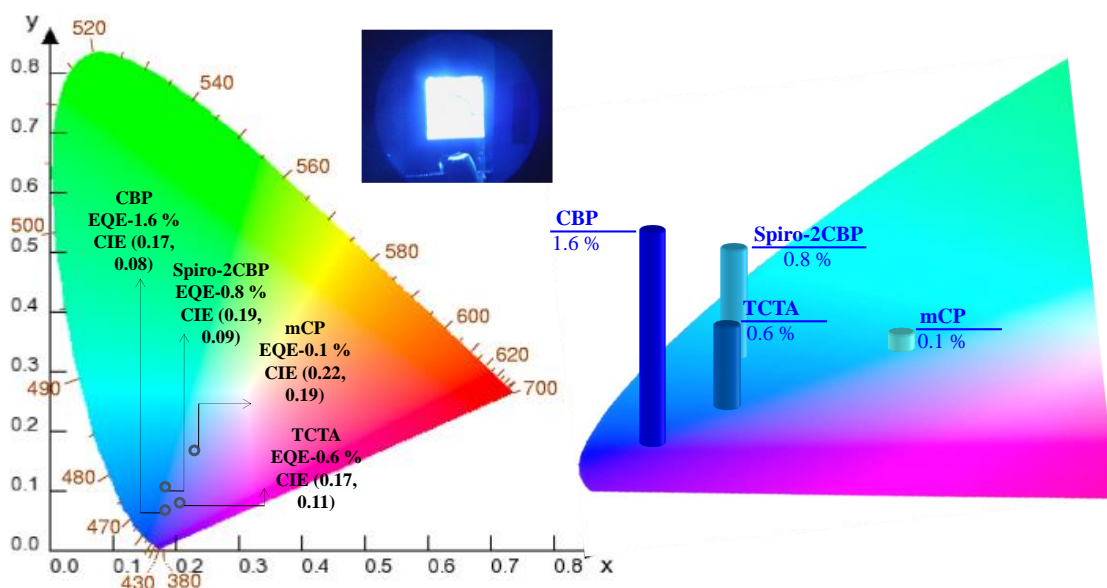


**Figure 2.16** CIE coordinates obtained for the device at 3 wt% dye concentration with CBP, Spiro-2CBP, mCP and TCTA host. Inset shows the image of the fabricated device.

Current density-voltage-luminescence (I-V-L) plots of the devices with different hosts are shown in Figure 2.15 and the pertinent EL parameters are tabulated in Table 2.3. The relatively low turn-on voltages and high current densities were observed for the TCTA, Spiro-CBP, and SimCP2 based devices when compared to the corresponding CBP host device at dopant 3 wt%. However, the CBP devices showed poor luminance when compared to the corresponding devices. This may be attributed to the leakage of charge carriers at the interface of respective electrodes without the formation of excitons in the emitting layer. The high current density of

the resultant OLED devices may be attributed to effective hole-transport feasibility in the devices.

The CBP and Spiro-2CBP host containing devices showed deep-blue emission with CIE coordinates of (0.17, 0.08) and (0.19, 0.09), respectively, while the TCTA and SimCP2 host containing devices showed bright blue emission with CIE coordinates of (0.17, 0.11) and (0.22, 0.19), respectively, as shown in Figure 2.16. The CIE coordinates of the CBP and Spiro-2CBP based devices are in good agreement with  $CIE_y < 0.10$  (Commission International de

**Table 2.3** Effects of different host materials and doping concentrations on the device parameters.

Host	Dopant (wt%)	OV (V) <sup>a</sup>	PE <sup>b</sup> (lm W <sup>-1</sup> )	CE <sup>c</sup> (cd A <sup>-1</sup> )	<sup>d</sup> EQE (%)	<sup>e</sup> CIE <sub>xy</sub> coordinates	<sup>f</sup> L <sub>max</sub> (cd/m <sup>2</sup> )
<b>CBP</b>	1	5.2	0.2	0.4	1.1	(0.17,0.07)	355
	3	5.1	0.3	0.4	1.6	(0.17, 0.08)	251
	5	6.1	0.2	0.4	1.1	(0.17, 0.08)	382
	100	-	-	-	-	-	5
<b>TCTA</b>	3	4.5	0.3	0.4	0.6	(0.17, 0.11)	889
<b>Spiro-2CBP</b>	3	5.1	0.1	0.2	0.8	(0.19, 0.09)	592
<b>SimCP2</b>	3	6.4	0.1	0.1	0.1	(0.22, 0.19)	127

<sup>a</sup>Operation voltage (OV), <sup>b</sup>power efficiency (PE), <sup>c</sup>current efficiency (CE), <sup>d</sup>external quantum efficiency (EQE) and CIE coordinates at 100 cd/m<sup>2</sup>. <sup>f</sup>Maximum luminance (L<sub>max</sub>) of solution-processed blue OLED devices.

L'Eclairage (CIE)) and match the National Television System Committee (NTSC) standard blue CIE (x, y) coordinates of (0.14, 0.08) for display applications.<sup>45</sup> The emission became deeper, the electroluminescent spectra shifted towards a lower wavelength and the EQE became higher as the dopant concentration decreased from 5 to 3 wt%, as shown in Figure 2.17a. Furthermore, at 3 wt% doping concentration, the synthesized dye showed CIE coordinates of (0.17, 0.08) and EQE of 1.6%, and as the dopant concentration further decreased to 1 wt%, the EQE dropped to 1.1%, but the emission was even slightly deeper, with CIE of (0.17, 0.07). The reason why the resulting device shows an extremely marked blue-shift may

be attributed to an effective emitter dispersion (Figure 2.17b). The employed host can be utilized to disperse the emitter to prevent the bathochromic-shift due to the increasing statistical probability that emitters are paired or to aggregation at high guest concentrations.

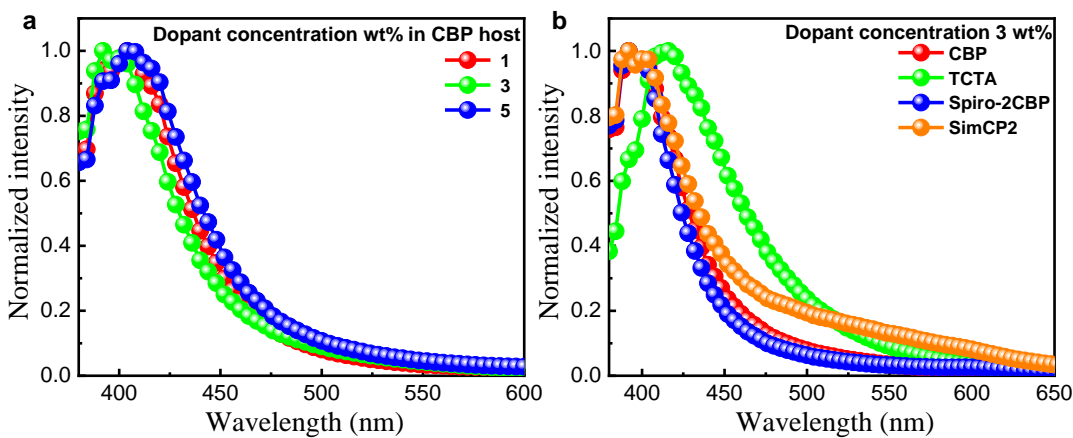


**Figure 2.17** (a) Doping concentration effects on the EL spectra of the solution-processed blue OLED devices using CBP host with 1, 3, and 5 wt% dopant concentration at brightness 100 cd m<sup>-2</sup>. (b) Host effect on the electroluminescence (EL) spectra of the devices containing the sky-blue emitter of the solution-processed blue OLED devices at 3 wt% dopant concentration and brightness 100 cd m<sup>-2</sup>.

### 2.1.3.6 Conductivity measurements

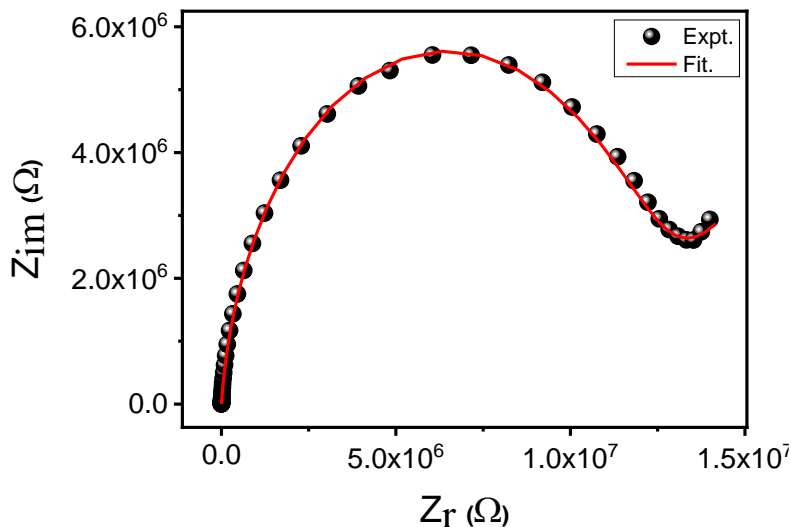


**Figure 2.18** Impedance  $Z_{im}$  vs  $Z_r$  of compound **3c** in their Col<sub>h</sub> phase (at 90 °C) and their corresponding circuit. Expt. represents plot obtained from measurement, Sim. represents plot obtained after fitting through software (“Nano-electronic Measurement Systems (NeMS), India”).

Conductivity measurements for compound **3c** were performed by ac impedance spectroscopy. The conductivity value obtained for compound **3c** in the Col<sub>h</sub> is  $1.12 \times 10^{-7} \text{ Sm}^{-1}$  (Figure 2.18). The conductivity values were calculated by using formula  $\sigma = d/(R.A)$ , where  $\sigma$  = Conductivity in  $\text{S m}^{-1}$ ,  $d$  = thickness of the cell,  $A$  = area of the cell, and  $R$  = bulk resistance.

### 2.1.4 Conclusions

This work presented the first report of heptazine-based DLCs, possessing a stable Col<sub>h</sub> phase and a smectic phase at ambient temperature. They are strong blue light emitters when fabricated into thin films. The derivatives showed aggregation enhanced emission behaviour. The solution-processed host-guest OLEDs, by using the columnar emitter in the emissive layer have been fabricated. The efficiency of the device has been tuned by varying the host molecule and the emitter concentration. At 3 wt% emitter concentration, the best performing CBP containing device attained a power efficiency of  $0.3 \text{ lm W}^{-1}$ , a current efficiency of  $0.4 \text{ cd A}^{-1}$ , an EQE of 1.6% and CIE coordinates of (0.17, 0.08) at brightness  $100 \text{ cd m}^{-2}$ . Hence, heptazine-based discotic liquid crystals will contribute for the further development of AIE-based blue emitters. The conductivity of the heptazine derivative in the columnar hexagonal phase is measured by AC conductivity method and found to be  $1.12 \times 10^{-7} \text{ Sm}^{-1}$ . Such materials are expected to be better candidates for future optoelectronic applications with the advantages that LCs offer.

***Acknowledgements.** The OLED device fabrication and measurement studies have been carried out in collaboration with Prof. J. H Jou's group at National Tsing Hua University, Taiwan and is greatly acknowledged and respected. Dr. Santosh Prasad Gupta (at Patna University) is duly acknowledged for the analysis of XRD data. We thank Dr. Kamalakannan Kailasam's group from INST Mohali for helping us in this project.*

### 2.1.5 Experimental section

**2.1.5.1 Synthesis of cyameluric chloride (1).** Heptazine (cyameluric) chloride ( $\text{C}_6\text{N}_7\text{Cl}_3$ ) **1** was synthesized from the polymeric material, melon which in turn synthesized from melamine. When melamine was heated in a closed crucible at  $330^\circ\text{C}$  in the furnace for 2 days, it condensed to form a white-beige colored solid, melem. On further heating the obtained beige-colored solid at  $520^\circ\text{C}$  for 1 day, it formed a light yellow-colored polymeric product called

the melon. The polymeric melon (10 g) was treated with 2.5 M aqueous KOH (250 ml) at 110 °C for 12 h, forming white-colored material, cyameluric acid (5g) which then further treated with PCl<sub>5</sub> (11.35g, 3 equiv.) and POCl<sub>3</sub> (100 ml) at 110 °C for 6-8 h under nitrogen atmosphere in ultra-dried conditions to form cyameluric chloride **1** having a bright yellow color.

**Cyameluric chloride:** <sup>13</sup>C NMR: δ 159.55 (CN<sub>3</sub>), 176.29 (CClN<sub>2</sub>); FTIR (ATR, cm<sup>-1</sup>): 1600, 1500, 1300, 1200, 938, 822, 648. UV-Vis (λ in nm): 310. Photoluminescence (λ in nm): 468.

**2.1.5.2 Synthesis of compounds 3a-c.** Cyameluric chloride (**1**) (50 mg, 1 equiv.) and 3,4,5-trialkoxy anilines (4 equiv.) were dissolved separately in 1ml and 4 ml dry THF in double-neck and one neck round bottom flask (R.B) in a glove box, respectively. The 3,4,5-trioctyloxy aniline solution was dissolved in dry THF by heating and then added to the cyameluric chloride solution dropwise at room temperature while the reaction starts immediately, as observed by a fast color change from yellow to turbid brown. After stirring for 15 minutes at room temperature, triethylamine (0.1 ml) was added to consume HCl formed during the reaction. Then the reaction mixture was stirred overnight. Subsequently, the yellow precipitate was filtered and repeatedly washed with THF, CHCl<sub>3</sub> and dried in a vacuum. After washing with several solvents, the compound was not able to purify as indicated by their NMR spectra.

**Compound 3a.** Elemental analysis for C<sub>33</sub>H<sub>36</sub>N<sub>10</sub>O<sub>9</sub>: calculated (%) – C 55.30, H 5.06, N 19.54; found (%) - C 57.85, H 6.04, N 17.85. FT-IR (cm<sup>-1</sup>): 3319.50, 3102.06, 2991.97, 2974.50 2938.82, 2840.30, 2484.94, 1667.00, 1601.60, 1499.36, 1444.66, 1417.42, 1375.82, 1347.30, 1302.01, 1123.80, 1041.06, 1000.63, 953.18, 929.67, 868.37, 835.85, 800.80, 755.71, 735.03, 719.78, 677.22, 627.11, 589.99, 510.46, 490.46, 444.15, 434.28, 415.97. <sup>1</sup>H NMR (400 MHz, dms<sub>o</sub>-d<sub>6</sub>, δ in ppm): δ 10.15-9.95 (m, 3H, -NH protons), δ 7.18 (s, 6H, aromatic protons), δ 3.76 (s, 18H), δ 3.65 (s, 9H), δ 3.40 (peak present in even reactant 3,4,5 trimethoxy aniline from sigma ), δ 4.29 (q, THF solvent), δ 1.18-1.14 (t, THF solvent). <sup>13</sup>C NMR (100 MHz, CDCl<sub>3</sub>, δ in ppm): 162.90, 162.68, 156.17, 153.05, 151.09, 135.12, 134.5, 99.91, 79.65, 60.67, 56.53, 56.43, 46.05, 9.29.

**Compound 3b.** Elemental analysis for C<sub>96</sub>H<sub>162</sub>N<sub>10</sub>O<sub>9</sub>: calculated (%) – C 72.05, H 10.20, N 8.75; found (%) - C 72.07, H 10.31, N 9.01. FT-IR (cm<sup>-1</sup>): 3378.99, 3134.21, 3075.18, 2955.30, 2925.71, 2855.67, 1643.13, 1598.40, 1539.26, 1498.31, 1463.9, 1434.88, 1344.25, 1296.31, 1230.00, 1114.68, 1042.37, 806.40, 723.37, 624.8. <sup>1</sup>H NMR (400 MHz, CDCl<sub>3</sub>, δ in ppm): δ

8.12-7.53 (m, 3H, -NH protons),  $\delta$  6.90-6.79 (m, 6H, aromatic protons),  $\delta$  3.95-3.91 (m, 18H),  $\delta$  1.78 (s, 18H),  $\delta$  1.47 (s, 18H),  $\delta$  1.30 (s, 72H),  $\delta$  0.91-0.88 (m, 27H).  $^{13}\text{C}$  NMR (100 MHz,  $\text{CDCl}_3$ ,  $\delta$  in ppm): 162.73, 162.58, 153.21, 152.91, 135.09, 132.21, 132.00, 102.62, 102.09, 101.27, 101.02, 69.39, 69.30, 69.23, 69.14, 31.95, 31.89, 30.37, 29.62, 29.48, 29.42, 29.36, 26.22, 26.17, 22.71, 14.13.

**Compound 3c.** Elemental analysis for  $\text{C}_{132}\text{H}_{234}\text{N}_{10}\text{O}_9$ : calculated (%) – C 75.30, H 11.20, N 6.65; found (%) - C 75.20, H 11.51, N 7.05. FT-IR ( $\text{cm}^{-1}$ ): 3384.70, 2954.64, 2923.00, 2852.87, 1644, 1595.31, 1540.60, 1498.68, 1463.9, 1437.55, 1348.90, 1291.4, 1231.23, 1116.22, 1038.3, 804.47, 720.13.  $^1\text{H}$  NMR (400 MHz,  $\text{CDCl}_3$ ,  $\delta$  in ppm):  $\delta$  7.91-7.39 (m, 3H, -NH protons),  $\delta$  6.88-6.77 (m, 6H, aromatic protons),  $\delta$  3.99-3.91 (m, 18H),  $\delta$  1.80-1.78 (m, 18H),  $\delta$  1.48-1.42 (m, 18H),  $\delta$  1.29-1.27 (m, 144H),  $\delta$  0.92-0.88 (m, 27H).  $^{13}\text{C}$  NMR (100 MHz,  $\text{CDCl}_3$ ,  $\delta$  in ppm): 162.63, 162.54, 153.21, 152.93, 135.93, 132.19, 102.63, 102.02, 101.37, 101.01, 69.31, 69.16, 31.97, 30.40, 29.74, 29.56, 29.44, 26.20, 22.73, 14.15.



## 2.2 Part B: Fluorescent H-bonded columnar liquid crystals based on heptazine derivatives

### 2.2.1 Introduction

Non-covalent interactions, in particular,  $\pi$ - $\pi$  interactions are the basis for the formation of 1D columnar (col) assemblies and realizing new classes of discotic liquid crystals (DLCs).<sup>1,2,4,46–48</sup> The other successful supramolecular approach to obtain such col organization is the combination of  $\pi$ - $\pi$  stacking and hydrogen (H) bonded interactions.<sup>49</sup> The dynamic and directional nature of the H-bond provides many advantages for the development of new functional DLCs. This approach has made widespread the use of DLCs which are often limited by lengthy synthetic routes and difficult purification steps. In 1989, Kato et al.<sup>50–52</sup> and Lehn et al.<sup>53</sup> reported the first examples of supramolecular LCs consisting of complementary intermolecular H-bonding between two different molecules (two-component systems). Sierra<sup>54–59</sup> and other groups<sup>60–64</sup> also investigated several H-bonded LCs that form well-defined supramolecular col assemblies. It is worth mentioning that for the formation of two-component H-bonded LCs, both the components are required to have appropriate H-donor and acceptor sites which can be used for self-assembly and molecular recognition. Such systems tend to self-assemble into mesophases, though they are not necessarily mesogenic by themselves.

The disc-shaped  $C_3$ -symmetric heptazine core ( $C_3N_7$ ) possesses 7 nitrogen (N) atoms, and the peripheral N-atoms can take part in H-bonding as a H-bond acceptor. If this core can be further modified by substituting with a hydrogen donor group like an  $-NH$  group, then the heptazine derivative can act as a H-bond donor and acceptor molecule and is a suitable candidate for the formation of H-bonded supramolecular complexes with its complementary systems. To our knowledge, there have been no attempts to construct rigid DLCs in heptazine systems involving H-bonding interactions by considering their strength and bonding directionality.

### 2.2.2 Objectives

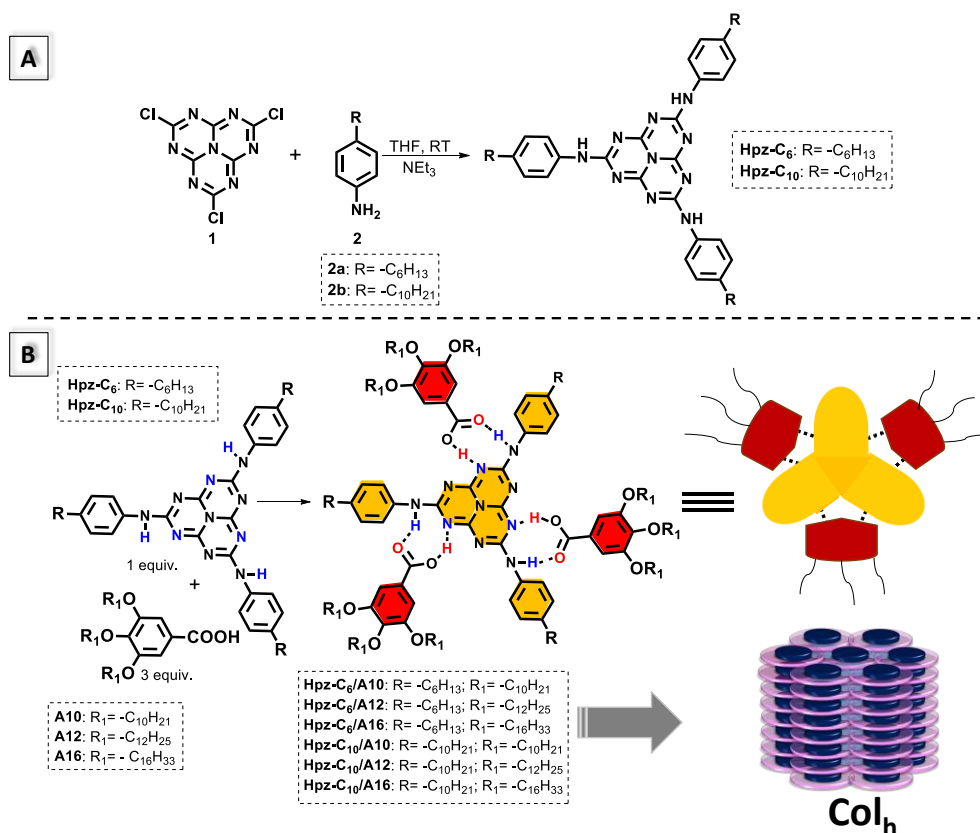
In two-component H-bonded systems, if one of them is intrinsically fluorescent, then new

FLCs can be achieved through non-covalent H-bonded interactions. In the literature, there are very few reports of such FLC systems achieved through H-bonding interactions.<sup>58,59,61–63</sup> Therefore, there is an increasing level of interest in developing new fluorophore components consisting of H-donor and acceptor moieties which can be non-covalently linked to their complementary systems in order to self-assemble into col superstructures. In the previous work (section 2.1), we have discovered heptazine as an electron-deficient core for DLCs. In the present work, we went a step further and explored the potentiality of a heptazine derivative (non-LC) to form complementary H-bonded complexes with 3,4,5-tri-alkoxy benzoic acids towards the realization of new classes of heptazine based DLCs.

## 2.2.3 Results and discussions

### 2.2.3.1 Synthesis and characterization

The fluorophore component heptazine derivatives, **Hpz-C<sub>m</sub>** (m = 6, 10) have been synthesized by following a simple and straightforward procedure (Scheme 2.2).<sup>13,65</sup>



**Scheme 2.2** (A). Synthetic route of fluorophore component **Hpz-C<sub>m</sub>** (n = 6, 10). (B) Formation of fluorescent supramolecular columnar LCs based on a C<sub>3</sub>-symmetric heptazine core.

The alkyl (hexyl and decyl) chains in **Hpz-C<sub>m</sub>** are introduced to facilitate their solubility in organic solvents for the formation of H-bonded supramolecular complexes. Then, tri-alkoxy benzoic acids, **A<sub>n</sub>** ( $n = 10, 12, 16$ ; Scheme 2.2) were prepared following the literature method.<sup>66</sup> The structures of all the acids and **Hpz-C<sub>m</sub>** derivatives were characterized using NMR and IR (Figure A11-A20, Appendix II, Page 138) while the Hpz-C<sub>m</sub> derivatives were additionally characterized by HRMS techniques (Figure A33 and A34, Page 149). After that, the complexes were prepared by dissolving the components in DCM of HPLC grade in the molar ratio of 1:3 of **Hpz-C<sub>m</sub>** and acids, **A<sub>n</sub>**, respectively (Scheme 2.2). Finally, after evaporating the solvent, the resultant mixtures were annealed at 80 °C for 3 hours. The complex formation was fully confirmed through spectroscopic (Figure A21-A32, Appendix II, Page 143) and thermal characterization techniques as discussed below.

### 2.2.3.2 Comparative infrared (IR) and NMR study of the complexes

The complex formation was first characterized and confirmed by comparative IR and NMR studies (Figure 2.19 and 2.20). The infrared (IR) spectra (KBr) of the pure acid **A<sub>16</sub>**, **Hpz-C<sub>6</sub>** and **Hpz-C<sub>6</sub>/A<sub>16</sub>** were recorded and are shown in Figure 2.19.

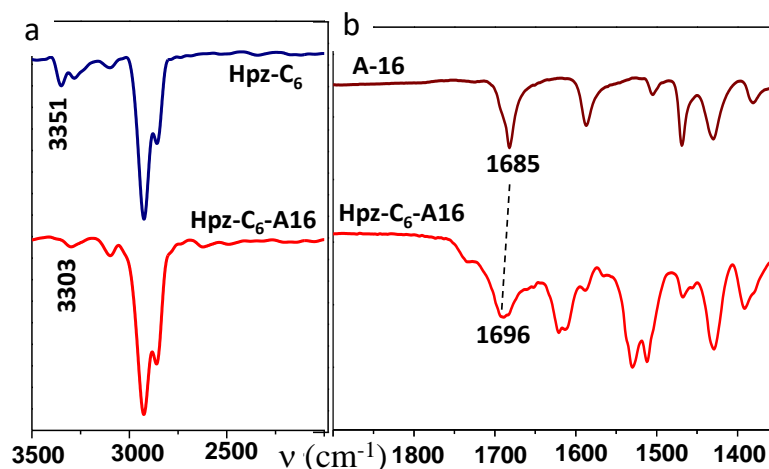


**Figure 2.19** FTIR spectra: (a) Comparison in –NH stretching region of pure component **Hpz-C<sub>6</sub>** and its complex **Hpz-C<sub>6</sub>/A<sub>16</sub>**. (b) Comparison in –C=O stretching region of acid **A<sub>16</sub>** and **Hpz-C<sub>6</sub>/A<sub>16</sub>**.

The –NH stretching peak in **Hpz-C<sub>6</sub>** was observed at 3351 cm<sup>-1</sup> which gets shifted to a lower wavenumber of 3310 cm<sup>-1</sup> in the resulting complex (**Hpz-C<sub>6</sub>/A<sub>16</sub>**). Besides, the carbonyl stretching peak in pure acid appeared at 1685 cm<sup>-1</sup> (corresponding to the dimeric form of the

acid) which became broadened and shifted to a higher wavenumber ( $1696\text{ cm}^{-1}$ ) after complexation. These observations were found to be consistent with the previously reported two-component H-bonded LCs.<sup>55,59,62,63</sup>

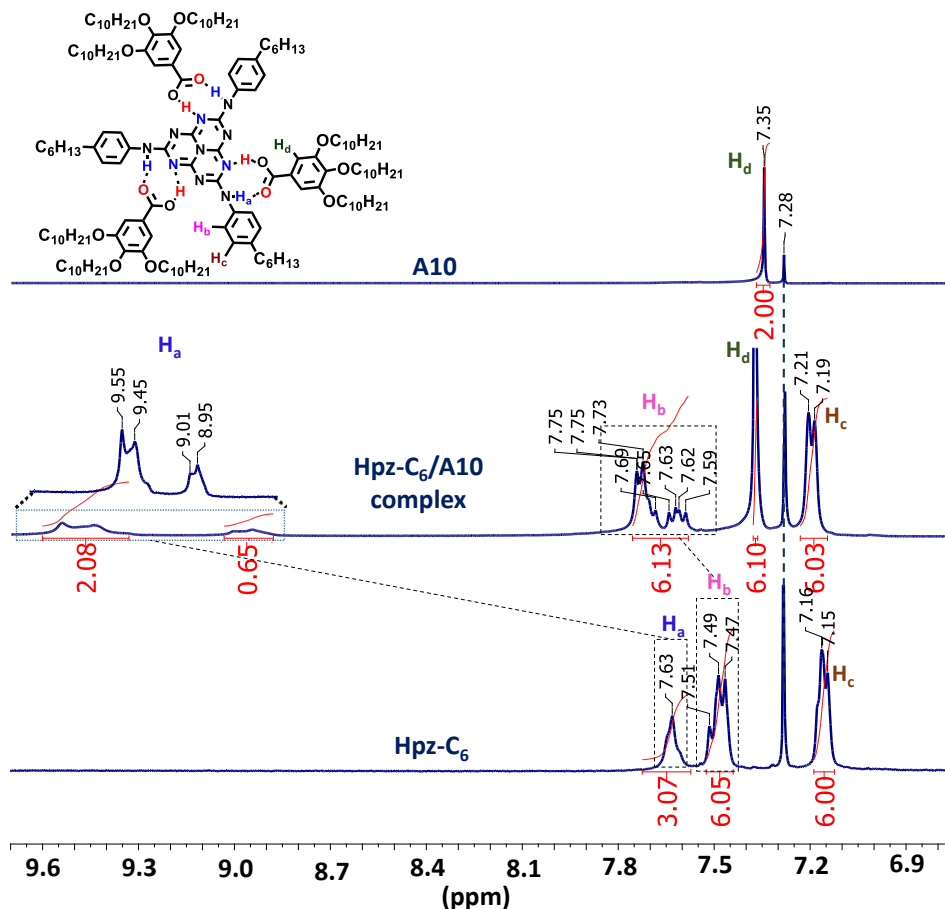


**Figure 2.20** Comparative  $^1\text{H}$  NMR studies of **A10**, **Hpz-C<sub>6</sub>/A10** complex and **Hpz-C<sub>6</sub>** of their 0.1 M concentration solution in  $\text{CDCl}_3$ .

Furthermore, the NMR studies also revealed the formation of H-bonded complexes (Figure 2.20). First, the proton integral peak ratio was found to be in a 1:3 ratio of **Hpz-C<sub>m</sub>** and **A<sub>n</sub>**, respectively. Second, the downfield shift for  $-\text{NH}$  protons in comparison to the pure heptazine derivative indicates the formation of a H-bonded system. It was also observed that while the aromatic protons ( $\text{H}_b$ ) of the **Hpz-C<sub>6</sub>** derivative split into two different sets of peaks in the **Hpz-C<sub>6</sub>/A10** complex, the  $\text{H}_c$  signals remain almost unaltered in both cases. This may be due to the different spatial environments of  $\text{H}_b$  protons in the complex and supports the formation of highly directional H-bonds.

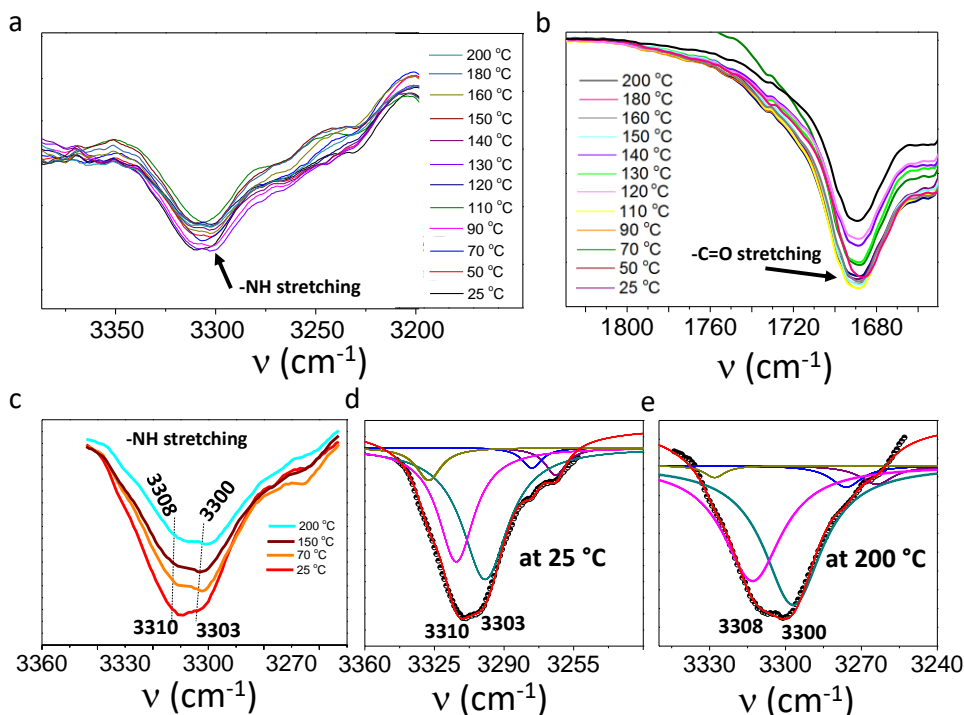


**Figure 2.21** Temperature-dependent FT-IR spectra of the complex **Hpz-C<sub>10</sub>/A<sub>10</sub>**: (a) –NH region from room temperature to above isotropic. (b) –C=O stretching region from room temperature to above isotropic. (c) Zoomed-in –NH stretching region at four different temperatures. Deconvolution of the merged peak in the –NH stretching region (d) at 25 °C (Col<sub>h</sub> phase), and (e) at 200 °C (isotropic phase).

Temperature-dependent FT-IR studies were carried out to get an insight into the strength of the H-bonding of the resulting complexes (Figure 2.21). It provides useful information on the nature and the extent of H-bonding within the system.<sup>67,68</sup> For temperature-dependent studies, we chose the **Hpz-C<sub>10</sub>/A<sub>10</sub>** complex which exhibits the broadest mesomorphic range (from 25 °C to 183 °C) out of all six complexes. The temperature-dependent studies were performed from 25 °C to 200 °C, a range that spans the Col<sub>h</sub> mesophase and an isotropic phase. We mainly focused on the change in the –NH stretching region and –C=O stretching region which take part in hydrogen bonding on changing the temperature. In the –NH region, it can be observed that the **Hpz-C<sub>10</sub>/A<sub>10</sub>** complex exhibits two merged bands which can be deconvoluted easily corresponding to 3310 cm<sup>-1</sup> (A-band) and 3303 cm<sup>-1</sup> (B-band) at room temperature (Figure 2.21d,e). It can be noted that the intensity of the A-band goes on decreasing while the intensity of the B-band increases and the bands get broadened on going from 25 to 200 °C (Fig. 2.21c).

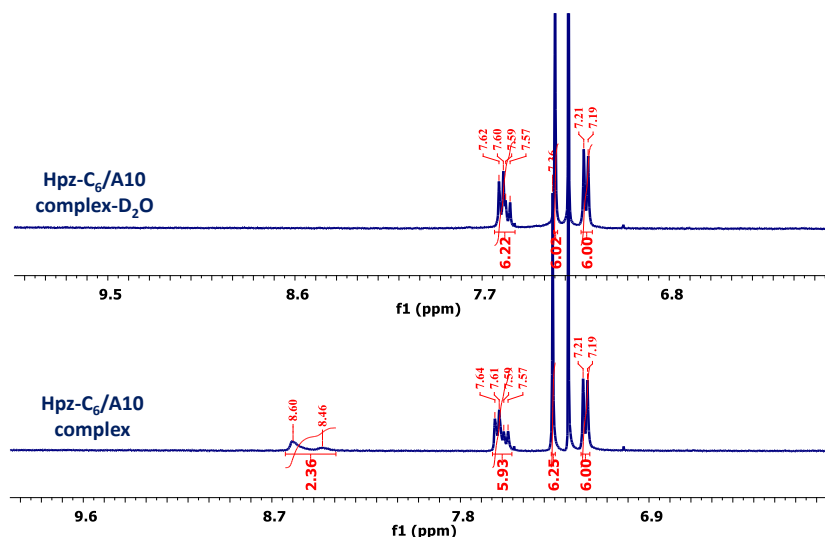


**Figure 2.22** Hydrogen-deuterium exchange studies of the complex **Hpz-C<sub>6</sub>/A10** of 0.17 M concentration solution in  $\text{CDCl}_3$ .

Along with this, a decrease in wavenumber has been observed for both bands at isotropic temperature by  $2\text{ cm}^{-1}$  in the A-band and  $3\text{ cm}^{-1}$  in the B-band i.e. the peaks get shifted to  $3308\text{ cm}^{-1}$  and  $3300\text{ cm}^{-1}$  (Figure 2.21c). The broadening of the  $-\text{NH}$  peak with an increase in temperature suggests the formation of the H-bonded complex. However, in the  $-\text{C}=\text{O}$  region, no appreciable change was observed in wavenumber while the intensity of the band occurring at  $1696\text{ cm}^{-1}$  dropped by an enormous amount accompanied by broadening of the bands (Figure 2.21b). As a result, from the temperature-dependent IR studies, it is revealed that the complexes exist as H-bonded aggregates even above their clearing temperatures. The results are consistent with the prior studies reported in the literature.<sup>69</sup>

The hydrogen–deuterium (H–D) exchange studies were also carried out for the complexes in order to evaluate the H-bonding (Figure 2.22). As we previously observed in Figure 2.20 the  $-\text{NH}$  protons get downfield shifted after the formation of the H-bond with the acid derivatives. Here we have studied the H–D exchange of the downfield shifted protons. We observed the disappearance of the  $-\text{NH}$  protons on adding a few drops of  $\text{D}_2\text{O}$  in a  $\text{CDCl}_3$  solution of the complex after shaking it well for 30 minutes.

### 2.2.3.3 Thermal behaviour

As the motive to make the complexes was to obtain a new class of supramolecular LCs, it is essential to check their mesomorphic behaviour first under a polarizing optical microscope

(POM). Firstly, both the pure components **Hpz-C<sub>m</sub>** and the acids **A<sub>n</sub>** were checked for their mesomorphic properties. Under POM, both the components were found to be non-mesomorphic. The heptazine derivative, **Hpz-C<sub>6</sub>** is crystalline at room temperature and did not show melting up to 250 °C (Figure 2.24). On the other hand, **Hpz-C<sub>10</sub>** showed a crystal to isotropic transition at 254 °C. All the acids, **A<sub>n</sub>** derivatives melted in the range of 55-62 °C. Interestingly, all the complexes (**Hpz-C<sub>m</sub>/A<sub>n</sub>**) exhibit enantiotropic well-defined col LC phases over a broad temperature range (Figure 2.23, Table 2.4). This observation is indicative of the strength of H-bonding between acids and heptazine derivatives, in good agreement with an earlier report.<sup>58</sup>

The occurrence of the mesophase in the complexes from non-mesogenic components also provides evidence for the formation of H-bonded assemblies. We note that except **Hpz-C<sub>10</sub>/A<sub>10</sub>**, all the complexes melted in the range of 140-150 °C. The complex **Hpz-C<sub>10</sub>/A<sub>10</sub>** exhibited the highest mesomorphic range up to 183 °C, probably due to the better packing of molecules in the col phase owing to the same alkyl chain length of both the **Hpz-C<sub>10</sub>** and **A<sub>10</sub>** components.

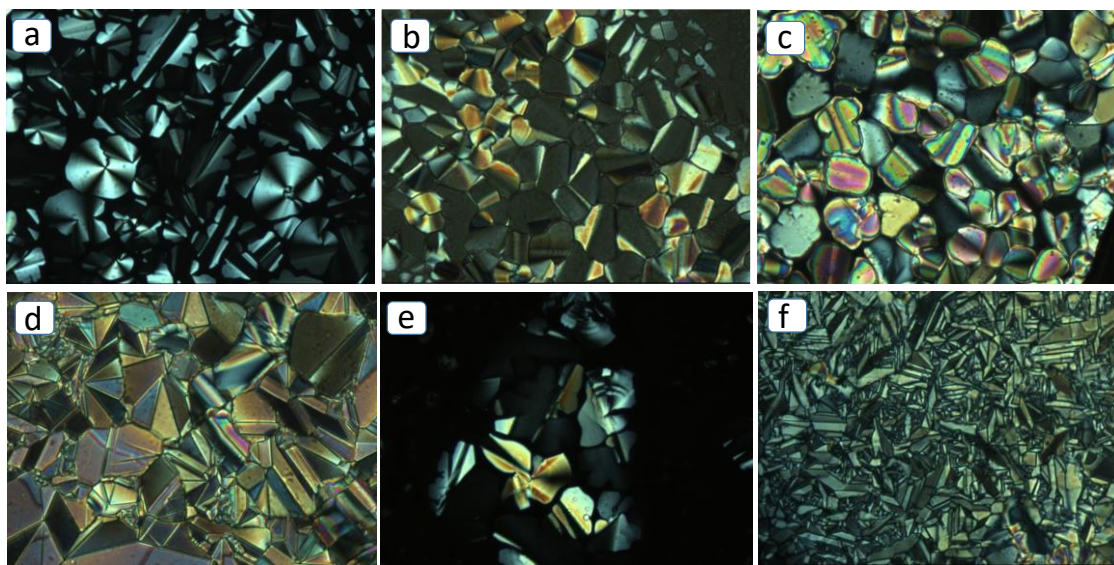


**Figure 2.23** Optical micrographs of heptazine derivative (**Hpz-C<sub>m</sub>**) complexes: (a) **Hpz-C<sub>6</sub>/A<sub>10</sub>** at 95.4 °C. (b) **Hpz-C<sub>6</sub>/A<sub>12</sub>** at 74 °C. (c) **Hpz-C<sub>6</sub>/A<sub>16</sub>** at 56.7 °C. (d) **Hpz-C<sub>10</sub>/A<sub>10</sub>** at 123.4 °C. (e) **Hpz-C<sub>10</sub>/A<sub>12</sub>** at 95.5 °C. (f) **Hpz-C<sub>10</sub>/A<sub>16</sub>** at 89.1 °C (scan rate 5 °C min<sup>-1</sup>, crossed polarizers, magnification ×500).



**Table 2.4** Thermal behaviour of the **Hpz-C<sub>m</sub>/A<sub>n</sub>** complexes.<sup>a</sup>

Compound	Heating	Cooling
<sup>b</sup> <b>Hpz-C<sub>6</sub>/A<sub>10</sub></b>	Col <sub>h</sub> 150 I	I 140 Col <sub>h</sub>
<sup>b</sup> <b>Hpz-C<sub>6</sub>/A<sub>12</sub></b>	Col <sub>h</sub> 147 I	I 130 Col <sub>h</sub>
<sup>b</sup> <b>Hpz-C<sub>6</sub>/A<sub>16</sub></b>	Col <sub>h</sub> 142 I	I 120 Col <sub>h</sub>
<b>Hpz-C<sub>10</sub>/A<sub>10</sub></b>	Col <sub>h</sub> 183 <sup>c</sup> (6.66) I	I 175 <sup>b</sup> Col <sub>h</sub>
<b>Hpz-C<sub>10</sub>/A<sub>12</sub></b>	Col <sub>hp</sub> 44 <sup>c</sup> (20.8) Col <sub>h</sub> 143.7 <sup>c</sup> (2.86) I	I 136 <sup>b</sup> Col <sub>h</sub> 40 <sup>c</sup> (12.98) Col <sub>hp</sub>
<b>Hpz-C<sub>10</sub>/A<sub>16</sub></b>	Col <sub>hp</sub> 62.5 <sup>c</sup> (26.21) Col <sub>h</sub> 150 <sup>c</sup> (3.94) I	I 145 <sup>b</sup> Col <sub>h</sub> 52 <sup>c</sup> (9.32) Col <sub>hp</sub>

<sup>a</sup>Phase transition temperature (°C) and transition enthalpies in kJmol<sup>-1</sup> (in parenthesis). Col<sub>h</sub> = Columnar hexagonal; Col<sub>hp</sub> = Columnar hexagonal plastic; I = Isotropic. <sup>b</sup>Phase transition observed through POM & XRD; <sup>c</sup>Phase transition observed through POM and DSC.

Under POM, no phase separation was observed upon reversibly heating and cooling the samples several times which indicates that the two components remain intact through strong H-bonding. For all the complexes, the birefringent columnar textures start to appear within a few degree ranges of 5-22 °C on cooling the sample from the isotropic melt. The complex **Hpz-C<sub>6</sub>** series complexes **Hpz-C<sub>6</sub>/A<sub>10</sub>**, **Hpz-C<sub>6</sub>/A<sub>12</sub>**, and **Hpz-C<sub>6</sub>/A<sub>16</sub>** exhibit mesophase to isotropic transition at 150 °C, 147 °C and 142 °C, respectively. In general, all the complexes form large homeotropic domains, which appear dark under crossed polarizers along with pseudo focal conic textures, mosaic textures, dendritical growth regions, spherulitic-like domains and linear defects. All the samples exhibited homeotropic regions. The presence of optically isotropic domains in the homeotropically aligned samples directs the observation of col phases with a hexagonal or square symmetry and points to the uniaxial nature of the mesophase. The complex **Hpz-C<sub>6</sub>/A<sub>10</sub>** shows a spherulitic-like texture with maltese crosses, suggesting a Col<sub>h</sub> mesophase when cooled from its isotropic state (Figure 2.23a). The **Hpz-C<sub>6</sub>/A<sub>12</sub>** complex shows mosaic-like textures while the **Hpz-C<sub>6</sub>/A<sub>16</sub>** exhibits a dendritic growth of textures with rectilinear defects, another characteristic texture of the Col<sub>h</sub> phase along with homeotropic regions. The **Hpz-C<sub>10</sub>** complexes, **Hpz-C<sub>10</sub>/A<sub>10</sub>**, **Hpz-C<sub>10</sub>/A<sub>12</sub>** and **Hpz-C<sub>10</sub>/A<sub>16</sub>** melt into an isotropic liquid at 183 °C, 143 °C and 150 °C, respectively. The **Hpz-C<sub>10</sub>** series complexes exhibit mosaic and dendritic growth of textures. The DSC curves for the **Hpz-C<sub>10</sub>** complexes are shown in Figure A35, Appendix II, Page 150.



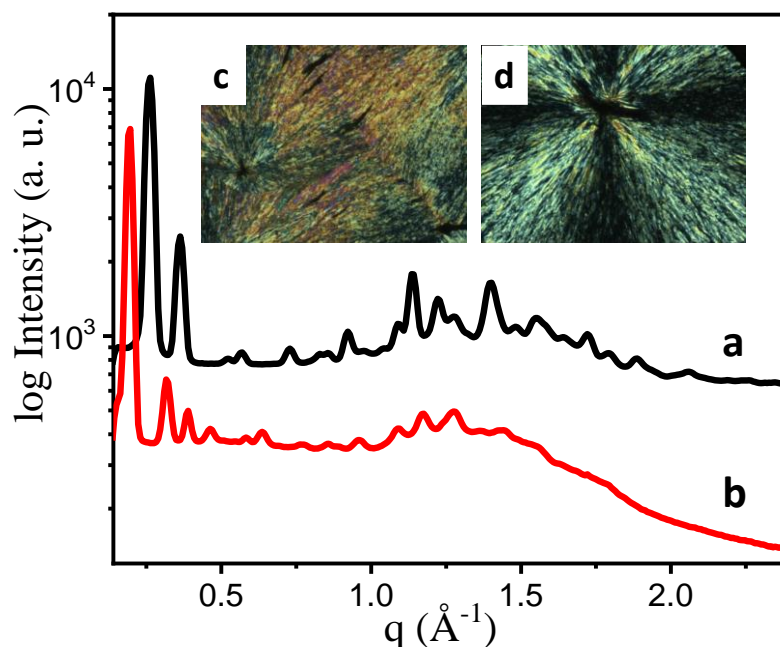


**Figure 2.24** X-ray diffraction (XRD) pattern of pure component: (a) **Hpz-C<sub>6</sub>**. (b) **Hpz-C<sub>10</sub>**. Inset shows the crystalline textures of (c) **Hpz-C<sub>6</sub>**. (d) **Hpz-C<sub>10</sub>** under polarized optical microscope (scan rate 10 °C/min, crossed polarizers, magnification  $\times 500$ ).

#### 2.2.3.4 X-ray diffraction studies

The quantitative phase behaviour of the complexes was examined by X-ray diffraction (XRD) studies on cooling the sample from the isotropic liquid. The pure components **Hpz-C<sub>6</sub>** and **Hpz-C<sub>10</sub>** exhibited many sharp peaks in the small-angle as well as in the wide-angle regime (Figure 2.24a,b) which is indicative of their crystalline nature. This behaviour is also well supported by the respective POM textures (Figure 2.24c,d). XRD study also confirmed the columnar nature of all the complexes. The details for the **Hpz-C<sub>6</sub>/A<sub>16</sub>** complex are given as below. In the range of 25-60 °C, it shows one intense diffraction peak with a  $d$ -spacing of 36.97 Å along with comparatively five weaker peaks with  $d$ -spacing ratios of  $1:1/\sqrt{3}:1/\sqrt{4}:1/\sqrt{7}:1/\sqrt{13}:1/\sqrt{19}$  in the small-angle region and a narrow peak ( $h_a$ ) at 4.58 Å and a broad peak ( $h_c$ ) at 3.81 Å in the wide-angle regime (Figure 2.25a, Table 2.5, Figure 2.27c). The  $d$ -spacing ratios in the small-angle region indicate the occurrence of columnar hexagonal ( $Col_h$ ) and the reflections were assigned to the (10), (11), (20), (21), (31) and (32) planes. The wide-angle peaks termed as  $h_a$  and  $h_c$  appear mainly due to alkyl chain to chain and disc to disc correlations, respectively.

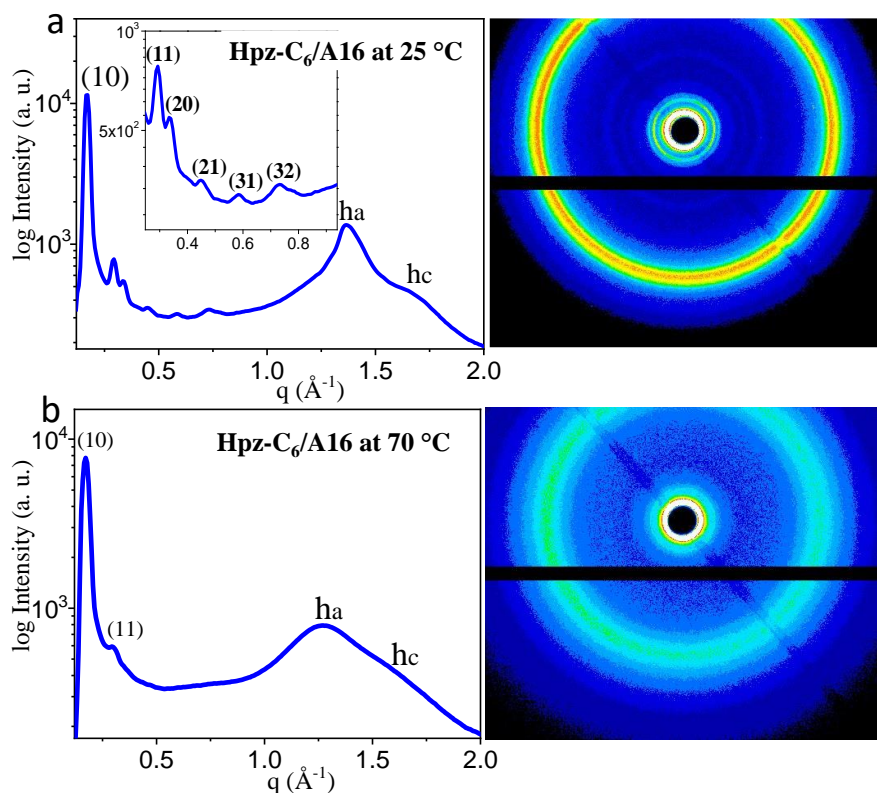


**Figure 2.25** X-ray diffraction pattern corresponding to mesophases of complex (a) **Hpz-C<sub>6</sub>/A16** at 25 °C (Col<sub>h</sub>). (b) **Hpz-C<sub>6</sub>/A16** at 70 °C (Col<sub>h</sub>). Right panel shows the respective 2D diffraction patterns.

Further,  $h_a$  peak is narrow which is attributed to the low mobility of the alkyl chains at room temperature. However, at a higher temperature (70 °C), the **Hpz-C<sub>6</sub>/A16** complex shows the lesser number of reflections in the small-angle region than at lower temperature and also the  $h_a$  peak became broader indicates alkyl chain mobility is higher (Figure 2.25b). But the structure remains still Col<sub>h</sub>. The detailed XRD data for **Hpz-C<sub>6</sub>/A16** are summarized in Table 2.5. The Col<sub>h</sub> mesophase behaviour was observed for the **Hpz-C<sub>6</sub>/A10** and **Hpz-C<sub>6</sub>/A12** complexes also (Figure 2.26b,a and Figure 2.27a,b).

The systematic variation of XRD lattice parameter ( $a$ ) and correlation length ( $\xi$ ) for all the three complexes of **Hpz-C<sub>6</sub>** series with temperature is shown in Figure 2.28a,b. The lattice parameter,  $a$ , is found to be increased on going from **Hpz-C<sub>6</sub>/A10** to **Hpz-C<sub>6</sub>/A16** (increase in the length of the alkyl chain of the acid) (Figure 2.28a) which is obvious as the overall molecular diameter of the molecule is increasing on increasing the acid chain lengths.

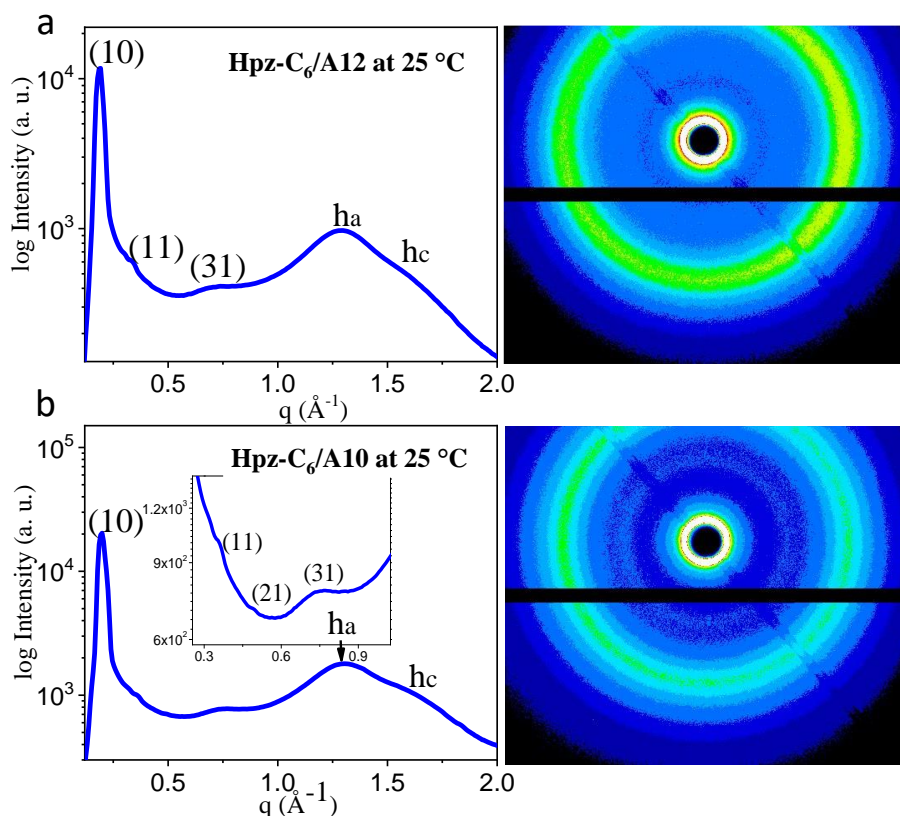


**Figure 2.26** X-ray diffraction pattern corresponding to mesophases of complex (a) **Hpz-C<sub>6</sub>/A12** at 25 °C (Col<sub>h</sub>). (b) **Hpz-C<sub>6</sub>/A10** at 25 °C (Col<sub>h</sub>) in 2D Col<sub>h</sub> phase; h<sub>a</sub>-alkyl chain-chain correlations, h<sub>c</sub>- disc to disc (face to face) correlations. Right panel shows the respective 2D diffraction patterns.

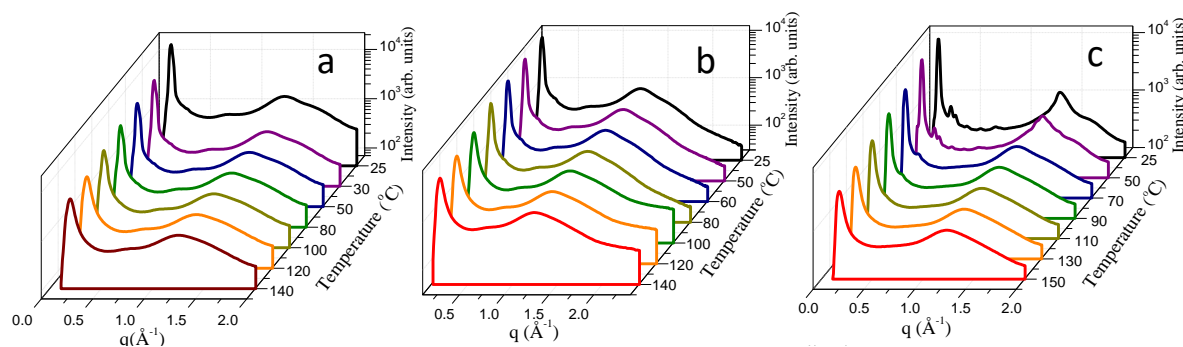


**Figure 2.27** Systematic temperature-dependent X-ray diffraction studies for **Hpz-C<sub>6</sub>** complexes from room temperature to their respective isotropic temperatures on cooling from the isotropic phase: (a) **Hpz-C<sub>6</sub>/A10**. (b) **Hpz-C<sub>6</sub>/A12**. (c) **Hpz-C<sub>6</sub>/A16**.

Moreover, the ‘ $a$ ’ value is more or less constant with temperature in the case of **Hpz-C<sub>6</sub>/A10** and **Hpz-C<sub>6</sub>/A12** but decreases smoothly for **Hpz-C<sub>6</sub>/A16** complex with an increase in temperature (Figure 2.28a). In addition, correlation length ( $\xi$ ) is found to be more in **Hpz-C<sub>6</sub>/A16** complex in comparison to the other two (**Hpz-C<sub>6</sub>/A10** & **Hpz-C<sub>6</sub>/A12**)(Figure 2.28b). However, the correlation lengths were found to decreasing with increasing temperature for all three complexes (Figure 2.28b).

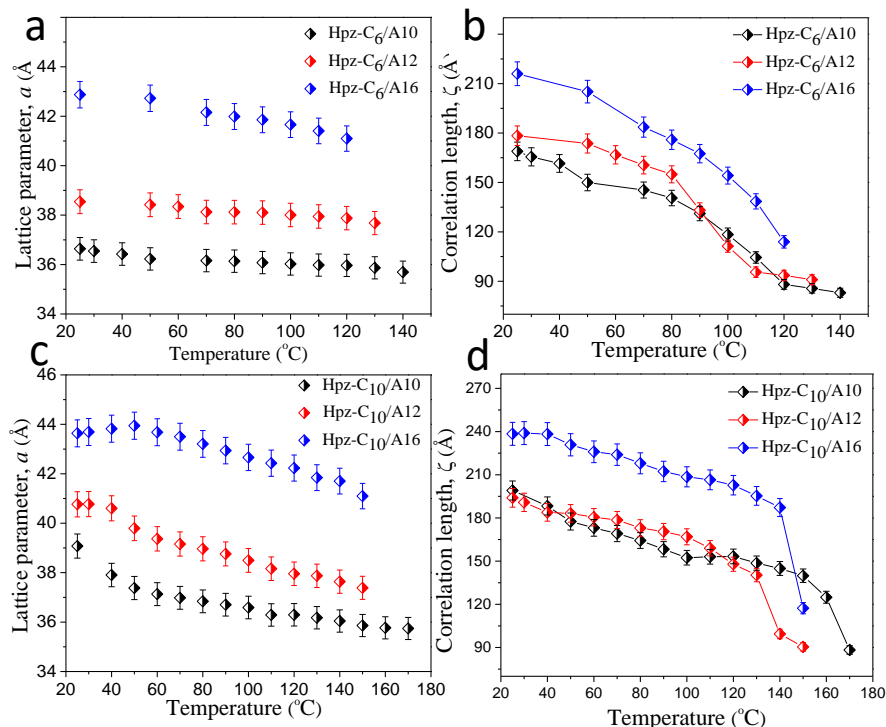


**Figure 2.28** (a) & (c) Variation of lattice parameter,  $a$ , and (b) & (d) corresponding correlation length ( $\xi$ ) with temperature for complexes **Hpz-C<sub>6</sub>/A10**, **Hpz-C<sub>6</sub>/A12** and **Hpz-C<sub>6</sub>/A16** and **Hpz-C<sub>10</sub>/A10**, **Hpz-C<sub>10</sub>/A12** and **Hpz-C<sub>10</sub>/A16**.

The systematic temperature-dependent XRD study for the **Hpz-C<sub>10</sub>/An** complexes (Figure 2.29) provides useful information about the change in mesophase structure on changing temperature. For instance, in case of **Hpz-C<sub>10</sub>** derivative complexes, the complex **Hpz-C<sub>10</sub>/A16** and **Hpz-C<sub>10</sub>/A12** exhibited many peaks in small and wide-angle region in the temperature ranges of 25-52 °C (Figure 2.25a and Figure 2.29c) and 25-40 °C, respectively. In the wide-angle region, the complexes show a bifurcated peak which is usually a characteristic of the plastic nature of the phase.<sup>70</sup> At these lower temperatures, the spacing can be indexed on hexagonal lattice for **Hpz-C<sub>10</sub>/A16** and **Hpz-C<sub>10</sub>/A12**. The bifurcated peaks are assigned to

(601) and (611) (Figure 2.30a) and thus the mesophase is characterized as columnar hexagonal plastic ( $\text{Col}_{\text{hp}}$ ) at a lower temperature.

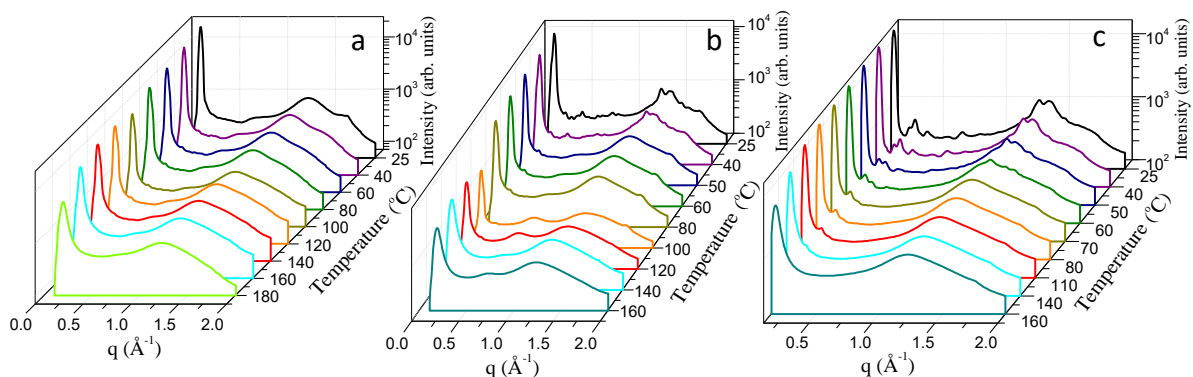


**Figure 2.29** Systematic temperature-dependent X-ray diffraction studies for **Hpz-C<sub>10</sub>** complexes from room temperature to their respective isotropic temperatures on cooling from the isotropic phase: (a) **Hpz-C<sub>10</sub>/A10**, (b) **Hpz-C<sub>10</sub>/A12** and (c) **Hpz-C<sub>10</sub>/A16**.

**Table 2.5** X-ray diffraction data for 1:3 complexes of heptazine derivative, **Hpz-C<sub>6</sub>** with the tri-alkoxy benzoic acids, **A10**, **A12** & **16**.

Compound	Mesophase	Lattice constants (Å)	$d_{\text{obs}}^a$ (Å)	$d_{\text{cal}}^b$ (Å)	MI <sup>c</sup> (hk)
<b>Hpz-C<sub>6</sub>/A10</b>	$\text{Col}_h$ at 25 °C	$a = 36.09$	31.75	31.96	10
		$c = 3.88$	18.21	18.45	11
			12.20	12.08	21
			8.75	8.86	31
			4.83		<b>h<sub>a</sub></b>
			3.88		<b>h<sub>c</sub></b>
<b>Hpz-C<sub>6</sub>/A12</b>	$\text{Col}_h$ at 25 °C	$a = 38.30$	33.17	33.17	10
		$c = 3.88$	19.02	19.15	11
			8.93	9.20	31
			4.89		<b>h<sub>a</sub></b>
			3.88		<b>h<sub>c</sub></b>
<b>Hpz-C<sub>6</sub>/A16</b>	$\text{Col}_h$ at 25 °C	$a = 42.90$	36.97	37.15	10
		$c = 3.81$	21.42	21.45	11
			18.45	18.58	20
			14.01	14.04	21
			10.65	10.30	31

		8.59	8.52	32
		4.58		<b>h<sub>a</sub></b>
		3.81		<b>h<sub>c</sub></b>
Col <sub>h</sub> at 70 °C	$a = 42.90$	36.34	36.29	10
	$c = 3.81$	20.94	20.95	11
		4.95		<b>h<sub>a</sub></b>
		3.95		<b>h<sub>c</sub></b>

$^a d_{obs}$  : experimental  $d$ -spacing;  $^b d_{cal}$  : calculated  $d$ -spacing by using the relation:  $\frac{1}{d^2} = \left[ \frac{4}{3} \left( \frac{h^2 + hk + k^2}{a^2} \right) + \frac{l^2}{c^2} \right]$ ;  $h, k, l$  are the indices of the reflections corresponding to the columnar hexagonal (Col<sub>h</sub>) phase;  $a$  &  $c$  are the unit cell parameters,  $h_a$  &  $h_c$  spacing appear due to alkyl chain-chain and core-core correlation, respectively.

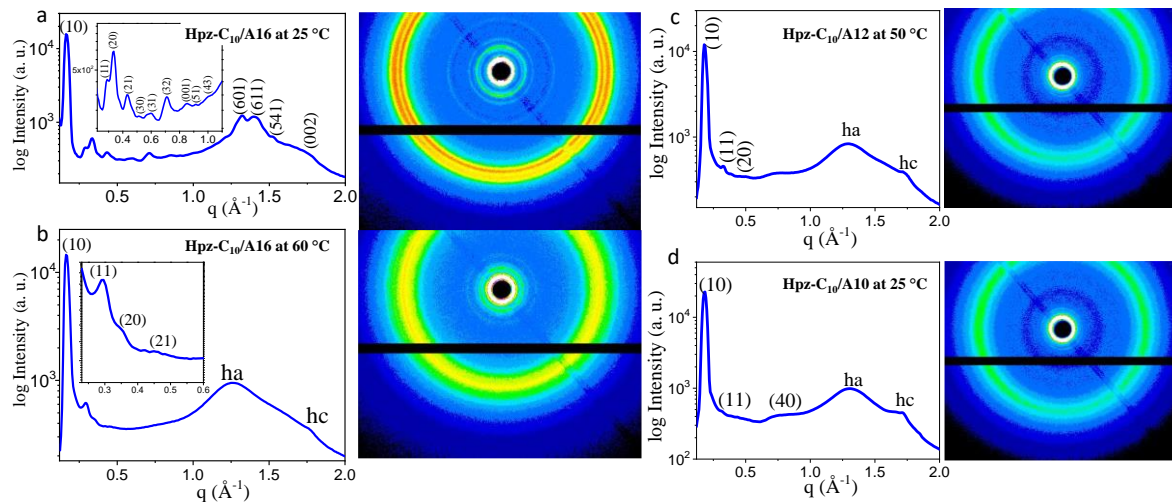


**Figure 2.30** X-ray diffraction pattern corresponding to mesophases of complex (a) **Hpz-C<sub>10</sub>/A16** at 25 °C (Col<sub>h</sub>), (b) **Hpz-C<sub>10</sub>/A16** at 60 °C (Col<sub>h</sub>), (c) **Hpz-C<sub>10</sub>/A12** at 50 °C (Col<sub>h</sub>) and (d) **Hpz-C<sub>10</sub>/A10** at 25 °C (Col<sub>h</sub>) in 2D Col<sub>h</sub> phase;  $h_a$ -alkyl chain-chain correlations,  $h_c$ -disc to disc (face to face) correlations. Right panel shows the respective 2D diffraction patterns. Right panel shows the respective 2D diffraction patterns.

Further, at higher temperatures ( $>52$  °C for **Hpz-C<sub>10</sub>/A16** and  $>40$  °C for **Hpz-C<sub>10</sub>/A12**), the XRD patterns were similar to that observed for complex **Hpz-C<sub>6</sub>/A16** at a higher temperature (Figure 2.30b,c, Figure 2.29b,c) which mainly consists of one strong diffraction peak, (10) accompanied with three or four weak diffraction peaks, (11), (20) & (21) which could be easily



indexed on the  $\text{Col}_h$  lattice. However, complex **Hpz-C<sub>10</sub>/A10** exhibits only  $\text{Col}_h$  phase in all the temperature ranges (Figure 2.30d and Figure 2.29a). The detailed XRD data for the **Hpz-C<sub>10</sub>** complexes are summarized in Table 2.6.

Variation of lattice parameter ( $a$ ) and correlation length ( $\xi$ ) for the **Hpz-C<sub>10</sub>/An** complexes with temperature were also studied (Figure 2.28c,d). The lattice constant,  $a$ , as well as correlation length ( $\xi$ ) are found to be decreased with increasing temperature for all the three complexes. The lattice parameter ( $a$ ) is found to be increased as **Hpz-C<sub>10</sub>/A10** < **Hpz-C<sub>10</sub>/A12** < **Hpz-C<sub>10</sub>/A16**. In summary, we have noticed that on increasing the alkyl chain lengths of acids e.g. from **A10-A16** as well as of the heptazine derivative **Hpz-C<sub>m=6</sub>** to **Hpz-C<sub>m=10</sub>**, the XRD becomes more ordered as going from isotropic to room temperature. That's why, all the **Hpz-C<sub>6</sub>/An** ( $n = 10, 12 \text{ \& } 16$ ) complexes exhibit only  $\text{Col}_h$  mesophase while in case of **Hpz-C<sub>10</sub>/An** ( $n = 10, 12 \text{ \& } 16$ ) complexes, the **Hpz-C<sub>10</sub>/A16** and **Hpz-C<sub>10</sub>/A12** with larger heptazine

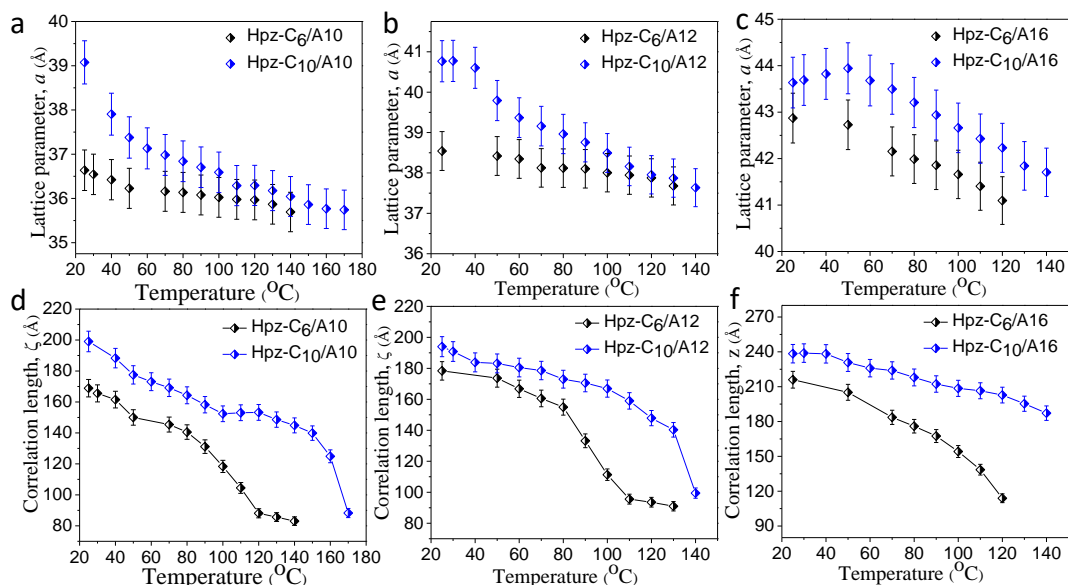


**Figure 2.31** Variation of lattice parameter,  $a$ , with temperature for complexes: (a) **Hpz-C<sub>6</sub>/A10** (black) and **Hpz-C<sub>10</sub>/A10** (blue). (b) **Hpz-C<sub>6</sub>/A12** (black) and **Hpz-C<sub>10</sub>/A12** (blue). (c) **Hpz-C<sub>6</sub>/A16** (black) and **Hpz-C<sub>10</sub>/A16** (blue) and corresponding variation of correlation length ( $\xi$ ) with temperature for compounds (d) **Hpz-C<sub>6</sub>/A10** (black) and **Hpz-C<sub>10</sub>/A10** (blue). (e) **Hpz-C<sub>6</sub>/A12** (black) and **Hpz-C<sub>10</sub>/A12** (blue). (f) **Hpz-C<sub>6</sub>/A16** (black) and **Hpz-C<sub>10</sub>/A16**.

derivative alkyl chain length, as well as larger acid alkyl chain length (A12 & A16), possesses  $\text{Col}_{hp}$  mesophase (more ordered) at lower temperatures and  $\text{Col}_h$  phase at higher temperatures.

And, the **Hpz-C<sub>10</sub>/A10** complex with lower acid chain length exhibits only Col<sub>h</sub> phase in all the temperature ranges. Furthermore, the lattice parameter as well as the correlation length is higher in **Hpz-C<sub>10</sub>/An** complexes in comparison to **Hpz-C<sub>6</sub>/An** (Figure 2.31).

The average number of molecules (*Z*) in a single disc of the column has been calculated for all six complexes. As all the complexes exhibit Col<sub>h</sub> phase, so *Z*, can be calculated by using the following formula.

$$Z = (a_{\text{hex}}^2)(\sqrt{3}/2)/(\rho N_A/M_w)$$

where  $a_{\text{hex}}$  is the hexagonal lattice parameter,  $h$  is maximum of the diffuse wide-angle scattering,  $\rho$  is density assuming 1 g cm<sup>-3</sup>,  $N_A$  is the Avogadro's constant,  $M_w$  is the molecular weight of the compound. After substituting the parameters, the number of molecules in one disc comes out to be 1.32, 1.37, 1.36, 1.45, 1.41 and 1.40 for **Hpz-C<sub>6</sub>/A10**, **Hpz-C<sub>6</sub>/A12**,

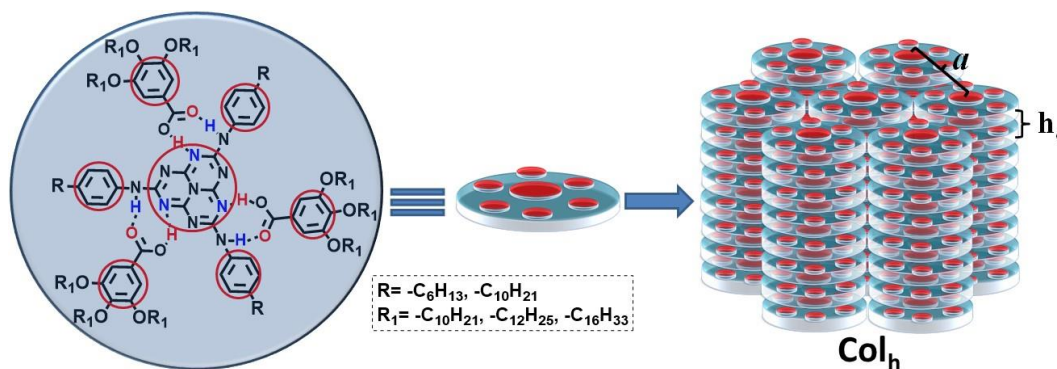


**Figure 2.32** General self-assembly principle of columnar hexagonal (Col<sub>h</sub>) assembly.

**Hpz-C<sub>6</sub>/A16**, **Hpz-C<sub>10</sub>/A10**, **Hpz-C<sub>10</sub>/A12** and **Hpz-C<sub>10</sub>/A16**, respectively. This indicates that on average one molecule which in turn composed of one **Hpz-C<sub>n</sub>** molecule surrounded by three acid (**An**) molecules that are non-covalently linked through H-bonding is forming the disc which finally arranges into the column to form a hexagonal lattice (Figure 2.32). Here, it seems that the heptazine core (C<sub>3</sub>N<sub>7</sub>) along with three benzene rings of **Hpz-C<sub>n</sub>** derivative and three benzene ring of acids are forming a rigid core and alkyl chain as a flexible unit. Hence, mesophase is arising because of the phase separation between the rigid core and flexible alkyl chains. The general self-assembly mechanism for the formation of Col<sub>h</sub> phase is shown in Figure 2.32. The same conclusion can be deduced from the reconstruction of electron density maps as described below.



Electron density map (EDM) is reconstructed for complex **Hpz-C10/A16** at 25 °C (Figure 2.33a) by using the procedure as reported earlier.<sup>72-74</sup> The map shows the arrangement of the cross-section of the columns on the 2D hexagonal lattice. Each cross-section exhibits the highest electron density at the center (O) and higher density at six hexagons (M) sites with respect to the centre (Figure 2.33b). The three benzene rings from three acids join to one heptazine core by intermolecular H-bonding forms a disc and these discs arrange on top of each other and form columns which finally amassed on a 2D hexagonal lattice.

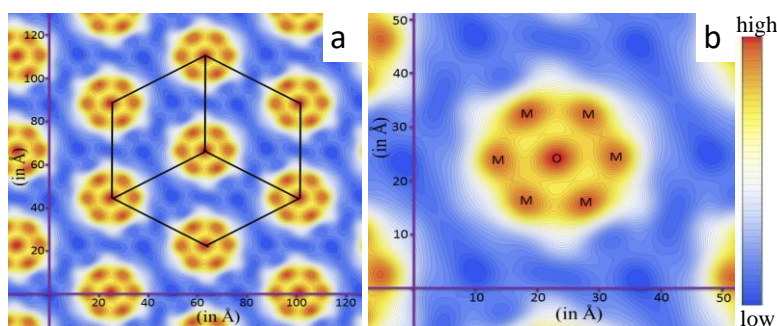


**Figure 2.33** Reconstructed electron density map (REDM) of compound **Hpz-C10/A16** at 25 °C: (a) in the Col<sub>hp</sub> phase. The black line drawn on the map is to guide and visualize 2D hexagonal structure, where the whole hexagon shows the conventional unit cell and rhombus displays the primitive unit cell. (b) REDM corresponding to the one disc unit. The map shows the highest electron density at the center (O) and higher density at six hexagons (M) sites. The center (O) is the location of heptazine core and six M are the location of six benzene rings; three from **Hpz-C10** derivative and three from Acid, **A10**. Red color represents the highest electron density and dark blue the lowest.

**Table 2.6** X-ray diffraction data for 1:3 complexes of heptazine derivative, **Hpz-C10** with the tri-alkoxy benzoic acids, **A10**, **A12** & **16**.

Compound	Mesophase	Lattice constants (Å)	$d_{\text{obs}}^a$ (Å)	$d_{\text{cal}}^b$ (Å)	MI <sup>c</sup> (hk)
<b>Hpz-C10/A10</b>	Col <sub>h</sub> at 25 °C	$a = 39.10$	33.89	33.86	10
		$c = 3.59$	19.60	19.55	11
			8.59	8.47	40
			4.83		<b>h<sub>a</sub></b>
			3.67		<b>h<sub>c</sub></b>
<b>Hpz-C10/A12</b>	Col <sub>h</sub> at 55 °C	$a = 40.10$	34.79	34.72	10

		$c = 3.65$	20.18	20.05	11
			17.38	17.36	20
			4.87		
			3.65		<b>h<sub>a</sub></b>
			3.88		<b>h<sub>c</sub></b>
<b>Hpz-C<sub>10</sub>/A16</b>	Col <sub>hp</sub> at 25 °C	$a = 43.90$	38.05	38.02	10
		$c = 7.34$	22.20	21.95	11
			19.06	19.01	20
			14.41	14.37	21
			12.48	12.67	30
			10.43	10.54	31
			8.86	8.72	32
			7.34	7.34	001
			6.86	6.83	51
			6.27	6.25	43
			4.75	4.80	601
			4.52	4.55	611
			4.08	4.06	541
			3.67	3.67	002
	Col <sub>h</sub> at 70 °C	$a = 42.90$	37.18	37.15	10
		$c = 3.59$	21.28	21.45	11
			18.38	18.58	20
			14.25	14.04	21
			4.97		<b>h<sub>a</sub></b>
			3.59		<b>h<sub>c</sub></b>

$^a d_{obs}$  : experimental  $d$ -spacing;  $^b d_{cal}$  : calculated  $d$ -spacing by using the relation:  $\frac{1}{d^2} = \left[ \frac{4}{3} \left( \frac{h^2 + hk + k^2}{a^2} \right) + \frac{l^2}{c^2} \right]$ ;  $h, k, l$  are the indices of the reflections corresponding to the columnar hexagonal (Col<sub>h</sub>) phase;  $a$  &  $c$  are the unit cell parameters,  $h_a$  &  $h_c$  spacing appear due to alkyl chain-chain and core-core correlation, respectively.

### 2.2.3.5 Photophysical behaviour

The photophysical properties were investigated for the pure components **Hpz-C<sub>m=6,10</sub>** as well as for all the complexes in solution as well as in solid-state (Figure 2.34, Table 2.7, Figure 2.35). The absorption and emission spectra for **Hpz-C<sub>10</sub>** and its complex **Hpz-C<sub>10</sub>/A10** in solution as well as in solid-state are shown in Figure 2.34. In solution state, the **Hpz-C<sub>10</sub>** shows

absorption maxima ( $\lambda_{\text{max}}$ ) at 317 nm and emission maxima at 444 nm. In all the complexes, the  $\lambda_{\text{max}}$  was centred at 274 nm while the emission maxima vary from 358-364 nm. Interestingly, the  $\lambda_{\text{max}}$  shifts from 317 nm to 274 nm in the complexes as that of pure components indicating the different self-assembly of the molecules. The emission peak gets shifted to a lower wavelength in the complexes. The complexes show purple-blue color weak fluorescence in chloroform (Figure 2.34c inset).

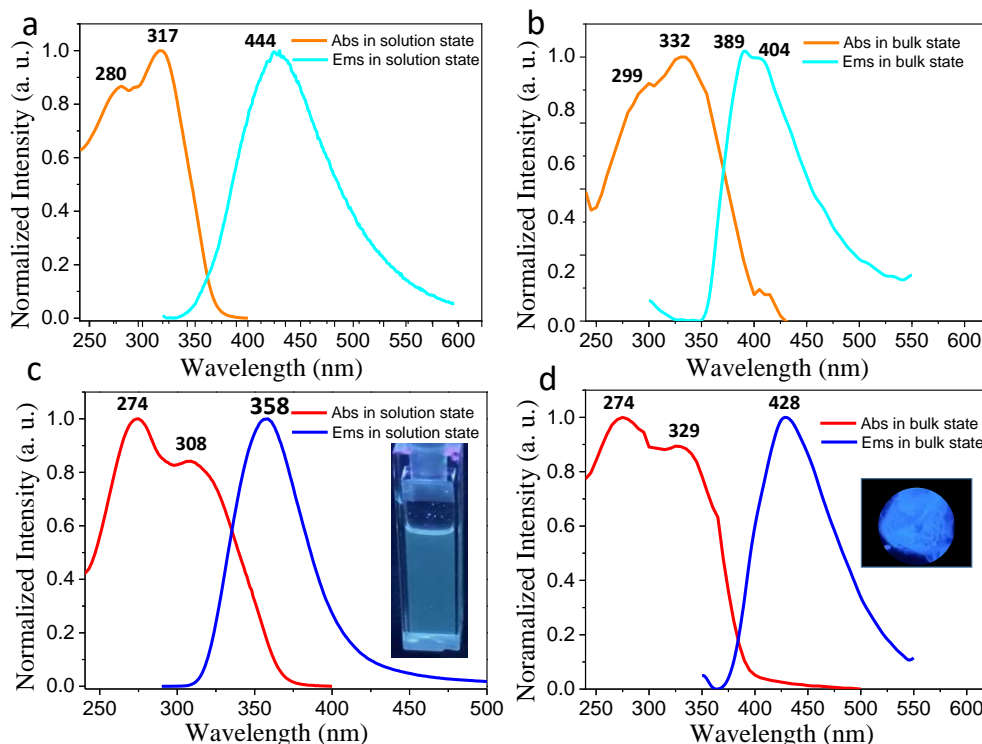


**Figure 2.34** Absorption and emission spectra of pure component **Hpz-C10** (a) in chloroform and (b) in the bulk state. Absorption and emission spectra of complex **Hpz-C10/A10**: (c) in chloroform. (d) in bulk state. Inset (c) shows purple-blue color weak fluorescence in the solution state, inset (d) shows blue emission in the neat state. Abs represents Absorption. Ems represents emissions in the graphs.

In solid-state absorption, the **Hpz-C10** displays peaks at 299 nm & 332 nm while emission spectra consist of peaks at 389 nm with one shoulder peak at 404 nm (Figure 2.34b). The complex **Hpz-C10/A10** displays absorption peaks at 274 nm & 329 nm and an emission peak located at 428 nm and also shows blue emission in a neat state (Figure 2.34d inset). Hence, the

different photophysical properties of the complexes from the pure fluorophore component also support the inference of H-bonded complex formation.

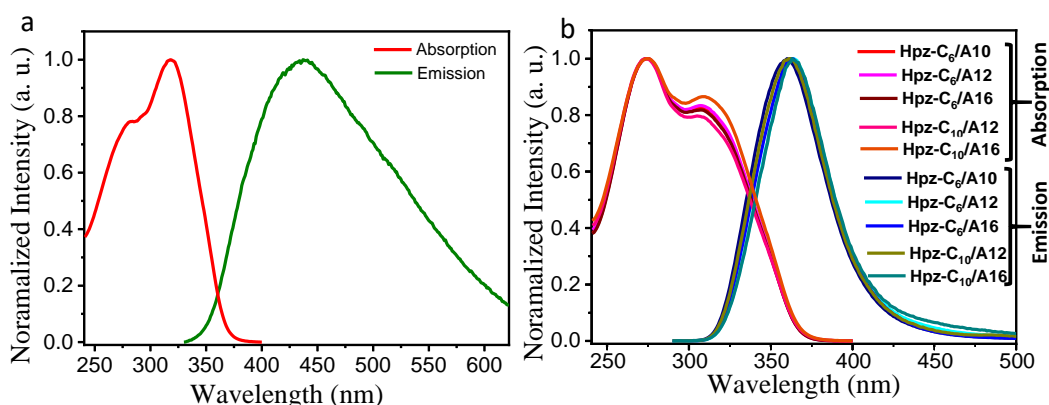


**Figure 2.35.** (a) Absorption and emission spectra of pure compounds in chloroform solution: (a) **Hpz-C6**. (b) Absorption and emission spectra of H-bonded complexes in chloroform solution.

**Table 2.7** Photophysical properties of the target compounds.

Compound	A <sub>solution</sub> <sup>a</sup> (nm)	E <sub>solution</sub> <sup>a,b</sup> (nm)	A <sub>solid</sub> (nm)	E <sub>solid</sub> <sup>b</sup> (nm)
<b>Hpz-C6</b>	280, 317 <sup>b</sup>	437	299, 332	389, 404
<b>Hpz-C10</b>	389, 404	444	299, 332	389, 404
<b>Hpz-C6/A10</b>	274, <sup>b</sup> 308	360	274, <sup>b</sup> 329	428
<b>Hpz-C6/A12</b>	274, <sup>b</sup> 308	364	274, <sup>b</sup> 329	428
<b>Hpz-C6/A16</b>	274, <sup>b</sup> 308	363	274, <sup>b</sup> 329	428
<b>Hpz-C10/A10</b>	274, <sup>b</sup> 308	358	274, <sup>b</sup> 329	428
<b>Hpz-C10/A12</b>	274, <sup>b</sup> 308	361	274, <sup>b</sup> 329	428
<b>Hpz-C10/A16</b>	274, <sup>b</sup> 308	363	274, <sup>b</sup> 329	428

<sup>a</sup>in chloroform solution. <sup>b</sup> $\lambda_{\max}$ . <sup>b</sup>obtained after exciting at their corresponding  $\lambda_{\max}$ .

A<sub>solution</sub>: Absorbance peaks in solution state, E<sub>solution</sub>: Emission peaks in solution state.

A<sub>solid</sub>: Absorbance peaks in bulk state, E<sub>solid</sub>: Emission peaks in bulk state.

## 2.2.4 Conclusions

In conclusion, a new series of fluorescent H-bonded col LCs are reported by incorporating the electron-deficient s-heptazine as a new fluorophore discotic component. The formation of complexes was confirmed by IR and NMR studies. The temperature-dependent studies were carried out to evaluate the strength of H-bonding with temperature. All the complexes exhibit

broad range Col<sub>h</sub> phases while **Hpz-C<sub>10</sub>/A12** and **Hpz-C<sub>10</sub>/A16**, in addition, to Col<sub>h</sub> phase at a higher temperature also possess Col<sub>hp</sub> phase at room temperature as determined by XRD. The UV-Vis and fluorescence studies of the pure heptazine component and complexes were carried out and compared. The complexes show different absorption and emission behaviour as that of their heptazine derivatives. All the complexes are weakly fluorescent in the solution state as compared to their neat state. Finally, the easy formation of these FLCs by the use of dynamic and versatile H-bonded non-covalent approach widespread the use of DLCs which are often limited by their difficult and lengthy synthetic procedures.

***Acknowledgements.** We are highly thankful to Dr. Kamalakannan Kailasam's group from INST Mohali for helping us in this project. Dr. Santosh Prasad Gupta (at Patna University) is duly acknowledged for the analysis of XRD data.*

## 2.2.5 Experimental section

**2.2.5.1 General synthetic procedure for the synthesis of Hpz-C<sub>m=6,10</sub>.** Cyameluric chloride (1) (Scheme 2.2) (150 mg, 1 equiv.) was dissolved in 5 ml dry THF in 25 ml double-neck round bottom flask (R.B) in a glove box. Then 4-alkyl aniline (4 equiv.) was added to the cyameluric chloride solution dropwise at room temperature. After stirring for 15 minutes at room temperature, triethylamine (0.1 ml) was added to consume HCl formed during the reaction. Then the reaction mixture was stirred overnight. Subsequently, the reaction mixture was washed several times with methanol to remove the excess amount of 4-alkyl aniline. The residue obtained was further purified through column chromatography (neutral alumina) to give the off-white color product. The <sup>1</sup>H, <sup>13</sup>C NMR [Figure A17-A20 (Page 141)], and HRMS spectra [Figure A33-A34 (Page 149)] are given in Appendix II.

**Hpz-C<sub>6</sub>:** FT-IR (cm<sup>-1</sup>): 3351.20, 3288.86, 3230.57, 3187.17, 3130.07, 3103.01, 2954.46, 2924.31, 2853.40, 1633.08, 1604.96, 1587.96, 1531.28, 1463.00, 1418.69, 1367.08, 1319.29, 1304.25, 1238.75, 1190.54, 1157.84, 1140.92, 1021.37, 856.94, 806.11, 737.28, 617.70. <sup>1</sup>H NMR (400 MHz, CDCl<sub>3</sub>, δ in ppm): δ 7.63 (s, 3H, -NH protons), δ 7.51-7.47 (m, 6H, aromatic protons), δ 7.18-7.15 (m, 6H, aromatic protons), δ 2.61-2.57 (t, 6H, *J* = 7.46 Hz), δ 1.63 (s, 6H), δ 1.32 (s, 12H), δ 1.27 (s, 8H), δ 0.92-0.89 (t, 9H, *J* = 5.70 Hz). <sup>13</sup>C NMR (100 MHz,

CDCl<sub>3</sub>,  $\delta$  in ppm): 177.86, 154.86, 129.06, 124.50, 121.52, 114.08, 68.40, 64.16, 43.16, 35.43, 31.95, 29.72, 22.72, 22.65, 14.14.

**Hpz-C10:** FT-IR (cm<sup>-1</sup>): 3360.00, 3286.61, 3224.42, 3096.19, 2956.41, 2922.96, 2853.06, 1703.98, 1632.35, 1603.99, 1593.24, 1512.06, 1470.16, 1422.36, 1390.67, 1368.43, 1316.01, 1299.22, 1245.21, 1190.16, 1157.52, 1139.56, 1121.49, 1019.30, 984.32, 887.65, 831.83, 805.49, 611.28. <sup>1</sup>H NMR (400 MHz, CDCl<sub>3</sub>,  $\delta$  in ppm): <sup>1</sup>H NMR (400 MHz, CDCl<sub>3</sub>,  $\delta$  in ppm):  $\delta$  7.52 (s, 3H, -NH protons),  $\delta$  7.49-7.47 (d, 6H, aromatic protons,  $J$  = 4.04 Hz),  $\delta$  7.17-7.15 (d, 6H, aromatic protons,  $J$  = 7.96 Hz),  $\delta$  2.61-2.57 (t, 6H,  $J$  = 7.56 Hz),  $\delta$  1.31-1.28 (m, 46H),  $\delta$  0.92-0.89 (t, 9H,  $J$  = 6.14 Hz). <sup>13</sup>C NMR (100 MHz, CDCl<sub>3</sub>,  $\delta$  in ppm): 162.29, 129.13, 128.95, 128.2, 121.41, 35.41, 35.12, 31.99, 31.94, 29.67, 29.38, 22.73, 14.16.

**2.2.5.2 General synthetic procedure for the synthesis of acids A10, A12, A16.** FT-IR (cm<sup>-1</sup>): 3,4,5-trialkoxybenzoic acids were prepared from the starting material gallic acid monohydrate according to the previously reported procedures.<sup>75</sup> The detailed <sup>1</sup>H and <sup>13</sup>C NMR, spectra are given in Appendix II [Figure A11-A16 (Page 138)].

**A10:** FT-IR (cm<sup>-1</sup>): 2955.13, 2924.78, 2854.79, 1685.00., 1587.00, 1504.13, 1468.06, 1433.16, 1382.11, 1330.88, 1265.83, 1229.76, 1117.35, 987.65, 931.74, 867.30, 768.55. <sup>1</sup>H NMR (400 MHz, CDCl<sub>3</sub>,  $\delta$  in ppm): 7.35 (s, 2H), 4.08-4.03 (m, 6H), 1.86-1.77 (m, 6H), 1.54-1.46 (m, 6H), 1.33-1.30 (m, 36H), 0.92-0.89 (t, 9H). <sup>13</sup>C NMR (100 MHz, CDCl<sub>3</sub>,  $\delta$  in ppm): 171.67, 152.84, 143.10, 123.62, 108.49, 73.57, 69.17, 31.97, 31.94, 30.35, 29.76, 29.70, 29.66, 29.61, 29.58, 29.43, 29.41, 29.38, 29.28, 26.10, 26.06, 14.15.

**A12:** FT-IR (cm<sup>-1</sup>): 2954.20, 2920.73, 2850.62, 1685.23, 1587.41, 1504.44, 1468.14, 1432.25, 1385.24, 1333.47, 1275.38, 1228.04, 1121.59, 864.03, 767.69. <sup>1</sup>H NMR (400 MHz, CDCl<sub>3</sub>,  $\delta$  in ppm): 7.34 (s, 2H), 4.08-4.03 (m, 6H), 1.86-1.77 (m, 6H), 1.53-1.46 (m, 6H), 1.32-1.29 (m, 48H), 0.92-0.89 (m, 9H). <sup>13</sup>C NMR (100 MHz, CDCl<sub>3</sub>,  $\delta$  in ppm): 152.87, 143.11, 108.51, 73.57, 69.18, 31.98, 31.96, 30.35, 29.79, 29.77, 29.73, 29.69, 29.67, 29.59, 29.42, 29.40, 29.29, 26.11, 26.07, 22.73, 14.16.

**A16:** FT-IR (cm<sup>-1</sup>): 2954.48, 2917.92, 2849.42, 1685.01, 1587.02, 1504.94, 1468.76, 1429.99, 1381.01, 1334.10, 1275.39, 1227.27, 1123.20, 984.81, 969.88, 863.06, 767.13. <sup>1</sup>H NMR (400 MHz, CDCl<sub>3</sub>,  $\delta$  in ppm): 7.34 (s, 2H), 4.08-4.03 (m, 6H), 1.88-1.73 (m, 6H), 1.53-1.46 (m, 6H), 1.37-1.28 (m, 72H), 0.92-0.88 (t, 9H). <sup>13</sup>C NMR (100 MHz, CDCl<sub>3</sub>,  $\delta$  in ppm): 171.67,

152.84, 143.10, 123.62, 108.49, 73.57, 69.17, 31.97, 31.94, 30.35, 29.76, 29.70, 29.66, 29.61, 29.58, 29.43, 29.41, 29.38, 29.28, 26.10, 26.06, 14.15.

**2.2.5.3 General synthetic procedure for the synthesis of complexes with the acids A10, A12, A16.** The acids **A10-16** were prepared according to the literature reports.<sup>66</sup> Then the complexes were prepared by mixing the **Hpz-C<sub>m</sub>** component with the acids **A<sub>n</sub>** in 1:3 ratio, respectively, in HPLC dichloromethane solution. Then the solution was evaporated to dryness and the resulting mixture was annealed at 80 °C for three hours to ensure the complexation. The complex formation was fully characterized through spectroscopic techniques *viz.* <sup>1</sup>H, <sup>13</sup>C NMR and FT-IR techniques. Their <sup>1</sup>H and <sup>13</sup>C NMR spectra are given in Appendix II (Figure A21-A32, Page 143).

**Complex Hpz-C<sub>6</sub>/A10:** FT-IR (cm<sup>-1</sup>): 3310.11, 3303.32, 3087.23, 2954.60, 2924.44, 2854.57, 1695.00, 1619.28, 1611.57, 1587.57, 1529.65, 1511.07, 1467.22, 1428.64, 1391.39, 1329.13, 1225.96, 826.60, 767.45, 720.24. <sup>1</sup>H NMR (400 MHz, CDCl<sub>3</sub>,  $\delta$  in ppm): 9.55-9.45 (m, 2H), 9.01-8.95 (m, 1H), 7.75-7.60 (m, 6H), 7.38 (s, 6H), 7.21-7.19 (d, 6H,  $J$  = 7.60 Hz), 4.08-4.04 (m, 18H), 2.63-2.58 (m, 6H), 1.88-1.75 (m, 24H), 1.52-1.49 (m, 18H), 1.30 (broad s, 126H), 0.92-0.89 (t, 36H,  $J$  = 6.48 Hz). <sup>13</sup>C NMR (100 MHz, CDCl<sub>3</sub>,  $\delta$  in ppm): 171.22, 152.86, 142.97, 128.86, 124.15, 121.13, 108.56, 73.57, 69.22, 35.54, 31.95, 31.81, 31.95, 31.81, 30.39, 29.77, 29.72, 29.69, 29.64, 29.62, 29.48, 29.44, 29.40, 29.38, 26.16, 26.10, 22.74, 22.72, 22.69, 14.16. **Complex Hpz-C<sub>6</sub>/A12:** FT-IR (cm<sup>-1</sup>): 3310.11, 3303.65, 3088.50, 2955.39, 2922.78, 2853.11, 1695.32, 1611.01, 1587.79, 1529.90, 1511.34, 1468.02, 1428.74, 1391.54, 1330.14, 1259.99, 1226.25, 1154.28, 1121.39, 1018.99, 864.48, 825.70, 799.88, 765.92, 720.76. <sup>1</sup>H NMR (400 MHz, CDCl<sub>3</sub>,  $\delta$  in ppm): 9.46 (broad s, 2H), 8.96 (s, 1H), 7.74-7.62 (m, 6H), 7.38 (s, 6H), 7.21-7.19 (d, 6H,  $J$  = 7.36 Hz), 4.08-4.04 (m, 18H), 2.63-2.57 (m, 6H), 1.88-1.76 (m, 24H), 1.51-1.44 (m, 18H), 1.29 (broad s, 163H), 0.92-0.89 (t, 36H,  $J$  = 6.52 Hz). <sup>13</sup>C NMR (100 MHz, CDCl<sub>3</sub>,  $\delta$  in ppm): 171.20, 152.86, 142.97, 128.86, 124.15, 121.16, 108.56, 73.57, 69.22, 35.55, 31.98, 31.96, 30.39, 29.79, 29.77, 29.75, 29.74, 29.71, 29.61, 29.63, 29.48, 29.44, 29.41, 29.38, 26.17, 26.11, 22.73, 22.69, 14.16.

**Complex Hpz-C<sub>6</sub>/A16:** FT-IR (cm<sup>-1</sup>): 3303.11, 3087.32, 2954.68, 2919.87, 2851.56, 1696.14, 1621.71, 1612.55, 1530.63, 1513.08, 1468.28, 1428.90, 1392.16, 1329.64, 1225.07, 1121.07, 823.68, 796.52, 763.51, 720.98. <sup>1</sup>H NMR (400 MHz, CDCl<sub>3</sub>,  $\delta$  in ppm): 9.36 (s, 2H), 8.92 (s,

1H), 7.73-7.59 (m, 6H), 7.38 (s, 6H), 7.21-7.20 (d, 6H,  $J = 7.00$  Hz), 4.08-4.04 (m, 18H), 2.63-2.58 (m, 6H), 1.88-1.75 (m, 24H), 1.51-1.47 (m, 18H), 1.28 (s, 234H), 0.92-0.88 (t, 36H,  $J = 6.66$  Hz).  $^{13}\text{C}$  NMR (100 MHz,  $\text{CDCl}_3$ ,  $\delta$  in ppm): 171.20, 152.86, 142.97, 128.88, 108.55, 73.57, 69.21, 35.55, 31.97, 31.81, 30.39, 29.77, 29.70, 29.64, 29.48, 29.42, 29.38, 26.17, 26.11, 22.73, 22.69, 14.16.

**Complex Hpz-C<sub>10</sub>/A10:** FT-IR ( $\text{cm}^{-1}$ ): 3310.11, 3303.05, 3090.36, 2955.69, 2923.65, 2853.73, 1696.11, 1620.97, 1612.884, 1588.31, 1529.92, 1511.85, 1467.64, 1429.15, 1391.32, 1329.40, 1226.48, 1116.59, 823.82, 765.54, 720.00.  $^1\text{H}$  NMR (400 MHz,  $\text{CDCl}_3$ ,  $\delta$  in ppm): 9.39-9.32 (m, 2H), 8.91 (s, 1H), 7.72-7.59 (m, 6H), 7.38 (s, 6H), 7.21-7.19 (d, 6H,  $J = 7.80$  Hz), 4.08-4.04 (m, 18H), 2.63-2.57 (m, 6H), 1.88-1.75 (m, 24H), 1.52-1.47 (m, 18H), 1.30 (broad s, 150H), 0.92-0.89 (t, 36H,  $J = 6.60$  Hz).  $^{13}\text{C}$  NMR (100 MHz,  $\text{CDCl}_3$ ,  $\delta$  in ppm): 171.09, 152.86, 142.96, 128.88, 108.56, 73.57, 69.23, 35.55, 31.98, 31.95, 30.39, 29.77, 29.72, 29.69, 29.64, 29.62, 29.48, 29.44, 29.40, 29.38, 26.16, 26.10, 22.74, 22.72, 14.15.

**Complex Hpz-C<sub>10</sub>/A12:** FT-IR ( $\text{cm}^{-1}$ ): 3310.11, 3303.12, 3082.17, 2954.98, 2920.14, 1696.41, 1620.42, 1610.39, 1588.61, 1527.97, 1511.36, 1467.93, 1429.30, 1390.86, 1331.01, 1259.82, 1227.41, 1150.18, 1020.65, 862.86, 801.12, 764.89, 722.25.  $^1\text{H}$  NMR (400 MHz,  $\text{CDCl}_3$ ,  $\delta$  in ppm): 9.26 (s, 3H), 7.71-7.61 (m, 6H), 7.36 (s, 6H), 7.21-7.19 (d, 6H,  $J = 8.00$  Hz), 4.08-4.03 (m, 18H), 2.63-2.55 (m, 6H), 1.85-1.74 (m, 24H), 1.60-1.50 (m, 18H), 1.29 (broad s, 186H), 0.91-0.88 (t, 36H,  $J = 6.00$  Hz).  $^{13}\text{C}$  NMR (100 MHz,  $\text{CDCl}_3$ ,  $\delta$  in ppm): 173.27, 152.86, 143.39, 128.91, 110.23, 108.55, 73.57, 69.2, 31.96, 30.38, 29.78, 29.74, 29.70, 29.69, 29.61, 29.43, 29.41, 29.36, 26.15, 26.09, 22.73, 14.16.

**Complex Hpz-C<sub>10</sub>/A16:** FT-IR ( $\text{cm}^{-1}$ ): 3310.11, 3303.21, 3090.33, 2954.93, 2920.14, 2852.39, 1695.00, 1621.21, 1614.68, 1530.48, 1512.67, 1468.76, 1429.20, 1392.41, 1329.68, 1225.79, 1120.15, 795.49, 720.88.  $^1\text{H}$  NMR (400 MHz,  $\text{CDCl}_3$ ,  $\delta$  in ppm): 9.32-9.30 (d, 3H,  $J = 8.12$  Hz), 7.72-7.61 (m, 6H), 7.37 (s, 6H), 7.21-7.19 (d, 6H,  $J = 8.20$  Hz), 4.08-4.03 (m, 18H), 2.60-2.57 (m, 6H), 1.87-1.74 (m, 24H), 1.50-1.47 (m, 18H), 1.28 (broad s, 258H), 0.92-0.89 (t, 36H,  $J = 6.68$  Hz).  $^{13}\text{C}$  NMR (100 MHz,  $\text{CDCl}_3$ ,  $\delta$  in ppm): 171.06, 152.87, 142.99, 128.88, 124.11, 121.18, 108.57, 73.56, 69.23, 35.54, 31.96, 31.63, 30.40, 29.80, 29.77, 29.71, 29.64, 29.49, 29.41, 26.17, 26.11, 22.72, 14.15.



## 2.3 Part C: Segregated donor-acceptor columnar assembly based on heptazine-triphenylene H-bonded system

### 2.3.1 Introduction

The quest for designing functional organic semiconductor materials, in particular, ambipolar charge transport materials, has increased and is being actively pursued worldwide. The use of ambipolar materials in devices cuts the high device fabrication cost on one hand and offers device miniaturization on the other by incorporating a single layer of active material.<sup>76-78</sup> However, the mobility of these materials is extremely reliant on the electronic coupling among the neighboring molecules which in turn depends on the molecular organization in the bulk state.<sup>79-81</sup> This poses a formidable yet exciting task for the material scientist to opt for the intriguing class of self-assembled materials to resolve diverse challenges at the molecular and morphological length scales. One such class of materials is liquid crystals (LCs),<sup>82</sup> in particular, discotic liquid crystals (DLCs)<sup>2,3,6,48</sup> where the columnar stacks exhibit quasi-one-dimensional charge transport behaviour. These materials exhibit the tendency of alignment that provides preorganized pathways for efficient charge-carrier transport.

Molecular design embedded with electron-donor (D) and acceptor (A) moiety is an appealing strategy to achieve ambipolar DLCs.<sup>83-99,54</sup> To integrate D-A units, the non-covalent hydrogen (H)-bonding strategy is a highly attractive and easy approach that largely avoids the difficult and lengthy synthetic as well as purification procedures of DLC systems.<sup>7,11a</sup> As donors, triphenylenes (TP) are the most widely investigated self-assembling discotics owing to their easy synthesis and mono-substitution.<sup>54,100,101</sup> On the other hand, the choice of electron-deficient discotic cores is rather critical due to their huge scarcity. At the same time, it is difficult to find a suitable core that can be modified with H-donor and acceptor sites mandated for complementary H-bonding. In literature, very few electron-deficient systems *viz.* triazine,<sup>87,91-94</sup> tris(triazolyl)triazine<sup>54,59,60</sup> and tris-benzimidazolyl benzene<sup>63,102</sup> are known for forming complementary H-bonded DLCs. In recent years, our group has introduced a new electron-deficient motif based on heptazine that can be modified for the formation of H-bonded

DLCs.<sup>103</sup> Heptazine ( $C_3N_7$ ), a  $C_3$  symmetric core consists of one central and six peripheral nitrogen (N) atoms (H-bond acceptor) shows the ability to form complementary H-bonding when substituted with the H-bond donor  $-NH$  groups. Here, we have employed heptazine and TP as A and D units linked non-covalently to each other through complementary H-bonding.

### 2.3.2 Objectives

In molecular architecture, segregation among D and A units is preferred for efficient ambipolar charge transport systems.<sup>54,85,86</sup> However, D and A molecules normally prefer to stack alternatively instead of segregating individually. The alternate stacking of D and A molecules leads to a disordered molecular arrangement, where the charge carriers are trapped and are thus annihilated.<sup>85</sup> Therefore, the segregation of D-A columns forms the basis for the realization of ambipolar charge transport behaviour. To attain the segregated columns, it is important to electronically decouple the D and A parts *via* distancing them apart. Up to now, few examples of D-A DLC systems are there that offer the possibility of forming separate conduction pathways for charge carriers, and very few have been studied for the ambipolar charge transport measurements.<sup>54,85,86,100</sup>

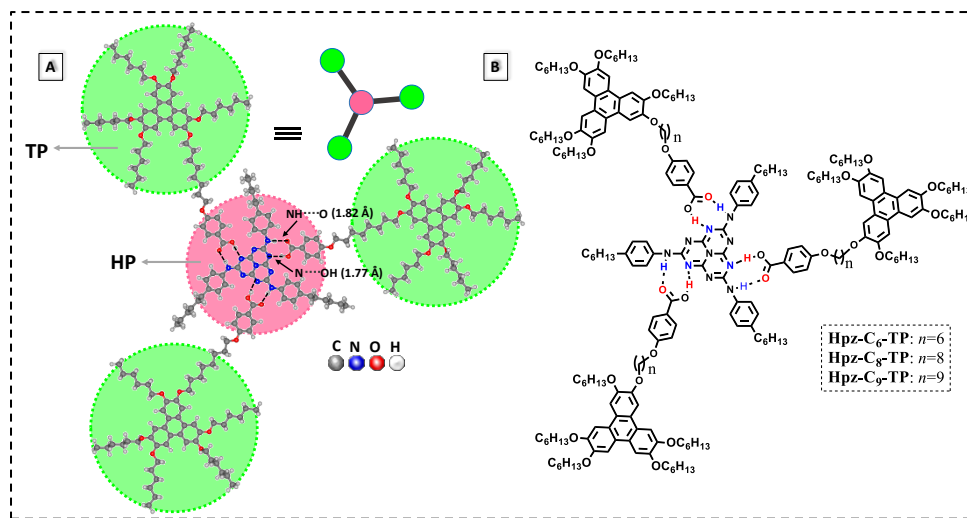


**Figure 2.36** (A) DFT optimized geometry (B3LYP/6-31G (d, p) of **Hpz-C8-TP** with triphenylene (TP) units at corners and HP unit at the center (pink color). Note: HP unit consists of the heptazine core together with six surrounded benzene rings (3 benzene rings connected through amine linkage + 3 benzene rings linked through H-bonding). (B) Molecular structure of **Hpz-C<sub>n</sub>-TP** complexes.

In the present work, we have developed such H-bonded D-A dyad system based on heptazine (A) and triphenylene (D), **Hpz-C<sub>n</sub>-TP** that are electronically decoupled with the aid of insulating alkyl chain spacers (Figure 2.36), led to the realization of highly efficient ambipolar charge transport when used in space-charge limited current (SCLC) devices. Together with the importance of the formation of segregated assemblies of D and A units, we also demonstrate a crucial role of homeotropic alignment in achieving efficient ambipolar charge transport. Three derivatives **Hpz-C<sub>6</sub>-TP**, **Hpz-C<sub>8</sub>-TP**, and **Hpz-C<sub>9</sub>-TP** were synthesized that differ in the length of alkyl spacers connecting D-A units. All the derivatives exhibit room temperature ordered columnar hexagonal self-assembly with a broad temperature range but differ in their alignment capabilities in the devices that led to the differences in the observed mobility values.

### 2.3.3 Results and discussions

#### 2.3.3.1 Molecular design and synthesis

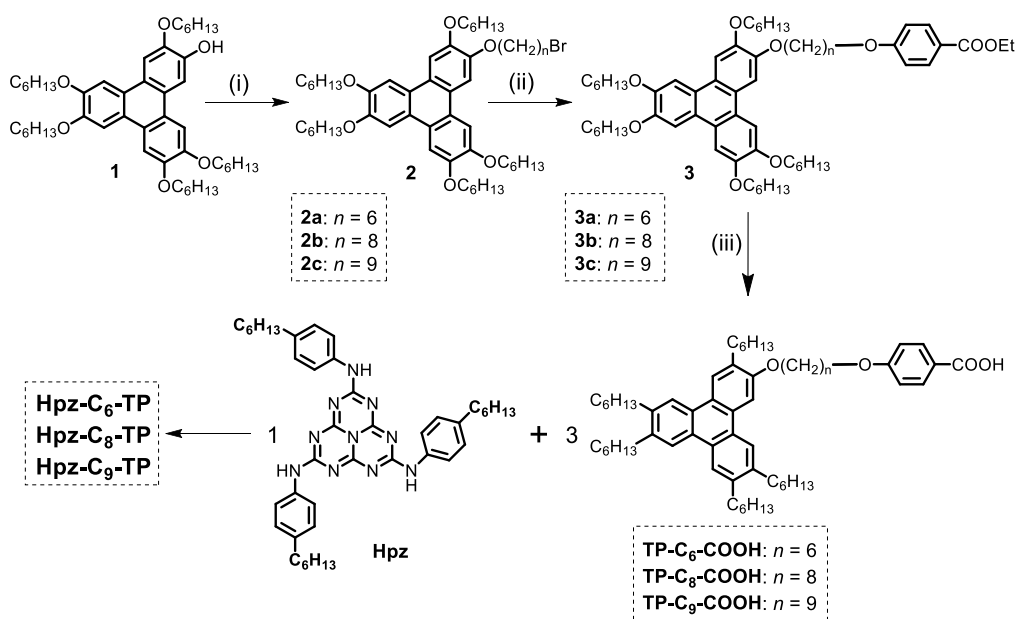
The molecular design of **Hpz-C<sub>n</sub>-TP** ( $n = 6, 8, 9$ ) complexes consists of central electron-deficient heptazine derivative **Hpz** attached to which three electron-donor TP acids, **TP-C<sub>n</sub>-COOH** through complementary H-bonding forming D-A molecular architectures (Figure 2.36). The structure of **Hpz-C<sub>8</sub>-TP** was optimized at the B3LYP/6-31G (d, p) level and the results demonstrate the occurrence of complementary H-bonding that directs the strong binding between the **Hpz** unit and **TP-C<sub>8</sub>-COOH** acids. The H-bond lengths obtained for  $\text{NH}^{\text{a}} \cdots \text{O}$  and  $\text{OH}^{\text{b}} \cdots \text{N}$  are 1.82 Å and 1.77 Å, respectively as shown in Figure 2.36a.

The heptazine derivative **Hpz** was prepared as per the previously reported procedure,<sup>103</sup> which involves the reaction between 4-hexyl aniline and heptazine chloride (NMR of heptazine chloride: Figure A36). The alkyl chain substituted aromatic amine was chosen to ensure the **Hpz** solubility in common organic solvents necessitates to form complexes. The three benzoic acids connected TP derivatives **TP-C<sub>6</sub>-COOH**, **TP-C<sub>8</sub>-COOH**, and **TP-C<sub>9</sub>-COOH** were achieved by varying the length of the flexible methylene spacer. The TP-based benzoic acid derivatives were chosen, as the TP unit is an electron-rich system that induces stable columnar mesomorphism<sup>4</sup> and it has been previously reported that **TP-C<sub>6</sub>-COOH** forms supramolecular H-bonded complexes with columnar mesomorphism.<sup>54</sup> Finally, the H-bonded **Hpz-C<sub>n</sub>-TP** complexes were formed by mixing the **Hpz** and **TP-C<sub>n</sub>-COOH** in 1:3 ratio, respectively in dichloromethane (DCM) (Scheme 2.3). The detailed synthesis and characterization of acids as

well as complexes are provided in the experimental section and their  $^1\text{H}$  and  $^{13}\text{C}$  NMR spectra are given in Appendix II (Figure A37-A48, Page 151). The formation of **Hpz-C<sub>n</sub>-TP** complexes was structurally confirmed by comparative FT-IR and NMR studies as described below.

### 2.3.3.2 Comparative IR and NMR studies

The IR spectra (KBr) of the individual components **Hpz** and **TP-C<sub>n</sub>-COOH** were compared with the resulting complexes **Hpz-C<sub>n</sub>-TP** (Figure 2.37 and Figure A49-A50, Appendix II, Page 157). The samples for the IR studies were prepared by taking approximately 5 mg of sample and grinding it with KBr powder. Subsequently, the KBr pellet was formed by using the grinded mixture.



**Scheme 2.3** Formation of supramolecular H-bonded complexes: (i)  $\text{K}_2\text{CO}_3$ ,  $\text{Br}(\text{CH}_2)_n\text{Br}$ , butanone, 80 °C, 24 hours; (ii) Ethyl 4-hydroxybenzoate,  $\text{K}_2\text{CO}_3$ , KI, butanone, 80 °C, 24 hours; (iii) KOH, 1,4-dioxane/ $\text{H}_2\text{O}$ , 80 °C, 20 hours.

Finally, the KBr pellet was used for the IR studies. In the case of **Hpz-C<sub>n</sub>-TP** complexes, the IR spectra were recorded by using both the thermally treated and without thermally treated KBr pellets. In both cases, the same values of  $-\text{NH}$  stretching and  $-\text{C}=\text{O}$  stretching were observed. For thermal treatment, the KBr pellet (containing sample) was first heated up to the isotropic temperatures (of the corresponding complex) and then cooled back to the room

temperature which was then used for the measurements. For **Hpz-C<sub>6</sub>-TP** (Figure 2.37), a sharp –NH stretching peak at 3350 cm<sup>-1</sup> (corresponding to nonassociated –NH) and along with other broad –NH peaks (equivalent to intermolecular H-bonded peaks) in **Hpz** gets converted to a much simpler one broad peak at 3295 cm<sup>-1</sup> in case of the complex. Interestingly, it can be noted that the carbonyl peak in complexes (1682 cm<sup>-1</sup>) shifts to lower wavenumber (i.e. weakening of C=O bond) in comparison to the carbonyl peak appears in free (1717 cm<sup>-1</sup>) and dimeric form of **TP-C<sub>n</sub>-COOH** acids (1688 cm<sup>-1</sup>)<sup>54</sup> which indicates the formation of relatively stronger H-bonding in heptazine based **Hpz-C<sub>n</sub>-TP** complexes (in comparison to the **TP-C<sub>n</sub>-COOH** acid dimers).

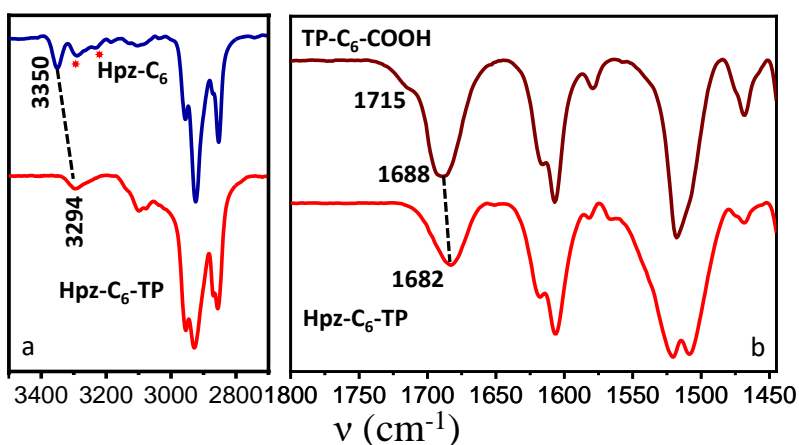


**Figure 2.37** FTIR spectral profiles of **Hpz-C<sub>6</sub>-TP** complex compared to those of (a) **Hpz** in the –NH stretching peak regime and (b) **TP-C<sub>6</sub>-COOH** in the carbonyl (–C=O) stretching region.

Furthermore, in comparative NMR studies of the resultant complexes (Figure 2.38 and Figure A51-A53, Appendix II, Page 158), the observed integration of all the protons in 1:3 ratio of **Hpz** and **TP-C<sub>n</sub>-COOH**, respectively confirmed the stoichiometric formation of complexes. In addition, the –NH protons H<sub>a</sub> (participating in H-bonding) in **Hpz** undergo obvious downfield shift (H<sub>a</sub>) upon complexation in **Hpz**. Interestingly, in CD<sub>2</sub>Cl<sub>2</sub>, the aromatic hydrogens H<sub>b</sub> of pure **Hpz**, present in the close proximity to the H-bonded functionalities become unsymmetrical (split into two different sets of peaks H<sub>b</sub>' and H<sub>b</sub>'') and shifted downfield (H<sub>b</sub>') in complexes. It can be noted that the –NH protons (H<sub>a</sub>) in CD<sub>2</sub>Cl<sub>2</sub> have merged with the aromatic protons (H<sub>b</sub>) while in CDCl<sub>3</sub> it is clearly separated from the H<sub>b</sub> protons (Figure A51, Appendix II, Page 158). Apart from these, the TP aromatic ring protons shifted

upfield due to increased  $\pi$ - $\pi$  interactions in complexes while other aromatic protons ( $H_c$ ,  $H_d$ , and  $H_e$ ) endured small shifts. The variation in chemical shifts indicated the formation of directional supramolecular H-bonded complexes. The **Hpz-C<sub>n</sub>-TP** complexes show concentration-dependent NMR (Figure 2.39 and Figure A54-A55, Appendix II, Page 160). For example, for **Hpz-C<sub>6</sub>-TP** complex, on increasing the concentration the  $-NH$  ( $H_a'$ ) and  $H_b'$  peak (in proximity to the H-bonded functionality) get shifted to downfield (indicating the strengthening of H-bonding) while the aromatic hydrogens corresponding to triphenylenes

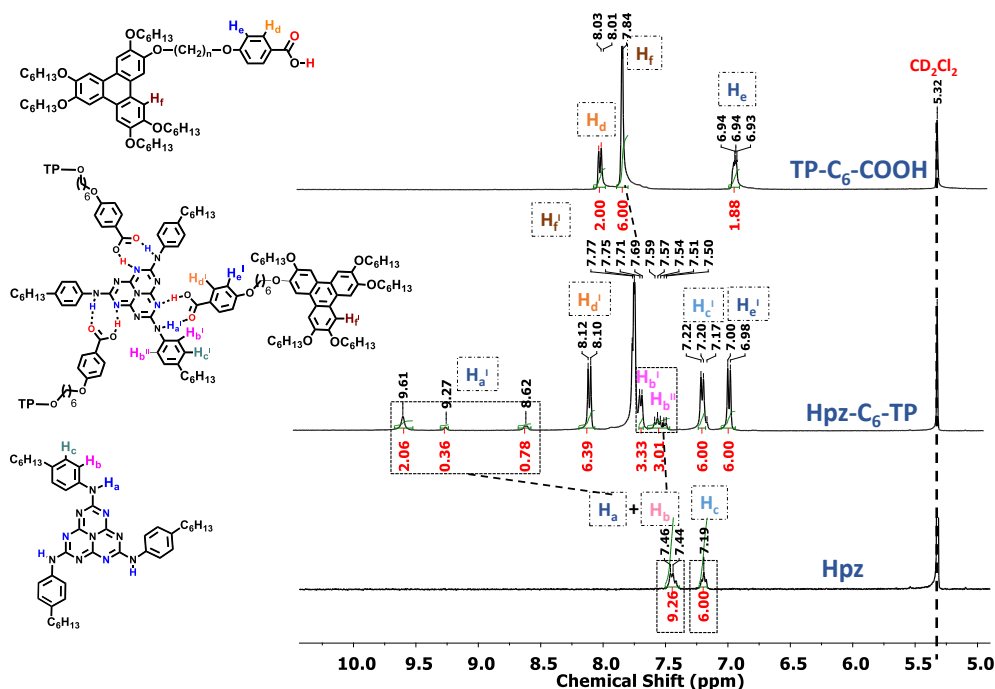


**Figure 2.38** Comparative <sup>1</sup>H NMR spectra (in CD<sub>2</sub>Cl<sub>2</sub>) of pure heptazine derivative **Hpz** (0.005 M), pure TP based benzoic acid **TP-C<sub>6</sub>-COOH** (0.015 M) and their corresponding complex, **Hpz-C<sub>6</sub>-TP** (0.005 M).

( $H_f'$ ) shifted upfield (indicating the occurrence of aggregation due to  $\pi$ - $\pi$  stacking) (Figure 2.39). It can be noted  $-NH$  protons in case of amine substituted heptazine derivatives (all the derivatives discussed in Part A, Part B and Part C of chapter 2) give rise to different  $-NH$  signals. The  $-NH$  functionality is attached to the highly electron-deficient heptazine ring which further increases the acidic nature of the  $-NH$  protons, hence making it more labile to undergo tautomerism. The tautomerism phenomena is very much prevailing in the  $-OH$  substituted heptazine derivative (i.e. cyameluric acid), where approximately 17 tautomeric structures are

in equilibrium in the solution state.<sup>104</sup> Similarly in the present case, the possibility of tautomeric structures in the solution state is obvious where the equilibrium between various tautomers may be present and in the NMR time scale, these tautomeric forms can be distinguishable which may rise to the different –NH signals. This can also be seen in the earlier reports of amine substituted heptazine derivatives where -NH hydrogens in the NMR spectra did not appear as equivalent.<sup>65,103,104</sup> The observed changes in IR as well as in NMR spectra of the complexes are in high accordance with the previous complementary H-bonded systems.<sup>55,63,103,105</sup> Furthermore, the polarized optical microscopy (POM) and wide-angle X-ray diffraction (XRD) studies also supported the realization of H-bonded complexes (*vide-infra*).

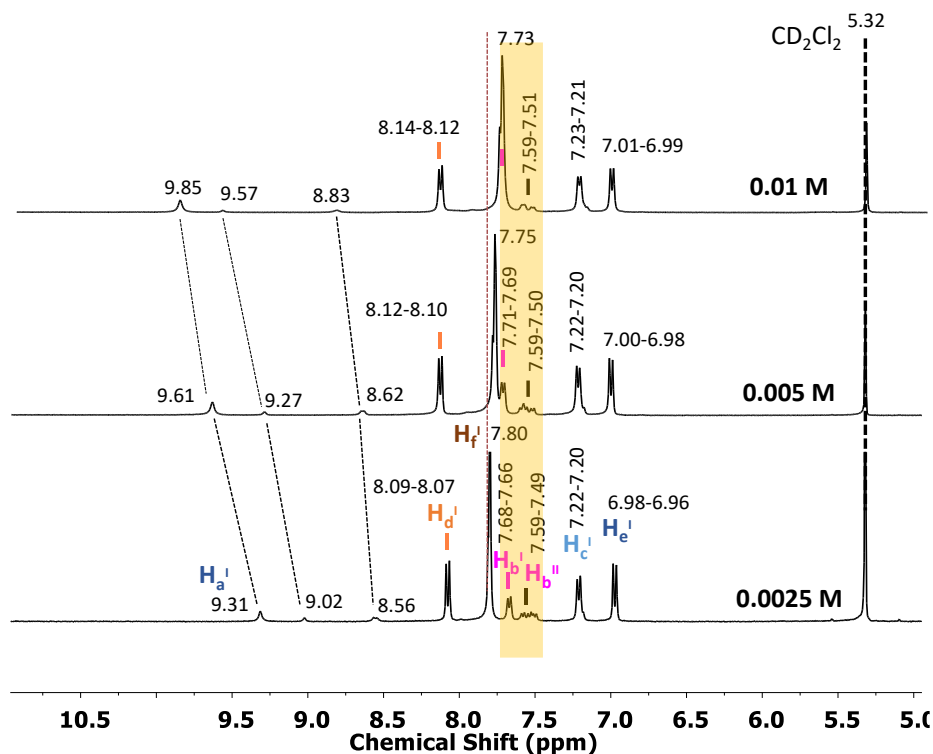


**Figure 2.39** Concentration-dependent  $^1\text{H}$  NMR spectra of the **Hpz-C<sub>6</sub>-TP** complex in  $\text{CD}_2\text{Cl}_2$ .

### 2.3.3.3 Thermal behaviour

The H-bonded **Hpz-C<sub>n</sub>-TP** complexes exhibited high thermal stability with decomposition temperatures ( $T_d$ ) above 330 °C (Table 2.8 and Figure 2.40). The pure components *viz.* heptazine derivative **Hpz** and TP-based benzoic acids **TP-C<sub>n</sub>-COOH** were found to be non-mesomorphic. The **Hpz** did not melt up to 250 °C<sup>103</sup> while all TP acids melted in the range of

60-107 °C. Under POM, **Hpz-C<sub>n</sub>-TP** complexes can be viewed as homogeneous materials and displayed characteristic columnar textures (pseudo focal conic textures) over a wide temperature range (Figure 2.41a-c). Hence, the observation of mesogenic behaviour from the non-mesogenic components directed the formation of H-bonded complexes. In DSC, all the complexes showed one peak corresponds to mesophase to isotropic phase transition on heating as well as on cooling which indicates the enantiotropic nature of the complexes (Figure 2.41d-f). The peaks were highly reversible over several thermal cycles which indicated the reversibility and stability of the complexes (Figure 2.42).

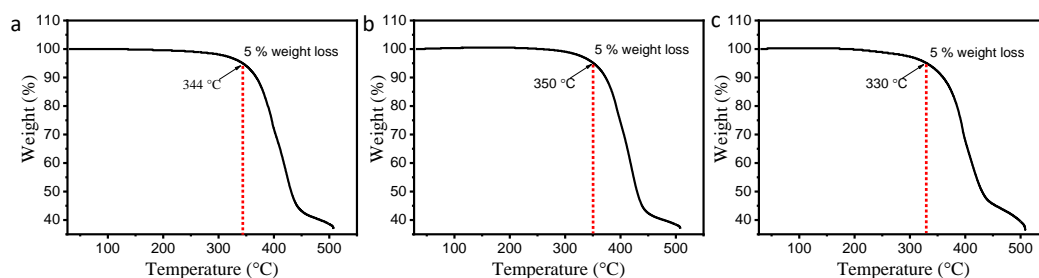


**Figure 2.40** TGA curves for **Hpz-C<sub>n</sub>-TP** complexes: (a) **Hpz-C<sub>6</sub>-TP**, (b) **Hpz-C<sub>8</sub>-TP** and (c) **Hpz-C<sub>9</sub>-TP** complexes recorded under a nitrogen atmosphere with a rate of 10 °C/min.

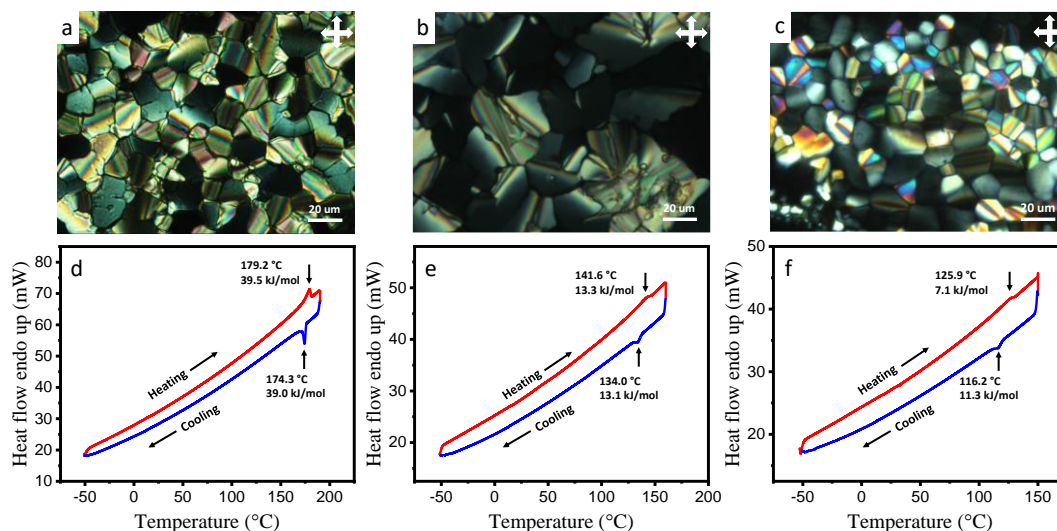


**Figure 2.41** (a) Optical microscopic images of (a) **Hpz-C<sub>6</sub>-TP** complex at 63 °C, (b) **Hpz-C<sub>8</sub>-TP** at 40 °C and (c) **Hpz-C<sub>9</sub>-TP** at 56.7 °C captured upon cooling the samples from isotropic state with the rate of 5 °C/min under crossed polarizer ( $\times 500$ ). DSC thermogram of (d) **Hpz-C<sub>6</sub>-TP** complexes, (e) **Hpz-C<sub>8</sub>-TP** complex and (f) **Hpz-C<sub>9</sub>-TP** complex recorded with the scanning rate of 10 °C/min.



**Table 2.8** Thermal behaviour of the **Hpz-C<sub>n</sub>-TP** complexes.

Complex	Heating <sup>a</sup>	Cooling <sup>a</sup>	<i>T<sub>d</sub></i> (°C) <sup>b</sup>
<b>Hpz-C<sub>6</sub>-TP</b>	Col <sub>ho</sub> 179.2 (39.5) Iso	Iso 174.3 (39.0) Col <sub>ho</sub>	344
<b>Hpz-C<sub>8</sub>-TP</b>	Col <sub>ho</sub> 141.6 (13.3) Iso	Iso 134.0 (13.1) Col <sub>ho</sub>	350
<b>Hpz-C<sub>9</sub>-TP</b>	Col <sub>ho</sub> 125.9 (7.1) Iso	Iso 116.2 (11.3) Col <sub>ho</sub>	330

<sup>a</sup>Phase transition temperatures are in °C as obtained by DSC with the scan rate of 10 °C/min and enthalpy values mentioned in brackets are in kJ/mol. <sup>b</sup>decomposition temperatures corresponding to 5% weight loss. Abbreviations: Col<sub>ho</sub>- ordered columnar hexagonal, Iso-isotropic phase.

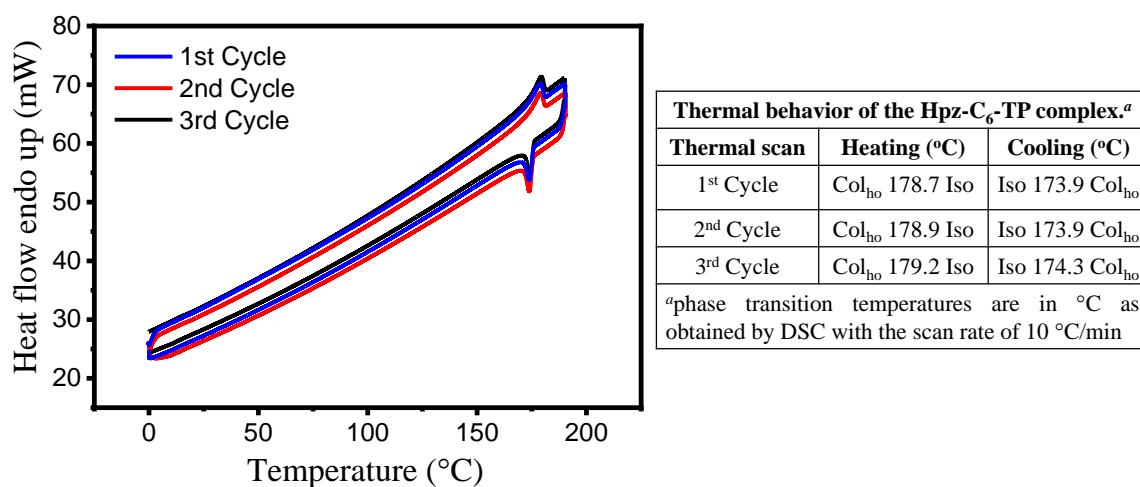


**Figure 2.42** (Left) Highly reversible DSC thermal cycles (No. of cycles are 3) of **Hpz-C<sub>6</sub>-TP** complex recorded under nitrogen atmosphere with 10 °C/min, and (Right table) corresponding observed phase transition temperatures.

In particular, DSC studies validate the realization of homogeneous supramolecular H-bonded complexes as the phase transition peaks appeared entirely at different temperatures than those of individual components. The phase transition temperatures and corresponding enthalpy values are mentioned in Table 2.8.

#### 2.3.3.4 X-ray diffraction studies

The phase behaviour of supramolecular H-bonded complexes was performed by variable temperature X-ray diffraction (XRD) studies. The **Hpz-C<sub>n</sub>-TP** complexes self-assembled in hexagonal lattice throughout the mesophase range. For example, **Hpz-C<sub>6</sub>-TP** at 20 °C, exhibited many peaks in the small-angle and mid-angle region with a *d*-spacing

ratio  $1: \frac{1}{\sqrt{3}}: \frac{1}{\sqrt{4}}: \frac{1}{\sqrt{7}}: \frac{1}{\sqrt{12}}: \frac{1}{\sqrt{16}}: \frac{1}{\sqrt{25}}$  that correspond to the reflections from (100), (110), (200), (210), (220), (400), and (500) planes of the two-dimensional (2D) hexagonal lattice, respectively (Figure 2.43a,b, Table 2.9). The quantitative comparison of the relative intensities and shapes of observed reflections revealed that (100) and (210) reflections are weak (and broad) while others are sharp. In the wide-angle region, a broad peak ( $h_a$ ) at 4.88 Å and a narrow peak ( $h_c$ ) at 3.76 Å appeared due to alkyl chain-chain correlation and core-core correlation ( $\pi$ - $\pi$  interaction), respectively (Figure 2.43c). The narrow and strong nature of  $h_c$

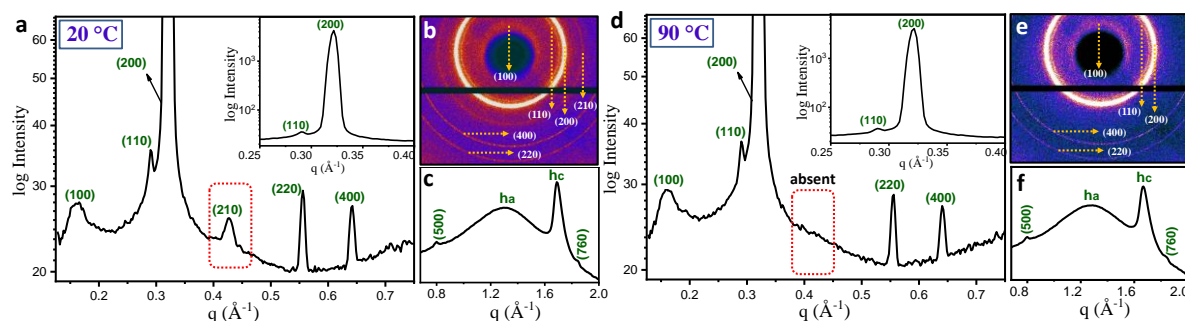


**Figure 2.43** 1D XRD profile of **Hpz-C6-TP** complex (a) at 20 °C and (d) at 90 °C in small-angle regime with indexing on 2D hexagonal lattice; Inset illustrates the zoomed version of the small-angle region showing the (110) and (200) peak. Corresponding 2D diffraction pattern of the small-angle regime (b) at 20 °C and (e) at 90 °C. 1D XRD profile of **Hpz-C6-TP** complex (c) at 20 °C and (f) at 90 °C in the wide-angle region;  $h_a$  represents fluid alkyl chain-chain correlations,  $h_c$  corresponds to core-core (face to face) correlations.

peak confirming the occurrence of ordered columnar structure and hence the phase is columnar hexagonal ( $\text{Col}_h$ ).<sup>106</sup> The  $h_c$  peak has Miller index (001) and its value is equal to the dimension of the unit cell normal to the 2D hexagonal lattice plane.<sup>105</sup> At higher temperature (90 °C), the (210) peak disappeared while the other peaks were equally present, indicating the obvious decrement in columnar order of hexagonal phase upon increasing the temperatures (Figure 2.43d,e), however, the phase remained  $\text{Col}_h$ . The hexagonal lattice parameter ( $a$ ) was found to be 44.67 Å at 20 °C and 44.78 Å at 90 °C (Table 2.9). **Hpz-C9-TP** complex showed a similar  $\text{Col}_h$  self-assembly behaviour to that of **Hpz-C6-TP** complex (Figure 2.44a-c), however, at a higher temperature (90 °C), both (100) and (210) peaks are absent (Figure 2.44d-f, Table 2.9). On the other hand, **Hpz-C8-TP** complex (Figure 2.45a-c) at 20 °C showed many peaks in the

small and mid-angle regime with  $d$ -spacing in ratios  $\frac{1}{\sqrt{3}} : \frac{1}{\sqrt{4}} : \frac{1}{\sqrt{7}} : \frac{1}{\sqrt{12}} : \frac{1}{\sqrt{13}} : \frac{1}{\sqrt{16}} : \frac{1}{\sqrt{25}}$  that can be fitted to the reflections from the (110), (200), (210), (220), (310), (400) and (500) planes of 2D hexagonal lattice while at a higher temperature (e.g. at 90 °C) only (110), (200), (220) and (500) reflections of the Col<sub>h</sub> phase were present. It is important to note that in all these complexes, the (100) reflection is very weak or absent in comparison to (200) reflection (which is found to be the strongest one). Since (200) planes lie at  $1/\sqrt{4}$  the interplanar distance of (100) planes, hence implies that there is a strong modulation of the electronic density<sup>54,107,108</sup> with a period  $1/\sqrt{4}$  times the (100) spacing. This is suggesting the formation of an additional hexagonal network or sub structure.

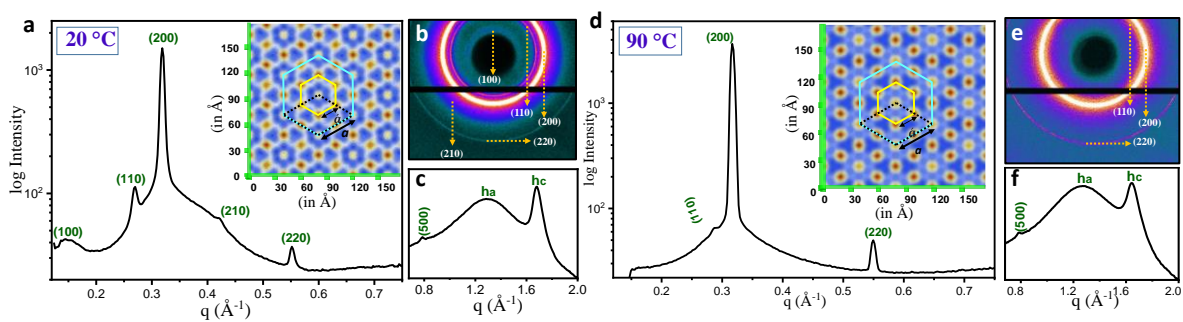


**Figure 2.44** (a) 1D XRD profile of **Hpz-C<sub>9</sub>-TP** complex in small-angle (a & d) and wide-angle regime (c & f): (a & c) at 20 °C and (d & f) at 90 °C with indexing on 2D hexagonal lattice; Insets of (a) and (d) illustrates the corresponding EDMs in the Col<sub>h</sub> phase showing the conventional unit cell of hexagonal lattice (cyan color) and sub structure with hexagonal symmetry (yellow color) having lattice parameter  $a$  and  $a'$ , respectively. The dotted rhombus in black color represents the primitive unit cell of the hexagonal lattice.. 2D diffraction pattern of **Hpz-C<sub>9</sub>-TP** complex in small-angle regime (b) at 20 °C and (e) at 90 °C as well as corresponding 1D XRD profile in the wide-angle region;  $h_a$  represents fluid alkyl chain-chain correlations,  $h_c$  corresponds to core-core (face to face) correlations.

In order to have a better understanding of the arrangement of the molecules on the 2D hexagonal lattice, the corresponding electron density maps (EDMs)<sup>74</sup> are reconstructed from the diffraction pattern of the **Hpz-C<sub>n</sub>-TP** complexes (Figure 2.44-2.45, Figure 2.46a). As shown in EDMs, the unit cell of the hexagonal lattice indicating the occurrence of sub structure with hexagonal symmetry. The observed value of  $a$  corresponds to the lattice parameter of the

hexagonal lattice which is just  $\sqrt{4}$  times the value of sub structure lattice parameter  $a'$  (Table 2.9). For example, in **Hpz-C6-TP** complex the calculated value of  $a'$  from EDM is 22.335 Å ( $\sqrt{4}$  times smaller than  $a$  (44.67 Å)) which relates roughly to the diameter of the hexa-substituted TP. This indicates that the sub-hexagonal structure is formed by segregated electron-rich TP units. It can be noted that EDMs exhibit two types of higher electron density regions; say 'I' and 'II' (Figure 2.46a) which are centred on 6- and 2-fold symmetry axes, respectively. The ratio of electron density region of 'II' to the region 'I', measured from the

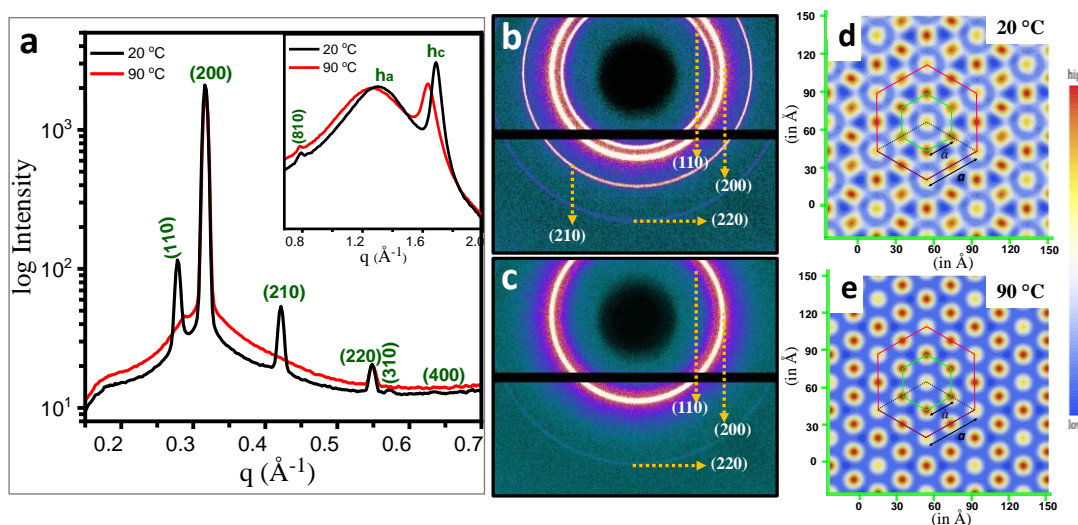


**Figure 2.45** (a) 1D XRD profile of **Hpz-C8-TP** complex at 20 °C and 90 °C in small-angle regime with indexing on 2D hexagonal lattice; Inset illustrates the corresponding 1D profile in the wide-angle region;  $h_a$  represents fluid alkyl chain-chain correlations,  $h_c$  corresponds to core-core (face to face) correlations. Corresponding 2D diffraction pattern of the small-angle regime (b) at 20 °C and (c) 90 °C. EDM of **Hpz-C8-TP** complex (d) at 20 °C and (e) at 90 °C in the Col<sub>h</sub> phase showing the conventional unit cell of hexagonal lattice (cyan color) and sub structure with hexagonal symmetry (yellow color) having lattice parameter  $a$  and  $a'$ , respectively. The dotted rhombus in black color represents the primitive unit cell of the hexagonal lattice.

EDMs are in the range of 1.25 to 1.40. On the other hand, the calculated value of electron density for the HP and TP core (excluding alkyl chains) are found to be 491.9 and 648.7 electrons nm<sup>-3</sup>, respectively. Thus, the ratio of electron density of HP unit to that of TP unit is calculated to be 1.32. This indicates that the region 'I' and 'II' of the EDM correspond to the

HP and TP units, respectively. The proposed structural model also accounts an interesting effect of the formation of the hexagonal lattice with sub structure where HP (pink circle) and TP (green circles) units of star-shaped complex molecules segregate into two different columns. As shown in Figure 2.46b-d, the segregation happens as the orientation of the knots between pink and green circles has two possibilities (Figure 2.46b,d), (Type-1:  $30^\circ$ ,  $150^\circ$ ,  $270^\circ$ ) or (Type-2:  $90^\circ$ ,  $210^\circ$ ,  $330^\circ$ ). These two orientations must be present with equal probability in the structure. However, the 2D arrangement of the molecule on the hexagonal lattice can be easily explained if one of the orientations takes place in a given 2D lamina. Besides, along the columnar axis, both orientations can fill-in successive lamina in ABAB... stacking manner (Figure 2.46d).

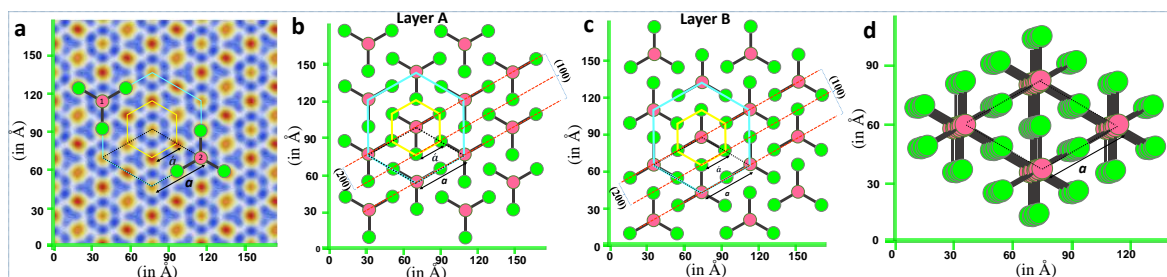


**Figure 2.46** (a) EDM of **HpZ-C<sub>6</sub>-TP** complex at 20 °C in the Col<sub>h</sub> phase showing conventional unit cell of the hexagonal lattice (cyan color) and sub structure with hexagonal symmetry (yellow color) having lattice parameter  $a$  and  $a'$ , respectively. Pink and green circles correspond to HP and TP units and are centred on 6- and 2-fold symmetry axes, respectively with two possible orientations: Type-1 and Type-2 of the complexes in different strata. The dotted rhombus in black color represents the primitive unit cell of the hexagonal lattice. 2D Projection of the structure showing hexagonal lattice with (b) layer A having Type-1 molecular orientation and (c) layer B having Type-2 orientation. The family of (100) and (200) planes is also shown. (d) Arrangement of the molecules in the Col<sub>h</sub> phase formed by ABAB.... stacking of layer A followed by layer B and so forth, along the direction of the column. Therefore, layer A which is having an orientation of Type-1 (Figure 2.46b) is followed by layer B with the orientation of Type-2 (Figure 2.46c), and so forth, separated by a distance corresponding to the spacing of  $h_c$  peak in such a way that HP and TP columns segregate. The green circle in the center of the unit cell (Figure 2.46d), causes an interference effect that contributes to reduce the intensity of the (100) reflection and also of the ( $h00$ ) reflections for odd  $h$  values.

**Table 2.9** The Miller indices, observed and calculated  $d$ -spacing corresponding to planes of the diffraction peaks of the 2D hexagonal lattice for **Hpz-C<sub>6</sub>-TP** complex.<sup>a</sup>

$(hk)$	$d$ -spacing Experimental $d_{\text{obs}} (\text{\AA})$	$d$ -spacing Calculated $d_{\text{cal}} (\text{\AA})$	Relative Intensity $I(hk)$	Multiplicity	Phase $\Phi(hk)$
<b>Hpz-C<sub>6</sub>-TP complex: Col<sub>h</sub> phase at 20 °C: <math>a = 44.67 \text{ \AA}</math>; <math>h_c = 3.76 \text{ \AA}</math></b>					
100	$38.66 \pm 0.30$	38.68	3.24	6	$\pi$
110	$22.12 \pm 0.08$	22.35	3.54	6	$\pi$
200	$19.34 \pm 0.08$	19.34	100.00	6	0
210	$14.63 \pm 0.12$	14.62	5.62	12	0
220	$11.22 \pm 0.08$	11.17	2.60	6	0
400	$9.71 \pm 0.08$	9.67	3.03	6	$\pi$
500	$7.85 \pm 0.08$	7.74	$\backslash\backslash$	$\backslash\backslash$	$\backslash\backslash$
$h_a$	$4.88 \pm 0.12$	Fluid alkyl chain			
$h_c$	$3.76 \pm 0.08$	$\pi$ - $\pi$ interaction			
(001)					
760	$3.41 \pm 0.08$	3.43			
<b>Col<sub>h</sub> phase at 90 °C: <math>a = 44.78 \text{ \AA}</math>; <math>h_c = 3.78 \text{ \AA}</math></b>					
100	$38.78 \pm 0.30$	38.78	4.23	6	$\pi$
110	$22.27 \pm 0.08$	22.39	2.79	6	$\pi$
200	$19.39 \pm 0.08$	19.39	100.00	6	0
220	$11.30 \pm 0.08$	11.19	2.94	6	0
400	$9.78 \pm 0.08$	9.70	3.35	6	$\pi$
500	$7.85 \pm 0.08$	7.76	$\backslash\backslash$	$\backslash\backslash$	$\backslash\backslash$
$h_a$	$4.88 \pm 0.12$	Fluid alkyl chain			
$h_c$	$3.78 \pm 0.08$	$\pi$ - $\pi$ interaction			
(001)					
760	$3.43 \pm 0.08$	3.44			
<b>Hpz-C<sub>8</sub>-TP complex: Col<sub>h</sub> phase at 20 °C: <math>a = 45.60 \text{ \AA}</math>; <math>h_c = 3.78 \text{ \AA}</math></b>					
110	$22.68 \pm 0.08$	22.48	7.05	6	$\pi$
200	$19.88 \pm 0.08$	19.88	100.00	6	0
210	$14.89 \pm 0.12$	14.93	3.16	12	0
220	$11.45 \pm 0.08$	11.40	0.61	6	0
310	$10.95 \pm 0.09$	10.95	0.18	12	$\pi$
400	$9.92 \pm 0.08$	9.87	0.15	6	$\pi$
500	$7.98 \pm 0.08$	7.90	$//$	$//$	$//$

$h_a$	$4.88 \pm 0.12$	Fluid alkyl chain			
$h_c$	$3.78 \pm 0.08$	$\pi$ - $\pi$ interaction			
(001)					
<b>Col<sub>h</sub> phase at 90 °C: <math>a = 44.95 \text{ \AA}</math>; <math>h_c = 3.80 \text{ \AA}</math></b>					
110	$22.29 \pm 0.08$	22.47	2.43	6	$\pi$
200	$19.46 \pm 0.08$	19.46	100.00	6	0
220	$11.32 \pm 0.08$	11.24	0.58	6	0
500	$7.92 \pm 0.08$	7.79	//	//	//
$h_a$	$4.96 \pm 0.12$	Fluid alkyl chain			
$h_c$	$3.80 \pm 0.08$	$\pi$ - $\pi$ interaction			
(001)					
<b>Hpz-C<sub>9</sub>-TP complex: Col<sub>h</sub> phase at 20 °C: <math>a = 46.22 \text{ \AA}</math>; <math>h_c = 3.77 \text{ \AA}</math></b>					
100	$40.03 \pm 0.30$	40.03	11.62	6	$\pi$
110	$23.11 \pm 0.08$	23.11	16.19	6	$\pi$
200	$20.01 \pm 0.08$	20.01	100.00	6	0
210	$15.10 \pm 0.12$	15.13	6.02	12	0
220	$11.40 \pm 0.08$	11.56	9.04	6	0
500	$7.99 \pm 0.08$	8.00	//	//	//
$h_a$	$4.86 \pm 0.12$	Fluid alkyl chain			
$h_c$	$3.77 \pm 0.08$	$\pi$ - $\pi$ interaction			
(001)					
<b>Col<sub>h</sub> phase at 90 °C: <math>a = 45.20 \text{ \AA}</math>; <math>h_c = 3.78 \text{ \AA}</math></b>					
110	$22.34 \pm 0.08$	22.60	4.92	6	$\pi$
200	$19.62 \pm 0.08$	19.57	100.00	6	0
220	$11.38 \pm 0.08$	11.30	4.21	6	0
500	$8.00 \pm 0.08$	7.83	//	//	//
$h_a$	$4.98 \pm 0.12$	Fluid alkyl chain			
$h_c$	$3.78 \pm 0.08$	$\pi$ - $\pi$ interaction			
(001)					
$a$ - $d$ -spacing are calculated by using the relation $d_{hk} = \frac{\sqrt{3}}{2} \frac{a}{\sqrt{h^2+hk+k^2}}$ where $a$ is the lattice parameter and $(hk)$ is the Miller indices of the plane. The $h_c$ peak has Miller index (001) and its value is equal to the dimension of the unit cell normal to the 2D hexagonal lattice plane.					

In contrast, the ( $h00$ ) reflections with even  $h$  values are reinforced and therefore, explain the occurrence of very low intensity (even absentee) of the (100) reflection in comparison to that



of the (200) peak. The calculated density value for all the complexes based on this model is in the range of 0.9-1.0 g cm<sup>-3</sup> which is reasonable and further authenticates our model.

### 2.3.3.5 Absorption studies in solution and solid-state

In addition, we have measured the UV-vis absorption spectra of **HPZ-C<sub>n</sub>-TP** ( $n = 6, 8$  and  $9$ ) complexes in both the solution ( $10^{-3}$  M in dichloromethane) and solid-state to get additional insight into their packing behaviours. From Figure 2.47, it is observed that all the complexes show absorption maxima ( $\lambda_{\text{max}}$ ) at 280 nm in the solution state which is corresponding to the triphenylene (TP) unit<sup>109-111</sup> of the complex. Whereas in the solid-state, the complexes exhibited a blue-shift of  $\sim 30$  nm (w.r.t.  $\lambda_{\text{max}}$ ) in comparison to its solution state. This clearly supports the co-facial arrangement (H-aggregation) of the TP units along with the columnar stack which is also consistent with the segregated columnar stacking.<sup>112</sup> For instances, Imahori and coworkers synthesized discotic liquid crystals consists of zinc phthalocyanine (ZnPc)-C60 dyad and explained its segregation based on blue-shift of the solid-state absorption arising from the ZnPc moiety relative to those in solution, supporting the face-to-face stacking of the ZnPc moieties in the discotic columnar structures.<sup>86</sup>

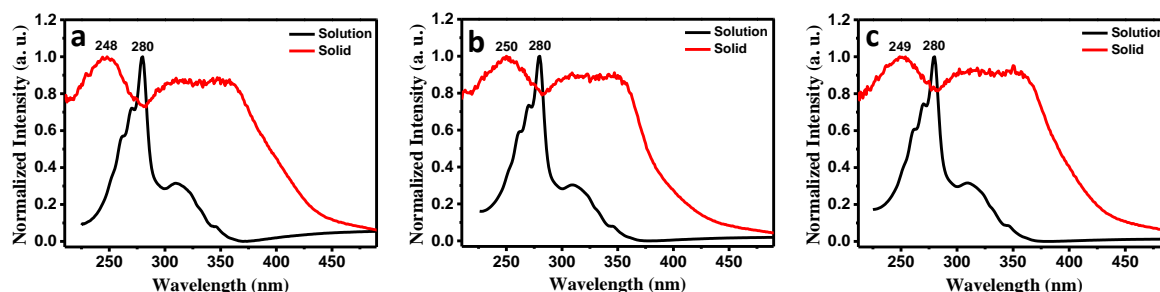


**Figure 2.47** UV-vis absorption spectra of (a) **HPZ-C<sub>6</sub>-TP**, (b) **HPZ-C<sub>8</sub>-TP** and (c) **HPZ-C<sub>9</sub>-TP** in solution ( $10^{-3}$  M dichloromethane) and solid state.

### 2.3.3.6 Theoretical and electrochemical studies

To get an insight into the electronic properties of the **Hpz-C<sub>n</sub>-TP** complexes, theoretical studies were carried out. The DFT calculations were performed for **Hpz-C<sub>8</sub>-TP** complex as well as for its individual components **Hpz** and **TP-C<sub>8</sub>-COOH**. The optimized geometry of **Hpz-C<sub>8</sub>-TP** complex (Figure 2.36) unveiled strong H-bonding between the complementary components as discussed before. Furthermore, HOMO and LUMO of the constituted components of the complex were first analyzed (Figure 2.48) and revealed that in case of TP



based molecular structures (e.g. in **TP-C<sub>8</sub>-COOH**), HOMO localized on the TP moiety while the LUMO lies on the benzoic acid part. On the other hand, in **Hpz** component, HOMO is not well distributed while the LUMO falls on the whole molecule. Interestingly, when both the components are mixed to form H-bonded **Hpz-C<sub>8</sub>-TP** complex, the HOMOs lie on the TP fragment while the LUMO is exclusively located on the central heptazine moiety and not on the TP connected benzoic acid groups. This indicated that the electronic properties get

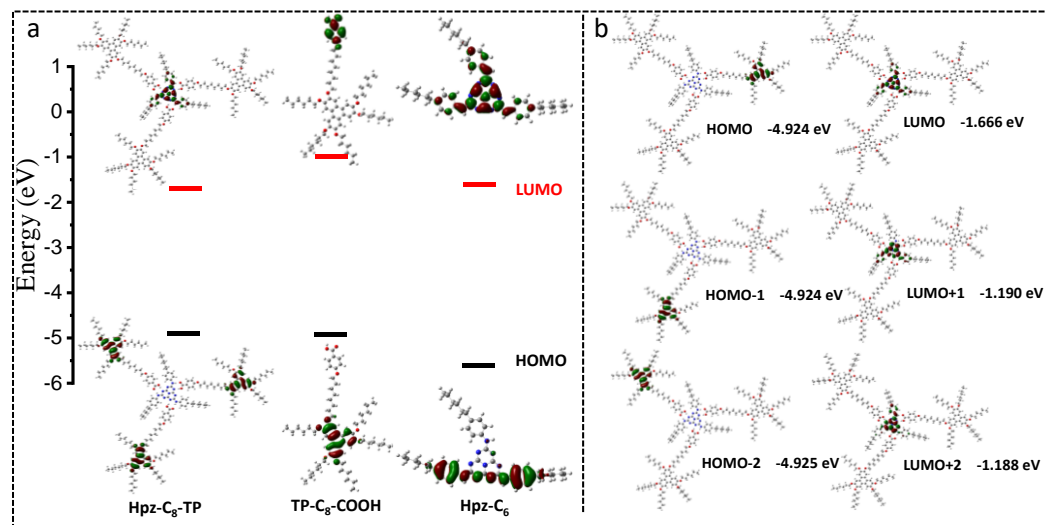


**Figure 2.48** (a) Frontier molecular orbitals and energy levels of **Hpz-C<sub>8</sub>-TP** complex and its individual components **TP-C<sub>8</sub>-COOH** and **Hpz** as obtained by DFT at B3LYP/6-31G (d,p) level of theory. (b) Frontier Molecular Orbitals (HOMO, HOMO-1, HOMO-2 and LUMO, LUMO-1, LUMO-2) and corresponding energy levels of complex **Hpz-C<sub>8</sub>-TP** as calculated at the B3LYP/6-31G (d,p) level of theory.

redistributed after the complex formation. It can be noted that in case of complex, the HOMO is composed of the combination of HOMO, HOMO-1 and HOMO-2 as these three energy levels are degenerate while in the case of LUMO, the degeneration of other energy levels was not perceived (Figure 2.48a). The spatial separation of molecular orbitals on the electron-rich (HOMO) and electron-deficient (LUMO) part in the resulting complexes indicates their ambipolar nature. The molecular orbitals and energy levels of **Hpz-C<sub>8</sub>-TP** complex and its individual components are plotted in Figure 2.48b.

Furthermore, the cyclic voltammetry technique was employed to estimate the energy levels that will further assist to choose the metal electrodes of appropriate work-function for the

charge transport studies of **Hpz-C<sub>n</sub>-TP** complexes. The HOMO and LUMO were calculated from the first onset oxidation and reduction potential, respectively (Table 2.10). The HOMO levels lie in the range of -5.24 eV to -5.28 eV that are likely to arise from the TP fragment<sup>113</sup> while the LUMO levels (-3.61 eV to -3.66 eV) are reminiscent of heptazine<sup>114</sup> moiety, **Hpz**. The CV details and voltammogram of all the complexes are given in Figure 2.49.

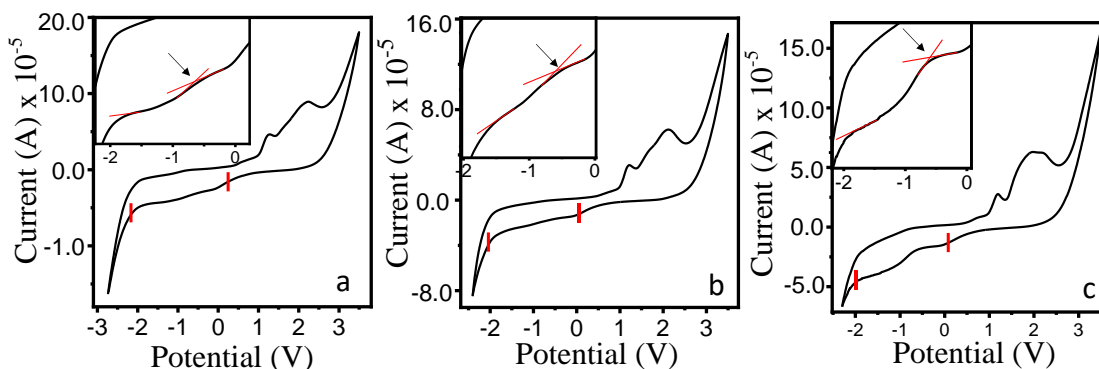


**Figure 2.49** Cyclic Voltammogram of **Hpz-C<sub>n</sub>-TP** complexes ( $1 \times 10^{-3}$  M): (a) **Hpz-C<sub>6</sub>-TP**, (b) **Hpz-C<sub>8</sub>-TP** and (c) **Hpz-C<sub>9</sub>-TP** complexes recorded in 0.1 M solution of TBAP in HPLC dichloromethane (Scan rate: 50 mV/s).

**Table 2.10.** Electrochemical data of **Hpz-C<sub>n</sub>-TP** series.<sup>a</sup>

Complex	E <sub>1ox</sub> <sup>b</sup> (V)	E <sub>1red</sub> <sup>c</sup> (V)	E <sub>HOMO</sub> <sup>d</sup> (eV)	E <sub>LUMO</sub> <sup>e</sup> (eV)
<b>Hpz-C<sub>6</sub>-Tp</b>	+1.02	-0.65	-5.28	-3.61
<b>Hpz-C<sub>8</sub>-Tp</b>	+0.99	-0.60	-5.25	-3.66
<b>Hpz-C<sub>9</sub>-Tp</b>	+0.98	-0.60	-5.24	-3.66

<sup>a</sup>in dichloromethane. <sup>b</sup>first onset oxidation potential. <sup>c</sup>first onset reduction potential. <sup>d</sup>Estimated as: E<sub>HOMO, CV</sub> = -[4.8-E<sub>1/2, Fc/Fc+</sub> + E<sub>1ox</sub>] eV, where E<sub>1/2, Fc/Fc+</sub> = 0.54 V. <sup>e</sup>Estimated as: E<sub>LUMO, CV</sub> = -[4.8-E<sub>1/2, Fc/Fc+</sub> + E<sub>1red</sub>] eV.

### 2.3.3.7 Charge transport measurements

To extract both electron and hole charge transport properties of **Hpz-C<sub>n</sub>-TP** complexes, space charge limited current (SCLC) technique, is used. One of the fundamental requirements of SCLC technique is to have an Ohmic contact between the injecting electrode and material (with HOMO level for a hole and with LUMO level for electron mobility). For hole mobility extraction of the reported **Hpz-C<sub>n</sub>-TP** complexes, having HOMO values of ~-5.25 eV, gold

(work function,  $\phi \sim -5.10$  eV) was chosen as injecting electrode. Gold can easily form an Ohmic contact with reported **Hpz-C<sub>n</sub>-TP** complexes (difference of  $\phi \sim 0.15$  eV between Au and **Hpz-C<sub>n</sub>-TP** HOMO) to ensure efficient injection of holes.<sup>115</sup> Indium tin oxide (ITO:  $\phi \sim -4.60$  eV) was chosen for a counter electrode in hole-only SCLC devices, ensuring a non-injecting electrode for electrons to minimize their charge carrier mobility contribution during current/voltage measurements. For electron mobility values reported in this work, ZnO (work function,  $\phi \sim -4.10$  eV), Cs<sub>2</sub>CO<sub>3</sub> (Device set-1;  $\phi \sim -2.9$  to  $-3.2$  eV) and Cs<sub>2</sub>CO<sub>3</sub> doped ZnO (by 1:9 ratio v/v; Device set-2,  $\phi \sim -3.4$  to  $-3.6$  eV) were used as injecting electrodes as well as counter electrodes in order to achieve Ohmic contact with the LUMO of **Hpz-C<sub>n</sub>-TP** complexes. Cs<sub>2</sub>CO<sub>3</sub> doping is known to lower the work function of ZnO by inducing interfacial dipoles, which is well established through ultraviolet photoelectron spectroscopy (UPS) in the literature.<sup>116</sup>

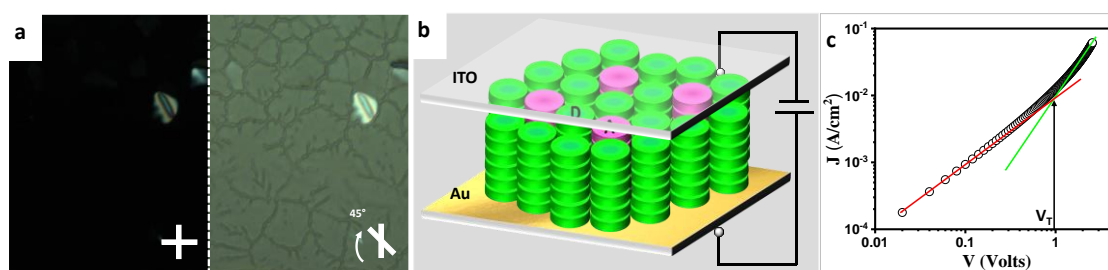


**Figure 2.50** (a) Optical microscopic images of **Hpz-C<sub>8</sub>-TP** complex in SCLC device cell under crossed polarizer at 90° (left) and 45° (right) (×500). (b) Schematic representation of SCLC device (Hole-only device) architecture. (c)  $J$ - $V$  curve for **Hpz-C<sub>8</sub>-TP** (at 25 °C) showing ideal Ohmic (slope 1, red line) and SCLC regimes (slope 2, green line).

The current density-voltage ( $J$ - $V$ ) characteristics obtained for **Hpz-C<sub>8</sub>-TP** in the hole-only device is shown in Figure 2.50c, where a linear as well as quadratic dependence of current with voltage, is clearly observed at lower and higher applied voltages, respectively. The transition at which current goes from linear to quadratic regime is referred to as threshold voltage ( $V_T$ ). A good match between experimentally calculated and theoretically extracted threshold value is a must for experiments considered to be reliable. It is evident from Table 2.11 that all **Hpz-C<sub>n</sub>-TP** complexes showed ambipolar charge transport behaviour except **Hpz-C<sub>6</sub>-TP**, where we were not able to extract electron mobility. Among **Hpz-C<sub>n</sub>-TP** complexes, **Hpz-C<sub>6</sub>-TP**

showed average hole mobility of  $1 \times 10^{-3} \text{ cm}^2 \text{ V}^{-1} \text{ s}^{-1}$  ( $4.5 \times 10^{-3} \text{ cm}^2 \text{ V}^{-1} \text{ s}^{-1}$  for champion device).

**Table 2.11** Mobility values (in  $\text{cm}^2 \text{ V}^{-1} \text{ s}^{-1}$ ) of **Hpz-C<sub>n</sub>-TP** complexes.<sup>a</sup>

Complex	Hpz-C <sub>6</sub> -TP	Hpz-C <sub>8</sub> -TP	Hpz-C <sub>9</sub> -TP
	$(1.00 \pm 0.35) \times 10^{-3}$ [ $4.50 \times 10^{-3}$ ]	$(1.01 \pm 0.36)$ [1.60]	$(4.98 \pm 1.48) \times 10^{-2}$ [ $8.30 \times 10^{-2}$ ]
		<b>Device set 1</b>	
		$(7.48 \pm 7.92) \times 10^{-7}$ [ $2.52 \times 10^{-6}$ ]	$(2.18 \pm 0.60) \times 10^{-3}$ [ $2.90 \times 10^{-3}$ ]
		<b>Device set 2</b>	
		$(6.83 \pm 3.82) \times 10^{-5}$ [ $1.50 \times 10^{-4}$ ]	
Electron	---		

<sup>a</sup>Average of 4-5 devices from a different area of the samples. The upper row consists of average mobility values and square brackets enclosed data of maximum or champion mobility.

**Hpz-C<sub>8</sub>-TP** and **Hpz-C<sub>9</sub>-TP** both showed ambipolar charge transport behaviour with **Hpz-C<sub>8</sub>-TP** showing average hole and electron mobility of 1.01 ( $1.60 \text{ cm}^2 \text{ V}^{-1} \text{ s}^{-1}$  for champion device) and  $6.83 \times 10^{-5} \text{ cm}^2 \text{ V}^{-1} \text{ s}^{-1}$  ( $1.5 \times 10^{-4} \text{ cm}^2 \text{ V}^{-1} \text{ s}^{-1}$  for champion device), respectively. Hole mobility of  $1.60 \text{ cm}^2 \text{ V}^{-1} \text{ s}^{-1}$  for **Hpz-C<sub>8</sub>-TP** is the highest ever reported mobility in H-bonded DLC systems. **Hpz-C<sub>9</sub>-TP** showed hole and electron mobility of values  $4.98 \times 10^{-2}$  ( $8.30 \times 10^{-2} \text{ cm}^2 \text{ V}^{-1} \text{ s}^{-1}$  for champion device) and  $2.18 \times 10^{-3} \text{ cm}^2 \text{ V}^{-1} \text{ s}^{-1}$  ( $2.90 \times 10^{-3} \text{ cm}^2 \text{ V}^{-1} \text{ s}^{-1}$  for champion device), respectively. POM images of hole-only device for **Hpz-C<sub>8</sub>-TP** (Figure 2.50a) showed a much improved columnar order and homeotropic alignment ( $\sim 98\%$ ) across the sample when compared with **Hpz-C<sub>9</sub>-TP** which showed  $\sim 52\%$  of homeotropic alignment (Figure 2.51a). The greater extent of homeotropic alignment observed in case of **Hpz-C<sub>8</sub>-TP** can be ascribed to its higher hole mobility value over **Hpz-C<sub>9</sub>-TP**. SCLC mobility in columnar discotic materials is highly anisotropic and needs perfect homeotropic alignment (Figure 2.50b) of the discotic columns along with its director as well as with the electrodes. The literature report suggests that a difference in the mobility values is observed in perfectly homeotropically aligned samples to that of partially or completely unaligned ones.<sup>117-123</sup> POM images of hole-only devices for **Hpz-C<sub>6</sub>-TP** (Figure 2.51b) revealed an unaligned sample ( $\sim 30\%$  of homeotropic alignment). Among various techniques reported to induce homeotropic alignment in DLCs such as introducing an alignment or surface anchoring layer,<sup>124,125</sup>

temperature treatment<sup>126</sup> roughness and surface energy of the substrate<sup>127</sup> used etc, temperature treatment was used to achieve the best possible homeotropic alignment in reported samples of hole and electron devices.

Electron mobility for **Hpz-C8-TP** extracted in Device set-1 and Device set-2 is also summarized in Table 2.11. Average electron mobility of  $7.48 \times 10^{-7}$  ( $2.52 \times 10^{-6} \text{ cm}^2 \text{ V}^{-1} \text{ s}^{-1}$  for champion device) for Device set-1 was observed as compared to  $6.83 \times 10^{-5}$  ( $1.50 \times 10^{-4} \text{ cm}^2 \text{ V}^{-1} \text{ s}^{-1}$  for champion device) for the same **Hpz-C8-TP** complex in Device set-2. This intriguing difference of two orders of magnitude in the electron mobility for **Hpz-C8-TP** complex can be best explained with the Ohmic contact of the injecting electrodes used in devices, which should ideally serve as an infinite reservoir of charges. Higher electron mobility observed for Device set-2 can be attributed to its near Ohmic contacts with **Hpz-C8-TP** complex as compared to Device set-1, where a difference of  $\sim 0.40 \text{ eV}$  in work function is observed with the LUMO value of **Hpz-C8-TP** complex. These results validate the importance of Ohmic contact requirements in SCLC technique in order to achieve efficient devices. The electron mobility for **Hpz-C9-TP** in Device set-2 geometry was found to be one order of magnitude higher than that of **Hpz-C8-TP** which was due to an improved alignment of the director along the column revealed in POM images (Figure 2.51c,d).

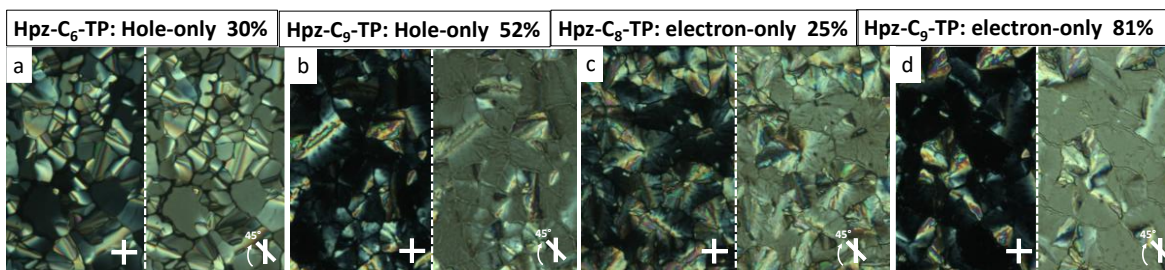


**Figure 2.51** POM images observed in SCLC hole-only device cells (a) **Hpz-C9-TP** (cell gap:  $3.41 \mu\text{m}$ ) (% of Homeotropic:  $\sim 52\%$ ), (b) **Hpz-C6-TP** (cell gap:  $3.63 \mu\text{m}$ ) (% of Homeotropic:  $\sim 30\%$ ), respectively. POM images observed in SCLC electron-only device cells with crossed polarizers at  $90^\circ$  and  $45^\circ$  for complexes (c) **Hpz-C8-TP** (cell gap:  $6.52 \mu\text{m}$ ) (% of Homeotropic:  $\sim 25\%$ , Device set-2) and (d) **Hpz-C9-TP** (Cell gap:  $3.03 \mu\text{m}$ ) (% of Homeotropic:  $\sim 81\%$ , Device set-2), respectively.

### 2.3.4 Conclusions

In summary, we have reported a series of three different **Hpz-C<sub>n</sub>-TP** complexes where electron-rich and electron-deficient components are linked together *via* means of non-covalent hydrogen-bonded approach. Supramolecular segregation of electron-rich and electron-deficient fragments which is broadly considered as an ideal architecture for efficient ambipolar transport is evident from the XRD studies. Furthermore, the formation of long-range, uniformly aligned homeotropic domains of **Hpz-C<sub>8</sub>-TP** complex in hole-only SCLC device contributed to the high hole mobility of  $1.60 \text{ cm}^2 \text{ V}^{-1} \text{ s}^{-1}$ , best known for H-bonded DLCs till date. Among reported **Hpz-C<sub>n</sub>-TP** complexes, **Hpz-C<sub>8</sub>-TP** and **Hpz-C<sub>9</sub>-TP** both showed electron mobilities of  $1.5 \times 10^{-4}$  and  $2.90 \times 10^{-3} \text{ cm}^2 \text{ V}^{-1} \text{ s}^{-1}$ , respectively. The present study reveals how a perfect blend of molecular properties with the supramolecular organization can be utilized effectively to achieve efficient ambipolar functional supramolecular materials for organic electronics.

**Acknowledgements.** *The SCLC device fabrication and measurement studies have been carried out in collaboration with Dr. Upendra Kumar Pandey at Shiv Nadar University and is greatly acknowledged and respected. Dr. Santosh Prasad Gupta (at Patna University) is duly acknowledged for the analysis of XRD data.*

### 2.3.5 Experimental section

**2.3.5.1 Synthesis of 4-(((6-((3,6,7,10,11-pentakis(hexyloxy)triphenylen-2-yl)oxy)alkyl)oxy)benzoic acids (TP-C<sub>n</sub>-COOH, n = 6, 8, 9).** In a one neck round bottom flask, 1,4-dioxane (10 ml) and water (2 ml) were taken in a 5:1 ratio. Then, compound **3** (1 equiv.) and potassium hydroxide (5.0 equiv.) was added into it and the mixture was stirred at 80 °C for 20 hours. After reaction completion, dilute HCl was added to the reaction mixture to adjust its pH value to 2-3. The obtained precipitates were filtered and air-dried to complete dryness.

**TP-C<sub>6</sub>-COOH:** FT-IR ( $\nu$  in  $\text{cm}^{-1}$ ): 3074.88, 2951.74, 2929.59, 2857.30, 2661.24, 2557.07, 1717.44, 1688.49, 1616.27, 1606.16, 1578.93, 1518.29, 1467.43, 1436.16, 1387.43, 1295.51, 1260.19, 1170.40, 1070.61, 1047.21, 928.46, 836.21, 800.14, 768.49, 726.70, 692.49, 645.34, 615.91, 601.20, 550.86, 506.90.  $^1\text{H}$  NMR (400 MHz,  $\text{CDCl}_3$ ,  $\delta$  in ppm):  $\delta$  8.03 (d,  $J = 7.7$  Hz,

2H), 7.84 (s, 6H), 6.92 (d,  $J = 8.8$  Hz, 2H), 4.23 (t,  $J = 6.5$  Hz, 12H), 4.06 (t,  $J = 6.5$  Hz, 2H), 2.00-1.87 (m, 14H), 1.68-1.49 (m, 14H), 1.40-1.26 (m, 20H), 0.93 (t,  $J = 6.7$  Hz, 15H).  $^{13}\text{C}$  NMR (100 MHz,  $\text{CDCl}_3$ ,  $\delta$  in ppm): 171.35, 163.71, 149.15, 149.09, 148.98, 132.44, 123.85, 123.79, 123.72, 121.57, 114.29, 107.59, 107.50, 107.38, 69.94, 69.86, 69.77, 69.66, 68.24, 31.83, 29.57, 29.26, 26.13, 26.00, 22.81, 14.20.

**TP-C<sub>8</sub>-COOH:** FT-IR ( $\nu$  in  $\text{cm}^{-1}$ ): 3073.71, 2951.57, 2929.00, 2855.32, 2665.79, 2558.69, 1717.51, 1688.19, 1616.58, 1606.73, 1578.68, 1517.52, 1467.77, 1437.10, 1387.56, 1295.13, 1260.40, 1171.30, 1049.02, 928.79, 837.65, 800.43, 769.30, 725.96, 693.05, 645.31, 615.21, 600.97, 551.80, 505.85.  $^1\text{H}$  NMR (400 MHz,  $\text{CDCl}_3$ ,  $\delta$  in ppm):  $\delta$  8.03 (d,  $J = 8.9$  Hz, 2H), 7.84 (s, 6H), 6.92 (d,  $J = 8.9$  Hz, 2H), 4.23 (t,  $J = 6.6$  Hz, 12H), 4.02 (t,  $J = 6.5$  Hz, 2H), 1.97-1.90 (m, 12H), 1.85-1.79 (m, 2H), 1.68-1.52 (m, 14H), 1.47-1.35 (m, 24H), 0.93 (t,  $J = 7.0$  Hz, 15H).  $^{13}\text{C}$  NMR (100 MHz,  $\text{CDCl}_3$ ,  $\delta$  in ppm): 171.60, 163.63, 148.95, 148.93, 148.89, 132.35, 132.29, 123.64, 123.61, 123.58, 121.38, 114.21, 114.10, 107.29, 69.76, 69.70, 69.65, 68.22, 31.72, 29.44, 29.14, 25.88, 22.70, 14.14, 14.05.

**TP-C<sub>9</sub>-COOH:** FT-IR ( $\nu$  in  $\text{cm}^{-1}$ ): 3075.41, 2952.22, 2927.72, 2855.31, 2666.49, 2553.13, 1716.70, 1688.38, 1615.47, 1606.16, 1579.04, 1517.53, 1467.48, 1436.16, 1387.24, 1294.43, 1261.70, 1171.75, 1049.06, 924.38, 836.43, 799.47, 771.29, 724.08, 694.03, 645.09, 615.22, 600.90, 550.49, 506.36.  $^1\text{H}$  NMR (400 MHz,  $\text{CDCl}_3$ ,  $\delta$  in ppm):  $\delta$  8.04 (d,  $J = 7.7$  Hz, 2H), 7.84 (s, 6H), 6.91 (d,  $J = 8.8$  Hz, 2H), 4.23 (t,  $J = 6.5$  Hz, 12H), 4.01 (t,  $J = 6.5$  Hz, 2H), 1.98-1.89 (m, 12H), 1.84-1.77 (m, 2H), 1.65-1.49 (m, 14H), 1.40-1.26 (m, 26H), 0.93 (t,  $J = 6.7$  Hz, 15H).  $^{13}\text{C}$  NMR (100 MHz,  $\text{CDCl}_3$ ,  $\delta$  in ppm): 171.15, 163.63, 148.96, 132.31, 123.59, 114.17, 107.27, 76.46, 69.67, 68.25, 29.41, 29.14, 28.38, 26.16, 26.01, 22.59, 14.13.

#### 2.3.5.2 General method adopted for the formation of Hpz-C<sub>n</sub>-TP ( $n = 6, 8, 9$ ) complexes.

The target complexes were prepared in HPLC dichloromethane by mixing the **Hpz** component and **TP-C<sub>n</sub>-COOH**, ( $n = 6, 8, 9$ ) acids in 1:3 ratio, respectively, in HPLC dichloromethane. After proper mixing of two components, the solvent was completely evaporated and then subsequently annealed at 80 °C for one hour to ensure the complexation process.

**Hpz-C<sub>6</sub>-TP:** FT-IR ( $\nu$  in  $\text{cm}^{-1}$ ): 3295.06, 3084.80, 2954.59, 2928.30, 2869.54, 2856.09, 2623.43, 2505.50, 1682.09, 1617.83, 1606.50, 1520.50, 1507.61, 1468.63, 1438.38, 1421.98, 1389.30, 1322.69, 1299.30, 1261.92, 1250.22, 1167.33, 1041.87, 848.11, 827.62, 795.97,

773.65, 725.16, 695.34, 640.14, 630.28, 600.68, 554.09, 504.98.  $^1\text{H}$  NMR (400 MHz,  $\text{CD}_2\text{Cl}_2$ ,  $\delta$  in ppm): 9.31-8.56 (m, 3H), 8.08 (d,  $J = 8.52$  Hz, 6H), 7.80 (s, 18H), 7.68-7.49 (m, 6H), 7.21 (d,  $J = 7.80$  Hz, 6H), 6.97 (d,  $J = 8.52$  Hz, 6H), 4.23-4.06 (m, 36H), 4.07 (t,  $J = 6.30$  Hz, 6H), 2.66-2.60 (m, 6H), 1.94-1.85 (m, 42H), 1.63-1.53 (m, 42H), 1.39-1.33 (m, 60H), 0.93 (t,  $J = 6.74$  Hz, 45H).  $^{13}\text{C}$  NMR (100 MHz,  $\text{CD}_2\text{Cl}_2$ ,  $\delta$  in ppm): 170.91, 163.90, 160.76, 154.17, 149.97, 149.51, 139.35, 136.36, 132.65, 129.04, 123.78, 123.74, 123.35, 121.17, 114.53, 107.18, 69.87, 68.86, 36.09, 32.51, 32.34, 32.04, 30.13, 30.04, 29.93, 29.88, 26.67, 26.61, 26.42, 23.35, 23.28, 14.57, 14.44.

**Hpz-C8-TP:** FT-IR ( $\nu$  in  $\text{cm}^{-1}$ ): 3294.95, 3085.43, 2953.88, 2927.61, 2869.69, 2856.35, 2623.42, 2503.43, 1682.29, 1617.56, 1606.48, 1519.93, 1508.75, 1467.67, 1437.77, 1421.92, 1390.23, 1323.27, 1297.95, 1261.50, 1167.71, 1042.96, 829.42, 797.94, 771.75, 723.96, 693.63, 639.64, 599.43, 552.10, 508.68.  $^1\text{H}$  NMR (400 MHz,  $\text{CD}_2\text{Cl}_2$ ,  $\delta$  in ppm): 9.41-8.58 (m, 3H), 8.07 (d,  $J = 8.04$  Hz, 6H), 7.80 (s, 18H), 7.68-7.50 (m, 6H), 7.20 (d,  $J = 7.36$  Hz, 6H), 6.96 (d,  $J = 8.08$  Hz, 6H), 4.18 (br m, 36H), 4.06 (t,  $J = 6.30$  Hz, 6H), 2.66-2.60 (m, 6H), 1.92-1.82 (m, 42H), 1.65-1.47 (m, 42H), 1.39-1.34 (br s, 72H), 0.93 (t,  $J = 6.22$  Hz, 45H).  $^{13}\text{C}$  NMR (100 MHz,  $\text{CD}_2\text{Cl}_2$ ,  $\delta$  in ppm): 170.89, 163.77, 159.69, 153.31, 149.26, 139.00, 136.44, 132.57, 128.85, 123.52, 123.23, 120.93, 114.42, 106.70, 69.61, 68.74, 36.04, 35.52, 32.28, 31.96, 30.04, 29.92, 29.81, 26.67, 26.57, 26.34, 23.35, 23.24, 14.57, 14.42.

**Hpz-C9-TP:** FT-IR ( $\nu$  in  $\text{cm}^{-1}$ ): 3295.31, 3086.51, 2954.17, 2926.99, 2869.62, 2854.94, 2628.36, 2506.85, 1681.83, 1617.60, 1606.26, 1519.93, 1508.41, 1466.22, 1436.79, 1422.26, 1389.64, 1326.01, 1298.36, 1260.95, 1167.14, 1042.07, 829.17, 798.07, 772.88, 724.98, 693.66, 639.41, 599.92, 552.03, 508.22.  $^1\text{H}$  NMR (400 MHz,  $\text{CD}_2\text{Cl}_2$ ,  $\delta$  in ppm): 9.93-8.54 (3H), 8.06 (d,  $J = 8.80$  Hz, 6H), 7.79 (s, 18H), 7.68-7.49 (m, 6H), 7.20 (d,  $J = 7.92$  Hz, 6H), 6.96 (d,  $J = 8.80$  Hz, 6H), 4.19-4.15 (m, 36H), 4.06 (t,  $J = 6.40$  Hz, 6H), 2.66-2.60 (m, 6H), 1.89-1.84 (m, 42H), 1.54 (br m, 42H), 1.41-1.37 (m, 78H), 0.95-0.90 (m, 45H).  $^{13}\text{C}$  NMR (100 MHz,  $\text{CD}_2\text{Cl}_2$ ,  $\delta$  in ppm): 170.90, 163.68, 159.55, 153.21, 149.25, 138.88, 136.50, 132.55, 128.79, 123.50, 123.34, 120.88, 114.40, 106.62, 69.57, 68.67, 36.02, 32.55, 32.30, 31.89, 30.25, 30.07, 30.01, 29.92, 29.66, 29.68, 26.47, 26.34, 23.38, 23.25, 14.59, 14.43.



## References

1. Cammidge A. N.; Bushby R. J.; Handbook of Liquid Crystals, ed. Demus D.; Goodby J. W.; Gray G. W.; Spiess H. W.; Vill V.; Wiley-WCH, Weinheim, **1998**, 7, 693.
2. Kumar, S. *Chem. Soc. Rev.* **2006**, 35, 83-109.
3. Kaafarani, B. R. *Chem. Mater.* **2010**, 23, 378-396.
4. Kumar S. *Liq. Cryst.* **2004**, 31, 1037-1059.
5. Kumar S. *Liq. Cryst.* **2005**, 32, 1089-1113.
6. Sergeyev, S.; Pisula, W.; Geerts, Y. H. *Chem. Soc. Rev.* **2007**, 36, 1902-1929.
7. Kumar, S.; Wachtel, E. J.; Keinan, E. *J. Org. Chem* **1993**, 58, 3821-3827.
8. Keinan, E.; Kumar, S.; Singh, S. P.; Ghirlando, R.; Wachtel, E. J. *Liq. Cryst.* **1992**, 11, 157-173.
9. Sienkowska, M. J.; Farrar, J. M.; Zhang, F.; Kusuma, S.; Heiney, P. A.; Kaszynski, P. *J. Mater. Chem.* **2007**, 17, 1399-1411.
10. Cristiano, R.; Eccher, J.; Bechtold, I. H.; Tironi, C. N.; Vieira, A. A.; Molin, F.; Gallardo, H. *Langmuir* **2012**, 28, 11590-11598.
11. Goettmann, F.; Thomas, A.; Antonietti, M. *Angew. Chem.* **2007**, 46, 2717-2720.
12. Wang, X. C.; Maeda, K.; Thomas, A.; Takanabe, K.; Xin, G.; Carlsson, J. M.; Domen, K.; Antonietti, M. *Nat. Mat.* **2009**, 8, 76-80.
13. Kailasam, K.; Mesch, M. B.; Möhlmann, L.; Baar, M.; Blechert, S.; Schwarze, M.; Schröder, M.; Schomäcker, R.; Senker, J.; Thomas, A. *Energy Technol.* **2016**, 4, 744-750.
14. Li, J.; Nomura, H.; Miyazaki, H.; Adachi, C. *Chem. Commun.* **2014**, 50, 6174-6176.
15. Jürgens, B.; Irran, E.; Senker, J.; Kroll, P.; Müller, H.; Schnick, W. *J. Am. Chem. Soc.* **2003**, 125, 10288-10300.
16. Li, J.; Nakagawa, T.; Macdonald, J.; Zhang, Q.; Nomura, H.; Miyazaki, H.; Adachi, C. *Adv. Mater.* **2013**, 25, 3319-3323.
17. Hosmane, R. S.; Rossman, M. A.; Leonard, N. J. *J. Am. Chem. Soc.* **1982**, 104, 5497-5499.
18. Kroke, E.; Schwarz, M.; Horath-Bordon, E.; Kroll, P.; Noll, B.; Norman, A. D. *New J. Chem.* **2002**, 26, 508-512.

19. Zheng, W.; Wong, N. B.; Wang, W.; Zhou, G.; Tian, A. *J. Phys. Chem. A* **2004**, *108*, 97-106.
20. Yadav, A. K.; Pradhan, B.; Ulla, H.; Nath, S.; De, J.; Pal, S. K.; Satyanarayana, M. N.; Achalkumar, A. S. *J. Mater. Chem. C* **2017**, *5*, 9345-9358.
21. Tokuhisa, H.; Era, M.; Tsutsui, T. *Appl. Phys. Lett.* **1998**, *72*, 2639-2641.
22. Moyano, S.; Barbera, J.; Diosdado, B. E.; Serrano, J. L.; Elduque, A.; Gimenez, R. *J. Mater. Chem. C* **2013**, *1*, 3119-3128.
23. An, Z.; Yu, J.; Jones, S. C.; Barlow, S.; Yoo, S.; Domercq, B.; Prins, P.; Siebbeles, L. D.; Kippelen, B.; Marder, S. R. *Adv. Mater.* **2005**, *17*, 2580-2583.
24. Liedtke, A.; Kelly, S. M.; Kitney, S. P.; Averbek, B. V.; Boudard, P.; Beljonne, D.; Cornil, J. *J. Phys. Chem. B* **2010**, *114*, 11975-11982.
25. Zhang, B.; Hsu, C. H.; Yu, Z. Q.; Yang, S.; Chen, E. Q. *Chem. Commun.* **2013**, *49*, 8872-8874.
26. Gimenez, R.; Pinol, M.; Serrano, J. L. *Chem. Mater.* **2004**, *16*, 1377-1383.
27. Luo, J. D.; Xie, Z. L.; Lam, J. W. Y.; Cheng, L.; Chen, H. Y.; Qiu, C. F.; Kwok, H. S.; Zhan, X. W.; Liu, Y. Q.; Zhu, D. B.; Tang, B. Z. *Chem. Commun.* **2001**, 1740-1741.
28. Mei, J.; Leung, N. L. C.; Kwok, R. T. K.; Lam, J. W. Y.; Tang, B. Z. *Chem. Rev.* **2015**, *115*, 11718-11940.
29. Zhao, Z.; Chen, S.; Deng, C.; Lam, J. W. Y.; Chan, C. Y. K.; Lu, P.; Wang, Z.; Hu, B.; Chen, X.; Lu, P.; Kwok, H. S.; Ma, Y.; Qiu, H.; Tang, B. Z. *J. Mater. Chem.* **2011**, *21*, 10949-10956.
30. Wang, Y.; Liao, Y.; Cabry, C. P.; Zhou, D.; Xie, G.; Qu, Z.; Bruce, D. W.; Zhu, W. *J. Mater. Chem. C* **2017**, *5*, 3999-4008.
31. Pathak, S. K.; Pradhan, B.; Gupta, R. K.; Gupta, M.; Pal, S. K.; Achalkumar, A. S. *J. Mater. Chem. C* **2016**, *4*, 6546-6561.
32. Jing, H.; Lu, L.; Feng, Y.; Zheng, J.-F.; Deng, L.; Chen, E.-Q.; Ren, X.-K. *J. Phys. Chem. C* **2016**, *120*, 27577-27586.
33. Sagara, Y.; Kato, T. *Angew. Chem., Int. Ed.* **2008**, *47*, 5175-5178.
34. Yamane, S.; Saqara, Y.; Mutai, T.; Araki, K.; Kato, T. *J. Mater. Chem. C* **2013**, *1*, 2648-2656.
35. Yamane, S.; Saqara, Y.; Kato, T. *Chem. Commun.* **2013**, *49*, 3839-3841.

36. Mitani, M.; Ogata, S.; Yamane, S.; Yoshio, M.; Hasegawa, M.; Kato, T. *J. Mater. Chem. C* **2016**, *4*, 2754-2760.
37. Jou, J. H.; Chen, Y. L.; Tseng, J. R.; Wu, R. Z.; Shyue, J. J.; Thomas, K. R. J.; Kapoor, N.; Chen, C. T.; Lin, Y. P.; Wang, P. H.; Hung, H. W.; Lie, J. Y.; Chen, S. P. *J. Mater. Chem.* **2012**, *22*, 15500-15506.
38. Dyjak, S.; Kiciński, W.; Huczko, A. *J. Mater. Chem. A* **2015**, *3*, 9621-9631.
39. Li, W.; Zhang, J.; Li, B.; Zhang, M.; Wu, L. *Chem. Commun.* **2009**, 5269-5271.
40. Schröter, J. A.; Tschierske, C.; Wittenberg, M.; Wendorff, J. H. *J. Am. Chem. Soc.* **2006**, *120*, 10669-10675.
41. Miller, D. R.; Swenson, D. C.; Gillan, E. G. *J. Am. Chem. Soc.* **2004**, *126*, 5372-5373.
42. Pati, A. K.; Gharpure, S. J.; Mishra, A. K. *J. Phys. Chem. A* **2015**, *119*, 10481-10493.
43. Zhang, L.; van Eersel, H.; Bobbert, P. A.; Coehoorn, R. *Chem. Phys. Lett.* **2016**, *662*, 221-227.
44. Zhang, L.; van Eersel, H.; Bobbert, P. A.; Coehoorn, R. *Chem. Phys. Lett.* **2016**, *652*, 142-147.
45. Tang, X.; Bai, Q.; Peng, Q.; Gao, Y.; Li, J.; Liu, Y.; Yao, L.; Lu, P.; Yang, B.; Ma, Y. *Chem. Mater.* **2015**, *27*, 7050-7057.
46. Kumar, S. *Chemistry of discotic liquid crystals-From monomers to polymers*, CRC, Taylor & Francis Group, Boca-Raton, **2011**, pp 493.
47. Bushby, R. J.; Kawata, K. *Liq. Cryst.* **2011**, *38*, 1415-1426.
48. Wohrle, T.; Wurzbach, I.; Kirres, J.; Kostidou, A.; Kapernaum, N.; Litterscheidt, J.; Haenle, J. C.; Staffeld, P.; Baro, A.; Giesselmann, F.; Laschat, S. *Chem. Rev.* **2016**, *116*, 1139-1241.
49. Kato, T.; Mizoshita, N.; Kishimoto, K. *Angew. Chem. Int. Ed.* **2006**, *45*, 38-68.
50. Kato, T.; Frechet, J. M. J.; *J. Am. Chem. Soc.* **1989**, *111*, 8533-8534.
51. Kato, T.; Frechet, J. M. J.; *Macromolecules* **1989**, *22*, 3818-3819.
52. Kato, T.; Frechet, J. M. J. *Macromolecules* **1990**, *23*, 360.
53. Brienne, M.-J.; Gabard, J.; Lehn, J.-M.; Stibor, I. *J. Chem. Soc. Chem. Commun.* **1989**, 1868-1870.

54. Feringán, B.; Romero, P.; Serrano, J. L.; Folcia, C. L.; Etxebarria, J.; Ortega, J.; Termine, R.; Golemme, A.; Giménez, R.; Sierra, T. *J. Am. Chem. Soc.* **2016**, *138*, 12511-12518.
55. Barbera, J.; Puig, L.; Serrano, J. L.; Sierra, T. *Chem. Mater.* **2004**, *16*, 3308-3317.
56. Alvarez, L.; Barbera, J.; Puig, L.; Romero, P.; Serrano, J. L.; Sierra, T. *J. Mater. Chem.* **2006**, *16*, 3768-3773.
57. Vera, F.; Tejedor, R. M.; Romero, P.; Barbera, J.; Ros, M. B.; Serrano, J. L.; Sierra, T. *Angew. Chem., Int. Ed.* **2007**, *46*, 1873-1877.
58. Vieira, A.; Gallardo, H.; Barberá, J.; Romero, P.; Serrano, J. L.; Sierra, T. *J. Mater. Chem.* **2011**, *21*, 5916-5922.
59. Feringán, B.; Romero, P.; Serrano, J. L.; Giménez, R.; Sierra, T. *Chem. Eur. J.* **2015**, *21*, 8859-8866.
60. Zhao, K.-Q.; Bai, X.-Y.; Xiao, B.; Gao, Y.; Hu, P.; Wang, B.-Q.; Zeng, Q.-D.; Wang, C.; Heinrich, B.; Donnio, B. *J. Mater. Chem. C* **2015**, *3*, 11735-11746.
61. Sautter, A.; Thalacker, C.; Wurthner, F. *Angew. Chem. Int. Ed.* **2001**, *40*, 4425-4428.
62. Ryu, M. H.; Choi, J. W.; Kim, H. J.; Park, N.; Cho, B. K. *Angew. Chem. Int. Ed.* **2011**, *123*, 5855-5858.
63. Xiong, J.-F.; Luo, S.-H.; Huo, J.-P.; Liu, J.-Y.; Chen, S.-X.; Wang, Z.-Y. *J. Org. Chem.* **2014**, *79*, 8366-8373.
64. Liu, C. Y.; Fechtenkötter, A.; Watson, M. D.; Müllen, K.; Bard, A. J. *Chem. Mater.* **2003**, *15*, 124-130.
65. Bala, I.; Singh, H.; Battula, V. R.; Gupta, S. P.; De, J.; Kumar, S.; Kailasam, K.; Pal, S. K. *Chem. Eur. J.* **2017**, *23*, 14718-14722.
66. Sayed, S. M.; Deng, L.-L.; Lin, B.-P.; Yang, H. *Liq. Cryst.* **2017**, *44*, 2175-2183.
67. Seo, S.; Park, J.; Chang, J. *Langmuir* **2009**, *25*, 8439-8441.
68. Jansze, S. M.; Felipe, A. M.; Storey, J. M. D.; Marcelis, A. T. M.; Imrie, C. T. *Angew. Chem. Int. Ed.* **2015**, *54*, 643-646.
69. Felipe, M.; Alfonso, G.; Abberley, J. P.; Walker, R.; Storey, J. M. D.; Imrie, C. T. *RSC Adv.* **2017**, *110*, 108164-108179.
70. Kleppinger, R.; Lillya, C. P.; Yang, C. *J. Am. Chem. Soc.* **1997**, *119*, 4097-4102.
71. De, J.; Setia, S.; Pal, S. K. *ChemistrySelect* **2016**, *1*, 5075-5082.

72. Bala, I.; Gupta, S. P.; De, J.; Pal, S. K. *Chem. Eur. J.* **2017**, *23*, 12767-12778.
73. De, J.; Gupta, S. P.; Bala, I.; Kumar, S.; Pal, S. K. *Langmuir* **2017**, *33*, 13849-13860.
74. Gupta, S. P.; Gupta, M.; Pal, S.K. *ChemistrySelect* **2017**, *2*, 6070-6077.
75. Seo, S.; Park, J.; Chang, J. *Langmuir* **2009**, *25*, 8439-8441.
76. Maiti, B.; Schubert, A.; Sarkar, S.; Bhandari, S.; Wang, K.; Li, Z.; Geva, E.; Twieg, R. J.; Dunietz, B. D. *Chem. Sci.* **2017**, *8*, 6947-6953.
77. Liao, Y. -L.; Lin, C. -Y.; Liu, Y. -H.; Wong, K. -T.; Hung, W. -Y.; Chen, W. -J. *Chem. Commun.* **2007**, 1831-1833.
78. Tsuji, H.; Mitsui, C.; Sato, Y.; Nakamura, E. *Adv. Mater.* **2009**, *21*, 3776-3779.
79. Shao, W.; Dong, H.; Jiang, L.; Hu, W. *Chem. Sci.* **2011**, *2*, 590-600.
80. Feng, X.; Marcon, V.; Pisula, W.; Hansen, M. R.; Kirkpatrick, J.; Grozema, F.; Andrienko, D.; Kremer, K.; Müllen, K. *Nat. Mater.* **2009**, *8*, 421-426.
81. Bashir, A.; Heck, A.; Narita, A.; Feng, X.; Nefedov, A.; Rohwerder, M.; Müllen, K.; Elstner, M.; Wöll, C. *Phys. Chem. Chem. Phys.* **2015**, *17*, 21988-21996.
82. Kato, T.; Uchida, J.; Ichikawa, T.; Sakamoto, T. *Angew. Chem. Int. Ed.* **2018**, *57*, 4355-4371.
83. Kushida, T.; Shuto, A.; Yoshio, M.; Kato, T.; Yamaguchi, S. *Angew. Chem. Int. Ed.* **2015**, *54*, 6922-6925.
84. Yasuda, T.; Shimizu, T.; Liu, F.; Ungar, G.; Kato, T. *J. Am. Chem. Soc.* **2011**, *133*, 13437-13444.
85. Li, W. S.; Yamamoto, Y.; Fukushima, T.; Saeki, A.; Seki, S.; Tagawa, S.; Masunaga, H.; Sasaki, S.; Takata, M.; Aida, T. *J. Am. Chem. Soc.* **2008**, *130*, 8886-8887.
86. Hayashi, H.; Nishihashi, W.; Umeyama, T.; Matano, Y.; Seki, S.; Shimizu, Y.; Imahori, H. *J. Am. Chem. Soc.* **2011**, *133*, 10736-10739.
87. Hahn, L.; Hermannsdorfer, A.; Günther, B.; Wesp, T.; Bühler, B.; Zschieschang, U.; Wadepohl, H.; Klauk, H.; Gade, L. H. *J. Org. Chem.* **2017**, *82*, 12492-12502.
88. Babel, A.; Zhu, Y.; Cheng, K. F.; Chen, W. C.; Jenekhe, S. A. *Adv. Funct. Mater.* **2007**, *17*, 2542-2549.
89. Stalder, R.; Puniredd, S. R.; Hansen, M. R.; Koldemir, U.; Grand, C.; Zajaczkowski, W.; Müllen, K.; Pisula, W.; Reynolds, J. R. *Chem. Mater.* **2016**, *28*, 1286-1297.

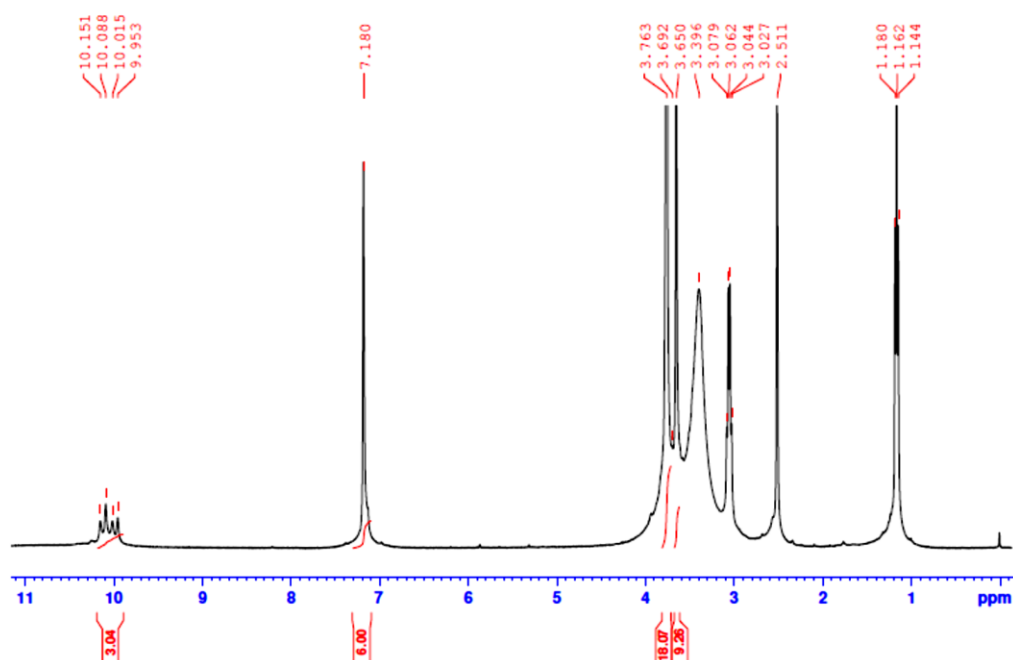
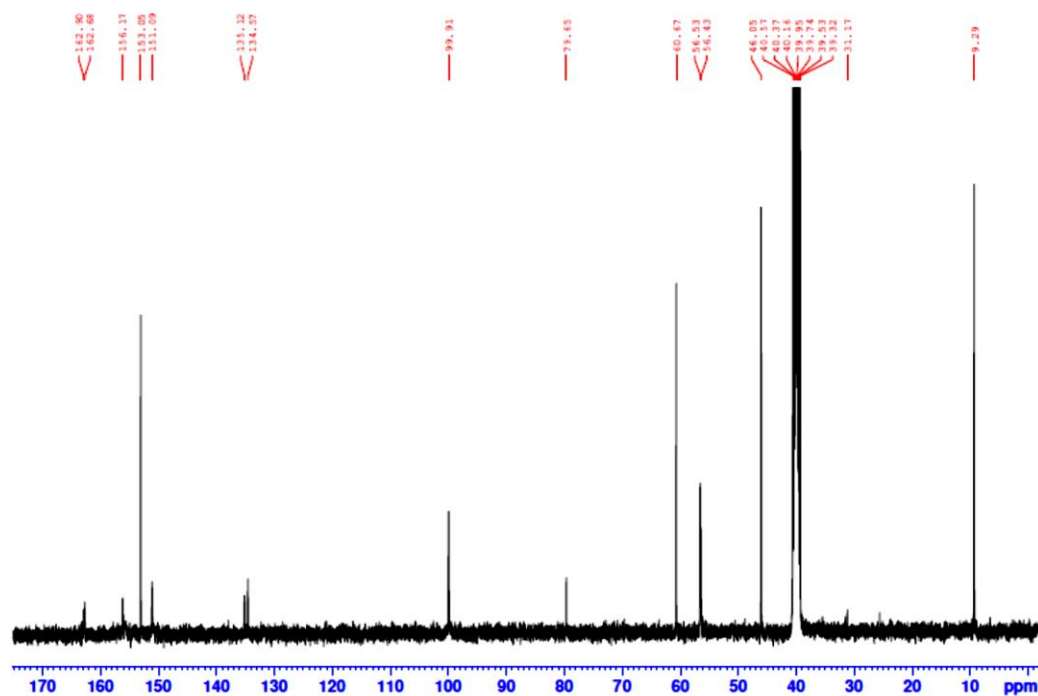
90. Shi, D.; Liu, Z.; Ma, J.; Zhao, Z.; Tan, L.; Lin, G.; Tian, J.; Zhang, X.; Zhang, G.; Zhang, D. *Adv. Funct. Mater.* **2020**, *30*, 1910235.
91. Cheng, S.; Yu, S. H.; Kwon, S. K.; Chung, D. S.; Kim, Y. H. *Dyes and Pigments* **2019**, *162*, 481-486.
92. Tan, L.; Guo, Y.; Yang, Y.; Zhang, G.; Zhang, D.; Yu, G.; Xu, W.; Liu, Y. *Chem. Sci.* **2012**, *3*, 2530-2541.
93. Gruber, M.; Jung, S. H.; Schott, S.; Venkateshvaran, D.; Kronemeijer, A. J.; Andreasen, J. W.; McNeill, C. R.; Wong, W. W.; Shahid, M.; Heeney, M.; Lee, J. K. *Chem. Sci.* **2015**, *6*, 6949-6960.
94. Liang, W. W.; Huang, C. F.; Wu, K. Y.; Wu, S. L.; Chang, S. T.; Cheng, Y. J.; Wang, C. L. *Chem. Sci.* **2016**, *7*, 2768-2774.
95. van Pruissen, G. W.; Pidko, E. A.; Wienk, M. M.; Janssen, R. A. *J. Mater. Chem. C* **2014**, *2*, 731-735.
96. Kreouzis, T.; Baldwin, R. J.; Shkunov, M.; Mcculloch, I.; Heeney, M.; Zhang, W. *Appl. Phys. Lett.* **2005**, *87*, 172110.
97. Iino, H.; Hanna, J. I.; Bushby, R. J.; Movaghar, B.; Whitaker, B. J.; Cook, M. J. *Appl. Phys. Lett.* **2005**, *87*, 132102.
98. Ye, Q.; Chang, J.; Huang, K. W.; Chi, C. *Org. Lett.* **2011**, *13*, 5960-5963.
99. Iino, H.; Takayashiki, Y.; Hanna, J. I.; Bushby, R. J. *Jpn. J. Appl. Phys.* **2005**, *44*, L1310.
100. Feringán, B.; Folcia, C. L.; Termine, R.; Golemme, A.; Granadino-Roldán, J. M.; Navarro, A.; Serrano, J. L.; Giménez, R.; Sierra, T. *Chem. Eur. J.* **2018**, *24*, 17459-17463.
101. Paraschiv, I.; Giesbers, M.; van Lagen, B.; Grozema, F. C.; Abellon, R. D.; Siebbeles, L. D.; Marcelis, A. T.; Zuilhof, H.; Sudhölter, E. J. *Chem. Mater.* **2006**, *18*, 968-974.
102. Lugger, J. A.; Mulder, D. J.; Bhattacharjee, S.; Sijbesma, R. P. *ACS nano* **2018**, *12*, 6714-6724.
103. Bala, I.; Gupta, S. P.; Kumar, S.; Singh, H.; De, J.; Sharma, N.; Kailasam, K.; Pal, S. K. *Soft Matter* **2018**, *14*, 6342-6352.
104. El-Gamel, N. E.; Seyfarth, L.; Wagler, J.; Ehrenberg, H.; Schwarz, M.; Senker, J.; Kroke, E. *Chem. Eur. J.* **2007**, *13*, 1158-1173.

105. Ryu, M. H.; Choi, J. W.; Kim, H. J.; Park, N.; Cho, B. K. *Angew. Chem. Int. Ed.* **2011**, *50*, 5737-5740.
106. Ichihara, M.; Suzuki, H.; Mohr, B.; Ohta, K. *Liq. Cryst.* **2007**, *34*, 401-410.
107. Beltrán, E.; Garzoni, M.; Feringán, B.; Vancheri, B. A.; Barberá, J.; Serrano, J. L.; Pavan, G. M.; Giménez, R.; Sierra, T. *Chem. Commun.* **2015**, *51*, 1811-1814.
108. McKenna, M. D.; Barberá, J.; Marcos, M.; Serrano, J. L. *J. Am. Chem. Soc.* **2005**, *127*, 619-625.
109. Markovitsi, D.; Germain, A.; Millie, P.; Le'cuyer, P.; Gallos, L. K.; Argyrakakis, P.; Bengs, H.; Ringsdorf, H. *J. Phys. Chem.* **1995**, *99*, 1005-1017.
110. Marguet, S.; Markovitsi, D.; Millie, P.; Sigal, H.; Kumar, S. *J. Phys. Chem. B* **1998**, *102*, 4697-4710.
111. Tritto, E.; Chico, R.; Sanz-Enguita, G.; Folcia, C. L.; Ortega, J.; Coco, S.; Espinet, P. *Inorg. Chem.* **2014**, *53*, 3449-3455.
112. Logsdon, J. L.; Hartnett, P. E.; Nelson, J. N.; Harris, M. A.; Marks, T. J.; Wasielewski, M. R. *ACS Appl. Mater. Interfaces* **2017**, *9*, 33493-33503.
113. Kong, X.; Xia, L.; Zhang, H.; Dai, S.; Yu, C.; Liu, Z.; Mu, L.; Wang, G.; He, Z. *RSC Adv.* **2017**, *7*, 17030-17037.
114. Mir Sayed, S.; Deng, L. L.; Lin, B. P.; Yang, H. *Liq. Cryst.* **2017**, *44*, 2175-2183.
115. Shen, Y.; Hosseini, A. R.; Wong, M. H.; Malliaras, G. G. *ChemPhysChem* **2004**, *5*, 16-25.
116. Kim, H. P.; Lee, H. J.; Lee, S. J.; Kim, H. J.; Seo, G. J.; Youn, J. H.; Jang, J. *Nanoscale Res. Lett.* **2014**, *9*, 323.
117. Eccher, J.; Faria, G. C.; Bock, H.; von Seggern, H.; Bechtold, I. H. *ACS Appl. Mater. Interfaces* **2013**, *5*, 11935-11943.
118. De, J.; Bala, I.; Gupta, S. P.; Pandey, U. K.; Pal, S. K. *J. Am. Chem. Soc.* **2019**, *141*, 18799-18805.
119. Bala, I.; De, J.; Gupta, S. P.; Singh, H.; Pandey, U. K.; Pal, S. K. *Chem. Commun.* **2020**, *56*, 5629-5632.
120. Chico, R.; de Domingo, E.; Domínguez, C.; Donnio, B.; Heinrich, R.; Termine, R.; Golemmé, A.; Coco, S.; Espinet, P. *Chem. Mater.* **2017**, *29*, 7587-7595.

121. García-Frutos, E. M.; Pandey, U. K.; Termine, R.; Omenat, A.; Barberá, J.; Serrano, J. L.; Golemme, A.; Gómez-Lor, B. *Angew. Chem. Int. Ed.* **2011**, *123*, 7537-7540.
122. Ruiz, C.; Pandey, U. K.; Termine, R.; Frutos, E. M. G.; Espejo, G. L.; Ortiz, R. P.; Huang, W.; Marks, T. J.; Facchetti, A.; Delgado, M. C. R.; Golemme, A.; Lor, B. G. *ACS Appl. Mater. Interfaces* **2016**, *8*, 26964-26971.
123. Benito-Hernández, A.; Pandey, U. K.; Cavero, E.; Termine, R.; Garcia-Frutos, E. M.; Serrano, J. L.; Golemme, A.; Lor, B. G. *Chem. Mater.* **2013**, *25*, 117-121.
124. Perova, T. S.; Vij, J. K. *Adv. Mater.* **1995**, *7*, 919-922.
125. Perova, T. S.; Vij, J. K.; Kocot, A. *Europhys. Lett.* **1998**, *44*, 198.
126. Bisoyi, H. K.; Li, Q. *Prog. Mater. Sci.* **2019**, *104*, 1-52.
127. Cupere, V. De; Tant, J.; Viville, P.; Lazzaroni, R.; Osikowicz, W.; Salaneck, W. R.; Geerts, Y. H. *Langmuir* **2006**, *22*, 7798-7806.



## Appendix II

Figure A1. <sup>1</sup>H NMR spectrum of compound 3a.Figure A2. <sup>13</sup>C NMR spectrum of compound 3a.

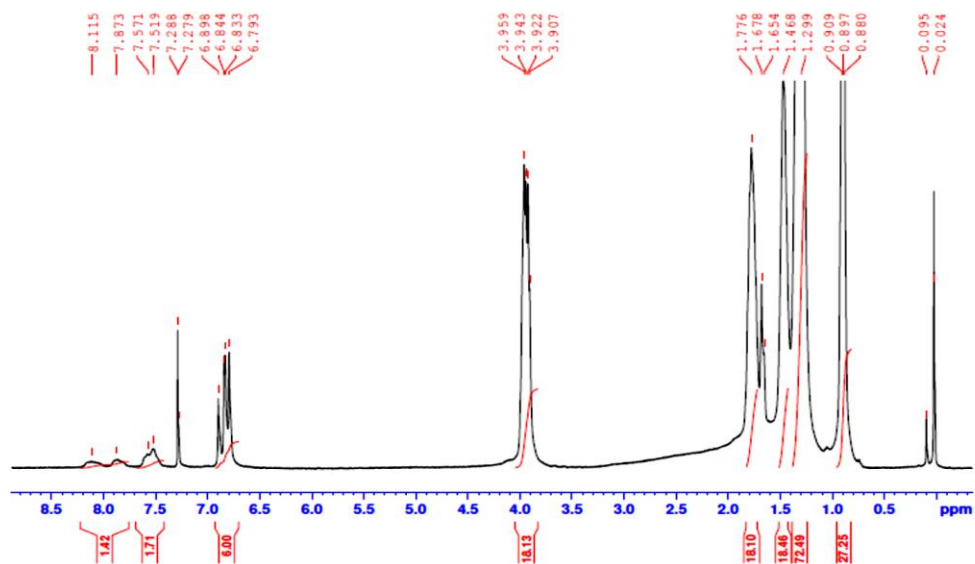


**Figure A3.** <sup>1</sup>H NMR spectrum of compound **3b**.

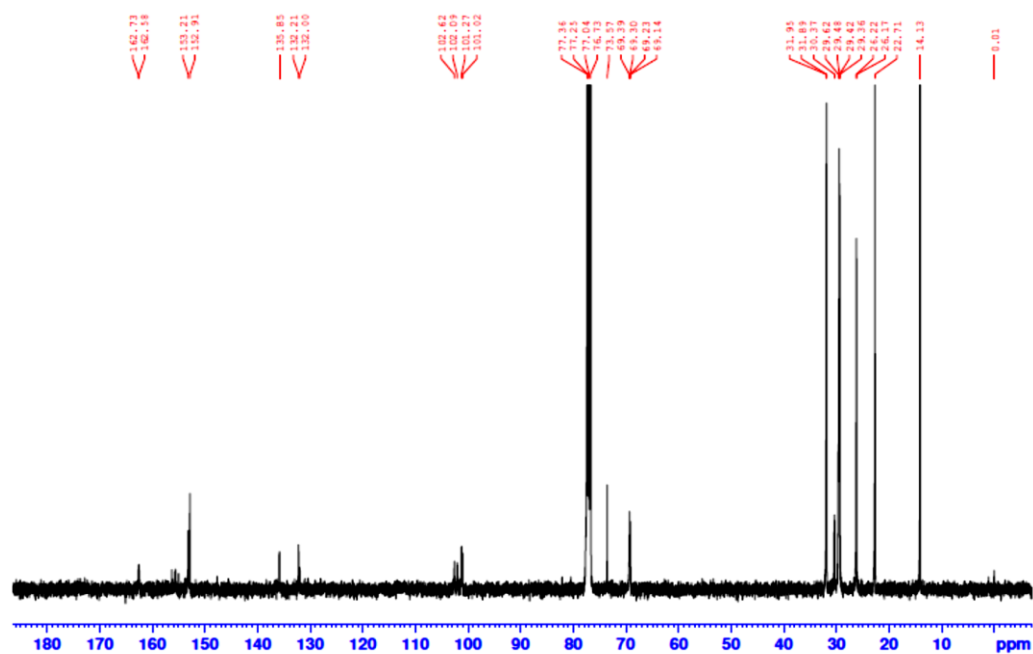


**Figure A4.** <sup>13</sup>C NMR spectrum of compound **3b**.

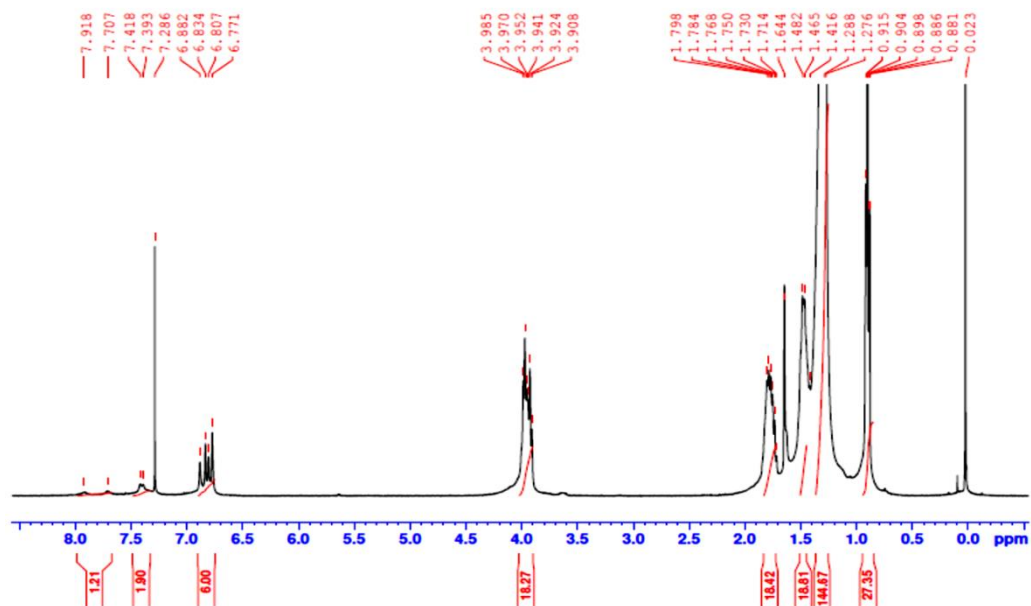


**Figure A5.** <sup>1</sup>H NMR spectrum of compound **3c**.

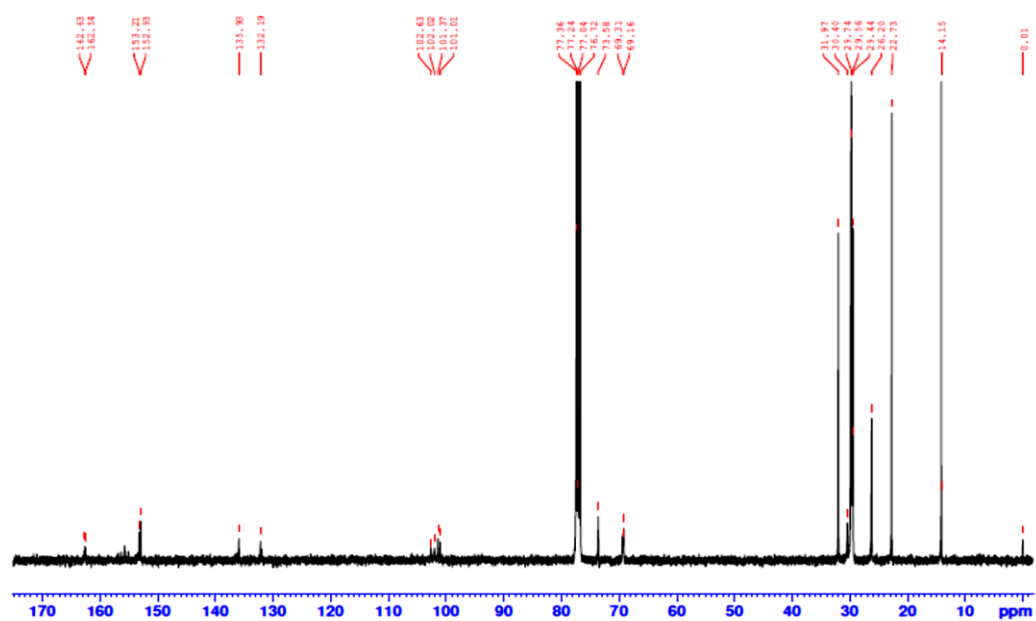


**Figure A6.** <sup>13</sup>C NMR spectrum of compound **3c**.

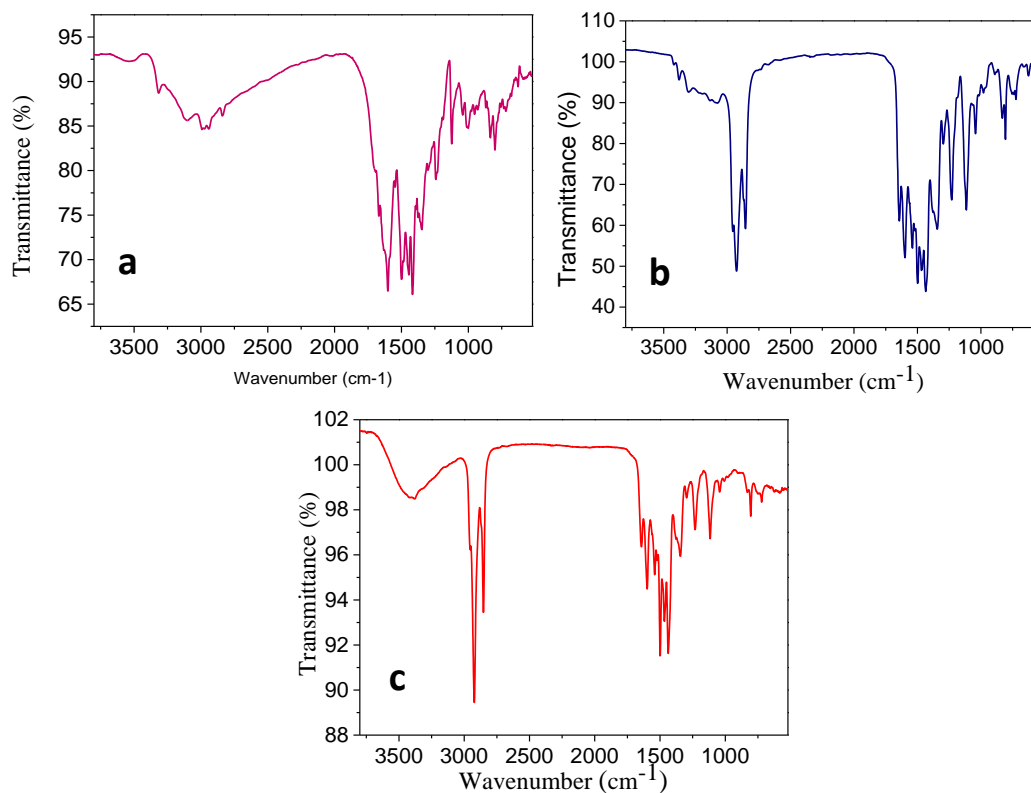


**Figure A7.** FT-IR spectra of compounds (a) **3a**, (b) **3b**, (c) **3c**.

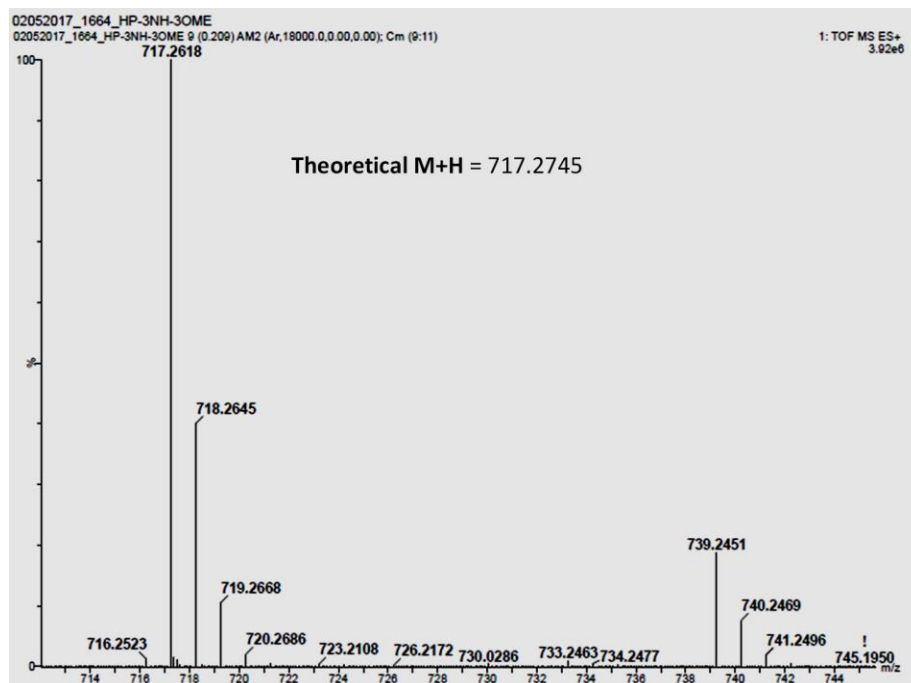


**Figure A8.** MALDI-TOF spectrum of compound **3a**.

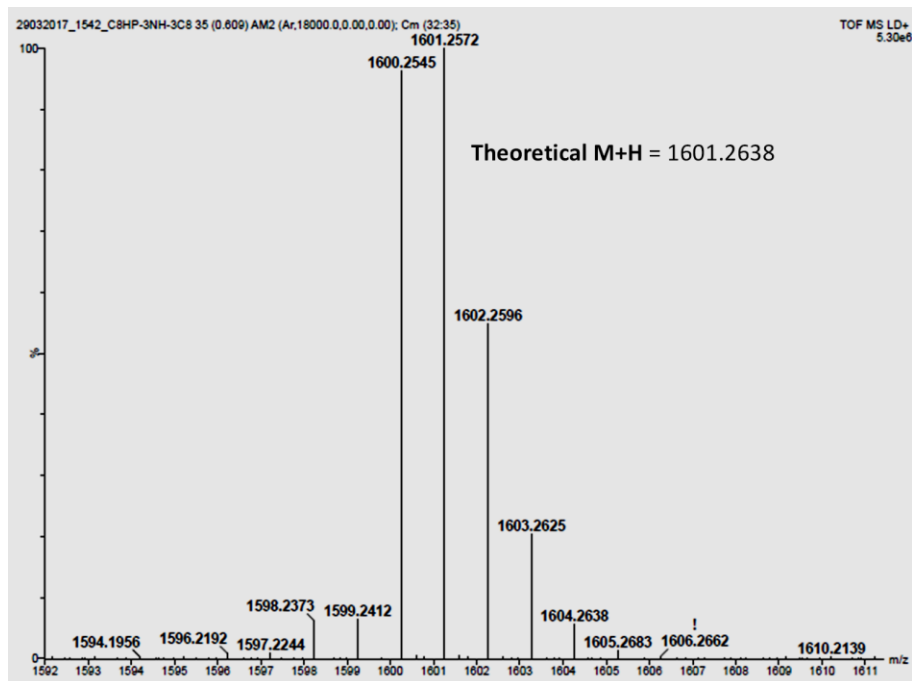


**Figure A9.** MALDI-TOF spectrum of compound **3b**.

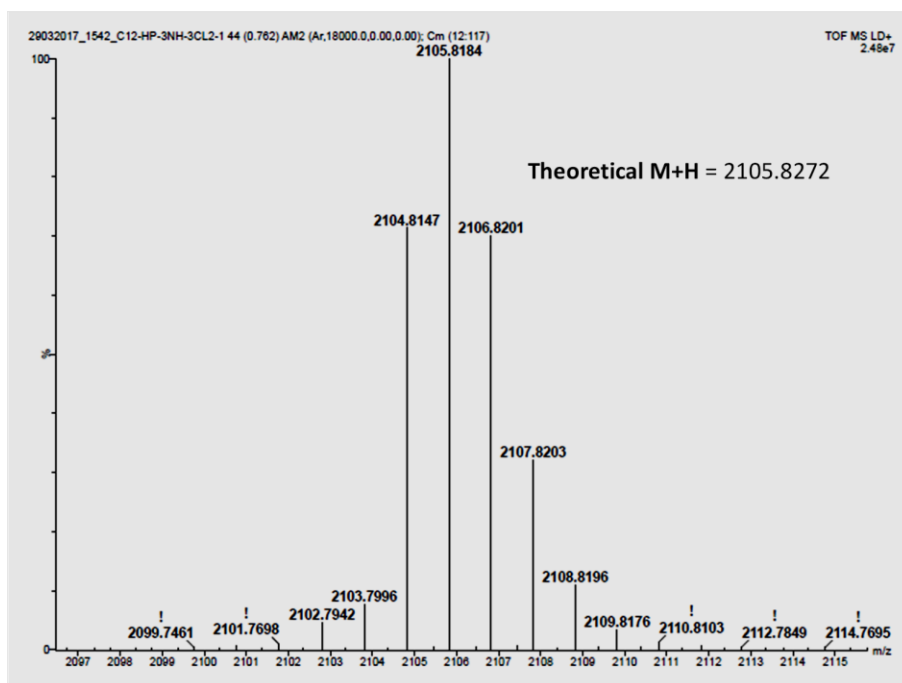


**Figure A10.** MALDI-TOF spectrum of compound **3c**.

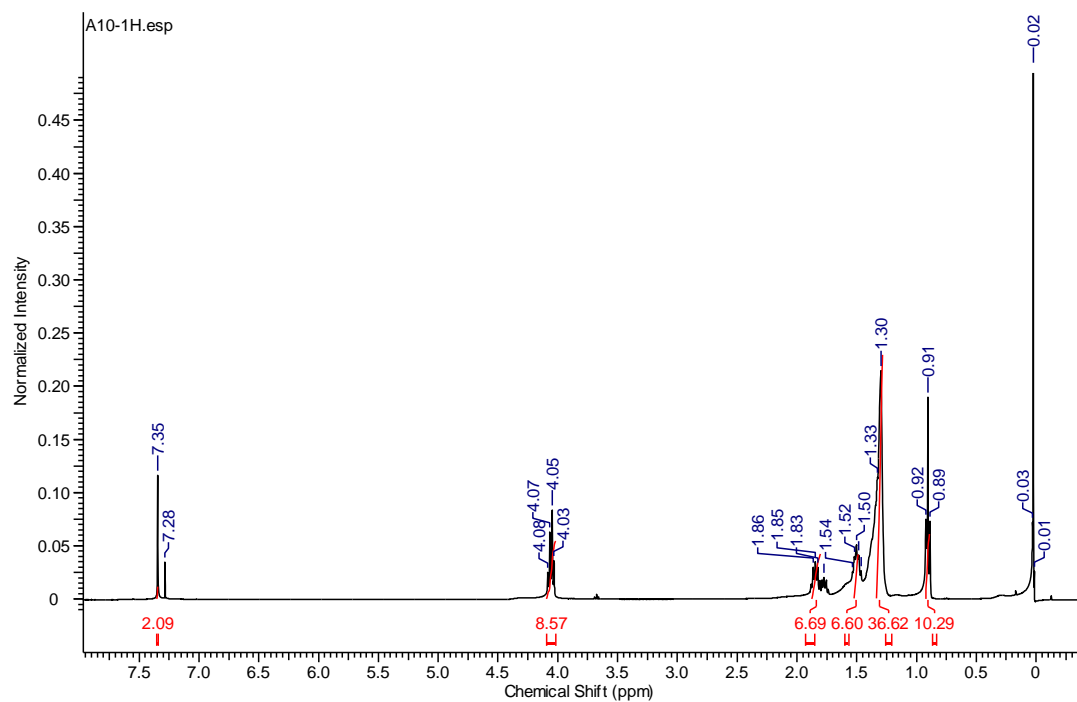


Figure A11. <sup>1</sup>H NMR spectrum of compound A10.

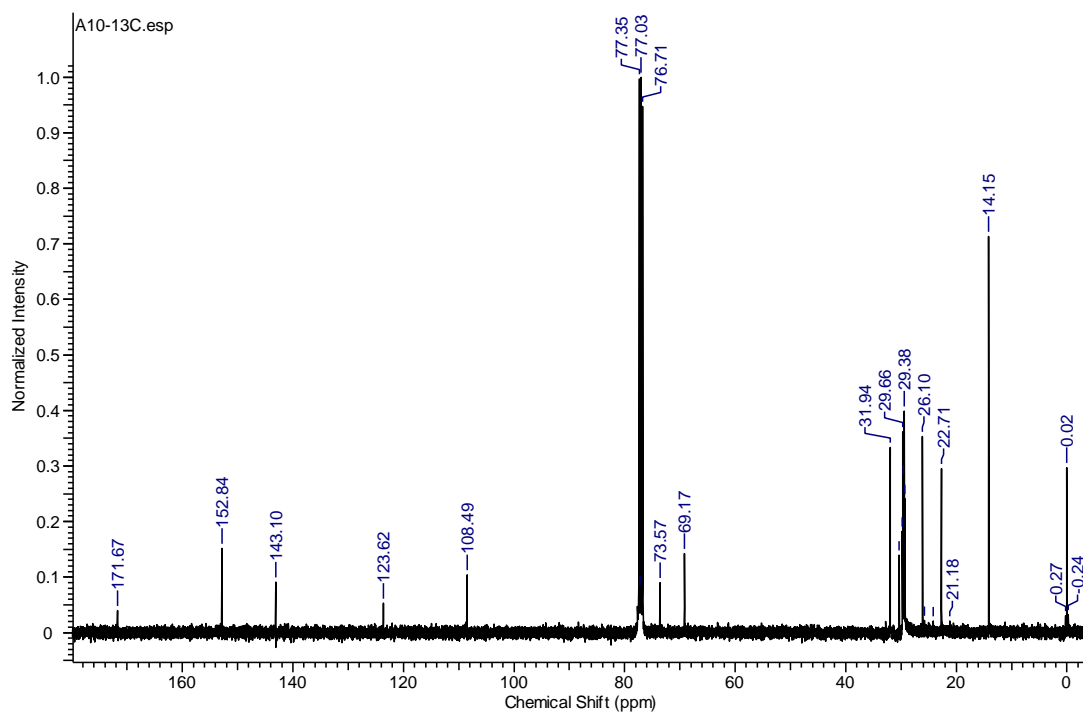


Figure A12. <sup>13</sup>C NMR spectrum of compound A10.

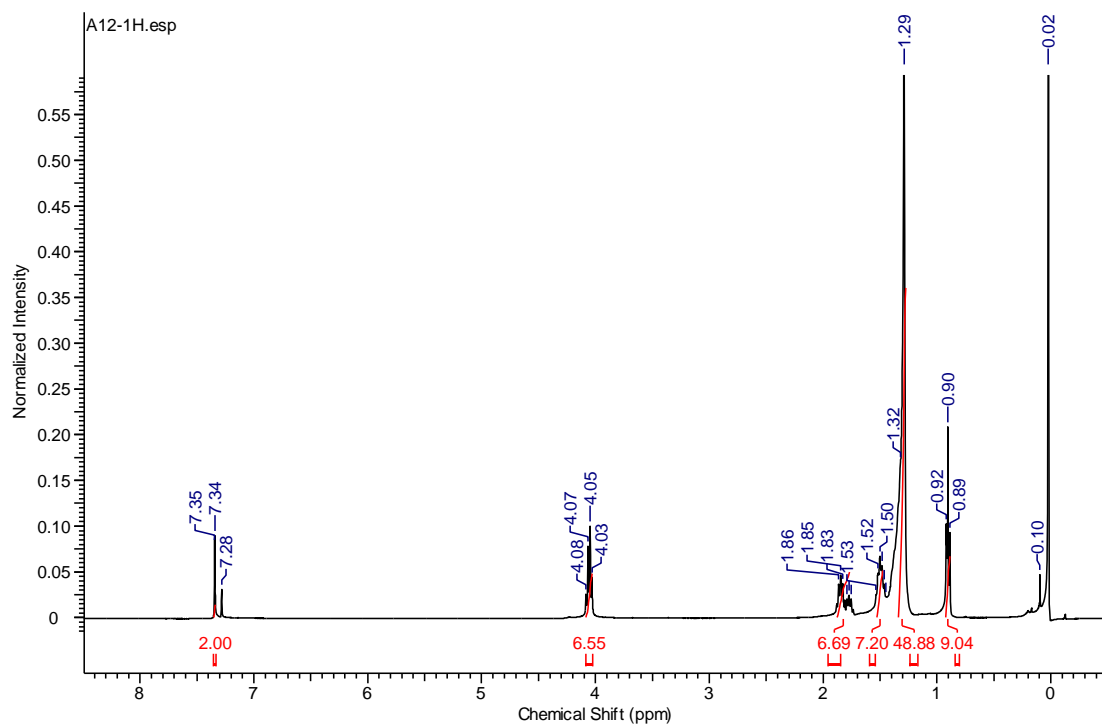


Figure A13.  $^1\text{H}$  NMR spectrum of compound A12.

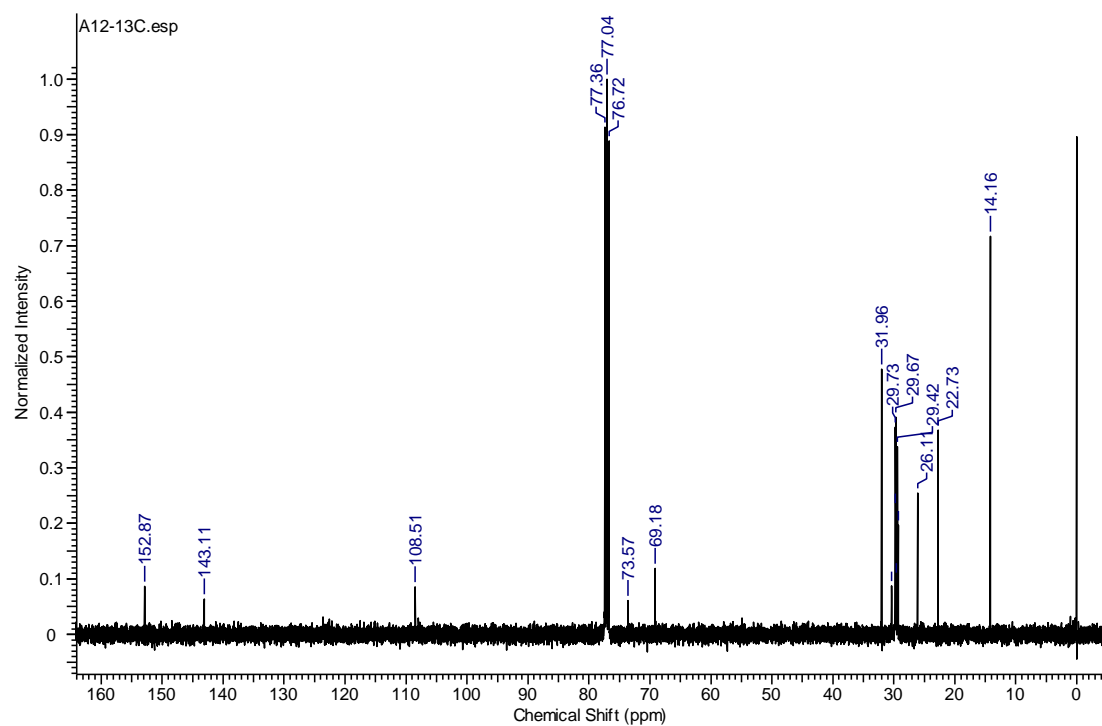
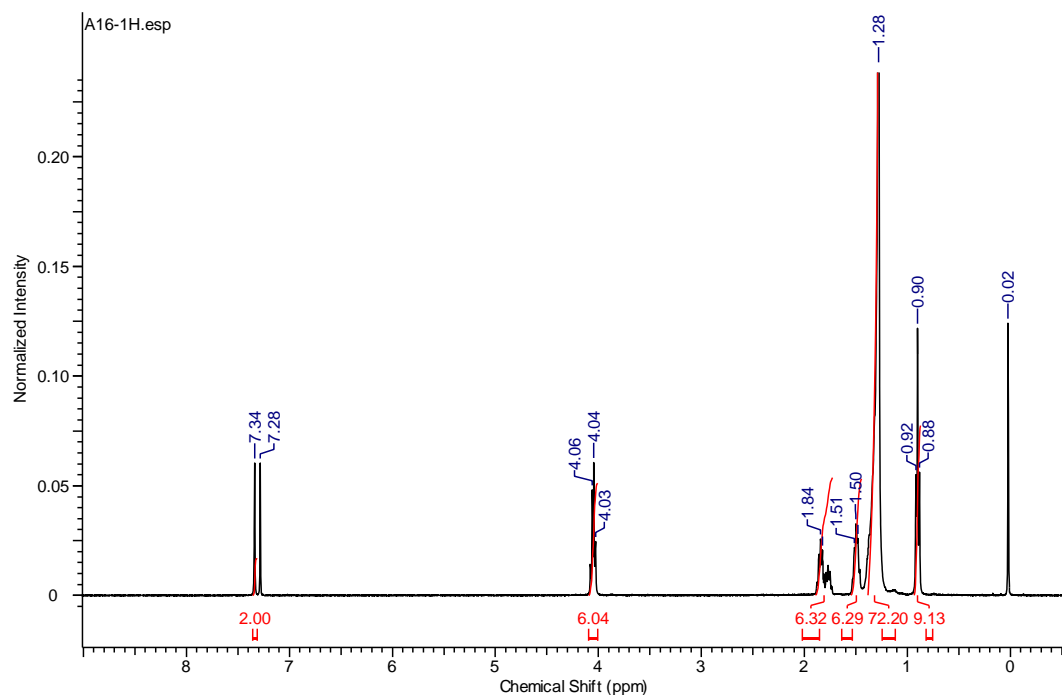
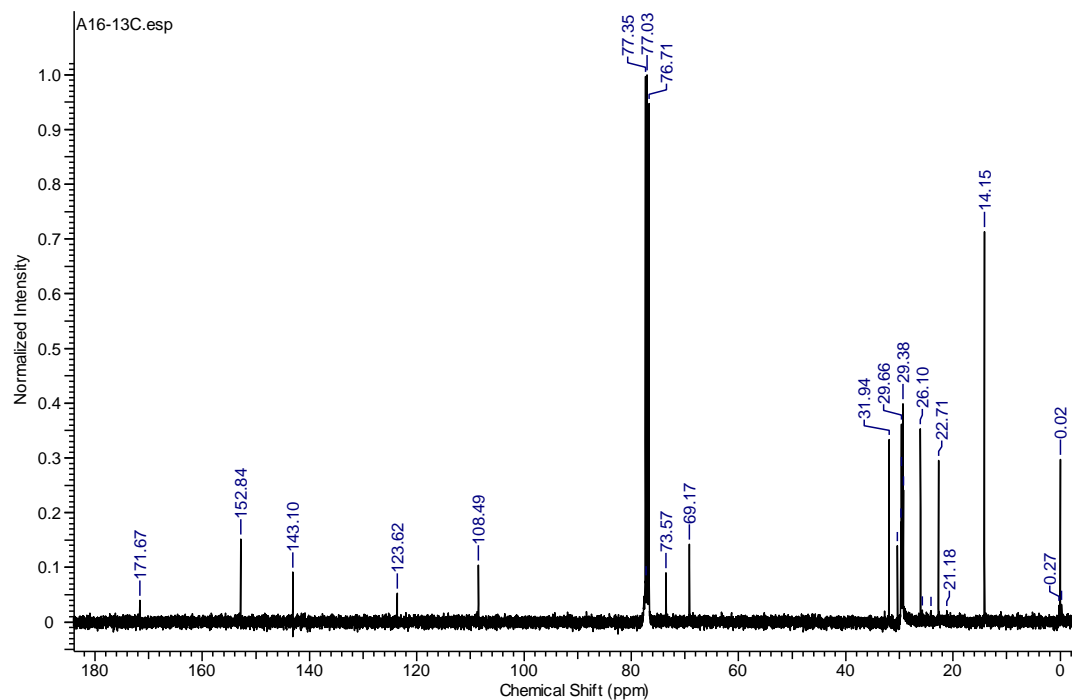


Figure A14.  $^{13}\text{C}$  NMR spectrum of compound A12.



**Figure A15.**  $^1\text{H}$  NMR spectrum of compound **A16**.



**Figure A16.**  $^{13}\text{C}$  NMR spectrum of compound **A16**.



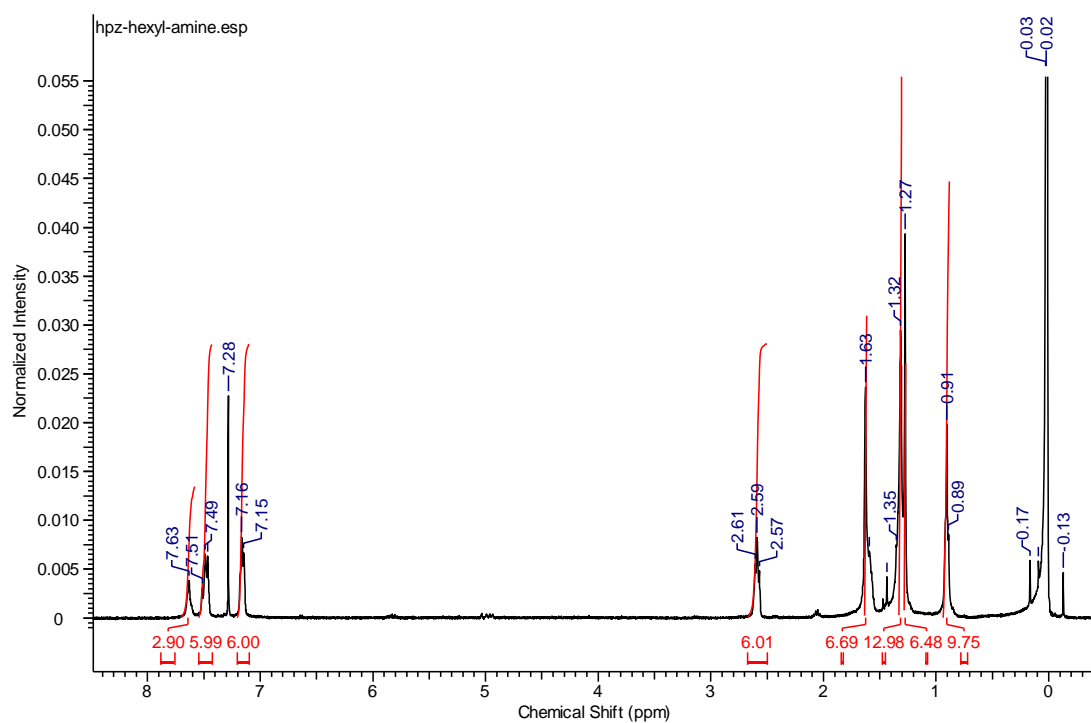


Figure A17.  $^1\text{H}$  NMR spectrum of compound **Hpz-C6**.

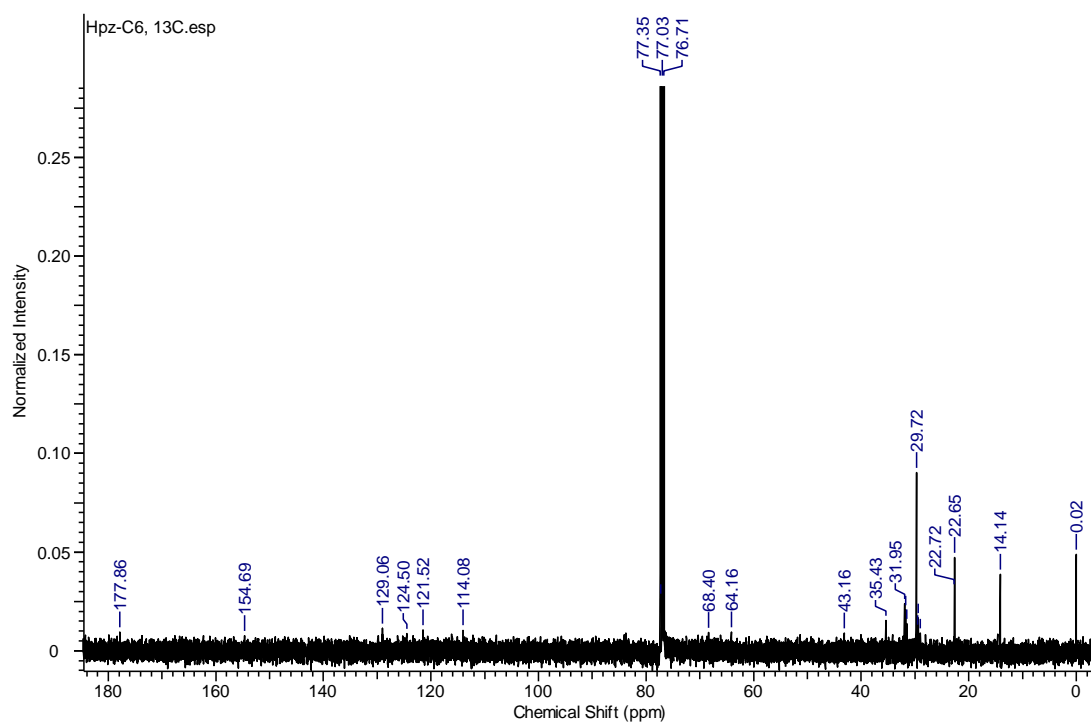


Figure A18.  $^{13}\text{C}$  NMR spectrum of compound **Hpz-C6**.

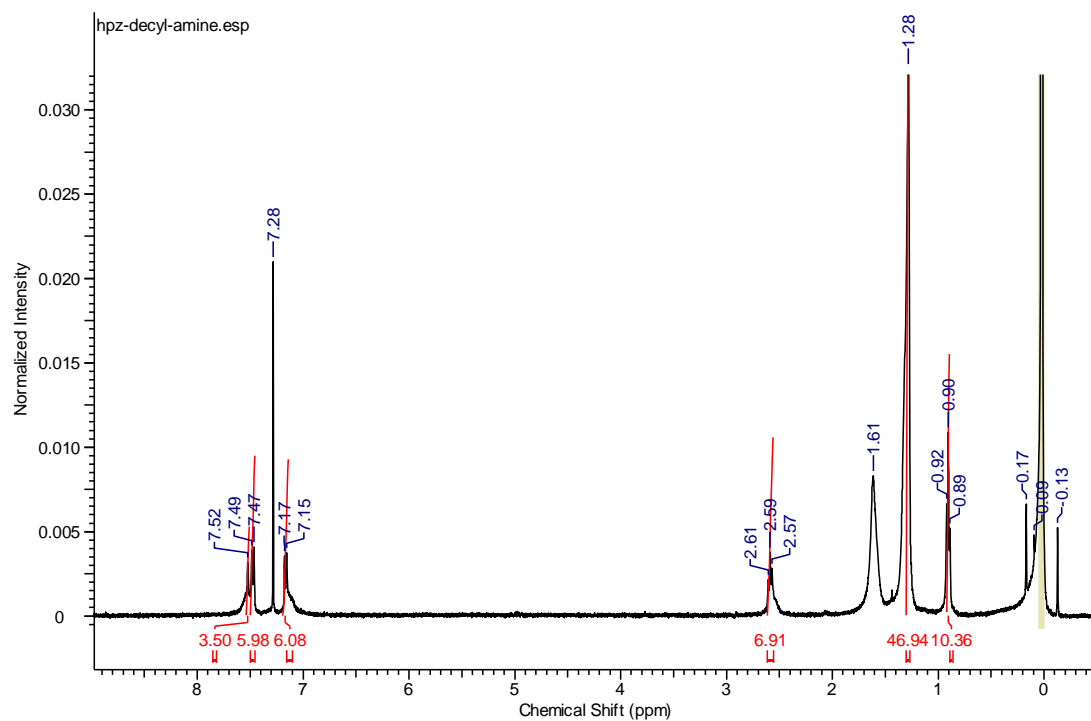


Figure A19.  $^1\text{H}$  NMR spectrum of compound **Hpz-C10**.

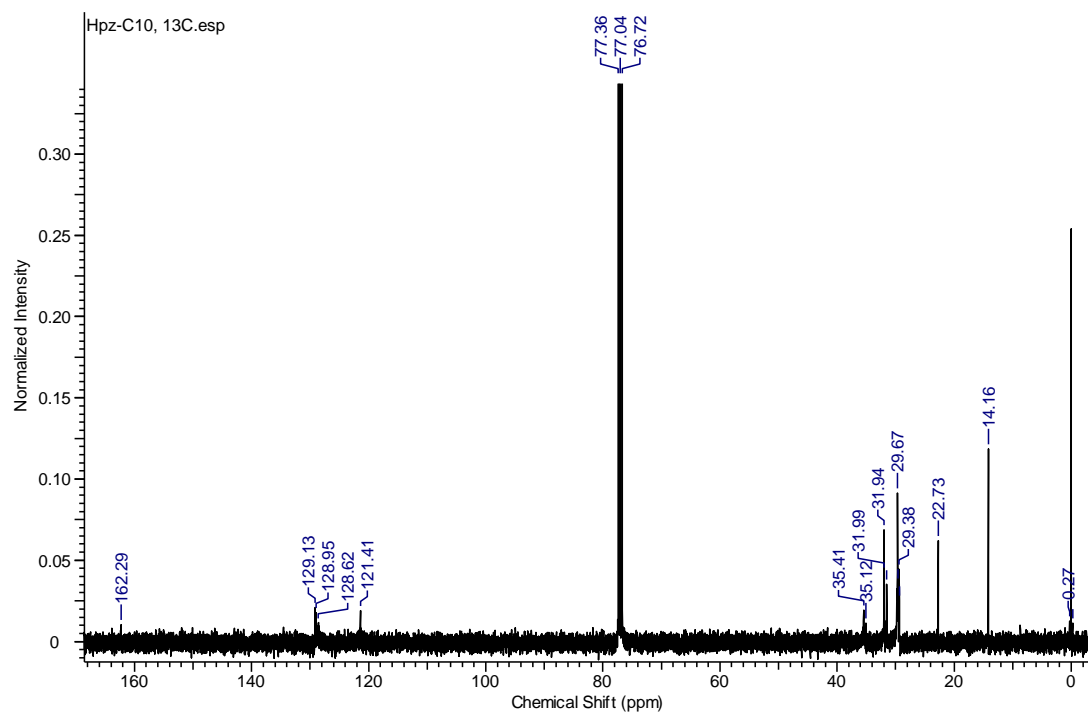


Figure A20.  $^{13}\text{C}$  NMR spectrum of compound **Hpz-C10**.

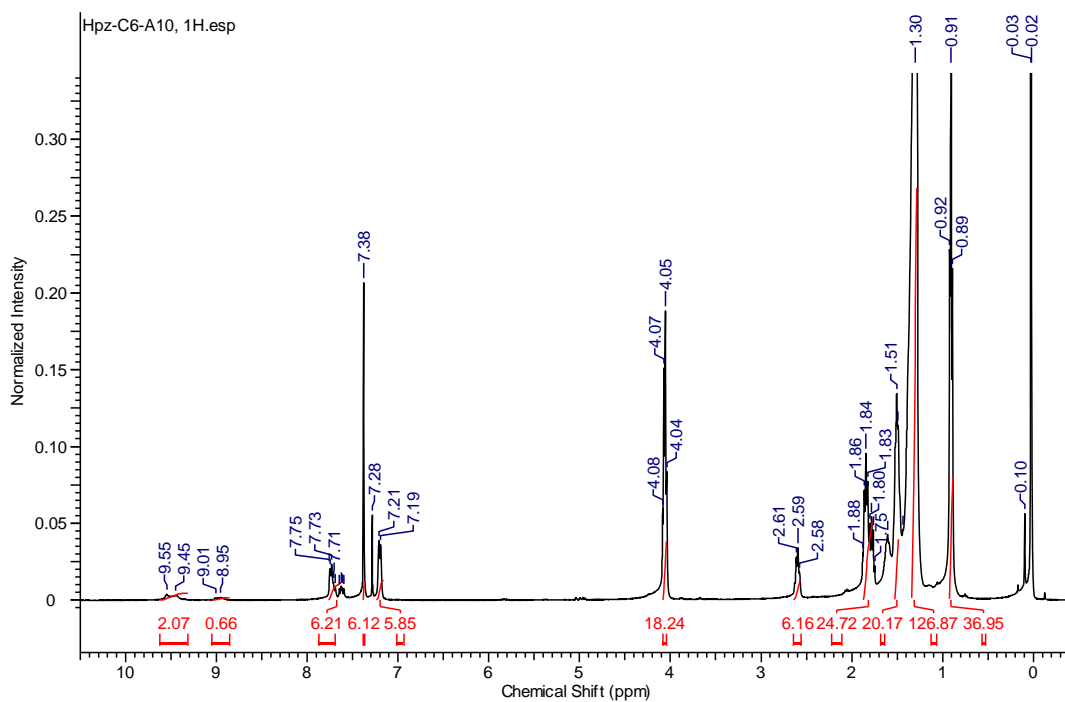


Figure A21.  $^1\text{H}$  NMR spectrum of compound **Hpz-C<sub>6</sub>/A10**.

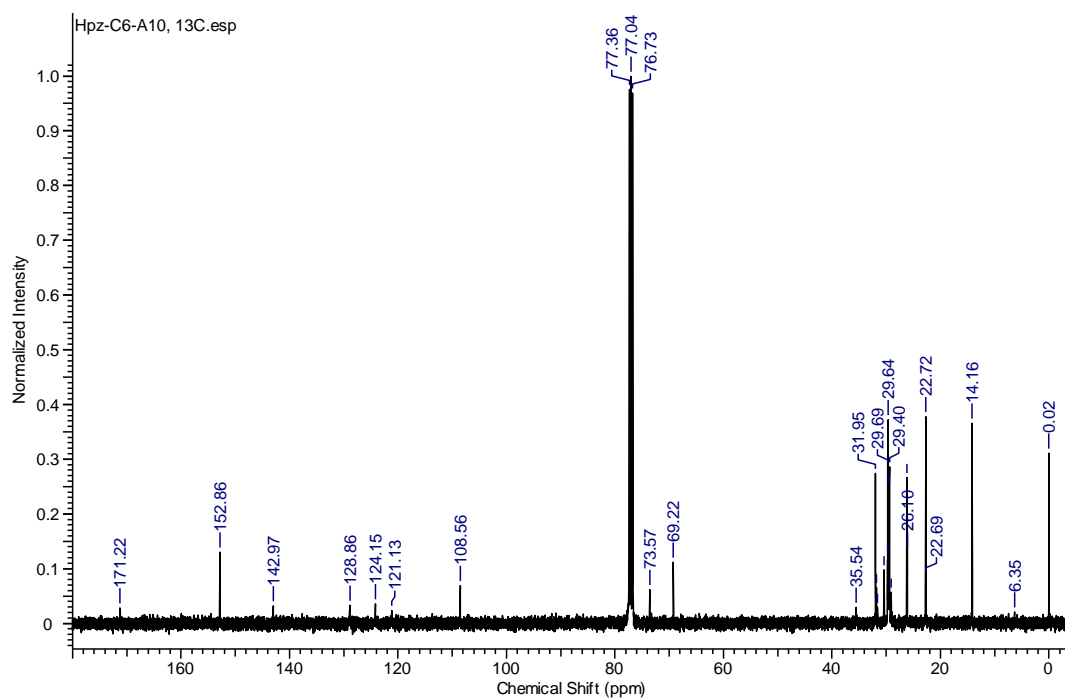


Figure A22.  $^{13}\text{C}$  NMR spectrum of compound **Hpz-C<sub>6</sub>/A10**.

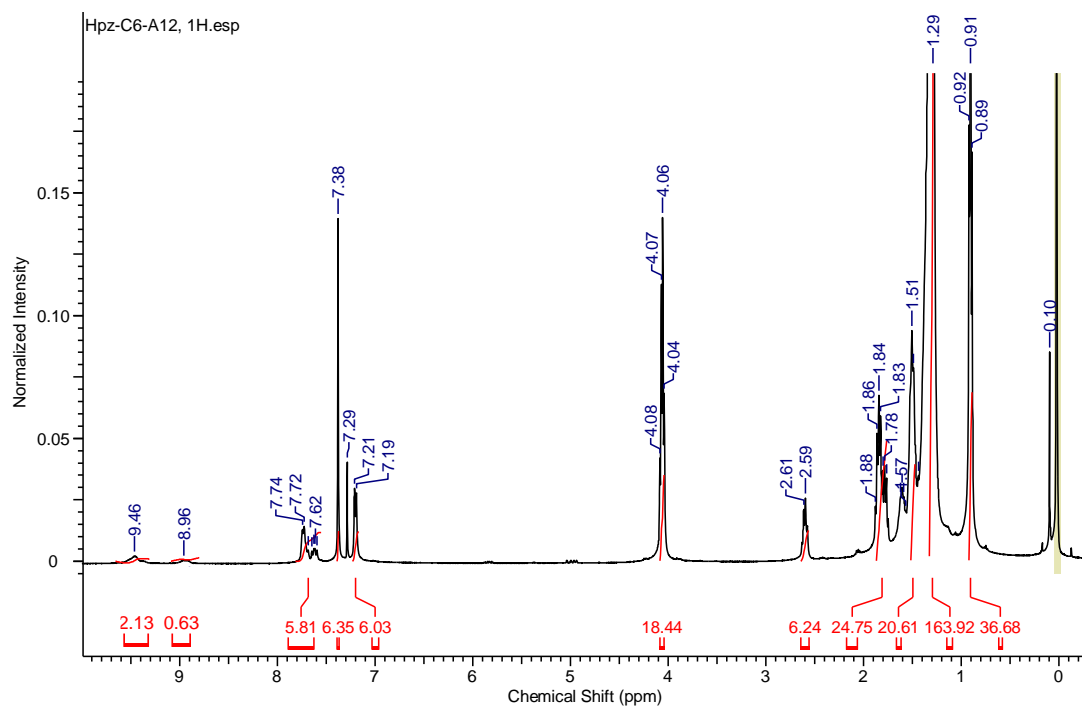


Figure A23.  $^1\text{H}$  NMR spectrum of compound **Hpz-C6/A12**.

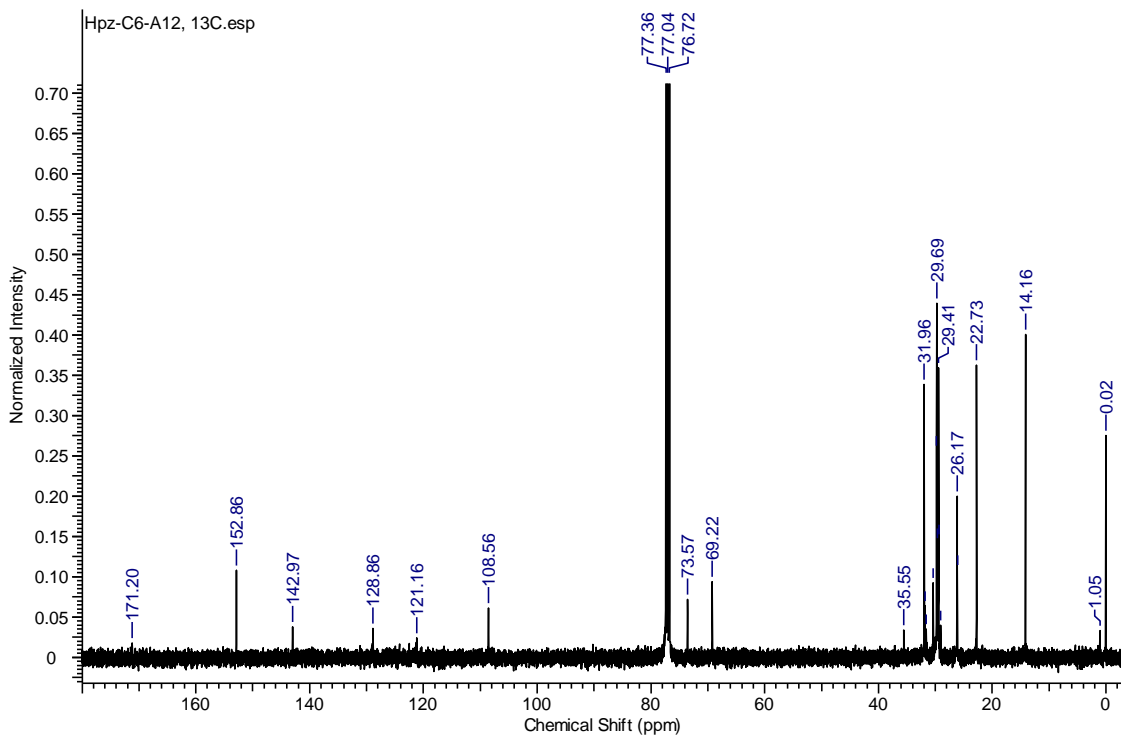


Figure A24.  $^{13}\text{C}$  NMR spectrum of compound **Hpz-C6/A12**.

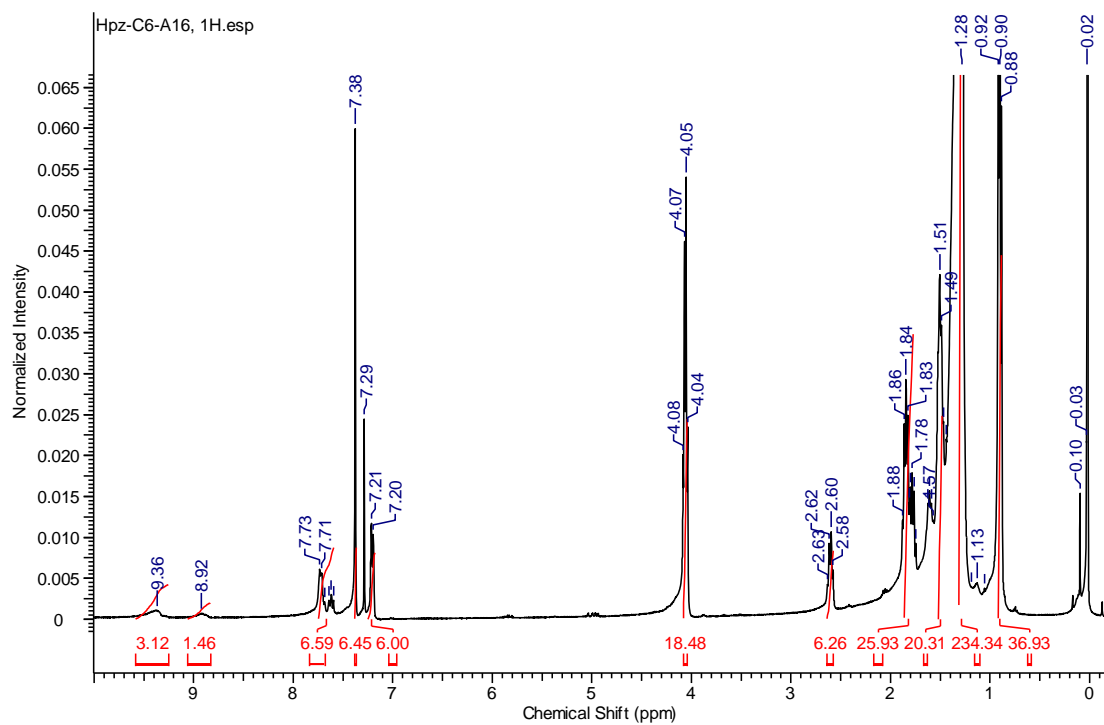


Figure A25.  $^1\text{H}$  NMR spectrum of compound **Hpz-C6/A16**.

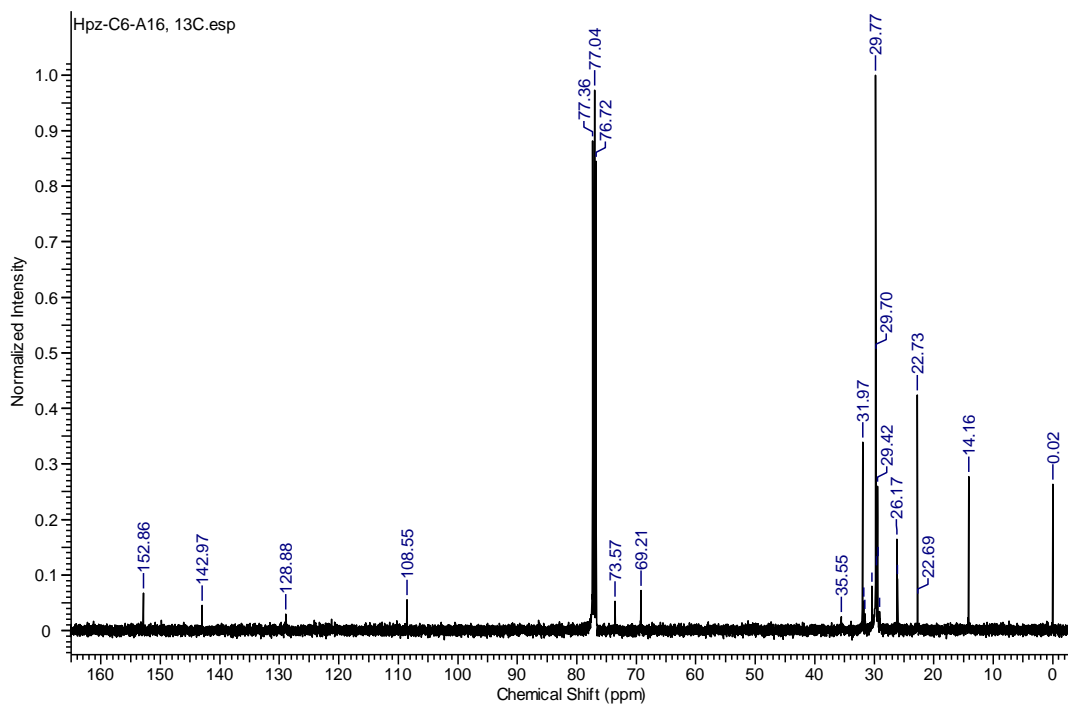


Figure A26.  $^{13}\text{C}$  NMR spectrum of compound **Hpz-C6/A16**.

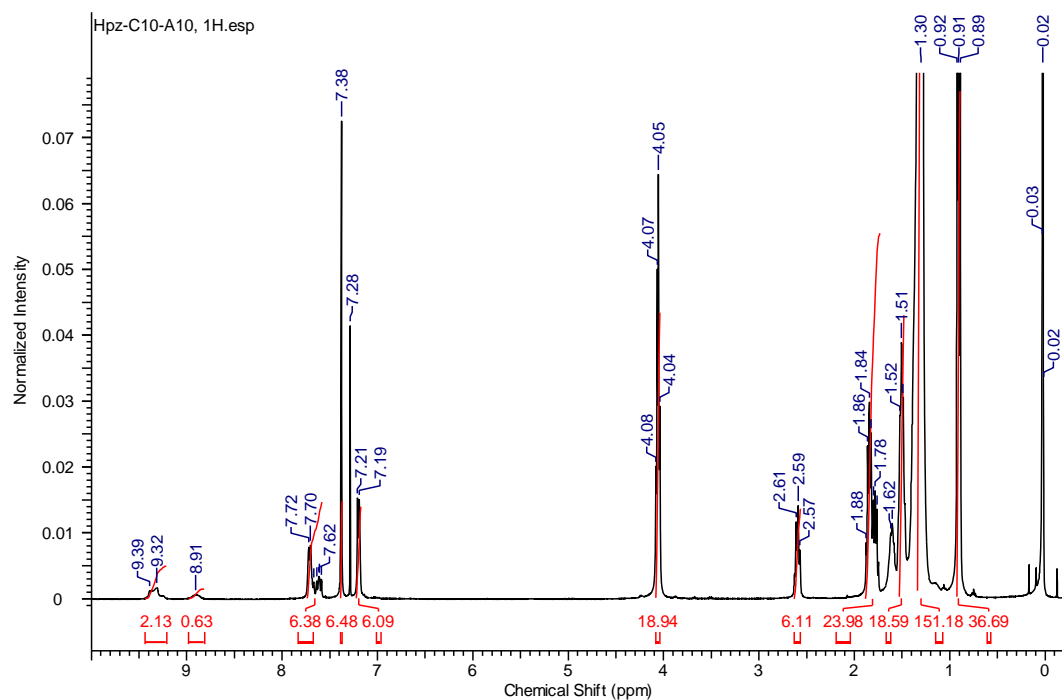


Figure A27.  $^1\text{H}$  NMR spectrum of compound **Hpz-C<sub>10</sub>/A10**.

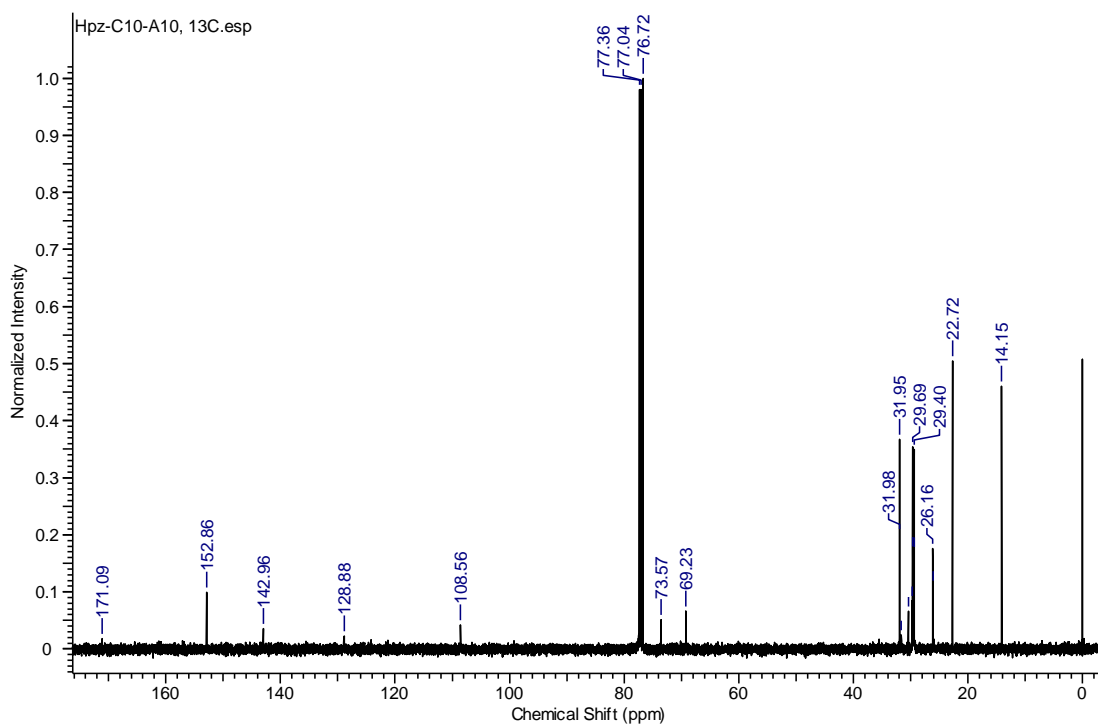
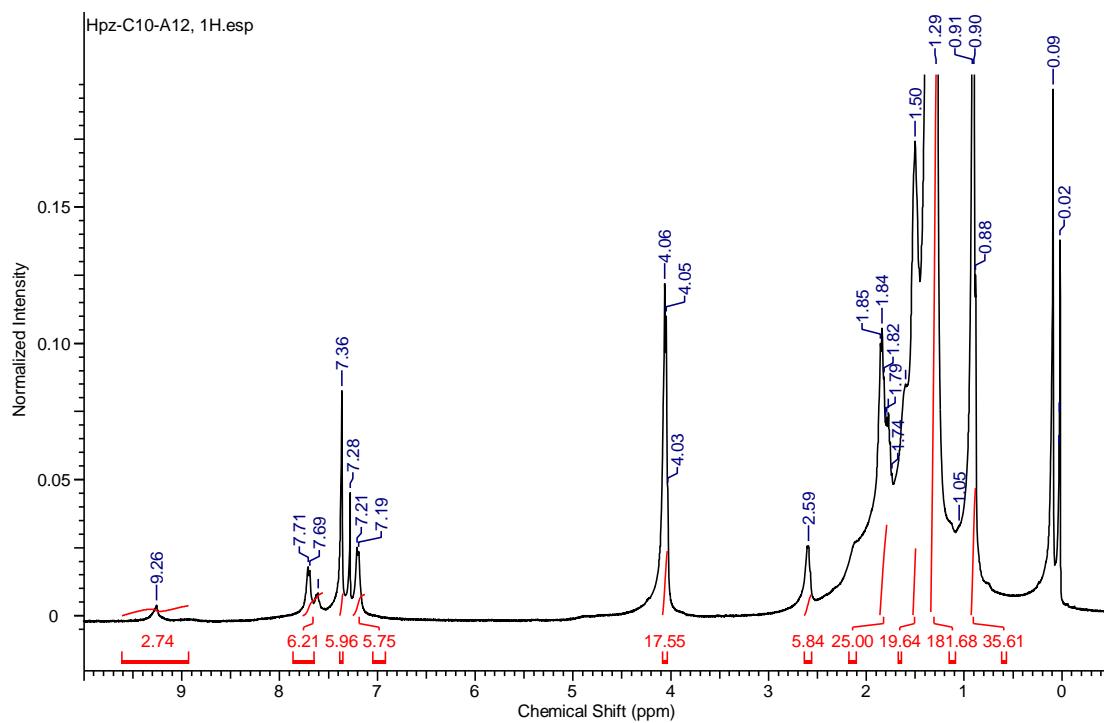
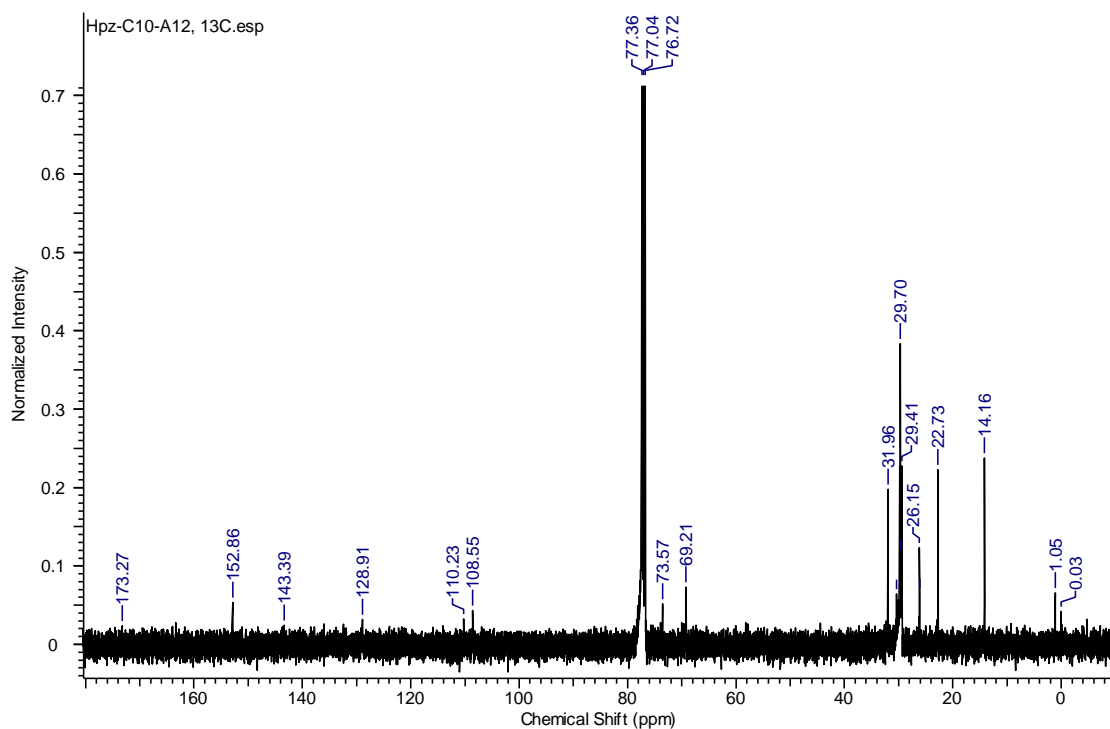


Figure A28.  $^{13}\text{C}$  NMR spectrum of compound **Hpz-C<sub>10</sub>/A10**.



**Figure A29.**  $^1\text{H}$  NMR spectrum of compound **Hpz-C<sub>10</sub>/A12**.



**Figure A30.**  $^{13}\text{C}$  NMR spectrum of compound **Hpz-C<sub>10</sub>/A12**.

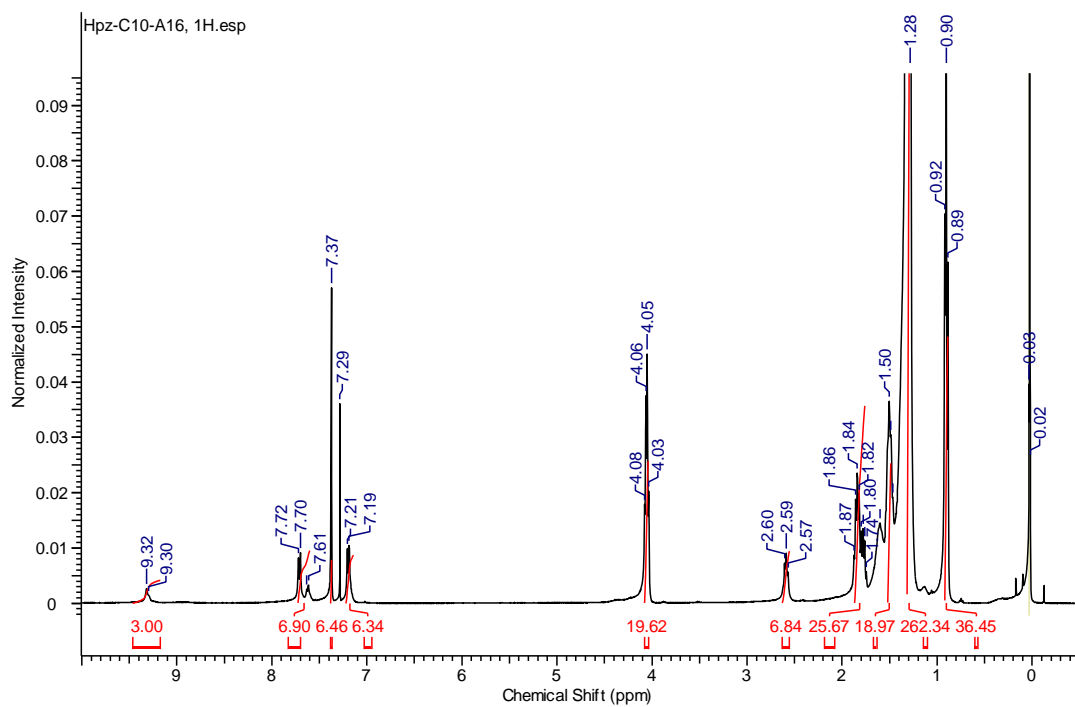


Figure A31.  $^1\text{H}$  NMR spectrum of compound **Hpz-C<sub>10</sub>/A16**.

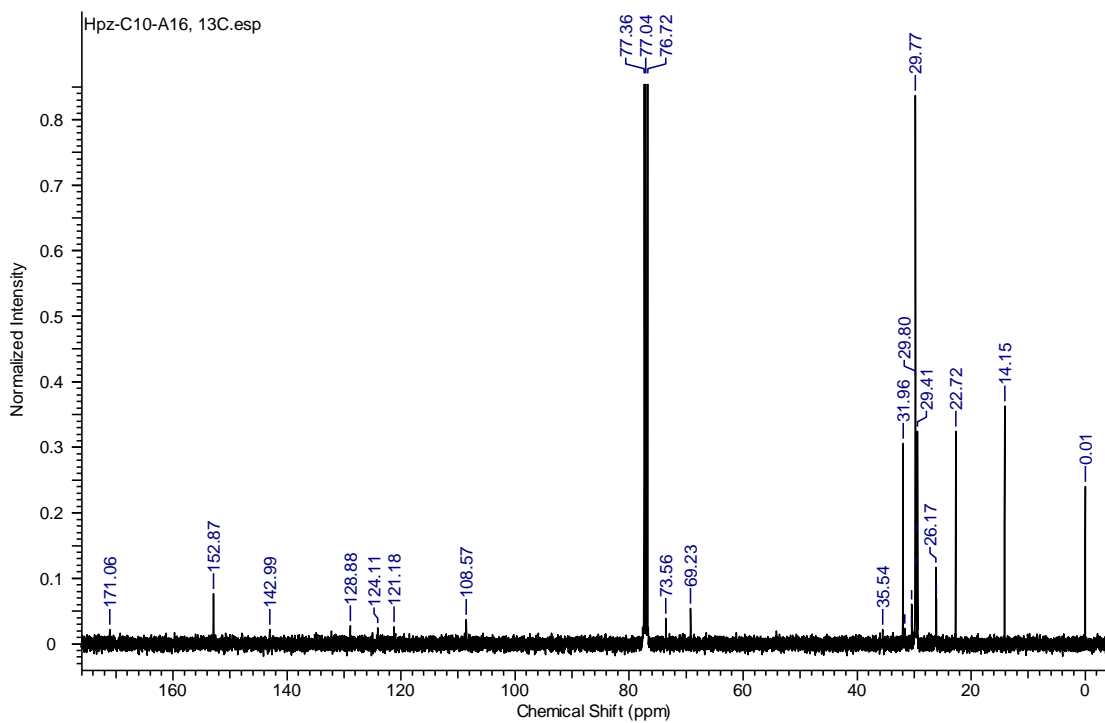


Figure A32.  $^{13}\text{C}$  NMR spectrum of compound **Hpz-C<sub>10</sub>/A16**.



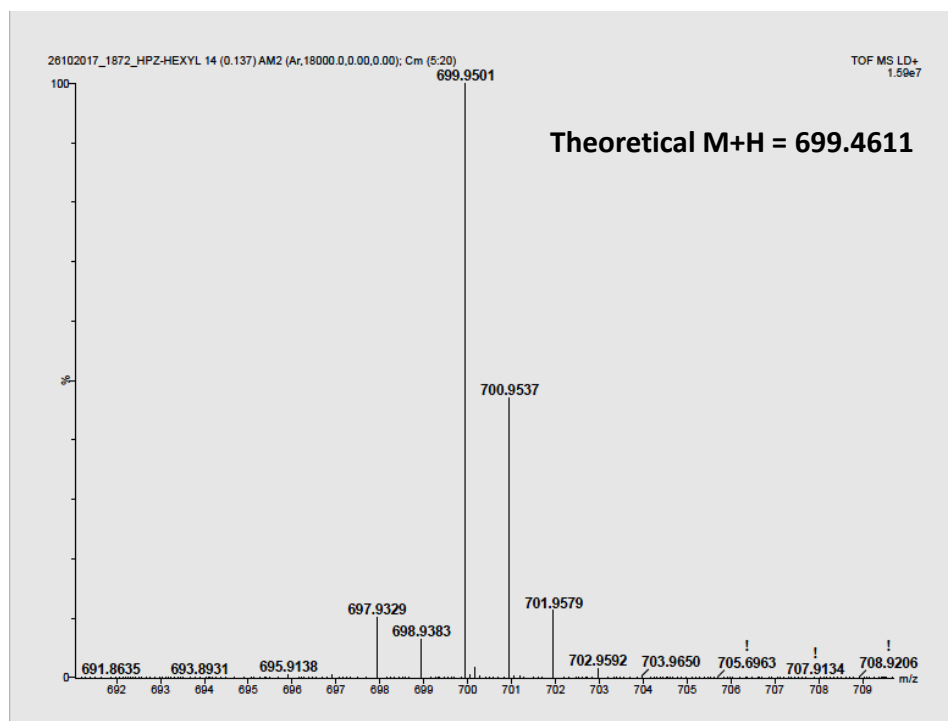


Figure A33. MALDI-TOF spectrum of compound **Hpz-C<sub>6</sub>**.

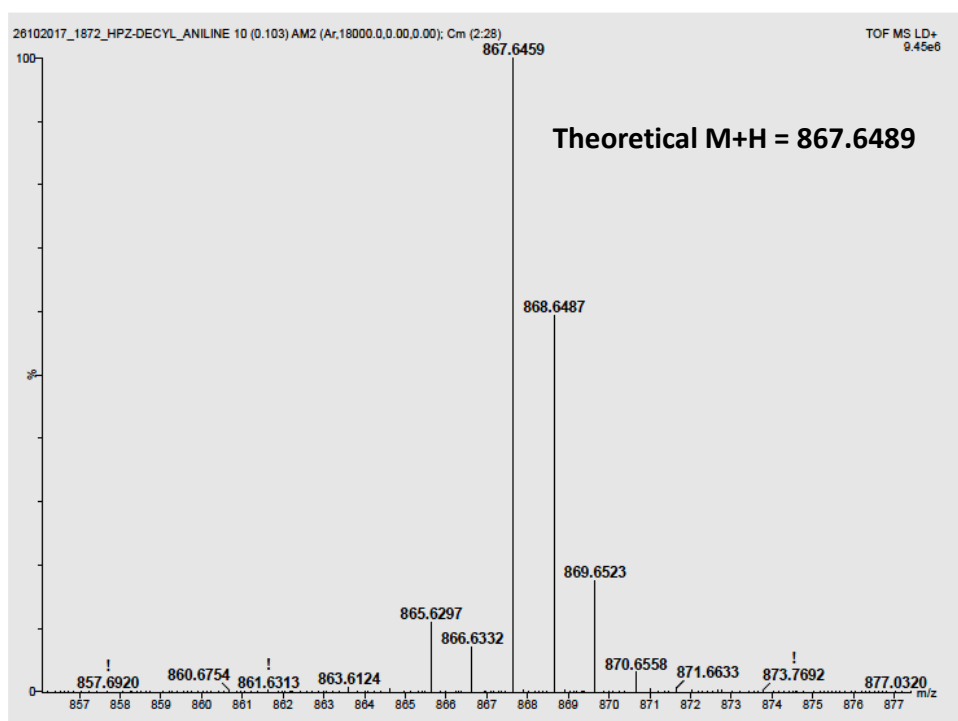
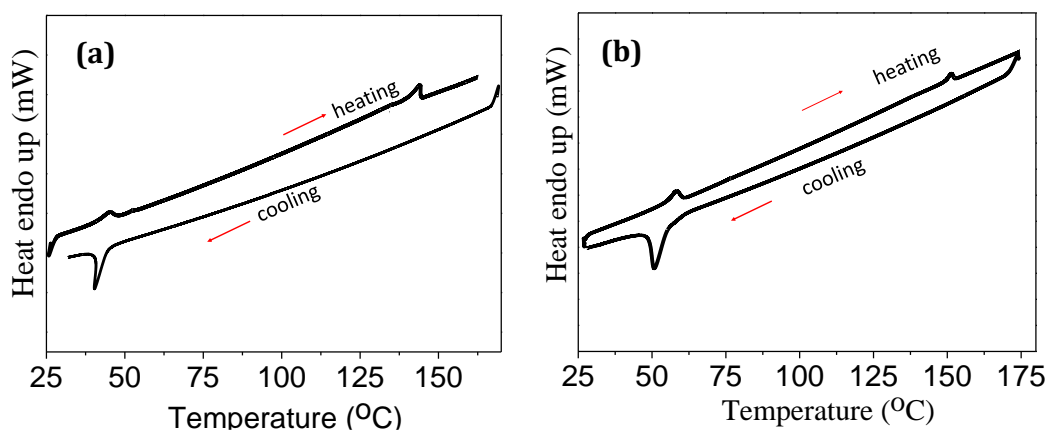
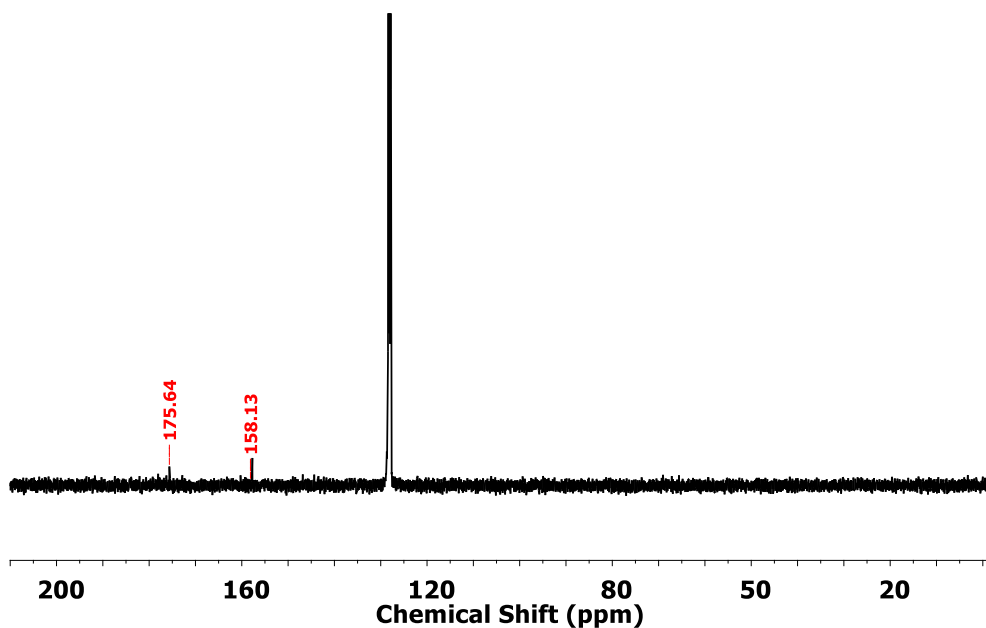


Figure A34. MALDI-TOF spectrum of compound **Hpz-C<sub>10</sub>**.



**Figure A35.** DSC spectra of the respective complexes of the **Hpz-C<sub>10</sub>** derivative: a) **Hpz-C<sub>10</sub>-A12** (1<sup>st</sup> heating & 2<sup>nd</sup> cooling); b) **Hpz-C<sub>10</sub>-A16** (2<sup>nd</sup> heating and 2<sup>nd</sup> cooling) with the scan rate of 10 °C/min.



**Figure A36.** <sup>13</sup>C NMR spectrum of cyameluric chloride in C<sub>6</sub>D<sub>6</sub> (deuterated benzene).

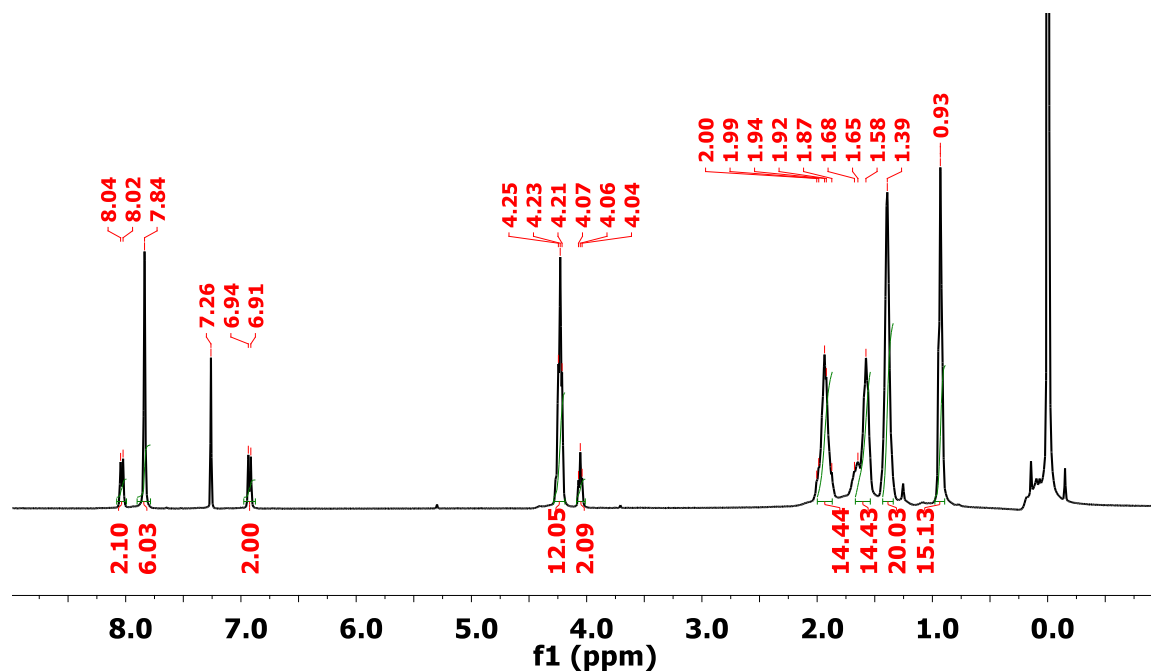


Figure A37. <sup>1</sup>H NMR spectrum of TP-C<sub>6</sub>-COOH in CDCl<sub>3</sub>.

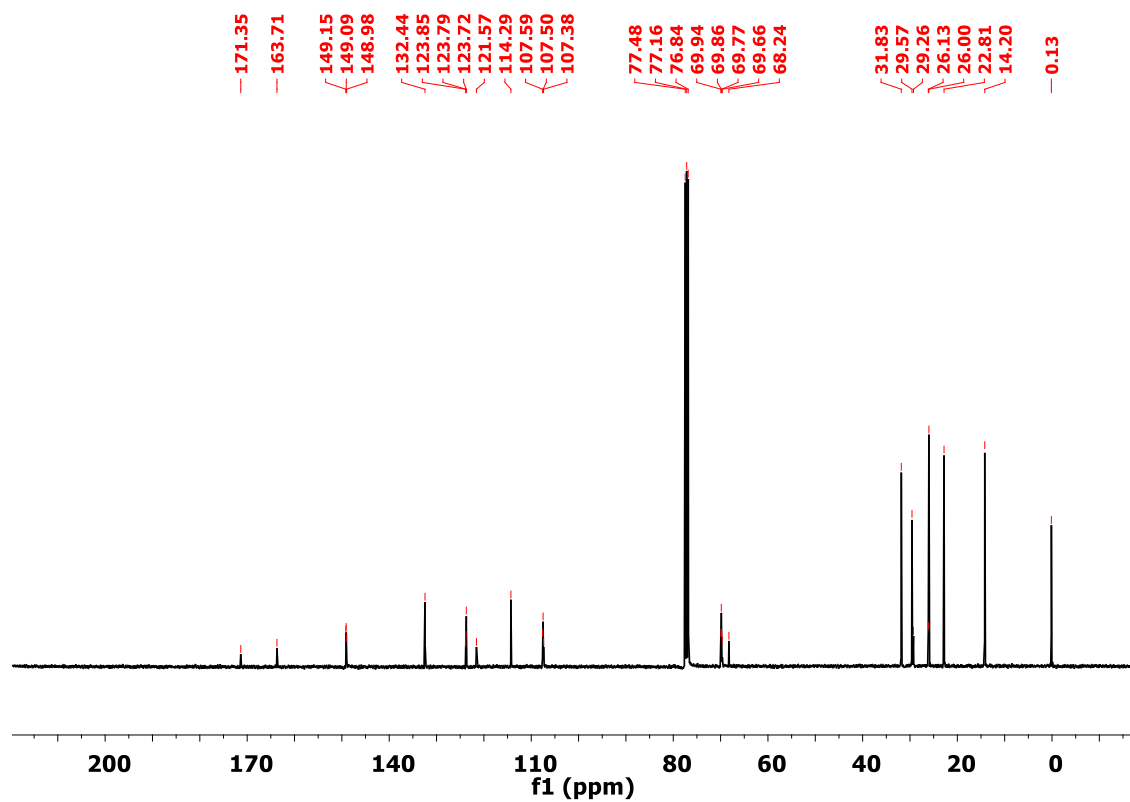


Figure A38. <sup>13</sup>C NMR spectrum of TP-C<sub>6</sub>-COOH in CDCl<sub>3</sub>.

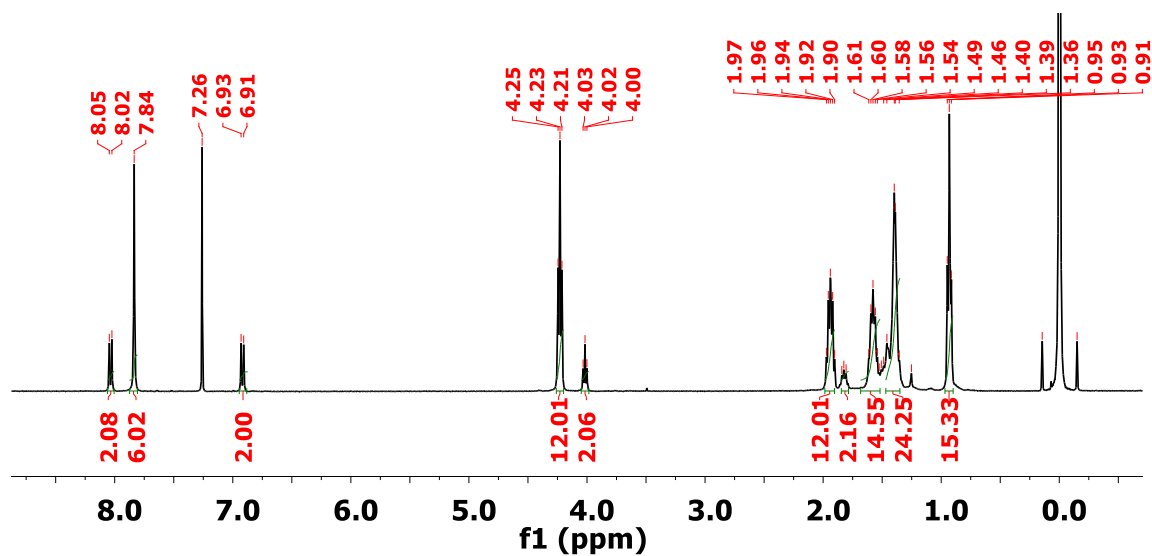


Figure A39. <sup>1</sup>H NMR spectrum of TP-C<sub>8</sub>-COOH in CDCl<sub>3</sub>.

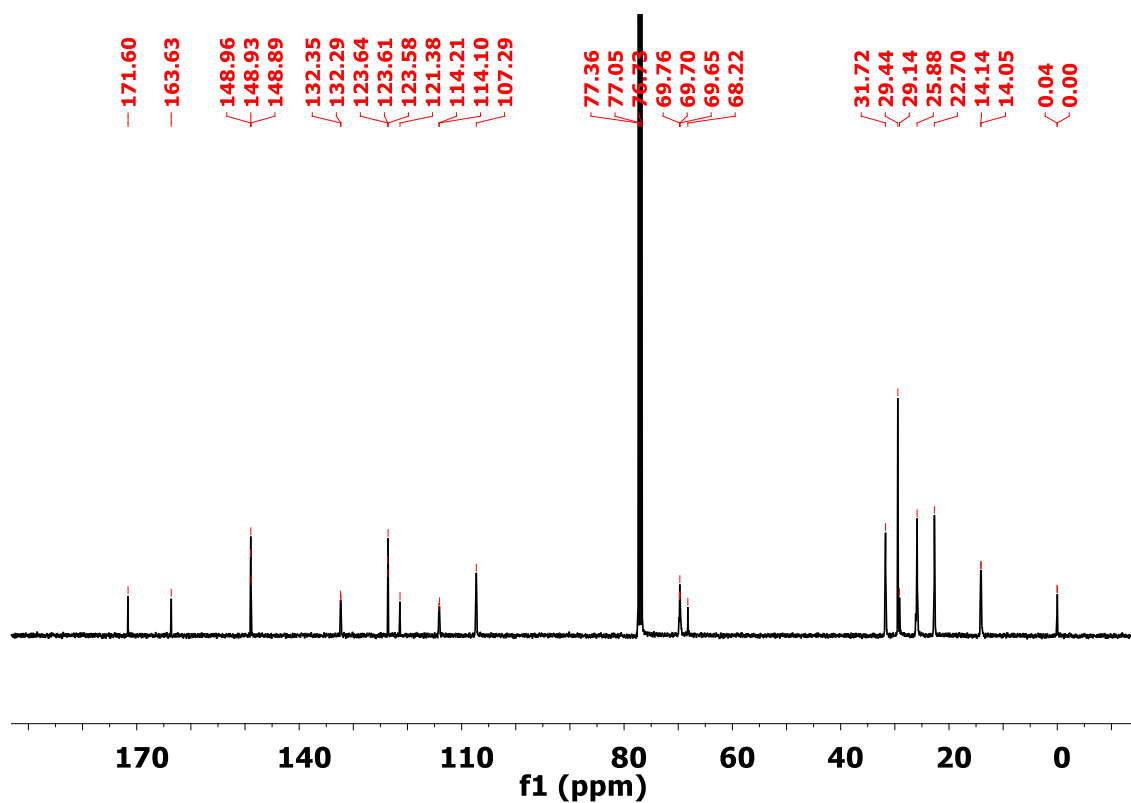


Figure A40. <sup>13</sup>C NMR spectrum of TP-C<sub>8</sub>-COOH in CDCl<sub>3</sub>.

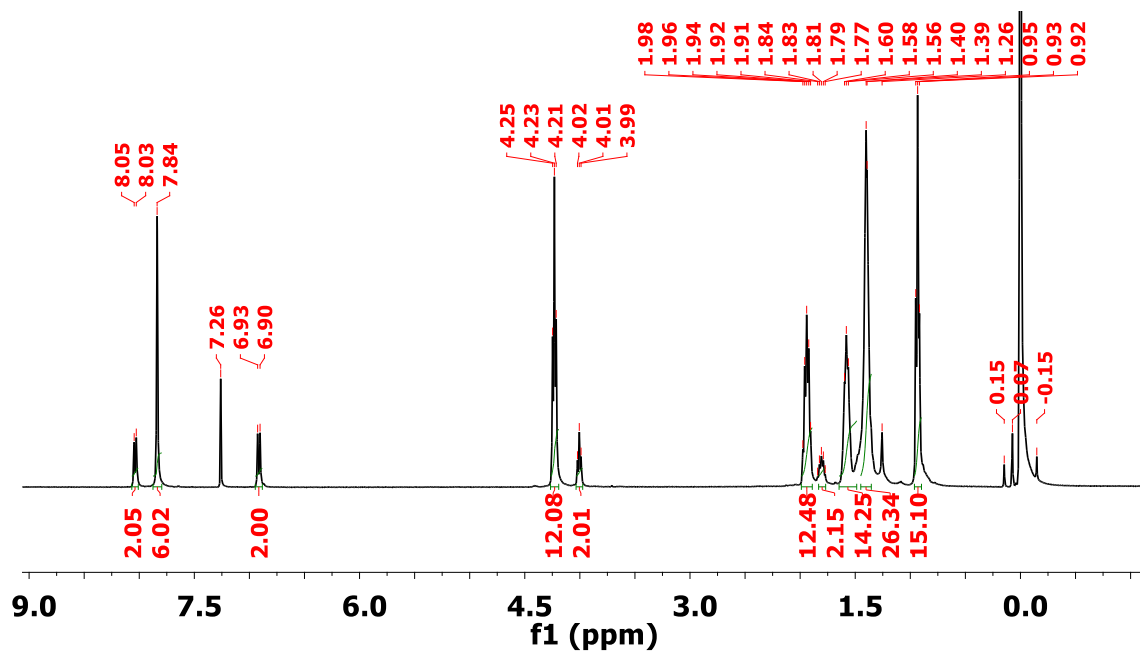


Figure A41. <sup>1</sup>H NMR spectrum of TP-C<sub>9</sub>-COOH in CDCl<sub>3</sub>.

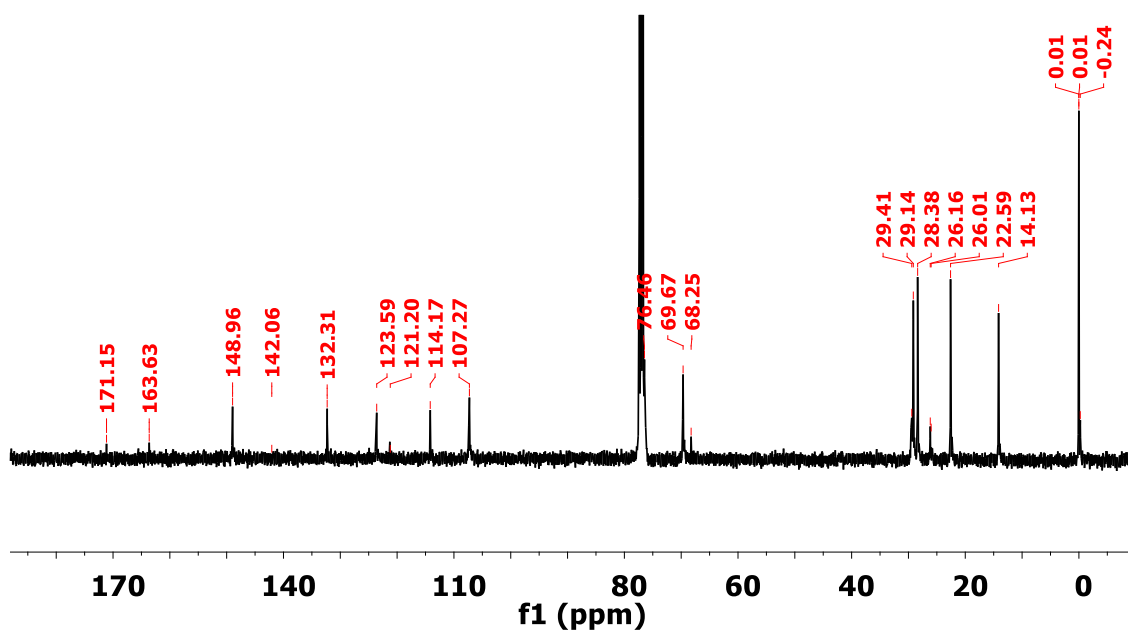


Figure A42. <sup>13</sup>C NMR spectrum of TP-C<sub>9</sub>-COOH in CDCl<sub>3</sub>.

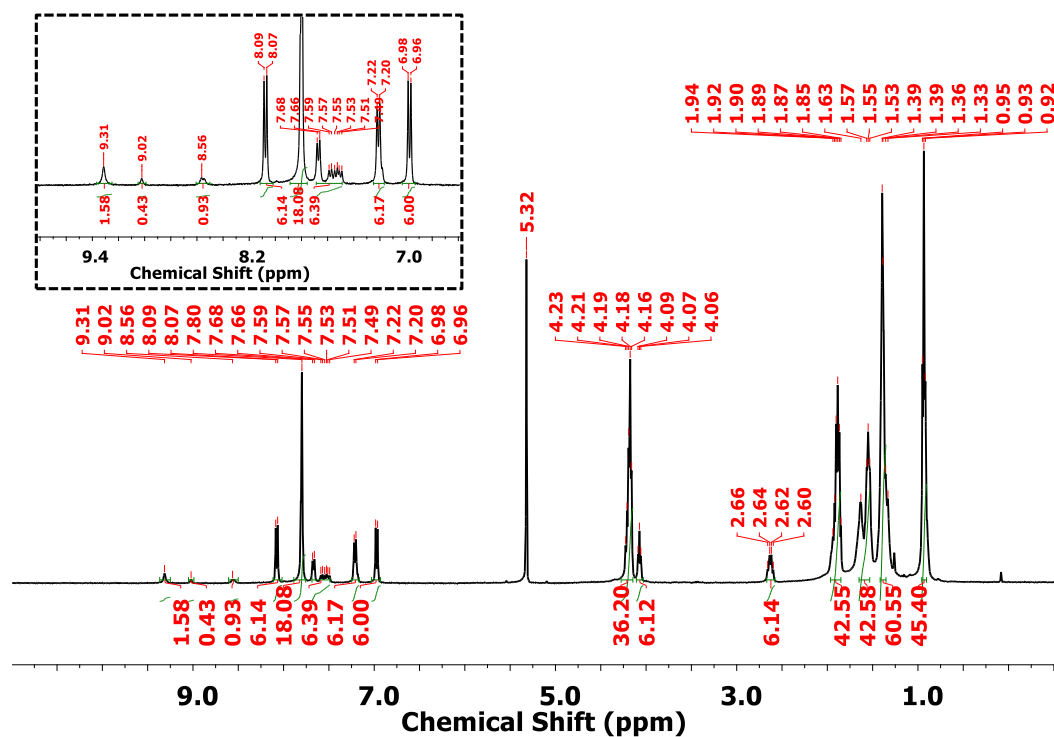


Figure A43. <sup>1</sup>H NMR spectrum of Hpz-C<sub>6</sub>-TP (0.0025 M) in CD<sub>2</sub>Cl<sub>2</sub>.

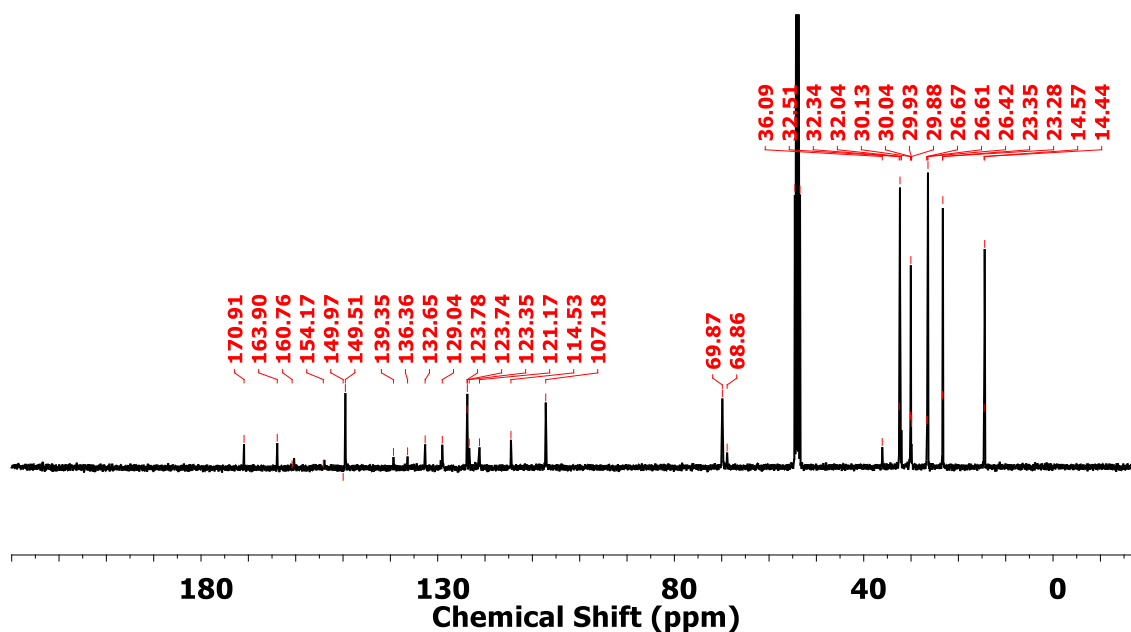


Figure A44. <sup>13</sup>C NMR spectrum of Hpz-C<sub>6</sub>-TP in CD<sub>2</sub>Cl<sub>2</sub>.

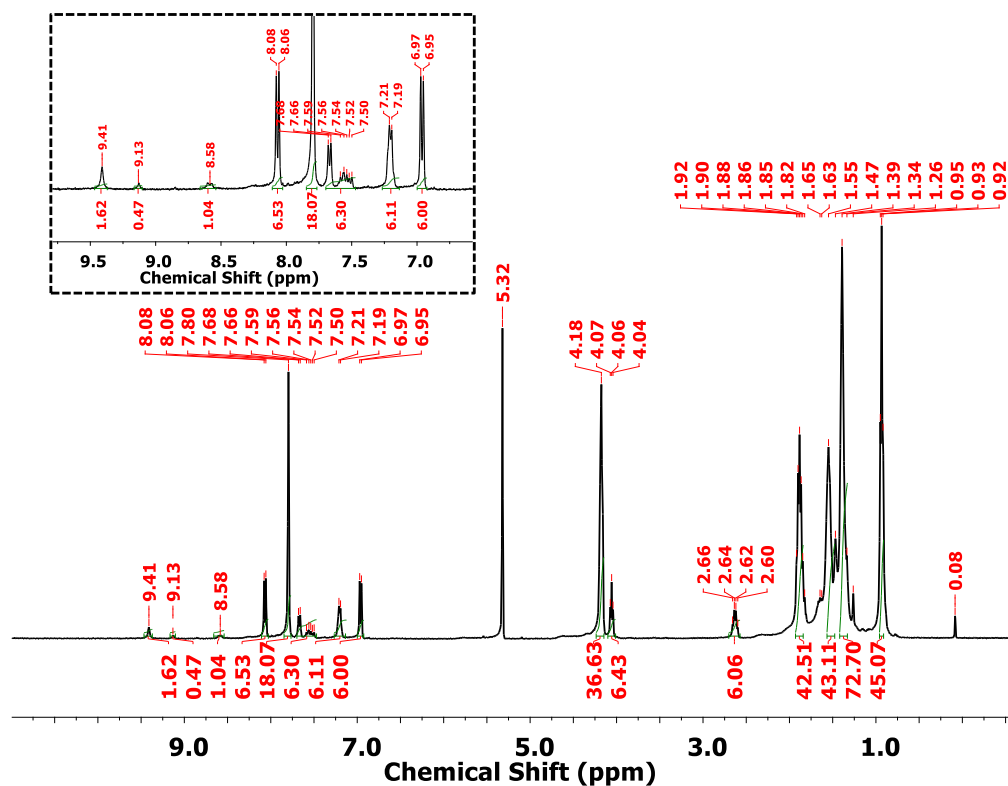


Figure A45. <sup>1</sup>H NMR spectrum of Hpz-C<sub>8</sub>-TP (0.0025 M) in CD<sub>2</sub>Cl<sub>2</sub>.

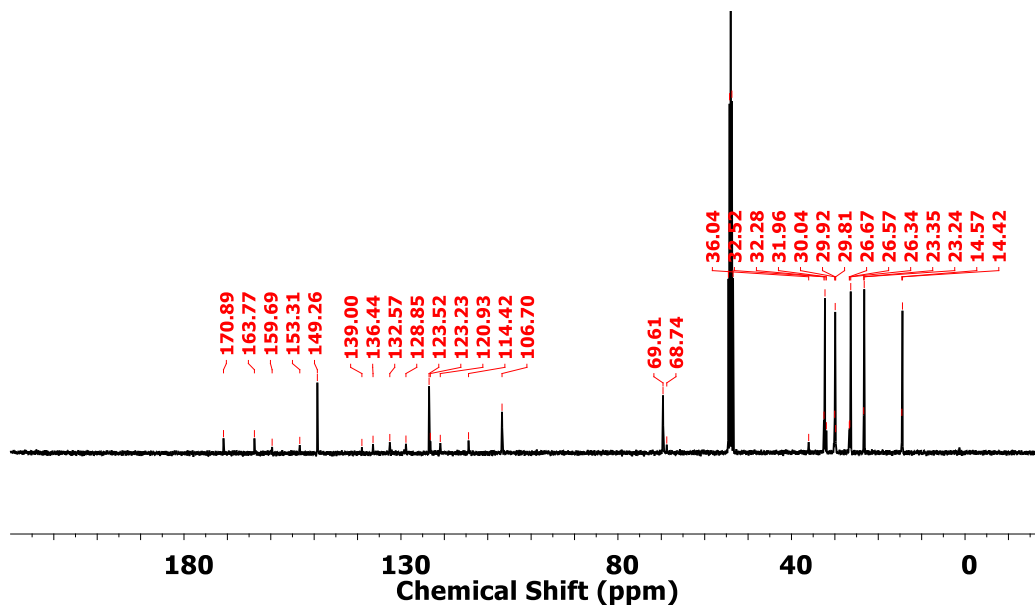


Figure A46. <sup>13</sup>C NMR spectrum of Hpz-C<sub>8</sub>-TP in CD<sub>2</sub>Cl<sub>2</sub>.

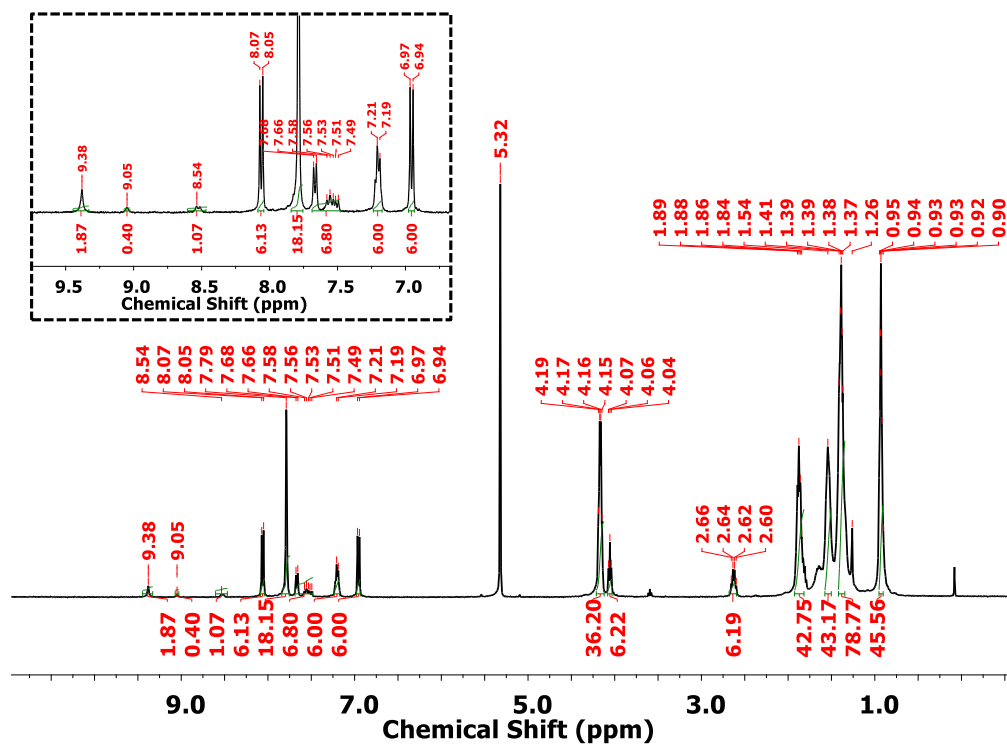


Figure A47. <sup>1</sup>H NMR spectrum of Hpz-C<sub>9</sub>-TP (0.0025 M) in CD<sub>2</sub>Cl<sub>2</sub>.

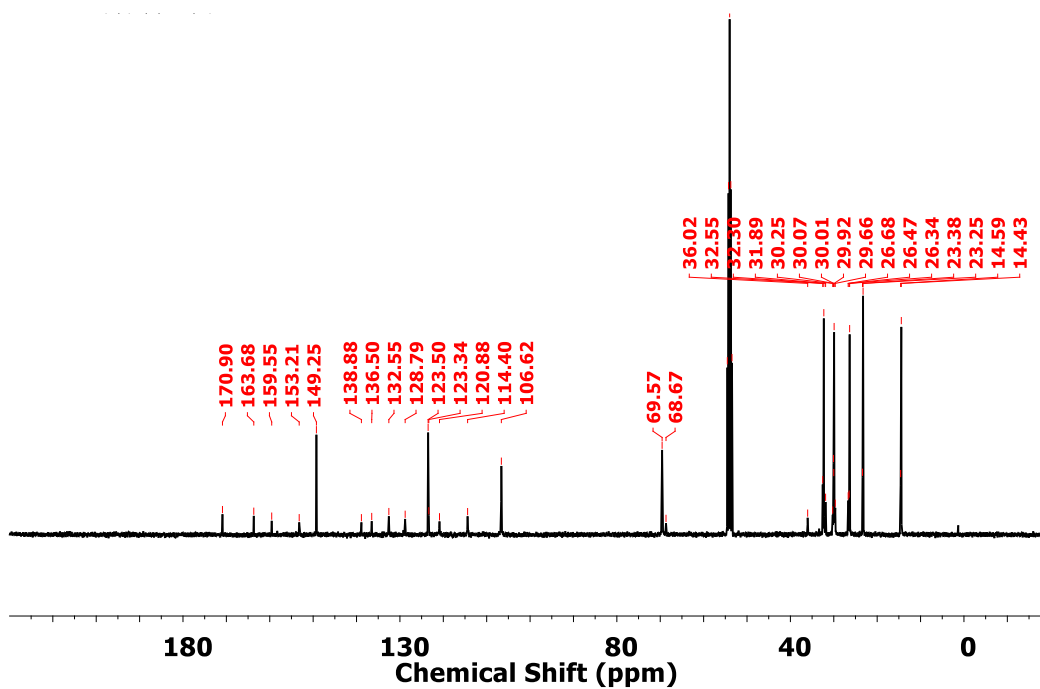
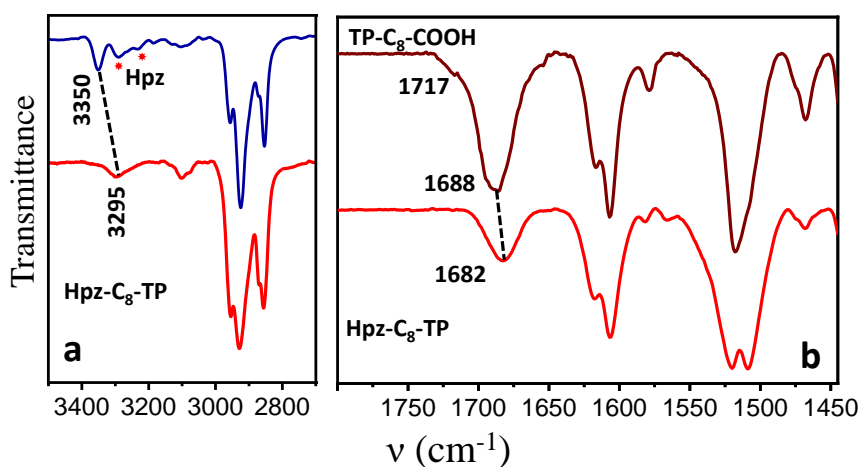
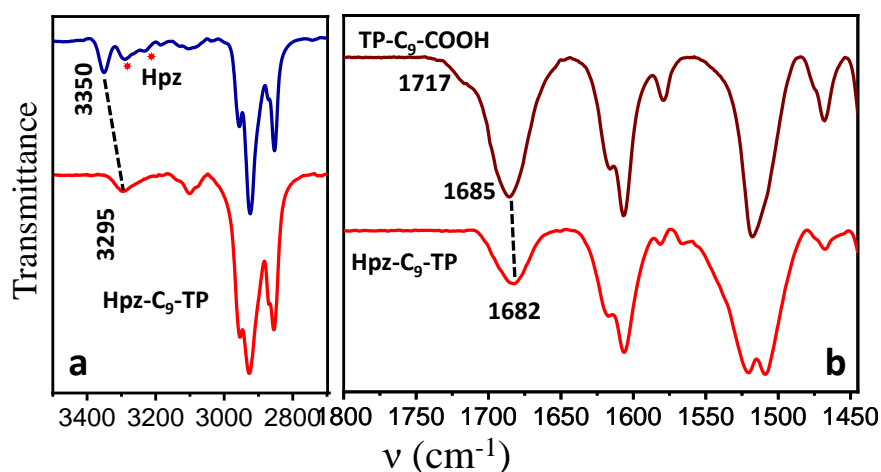


Figure A48. <sup>13</sup>C NMR spectrum of Hpz-C<sub>9</sub>-TP in CD<sub>2</sub>Cl<sub>2</sub>.





**Figure A49.** FT-IR spectral profiles of **Hpz-C<sub>8</sub>-TP** complex compared to those of (a) **Hpz** in the  $\text{-NH}$  stretching peak regime and (b) **TP-C<sub>8</sub>-COOH** in the carbonyl ( $\text{-C=O}$ ) stretching region.



**Figure A50.** FT-IR spectral profiles of **Hpz-C<sub>9</sub>-TP** complex compared to those of (a) **Hpz** in the  $\text{-NH}$  stretching peak regime and (b) **TP-C<sub>9</sub>-COOH** in the carbonyl ( $\text{-C=O}$ ) stretching region.

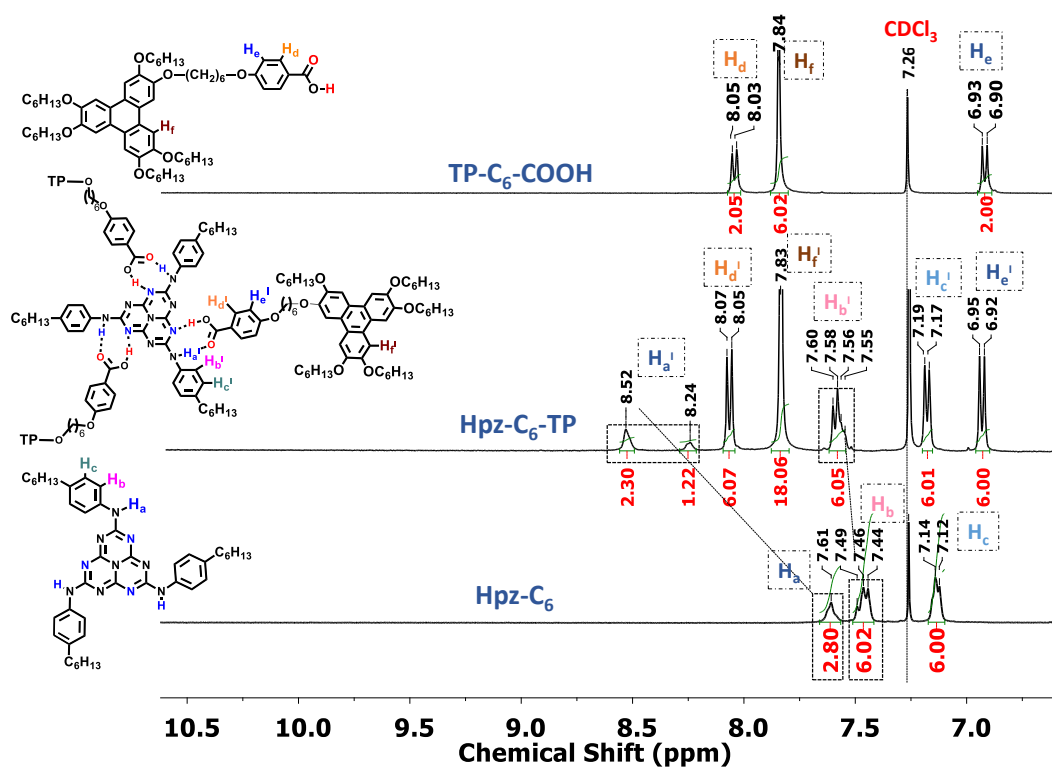


**Figure A51.** Comparative <sup>1</sup>H NMR spectra (in CDCl<sub>3</sub>) of pure heptazine derivative **Hpz** (0.01 M), pure TP based benzoic acid **TP-C<sub>6</sub>-COOH** (0.03 M) and their corresponding complex, **Hpz-C<sub>6</sub>-TP** (0.01 M).

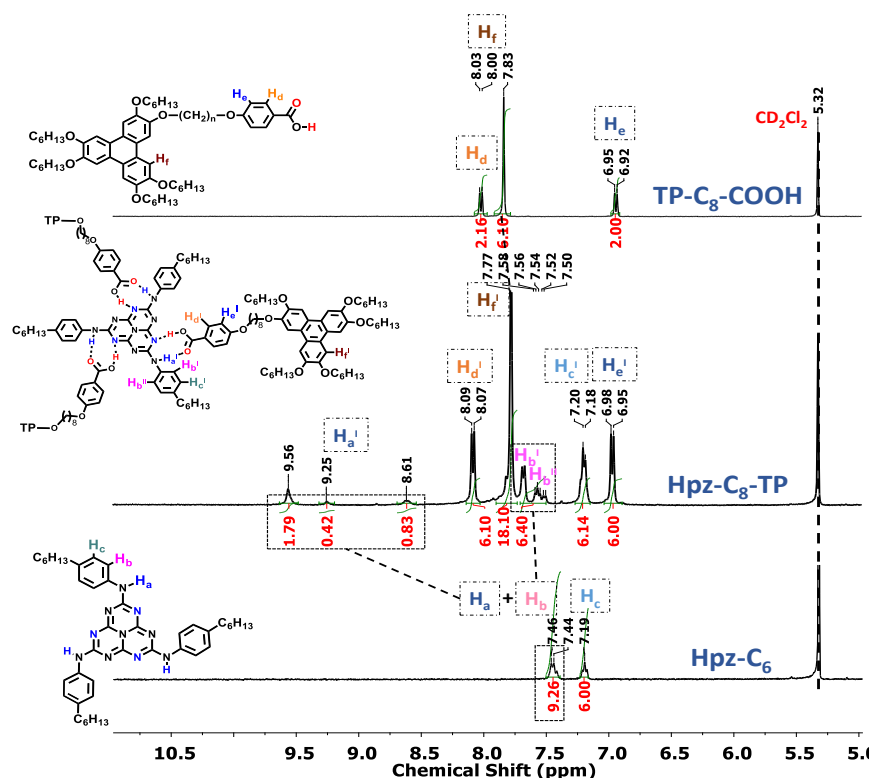


**Figure A52.** Comparative  $^1\text{H}$  NMR spectra (in  $\text{CD}_2\text{Cl}_2$ ) of pure heptazine derivative **Hpzc** (0.005 M), pure TP based benzoic acid **TP-C<sub>8</sub>-COOH** (0.015 M) and their corresponding complex, **Hpzc-C<sub>8</sub>-TP** (0.005 M).

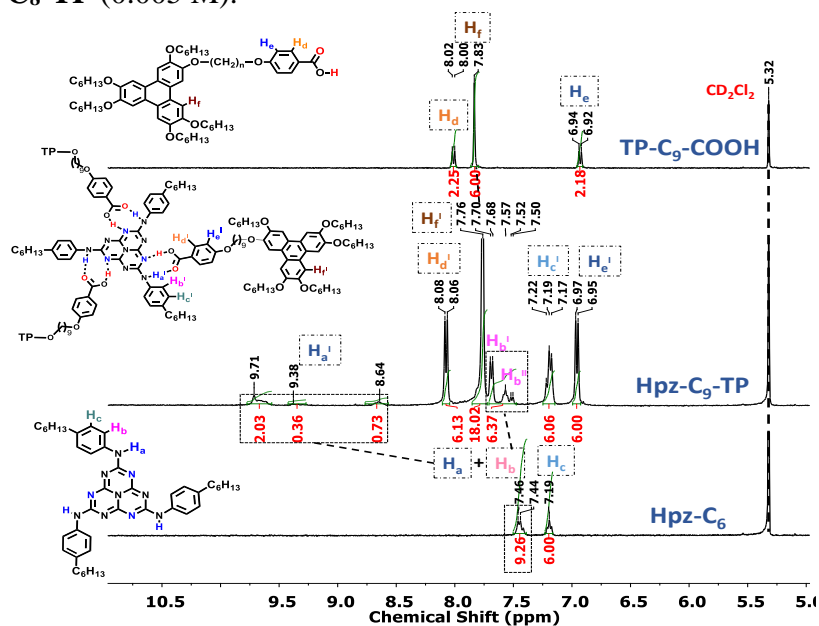


**Figure A53.** Comparative  $^1\text{H}$  NMR spectra (in  $\text{CD}_2\text{Cl}_2$ ) of pure heptazine derivative **Hpzc** (0.005 M), pure TP based benzoic acid **TP-C<sub>9</sub>-COOH** (0.015 M) and their corresponding complex, **Hpzc-C<sub>9</sub>-TP** (0.005 M).

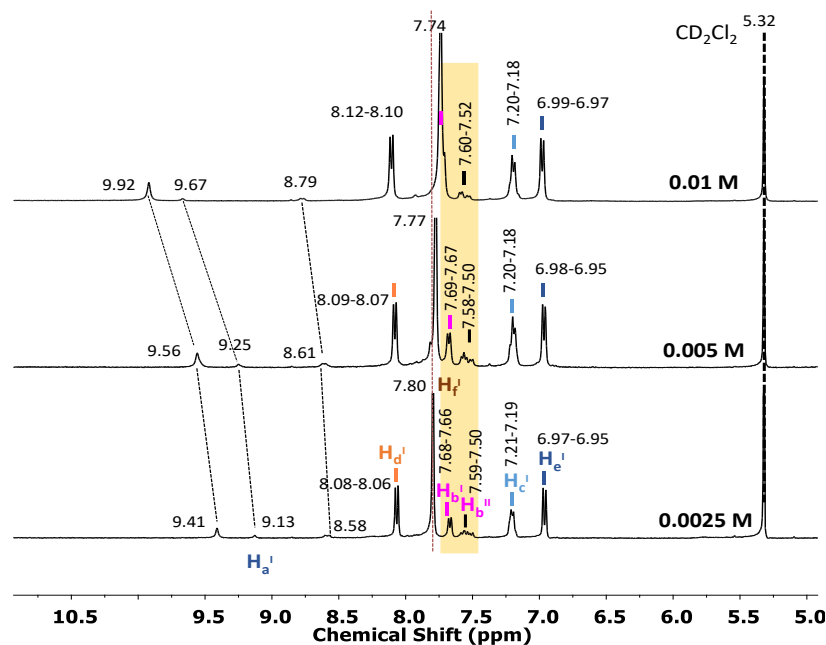


**Figure A54.** Concentration dependent  $^1\text{H}$  NMR spectra of the **Hpz-C8-TP** complex in  $\text{CD}_2\text{Cl}_2$ .

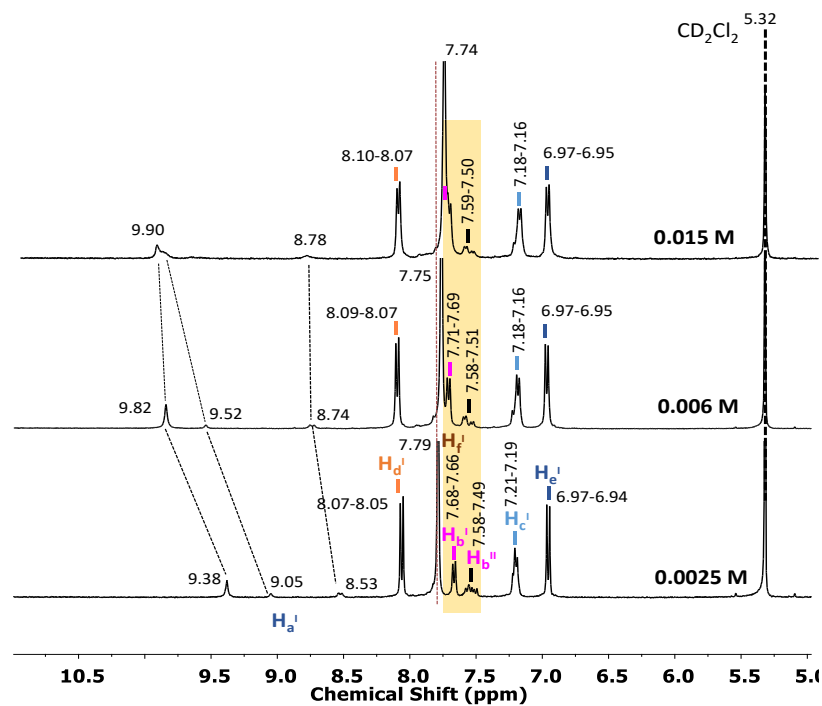
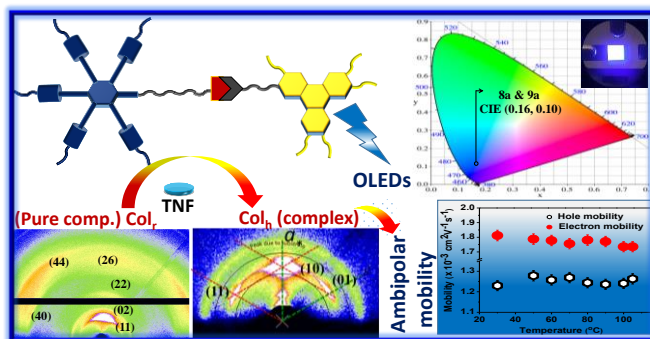


**Figure A55.** Concentration dependent  $^1\text{H}$  NMR spectra of the **Hpz-C9-TP** complex in  $\text{CD}_2\text{Cl}_2$ .

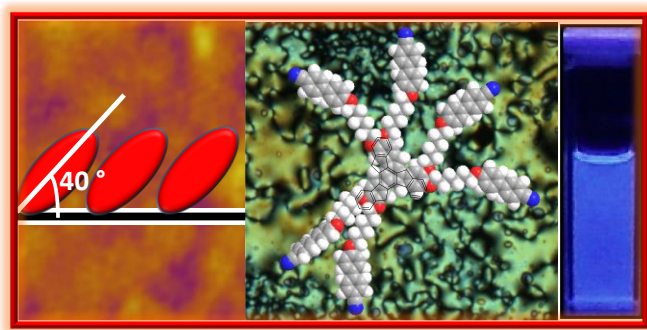
## Chapter 3

### Functional Triphenylene-Pentaalkynylbenzene based Disc-Disc and Truxene-Cyanobiphenylene based Rod-Disc Oligomers

**Part A:** Discotic liquid crystalline (DLC) dimers composed of pentaalkynylbenzene (PA) and triphenylene (TP) moieties were reported by using the  $\text{CuI-Et}_3\text{N}$  catalyzed click reaction between terminal TP alkyne and PA azide. Room temperature columnar behaviour and blue light-emitting property were aimed to introduce with the involvement of PA moiety and consequently used as a potential emitter in blue OLED devices. TP core with the favourable columnar organization along with additionally introduced inter-disc interactions by doping the TP-PA dimers with disc-shaped 2,4,7-trinitrofluorenone (TNF) electron acceptors resulted into efficient ambipolar charge transport.



**Part B:** A facile synthesis of a novel covalently linked disc-rod mesogen is reported consisting of a truxene-based core attached to which are six 4-cyanobiphenyl units via flexible alkyl spacers. The compound formed a stable Langmuir monolayer at the air-water interface. The atomic force microscope study on the Langmuir-Blodgett film of the molecule reveals a tilted orientation at air-solid interfaces.





### 3.1 Part A: Triphenylene-pentalkynylbenzene discotic liquid crystalline dyads as an emitter in blue OLEDs and their charge transfer complexes with ambipolar charge transport behaviour

#### 3.1.1 Introduction

Non-symmetric LC dimers<sup>1-4</sup> comprising of two different mesogenic units have attracted their own significance as they can combine the properties of both the individual mesogenic units into just one single component. As a result, one can connect two different mesogenic units of their own interest to form new LC materials of new interesting properties. Triphenylene (TP) derivatives are the pillars of discotic liquid crystals (DLCs) which mainly favours columnar organization due to their rigid conjugated core.<sup>5</sup> In contrary, multialkynyl benzenes are the most investigated discotic nematogens in the literature.<sup>3,6</sup> The induction of the discotic nematic ( $N_D$ ) phase in these systems is a result of rotational freedom provided by the ethynyl linkers which prevents effective columnar stacking of the pentayne disks.<sup>6</sup> In addition, multiynes are known as blue-light emitter discotic nematogens,<sup>1-3</sup> so their incorporation with the non-emissive rigid  $\pi$ -conjugated molecules can modify their self-assembly behaviour and can induce the emissive properties in the resulting new material.

There are numerous reports on TP dimers, oligomers, and polymers<sup>7</sup> while there are a few reports on pentaalkynylbenzene (PA) ones.<sup>1-3,8</sup> Conventionally, TP-containing DLC oligomers are largely connected *via* ether, ester, amide, siloxane, or oligo methylene functional groups.<sup>9-16</sup> A variety of pentayne dimers, oligomers and side-chain polymers have been synthesized differing in peripheral substituents and nature of spacers which involves alkyl, amide, oligo(ethylene oxide), perfluoroalkyl and siloxane groups.<sup>17,18</sup> Symmetric TP and PA dimers linked *via* flexible alkyl spacers show glassy structures<sup>9</sup> and  $N_D$  phases, respectively. In addition, chemoselective click chemistry approach has been widely used to produce new LC materials with different molecular structures and physical properties. This includes molecular propeller DLCs,<sup>19,20</sup> gold nanoparticles,<sup>21,22</sup> LC dendrimers,<sup>23</sup> fullerenes,<sup>24</sup> metal complexes,<sup>25</sup> aggregation-induced light-emitting oligomers<sup>26</sup> and so on. A variety of TP-containing DLC oligomers have been synthesized *via* a triazole linkage.<sup>27-39</sup> Both PA and TP are known to form

---

Reproduced/Adapted from (Bala, I.; Yang, W. Y.; Gupta, S. P.; De, J.; Yadav, R. A. K.; Singh, D. P.; Dubey, D. K.; Jou, J. H.; Douali, R.; Pal, S. K. *J. Mater. Chem. C* **2019**, 7, 5724-5738.) with permission from The Royal Society of Chemistry.

a variety of mesophases in their neat as well as in complex form due to their tendency to form charge transfer complexes with multinitro fluorenone electron acceptors owing to their high electron richness.<sup>40-45</sup> This provides an easy and efficient way to manipulate the mesomorphic properties and also gives rise to the good charge transport properties of the resulting complexes. In literature, triphenylene containing DLCs are known to exhibit good charge carrier conducting properties.<sup>46-50</sup>

This work deals with the first representatives of TP and PA dimers modified with the triazole ring in between the ether chains (Figure 3.1). The synthesis, thermal behaviour, and the mesomorphic properties of neat compounds and their binary systems attained after doping with electron acceptor 2,4,7-trinitrofluorenone (TNF) are discussed in detail. The compounds were doped in different ratios with TNF such as in TNF:compound ratio of 1:1, 1:2, 2:1. The mesomorphic behaviour was found to be perfectly Col<sub>h</sub> in case of 2:1 ratio of TNF:compound while in other cases the intermediate kind of behaviour was found which was not clear from X-ray diffraction (XRD) techniques. The doped devices have been fabricated by using neat compounds **8a** and **9a** as an emitter with the configuration ITO/PEDOT:PSS/Host:Emitter/TPBi/LiF/Al which shows a maximum EQE of 2.1%. Additionally, the studied complex **8b/TNF** exhibited both electron and hole charge carrier mobility of value  $1.78 \times 10^{-3} \text{ cm}^2 \text{ V}^{-1} \text{ s}^{-1}$  and  $1.25 \times 10^{-3} \text{ cm}^2 \text{ V}^{-1} \text{ s}^{-1}$  which revealed its ambipolar nature. The donor-acceptor molecular interactions among discogens (electron donor) and TNF (electron acceptor) stabilise the mesophase and contribute towards the ambipolar nature of the resulting complexes.

### 3.1.2 Objectives

To date, there are only three reports based on multialkynylbenzene and TP non-symmetric oligomers which were reported by our group.<sup>1-3</sup> In one report, we have synthesized TP-PA dimer connected *via* flexible alkyl spacer in between rigid ester group<sup>1</sup> showing Col<sub>h</sub> phase at ambient temperature while in another *via* simple flexible alkyl spacer exhibits N<sub>D</sub> phase at room temperature.<sup>3</sup> In the third report, the triphenylene-multiynes-triphenylene triad connected *via* flexible alkyl spacers possess highly ordered columnar plastic and Col<sub>r</sub> mesophases.<sup>2</sup> As the nature of mesophases is highly dependent on the type of linkage unit. So it becomes very important to explore and exploit new discotic dimers with different linkages from a structure-



property relationship point of view. The formation of TP-PA dyad *via* triazole linkage was motivated by three goals. Firstly, the columnar assembly of TP can be stabilized in a better manner at room temperature *via* the introduction of the triazole ring along with the PA moiety.

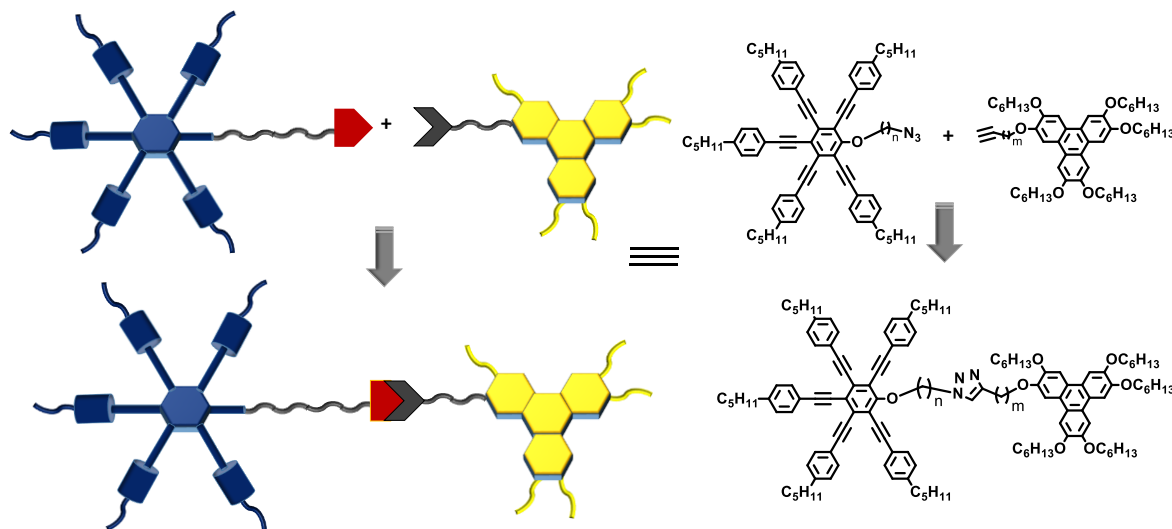


**Figure 3.1** Formation of the TP-PA non-symmetric discotic dimer.

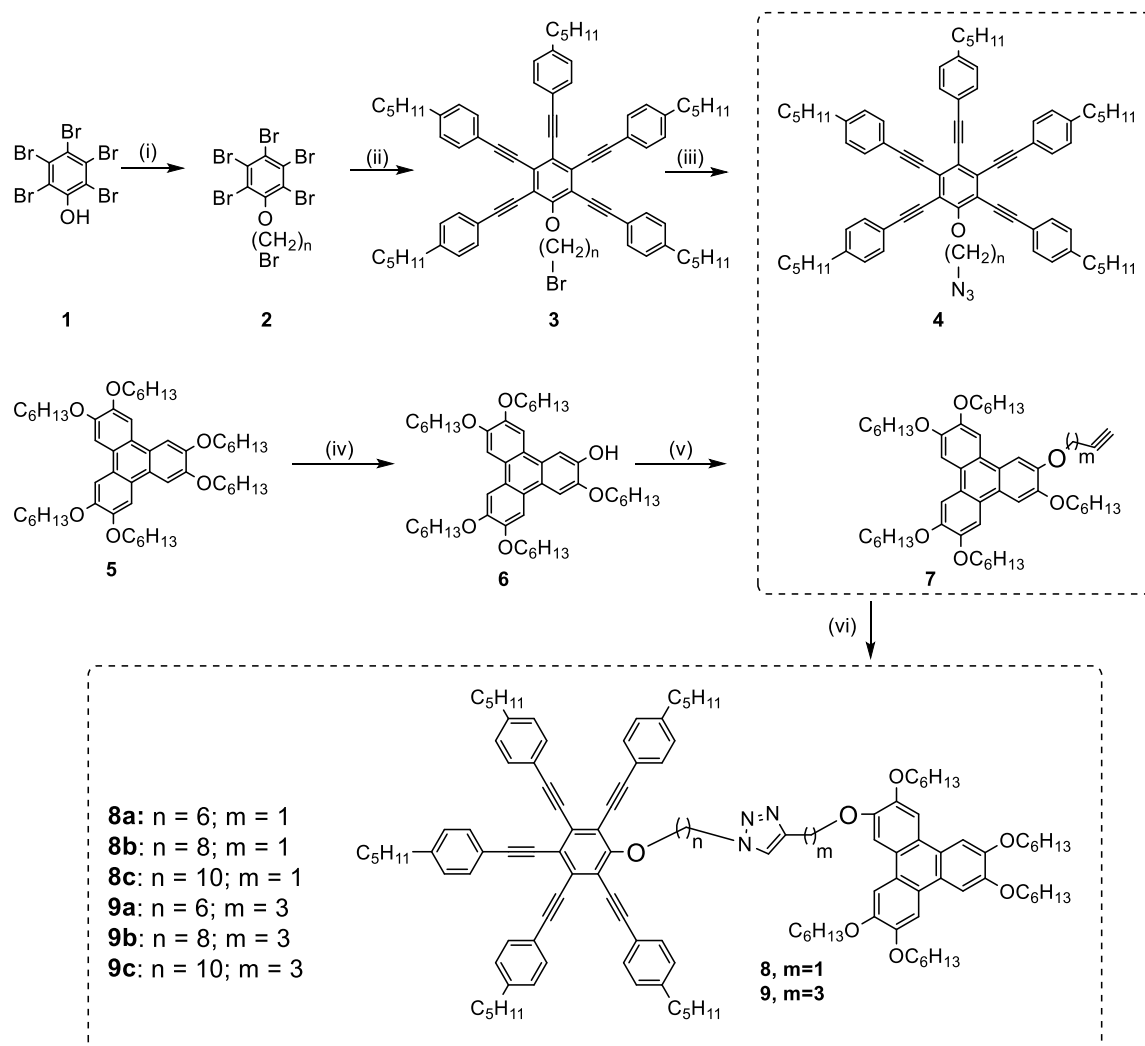
Secondly, in addition to their room temperature columnar behaviour, the blue light-emitting property can be induced to the resulting mesogen by the involvement of PA moiety and hence used as a potential emitter in fabricating blue OLED devices. Thirdly, in continuation to these, additional inter-disc interactions were introduced by doping the mesogens with disc-shaped electron acceptors for the realization of charge transfer complexes and the ambipolar characteristics of the complex have been revealed from the time of flight mobility experiments.

### 3.1.3 Results and discussions

#### 3.1.3.1 Synthesis and characterization

The synthesis of the target compounds is depicted in Scheme 3.1. The synthesis of non-symmetric dimers has been started from the Williamson alkylation of the pentabromophenol as reported in earlier reports.<sup>1-3</sup> Then the fivefold sonogshira coupling of compound **2** with 4-pentylphenylacetylene results in the formation of compound **3**. Afterward, the reaction of compound **3** with sodium azide ( $\text{NaN}_3$ ) in DMF leads to the replacement of bromo to azido group by the nucleophilic attack of azide anion. Moreover, the hexaalkoxytriphenylene **5**, monohydroxytriphenylene **6** and propargyl bromide and 5-chloropentayne substituted

triphenylenes **7**, were prepared as reported previously.<sup>1,30</sup> Then the CuI catalyzed click reaction between TP substituted terminal alkynes **7** and PA substituted aliphatic azides **4** leads to the formation of target compounds **8** and **9**. All the target compounds are characterized by NMR, FT-IR (Figure A1-A13, Appendix III, Page 211) and HRMS techniques.



**Scheme 3.1** Synthesis of the target compounds **8a-c** and **9a-c**, Reagents and conditions: (i)  $K_2CO_3$ , KI,  $Br(CH_2)_nBr$ , acetone, reflux, 12 hrs, Yield-80% (ii)  $Pd(PPh_3)_2Cl_2$ , 4-pentylphenylacetylene, CuI,  $Et_3N$ , 100 °C, Yield-80% (iii)  $NaN_3$ , DMF, RT, 12 hrs, Yield-99% (iv) Cat-B-Br,  $CH_2Cl_2$ , RT, 48 h, Yield-40%; (v) 3-bromo-1-propyne/5-chloro-1-pentyne,  $Cs_2CO_3$ , KI, butanone, 80 °C, 18 h, Yield-88%; (vi) CuI,  $NEt_3$ , toluene, RT, overnight, Yield for **8a**-60%, **8b**-64%, **8c**-58% and **9a**-68%, **9b**-71%, **9c**-66%.

### 3.1.3.2 Thermal behaviour of pure PA-TP oligomers (8a-c and 9a-c)

The thermal behaviour of all the compounds were examined by polarising optical microscopy (POM), differential scanning calorimetry (DSC), and wide-angle X-ray diffraction (WAXD) studies. All the compounds **8a-c**, **9a-c** in their pure form were showing the highly fluidic birefringent textures started appearing from the room temperature upon heating (Figure 3.2) while on cooling with the rate of 10 °C/min, the weak birefringence appears (Figure A15, Appendix III, Page 218) but only at lower temperatures (below 15 °C, Table 3.1). This was the case examined for all the compounds. The reappearance of textures at such lower temperatures on cooling can be possibly explained due to the inability of the mesogens to overcome its flexibility that the molecules have gained into their isotropic state and hence required lower temperature to reassemble. Similar behaviour was also supported by a DSC study for the pure series of compounds **8a-c** and **9a-c** (Figure A14, Appendix III, Page 217).

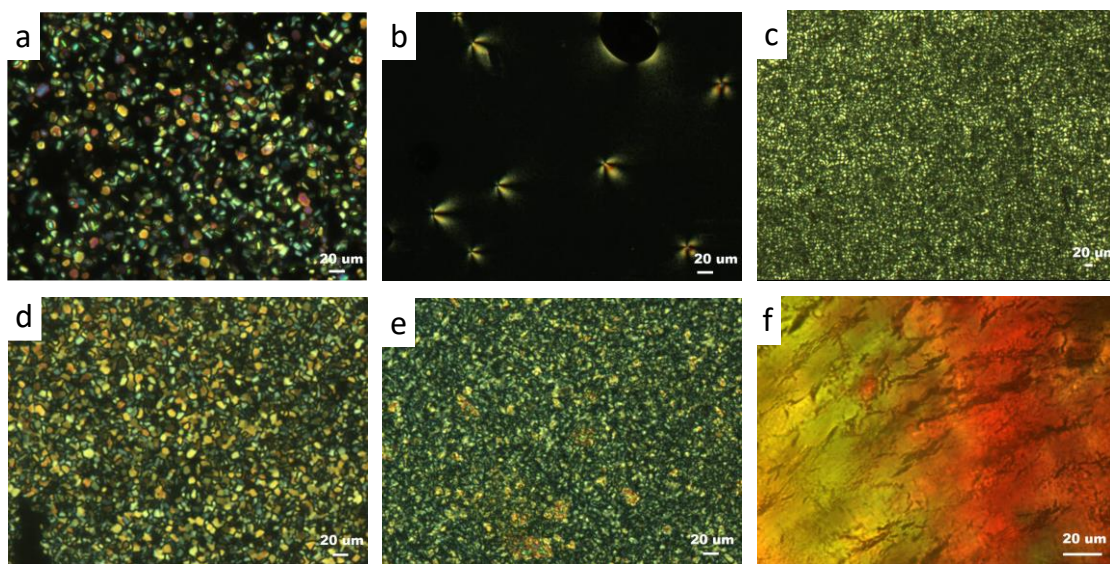


**Figure 3.2** Polarised optical micrographs (POM) of pure compounds: (a) **8a** at 35.2 °C; (b) **8b** at 40.2 °C; (c) **8c** at 33.4 °C; (d) **9a** at 37.1 °C; (e) **9b** at 45.3 °C; (f) **9c** at 57.4 °C, on heating with the rate of 5 °C/min (crossed polarizers).

For all the pure compounds, the DSC thermograms were recorded in the temperature range of -50 °C to the respective isotropic temperatures. In the heating cycle in the DSC thermogram, the compounds showed one peak corresponding to its mesophase to isotropic transition and on cooling cycle, weak peak associated with low enthalpy appears at lower temperatures (also

supported by weak birefringence under POM) and suggests some weakly ordered mesophase. The weak birefringence becomes brighter when the sample is kept at room temperature for one day. The transition temperatures of compounds **8a-c** and **9a-c** are listed in Table 3.1.

**Table 3.1** Phase transition temperatures of pure PA-TP oligomers (**8a-c** and **9a-c**).

Compound	Heating	Cooling
<b>8a</b>	Col <sub>r</sub> 46.1 (25.15) Iso	Iso 13.2 (0.04) N <sub>C</sub> <sup>d</sup>
<b>8b</b>	Col <sub>r</sub> 62.5 (27.32) Iso	Iso 11.5 (0.27) N <sub>C</sub>
<b>8c</b>	Sm 51.8 (12.51) Iso	Iso 11.0 (0.01) Sm <sup>d</sup>
<b>9a</b>	Col <sub>r</sub> 53.0 (33.07) Iso	Iso 12.8 (0.03) N <sub>C</sub>
<b>9b</b>	Col <sub>r</sub> 68.8 (36.52) Iso	Iso -3.0 <sup>c</sup> N <sub>C</sub> <sup>d</sup>
<b>9c</b>	Sm 76.5 (23.47) Iso	Iso -14.5 (4.85) Sm

<sup>a</sup>Phase transition behaviour observed on heating (°C) and enthalpy values in parentheses in kJ/mol; Abbreviation: Col<sub>r</sub> = centered Columnar rectangular; Sm = Disordered smectic; Iso = Isotropic. <sup>b</sup>Phase transition observed through DSC. <sup>c</sup>Phase transition through POM. <sup>d</sup>corresponding diffractograms are in Appendix III, Page 218.

### 3.1.3.3 X-Ray diffraction studies of pure PA-TP oligomers (**8a-c** and **9a-c**)

From the careful microscopic studies, it was observed that once the **8a-c** and **9a-c** compounds are heated to their isotropic temperatures, it took a time of one day to reassemble properly into columnar rectangular phase. Hence, the WAXD studies were carried out for the assembled samples. The X-ray diffractograms for the compounds **9a-b** (Figure 3.3a,b) and **8a-b** (Figure 3.4a,b) that differ from each other in the length of the alkyl spacer connecting the PA and TP moiety through triazole linkage were found to be similar. The diffractograms for **8a-b** and **9a-b** could be indexed on Col<sub>r</sub> lattice. However, for the compound **9c** ( $n = 10$ ,  $m = 1$ ) (Figure 3.3c) and **8c** ( $n = 10$ ,  $m = 3$ ) (Figure 3.4c) in which PA and TP components are connected through the longest alkyl spacers weakening the inter-columnar stacking exhibited the diffractograms similar for the N<sub>D</sub> phases. Although, from the microscopic investigation, no representative textures of N<sub>D</sub> were found (Figure 3.2c,f). Hence, later on, upon combining the microscopic and XRD information, the phase was best described to be a weak smectic phase(Sm). For all the hybrid PA-TP dimers **8a-c** and **9a-c**, the imbalanced molecular geometrical structure

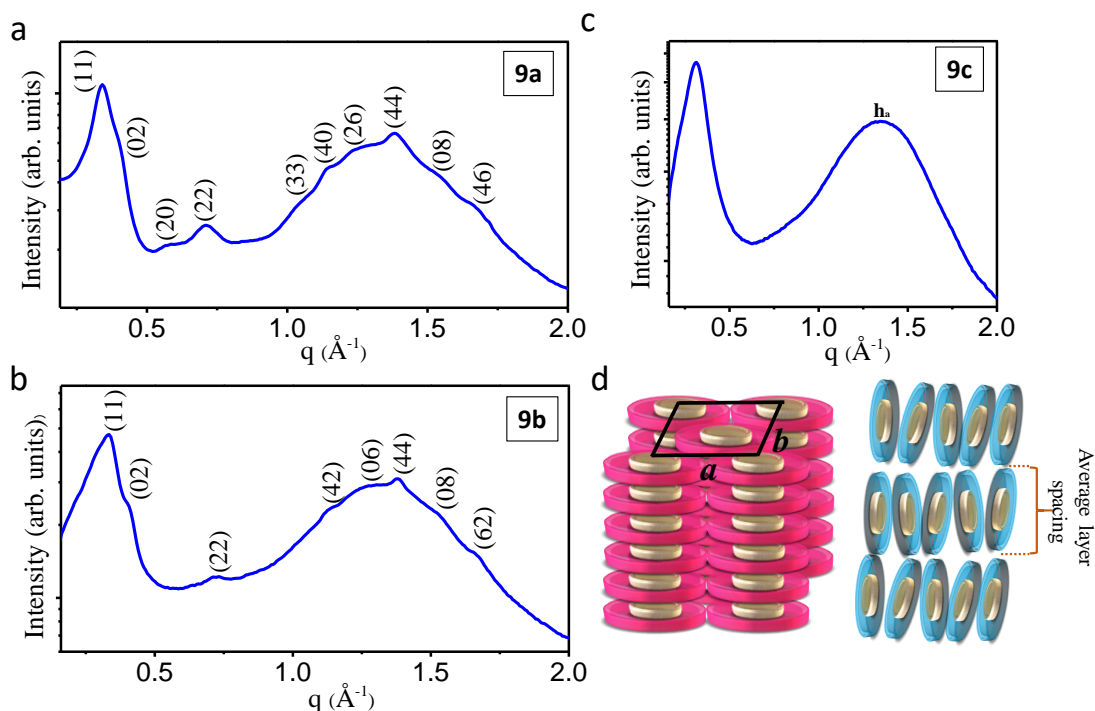


**Figure 3.3** X-Ray diffraction pattern for the pure compounds: (a) Col<sub>r</sub> phase at 25 °C for **9a**; (b) Col<sub>r</sub> phase at 25 °C for **9b**; (c) Sm phase for **9c**; (d) Proposed molecular stacking model for Col<sub>r</sub> phase in case of **9a** and **9b** and weak smectic phase in case of **9c**.

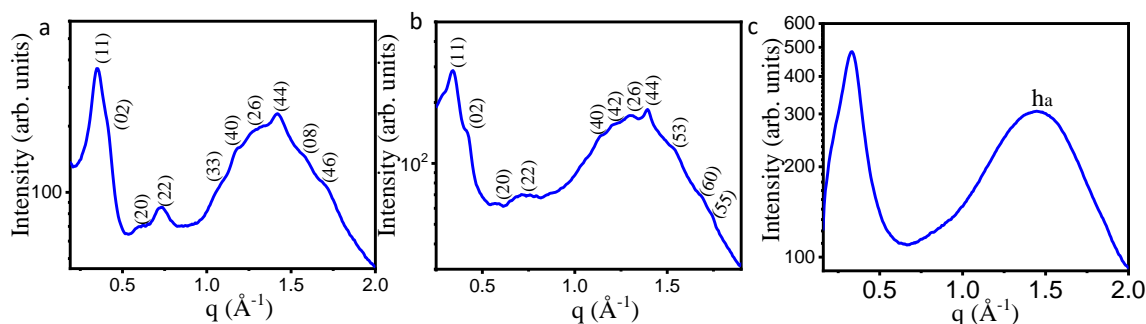


**Figure 3.4** X-Ray diffraction pattern for the pure compounds: (a) Col<sub>r</sub> phase at 25 °C for **8a**; (b) Col<sub>r</sub> phase at 25 °C for **8b**; (c) weak smectic phase at 25 °C for **8c**.

suppressed their tendency to form long-range ordered columnar structures as indicated by the characteristic WAXD patterns with no sharp reflection peaks. The XRD pattern for **9a** is shown in Figure 3.3a. It exhibited many narrow peaks in small as well as in the wide-angle region. The diffraction pattern could be indexed on a 2D centered rectangular lattice (Table 3.2). The lattice parameter was found to be  $a = 22.27 \text{ \AA}$  and  $b = 32.02 \text{ \AA}$ . The peak indexed as (46) is

also having a contribution from  $\pi$ - $\pi$  interaction between discs. Similarly, compound **9b** showed Col<sub>r</sub> phase with lattice parameters;  $a = 22.38$  Å and  $b = 30.62$  Å (Figure 3.3b, Table 3.2). However, compound **9c** exhibited one narrow peak in small-angle region with spacing 20.09 Å and one broad peak in the wide-angle regime with spacing 4.62 Å, indicating the occurrence of a weak smectic phase (Figure 3.3c, Table 3.2). As for the long spacer chain length, the disorder effect is getting pronounced which leads to the destabilization of the Col<sub>r</sub> phase and resulting in weak smectic phase. Lattice parameters and indexing for **9a-c** are listed in Table 3.2.

**Table 3.2** The Indices observed and calculated  $d$ -spacings and planes of the diffraction peaks observed for the pure compounds **8a-c** and **9a-c**.

Compound	Mesophase	Lattice constants (Å)	$d_{\text{obs}}^a$ (Å)	$d_{\text{cal}}^b$ (Å)	MI <sup>c</sup> (hk)
<b>8a</b>	Col <sub>r</sub> at 25 °C	$a = 21.87$ $b = 31.02$	17.88	17.87	11
			15.51	15.51	02
			10.65	10.94	20
			8.73	8.94	22
			5.95	5.96	33
			5.33	5.47	40
			4.83	4.67	26
			4.43	4.47	44
			3.97	3.88	08
			3.69	3.76	(46) <b>h<sub>c</sub></b>
<b>8b</b>	Col <sub>r</sub> at 25 °C	$a = 22.26$ $b = 30.72$	18.59	18.58	11
			15.31	15.31	02
			9.05	9.29	20
			5.57	5.46	22
			5.00	5.10	40
			4.55	4.64	42
			4.04	3.83	26
			4.50	4.51	44
			4.10	4.08	53
			3.71	3.71	60
<b>8c</b>	Sm at 25 °C		18.93	-	
			4.34	-	<b>h<sub>a</sub></b>
<b>9a</b>	Col <sub>r</sub> at 25 °C	$a = 22.27$	18.29	18.28	11

		$b = 32.02$	16.01	16.01	02
			11.07	11.13	20
			8.90	9.14	22
			6.12	6.09	33
			5.52	5.57	40
			4.92	4.81	26
			4.55	4.57	44
			4.05	4.00	08
			3.74	3.85	<b>h<sub>c</sub></b>
<b>9b</b>	Col <sub>r</sub> at 25 °C	$a = 22.38$	18.59	18.58	11
		$b = 30.62$	15.31	15.31	02
			9.05	9.29	22
			5.57	5.46	42
			5.00	5.10	06
			4.55	4.64	44
			4.04	3.83	08
			3.76	3.78	<b>h<sub>c</sub></b>
<b>9c</b>	Sm at 25 °C		20.09		
			4.62		<b>h<sub>a</sub></b>

<sup>a</sup> $d_{\text{obs}}$  : experimental  $d$ -spacing; <sup>b</sup> $d_{\text{cal}}$  : calculated  $d$ -spacing by using the relation:  $\frac{1}{d_{\text{cal}}^2} = \left[ \frac{h^2}{a^2} + \frac{k^2}{b^2} \right]$ ; with  $h+k = \text{even}$ ,  $h$  and  $k$  are the miller indices of the reflections corresponding to the columnar centered rectangular (Col<sub>r</sub>);  $a$  &  $b$  are the unit cell parameters,  $h_a$  &  $h_c$  spacing appear due to alkyl chain-chain and core-core correlation, respectively.

On careful microscopic and DSC investigations of series **8a-c** and **9a-c**, it has been found that all the compounds show Col<sub>r</sub> mesophase on heating while on cooling the mesophase reappears at lower temperatures which correspond to columnar nematic (N<sub>C</sub>) for **8a-b** & **9a-b** and smectic for **8c** & **9c** as shown in Figure A15, Appendix III, Page 218. The same Col<sub>r</sub> mesophase reappears for **8a-b** and **9a-b** after keeping the sample showing N<sub>C</sub> phase for one day.

In conclusion, **8a-b** and **9a-b** show Col<sub>r</sub> phase on heating while on cooling back from the isotropic phase, it self-assembles into N<sub>C</sub> at lower temperatures which turns into Col<sub>r</sub> on keeping the sample for one day at room temperature. For **8c** and **9c** smectic mesophase was found at heating and cooling as well.



### 3.1.3.4 Thermal behaviour and X-Ray diffraction studies of PA-TP oligomers/TNF complexes (8a-c/TNF and 9a-c/TNF)

The induction of stable Col<sub>h</sub> mesomorphism is driven through charge-transfer interactions of electron-rich PA and TP moiety with electron-acceptor TNF molecule. When the compounds were doped with the electron acceptor molecule TNF, it shows enantiotropic mesomorphic behaviour (Table 3.3). After mixing the compounds with TNF in different TNF/compound molar ratio of 1/2:1 and 1:1, the intermediate phase behaviour of Col<sub>r</sub> and Col<sub>h</sub> was observed but convert to Col<sub>h</sub> on increasing the TNF ratio to 2. We have described detailed microscopy (Figure 3.5) and XRD studies in case of 2:1 molar ratio of TNF:compound (Figure 3.6 and Figure 3.7).

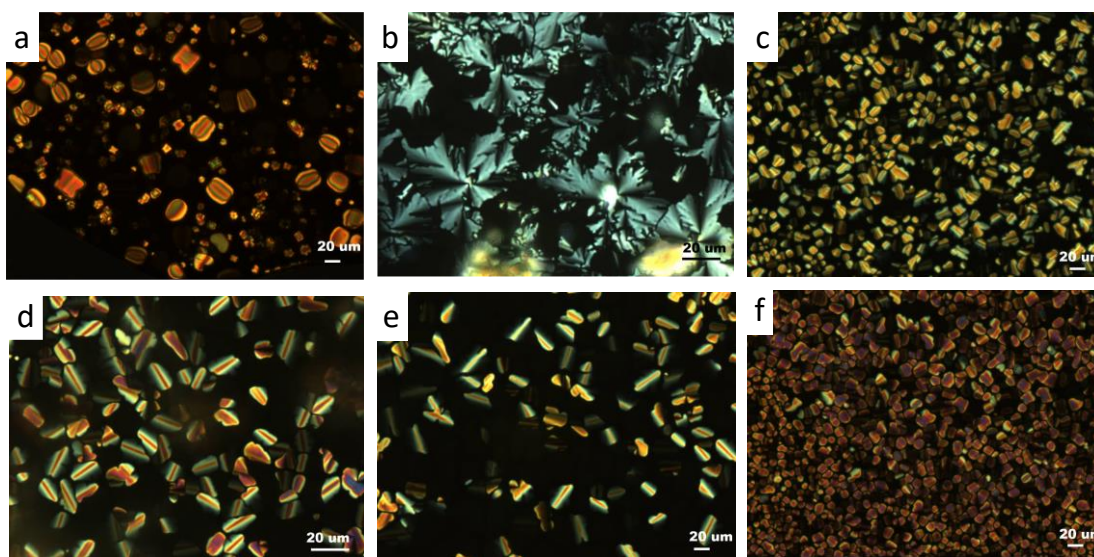


**Figure 3.5** POM images of 2:1 TNF: Compound ratio (a) **8a** at 57.7 °C; (b) **8b** at 93.2 °C; (c) **8c** at 62 °C; (d) **9a** at 89.9 °C; (e) **9b** at 111.1 °C; (f) **9c** at 52.2 °C observed on cooling from isotropic phase with the rate of 5 °C/min (crossed polarizers).

In the complex form, all the compounds **8a-c/TNF** and **9a-c/TNF** were showing characteristic columnar textures on heating as well as on cooling (Figure 3.5). The phase was described to be Col<sub>h</sub> on the basis of POM with the support of XRD technique. The XRD patterns for 2:1 TNF/**9a**, **9b** & **9c** are shown in Figure 3.6. In case of **9a/TNF**, the diffraction pattern showed four peaks in the small-angle region with *d*-spacing in ratios  $1:1/\sqrt{3}:1/\sqrt{4}:1/\sqrt{7}$



corresponding to the reflections from (10), (11), (20) and (21) planes of the Col<sub>h</sub> phase, respectively.

**Table 3.3** Phase transition temperatures of PA-TP/TNF (1:2) complexes.<sup>a,b</sup>

Compound	Heating	Cooling
<b>8a/TNF</b>	Col <sub>h</sub> 70.1 Iso	Iso 63.3 Col <sub>h</sub>
<b>8b/TNF</b>	Col <sub>h</sub> 132.8 Iso	Iso 106.3 Col <sub>h</sub>
<b>8c/TNF</b>	Col <sub>h</sub> 83.8 Iso	Iso 69.1 Col <sub>h</sub>
<b>9a/TNF</b>	Col <sub>h</sub> 108.9 Iso	Iso 100.3 Col <sub>h</sub>
<b>9b/TNF</b>	Col <sub>h</sub> 135.6 Iso	Iso 129.8 Col <sub>h</sub>
<b>9c/TNF</b>	Col <sub>h</sub> 73.2 Iso	Iso 68.5 Col <sub>h</sub>

<sup>a</sup>Phase transition temperature (°C) and transition enthalpies in kJmol<sup>-1</sup> (in parenthesis). Abbreviation: Col<sub>h</sub> = Columnar hexagonal; Iso = Isotropic. <sup>b</sup>Phase transition observed through POM & XRD.

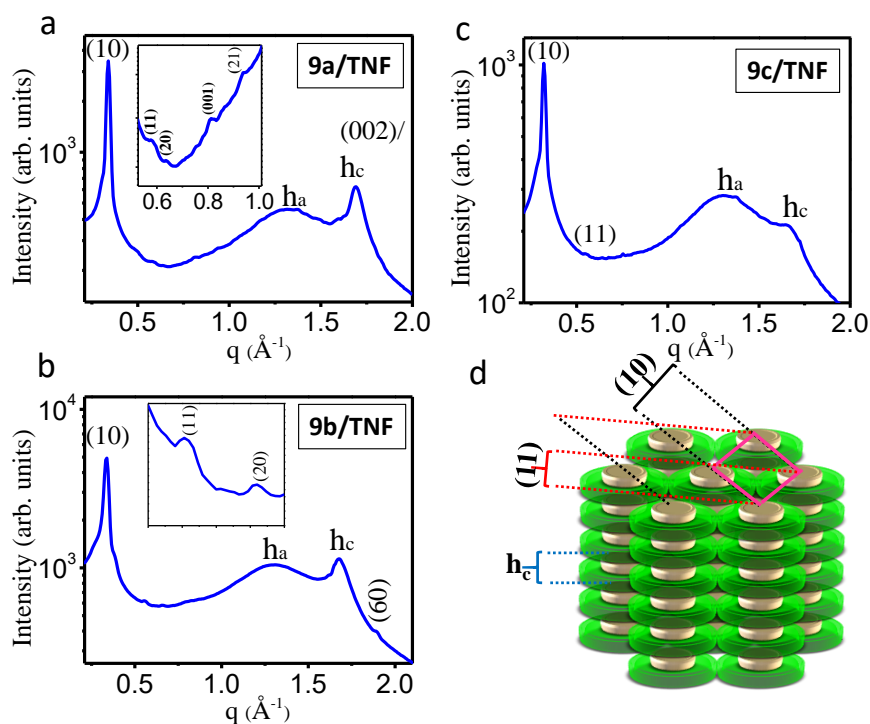


**Figure 3.6** X-Ray diffraction pattern for 2:1 ratio of TNF: compound complex: (a) Col<sub>h</sub> phase at 25 °C for **9a/TNF** complex; (b) Col<sub>h</sub> phase at 25 °C for **9b/TNF** complex; (c) Col<sub>h</sub> phase at 25 °C **9c/TNF** complex; (d) Proposed molecular stacking model for Col<sub>h</sub> phase.

In addition, there are two peaks in the wide-angle regime, namely,  $h_a$  and  $h_c$   $\{(002)\}$  along with (001) peak of the small-angle region. The wide-angle  $h_a$  peak attributes the correlation mainly due to the molten chains whereas  $h_c$  peak is indicative of the  $\pi$ - $\pi$  interaction of the discs in the column. The XRD pattern for complex **9b**/TNF and **9c**/TNF exhibited (10), (11), (20) and (10), (11) peaks, corresponding to  $Col_h$  phase, respectively. Similarly, the complexes **8a-c**/TNF also arranges in  $Col_h$  manner (Figure 3.7, Table 3.4). Variation of lattice parameter for pure compounds **8a-c** (Figure 3.8c), **9a-c** (Figure 3.8a) and their corresponding 2:1 TNF complexes (Figure 3.8d and Figure 3.8b) are shown in Figure 3.8.

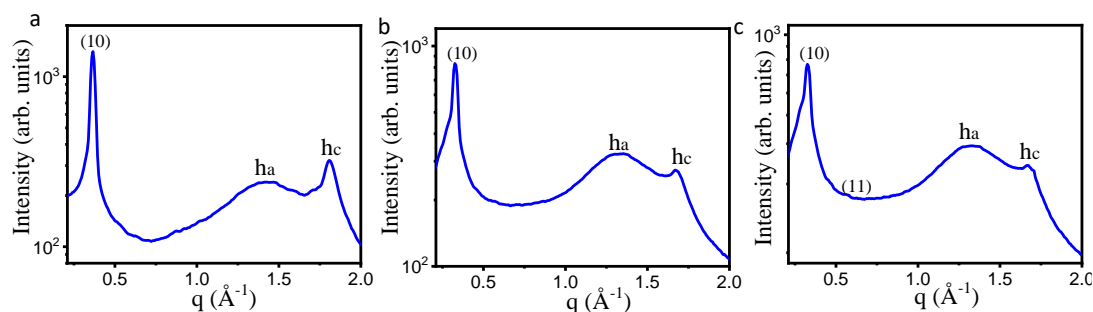


**Figure 3.7** X-Ray diffraction pattern for 2:1 ratio of TNF: compound complex: (a)  $Col_h$  phase at 25 °C for **8a**/TNF complex; (b)  $Col_h$  phase at 25 °C for **8b**/TNF complex; (c)  $Col_h$  phase at 25 °C **8c**/TNF complex.

In order to have a better understanding of the  $Col_h$  and  $Col_r$  phase, the compounds were additionally investigated by GIWAXS/GISAXS on aligned films. All the experiments were carried out on an ITO-coated glass substrate. The thin films were prepared by shearing the gummy sample in one direction at room temperature. The morphological observation of the thin films was observed under POM showing uniformly oriented films along one direction (Figure 3.9b,c). The aligned patterns were obtained by exposing the X-ray incident beam perpendicular to the mechanical shearing direction (Figure 3.9a).

Firstly, the GIWAXS of the blank substrate was recorded to subtract the background peaks (Figure 3.9d). The partially aligned pattern of the compound **9a** in  $Col_r$  phase was obtained (Figure 3.9e). In the partly aligned pattern for compound **9a** in  $Col_r$  phase, the intensity maximum in small-angle regime is along the shearing direction as shown in Figure 3.9e. Significantly, the GIWAXS pattern also shows aligned peaks and the pattern is well matching with the un-oriented pattern.

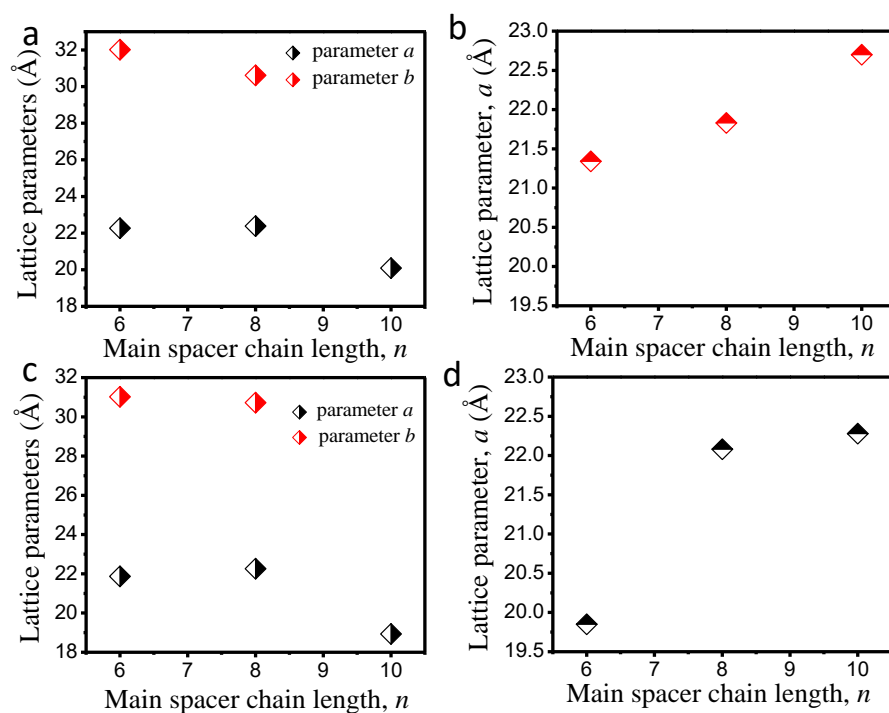


**Figure 3.8** Variation of lattice parameter for (a) pure compounds **9a**, **9b** and **9c** and (c) **8a**, **8b** and **8c**, 2:1 TNF/compound complex: (b) **9a**/TNF, **9b**/TNF and **9c**/TNF and (d) **9a**/TNF, **9b**/TNF and **9c**/TNF.

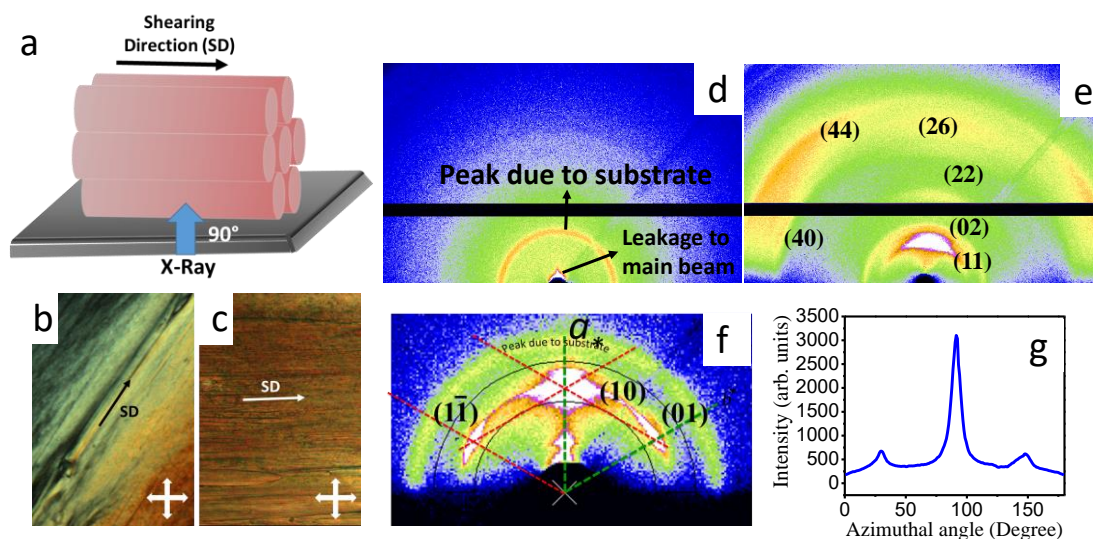


**Figure 3.9** (a) Schematic showing the X-ray incident beam was parallel to the film normal direction and mechanical shearing direction; (b & c) POM morphological observation of thin films used in GIWAXS experiments for **9a** and **9a**/TNF complex, respectively, sheared at room temperature; (d) GIWAXS of blank ITO-coated glass substrate; (e) Aligned GIWAXS

pattern for **9a** in Col<sub>r</sub> phase; (f) GISAXS pattern for **9a/TNF** complex in Col<sub>h</sub> phase; (g) azimuthal profiles corresponding to the Col<sub>h</sub> GIWAXS pattern shown in “f” recorded along a circle going through the scattering maximum.

On the other hand, the aligned pattern of the complex **9a/TNF** in Col<sub>h</sub> phase showed strong Bragg peaks represented by three lattice points in the annular region between 0° to 180° corresponding to (10), (01) and (1 $\bar{1}$ ) planes of the hexagonal (Col<sub>h</sub>) lattice (Figure 3.9f). The columnar LC phase has a planar orientation as indicated by intense meridional reflections with the high in-plane alignment of the columns (normal to *z*) but random orientation in the *x,y* plane.<sup>51</sup> Moreover, the azimuthal plot (Figure 3.9g) showed three peaks at 30°, 90° and 150°, respectively, further confirming the occurrence of Col<sub>h</sub> phase. The modeling of the corresponding mesophases shown by the pure compounds as well as the complexes is shown in Figure 3.10.

**Table 3.4** The Indices observed and calculated *d*-spacings and planes of the diffraction peaks for the columnar hexagonal (Col<sub>h</sub>) phase observed for 2:1 TNF/compound complex for series of compounds **8** and **9**.

Compound	Mesophase	Lattice constants (Å)	<i>d</i> <sub>obs</sub> <sup>a</sup> (Å)	<i>d</i> <sub>cal</sub> <sup>b</sup> (Å)	MI <sup>c</sup> ( <i>hk</i> )
<b>8a/TNF</b>	Col <sub>h</sub> at 25 °C	<i>a</i> = 19.85	17.19	17.19	10
			4.42		<b>h<sub>a</sub></b>
			3.48		<b>h<sub>c</sub></b>
<b>8b/TNF</b>	Col <sub>h</sub> at 25 °C	<i>a</i> = 22.08	19.12	19.12	10
			4.74		<b>h<sub>a</sub></b>
			3.74		<b>h<sub>c</sub></b>
<b>8c/TNF</b>	Col <sub>h</sub> at 25 °C	<i>a</i> = 22.28	19.30	19.66	10
			11.10		11
			4.74		<b>h<sub>a</sub></b>
			3.73		<b>h<sub>c</sub></b>
<b>9a/TNF</b>	Col <sub>h</sub> at 25 °C	<i>a</i> = 21.34 <i>c</i> = 7.50	18.48	18.48	10
			10.63	10.67	11
			9.63	9.24	20
			7.65	7.50	001
			6.73	6.98	21
			4.72	-	<b>h<sub>a</sub></b>
			3.75	3.75	<b>h<sub>c</sub></b> (002)
<b>9b/TNF</b>	Col <sub>h</sub> at 25 °C	<i>a</i> = 21.83	18.96	19.08	10

			11.20	11.02	11
			9.54	9.54	20
			4.84		<b>h<sub>a</sub></b>
			3.74		<b>h<sub>c</sub></b>
			3.32	3.18	60
<b>9c/TNF</b>	Col <sub>h</sub> at 25 °C	<i>a</i> = 22.70	19.64	19.66	10
			11.39	11.35	11
			4.78		<b>h<sub>a</sub></b>
			3.77		<b>h<sub>c</sub></b>

<sup>a</sup>*d*<sub>obs</sub> : experimental *d*-spacing; <sup>b</sup>*d*<sub>cal</sub> : calculated *d*-spacing by using the relation:  $\frac{1}{d_{cal}^2} = \left[ \frac{4}{3} \left( \frac{h^2 + hk + k^2}{a^2} \right) + \frac{l^2}{c^2} \right]$ ; *h*, *k*, *l* are the indices of the reflections corresponding to the columnar hexagonal (Col<sub>h</sub>) phase; *a* & *c* are the unit cell parameters, *h<sub>a</sub>* & *h<sub>c</sub>* spacing appear due to alkyl chain-chain and core-core correlation, respectively.

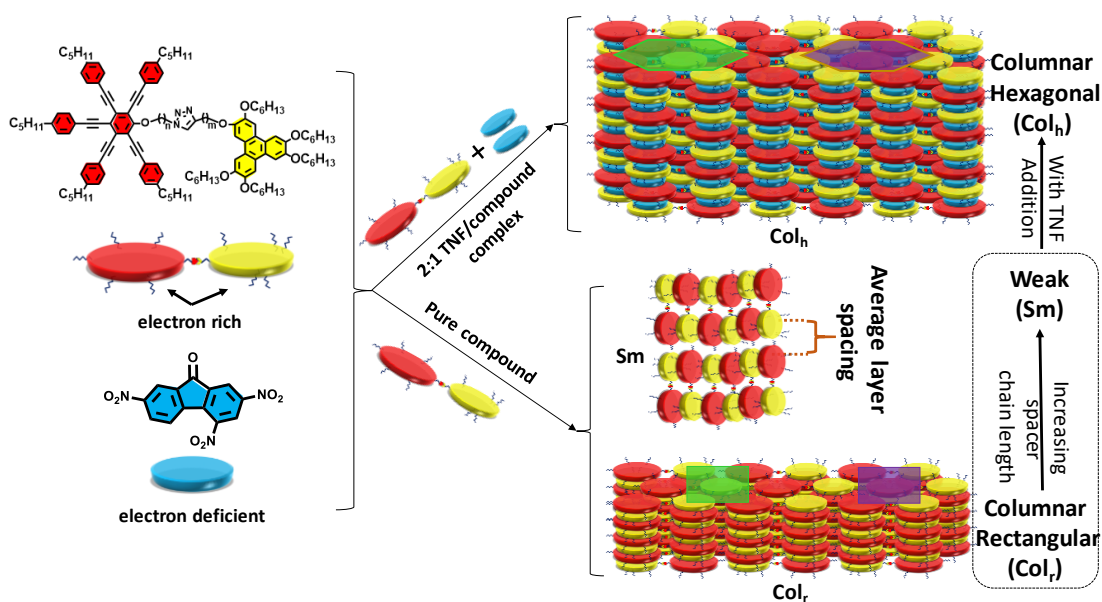


**Figure 3.10** Schematic showing the self-assembly behaviour of the non-symmetric oligomer in pure state and in 2:1 TNF/compound complex.

The arrangement of molecules in their respective phases has been deduced by reconstructing the electron density map (EDM) by using the information of their respective peak indexes and intensities. The EDM for the pure compound **9a** in the Col<sub>r</sub> phase and for complex **9a/TNF** in the Col<sub>h</sub> phase are shown in Figure 3.11a and Figure 3.11b, respectively.

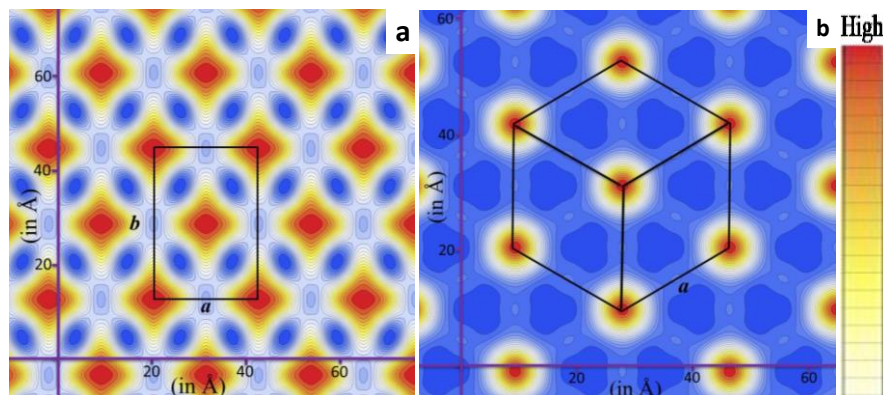


**Figure 3.11** Electron density maps of (a) **9a** in centered  $\text{Col}_r$  phase; (b) complex **9a/TNF** in  $\text{Col}_h$  phase. Red color represents the high electron density region and deep blue is the lowest. Rectangle in “Fig. a” represents unit cell of  $\text{Col}_r$  phase with lattice parameter  $a$  &  $b$  and hexagon in “Fig. b” displayed conventional unit cell of  $\text{Col}_h$  phase with a lattice parameter,  $a$ .

### 3.1.3.5 Photophysical, electrochemical and theoretical studies

The photophysical studies for **8a-c** and **9a-c** were done in solution as well as in thin-film state. The UV/Vis absorption and fluorescence spectroscopic data of newly synthesized TP-PA dyads in dilute chloroform solution at room temperature are presented in Table 3.5. And the normalized UV/Vis and emission spectra in  $\text{CHCl}_3$  for compounds **8a-c** and **9a-c** is shown in Figure 3.12a. All the compounds showed similar absorption and emission behaviour as they only differ in the length of flexible alkyl spacer which usually has no effect on the photophysical properties until or unless it does not affect the assembly of the molecules. All the compounds were showing a blue tinge in dilute chloroform solution even under daylight and proper blue light emission under UV light (Figure 3.12d). Absorption spectra of compound **8a** displayed absorption maxima mainly centred at 280 and 337 nm with four shoulder peaks at 261, 270, 381 & 420 nm. The photophysical studies were also performed in neat form for all the compounds **8a-c** and **9a-c** (Figure 3.12b). In solid-state absorption spectrum, the number and position of the peaks were observed at around the same wavelength as that of in solution state. While the number of emission peaks varies for all the derivatives. In addition, in comparison to the solution state, the absorption bands in the solid state are broad and emission peaks become broader and red-shifted because of aggregation. In the neat film, the compounds



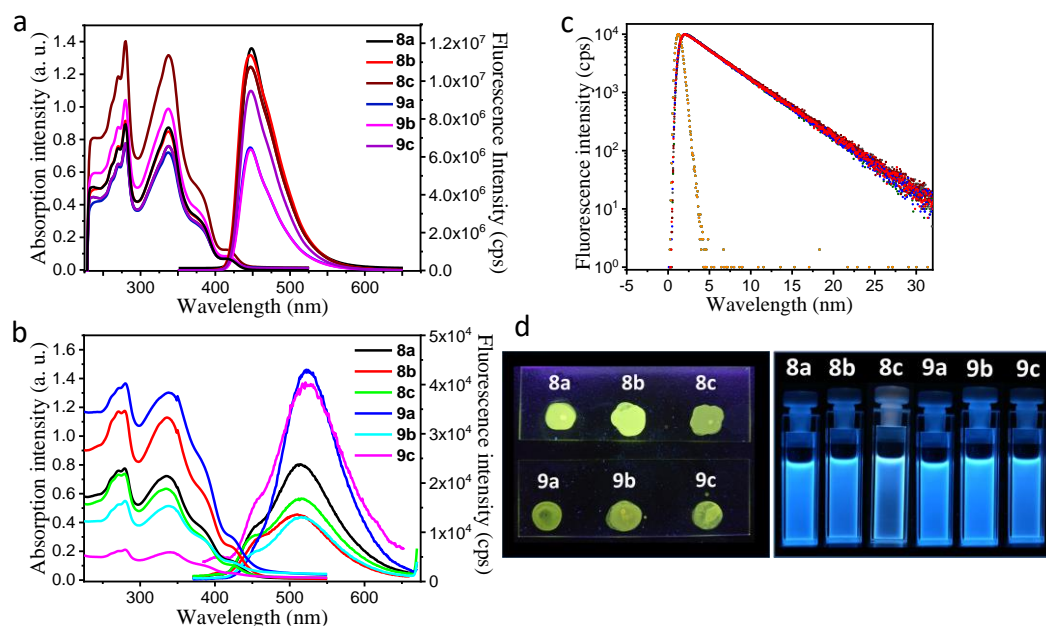


**Figure 3.12** (a) Absorption (left) and Emission (right) spectra of compounds **8a-c** and **9a-c** in HPLC chloroform solution; (b) Absorption (left) and Emission (right) spectra of compounds **8a-c** and **9a-c** in thin-film; (c) Fluorescence decay curve (log-linear plot) of compound **8a** in chloroform solution fitted by the bi-exponential fitting; (d) Photomicrographs showing green (preparing by drop cast) and blue light emission in thin-film and solution (DCM) state, respectively.

were showing green fluorescence (Figure 3.12d). The absorption and emission peaks for all the TP-PA oligomers in solution and thin film state are listed in Table 3.5. To obtain further insight into the fluorescence behaviour of the newly synthesized series, fluorescence decay and lifetime measurement studies were carried out in chloroform solutions using a time-correlated single-photon counting technique. The excitation wavelength is 337 nm corresponding to the absorption maxima of the compounds and a band-pass filter at 447 nm is used to measure the fluorescence decay curves shown in Figure 3.12c and Figure A17 (Appendix III, Page 219) for compounds **8a-c** and **9a-c**. The decay curves (red colored) were fitted with the instrument response function (IRF) (black colored). The fitted (blue) curve is overlapping with the decay curve (red). In all the cases, the curves were better fitted by using a bi-exponential function. This implies two radiative decay processes occurring from the excited states and giving two-lifetime decay values  $\tau_1$  and  $\tau_2$ . The average lifetime varied from 4.16-4.28 ns for all the compounds (Table 3.5). Besides this, quantum yield measurements [Appendix III, Figure A16

(Page 219), Table A1 (Page 218)] were done in THF by taking quinine sulfate as a standard as its absorption maxima ( $\lambda_{\text{max}}$ ) centred at around the same wavelength ( $\lambda_{\text{max}} = 340 \text{ nm}$ ) as that of our target compounds ( $\lambda_{\text{max}} = 337 \text{ nm}$ ).

**Table 3.5** Photophysical properties of the PA-TP oligomers.

C	A <sub>solution</sub> <sup>a</sup> Peaks (nm)	E <sub>solution</sub> <sup>a,c</sup> Peaks (nm)	A <sub>solid</sub> Peaks (nm)	E <sub>solid</sub> <sup>c</sup> Peaks (nm)	T <sub>1</sub> (a <sub>1</sub> ) (ns)	T <sub>2</sub> (a <sub>2</sub> ) (ns)	T <sub>av</sub> <sup>d</sup> (ns)
<b>8a</b>	261, 270, 280 337, <sup>b</sup> 382, 419	446, 470	261, 270, 280 335, <sup>b</sup> 384, 425	454, 513	2.40 (0.16)	4.41 (0.84)	4.10
<b>8b</b>	261, 270, 280 337, <sup>b</sup> 382, 420	446, 470	262, 271, 279 336, <sup>b</sup> 384, 423	401, 461, 510	2.20 (0.10)	4.52 (0.90)	4.28
<b>8c</b>	261, 270, 280 337, <sup>b</sup> 382, 419	446, 470	263, 270, 279 335, <sup>b</sup> 381, 423	402, 452, 515	1.02 (0.10)	4.52 (0.90)	4.17
<b>9a</b>	261, 270, 280 337, <sup>b</sup> 382, 419	446, 470	262, 270, 280 338, <sup>b</sup> 381, 422	523	2.16 (0.10)	4.45 (0.89)	4.23
<b>9b</b>	261, 270, 280 337, <sup>b</sup> 382, 419	446, 470	262, 270, 280 338, <sup>b</sup> 381, 422	455, 515	2.12 (0.11)	4.41 (0.89)	4.16
<b>9c</b>	261, 270, 280 337, <sup>b</sup> 381, 420	446, 471	261, 268, 280 340, <sup>b</sup> 384, 425	453, 515	2.19 (0.11)	4.48 (0.89)	4.23

<sup>a</sup>in micromolar chloroform solution. <sup>b</sup> $\lambda_{\text{max}}$ . <sup>c</sup>obtained after exciting at their corresponding  $\lambda_{\text{max}}$ . A<sub>solution</sub>: Absorbance in solution state, E<sub>solution</sub>: Emission in solution state. A<sub>solid</sub>: Absorbance in thin-film, E<sub>solid</sub>: Emission in thin-film. <sup>d</sup>T<sub>av</sub> = average lifetime. <sup>e</sup> $\phi_F$  = Fluorescence quantum yield. Abbreviation: C- compound.

The quantum yield values lied in the range of 0.35-0.47 for the series of compounds. The electronic energy levels of the chosen TP-PA oligomers **8a** and **9a** used to fabricate OLED devices were estimated by using the cyclic voltammetry (CV) technique. The CV experiments were carried out by using millimolar solutions of **8a** and **9a** in oxygen-free dichloromethane (Figure 3.13a,b). 0.1 M solution of TBAH was used as a supporting electrolyte. The experimental setup conditions for CV experiments and electrochemical data for **8a** and **9a** are listed in Table 3.6. Both the derivatives show reversible oxidation and reduction potential. The HOMO and LUMO energy levels for **8a** and **9a** are found to be -5.36 and -5.43 eV, while the LUMO energy levels are -3.68 and -3.52 eV, respectively (Table 3.6). The electrochemical bandgap was calculated as,  $\Delta E_{g, CV} = E_{\text{LUMO}} - E_{\text{HOMO}}$  and found to be 1.69 and 1.90 eV for **8a**



and **9a**, respectively. The optical bandgap ( $\Delta E_{UV}$ ) was obtained by using the red edge absorption wavelength of the UV-vis spectrum and is estimated to be 2.72 eV for both **8a** and **9a** oligomers. The electrochemical bandgaps ( $\Delta E_{g,CV}$ ) were found to be lesser than its optical bandgap ( $\Delta E_{UV}$ ).

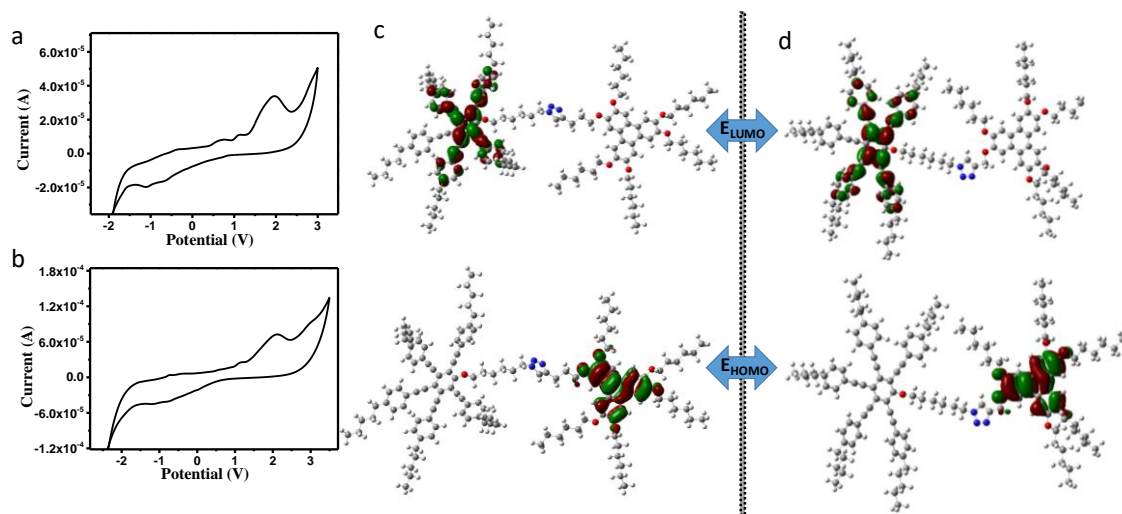


**Figure 3.13** (a & b) Cyclic voltammograms, (c & d) HOMO and LUMO frontier molecular orbitals for **8a** and **9a**, respectively.

**Table 3.6** Electrochemical data<sup>a</sup>

C	$E_{1red}$ (V) <sup>b</sup>	$E_{1oxd}$ (V) <sup>c</sup>	$E_{LUMO}$ (eV) <sup>d</sup>	$E_{HOMO}$ (eV) <sup>e</sup>	$\Delta E_{CV}$ (eV) <sup>f</sup>	$\Delta E_{UV}$ <sup>g</sup> (eV)
<b>8a</b>	-0.61	+1.08	-3.68	-5.36	1.69	2.72
<b>9a</b>	-0.77	+1.14	-3.52	-5.43	1.90	2.72

<sup>a</sup>recorded in micromolar DCM solution. Experimental conditions: Ag/AgNO<sub>3</sub> as a reference electrode, glassy carbon working electrode, platinum wire counter electrode, and TBAH (0.1M) as a supporting electrolyte. <sup>b</sup>onset reduction potential. <sup>c</sup>onset oxidation potential. <sup>d</sup>Estimated by using the formula:  $E_{LUMO} = -[4.8 - E_{1/2,Fe/Fe^+} + E_{1red}]$  eV. <sup>e</sup>Estimated by using the formula:  $E_{HOMO} = -[4.8 - E_{1/2,Fe/Fe^+} + E_{1oxd}]$  eV, where  $E_{1/2,Fe/Fe^+} = 0.55$  V. <sup>f</sup>Calculated from the formula:  $\Delta E_{g,CV} = E_{LUMO} - E_{HOMO}$ . <sup>g</sup>Calculated from the formula:  $\Delta E_{UV} = 1240/\lambda_{onset}$ . Abbreviation: C- Compound.

Further, the energy minimized structures for chosen compounds **8a** and **9a** were obtained by using Density functional theory (DFT) calculations using Gaussian 09 software with B3LYP/6-31G (d,p). The frontier molecular orbitals of **8a** and **9a** oligomers are shown in

Figure 3.13c,d and HOMO of the compound is primarily located on the electron-rich TP while the LUMO is distributed on the PA moiety.

### 3.1.3.6 Electroluminescent properties

To fully evaluate the electroluminescence (EL) characteristics of the newly synthesized deep-blue emitters **8a** and **9a** initially non-doped devices with structure ITO/PEDOT:PSS/Emitter/TPBi/LiF/Al are fabricated by employing the dyes as emitting layer. Since the non-doped devices exhibited unsatisfactory EL performance due to the poor thin film stability and formation of aggregates in solid-state, we fabricated doped devices with the configuration ITO/PEDOT:PSS/Host:Emitter/TPBi/LiF/Al, to mitigate aggregation caused emission quenching and thereby improve the EL performances.

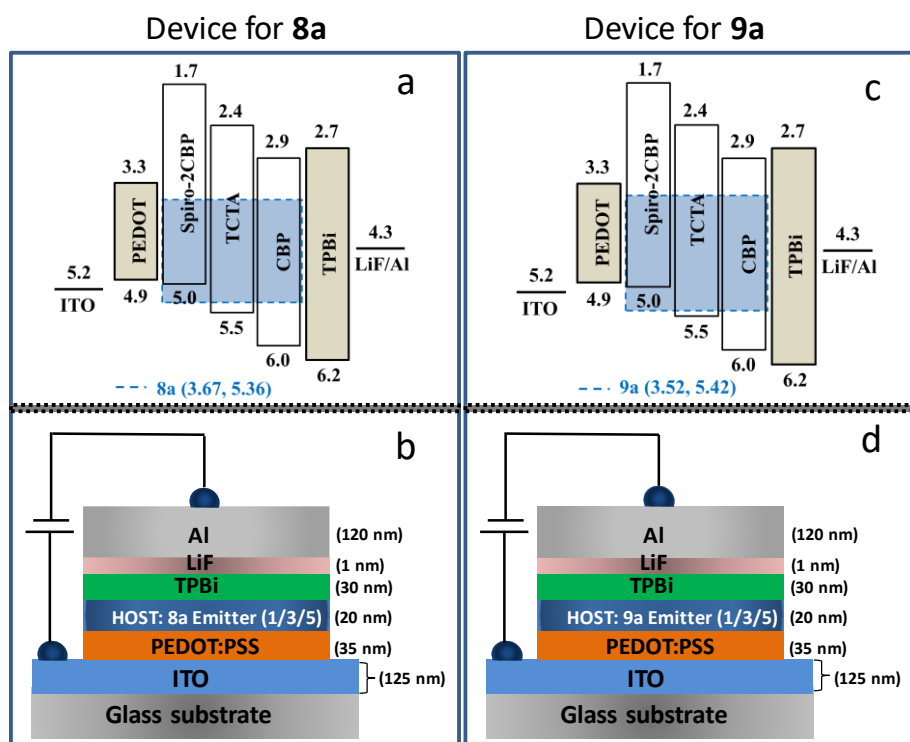


**Figure 3.14** Schematic diagram of the energy levels of the solution-processed deep-blue OLED devices composed of three different hosts Spiro-2CBP, TCTA and CBP: (a & b) Device for **8a**, (b & d) Device for **9a**.

Figure 3.14 illustrates the schematic energy-level diagram of the solution-processed deep-blue OLED devices composed of three different hosts Spiro-2CBP, TCTA and CBP. The voltage-

luminance, voltage-current density, luminance-power efficiency, and EL spectra plots are presented in Figure 3.15 and Figure 3.16, and the EL characteristics are summarized in Table 3.7. For the doped devices, first, the emitters are doped in the CBP host at different concentrations (1, 3 and 5 wt%). CBP owes to its favourable alignment of energy levels with those of the emitters, as this could facilitate host-to-guest energy transfer and the uniform dispersion of the dopant into the host. Doped devices illustrate the restoration of EL spectrum to narrow and blue-shifted photoluminescence spectrum which indicates the suppression of aggregates (Figure 3.15d and Figure 3.16d). The fabricated devices of compound **8a** (1 wt%) and **9a** (1 and 3 wt%), possessed a small hump around 392 nm. It might be because of the CBP host emission and indicates the incomplete photoexcitation energy transfer from CBP host to dopant. This is evident from the decreasing intensity of hump at higher dopant concentrations (5 wt%) as the number of emitting molecules to confine excitons from the CBP host increased. The doped devices exhibited high luminance when compared to non-doped devices of analogous dyes (Table 3.7). It might be due to the effective capture of excitons

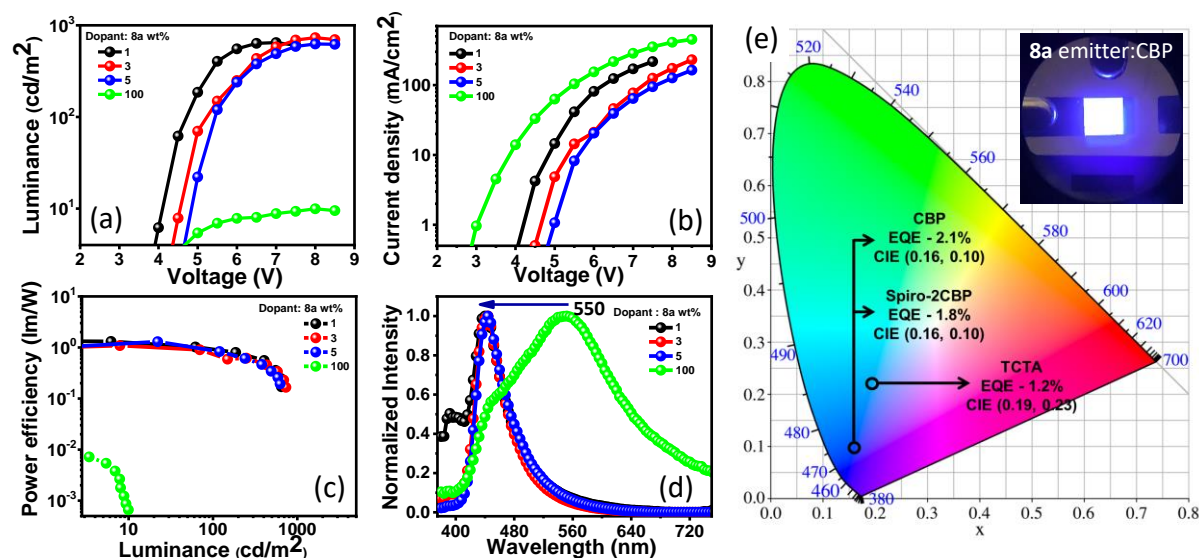


**Figure 3.15** Dopant (Emitter **8a**) concentration effect on (a) luminance, (b) current density, (c) power efficiency and (d) electroluminescent (EL) spectra of the solution-processed deep-blue OLED devices using CBP host with 1, 3, and 5 wt% dopant concentrations. (e) CIE coordinates obtained for devices at 5 wt% dye concentration with CBP, Spiro-2CBP and TCTA host. Inset “e” shows the image of the fabricated device by using **8a** emitter doped (5 wt%) with CBP host.

formed in the CBP host by dopants *via* favourable energy transfer. A large current density was observed for compound **8a** based devices at low drive voltage when compared to the counter device. This may be associated with the imbalance in the charge transport and leakage of charges at the terminal electrodes. This could arise due to the facile injection of holes from PEDOT:PSS into the emitting layer and poor injection of electrons from TPBi to emitter. The doped devices exhibited high operating voltage ( $> 4.7$  V at  $100 \text{ cd m}^{-2}$ ) that may arise due to the poor blending of the emitter in CBP host which resulted in poor-film stability. Generally, the doped devices showed superior performance compared to the non-doped emitting devices. This clearly indicates the role of balanced charge transport at low dopant concentration and confinement of recombination well across the CBP layer.<sup>52-54</sup> The poor performance of non-doped and doped devices with low concentration may be attributed to the increased crystallinity which could affect the film integrity.

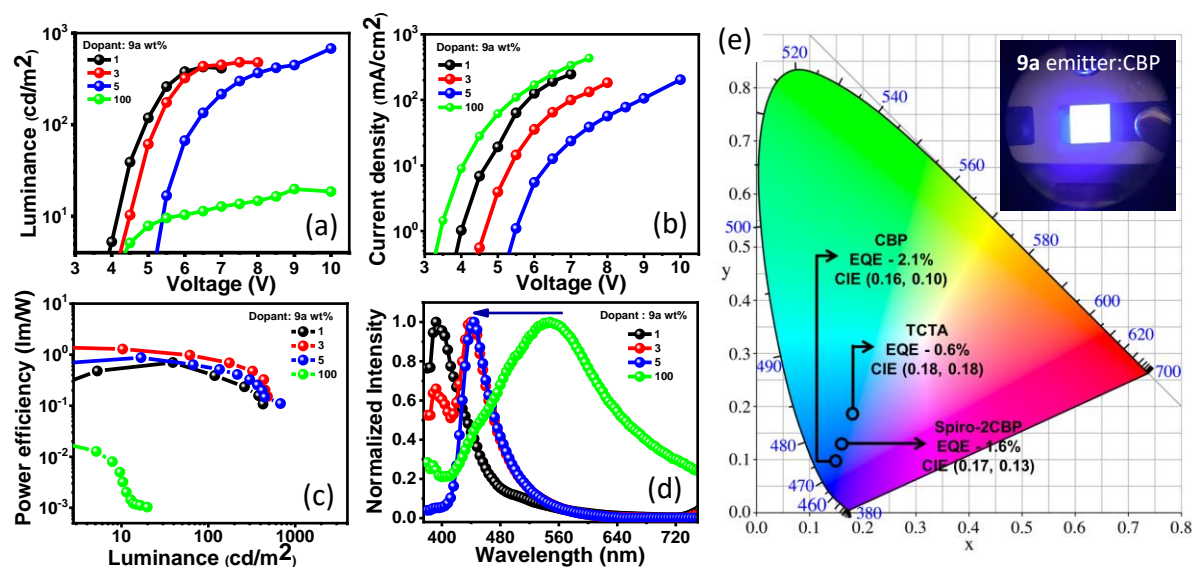


**Figure 3.16** Dopant (Emitter **9a**) concentration effect on (a) luminance, (b) current density, (c) power efficiency and (d) electroluminescent (EL) spectra of the solution-processed deep-blue OLED devices using CBP host with 1, 3, and 5 wt% dopant concentration. (e) CIE coordinates obtained for device at 3 wt% dye concentration with CBP, Spiro-2CBP and TCTA host. Inset of (e) shows the image of the fabricated device by using **9a** emitter doped (3 wt%) with CBP host.

The dopant concentration and host material increased as a result of an increasing number of emitting species. Furthermore, the EL performance of the emitters is optimized by employing

different host materials such as TCTA and Spiro-2CBP at their best dopant concentration (Table 3.7). Among the different hosts, the energy level of the CBP host is well aligned with the emitters for facile charge injection. As a result, the device containing the CBP host showed superior EL performance compared to the other devices containing different host material.

**Table 3.7** Effect of doping concentration on the operation voltage (OV), power efficiency (PE), current efficiency (CE), external quantum efficiency (EQE), CIE coordinates, and maximum luminance ( $L_{\max}$ ) of solution-processed deep-blue OLED devices with host CBP, TCTA and Spiro-2CBP.

	Host	Conc. (wt%)	OV (V) <sup>a</sup>	PE <sub>max</sub> /CE <sub>max</sub> /EQE <sub>max</sub> <sup>b</sup> (lm W <sup>-1</sup> /cd A <sup>-1</sup> /%)	PE <sub>100</sub> /CE <sub>100</sub> /EQE <sub>100</sub> <sup>c</sup> (lm W <sup>-1</sup> /cd A <sup>-1</sup> /%)	CIE <sup>d</sup>	L <sub>max</sub> (cd/m <sup>2</sup> )
<b>8a</b>	<b>CBP</b>	1	4.7	1.2/1.6/1.7	1.0/1.4/1.5	(0.17, 0.11)	648
		3	5.2	0.9/1.4/1.7	0.8/1.3/1.5	(0.16, 0.09)	733
		5	5.4	1.2/2.0/2.1	0.9/1.6/1.7	(0.16, 0.10)	625
		100	-	- / - / -	- / - / -	-/-	10
	<b>TCTA</b>	5	4.0	1.8/2.1/1.2	1.6/2.0/1.1	(0.19, 0.23)	1289
	<b>Spiro-2CBP</b>	5	5.1	1.3/1.7/1.8	0.9/1.4/1.5	(0.16, 0.10)	694
		1	4.9	0.7/1.0/2.1	0.5/0.7/1.5	(0.17, 0.09)	427
<b>9a</b>	<b>CBP</b>	3	5.2	1.2/1.8/2.1	0.9/1.4/1.9	(0.16, 0.10)	481
		5	6.1	0.9/1.6/1.7	0.6/1.2/1.3	(0.16, 0.10)	566
		100	-	- / - / -	- / - / -	-/-	19
	<b>TCTA</b>	3	5.2	0.2/0.7/0.6	0.2/0.7/0.6	(0.18, 0.18)	2414
	<b>Spiro-2CBP</b>	3	4.9	1.8/2.4/1.6	0.8/1.3/1.3	(0.17, 0.13)	750

<sup>a</sup>Operation voltage (the voltage at 100 cd/m<sup>2</sup>). <sup>b</sup>Power efficiency (PE), Current efficiency (CE) and EQE at maximum luminance ( $L_{\max}$ ), <sup>c</sup>Power efficiency (PE), Current efficiency (CE) and EQE at 100 cd/m<sup>2</sup>, <sup>d</sup>CIE coordinates at 100 cd/m<sup>2</sup>.

### 3.1.3.7 Charge Carrier Mobility for the complex

The introduced donor-acceptor interactions among discogen and TNF molecule in the complexes prompted us to measure their charge transport properties. The charge carrier

mobility measurement for the complex **8b/TNF** was carried out by using the time of flight (ToF) technique (Figure 3.17). To execute ToF measurement, the complex was filled in a commercially purchased homeotropic anchored ITO cell (from AWAT, Poland) of thickness 5  $\mu\text{m}$ . The sample was excited by a Nd:YAG pulsed laser having an excitation wavelength of 355 nm and 5 ns pulse width. The measurement was performed in the cooling cycle started from its isotropic temperature with a rate of 2  $^{\circ}\text{C}/\text{min}$ . The filling of the sample cell was conducted in  $\text{N}_2$  atmosphere in order to avoid the recombination of electrons with the space charges and/or oxygen molecules. To measure the ambipolar charge mobility, the bipolar voltage of  $\pm 10\text{V}$  was applied with the help of Keithley 6487. The induced charge displacement was observed *via* a transient photocurrent curve which was recorded by a digital oscilloscope (Agilent, DSO 1012A) connected to a voltage amplifier. The output transient photocurrent curve was used to calculate the ambipolar charge carrier mobility.

The investigated complex **8b/TNF** consists of both electron-rich and electron-deficient moieties; therefore ambipolar charge mobility was measured at an optimized voltage of  $\pm 10\text{V}$ . We obtained dispersive transient photocurrent curves under the application of applied bipolar

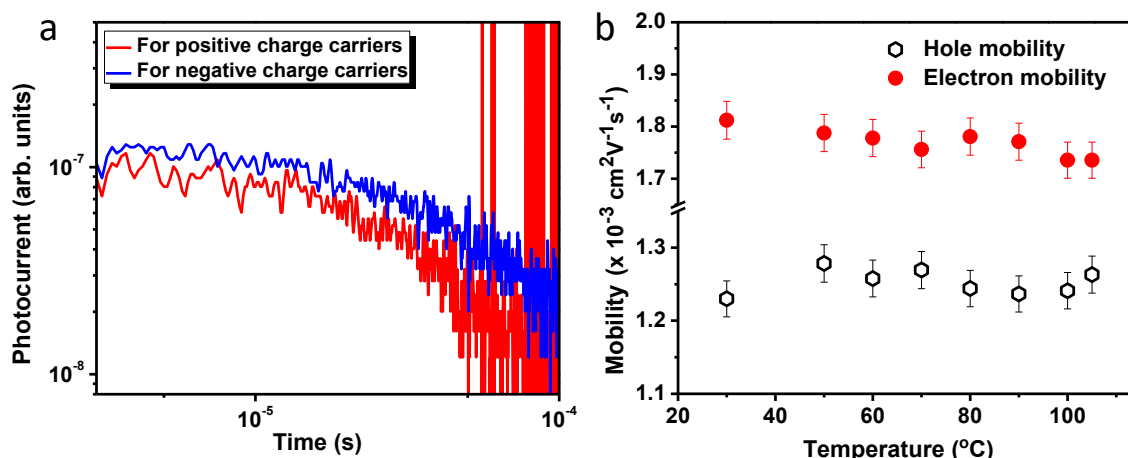


**Figure 3.17** (a) Ambipolar dispersive transient photocurrent curves of complex, recorded at  $\pm 10\text{V}$ , whereas (b) shows the electron and hole mobility curves as a function of temperature. Error bars represent the maximum error of  $\pm 2\%$  in the experimental data.

voltage that is attributed to the positive and negative charge carriers. The transit time ( $T_r$ ) of charge carriers was obtained by the photocurrent curves and the mobility ( $\mu$ ) was calculated using the formula  $\mu = d^2 / T_r V$  where  $T_r$  is the transit time obtained by photocurrent curves,  $V$  is

the applied voltage and  $d$  is the thickness of ITO cell. The photocurrent curves and electron/hole mobility as a function of temperature are shown in Figure 3.17a and Figure 3.17b, respectively. It is evident from Figure 3.17b that the electron and hole mobilities are almost temperature invariant which is usually observed in the Col<sub>h</sub> phase of liquid crystalline materials. At room temperature (30 °C), DLC exhibited the average ambipolar charge carrier mobility of  $1.78 \times 10^{-3} \text{ cm}^2 \text{ V}^{-1} \text{ s}^{-1}$  and  $1.25 \times 10^{-3} \text{ cm}^2 \text{ V}^{-1} \text{ s}^{-1}$ , for the electron and hole, respectively. We also noticed that the electron mobility is higher than that of hole mobility. Hence, the additionally introduced donor-acceptor interactions among the electron donor discogens (**8a-c** and **9a-c**) and electron acceptor TNF molecules stabilize the mesophase and resulting in ambipolar behaviour of the complexes.

### 3.1.4 Conclusions

A new series of non-symmetric discotic liquid crystals based on TP and PA moiety has been successfully synthesized by connecting both discotic components by triazole linkage. All the discotic dimers exhibit blue light emission in solution state. The pure dimers display Col<sub>r</sub> and D<sub>Lam</sub> phases while on doping with electron acceptor TNF exhibits enantiotropic Col<sub>h</sub> phase. GISAXS/GIWAXS experiments performed on the mechanically sheared sample for the representative compounds showing desirable alignment properties of the materials in Col<sub>r</sub> (**9a**) and Col<sub>h</sub> mesophases (**9a**/TNF). The fabrication of doped OLED devices by using **8a** and **9a** as an emitter with the configuration ITO/PEDOT:PSS/Host:Emitter/TPBi/LiF/Al, has been carried out with three different hosts: carbazoyl-1,1'-biphenyl (CBP), 4',4''-tri(N-carbazoyl)triphenylamine (TCTA) and 2,7-Bis(carbazol-9-yl)-9,9-spirobifluorene (Spiro-2CBP) by varying dopant concentration. The best electroluminescence performance is observed for the device fabricated with **8a** (5 wt% on CBP host) with maximum external quantum efficiency (EQE) of 2.1%, power efficiency (PE) of  $1.2 \text{ lm W}^{-1}$ , current efficiency (CE) of  $2.0 \text{ cd A}^{-1}$  and CIE coordinates of (0.16, 0.10). Hence, the synthesized TP-PA dyads owing to their good efficiency in blue OLEDs combining with the desirable alignment property make them highly promising materials for device application. In addition, one of the studied complex **8b**/TNF showing Col<sub>h</sub> mesophase exhibited hole and electron mobility of  $1.78 \times 10^{-3} \text{ cm}^2 \text{ V}^{-1} \text{ s}^{-1}$  and  $1.25 \times 10^{-3} \text{ cm}^2 \text{ V}^{-1} \text{ s}^{-1}$  reveals its potential application as organic semiconducting material as an ambipolar material.

**Acknowledgements.** *The OLED device studies and TOF measurements carried out in collaboration with Prof. J. H Jou's group (at National Tsing Hua University, Taiwan) and Dr. Dharmendra Pratap Singh (at Université du Littoral Côte d'Opale, France) are greatly acknowledged and respected. Dr. Santosh Prasad Gupta (at Patna University) is duly acknowledged for the analysis of XRD data.*

### 3.1.5 Experimental section

**3.1.5.1 Synthesis of compound 5a.** The compounds **2a-c** were prepared according to the procedure as reported in earlier reports.<sup>3,93</sup>

**3.1.5.2 General procedure for the synthesis of the compounds 2a-c.** In a round bottom flask (R.B), pentabromophenol (1equiv.), potassium carbonate (5 equiv.) and alkyl bromide (5 equiv.) was refluxed in a 30 ml dry acetone for 12 hours. Potassium iodide was added in a catalytic amount. After completion of the reaction, the acetone was evaporated and then extracted with DCM. The reaction mixture was purified in 100-120 silica gel by using hexane/EtOAc as eluent.

**3.1.5.3 General procedure for the synthesis of the compounds 3a-c.** The sonogshira of alkylated compound **2** (500 mg) was done by taking 30 ml of dry triethylamine in a round bottom flask which was degassed followed by the addition of Pd(PPh<sub>3</sub>)<sub>2</sub>Cl<sub>2</sub> (50 mg), CuI (50 mg) & PPh<sub>3</sub> (100 mg). The mixture was stirred for 15 minutes followed by the gradual addition of 4-pentylphenylacetylene. The reaction mixture was stirred at 100 °C for 24 h under nitrogen atmosphere & after cooling to room temperature it was poured into 30 ml of 5M HCl. After extracting the reaction mixture with DCM, the compound was purified in 230-400 silica gel by using hexane/EtOAc as an eluent.

**3.1.5.4 General procedure for the synthesis of the compounds 4a-c.** A mixture of compound **2** (1 equiv.) and NaN<sub>3</sub> (13 equiv.) in DMF (10 mL) was stirred at room temperature for 12 h. After the addition of water, it was extracted with diethyl ether. The organic layer was dried with Na<sub>2</sub>SO<sub>4</sub>, and the solvent was removed under reduced pressure. The compound was used without further purification.

**3.1.5.5 General procedure for the synthesis of compound 7 (m = 1 & m = 2, see Scheme 1 in main manuscript).** To the mixture of compound **6** (1 equiv.) and K<sub>2</sub>CO<sub>3</sub> (4 equiv.) in DMF



(3 mL), the terminal alkyne (1-bromo-propyne,  $m = 1$  & 3-bromo-1-propyne,  $m = 2$ ) (16 equiv.) was added, and the mixture was stirred over 12 h at 50 °C. After removing the solvent, the residue was washed with water and extracted with diethyl ether. The organic layer was dried with  $\text{Na}_2\text{SO}_4$ , and the organic solvent was removed under vacuum. The crude product was purified by column chromatography with 60-120 silica gel by using hexane/ethyl acetate as an eluent to get the product as a white solid.

#### 3.1.5.6 General procedure for the synthesis of the target compounds **8a-c** & **9a-c**.

Compound **4** (1 equiv.) and **7** ( $m = 1$  &  $m = 2$ ) (1 equiv.) were dissolved in toluene (2 mL), then CuI (1.4 equiv.) and  $\text{NEt}_3$  (0.24 equiv.) was added. The resulting mixture was stirred for 12 h at room temperature. Then toluene was removed under reduced pressure, and the residual solid was purified by column chromatography with 100-200 silica gel by using hexane/ethyl acetate as an eluent to obtain the product as a yellowish-brown solid.

**Compound 8a.** FT-IR ( $\text{cm}^{-1}$ ): 2955.50, 2929.29, 2857.60, 2208.29, 1741.7, 1616.47, 1513.31, 1466.87, 1434.80, 1379.78, 1346.81, 1262.10, 1168.74, 1085.9, 1043.22, 838.01, 726.72, 597.89, 551.11.  $^1\text{H}$  NMR (400 MHz,  $\text{CDCl}_3$ ,  $\delta$  in ppm):  $\delta$  8.08 (s, 1H),  $\delta$  7.83 (s, 1H),  $\delta$  7.81 (s, 4H),  $\delta$  7.58 (s, 1H),  $\delta$  7.54-7.47 (m, 10H),  $\delta$  7.18-7.15 (m, 10H),  $\delta$  5.49 (s, 2H), 4.29-4.19 (m, 14H), 2.65-2.58 (m, 10H), 1.98-1.88 (m, 10H), 1.86-1.81 (m, 4H), 1.62-1.56 (m, 22H), 1.43-1.28 (m, 42H), 0.94-0.86 (m, 30H).  $^{13}\text{C}$  NMR (100 MHz,  $\text{CDCl}_3$ ,  $\delta$  in ppm):  $\delta$  160.11, 149.44, 149.26, 148.87, 147.83, 144.70, 144.19, 144.16, 143.87, 131.90, 131.78, 131.66, 128.94, 128.72, 128.67, 128.64, 124.28, 123.83, 123.61, 123.38, 123.27, 122.75, 120.78, 120.57, 120.54, 120.10, 108.95, 107.59, 107.21, 106.77, 106.49, 99.76, 99.41, 97.52, 87.15, 84.15, 74.26, 70.03, 69.92, 69.70, 64.15, 50.40, 36.12, 36.07, 32.07, 31.85, 31.82, 31.62, 31.60, 31.09, 30.31, 29.85, 29.59, 29.56, 29.48, 26.51, 26.00, 25.99, 25.91, 22.81, 22.68, 22.66, 14.58, 14.21, 14.19. HRMS (MALDI) for  $\text{C}_{128}\text{H}_{161}\text{N}_3\text{O}_7$  ( $\text{M} + \text{H}$ ): calculated – 1854.2446; found-1854.2546.

**Compound 8b.** FT-IR ( $\text{cm}^{-1}$ ): 2955.70, 2928.78, 2857.00, 2208.11, 1737.80, 1616.56, 1513.26, 1466.75, 1434.99, 1379.64, 1346.81, 1262.43, 1169.64, 1085.9, 1042.80, 838.12, 726.08, 593.98, 547.14.  $^1\text{H}$  NMR (400 MHz,  $\text{CDCl}_3$ ,  $\delta$  in ppm):  $\delta$  8.09 (s, 1H),  $\delta$  7.84 (s, 1H),  $\delta$  7.82 (s, 4H),  $\delta$  7.64 (s, 1H),  $\delta$  7.55-7.49 (m, 10H),  $\delta$  7.18-7.15 (m, 10H),  $\delta$  5.50 (s, 2H), 4.35-4.20 (m, 14H), 2.64-2.59 (m, 10H), 1.99-1.83 (m, 14H), 1.67-1.55 (m, 22H), 1.44-1.25 (m,

46H), 0.95-0.87 (m, 30H).  $^{13}\text{C}$  NMR (100 MHz,  $\text{CDCl}_3$ ,  $\delta$  in ppm):  $\delta$  160.25, 149.44, 149.26, 148.91, 148.86, 147.86, 144.72, 144.17, 144.08, 143.85, 131.89, 131.77, 131.69, 128.91, 128.68, 128.64, 124.27, 124.24, 124.06, 123.83, 123.63, 123.38, 123.25, 122.73, 120.79, 120.63, 120.56, 120.14, 108.95, 107.61, 107.22, 106.48, 99.70, 99.46, 97.46, 87.17, 86.68, 84.22, 74.70, 70.03, 69.93, 69.71, 69.54, 69.34, 64.17, 50.54, 36.12, 31.84, 31.62, 31.60, 31.11, 31.08, 30.59, 30.37, 29.85, 29.58, 29.55, 29.48, 29.40, 29.04, 26.59, 26.34, 26.00, 22.82, 22.68, 14.21, 14.19. HRMS (MALDI) for  $\text{C}_{130}\text{H}_{165}\text{N}_3\text{O}_7$  (M + H): calculated – 1882.2759; found- 1882.2852.

**Compound 8c.** FT-IR ( $\text{cm}^{-1}$ ): 2959.70, 2928.61, 2856.84, 2210.10, 1733.90, 1616.08, 1512.89, 1468.40, 1434.65, 1379.77, 1262.10, 1170.59, 1085.90, 1041.72, 839.92, 802.90, 730.61, 597.89, 558.85.  $^1\text{H}$  NMR (400 MHz,  $\text{CDCl}_3$ ,  $\delta$  in ppm):  $\delta$  8.09 (s, 1H),  $\delta$  7.84 (s, 1H),  $\delta$  7.82 (s, 4H),  $\delta$  7.65 (s, 1H),  $\delta$  7.55-7.49 (m, 10H),  $\delta$  7.17-7.15 (m, 10H),  $\delta$  5.50 (s, 2H), 4.34-4.20 (m, 14H), 2.64-2.60 (t, 10H,  $J = 6.94$  Hz), 1.96-1.87 (m, 14H), 1.62-1.57 (m, 22H), 1.41-1.32 (m, 50H), 0.94-0.86 (m, 30H).  $^{13}\text{C}$  NMR (100 MHz,  $\text{CDCl}_3$ ,  $\delta$  in ppm):  $\delta$  149.45, 149.27, 148.97, 148.86, 148.36, 147.87, 146.85, 144.16, 144.09, 144.03, 131.90, 131.78, 131.71, 128.88, 128.66, 124.28, 123.64, 123.57, 122.71, 121.36, 120.66, 120.58, 120.17, 107.62, 107.24, 99.66, 99.47, 98.90, 97.43, 87.19, 84.23, 74.84, 70.19, 70.03, 69.85, 69.71, 69.65, 69.55, 69.35, 64.19, 50.59, 36.10, 32.08, 31.84, 31.62, 31.11, 30.69, 30.44, 29.85, 29.59, 29.48, 29.10, 26.65, 26.45, 26.00, 22.82, 22.68, 14.21, 14.19. HRMS (MALDI) for  $\text{C}_{132}\text{H}_{169}\text{N}_3\text{O}_7$  (M + H): calculated – 1910.3072; found- 1910.3203.

**Compound 9a.** FT-IR ( $\text{cm}^{-1}$ ): 2959.10, 2929.57, 2857.79, 2210.30, 1733.90, 1616.13, 1512.99, 1468.40, 1434.70, 1379.93, 1262.38, 1170.52, 1085.90, 1042.84, 838.28, 802.90, 732.25, 595.03, 555.83.  $^1\text{H}$  NMR (400 MHz,  $\text{CDCl}_3$ ,  $\delta$  in ppm):  $\delta$  7.82-7.81 (m, 6H),  $\delta$  7.55-7.47 (m, 10H),  $\delta$  7.23 (s, 1H),  $\delta$  7.18-7.15 (m, 10H),  $\delta$  4.28-4.17 (m, 16H),  $\delta$  3.05-3.01 (t, 2H,  $J = 7.40$  Hz),  $\delta$  2.62-2.61 (m, 10H), 2.34-2.31 (t, 2H,  $J = 6.68$  Hz), 1.92-1.83 (t, 10H,  $J = 7.16$  Hz), 1.81-1.79 (m, 4H), 1.63-1.57 (m, 22H), 1.39-1.33 (m, 42H), 0.92-0.87 (m, 30H).  $^{13}\text{C}$  NMR (100 MHz,  $\text{CDCl}_3$ ,  $\delta$  in ppm):  $\delta$  149.14, 146.71, 144.15, 131.90, 131.78, 131.65, 128.72, 128.68, 123.84, 120.53, 107.26, 106.78, 99.41, 69.81, 36.12, 31.85, 31.62, 31.09, 29.58, 26.00, 22.81, 22.68, 14.22, 14.19. HRMS (MALDI) for  $\text{C}_{130}\text{H}_{165}\text{N}_3\text{O}_7$  (M + H): calculated – 1882.2759; found- 1882.2706.

**Compound 9b.** FT-IR ( $\text{cm}^{-1}$ ): 2959.70, 2928.25, 2856.63, 2210.10, 1737.80, 1616.08, 1512.89, 1468.40, 1434.49, 1379.43, 1262.10, 1170.45, 1085.90, 1042.32, 838.32, 802.90, 726.71, 597.89, 558.85.  $^1\text{H}$  NMR (400 MHz,  $\text{CDCl}_3$ ,  $\delta$  in ppm):  $\delta$  7.83-7.81 (m, 6H),  $\delta$  7.54-7.48 (m, 10H),  $\delta$  7.27 (s, 1H),  $\delta$  7.17-7.68 (m, 10H),  $\delta$  4.35-4.32 (t, 2H,  $J = 6.12$  Hz),  $\delta$  4.28-4.20 (m, 14H),  $\delta$  3.05-3.01 (t, 2H,  $J = 7.16$  Hz),  $\delta$  2.66-2.62 (m, 10H), 2.34-2.31 (t, 2H,  $J = 7.06$  Hz), 1.95-1.87 (m, 12H), 1.80-1.77 (m, 2H), 1.61-1.57 (m, 22H), 1.38-1.28 (m, 46H), 0.92-0.89 (m, 30H).  $^{13}\text{C}$  NMR (100 MHz,  $\text{CDCl}_3$ ,  $\delta$  in ppm):  $\delta$  160.25, 148.97, 147.41, 144.18, 131.89, 131.77, 131.69, 128.91, 128.68, 123.68, 120.99, 120.55, 120.15, 107.53, 107.26, 99.70, 87.17, 84.21, 69.78, 50.32, 36.12, 31.84, 31.62, 31.12, 31.09, 30.60, 29.85, 29.57, 29.24, 29.08, 26.63, 26.33, 26.01, 2282, 22.68, 14.22, 14.20. HRMS (MALDI) for  $\text{C}_{132}\text{H}_{169}\text{N}_3\text{O}_7$  (M + H): calculated – 1910.3072; found- 1910.3152.

**Compound 9c.** FT-IR ( $\text{cm}^{-1}$ ): 2959.70, 2928.61, 2856.84, 2210.10, 1741.70, 1616.08, 1512.89, 1468.40, 1434.65, 1379.77, 1262.10, 1170.59, 1085.90, 1041.72, 839.92, 802.90, 730.61, 597.89, 547.14.  $^1\text{H}$  NMR (400 MHz,  $\text{CDCl}_3$ ,  $\delta$  in ppm):  $\delta$  7.83-7.81 (m, 6H),  $\delta$  7.54-7.49 (m, 10H),  $\delta$  7.29 (s, 1H),  $\delta$  7.17-7.16 (m, 10H),  $\delta$  4.36-4.33 (t, 2H,  $J = 6.14$  Hz),  $\delta$  4.27-4.21 (m, 14H),  $\delta$  3.05-3.01 (t, 2H,  $J = 7.28$  Hz),  $\delta$  2.64-2.61 (t, 10H,  $J = 7.10$  Hz), 2.34-2.31 (t, 2H,  $J = 6.68$  Hz), 1.95-1.82 (m, 14H), 1.65-1.57 (m, 22H), 1.39-1.22 (m, 50H), 0.95-0.90 (m, 30H).  $^{13}\text{C}$  NMR (100 MHz,  $\text{CDCl}_3$ ,  $\delta$  in ppm):  $\delta$  149.33, 149.15, 148.74, 147.75, 144.03, 143.90, 131.77, 131.65, 131.59, 128.76, 128.54, 124.16, 123.52, 122.58, 120.54, 120.46, 120.04, 107.49, 107.16, 107.11, 99.54, 99.34, 98.78, 97.31, 87.07, 84.10, 74.71, 69.91, 69.58, 69.43, 69.23, 64.07, 50.46, 35.98, 31.95, 31.72, 31.49, 30.98, 30.57, 30.31, 29.73, 29.46, 29.35, 28.98, 26.53, 26.33, 25.88, 14.09, 14.06. HRMS (MALDI) for  $\text{C}_{134}\text{H}_{173}\text{N}_3\text{O}_7$  (M + H): calculated – 1938.3385; found- 1938.3344.

**3.1.5.7 Quantum yield calculation.** Relative quantum yield values were calculated according to the following equation:  $Q_S = Q_R \times (m_S/m_R) \times (n_S/n_R)^2$ , Where Q: Quantum yield, m: the slope of the plot of integrated fluorescence intensity vs absorbance, n = refractive index. In order to minimize the re-absorption effects, the absorbance value was kept below 0.15 at the excitation wavelength of 337 nm. Quantum yield of quinine sulfate in 0.1M  $\text{H}_2\text{SO}_4$  solution is 0.54. After substituting the appropriate values, the simplified equation is:  $Q_S = 0.54 \times (m_S/m_R) \times (1.445/1.33)^2 = 0.5867 \times (m_S/m_R)$ .



## 3.2 Part B: Rod-disc oligomeric liquid crystal based on 4-cyanobiphenyl and truxene core

### 3.2.1 Introduction

Liquid crystal (LC) oligomers such as rod-rod, disc-disc and rod-disc mesogenic units interconnected *via* flexible alkyl spacers are focussing great attention on research activity in LC field.<sup>55,56</sup> Among them, rod-disc hybrid oligomers have emerged as a new sub-field in research providing significant insight into several unconventional structure-mesophase morphology relationships.<sup>57,58</sup> In other words, they fulfill the significant knowledge gap in understanding the structure-property behaviour between calamitic and discotic liquid crystals (LCs). Theoretical studies predict that the LC containing both rod-shaped and disc-shaped moiety can result in the biaxial nematic ( $N_b$ ) phase.<sup>59,60</sup> But this prediction has proven to be unsuccessful as physical mixtures of rod and disc lead to phase separation into two uniaxial N phases.<sup>61</sup> To prevent phase separation and to introduce attractive interactions within rod and disc systems, a covalent attachment approach between two moieties *via* flexible alkyl spacers has been explored.<sup>59,62</sup> In these molecular systems mostly one, two or three rods have been attached to a single disc that results unconventional micro-segregated structures.<sup>6,63,64</sup> To get conventional mesophase morphology, a recent trend has been to attach six rods radially to the central disc core,<sup>57,58,65-67</sup> closely related to the idea of distributing discs around a discotic core.<sup>68</sup> Such systems indicate rod-like units in the tail can significantly change the overall molecular shape resulting in either discotic or calamitic mesophases.<sup>65,69</sup> 4-cyanobiphenyl units are the most used rod-like units that usually disrupt the  $\pi$ - $\pi$  intermolecular interactions among the disc-like units and induced discotic nematic mesophase in the discotic LCs.<sup>60,70,71</sup> For instance, Imrie et al. reported triphenylene-based oligomeric nematic liquid crystals (**1**) where triphenylene discotic core attached to six 4-cyanobiphenyl units *via* flexible alkyl spacers (Figure 3.18).<sup>70</sup> Pal and co-workers reported perylene tetraesters (**2**)<sup>71</sup> and anthraquinone (**3**)<sup>6</sup> based discotic nematic LCs achieved by substituting the 4-cyanobiphenyl rod units to the respective discotic cores. It can be noted that the liquid crystalline derivatives of triphenylene<sup>72</sup> perylene<sup>73-77</sup> and anthraquinone<sup>78-80</sup> based discotic cores are very much known to show

columnar mesophases, however, showed discotic nematic phase on the introduction of 4-cyanobiphenyl units in the molecular structure.

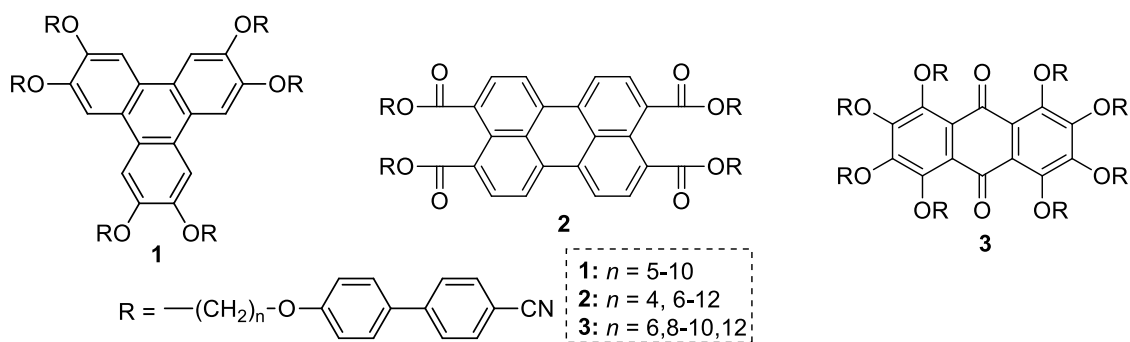


**Figure 3.18** Molecular structures of discotic LC derivative (**1-3**) based on triphenylene, perylene, and anthraquinone derivatives attached to which 4-cyanobiphenyl units at the peripheral positions.

### 3.2.2 Objectives

Intending to study the influence of the introduction of six 4-cyanobiphenyl nematogens on the truxene core, we have synthesized a new rod-disc oligomer, **5** (Figure 3.19) containing six cyanobiphenyl based rod-like moieties attached radially to a central truxene (TX) discotic core *via* flexible alkyl spacers. The TX core was chosen because it is known as a promising scaffold<sup>81</sup> for potential construction of large molecular architectures, easy functionalization, high thermal stability, good fluorescence capacity,  $C_3$  symmetrical structure *etc.* Thus TX derivatives can act as an attractive building block for many applications in the field of

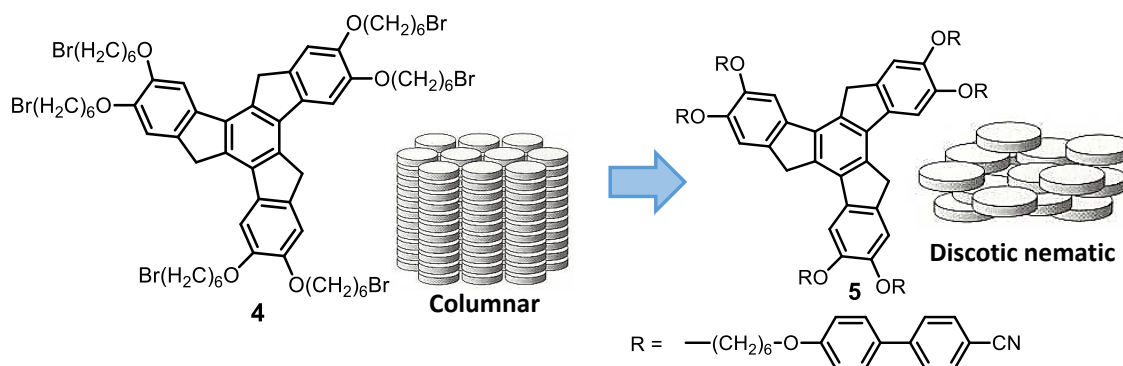


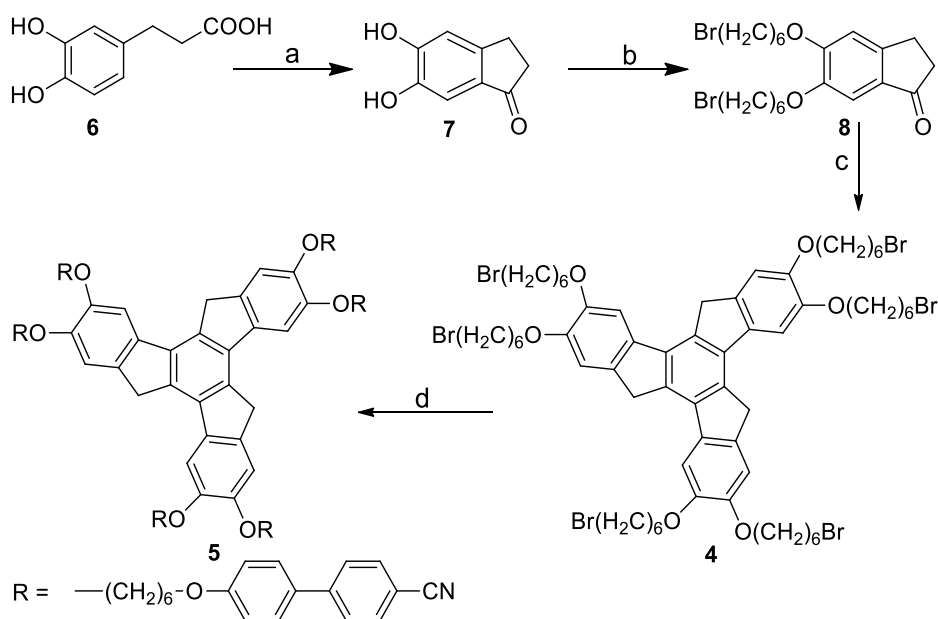
**Figure 3.19** Schematic representation showing the transformation of columnar phase to nematic in truxene based discotic LC on substitution with rod-like 4-cyanobiphenyl units.

optoelectronics, organic photovoltaics, organic light emitting diodes (OLEDs), organic lasers, fluorescent probes, organogels, and non-linear optical systems.<sup>70</sup> In addition, TX core is also known to promote LC behaviour in a wide range of molecular systems and has variable synthetic chemistry.<sup>82-89</sup> In addition, TX core is also known to promote LC behaviour in a wide range of molecular systems and has a variable synthetic chemistry. In this work, we have shown that how the discotic columnar phase transformed to discotic nematic phase upon the introduction of 4-cyanobiphenyl units. To this end, we have studied ultrathin films of newly synthesized oligomers at air–water interface (Langmuir film) and air–solid interface (Langmuir–Blodgett (LB) film).

### 3.2.3 Results and discussions

#### 3.2.3.1 Synthesis and characterization

The synthesis of **5** is outlined in Scheme 3.2. First, acid-treated aldol cyclotrimerization of 3, 4 dihydroxyhydrocinnamic acid **6** using polyphosphoric acid (PPA) as a dehydrating agent resulted in the formation of 5, 6-dihydroxy-1-indanone, **7**. **7** was then alkylated using  $\alpha$ ,  $\omega$ -



**Scheme 3.2** Synthesis of compound **5**. (a) PPA, 110 °C, 1.5 h, yield 20%; (b) Br(CH<sub>2</sub>)<sub>6</sub>Br, K<sub>2</sub>CO<sub>3</sub>, tetra-*n*-butylammonium bromide, acetone, 65 °C, 9 h, yield 50%; (c) PPE, 140 °C, 25 min, yield 25%; (d) 4'-hydroxy-4-biphenyl carbonitrile, K<sub>2</sub>CO<sub>3</sub>, KI, acetone, 65 °C, 24 h, yield 20%.

dibromoalkane according to the previously reported procedure.<sup>90</sup> The alkylated product **8** was then trimerised using polyphosphoric ester (PPE) to furnish **4**.<sup>86</sup> Finally, **4** was reacted with 4'-hydroxy-4-biphenylcarbonitrile in the presence of potassium carbonate in refluxing acetone to give the expected product **5**.<sup>70</sup> The experimental details are given in the experimental section and the <sup>1</sup>H NMR of final TX derivative is given in Figure 3.20.

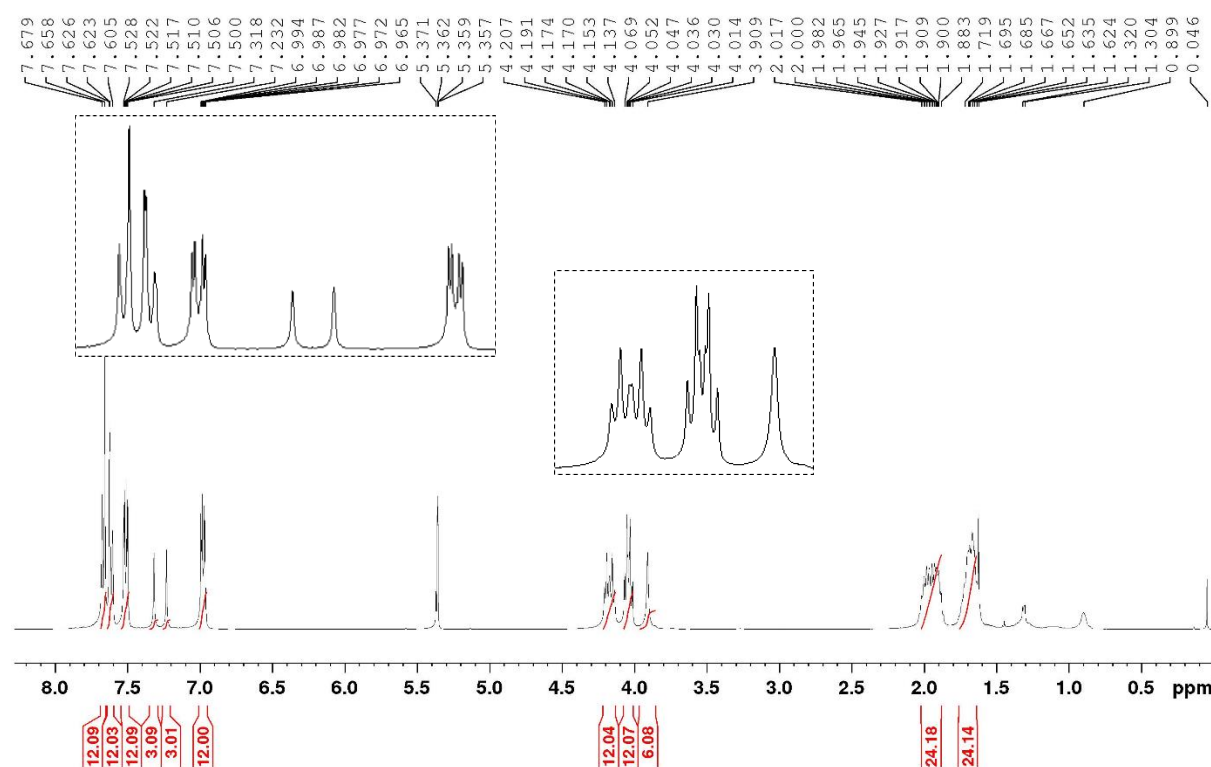


**Figure 3.20** <sup>1</sup>H NMR spectra of compound **5**.

### 3.2.3.2 Thermal and photophysical behaviour

The thermal behaviour of the newly synthesized truxene derivative **5** was studied by POM, DSC and X-ray diffraction studies (SAXS/WAXS system). When viewed under POM, a classical schlieren texture indicative of a nematic (N) phase was observed for **5** (Figure 3.21a). Compound **5** exhibited only a monotropic N phase as confirmed by DSC. It melted at 181 °C ( $\Delta H = 25.5 \text{ kJ mol}^{-1}$ ) to the isotropic phase. However, on cooling the N phase appeared at 177 °C ( $\Delta H = 0.5 \text{ kJ mol}^{-1}$ ) and then crystallized at 172.5 °C ( $\Delta H = 27 \text{ kJ mol}^{-1}$ ). The entropy of the nematic-isotropic transition temperature ( $\Delta S_{N-I}/R = 0.13$ ) is quite small. This is likely due to the enhanced biaxiality of this molecule.<sup>91,92</sup> The DSC traces obtained on heating and



cooling (at a scan rate of 10 °C/min) are shown in Figure 3.22. The compound **4**, precursor for compound **5** was also found to be mesomorphic. Interestingly, as expected, it shows classical columnar texture under POM (Figure 3.21b), very similar to its hexa-hexyloxy-truxene analogue.<sup>83</sup>

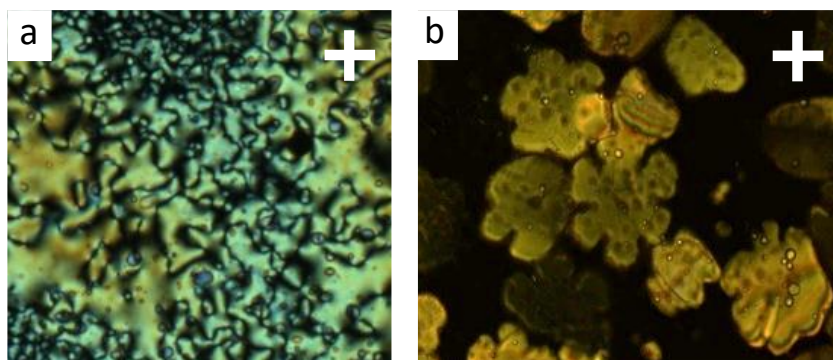


**Figure 3.21** (a) Schlieren texture of the N phase of compound **5** at 175 °C, obtained upon cooling from isotropic phase with a scan rate of 5 °C min<sup>-1</sup>. (b) Optical photomicrograph of the Col<sub>h</sub> phase of compound **4** obtained on heating at 192 °C with a scan rate of 10 °C min<sup>-1</sup>. (crossed polarizers, magnification ×200).

In DSC, on heating, it melted at 82 °C to the columnar hexagonal phase (Col<sub>h</sub>) which gets decomposed at a very high temperature (> 250 °C). In summary, the addition of rod-like moieties to **4**, has sufficiently perturbed the average molecular shape to yield N mesophase.

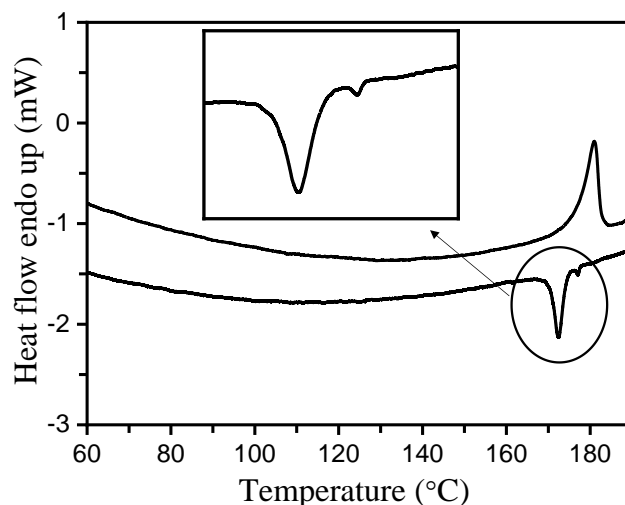


**Figure 3.22** DSC traces of compound **5** on heating and cooling with a scan rate of 10 °C min<sup>-1</sup>.

The UV-Vis absorption spectra and emission spectra of compound **5** were recorded in dichloromethane ( $1 \times 10^{-5}$  M) at room temperature (Figure 3.23). It shows two absorption bands. The sharp band at 224 nm corresponds to the  $\pi$ - $\pi^*$  transitions due to cyanobiphenyl moiety. The other broadband that composed of two bands at 293 nm and 308 nm, corresponds to the  $\pi$ - $\pi^*$  transitions due to cyanobiphenyl moiety at longer wavelength<sup>84</sup> and the  $\pi$ - $\pi^*$  transitions due to truxene core,<sup>85</sup> respectively (Figure 3.23a). For the emission spectra measurements, the sample was excited with light of 297 nm, two emission bands were observed (Figure 3.23b).

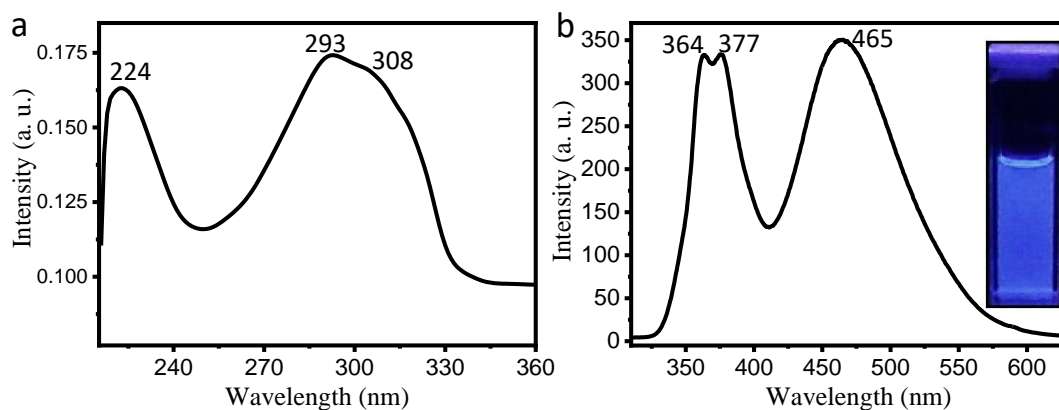


**Figure 3.23** (a) UV-Vis and (b) fluorescence spectra of compound **5** in  $\text{CHCl}_3$ .

One bifurcated band at 364 and 377 nm with a blue fluorescence peak at 465 nm suggest that compound **5** exhibits a blue light-emitting property.

### 3.2.3.3 X-ray diffraction

The supramolecular organization of compound **5** was further investigated by X-ray diffraction studies (XRD). In the nematic phase of compound **5**, two diffuse reflections were observed in the wide and the small-angle region (Figure 3.24a). These observations indicate the absence of any positional order in the N mesophase and thus exclude the possibility of the existence of a smectic and columnar phase structure of this rod-disc oligomer, consistent with their microscopic textures. The small-angle reflection for compound **5** showed a  $d$ -spacing of 16.44 Å in the mesophase (at 175 °C). This corresponds to the average length of the truxene core ( $\sim 11$  Å) and rod-like cyanobiphenyl units along with alkyl chains (21 Å), indicating a molecularly mixed nematic phase. In fact, the considerably smaller reflection at a smaller angle

than that of the total length of the hybrid, confirms the compatibility of both the components in the mesophase. A significantly diffused peak at around  $4.92 \text{ \AA}$  was observed which can be attributed to the average lateral separation of the molecules in the mesophase. Based on the X-ray diffraction studies and microscopy textures, we propose a sketch of the order of the nematic phase (Figure 3.24b).

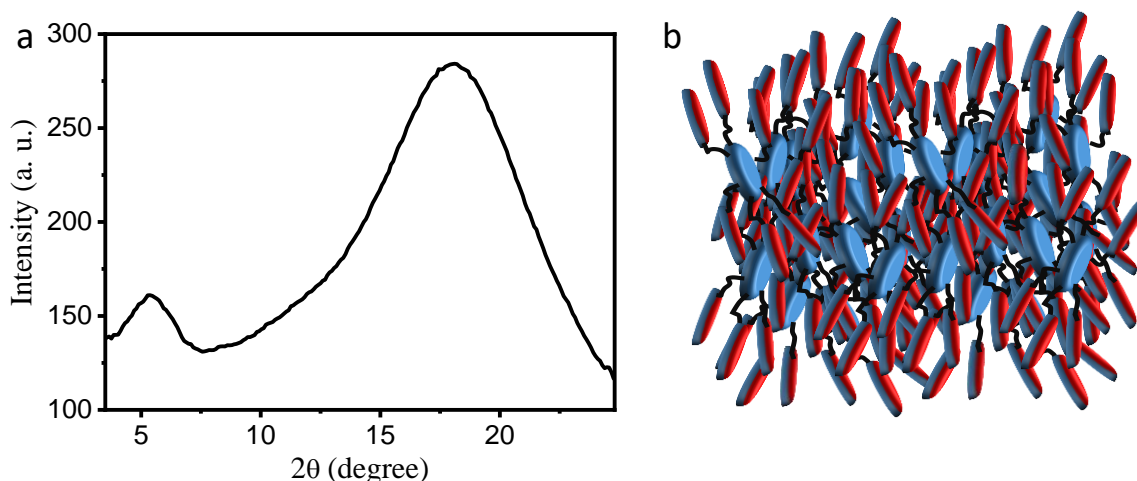


**Figure 3.24** (a) An intensity versus  $2\theta$  graph derived from the X-ray diffraction pattern of compound **5** in the mesophase. (b) Sketch of the order in the mixed nematic phase.

### 3.2.3.4 Surface Manometry, BAM and AFM studies

The ultrathin monolayer of six 4-cyanobiphenyl substituted truxene (TX) compound **5** was studied at air-water and air-solid interface. Because of the presence of strong polar groups and long alkyl chains these molecules are expected to show monolayer properties. The surface pressure ( $\pi$ )-area per molecule ( $A_m$ ) isotherm of compound **5** formed on ultrapure deionized water subphase is shown in Figure 3.25. The surface-pressure was approximately zero at a large area per molecule ( $A_m \sim 1.58 \text{ nm}^2$ ). On compression, the isotherm indicates a change in the slope which then starts increasing on compression and finally collapsed at an  $A_m$  of  $0.42 \text{ nm}^2$  (with a collapse pressure of  $70 \text{ mN/m}$ ). The high collapse pressure can be due to the presence of strong polar groups and strong chain-chain interactions associated with 4-cyanobiphenyl units *via* flexible alkyl spacers. In the  $\pi$ - $A_m$  isotherm (Figure 3.25), we make two observations. First, a gradual increase in slope up to  $40 \text{ mN/m}$  and second, a steep increase in slope after that. The average molecular area in a phase can be estimated by extrapolating the corresponding region of the isotherm at zero surface pressure.<sup>92</sup> The extrapolation to the zero

surface pressure of the region where the surface pressure is gradually increasing yields an  $A_m$  value of around  $1.4 \text{ nm}^2$  ( $A_0^1$ ) which corresponds to an expanded phase ( $L_1$ ). The rapidly increasing surface pressure region of the isotherm yields a limiting area per molecule of around  $1.02 \text{ nm}^2$  ( $A_0$ ) which corresponds to a condensed phase ( $L_2$ ). If the compound **5** is considered

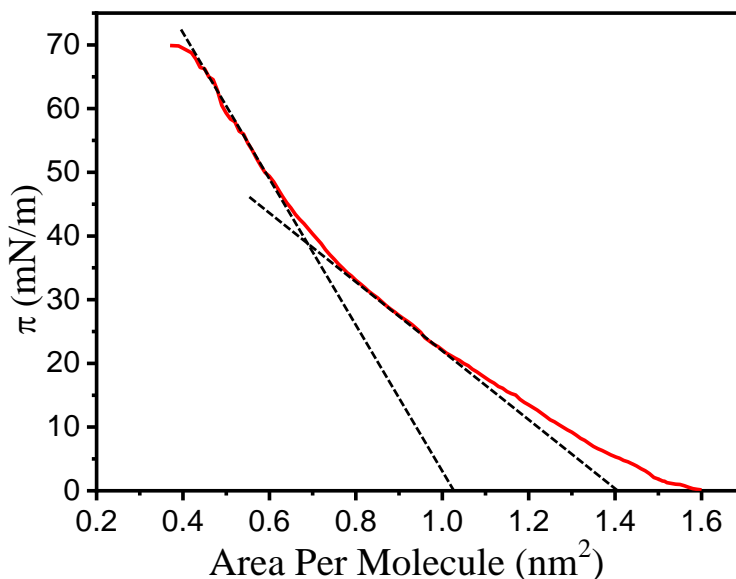


**Figure 3.25**  $\pi$ - $A_m$  isotherm of compound **5**.

to have a face-on conformation on the water surface, then their average molecular area should be around  $21 \text{ nm}^2$ . However, the surface pressure-area isotherm of compound **5** indicates the average molecular area in expanded ( $L_1$ ) and condensed phase ( $L_2$ ) to be around  $1.4 \text{ nm}^2$  and  $1.02 \text{ nm}^2$ , respectively. This much smaller average molecular area excludes the possibility of compound **5** being in face-on conformation. As a result, it can be concluded that  $L_1$  and  $L_2$  are low density and high-density liquid phases wherein the compound **5** molecules probably in the

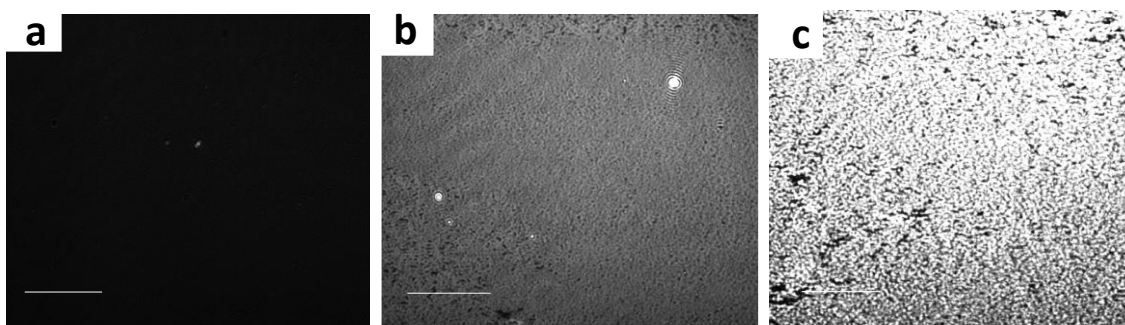


**Figure 3.26** BAM images of Langmuir film of compound **5** at area (a)  $1.6 \text{ nm}^2$ , (b)  $1.04 \text{ nm}^2$  and (c)  $0.43 \text{ nm}^2$ . Scale bar =  $100 \mu\text{m}$ .

edge-on conformation (see details from AFM studies below).

The BAM images show that the brightness increases gradually upon compression from nearly zero surface pressure (Figure 3.26a). This transforms to 3D crystals (Figure 3.26c) at the collapsed state. A very uniform grey-colored region was observed in the monolayer state (Figure 3.26b). AFM has been employed to know the morphology of the film in the compound at an air-solid interface. The AFM topography of compound **5** deposited at three different surface pressures on hydrophilic glass substrates is shown in Figure 3.27.

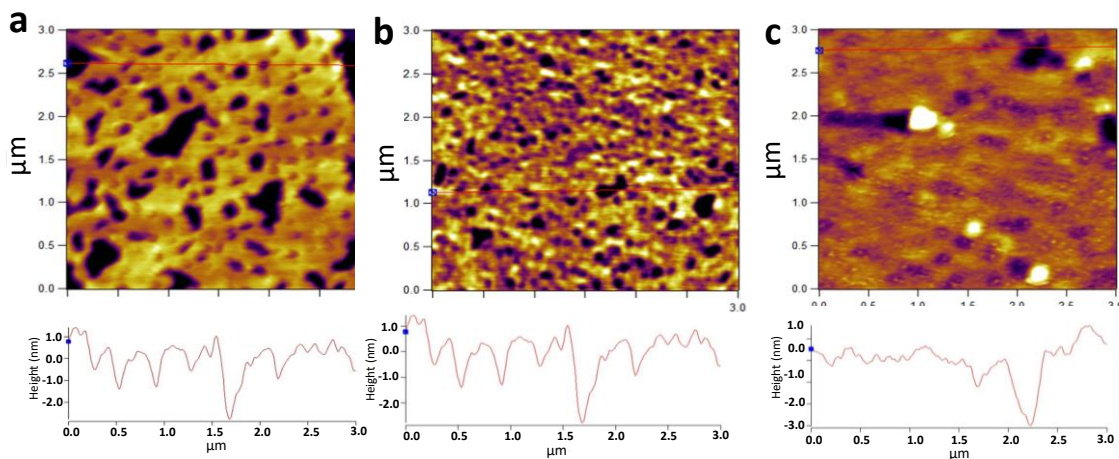


**Figure 3.27** AFM images of the LB film of compound **5** on hydrophilic glass substrates at target pressure: (a) 10 mN/m, (b) 20 mN/m and (c) 35 mN/m.

The deposition of a single layer of LB films was done by a single upstroke of the dipper in a vertical direction. The AFM topography images of compound **5** transferred at a surface pressure of 10 mN/m by vertical method shows the height of about 4.0 nm with reference to the substrate. This height is less than the actual height (5.1 nm) of compound **5** if lying in the vertical direction. This can be accounted by the tilt of the molecules as evidenced from earlier studies.<sup>92</sup> The AFM image (Figure 3.27a) at 10 mN/m consist voids which gets filled as we compress the film. At 20 mN/m the height is close to 4 nm with decreasing voids sizes (Figure 3.27b). At 35 mN/m the voids get disappeared and form a homogeneous film showing a height of  $\sim 4.0 \pm 0.4$  nm (Figure 3.27c). So it can be concluded that compound **5** exist in edge-on conformation with a tilted orientation from their vertical direction.

### 3.2.3 Conclusions

In conclusion, we have reported the first example of the oligomeric rod-disc hybrid based on truxene and 4-cyanobiphenyl core. The target compound shows a monotropic nematic phase on cooling. This is interesting as rod-like moieties sufficiently perturbed the average molecular shape of the compound to yield a nematic mesophase. The compound shows a stable monolayer at the air-water interface. AFM studies revealed the tilted orientation of the molecule at the air-solid interface.

**Acknowledgements.** *We are highly thankful to Dr. Goutam Sheet's group from IISER Mohali for carrying out AFM measurements.*

### 3.2.4 Experimental section

**3.2.4.1 Synthesis of 2,3-Dihydro-5,6-dihydroxyinden-1-one (compound 7).** A mixture of 3,4-Dihydroxyhydrocinnamic acid (3 g, 0.016 mmol) and PPA (100 g) was taken in 50 mL round bottom flask (the flask was already equipped with a guard tube), the mixture was heated to 110 °C with stirring for 1.5 hours. After cooling, the solution was poured over ice, the organic product was extracted with ethyl acetate. The crude red colored solid was purified by column chromatography using hexane/ethyl acetate as an eluant to give compound **2** as yellow solid (20%).

**3.2.4.2 Synthesis of 2,3-Dihydro-5,6-dibromoalkoxyinden-1-one (compound 8).** A mixture of **2** (1 g, 0.006 mol), dibromohexane (0.073 mol), K<sub>2</sub>CO<sub>3</sub> (4.15 g, 0.030 mol), acetone (30 mL) and tetrabutyl ammonium bromide (200 mg, 0.620 mmol) was taken into a 100 mL round bottom flask with a water condenser and a mechanical stirrer. The mixture was brought to a temperature 65 °C for 12 hours and then distilled off the solvent, diluted with water. The aqueous layer was extracted with dichloromethane, and the extract was washed with water, dried and evaporated in the rota vapor under reduced pressure to get a crude mixture. The crude mixture was purified by column chromatography using hexane/ethylacetate to get white solid (yield 50%). <sup>1</sup>H NMR (CDCl<sub>3</sub>, 400 MHz, ppm): δ 7.18 (s, 1H), 6.88 (s, 1H), 4.10-4.07 (t, *J* = 6.7 Hz, 6.6 Hz, 2H), 4.04-4.01 (t, *J* = 6.7 Hz, 2H), 3.45-3.41 (t, *J* = 6.8 Hz, 2H), 3.07-3.04 (t, *J* = 5.3 Hz, 5.7 Hz, 2H), 2.70-2.67 (t, *J* = 5.7 Hz, 5.5 Hz, 2H), 1.91-1.37 (m, 8H), 1.48-1.37 (m, 8H).

**3.2.4.3 Synthesis of 2,3,7,8,12,13-Hexakis-(6-bromo-hexyloxy)-10,15-dihydro-5H diindeno[1,2-a;1',2'-c]flourene (compound 4).** PPE (300 mg) was taken in a 25 mL round bottom flask which was placed in a preheated oil bath at 140 °C. When the PPE had reached a temperature of 140 °C, compound **3** (200 mg, 0.408 mmol) was added to the flask (equipped with a guard tube, magnetic stirrer and thermometer) over a 5 min period. This mixture was subsequently heated for 25 min at 160 °C. During this reaction condition, excessive foaming occurred. The reaction mixture was then hydrolyzed with 20 mL of water. The reaction mixture was extracted with dichloromethane (DCM). The crude mixture was purified by column chromatography using hexane/DCM to get a yellow product (yield 25%). <sup>1</sup>H NMR (CDCl<sub>3</sub>, 400 MHz, ppm): δ 7.41 (s, 3H), 7.26 (s, 3H), 4.21-4.18 (t, *J* = 6.4 Hz, 6H), 4.15-4.12 (t, *J* = 6.5 Hz, 6H), 4.07 (s, 6H), 3.51-3.47 (m, 12H), 1.98-1.94 (m, 24H), 1.64-1.60 (m, 24H).

**3.2.4.4 Synthesis of target compound 5.** In a 50 mL round bottom flask (fitted with a condenser), a mixture of 4'-Hydroxy-4-biphenyl carbonitrile (332 mg, 1.702 mmol), acetone (20 mL) and K<sub>2</sub>CO<sub>3</sub> (392 mg, 2.836 mmol) was stirred for 15 min. Then compound **4** (200 mg, 0.142 mmol) was added into it. A pinch of KI was also added to the reaction mixture. After that it was heated at 65 °C for 24 hours followed by extraction with chloroform and then purified by column chromatography using DCM/ethylacetate (yield 20%). <sup>1</sup>H NMR (CD<sub>2</sub>Cl<sub>2</sub>, 400 MHz, ppm): δ 7.68-7.61 (m, 24H, ArH from biphenyl), 7.53-7.50 (m, 12H, ArH from biphenyl), 7.32 (s, 3H, ArH from truxene), 7.23 (s, 3H, ArH from truxene), 7.00-6.96 (m, 12H, ArH from biphenyl), 4.21-4.14 (m, 12H, ArOCH<sub>2</sub>), 4.07-4.01 (m, 12H, CH<sub>2</sub> from truxene), 3.91 (s, 6H, CH<sub>2</sub> from truxene), 2.01-1.88 (m, 24H, alkyl chain), 1.71-1.63 (m, 24H, alkyl chain). Figure 1 represents the <sup>1</sup>H NMR spectra of compound **5**. <sup>13</sup>C NMR (CD<sub>2</sub>Cl<sub>2</sub>, 100 MHz, ppm): δ 159.77, 148.68, 148.56, 144.89, 136.81, 136.74, 134.61, 132.99, 132.53, 131.06, 128.23, 126.84, 118.99, 114.92, 111.02, 109.99, 108.02, 69.59, 69.41, 68.05, 68.02, 35.82, 29.6459, 29.53, 29.32, 29.29, 26.07, 26.01, 25.96, 25.89. IR (ν<sub>max</sub>/cm<sup>-1</sup>): 2922.56, 2853.47, 2360.69, 2222.72, 2038.69, 1600.71, 1578.83, 1522.17, 1492.08, 1466.36, 1372.91, 1289.99, 1248.49, 1204.39, 1177.84, 1097.55, 1059.78, 1030.76, 998.80, 849.15, 819.11, 658.87. HRMS (Maldi-MS): *m/z* (C<sub>141</sub>H<sub>132</sub>N<sub>6</sub>O<sub>12</sub>) 2100.9941 (observed), 2100.9901 (calculated).



## References

1. Gupta, M.; Bala, I.; Pal, S. K. *Tetrahedron Lett.* **2014**, *55*, 5836-5840.
2. Gupta, M.; Pal, S. K. *Langmuir* **2016**, *32*, 1120-1126.
3. Gupta, M.; Gupta, S. P.; Rasna, M. V.; Adhikari, D.; Dhara, S.; Pal, S. K. *Chem. Commun.* **2017**, *53*, 3014-3017.
4. Varshney, S. K.; Monobe, H.; Shimizu, Y.; Takezoe, H.; Prasad, V. *Liq. Cryst.* **2010**, *37*, 607-615.
5. Kumar, S. *Liq. Cryst.* **2004**, *31*, 1037-1059.
6. Bisoyi, H. K.; Kumar, S. *Chem. Soc. Rev.* **2010**, *39*, 264-285.
7. Kumar, S. *Liq. Cryst.* **2005**, *32*, 1089-1113.
8. Zhao, K. Q.; Bai, X. Y.; Xiao, B.; Gao, Y.; Hu, P.; Wang, B. Q.; Zeng, Q. D.; Wang, C.; Heinrich, B.; Donnio, B. *J. Mater. Chem. C* **2015**, *3*, 11735-11746.
9. Boden, N.; Bushby, R. J.; Cammidge, A. N.; El-Mansoury, A.; Martin, P. S.; Lu, Z. *B. J. Mater. Chem.* **1999**, *9*, 1391-1402.
10. Kumar, S.; Manickam, M.; Schonherr, H. *Liq. Cryst.* **1999**, *26*, 1567-1571.
11. Maliszewskyj, N. C.; Heiney, P. A.; Josefowicz, J. Y.; Plesnivý, T.; Ringsdorf, H.; Schuhmacher, P. *Langmuir* **1995**, *11*, 1666-1674.
12. Paraschiv, I.; Giesbers, M.; Lagen, B. V.; Grozema, F. C.; Abellon, R. D.; Siebbeles, L. D. A.; Marcelis, A. T. M.; Zuilhof, H.; Sudholter, E. J. R. *Chem. Mater.* **2006**, *18*, 968-974.
13. Markovitsi, D.; Marguet, S.; Bondkowski, J.; Kumar, S. *J. Phys. Chem. B* **2001**, *105*, 1299-1306.
14. Zelcer, A.; Donnio, B.; Bourgogne, C.; Cukiernik, F. D.; Guillon, D. *Chem. Mater.* **2007**, *19*, 1992-2006.
15. Zelcer, A.; Cecchi, F.; Albore's, P.; Guillon, D.; Heinrich, B.; Donnio, B.; Cukiernik, F. D. *Liq. Cryst.* **2013**, *40*, 1121-1134.
16. Han, B.; Hu, P.; Wang, B. Q.; Redshaw, C.; Zhao, K. Q. *Beilstein J. Org. Chem.* **2013**, *9*, 2852-2861.
17. Janietz, D.; Praefcke, K.; Singer, D. *Liq. Cryst.* **1993**, *13*, 247-253.



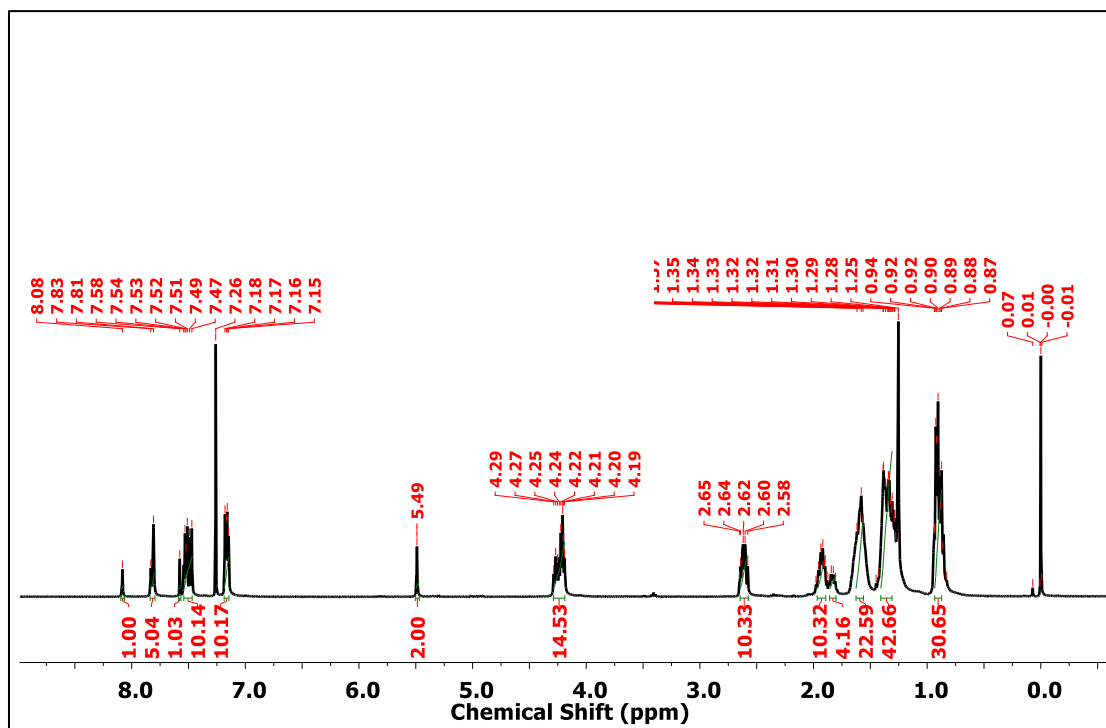
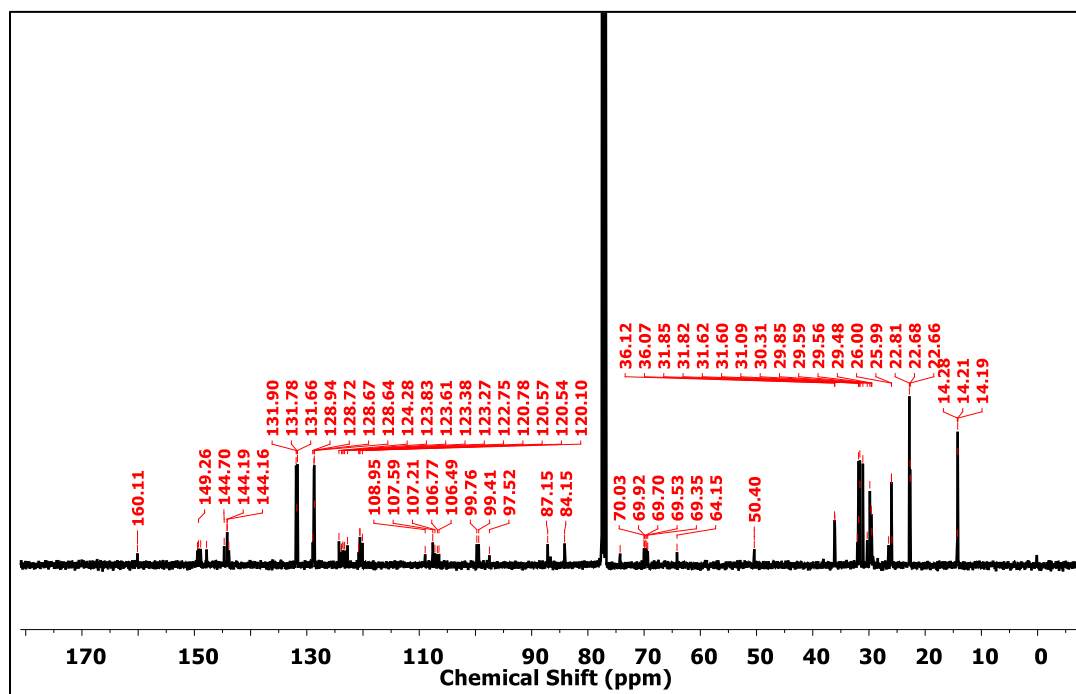
18. Kouwer, P. H. J.; Mehl, G. H.; Picken, S. J. *Mol. Cryst. Liq. Cryst.* **2004**, *411*, 387-396.
19. Kim, J.; Cho, S.; Cho, B.-K. *Chem. Eur. J.* **2014**, *20*, 12734-12739.
20. Park, S.; Cho, B.-K. *Soft Matter* **2015**, *11*, 94-101.
21. Mischler, S.; Guerra, S.; Deschenaux, R. *Chem. Commun.* **2012**, *48*, 2183-2185.
22. Nguyen, T. T.; Albert, S.; Nguyen, T. L. A.; Deschenaux, R. *RSC Adv.* **2015**, *5*, 27224-27228.
23. Fedeli, E.; Lancelot, A.; Serrano, J.-L.; Calvo, P.; Sierra, T. *New J. Chem.* **2015**, *39*, 1960-1967.
24. Guerra, S.; Iehl, J.; Holler, M.; Peterca, M.; Wilson, D. A.; Partridge, B. E.; Zhang, S.; Deschenaux, R.; Nierengarten, J.-F.; Percec, V. *Chem. Sci.* **2015**, *6*, 3393-3401.
25. Krikorian, M.; Liu, S.; Swager, T. M. *J. Am. Chem. Soc.* **2014**, *136*, 2952-2955.
26. Yu, W. H.; Chen, C.; Hu, P.; Wang, B. Q.; Redshaw, C.; Zhao, K. Q. *RSC Adv.* **2013**, *3*, 14099-14105.
27. Zhao, K. Q.; Bai, Y. F.; Hu, P.; Wang, B. Q.; Shimizu, Y. *Mol. Cryst. Liq. Cryst.* **2009**, *509*, 819-830.
28. Yu, W. H.; Nie, S. C.; Bai, Y. F.; Jing, Y.; Wang, B. Q.; Hu, P.; Zhao, K. Q. *Sci. China: Chem.* **2010**, *53*, 1134-1141.
29. Bai, Y. F.; Bao, L.; Hu, P.; Wang, B. Q.; Redshaw, C.; Zhao, K. Q. *Liq. Cryst.* **2013**, *40*, 97-105.
30. Bai, Y. F.; Zhao, K. Q.; Hu, P.; Wang, B. Q.; Redshaw, C. *Curr. Org. Chem.* **2013**, *17*, 871-885.
31. Beltran, E.; Garzoni, M.; Feringan, B.; Vancheri, A.; Barbera, J.; Serrano, J. L.; Pavan, G. M.; Gimenez, R.; Sierra, T. *Chem. Commun.* **2015**, *51*, 1811-1814.
32. Umesh, C. P.; Gangarapu, S.; Marcelis, A. T. M.; Zuilhof, H. *Liq. Cryst.* **2014**, *41*, 1862-1872.
33. Cho, B.-K.; Kim, S.-H. *Soft Matter* **2014**, *10*, 553-559.
34. Park, S.; Ryu, M.-H.; Shin, T. J.; Cho, B.-K. *Soft Matter* **2014**, *10*, 5804-5809.
35. Ryu, M. H.; Choi, J. W.; Kim, H. J.; Park, N.; Cho, B. K. *Angew. Chem. Int. Ed.* **2011**, *50*, 5737-5740.

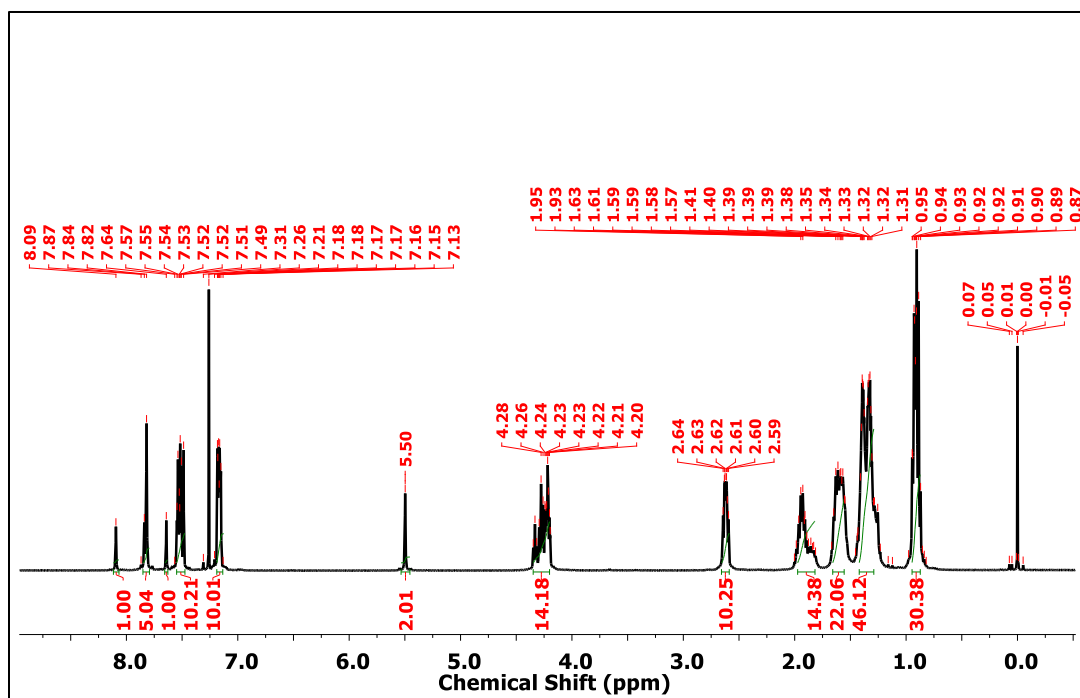
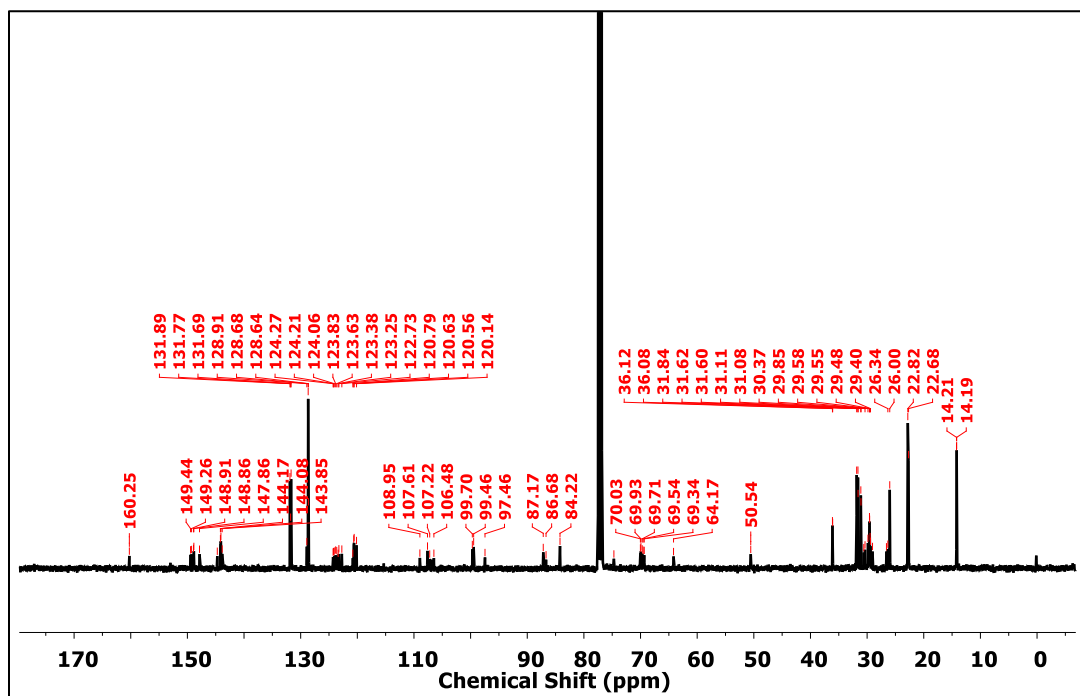
36. Feringa, B.; Romero, P.; Serrano, J. L.; Giménez, R.; Sierra, T. *Chem. Eur. J.* **2015**, *21*, 8859-8866.
37. Xiong, J. F.; Luo, S. H.; Huo, J. P.; Liu, J. Y.; Chen, S. X.; Wang, Z. Y. *J. Org. Chem.* **2014**, *79*, 8366-8373.
38. Xu, Y. Y.; Jiang, H.; Zhang, Q. J.; Wang, F.; Zou, G. *Chem. Commun.* **2014**, *50*, 365-367.
39. Krikorian, M.; Liu, S.; Swager, T. M. *J. Am. Chem. Soc.* **2014**, *136*, 2952-2955.
40. Kouwer, P. H. J.; Jager, W. F.; Mijs, W. J.; Picken, S. J. *J. Mater. Chem.* **2003**, *13*, 458-469.
41. Fornasier, R.; Tornatore, M.; Chapoy, L. L. *Liq. Cryst.* **1990**, *8*, 787-796.
42. Janietz, D.; Festag, R.; Schmidt, C.; Wendorff, J. H. *Liq. Cryst.* **1996**, *20*, 459-467.
43. Kranig, W.; Boeffel, C.; Spiess, H. W.; Karthaus, O.; Ringsdorf, H.; Wüstefeld, R. *Liq. Cryst.* **2006**, *8*, 375-388.
44. Bengs, H.; Ebert, M.; Karthaus, O.; Kohne, B.; Praefcke, K.; Ringsdorf, H.; Wendorff, J. H.; Wüstefeld, R. *Adv. Mater.* **1990**, *3*, 141-144.
45. Janietz, D.; Praefcke, K.; Singer, D. *Liq. Cryst.* **1993**, *13*, 247-253.
46. Gowda, A.; Jacob, L.; Singh, D. P.; Douali, R.; Kumar, S. *ChemistrySelect* **2018**, *3*, 6551.
47. Zhao, K. Q.; An, L. L.; Zhang, X. B.; Yu, W. H.; Hu, P.; Wang, B. Q.; Xu, J.; Zeng, Q. D.; Monobe, H.; Shimizu, Y.; Heinrich, B. *Chem. Eur. J.* **2015**, *21*, 10379-10390.
48. Iino, H.; Takayashiki, Y.; Hanna, J. I.; Bushby, R. J.; Haarer, D. *Appl. Phys. Lett.* **2015**, *87*, 192105.
49. Donnio, B.; Zhao, K. C.; Du, J. Q.; Wang, H. F.; Zhao, K. Q.; Hu, P.; Wang, B. Q.; Monobe, H.; Heinrich, B. *Chem. Asian J.* **2018**, *14*, 462-470.
50. Kondratenko, K.; Singh, D. P.; Boussoualem, Y.; Douali, R.; Legrand, C.; Daoudi, A. *J. Mol. Liq.* **2019**, *276*, 27-31.
51. Ungar, G.; Liu, F.; Zeng, X. B.; Glettner, B.; Prehm, M.; Kieffer, R.; Tschierske, C. *J. Phys.: Conf. Ser.* **2010**, *247*, 012032.
52. De, J.; Gupta, S. P.; Swayamprabha, S. S.; Dubey, D. K.; Bala, I.; Sarkar, I.; Dey, G.; Jou, J.-H.; Ghosh, S.; Pal, S. K. *J. Phys. Chem. C* **2018**, *122*, 23659-23674.

53. Bala, I.; Ming, L.; Yadav, R. A. K.; De, J.; Dubey, D. K.; Kumar, S.; Singh, H.; Jou, J.-H.; Kailasam, K.; Pal, S. K. *ChemistrySelect* **2018**, *3*, 7771-7777.
54. De, J.; Yang, W. -Y.; Bala, I.; Gupta, S. P.; Yadav, R. A. K.; Dubey, D. K.; Chowdhury, A.; Jou, J. -H.; Pal, S. K. *ACS Appl. Mater. Interfaces* **2019**, *11*, 8291-8300.
55. Imrie C. T.; Henderson P. A. *Chem. Soc. Rev.* **2007**, *36*, 2096-2124.
56. Imrie C. T.; Henderson P. A.; Yeap G. Y. *Liq. Cryst.* **2009**, *36*, 755-777.
57. Pal S. K.; Kumar S.; Seth J. *Liq. Cryst.* **2008**, *35*, 521-525.
58. Kumar S. *Liq. Cryst.* **2013**, *40*, 281-292.
59. Bisoyi H. K.; Raghunathan V. A.; Kumar S. *Chem. Commun.* **2009**, 7003-7005.
60. Setia S.; Sidiq S.; Pal S. K. *Tetrahedron Lett.* **2012**, *53*, 6446-6450.
61. Gupta, M.; Agarwal, N.; Arora, A.; Kumar, S.; Kumar, B.; Sheet, G.; Pal, S. K. *RSC Adv.* **2014**, *4*, 41371-41377.
62. Gupta M.; Pal S. K. *Liq. Cryst.* **2015**, *42*, 1250-1256.
63. Kouwer P. H. J.; Mehl G. H. *J. Am. Chem. Soc.* **2003**, *125*, 11172-11173.
64. Kouwer P. H. J.; Mehl G. H. *Angew. Chem. Int. Ed.* **2003**, *42*, 6015-6018.
65. Kouwer P. H. J.; Pourzand J.; Mehl G. H. *Chem. Commun.* **2004**, 66-67.
66. Kouwer, P. H. J.; Welch, C. J.; McRobbie, G.; Dodds, B. J.; Priest, L.; Mehl, G. H. *J. Mater. Chem.* **2004**, *14*, 1798-1803.
67. Galindo A.; Haslam A. J. *J. Chem. Phys.* **2003**, *119*, 5216-5225.
68. Fletcher I. D.; Luckhurst, G. R. *Liq. Cryst.* **1995**, *18*, 175-183.
69. Hunt, J. J.; Date, R. W.; Timimi, B. A.; Luckhurst, G. R.; Bruce, D. W. *J. Am. Chem. Soc.* **2001**, *123*, 10115-10116.
70. Imrie, C. T.; Lu, Z.; Picken, S. J.; Yildirim, Z. *Chem. Commun.* **2007**, 1245-1247.
71. Gupta, S. K.; Setia, S.; Sidiq, S.; Gupta, M.; Kumar, S. Pal, S. K. *RSC Adv.* **2013**, *3*, 12060-12065.
72. Kumar, S. *Liq. Cryst.* **2004**, *31*, 1037-1059.
73. Mo, X.; Chen, H.-Z.; Shi, M.-M.; Wang, M. *Chem. Phys. Lett.* **2006**, *417*, 457-460.
74. Mo, X.; Shi, M.-M.; Huang, J.-C.; Wang, M.; Chen, H.-Z. *Dyes Pigm.* **2008**, *76*, 236-242.
75. Saidi-Besbes, S.; Grelet, E.; Bock, H. *Angew. Chem. Int. Ed.* **2006**, *45*, 1783-1786.

76. Wolarz, E.; Mykowska, E.; Martyński, T.; Stolarski, R. *J. Mol. Struct.* **2009**, 929, 79-84.
77. Stolarski, R.; Fiksiński, K. *Dyes Pigm.* **1994**, 24, 295-303.
78. Setia, S.; Soni, A.; Gupta, M.; Sidiq, S.; Pal, S. K. *Liq. Cryst.* **2001**, 40, 1364-1372.
79. Murschell, A. E.; Sutherland, T. C. *Langmuir* **2010**, 26, 12859-12866.
80. Prasad, V.; Roy, A.; Nagaveni, N. G.; Gayathri, K. *Liq. Cryst.* **2011**, 38, 1301-1314.
81. Goubard F.; Dumur F. *RSC Adv.* **2015**, 5, 3521-3551.
82. Destrade, C.; Gasparoux, H.; Babeau, A.; Tinh, N. H.; Malthete, *Mol. Cryst. Liq. Cryst.* **1981**, 67, 37-47.
83. Foucher P.; Destrade C.; Tinh N. H. *Mol. Cryst. Liq. Cryst.* **1984**, 108, 219-229.
84. Sandström, D.; Nygren, M.; Zimmermann, H.; Maliniak, A. *J. Phys. Chem.* **1995**, 99, 6661-6669.
85. Warmerdam T. W.; Frenkel D.; Zijlstra J. J. *Liq. Cryst.* **1988**, 3, 149-152.
86. Warmerdam, T. W.; Nolte, R. J. M.; Drenth, W.; Van Miltenburg, J. C.; Frenkel, D.; Zijlstra, R. J. *Liq. Cryst.* **1988**, 3, 1087-1104.
87. Li, L. L.; Hu, P.; Wang, B. Q.; Yu, W. H.; Shimizu, Y.; Zhao, K. Q. *Liq. Cryst.* **2010**, 37, 499-506.
88. Ni, H. L.; Monobe, H.; Hu, P.; Wang, B. Q.; Shimizu, Y.; Zhao, K. Q. *Liq. Cryst.* **2013**, 40, 411-420.
89. Vinayakumara, D. R.; Kumar, M.; Sreekanth, P.; Philip, R.; Kumar, S. *RSC Adv.* **2015**, 5, 26596-26603.
90. Chinnapillai R.; Arava V. R.; Athukuru V. S. R., et al. Patent US872132 **2011**.
91. Chan, T. N.; Lu, Z.; Yam, W. S.; Yeap, G. Y.; Imrie, C. T. *Liq. Cryst.* **2012**, 39, 393-402.
92. Lee, H. C.; Lu, Z.; Henderson, P. A.; Achard, M. F.; Mahmood, W. A. K.; Yeap, G. Y.; Imrie, C. T. *Liq. Cryst.* **2012**, 39, 259-268.
93. Bala, I.; Gupta, S. P.; De, J.; Pal, S. K. *Chem. Eur. J.* **2017**, 23, 12767-12778.

## Appendix III

Figure A1. <sup>1</sup>H NMR spectrum of compound 8a.Figure A2. <sup>13</sup>C NMR spectrum of compound 8a.

Figure A3. <sup>1</sup>H NMR spectrum of compound **8b**.Figure A4. <sup>13</sup>C NMR spectrum of compound **8b**.

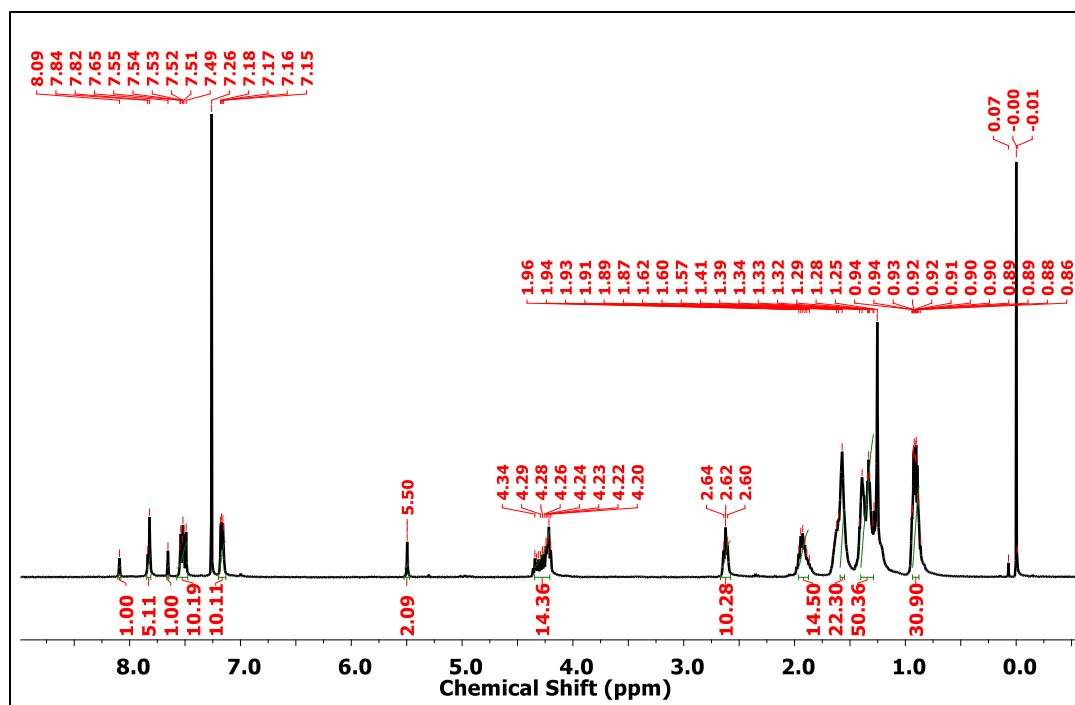


Figure A5. <sup>1</sup>H NMR spectrum of compound **8c**.

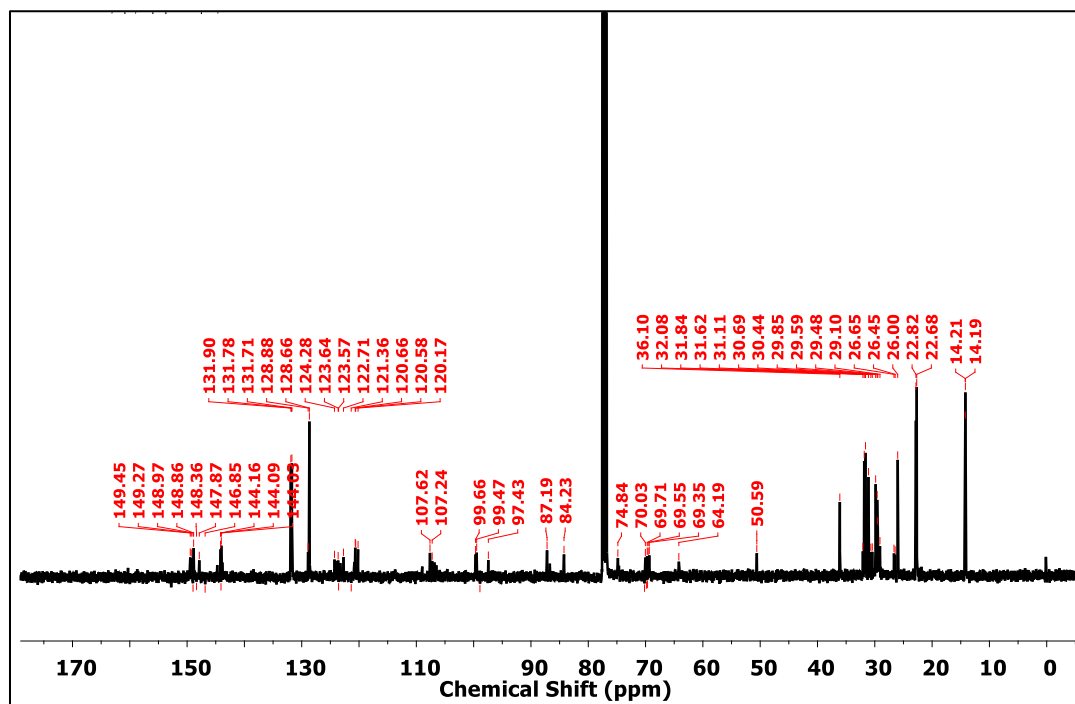


Figure A6. <sup>13</sup>C NMR spectrum of compound **8c**.

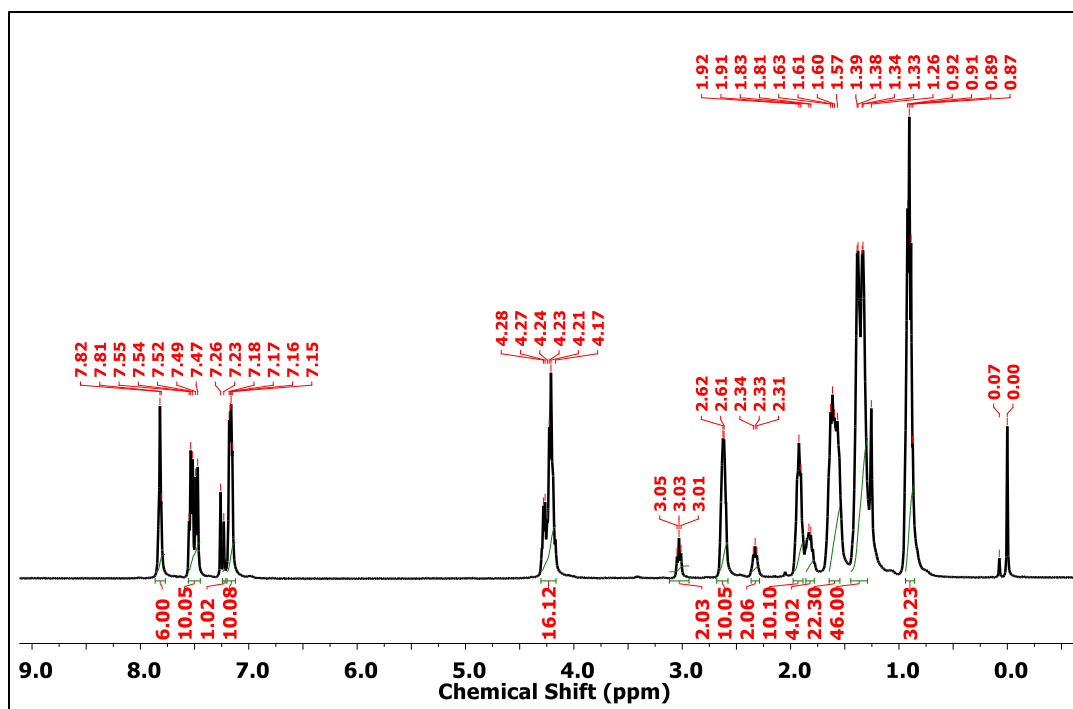


Figure A7. <sup>1</sup>H NMR spectrum of compound 9a.

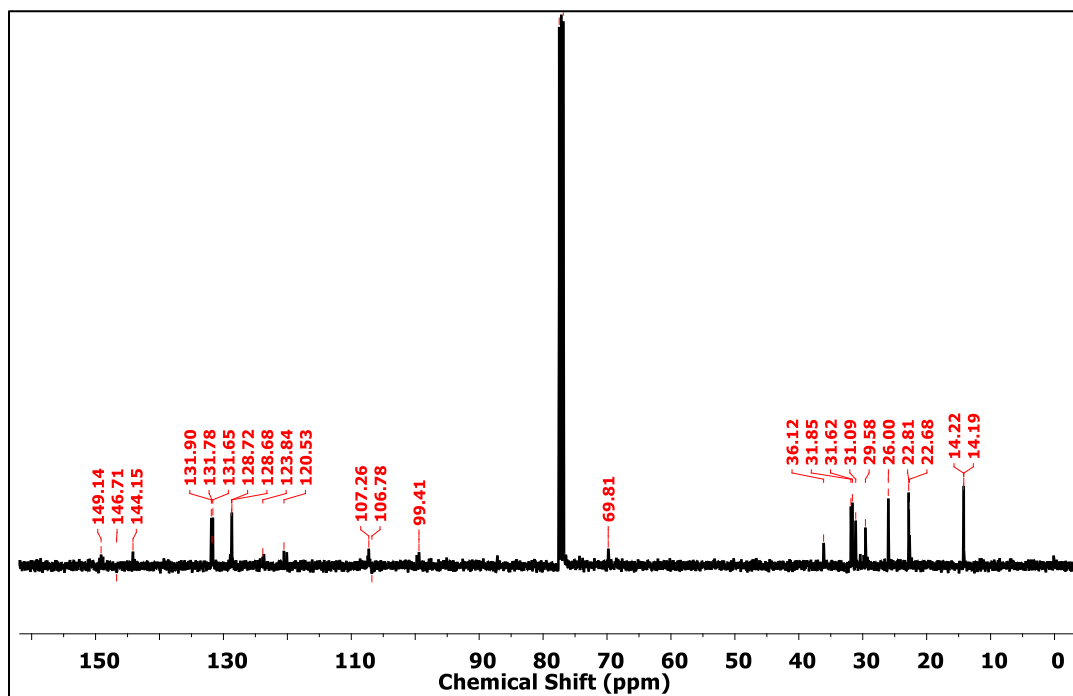


Figure A8. <sup>13</sup>C NMR spectrum of compound 9a.



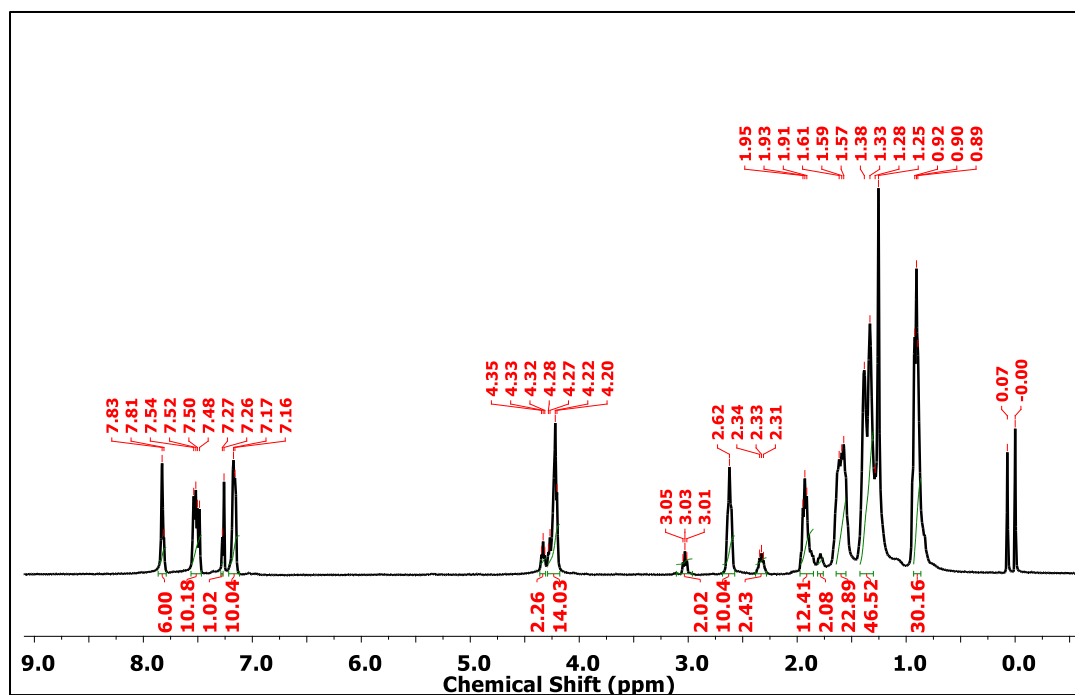


Figure A9. <sup>1</sup>H NMR spectrum of compound 9b.

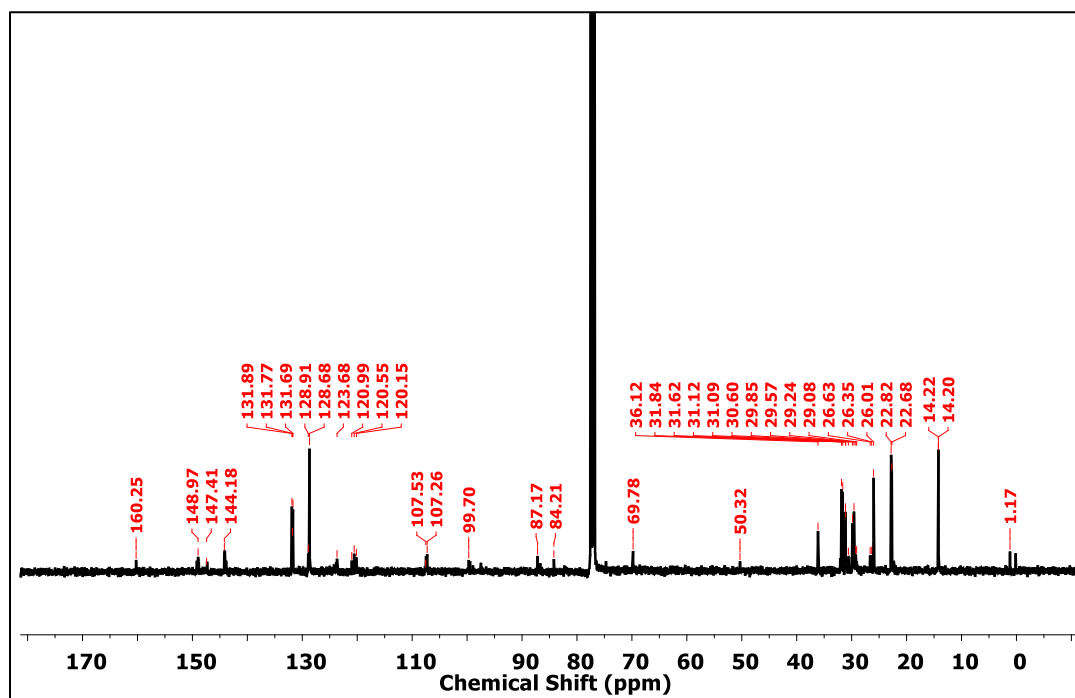
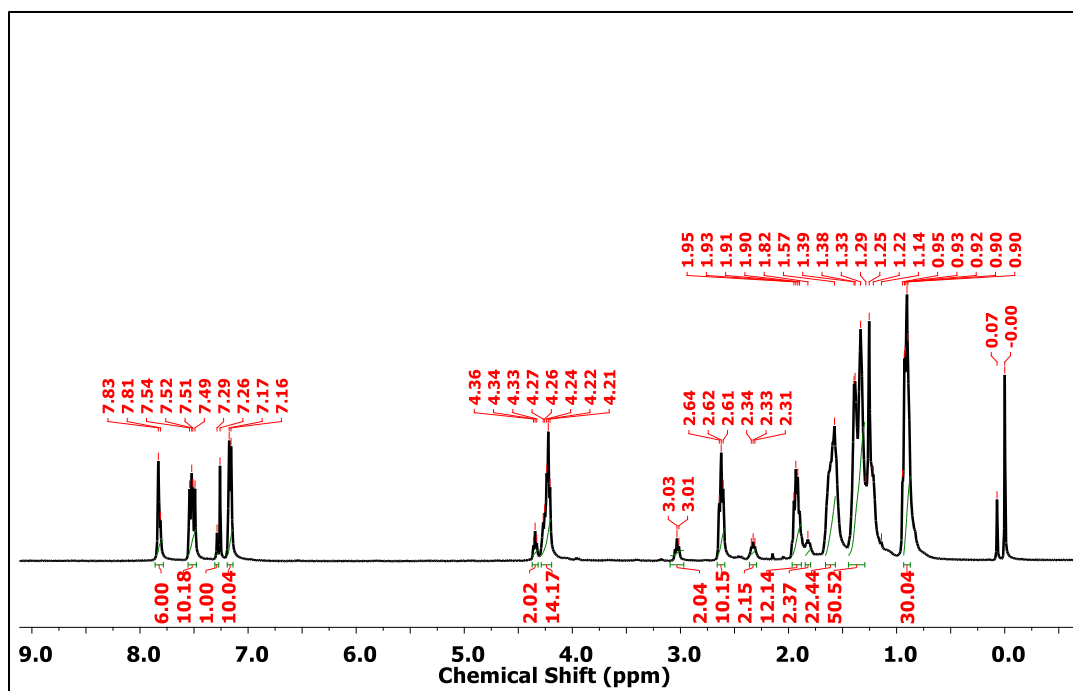
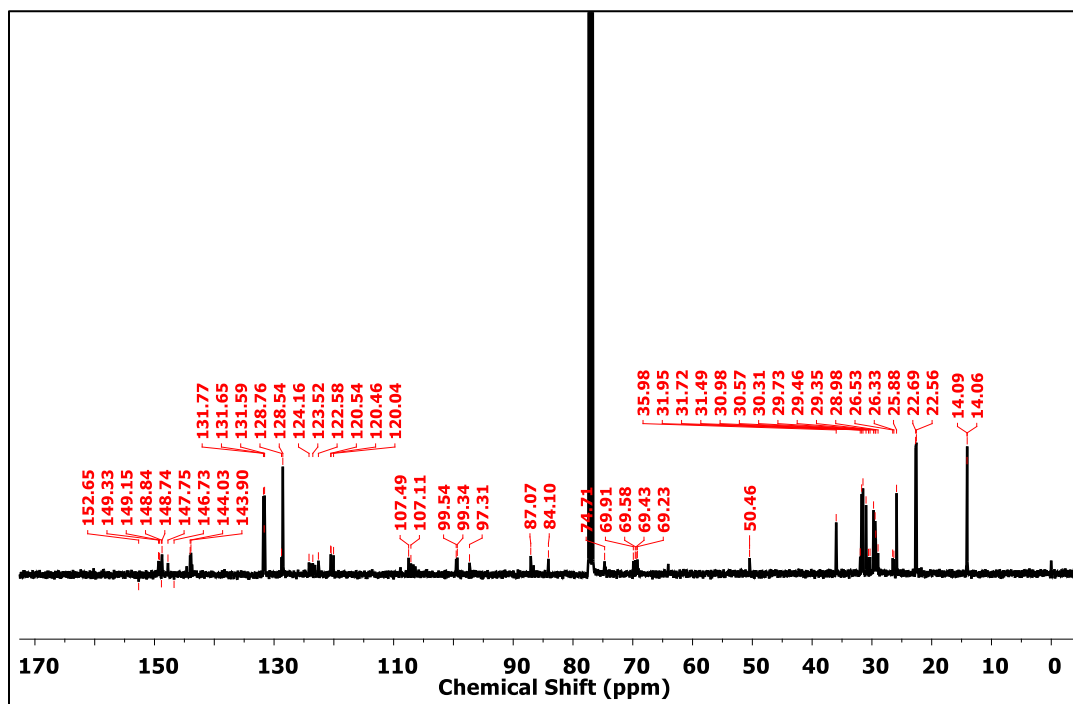
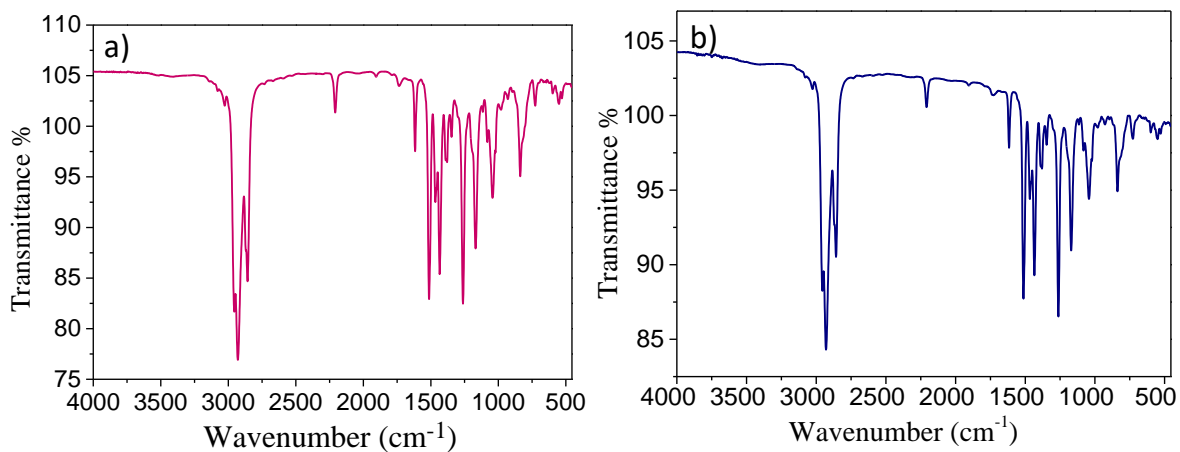
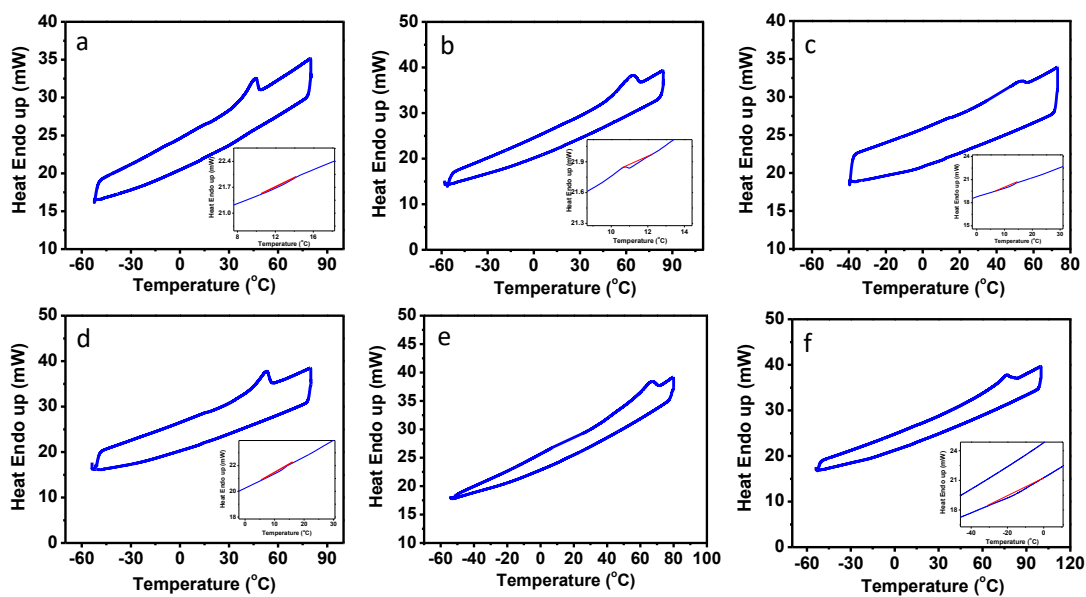


Figure A10. <sup>13</sup>C NMR spectrum of compound 9b.

Figure A11. <sup>1</sup>H NMR spectrum of compound 9c.Figure A12. <sup>13</sup>C NMR spectrum of compound 9c.



**Figure A13.** FT-IR spectra of compounds **8a** and **9a**, respectively.



**Figure A14.** DSC thermogram for the pure series of compounds (a) **8a**; (b) **8b**; (c) **8c**; (d) **9a**; (e) **9b**; (f) **9c**, recorded with the scan rate of 10 °C/ min.

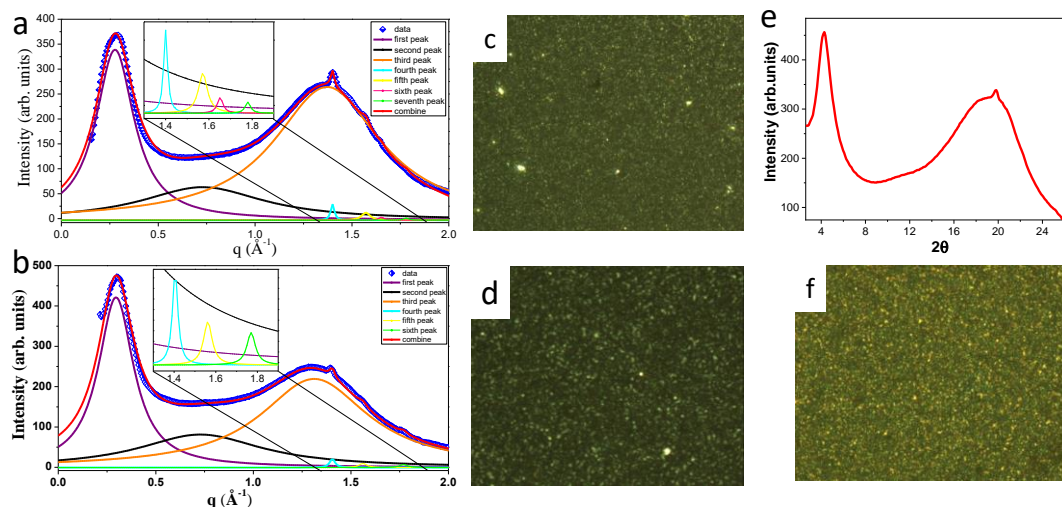


**Figure A15.** X-Ray diffraction pattern for the pure compounds: (a)  $N_C$  phase at 10.0 °C for **8a**; (b)  $N_C$  phase at 5.0 °C for **9a**; (e) smectic phase at -20.0 °C for **9c**; POM textures on upon cooling: (c) for **8a** at 10.4 °C; (d) for **9a** at 5.8 °C; (f) for **9c** at -20.0 °C, recorded with the rate of 10 °C/min.

**Table A1.** Quantum yield values of compounds **8a-c** and **9a-c**.

C	ms	MR	$Q_s^{a,b,c}$
<b>8a</b>	$10.957 \times 10^7$	$13.937 \times 10^7$	0.461
<b>8b</b>	$11.198 \times 10^7$	$13.937 \times 10^7$	0.471
<b>8c</b>	$10.358 \times 10^7$	$13.937 \times 10^7$	0.436
<b>9a</b>	$8.261 \times 10^7$	$13.937 \times 10^7$	0.348
<b>9b</b>	$9.846 \times 10^7$	$13.937 \times 10^7$	0.414
<b>9c</b>	$10.125 \times 10^7$	$13.937 \times 10^7$	0.426

<sup>a</sup>Measured in THF. <sup>b</sup>Excited at absorption maxima. <sup>c</sup>Standard Quinine sulphate ( $Q_f = 0.54$ ) in 0.1 M  $H_2SO_4$ . Abbreviation: C-Compound.

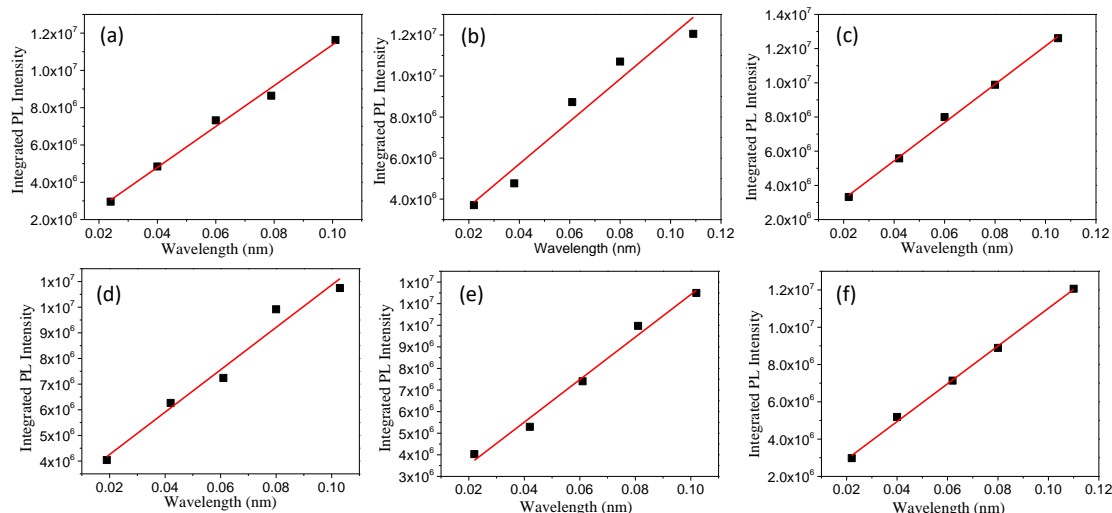


**Figure A16.** Plots of integrated photoluminescence intensity vs absorbance of compounds **8a** (a); **8b** (b); **8c** (c); **9a** (d); **9b** (e); **9c** (f) measured in HPLC chloroform excited at 337 nm.

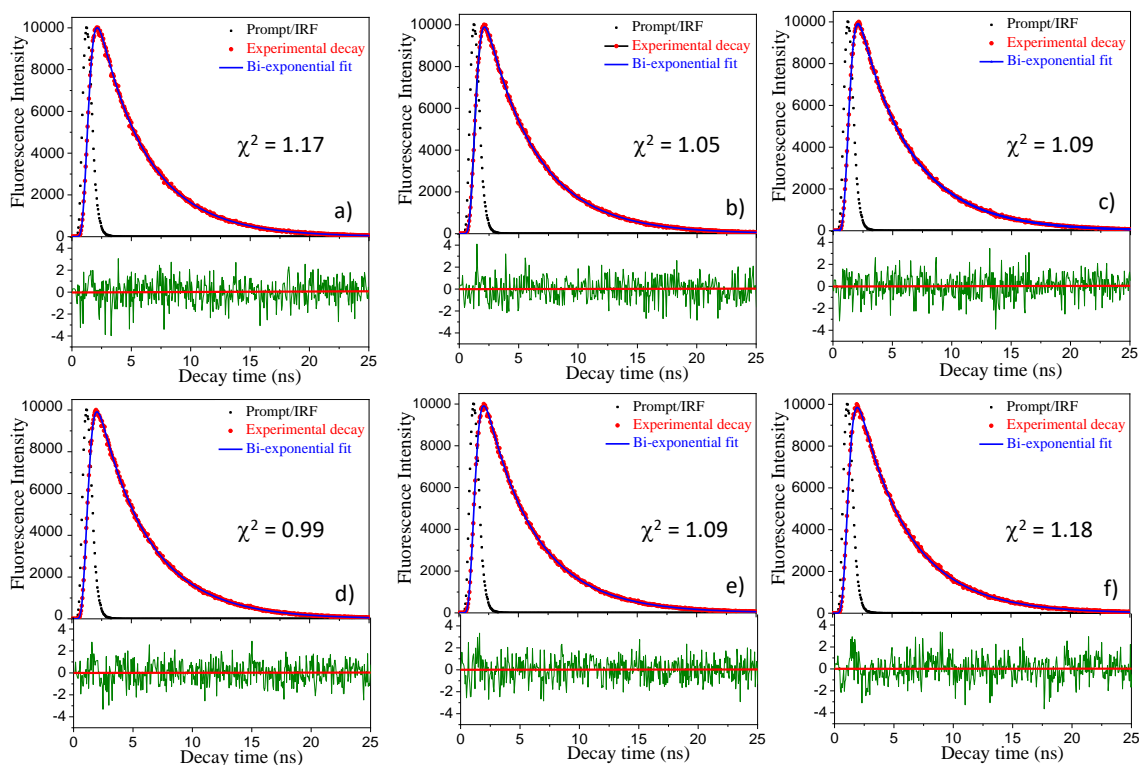


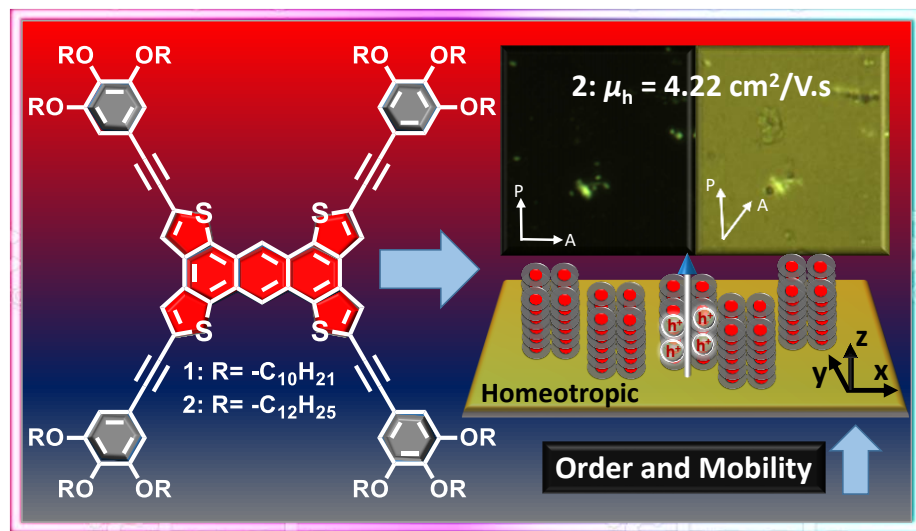
**Figure A17.** Fluorescence decay spectra (linear-linear plot) of compounds (a) **8a**; (b) **8b**; (c) **8c**; (d) **9a**; (e) **9b**; (f) **9c**; for  $\lambda_{\text{exc}} = 337$  nm &  $\lambda_{\text{ems}} = 447$  nm in micromolar chloroform solution.



## Chapter 4

### Design Strategy Enabling High Charge Transport in Room Temperature Columnar Liquid Crystalline Tetrathienoanthracene based Discotics

*This chapter illustrates a new design system that showed remarkably high hole mobility of  $4.22 \text{ cm}^2 \text{ V}^{-1} \text{ s}^{-1}$  at room temperature when used in space-charge limited current (SCLC) devices. Our strategy was to use a new core fragment for DLCs namely, tetrathienoanthracene (TTA) attached to which are four tri-alkoxybenzene units via alkynyl spacers which results in the formation of room temperature columnar phase. Strong co-facial interactions ( $\pi$ - $\pi$ ,  $S \cdots S$ ) among TTA core along with a high tendency of one of its derivatives to align homeotropically over a large area in SCLC cells contributed to the top-class charge carrier mobility.*



Reproduced/Adapted from (Bala, I.; De, J.; Gupta, S. P.; Singh, H.; Pandey, U. K.; Pal, S. K. *Chem. Commun.* **2020**, 56, 5629-5632) with permission from The Royal Society of Chemistry.





## 4.1 Introduction

Significant advances have been made in the engineering of discotic materials, however, the development of highly efficient, stable and inexpensive hole-transporting materials suffers intriguing challenges. The advancement of high-performance organic semiconducting devices at low cost demands the synergy of various parameters such as the rational design of electroactive materials coupled with cost-effectiveness and easy processability of large-area devices.<sup>1,2</sup> The crucial factor in structural design is to regulate the molecular organization by incorporating highly planar  $\pi$ -conjugated scaffolds to achieve high charge carrier mobilities.<sup>3</sup> The introduction of alkyl chains in the  $\pi$ -conjugated motifs not only provides the ease of fabrication by low-cost solution-processable techniques but also plays a pivotal role in controlling the molecular self-assembly and thin-film morphology.<sup>4,5</sup> Discotic liquid crystals (DLCs), having a supramolecular columnar (Col) architecture, can act as appropriate candidates in devices as efficient charge transporting materials due to strong  $\pi$ - $\pi$  interactions among the discs in columns.<sup>6-9</sup> Besides that, peripheral alkyl chains connected to the rigid aromatic core enable the devices to be a solution or melt processable.<sup>10-12</sup> DLC systems inherently endowed with self-healing properties are advantageous with respect to fragile single/polycrystalline conjugated systems in flexible devices. In DLCs, the preferred strategy that results in high mobility is associated with an enhanced intermolecular order within the  $\pi$ -stacks in discs ( $\pi$ - $\pi$  interactions),<sup>13</sup> which can be further amplified by introducing additional noncovalent interactions such as S $\cdots$ S, van der Waals and H-bonding.<sup>13-15</sup> Another way to improve the 1-D migration of charge carriers is by controlling the orientations of the columns macroscopically with more defined conducting channels.<sup>16,17</sup>

In recent years, thiophene fused aromatic cores drive attention because of their potential to be used as mesogenic discotic cores with the ability of charge carrier transport (Figure 4.1).<sup>18-23</sup> There are many rod-shaped liquid crystals (LCs) incorporated thiophene heterocycles are reported in the literature<sup>24-31</sup> but few examples of the same in DLCs<sup>18-23</sup> are known. Recently, Donnio *et al.* reported benzothienobenzothiophene cored Col LC (**3**) and measured charge carrier mobility of the order of  $10^{-3} \text{ cm}^2 \text{ V}^{-1} \text{ s}^{-1}$  by TOF method in the temperature range of 100-230 °C in the mesophase.<sup>18</sup> Board-shaped thiophene fused DLCs (**4** and **5**) enabling hole transport values in the range of  $10^{-3}$  to  $10^{-2} \text{ cm}^2 \text{ V}^{-1} \text{ s}^{-1}$  are also reported by the same group.<sup>19</sup>

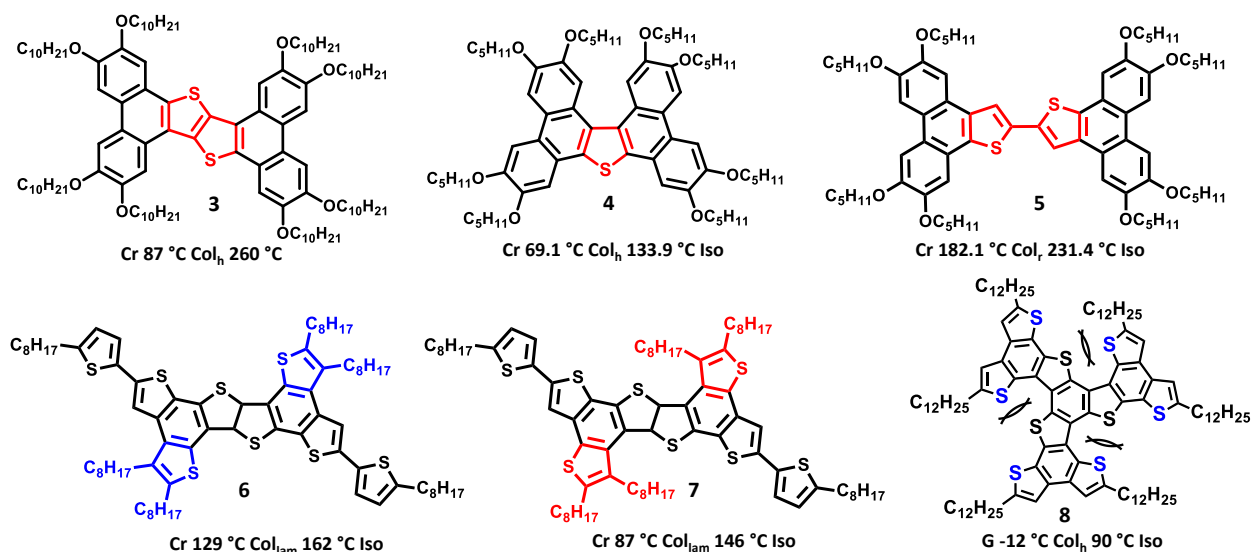


**Figure 4.1** Thiophene based Col DLCs studied as charge transport systems, along with the phase transition temperatures observed on heating.

Dang et al. measured the charge transport mobilities in the isomeric fused thiophene derivatives **6** and **7** and measured OFET mobility of  $1.7 \times 10^{-4} \text{ cm}^2 \text{ V}^{-1} \text{ s}^{-1}$  for **6** and  $3.5 \times 10^{-4} \text{ cm}^2 \text{ V}^{-1} \text{ s}^{-1}$  for **7** at room temperature.<sup>32</sup> Aida's group reported propeller-shaped fused oligothiophene derivative **8**.<sup>33</sup> The electronic mobilities of the LC derivative (**8**) was evaluated by TOF method which showed a significant amount of balanced ambipolar charge transport with hole and electron mobility of  $0.02 \text{ cm}^2 \text{ V}^{-1} \text{ s}^{-1}$  and  $0.03 \text{ cm}^2 \text{ V}^{-1} \text{ s}^{-1}$ .

## 4.2 Objectives

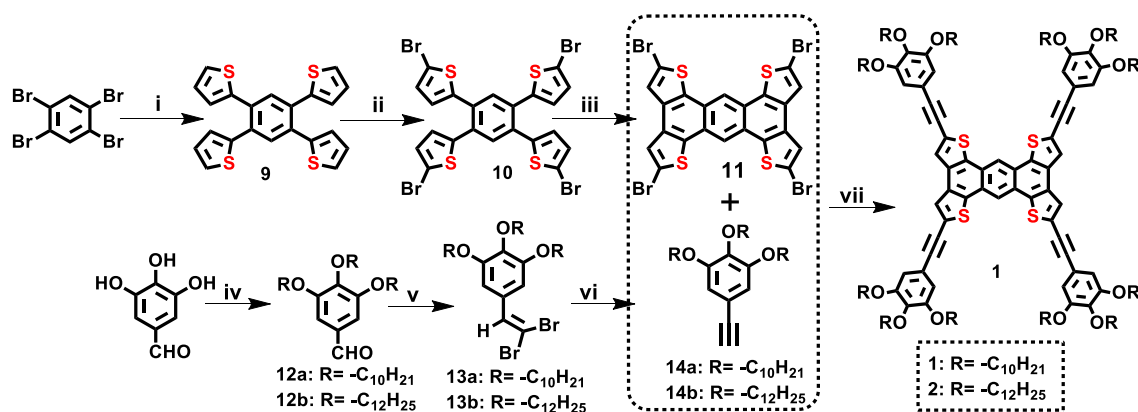
In recognition of the fact that fused systems are known to enjoy increased stability together with a more efficient conjugation, here, we employed a molecular design (**1–2**) consisting of a TTA core connected to four tri-alkoxybenzene peripheral groups *via* ethynyl spacers. The design is motivated by the following two goals. First, the inclusion of multiple S...S interactions coupled with  $\pi$ - $\pi$  stacking in TTA derivatives could provide an effective spatial overlap of the electronic wave functions of the molecules in discs and may lead to excellent hole-carrier mobilities.<sup>26–30</sup> In addition, by varying the lateral alkyl chains, the self-assembly of the Col phase can be controlled and thus so can the overall electronic properties of the system.<sup>9</sup> Second, the presence of triple bond spacers will provide extended conjugation over the whole molecule and at the same time can reduce the stacking distances favourable for high charge

transport.<sup>13,39,40</sup> The materials reported in this paper show homeotropic Col ordering at room temperature over a macroscopic area induced by boundary interfaces, extremely warranted from a device point of view. When employed in SCLC devices, maximum hole mobility ( $\mu_h$ ) of  $4.13 \times 10^{-2} \text{ cm}^2 \text{ V}^{-1} \text{ s}^{-1}$  and  $4.22 \text{ cm}^2 \text{ V}^{-1} \text{ s}^{-1}$  for **1** and **2**, respectively, was observed at ambient temperature. The  $\mu_h$  value of  $4.22 \text{ cm}^2 \text{ V}^{-1} \text{ s}^{-1}$  is remarkable and 2 orders higher mobility than previously reported thiophene-based DLCs.

## 4.3 Results and discussions

### 4.3.1 Synthesis and characterization

The synthetic scheme is shown in Scheme 4.1. For the synthesis of target materials **1-2**, the synthetic process commenced from the four-fold Stille coupling of 1,2,4,5 tetrabromobenzene with 2-(tributylstannyl)thiophene which results in the formation of tetrathiophene substituted product **9**.<sup>35</sup> The bromination of compound **9** at four positions using N-bromosuccinimide (NBS) as a brominating agent enables to yield compound **10** in an appropriate amount.<sup>35</sup> After that, the formation of  $\pi$ -extended derivative **11** involves the  $\text{FeCl}_3$ -mediated Scholl reaction in a good yield.<sup>35</sup> To achieve the liquid crystalline material, the tri-alkoxyethynylbenzene, **14** were chosen as the connecting unit. The synthesis of the promesogenic unit **14** was carried out by following the Corey-Fuchs reaction pathway.<sup>41</sup>



**Scheme 4.1** Materials and reagents: (i) 2-(tributylstannyl)thiophene,  $\text{PdCl}_2(\text{PPh}_3)_2$ , DMF,  $140^\circ\text{C}$ , 16h, 82%; (ii) NBS, THF, RT, 16h, 80%; (iii)  $\text{FeCl}_3$ ,  $\text{CH}_3\text{NO}_2$ , chlorobenzene, overnight, 78%; (iv)  $\text{RBr}$ ,  $\text{K}_2\text{CO}_3$ , DMF,  $80^\circ\text{C}$ , 12h, 93%; (v)  $\text{CBr}_4$ ,  $\text{PPh}_3$ , dry DCM, 5 min, 80%; (vi)  $n\text{-BuLi}$ , dry THF, 24 h, 60%; (vii)  $\text{Pd}(\text{PPh}_3)_4$ ,  $\text{CuI}$ ,  $\text{Et}_3\text{N}$ , DMF,  $110^\circ\text{C}$ , 72h, 36% for **1**, 32% for **2**.

First, the Williamson etherification of trihydroxybenzaldehyde<sup>42</sup> gives the trialkoxy-substituted benzaldehyde **12** which on reaction with  $\text{CBr}_4$  and  $\text{PPh}_3$  reagent generates the isolable dibromoalkene intermediate **13**. On treating the intermediate **13** with  $n\text{-BuLi}$  yields the terminal alkyne **14**.<sup>41</sup> Finally, the tetrabromosubstituted TTA derivative **11** and the promesogenic moiety **14** were reacted together *via* a four-fold sonogashira coupling reaction leads to the target materials in good to moderate yields. The TTA derivatives **1-2** were purified by employing column chromatography (Alumina gel) giving rise to the material **1** ( $\text{R} = \text{C}_{10}\text{H}_{21}$ ) and **2** ( $\text{R} = \text{C}_{12}\text{H}_{25}$ ) in 36% and 32% yield, respectively, and then fully characterized by  $^1\text{H}$  and  $^{13}\text{C}$  NMR, FT-IR and HRMS. The full details of synthetic procedures are given in the experimental section (Section 4.5) and NMR spectra are given in Appendix IV (Figure A1-A20, Page 247).

#### 4.3.2 Thermal behaviour (TGA, POM, DSC)

Both compounds **1-2** show good thermal stability as determined by thermogravimetric analysis (TGA), and 5% weight loss temperature ( $T_{5\%}$ ) was perceived well above the clearing temperatures of the respective compounds (Figure 4.2).

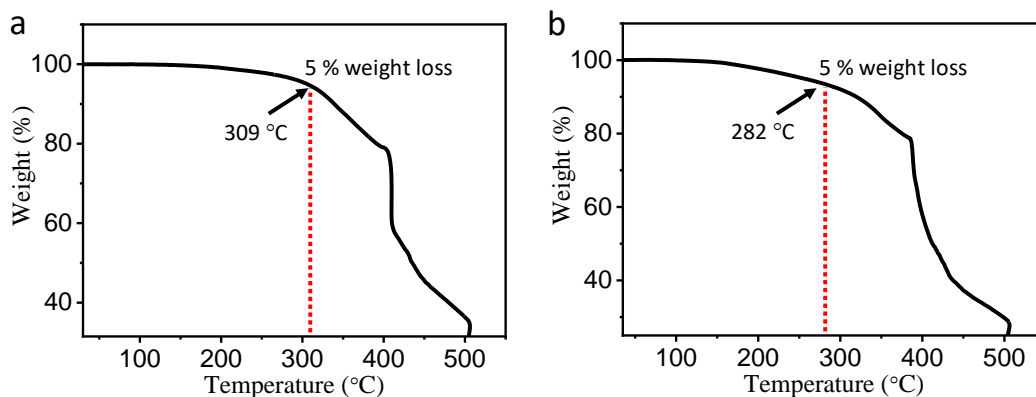


**Figure 4.2** TGA curve of compound (a) **1** and (b) **2** recorded (rate 10 °C/min) under nitrogen atmosphere. Red dotted line indicates the decomposition temperature equivalent to ~5% weight loss.

The mesomorphic properties and thermal transitions (Table 4.1) were studied by polarized optical microscopy (POM) and differential scanning calorimetry (DSC), respectively. The mesophases of **1** (Figure 4.3a,b) and **2** (Figure 4.4a,b) were identified as Col phases based on fan-shaped textures concomitant with rectilinear defects. Furthermore, as deduced from DSC,

both **1** and **2** retain LC phases down to room temperature and no crystallization was observed (Figure A21, Appendix IV, Page 257).

**Table 4.1** Phase transition temperatures of **1-2**.<sup>a</sup>

Compound	Heating	Cooling
<b>1</b>	Col <sub>r</sub> 88.2 Col <sub>h</sub> 181.2 I	I 161.3 Col <sub>h</sub> 48.4 Col <sub>r</sub>
<b>2</b>	Col <sub>r</sub> 78.7 Col <sub>h</sub> 164.7 I	I 158.6 Col <sub>h</sub> 43.5 Col <sub>r</sub>

<sup>a</sup>Transition temperature in °C (peak) from DSC data (rate: 10 °C/min).

### 4.3.3 X-ray diffraction

To understand the self-assembly behaviour of compounds **1** and **2**, variable temperature X-ray diffraction (XRD) studies were performed. The X-ray pattern of **1** at 30 °C exhibits many narrow peaks in a small-angle which could be indexed on a 2D rectangular lattice with lattice parameters  $a = 39.81$  Å,  $b = 28.66$  Å (Figure 4.3c). At a high angle, observed reflection at  $3.74$  Å ( $h_c$ ) indicates periodicity along the Col axis.

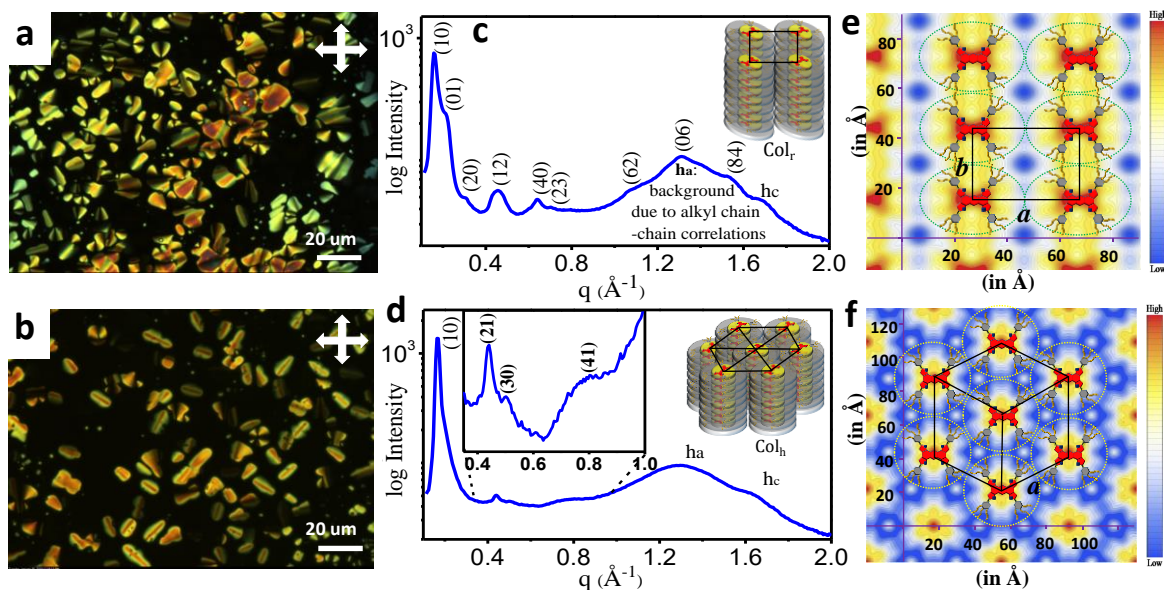


**Figure 4.3** Optical microscopic images of **1**: (a) at 42 °C (Col<sub>r</sub> phase) and (b) at 117.2 °C (Col<sub>h</sub> phase). X-Ray diffraction pattern of **1**: (c) at 30 °C (Col<sub>r</sub> phase) and (d) at 95 °C (Col<sub>h</sub> phase) obtained on cooling from the isotropic liquid. Electron density maps of compound **1** in (e) Col<sub>r</sub>

and (f) Col<sub>h</sub> phase. Red color signifies the high electron density region and deep blue is the lowest.

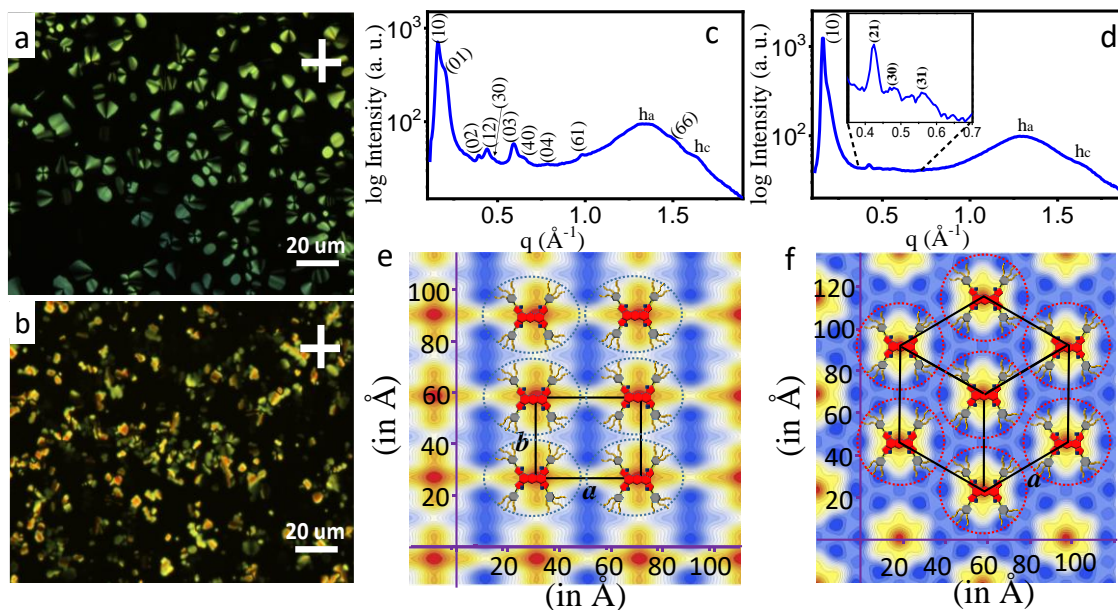


**Figure 4.4** Microscopic texture of compound **2** sandwiched between normal glass slides: (a) at 117.1 °C and (b) at 49.9 °C recorded with the rate of 10 °C/min under crossed polarizer (magnification  $\times 500$ ). X-Ray diffraction pattern of **2** (c) at 30 °C in columnar rectangular (Col<sub>r</sub>) phase and (d) at 90 °C in columnar hexagonal (Col<sub>h</sub>) phase. EDMs of compound **2** in (e) Col<sub>r</sub> phase at temperature 30 °C and (f) Col<sub>h</sub> phase at temperature 90 °C. Red color in the EDM corresponds to the high electron density region while the lowest electron density areas are represented by deep blue color. Rectangle in Figure (e) draws the unit cell of Col<sub>r</sub> phase with lattice parameter '*a*' & '*b*' and hexagon in Figure (f) displayed the conventional unit cell of Col<sub>h</sub> phase with lattice parameter '*a*'. (e) & (f) exhibit the corresponding molecular arrangement in the Col<sub>r</sub> and Col<sub>h</sub> phase, respectively.

At higher temperature (95 °C) in the small-angle region, four peaks were observed with *d*-spacing in ratios  $1:1/\sqrt{3}:1/\sqrt{9}:1/\sqrt{21}$  which are characteristics of a hexagonal lattice and correspond to the reflections (10), (21), (30) and (41), respectively (Figure 4.3d). Compound **2** also showed a similar diffraction pattern i.e. Col<sub>r</sub> phase at lower temperature and Col<sub>h</sub> at higher (Figure 4.4c,d). The detailed diffraction data for **1** and **2** are summarized in Table 4.2. XRD lattice parameters with temperature exhibit more or less constant values in respective Col<sub>r</sub> and Col<sub>h</sub> phases of **1** and **2**; however, the value changed rapidly when transformed from



Col<sub>r</sub> to Col<sub>h</sub> phase (Figure 4.5). The calculated electron density maps (EDM)<sup>43</sup> provided a clear visualization of molecules in their respective Col lattices (Figure 4.3e,f, and Figure 4.4e,f). The variation of electron density on moving away from the central aromatic core towards the peripheral alkyl chains indicates nanosegregated Col LC phase.

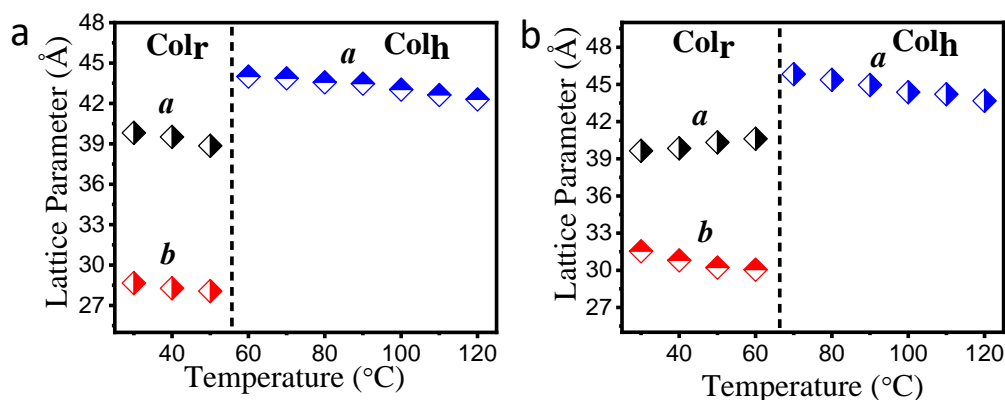


**Figure 4.5** Variation of lattice parameter of compound (a) **1** and (b) **2** with temperature (on cooling). In the Col<sub>r</sub> phase ‘a’ and ‘b’ represents the lattice parameter. In the Col<sub>h</sub> phase ‘a’ shows the inter-columnar separation.

**Table 4.2** Phase behaviour, Miller Indices, lattice constants and *d*-spacing observed from the X-ray diffraction studies for compounds **1-2**.

Compound	Mesophase	Lattice constants (Å)	$d_{\text{obs}}^a$ (Å)	$d_{\text{cal}}^b$ (Å)	MI <sup>c</sup> (hk)	RI (Φ)(M) <sup>c</sup>
<b>1</b>	Col <sub>r</sub> at 30 °C	$a = 39.81$	39.82	39.81	10	100.00(0)(2)
		$b = 28.66$	28.66	28.66	01	30.07(0)(2)
			20.08	19.90	20	6.49(π)(2)
			13.60	13.48	12	7.42(0)(4)
			9.80	9.95	40	6.36(π)(2)
			8.88	8.61	23	5.30(0)(4)
			5.93	6.02	62	
			4.77	4.78	06	
			4.09	4.09	84	
			3.74		<b>h<sub>c</sub></b>	
	Col <sub>h</sub> at 95 °C	$a = 43.44$	37.62	37.62	10	100.00(0)(6)
			14.21	14.22	21	3.73(π)(12)
			12.54	12.54	30	3.29(0)(6)
			8.22	8.21	41	3.37(0)(12)
			4.87		<b>h<sub>a</sub></b>	
			3.85		<b>h<sub>c</sub></b>	

2	Col <sub>r</sub> at 30 °C	$a = 39.64$	39.64	39.64	10	100.00 (0)(2)
		$b = 31.54$	31.54	31.54	01	51.26(0)(2)
			15.85	15.77	02	6.02(0)(2)
			14.41	14.65	12	7.14( $\pi$ )(4)
			13.09	13.21	30	2.80(0)(2)
			10.63	10.51	03	8.12(0)(2)
			9.72	9.91	40	
			8.00	7.89	04	
			6.41	6.47	61	
			4.65		<b>h<sub>a</sub></b>	
			4.19	4.11	66	
			3.82		<b>h<sub>c</sub></b>	
	Col <sub>h</sub> at 90 °C	$a = 45.44$	39.35	39.35	10	100.00(0)(6)
			14.80	14.87	21	3.80( $\pi$ )(12)
			13.13	13.12	30	3.47(0)(6)
			10.94	10.91	31	3.39(0)(12)

<sup>a</sup> $d_{\text{obs}}$ : experimental  $d$ -spacing; <sup>b</sup> $d_{\text{cal}}$ : calculated  $d$ -spacing by using the relation for Col<sub>r</sub>:  $\frac{1}{d_{\text{cal}}^2} = \left[ \frac{h^2}{a^2} + \frac{k^2}{b^2} \right]$ ; Col<sub>h</sub>:  $\frac{1}{d_{\text{cal}}^2} = \left[ \frac{4}{3} \left( \frac{h^2 + hk + k^2}{a^2} \right) + \frac{l^2}{c^2} \right]$ ;  $h, k, l$ : Miller indices of observed reflections;  $a, b$  &  $c$ : unit cell parameters,  $h_a$ : alkyl chain-chain correlation;  $h_c$ : core-core correlation. <sup>c</sup>Abbreviations: MI- Miller Indices; RI ( $\Phi$ )(M)- Relative Intensity (Phase value)(Multiplicity).

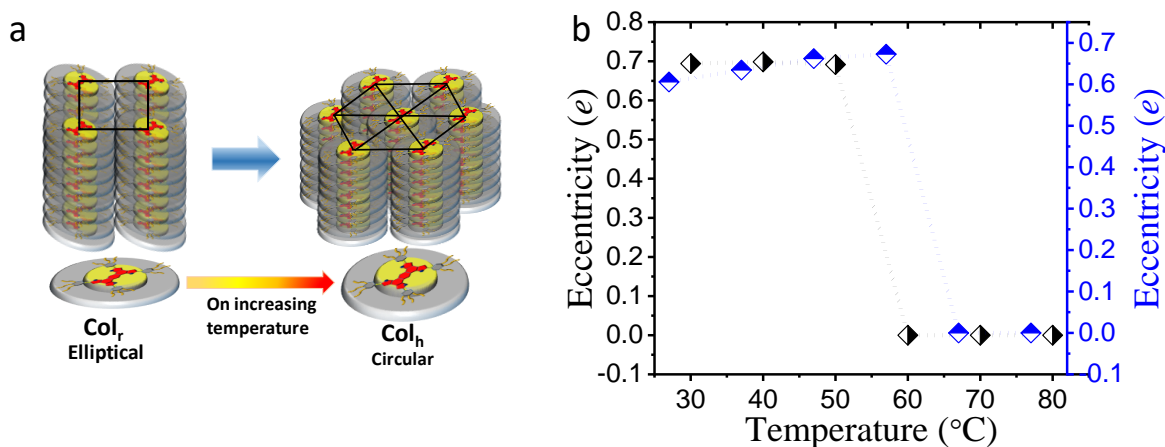


**Figure 4.6** (a) Schematic showing the switching of Col<sub>r</sub> to Col<sub>h</sub> due to the shape change of the molecule. (b) Variation of eccentricity ( $e$ ) of the compound with temperature on cooling for compound **1** (Black diamond) and **2** ((Blue diamond)). Eccentricity is calculated by assuming the elliptical shape and circular shape of the compound in Col<sub>r</sub> and Col<sub>h</sub> phase, respectively.



The EDM suggested that the shape of the Col section is better represented by elliptical in Col<sub>r</sub> phase and circular in Col<sub>h</sub> phase. To characterize uniquely its shape, eccentricity ( $e$ ) is calculated by using the value of the lattice parameter, as shown in Figure 4.6. The value of  $e$  is  $\sim 0.70$  in Col<sub>r</sub> which rapidly changes to 0 in Col<sub>h</sub> phase for both **1** and **2**. This suggests the phase transition (Col<sub>r</sub> to Col<sub>h</sub>) on increasing temperature is likely to accompany with shape transformation of a molecule from elliptical to circular. Moreover, as temperature increases, the entropy of the system increases, thereby giving rise to an average circular shape of the molecule resulting in Col<sub>h</sub> phase.<sup>43</sup>

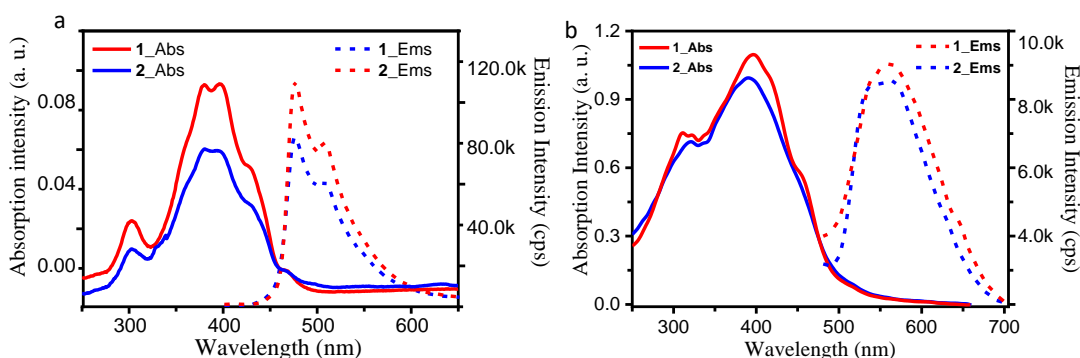


**Figure 4.7** Absorption (Abs) and emission (Ems) spectra of compounds **1** and **2** (a) in solution state (chloroform) and (b) in thin-film state.

#### 4.3.4 Photophysical, Electrochemical, and Theoretical studies

The derivatives **1-2** were tested for their absorption and emission properties in solution and in the thin-film state as well (Figure 4.7). They showed identical absorption and emission features due to the common  $\pi$ -structural skeleton. In the thin-film state, absorption and emission peaks (Table 4.3) get red-shifted and broadened relative to the solution state due to increased intermolecular interactions. To get an insight into the redox behaviour of the electroactive TTA derivatives, cyclic voltammetry was performed (Figure 4.8a,b). The voltammogram in oxidation cycle exhibits three oxidation peaks for **1** ( $E_{\text{oxd, peak potential}} = 1.47 \text{ V}, 1.93 \text{ V}, 2.31 \text{ V}$ ) and **2** ( $E_{\text{oxd, peak potential}} = 1.44 \text{ V}, 1.94 \text{ V}, 2.28 \text{ V}$ ) whereas one peak ( $E_{\text{red, peak potential}} = -1.12 \text{ V}, -1.08 \text{ V}$  for **1** and **2**, respectively) was observed in reduction cycle. The HOMO/LUMO levels were predicted at  $-5.21 \text{ eV}/-3.36 \text{ eV}$  for **1** and  $-5.27 \text{ eV}/-3.38 \text{ eV}$  for **2** as summarized in Table 4.4. The observed low-lying HOMO levels are highly favourable for the air-stability of the

**Table 4.3** Photophysical data of the TTA derivatives.

C	A <sub>solution</sub> <sup>a</sup> Peaks (nm)	E <sub>solution</sub> <sup>a,c</sup> Peaks (nm)	A <sub>solid</sub> Peaks (nm)	E <sub>solid</sub> <sup>c*</sup> Peaks (nm)
1	303, 380, 396, <sup>b</sup> 423, 469	476, 507, 545*	323, 398, <sup>b</sup> 455, 515	537, 560, 645
2	303, 380, 395, <sup>b</sup> 428, 467	475, 506, 546*	321, 390, <sup>b</sup> 454, 515	540, 563, 634

<sup>a</sup>in micromolar chloroform solution. <sup>b</sup>Excitation wavelength,  $\lambda_{\text{exc}}$ . <sup>c</sup>obtained after exciting at respective  $\lambda_{\text{exc}}$ . \*Peaks can be visualized after zooming the respective region. Abbreviation: C: Compound, A<sub>solution</sub>: Solution state absorbance, E<sub>solution</sub>: Solution state emission. A<sub>solid</sub>: Thin-film absorbance, E<sub>solid</sub>: Thin-film emission.

materials.<sup>44</sup> The calculated electrochemical bandgap was found to be 1.85 eV for **1** and 1.89 eV for **2**. Moreover, the optical bandgap was estimated (from the red absorption edge) as 2.04 eV and 2.06 eV for **1** and **2**, respectively (Table 4.4).

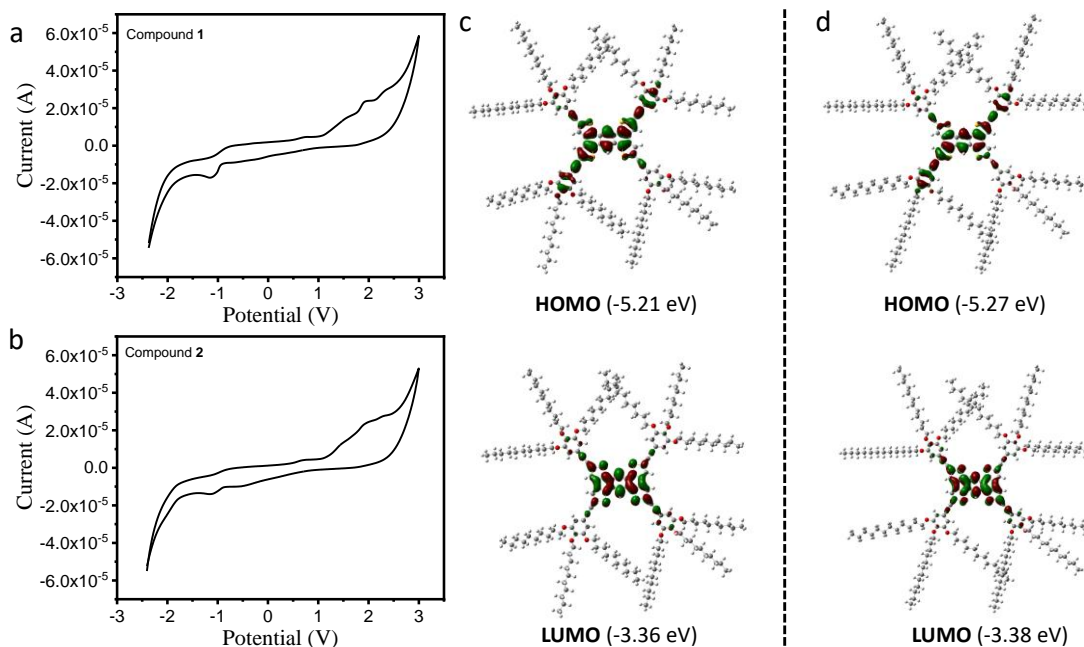


**Figure 4.8** Cyclic Voltammograms of compound (a) **1** and (b) **2** in HPLC dichloromethane solution of tetrabutylammonium hexafluorophosphate (0.1 M) performed at a scanning rate 50 mVs<sup>-1</sup>. Frontier molecular orbitals of compound (c) **1** and (d) **2** obtained by using B3LYP/6-31G (d,p) basis set.

**Table 4.4** Electrochemical properties of TTA derivatives.<sup>a</sup>

Compound	$E_{\text{red}}$ (V) <sup>b</sup>	$E_{\text{oxd}}$ (V) <sup>c</sup>	$E_{\text{LUMO}}$ (eV) <sup>d</sup>	$E_{\text{HOMO}}$ (eV) <sup>e</sup>	$\Delta E_{\text{g,CV}}$ (eV) <sup>f</sup>	$\Delta E_{\text{g,opt}}$ (eV) <sup>g</sup>
<b>1</b>	-0.89	+1.02	-3.36	-5.21	1.85	2.04
<b>2</b>	-0.86	+0.96	-3.38	-5.27	1.89	2.06

<sup>a</sup>Experimental conditions: reference electrode-Ag/AgNO<sub>3</sub> electrode, counter electrode-platinum wire electrode, working electrode-glassy carbon electrode, supporting electrolyte-tetrabutylammonium perchlorate (0.1 M). <sup>b</sup>Reduction onset potential. <sup>c</sup>Oxidation onset potential. Estimated from the formula: <sup>d</sup> $E_{\text{LUMO}} = -(4.8 - E_{1/2,\text{Fc,Fc}^+} + E_{\text{red,onset}})$  eV. <sup>e</sup> $E_{\text{HOMO}} = -(4.8 - E_{1/2,\text{Fc,Fc}^+} + E_{\text{oxd,onset}})$  eV. <sup>f</sup>Electrochemical bandgap:  $\Delta E_{\text{g,CV}} = E_{\text{LUMO}} - E_{\text{HOMO}}$ . <sup>g</sup>Optical bandgap estimated from red absorption edge.

To predict the geometries and electronic structures of **1** and **2**, density functional theory (DFT) studies (Figure 4.8c,d) were performed at B3LYP/6-31G (d,p) level. The energy minimized structures displayed a nearly flat geometry of the TTA derivatives. The HOMOs were bonding in nature and the electron density is found to be delocalized over the entire aromatic system including central core and triple bond linked peripheral groups. However, LUMOs were predominantly spread only over the core with contribution from the extended alkynyl linkers and are antibonding in nature. It can be noted that HOMOs and LUMOs of TTA DLCs are highly delocalized over the central core which is likely to increase the time-averaged overlap of molecular orbitals.<sup>45</sup> These structural aspects indicate the possibility of having excellent charge transport properties of the material (**1** and **2**) since the effective orbital overlap among aromatic cores is considered to be one of the prerequisites for high-performance semiconducting devices.<sup>45,46</sup>

### 4.3.5 Charge transport studies

Charge carrier transport properties of TTA derivatives (**1-2**) were investigated by extensively used space charge limited current (SCLC) technique.<sup>13,47-49</sup> The materials of interest were sandwiched in hole-only devices with configuration: Au/**1** or **2**/FTO following the basic Ohmic contact requirement between injecting electrode and energy level (HOMO) of material in order to extract charge (hole) mobility. The low-lying HOMOs of **1** (-5.21 eV) and **2** (-5.27 eV) favour efficient hole injection from Au electrode (work function ~ -5.10 eV) by providing Ohmic contact (low barrier) whereas significant injection barrier between LUMOs (Table 4.4)

and cathode work function (FTO  $\sim$  -4.46 eV) was maintained to block the injection of electrons. The obtained  $J$ - $V$  curves for compounds **2** and **1** at room temperature are shown in Figure 4.9e and Figure 4.10, respectively. Similar to prior reports,<sup>13,47-49</sup> charge mobility measurements for **1** and **2**, at lower voltages current showed a linear dependence (slope 1) indicating Ohmic behaviour whereas at higher applied voltages, due to injection of excess charge carriers quadratic region (slope 2) of SCLC was observed. In the SCLC regime, current solely depends on the charge mobility considering contacts as Ohmic and material to be trap free,<sup>13</sup> therefore, mobility can be extracted by fitting the obtained  $J$ - $V$  curves using Mott-Gurney equation<sup>50</sup>:

$$J = \frac{9}{8} \varepsilon_0 \varepsilon_r \mu \frac{V^2}{L^3} \quad (1)$$

where  $J$  is current density measured at applied voltage  $V$ ,  $\varepsilon_0$  is the permittivity of free space,  $\varepsilon_r$  is the dielectric constant of the material,  $\mu$  is the charge mobility of material and  $L$  is the thickness of the sample used for SCLC measurements.

The sample thickness of the effective SCLC cells was measured as 3.18  $\mu\text{m}$  for **1** and 3.14  $\mu\text{m}$  for **2** and filled from the isotropic melt *via* capillary action (followed by slow cooling to room temperature). Average hole mobility of  $4.13 \times 10^{-2} \text{ cm}^2 \text{ V}^{-1} \text{ s}^{-1}$  for **1** and  $3.42 \text{ cm}^2 \text{ V}^{-1} \text{ s}^{-1}$  for **2** was obtained with a maximum of  $4.22 \text{ cm}^2 \text{ V}^{-1} \text{ s}^{-1}$  for compound **2** (Table 4.5). Although both **1** and **2** differ only in the length of the peripheral alkyl chain, a charge mobility difference of  $\sim 2$  orders of magnitude was observed. It is well established that mobility is highly dependent on the molecular alignment,<sup>17</sup> sizes of the domain,<sup>15</sup> and the techniques<sup>16,51-53</sup> being used to extract mobility. In the SCLC technique, charge injection effectiveness from the injecting contact as well as macroscopic degree of order within the columns plays a significant role in deciding the charge mobility. Moreover, different alkyl chains length is known to induce different structural arrangements and/or morphology which results in different mobility values in organic semiconductors.<sup>4,5,15,54</sup> In order to investigate the difference in observed mobility values for **1** and **2**, POM texture of samples in SCLC cell was carefully examined. The photomicrograph of the corresponding SCLC cell (at  $90^\circ$  angle) revealed that compound **1** with lower mobility displays the birefringent areas (random planar alignment) along with partially aligned homeotropic domains (Figure 4.9a).

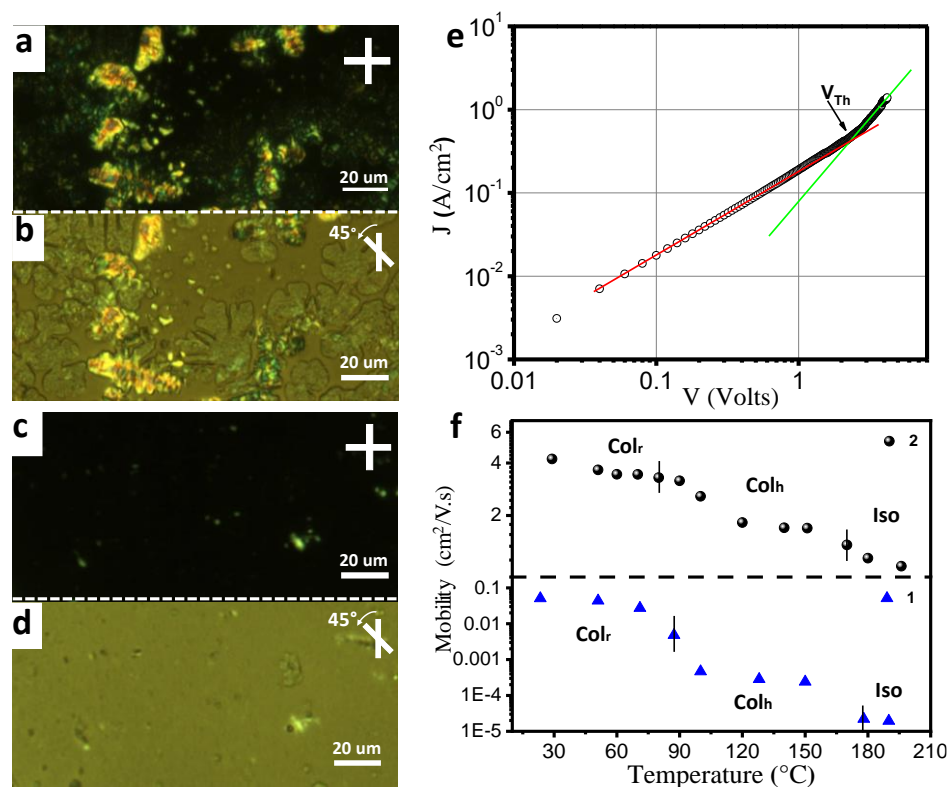


**Figure 4.9** POM image of SCLC cell under crossed polarizer: For compound **1** (3.18 μm) with crossed polarizer angle (a) at 90°, (b) 45° and for compound **2** (3.14 μm) with crossed polarizer angle (c) at 90°, (d) 45°. Image “b” shows the flower-like domains corresponding to image “a” for **1** while Image “d” displays the uniform homeotropic background for **2** which becomes visible at 45° angle between polarizer and analyzer in SCLC mobility measured cell. (e)  $J$ - $V$  curve for **2** (at 25 °C) showing ideal Ohmic (slope 1, red line) and SCLC regimes (slope 2, green line). (f) Temperature-dependent SCLC Mobility of **1** and **2** on heating.

**Table 4.5** Hole charge carrier mobility values for **1-2**.

Compound	Mobility (cm <sup>2</sup> V <sup>-1</sup> s <sup>-1</sup> ) <sup>a</sup>
<b>1</b>	(4.13 ± 0.69) × 10 <sup>-2</sup>
<b>2</b>	3.42 (4.22) ± 0.86 <sup>b</sup>

<sup>a</sup>Mobility values are an average of five samples measured in different regions. <sup>b</sup>value in bracket indicates the highest mobility value obtained at room temperature.

However, almost uniform homeotropic alignment was observed over the whole area of sample **2** showing higher mobility (Figure 4.9c). SCLC mobility is sensitive to macroscopic

orientational order and has varied up to several orders ( $\sim 1$ -5) of magnitude in homeotropically aligned (more mobility) versus non-aligned samples/areas (less mobility) in several prior reports on DLCs.<sup>17,54,55</sup>

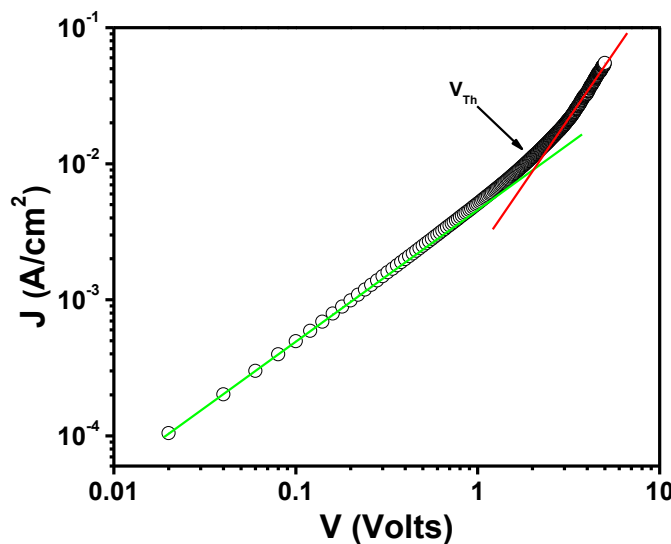


**Figure 4.10**  $J$ - $V$  characteristics for compound **1** (at 25 °C) representing ideal Ohmic and SCLC regimes.

Additionally, the grain boundaries of the homeotropic domains of the samples can be visualized upon rotating the crossed polarizers to  $45^\circ$  angle (Figure 4.9b and 4.9d). It can be noted that homeotropic domains for **1** have grown in flower-like domains (Figure 4.9b); however, the uniform homeotropic background was observed in the case of **2** (Figure 4.9d). Consistent with this finding, the grain boundaries associated with flower-like domains in case of sample **1** may act as a barrier for charge transport and might be contributing to its lower mobility values.<sup>15</sup> Apparently, the temperature-dependent mobility measurements for both **1** and **2** showed a slight variation in the mobility values from Col<sub>r</sub> to Col<sub>h</sub> phase change (Figure 4.9f), which echoes well with the previous findings.<sup>56,57</sup> It is widely acknowledged that mobility values measured in the SCLC technique are always towards their lower limit and can be further enhanced by optimizing various factors.<sup>58</sup> In order to give additional insight into the observed trend in charge mobility values of **1** and **2**, GISAXS studies (Figure 4.11a-d) were carried out to estimate their orientational order.

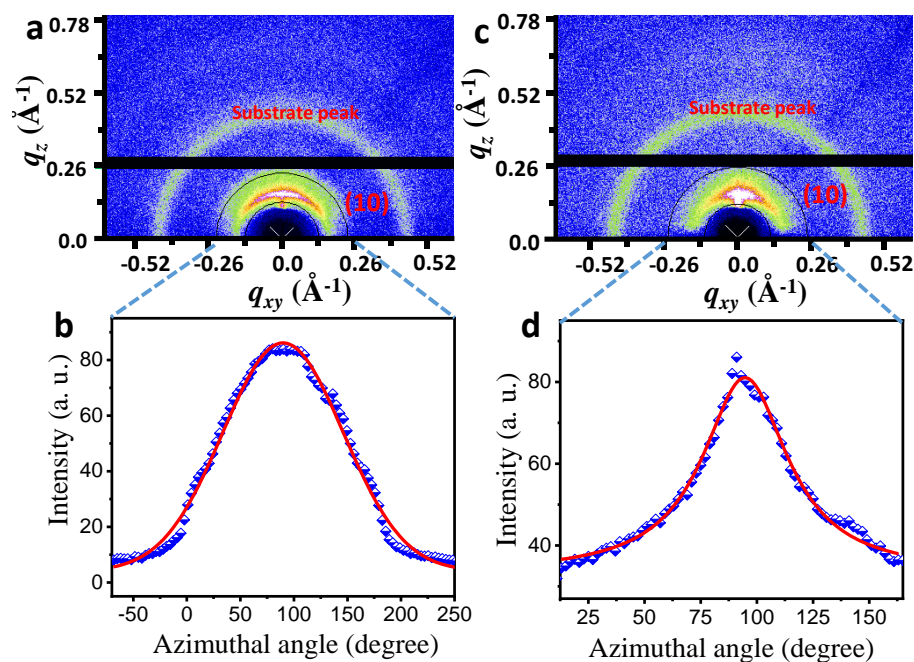


**Figure 4.11** GISAXS pattern of a partially aligned sample of (a) **1** and (b) **2** in Col<sub>r</sub> phase (25 °C) with indexing and cake for (10) peak shown by annular region in black color. Respective Intensity vs. azimuthal plots of (c) **1** and (d) **2** in blue color half-filled diamond with Gaussian fit in red color.

Both **1** and **2** exhibit Col<sub>r</sub> phases at room temperature. In these phases, the assembly has both positional and orientational order which can be calculated from their XRD patterns. Orientational order could be calculated from the first peak of the diffraction pattern in the small-angle region and it is inversely proportional to the full width at half maxima (FWHM) of an azimuthal plot (Figure 4.11b,d) of the peak. A lower FWHM value is an indication of better orientational order than that of higher. In our case, FWHM values extracted for **1** and **2** from their azimuthal plot of (10) peak of Col<sub>r</sub> phase are found to be 133° and 45°, respectively, at room temperature. This indicates a much better orientational order for **2** in Col<sub>r</sub> phase as compared to **1**. Higher orientational order for **2** from GISAXS also supports the observed higher (~ 2 orders) mobility (hole) values over **1**.

## 4.4 Conclusions

In summary, we have utilized a fused  $\pi$ -conjugated tetrathienoanthracene (TTA) unit as a convenient building block to the development of novel DLCs to the realization of highly

efficient hole transporting systems. The rational design of attaching tri-alkoxy benzenes with different chain lengths (**1**: R = C<sub>10</sub>H<sub>21</sub> and **2**: R = C<sub>12</sub>H<sub>25</sub>) attached to TTA core *via* alkynyl linker were successful to achieve high hole transport for **1** and **2**, possibly arising from the molecular packing features ( $\pi$ - $\pi$  stacking along with S $\cdots$ S interactions) common to the fused thiophene systems. The observed SCLC hole mobility value of 4.22 cm<sup>2</sup> V<sup>-1</sup> s<sup>-1</sup> for **2** is remarkable and surprisingly, 2 orders of magnitude higher than **1**. This is due to a high tendency of **2** to align homeotropically over a large area in SCLC cells than **1** as confirmed through POM studies and GI-SAXS investigations. Our strategy establishes to be a robust and effective tool to achieve high hole mobility in the field of discotics, in general, while highest in thiophene-based DLCs reported to date. Therefore, the findings of this work can certainly guide to develop new rational designs of high-performance charge transport materials based on DLCs with an appropriate balance between mobility and processability in devices.

**Acknowledgements.** *The SCLC device fabrication and measurement studies have been carried out in collaboration with Dr. Upendra Kumar Pandey at Shiv Nadar University and is greatly acknowledged and respected. Dr. Santosh Prasad Gupta (at Patna University) is duly acknowledged for the analysis of XRD data.*

## 4.5 Experimental section

**4.5.1 Synthesis of compound 9.** In a double-neck round bottom flask (RBF), 30 ml dry DMF was taken and purged it with nitrogen for 15 minutes. To that, 1,2,4,5-tetrabromobenzene (1 g, 2.54 mmol) was added followed by Pd(PPh<sub>3</sub>)<sub>2</sub>Cl<sub>2</sub> (126 mg, 0.18 mmol). After 5 minutes, 2-(tributylstannyl)thiophene (4.83 g, 12.95 mmol) was dropwise added. The reaction was left to stir for 16 hours at 140 °C. After the completion of the reaction, extraction of the reaction mixture with diethyl ether was done and then well dried using sodium sulfate. Column chromatographic using silica-gel as adsorbent and hexane-ethyl acetate as an eluent were done to get the white-colored product in 82% yield. <sup>1</sup>H NMR (400 MHz, CDCl<sub>3</sub>,  $\delta$  in ppm):  $\delta$  7.67 (s, 2H), 7.31-7.30 (dd, 4H,  $J$  = 4.96 Hz), 7.00-6.96 (m, 8H). <sup>13</sup>C NMR (100 MHz, CDCl<sub>3</sub>,  $\delta$  in ppm): 141.74, 133.55, 133.40, 127.56, 127.18, 126.50. FT-IR (cm<sup>-1</sup>): 3100.10, 2929.00, 1738.00, 1661.90, 1593.40, 1544.00, 1532.50, 1481.36, 1441.52, 1422.20, 1376.50, 1262.40, 1237.84, 1201.50, 1079.70, 1053.00, 946.54, 900.95, 847.48, 835.20, 737.27, 702.98, 524.00.



**4.5.2 Synthesis of compound 10.** To a solution of compound **9** (1 g, 2.46 mmol) in 20 ml dry THF, N-Bromosuccinimide (2.69 g, 15.10 mmol) was added and reaction mixture was kept for stirring for 16 hours. After completing reaction, solvent was evaporated and the slurry was prepared in 60-120 mesh silica gel in order to purify it. The purification gives rise to white colored pure product in 80% yield.  $^1\text{H}$  NMR (400 MHz,  $\text{CDCl}_3$ ,  $\delta$  in ppm):  $\delta$  7.50 (s, 2H), 6.97-6.96 (d, 4H,  $J = 3.84$  Hz), 6.75-6.74 (d, 4H,  $J = 3.80$  Hz).  $^{13}\text{C}$  NMR (100 MHz,  $\text{CDCl}_3$ ,  $\delta$  in ppm): 142.34, 133.28, 132.85, 130.29, 128.15, 113.74. FT-IR ( $\text{cm}^{-1}$ ): 3093.00, 2963.20, 2925.10, 2852.80, 1749.40, 1734.20, 1601.00, 1551.50, 1483.00, 1443.25, 1422.20, 1368.90, 1323.20, 1228.10, 1193.90, 1167.20, 1056.90, 1022.60, 976.27, 969.37, 931.32, 904.69, 866.64, 791.04, 737.27, 703.03, 661.17, 581.27, 528.00, 474.73.

**4.5.3 Synthesis of compound 11.** To a solution of compound **10** (1.23 g, 1.70 mmol) in warm chlorobenzene (60 ml),  $\text{FeCl}_3$  (1.70 g, 10.47 mmol) solution in 30 ml nitromethane was slowly poured (dropwise) for over 5 minutes. The reaction was kept for stirring at room temperature for overnight. The yellow-colored solution was filtered and the filtered precipitates were allowed to stir with 10%  $\text{HCl}/\text{H}_2\text{O}$  mixture for 30 minutes and washed with an excess amount of methanol. The resultant mustard yellow precipitates were dried and quantitatively obtained in the crude form with a yield of 78%. The product was almost insoluble in all common inorganic solvents and hence limits its characterization by NMR Spectroscopy. FT-IR ( $\text{cm}^{-1}$ ): 2917.50, 2852.80, 1546.09, 1482.83, 1429.80, 1392.84, 1298.16, 12585.29, 1190.00, 1133.00, 973.18, 961.03, 858.80, 817.18, 803.29, 741.08, 615.51, 559.09, 494.19.

**4.5.4 Synthesis of compound 12a.** In a double neck RBF, dry DMF was purged with nitrogen for 15 minutes. Then, 3,4,5-trihydroxybenzaldehyde monohydrate (1 g, 5.81 mmol) and  $\text{K}_2\text{CO}_3$  (29.04 mmol, 4.01 g) were stirred for 15 minutes. After that, the addition of 1-bromodecane (3.98 g, 18.01 mmol) followed by a pinch of potassium iodide was done. The reaction was kept for stirring at 80 °C for 12 hours. The extraction with diethylether was performed and reaction mixture was evaporated and then purified by column chromatography. The purification enable to get the white colored product in 93% yield.  $^1\text{H}$  NMR (400 MHz,  $\text{CDCl}_3$ ,  $\delta$  in ppm):  $\delta$  9.83 (s, 1H), 7.08 (s, 2H), 4.07-4.01 (m, 6H), 1.83-1.71 (m, 6H), 1.49-1.44 (m, 6H), 1.35-1.27 (m, 36H), 0.89-0.86 (t, 9H,  $J = 6.84$  Hz).  $^{13}\text{C}$  NMR (100 MHz,  $\text{CDCl}_3$ ,  $\delta$  in ppm):  $\delta$  191.44, 161.35, 153.66, 144.00, 131.58, 108.00, 73.78, 69.39, 64.28, 32.09, 32.06, 32.03, 30.49, 29.87, 29.81,

29.77, 29.73, 29.69, 29.65, 29.53, 29.50, 29.44, 29.41, 29.33, 28.66, 26.22, 26.18, 25.97, 22.84, 14.26. FT-IR ( $\text{cm}^{-1}$ ): 2955.50, 2923.88, 2854.09, 2723.40, 1697.85, 1585.80, 1497.97, 1468.45, 1440.90, 1381.47, 1331.43, 1228.20, 1148.20, 1116.95, 986.98, 825.84, 721.37, 653.56, 585.08.

**4.5.5 Synthesis of compound 12b.** Compound **12b** was synthesized according to a similar procedure as explained for **12a** (yield: 93%).  $^1\text{H}$  NMR (400 MHz,  $\text{CDCl}_3$ ,  $\delta$  in ppm):  $\delta$  9.83 (s, 1H), 7.08 (s, 2H), 4.07-4.01 (m, 6H), 1.83-1.73 (m, 6H), 1.49-1.45 (m, 6H), 1.30-1.26 (m, 48H), 0.89-0.86 (t, 9H,  $J = 6.84$  Hz).  $^{13}\text{C}$  NMR (100 MHz,  $\text{CDCl}_3$ ,  $\delta$  in ppm): 191.42, 161.33, 153.66, 144.00, 131.58, 107.99, 73.78, 69.38, 64.27, 32.08, 30.49, 29.90, 29.87, 29.84, 29.81, 29.70, 29.64, 29.53, 29.52, 29.41, 29.33, 28.66, 26.22, 26.18, 25.96, 22.84, 14.26. FT-IR ( $\text{cm}^{-1}$ ): 2954.48, 2917.89, 2849.10, 2727.30, 1692.99, 1583.40, 1501.38, 1469.20, 1440.87, 1380.33, 1336.97, 1224.47, 1145.73, 1119.15, 1011.20, 988.40, 967.49, 823.53, 720.07, 649.76, 619.32.

**4.5.6 Synthesis of compound 13a.** In one neck 100 ml RBF, compound **12a** (1 g, 1.74 mmol) was taken in 15 ml dry DCM and cooled to 0 °C. To that,  $\text{CBr}_4$  (1.15 g, 3.48 mmol) was added for 10 minutes and the solution was allowed to stir. After 5 minutes,  $\text{PPh}_3$  (1.59 g, 6.08 mmol) was added and kept the solution to stir for another 5 minutes. After checking the TLC and on comparing it with reactant **12a**, the reaction was stopped. A new non-polar spot as compared to the reactant indicated the occurrence of reaction. Further the evaporation of the solvent for making slurry using silica-gel for column chromatography was done, giving rise to colorless liquid in 80% yield.  $^1\text{H}$  NMR (400 MHz,  $\text{CDCl}_3$ ,  $\delta$  in ppm):  $\delta$  7.37 (s, 1H), 6.77 (s, 2H), 3.99-3.94 (m, 6H), 1.81-1.72 (m, 6H), 1.48-1.43 (m, 6H), 1.34-1.27 (m, 36H), 0.90-0.87 (t, 9H,  $J = 6.86$  Hz).  $^{13}\text{C}$  NMR (100 MHz,  $\text{CDCl}_3$ ,  $\delta$  in ppm): 153.01, 148.23, 138.84, 136.95, 130.14, 107.38, 88.20, 73.59, 69.35, 32.09, 32.06, 30.47, 29.88, 29.82, 29.79, 29.73, 29.65, 29.50, 26.23, 22.84, 14.26. FT-IR ( $\text{cm}^{-1}$ ): 2959.40, 2924.95, 2854.59, 1575.81, 1504.63, 1467.76, 1429.11, 1379.52, 1332.95, 1239.35, 1116.82, 835.85, 721.79, 684.00, 626.93.

**4.5.7 Synthesis of compound 13b.** Compound **13b** was synthesized according to a similar procedure as explained for **13a** (yield: 80%).  $^1\text{H}$  NMR (400 MHz,  $\text{CDCl}_3$ ,  $\delta$  in ppm):  $\delta$  7.37 (s, 1H), 6.76 (s, 2H), 3.98-3.94 (m, 6H), 1.81-1.71 (m, 6H), 1.48-1.31 (m, 6H), 1.34-1.26 (m, 48H), 0.90-0.86 (t, 9H,  $J = 6.84$  Hz).  $^{13}\text{C}$  NMR (100 MHz,  $\text{CDCl}_3$ ,  $\delta$  in ppm): 153.01, 148.23,

138.85, 136.95, 130.13, 107.38, 88.20, 73.58, 69.34, 32.08, 30.47, 29.89, 29.85, 29.81, 29.79, 29.74, 29.56, 29.52, 29.49, 26.24, 22.84, 14.26. FT-IR ( $\text{cm}^{-1}$ ): 2955.50, 2921.64, 2851.79, 1575.11, 1506.05, 1467.99, 1430.21, 1379.66, 1335.51, 1244.09, 1123.20, 1015.00, 992.78, 868.65, 831.67, 809.87, 721.04, 680.40, 623.30.

**4.5.8 Synthesis of compound 14a.** In a Schenk flask, addition of *n*-BuLi to a solution of **13a** (2.30 g, 3.15 mmol) in dry THF under  $\text{N}_2$  atmosphere, *n*-BuLi (1.6 M in hexane) (7.87 mmol, 4.9 ml) in dry THF was carried out at  $-78^\circ\text{C}$  in a slow manner. Then the reaction was stirred for 24 hours at room temperature. After checking the TLC, the reaction was stopped and quenched with saturated  $\text{NH}_4\text{Cl}$  solution. After extraction with DCM, the organic layer was dried and evaporated to dryness and further subjected to purification. The purification by column chromatography using hexane-ethyl acetate as an eluent leads to obtain the product in 60% yield as a colorless liquid.  $^1\text{H}$  NMR (400 MHz,  $\text{CDCl}_3$ ,  $\delta$  in ppm):  $\delta$  6.69 (s, 2H), 3.97-3.93 (m, 6H), 2.99 (s, 1H) 1.81-1.71 (m, 6H), 1.45-1.41 (m, 6H), 1.30-1.27 (m, 36H), 0.90-0.86 (t, 9H,  $J = 6.78$  Hz).  $^{13}\text{C}$  NMR (100 MHz,  $\text{CDCl}_3$ ,  $\delta$  in ppm): 153.07, 139.65, 116.53, 110.79, 84.17, 75.89, 73.65, 69.26, 32.09, 32.06, 30.45, 29.88, 29.82, 29.78, 29.74, 29.55, 29.53, 29.50, 29.45, 26.23, 26.21, 22.84, 14.26. FT-IR ( $\text{cm}^{-1}$ ): 3315.10, 2959.40, 2923.29, 2854.86, 2106.45, 1574.74, 1501.01, 1468.80, 1421.62, 1380.56, 1333.95, 1234.64, 1116.84, 999.83, 832.38, 721.91, 680.20, 645.61, 596.63.

**4.5.9 Synthesis of compound 14b.** Compound **14b** was synthesized according to a similar procedure as explained for **14a** (yield: 60%).  $^1\text{H}$  NMR (400 MHz,  $\text{CDCl}_3$ ,  $\delta$  in ppm):  $\delta$  6.69 (s, 2H), 3.97-3.93 (m, 6H), 2.99 (s, 1H) 1.81-1.73 (m, 6H), 1.45-1.42 (m, 6H), 1.30-1.26 (m, 48H), 0.90-0.86 (t, 9H,  $J = 6.76$  Hz).  $^{13}\text{C}$  NMR (100 MHz,  $\text{CDCl}_3$ ,  $\delta$  in ppm): 153.08, 139.65, 116.54, 110.80, 84.18, 75.89, 73.66, 69.27, 32.09, 30.45, 29.89, 29.85, 29.82, 29.79, 29.74, 29.53, 29.45, 26.24, 26.22, 22.85, 14.27. FT-IR ( $\text{cm}^{-1}$ ): 3314.22, 2959.40, 2924.07, 2853.85, 2110.90, 1575.33, 1500.33, 1467.40, 1420.66, 1380.04, 1333.94, 1234.89, 1117.36, 999.81, 831.91, 721.59, 645.55, 596.39.

**4.5.10 Synthesis of tetrathienoanthracene derivative (1).** In an oven-dried double neck RBF, dry DMF (15 ml) and triethylamine (30 ml) was taken in 1:2 ratio. The solvent mixture was purged out vigorously with nitrogen for 30 minutes. Compound **11** (107 mg, 0.15 mmol) was then added and again purged it for 5 minutes. After that, addition of  $\text{Pd}(\text{PPh}_3)_4$  (13.77 mg,

0.012 mmol) followed by CuI (2.8 mg, 0.015 mmol) was done and the reaction mixture was kept for stirring for further 10 minutes under N<sub>2</sub> atmosphere. Finally, addition of alkyne **14a** (680 mg, 1.19 mmol) was done and then stirred the reaction 110 °C for 3 days. The reaction was quenched with dilute HCl under cold condition and then extraction with ether was performed. The organic layer separation followed by evaporated to dryness and purification by using alumina-gel column chromatography enable to yield the orange-brown colored product in 36% yield. <sup>1</sup>H NMR (400 MHz, CDCl<sub>3</sub>,  $\delta$  in ppm):  $\delta$  8.63 (s, 2H), 7.75 (s, 4H), 6.80 (s, 8H), 4.03-4.00 (m, 24H), 1.87-1.73 (m, 24H), 1.48-1.46 (m, 24H), 1.30-1.25 (m, 144H), 0.89-0.87 (m, 36H). <sup>13</sup>C NMR (100 MHz, CDCl<sub>3</sub>,  $\delta$  in ppm): 153.23, 139.67, 135.92, 132.72, 127.48, 125.52, 123.74, 116.99, 110.10, 96.24, 81.82, 73.73, 69.31, 32.11, 30.58, 29.95, 29.87, 29.83, 29.67, 29.59, 29.56, 26.33, 22.87, 14.28. FT-IR (cm<sup>-1</sup>): 2955.50, 2923.51, 2853.61, 2202.20, 1738.00, 1574.14, 1510.25, 1502.00, 1468.06, 1422.20, 1376.50, 1354.59, 1308.00, 1236.76, 1119.02, 1018.80, 847.62, 824.06, 721.76. MALDI-MS (m/z): M<sup>+</sup> 2677.9734 (calculated for C<sub>174</sub>H<sub>266</sub>O<sub>12</sub>S<sub>4</sub> = M<sup>+</sup> 2677.9199).

**4.5.11 Synthesis of tetrathienoanthracene derivative (2).** Compound **2** was synthesized according to a similar procedure as explained for **1** (yield: 32%). <sup>1</sup>H NMR (400 MHz, CDCl<sub>3</sub>,  $\delta$  in ppm):  $\delta$  8.62 (s, 2H), 7.75 (s, 4H), 6.80 (s, 8H), 4.03-4.00 (m, 24H), 1.87-1.73 (m, 24H), 1.50-1.41 (m, 24H), 1.30-1.25 (m, 192H), 0.89-0.86 (t, 36H, *J* = 5.80 Hz). <sup>13</sup>C NMR (100 MHz, CDCl<sub>3</sub>,  $\delta$  in ppm): 153.27, 139.76, 136.00, 132.83, 127.96, 123.89, 119.18, 116.96, 110.20, 96.30, 81.73, 73.76, 69.35, 37.26, 32.91, 32.11, 30.56, 30.20, 29.95, 29.64, 29.56, 27.25, 26.32, 22.86, 19.89, 14.28. FT-IR (cm<sup>-1</sup>): 2955.50, 2923.29, 2853.12, 2206.00, 1738.00, 1574.26, 1505.10, 1466.97, 1422.20, 1376.50, 1352.06, 1236.48, 1117.98, 1030.30, 851.42, 823.83, 721.20. MALDI-MS (m/z): M<sup>+</sup> 3015.3357 (calculated for C<sub>198</sub>H<sub>314</sub>O<sub>12</sub>S<sub>4</sub> = M<sup>+</sup> 3015.2989).

## References

1. Feng, X.; Marcon, V.; Pisula, W.; Hansen, M. R.; Kirkpatrick, J.; Grozema, F.; Andrienko, D.; Kremer, K.; Müllen, K. *Nat. Mater.* **2009**, *8*, 421-426.
2. Forrest, S. R. *Nature* **2004**, *428*, 911-918.
3. Bashir, A.; Heck, A.; Narita, A.; Feng, X.; Nefedov, A.; Rohwerder, M.; Müllen, K.; Elstner, M.; Wöll, C. *Phys. Chem. Chem. Phys.* **2015**, *17*, 21988-21996.
4. Back, J. Y.; An, T. K.; Cheon, Y. R.; Cha, H.; Jang, J.; Kim, Y.; Baek, Y.; Chung, D. S.; Kwon, S. K.; Park, C. E.; Kim, Y. H. *ACS Appl. Mater. Interfaces* **2014**, *7*, 351-358.
5. Ma, Z.; Geng, H.; Wang, D.; Shuai, Z. *J. Mater. Chem. C* **2016**, *4*, 4546-4555.
6. Kato, T.; Yoshio, M.; Ichikawa, T.; Soberats, B.; Ohno, H.; Funahashi, *Nat. Rev.* **2017**, *2*, 17001.
7. Kumar, S. *Chem. Soc. Rev.* **2006**, *35*, 83-109.
8. Wöhrle, T.; Wurzbach, I.; Kirres, J.; Kostidou, A.; Kapernaum, N.; Litterscheidt, J.; Haenle, J. C.; Staffeld, P.; Baro, A.; Giesselmann, F.; Laschat, S. *Chem. Rev.* **2016**, *116*, 1139-1241.
9. Kaafarani, B. R. *Chem. Mater.* **2010**, *23*, 378-396.
10. Murphy, A. R.; Fréchet, J. M. J. *Chem. Rev.* **2007**, *107*, 1066-1096.
11. Funahashi, M.; Zhang, F.; Tamaoki, N. *Adv. Mater.* **2007**, *19*, 353.
12. Feng, X.; Liu, M.; Pisula, W.; Takase, M.; Li, J.; Müllen, K. *Adv. Mater.* **2008**, *20*, 2684-2689.
13. García-Frutos, E. M.; Pandey, U. K.; Termine, R.; Omenat, A.; Barberá, J.; Serrano, J. L.; Golemme, A.; Gómez-Lor, B. *Angew. Chem. Int. Ed.* **2011**, *50*, 7399-7402.
14. Paraschiv, I.; Giesbers, M.; Van Lagen, B.; Grozema, F. C.; Abellon, R. D.; Siebbeles, L. D. A.; Marcelis, A. T. M.; Zuilhof, H.; Sudhoelter, E. J. R. *Chem. Mater.* **2006**, *18*, 968-974.
15. Ruiz, C.; García-Frutos, E. M.; Hennrich, G.; Gomez-Lor, B. *J. Phys. Chem. Lett.* **2012**, *3*, 1428-1436.
16. Zhen, Y.; Inoue, K.; Wang, Z.; Kusamoto, T.; Nakabayashi, K.; Ohkoshi, S. I.; Hu, W.; Guo, Y.; Harano, K.; Nakamura, E. Acid Responsive Conductive Nanofiber of

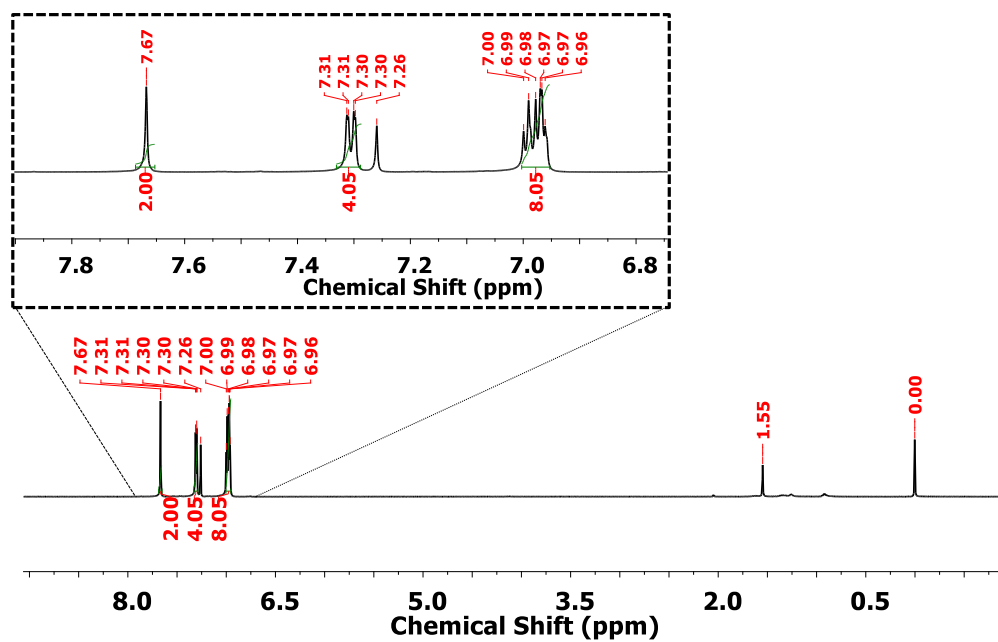
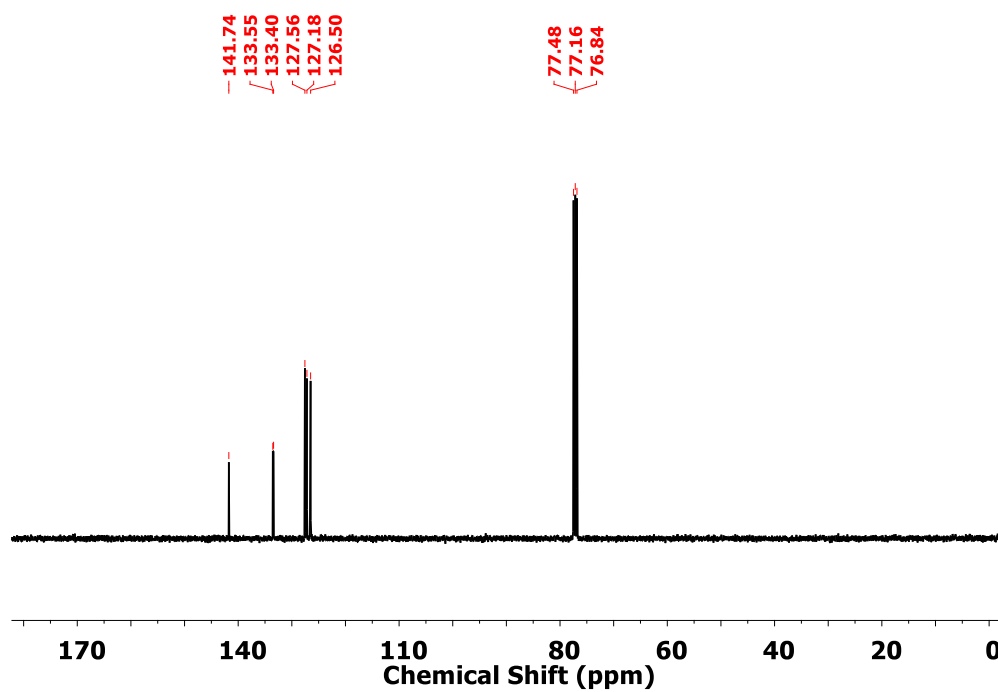
- Tetrabenzoporphyrin Made by Solution Processing. *J. Am. Chem. Soc.* **2018**, *140*, 62-65.
17. Eccher, J.; Faria, G. C.; Bock, H.; von Seggern, H.; Bechtold, I. H. *ACS Appl. Mater. Interfaces* **2013**, *5*, 11935-11943.
18. Liu, C. X.; Wang, H.; Du, J. Q.; Zhao, K. Q.; Hu, P.; Wang, B. Q.; Monobe, H.; Heinrich, B.; Donnio, B. *J. Mater. Chem. C* **2018**, *6*, 4471-4478.
19. Zhao, K. C.; Du, J. Q.; Wang, H. F.; Zhao, K. Q.; Hu, P.; Wang, B. Q.; Monobe, H.; Heinrich, B.; Donnio, B. *Chem. Asian J.* **2019**, *14*, 462-470.
20. Ma, T.; Wang, H. F.; Zhao, K. Q.; Wang, B. Q.; Hu, P.; Monobe, H.; Heinrich, B.; Donnio, B. *ChemPlusChem* **2019**, *84*, 1439-1448.
21. Yasuda, T.; Shimizu, T.; Liu, F.; Ungar, G.; Kato, T. *J. Am. Chem. Soc.* **2011**, *133*, 13437-13444.
22. Isoda, K.; Yasuda, T.; Kato, T. *Chem. Asian J.* **2009**, *4*, 1619-1625.
23. Li, Y.; Clevenger, R. G.; Jin, L.; Kilway, K. V.; Peng, Z. *J. Mater. Chem. C* **2014**, *2*, 7180-7183.
24. Funahashi, M.; Hanna, J. I. *Appl. Phys. Lett.* **2000**, *76*, 2574-2576.
25. Funahashi, M.; Hanna, J. I. *Adv. Mater.* **2005**, *17*, 594-598.
26. van Breemen, A. J.; Herwig, P. T.; Chlon, C. H.; Sweelssen, J.; Schoo, H. F.; Setayesh, S.; Hardeman, W. M.; Martin, C. A.; de Leeuw, D. M.; Valeton, J. J.; Bastiaansen, C. W. *J. Am. Chem. Soc.* **2006**, *128*, 2336-2345.
27. Funahashi, M.; Zhang, F.; Tamaoki, N. *Adv. Mater.* **2007**, *19*, 353-358.
28. Zhang, F.; Funahashi, M.; Tamaoki, N. *Org. Electron.* **2010**, *11*, 363-368.
29. Zhang, X.; Richter, L. J.; DeLongchamp, D. M.; Kline, R. J.; Hammond, M. R.; McCulloch, I.; Heeney, M.; Ashraf, R. S.; Smith, J. N.; Anthopoulos, T. D.; Schroeder, B. *J. Am. Chem. Soc.* **2011**, *133*, 15073-15084.
30. Funahashi, M.; Zhang, F.; Tamaoki, N.; Hanna, J. I. *ChemPhysChem* **2008**, *9*, 1465-1473.
31. Sun, K.; Xiao, Z.; Lu, S.; Zajackowski, W.; Pisula, W.; Hanssen, E.; White, J. M.; Williamson, R. M.; Subbiah, J.; Ouyang, J.; Holmes, A. B. *Nat. Commun.* **2015**, *6*, 6013.

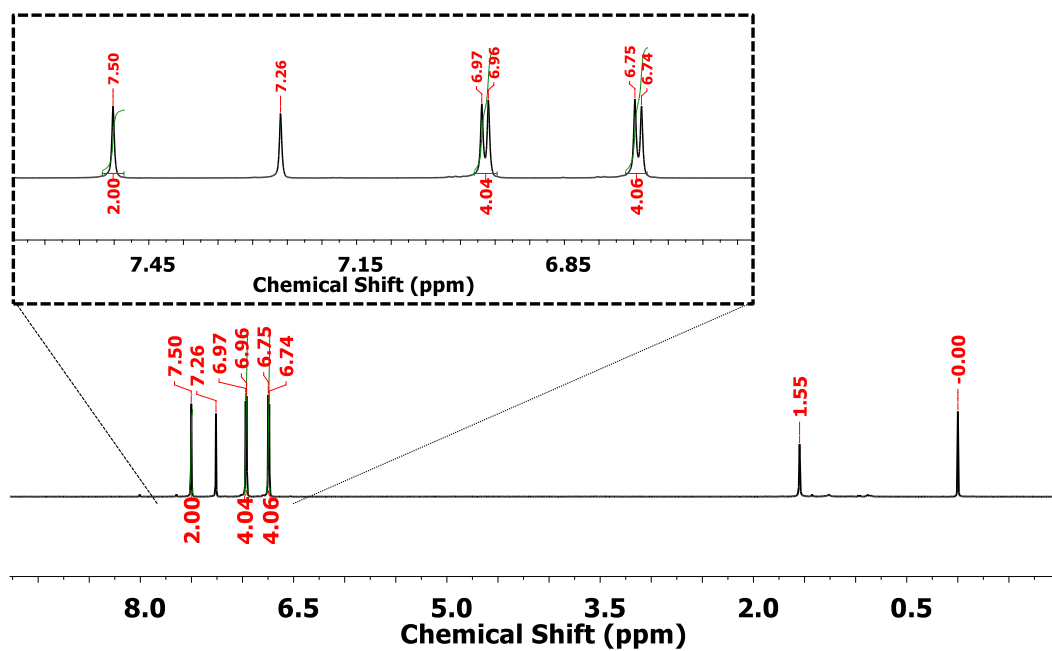
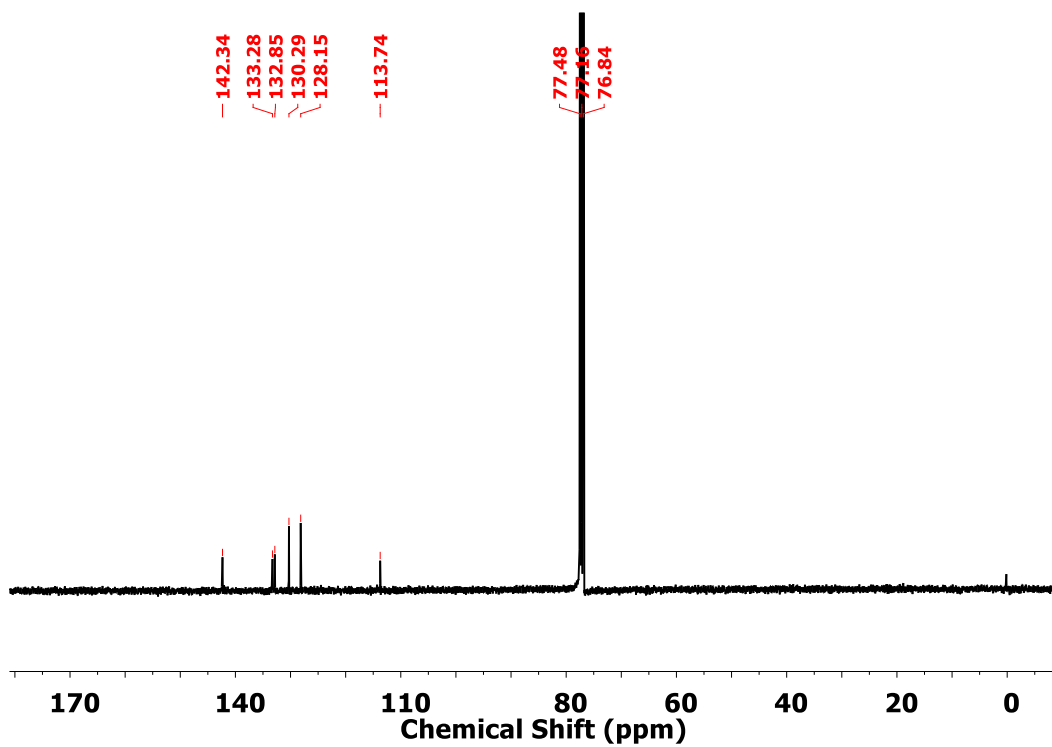
32. Dang, D.; Zhou, P.; Wu, Y.; Xu, Y.; Zhi, Y.; Zhu, W. *Phys. Chem. Chem. Phys.* **2018**, *20*, 13171-13177.
33. Xiao, Q.; Sakurai, T.; Fukino, T.; Akaike, K.; Honsho, Y.; Saeki, A.; Seki, S.; Kato, K.; Takata, M.; Aida, T. *J. Am. Chem. Soc.* **2013**, *135*, 18268-18271.
34. Zimmermann, I.; Urieta-Mora, J.; Gratia, P.; Aragó, J.; Grancini, G.; Molina-Ontoria, A.; Ortí, E.; Martín, N.; Nazeeruddin, M. K. *Adv. Energy Mater.* **2017**, *7*, 1601674.
35. Brusso, J. L.; Hirst, O. D.; Dadvand, A.; Ganesan, S.; Cicoira, F.; Robertson, C. M.; Oakley, R. T.; Rosei, F.; Perepichka, D. F. *Chem. Mater.* **2008**, *20*, 2484-2494.
36. He, F.; Wang, W.; Chen, W.; Xu, T.; Darling, S. B.; Strzalka, J.; Liu, Y.; Yu, L. *J. Am. Chem. Soc.* **2011**, *133*, 3284-3287.
37. Wu, W.; Liu, Y.; Zhu, D. *Chem. Soc. Rev.* **2010**, *39*, 1489-1502.
38. García-Benito, I.; Zimmermann, I.; Urieta-Mora, J.; Aragó, J.; Molina-Ontoria, A.; Ortí, E.; Martín, N.; Nazeeruddin, M. K. *J. Mater. Chem. A* **2017**, *5*, 8317-8324.
39. Cuesta, V.; Vartanian, M.; Malhotra, P.; Biswas, S.; de la Cruz, P.; Sharma, G. D.; Langa, F. *J. Mater. Chem. A* **2019**, *7*, 11886-11894.
40. Volpi, R.; Camilo, A. C. S.; da Silva Filho, D. A.; Navarrete, J. T. L.; Gómez-Lor, B.; Delgado, M. C. R.; Linares, M. *Phys. Chem. Chem. Phys.* **2017**, *19*, 24202-24208.
41. Heinz, P.; Hindelang, K.; Golosova, A.; Papadakis, C. M.; Rieger, B. *ChemPhysChem* **2011**, *12*, 3591-3603.
42. Blanco, H.; Iguarbe, V.; Barberá, J.; Serrano, J. L.; Elduque, A.; Giménez, R. *Chem. Eur. J.* **2016**, *22*, 4924-4930.
43. De, J.; Gupta, S. P.; Bala, I.; Kumar, S.; Pal, S. K. *Langmuir* **2017**, *33*, 13849-13860.
44. Takimiya, K.; Yamamoto, T.; Ebata, H.; Izawa, T. *Sci. Technol. Adv. Mater.* **2007**, *8*, 273-276.
45. Mahoney, S. J.; Ahmida, M. M.; Kayal, H.; Fox, N.; Shimizu, Y.; Eichhorn, S. H. *J. Mater. Chem.* **2009**, *19*, 9221-9232.
46. Mitsui, C.; Soeda, J.; Miwa, K.; Tsuji, H.; Takeya, J.; Nakamu-ra, E. *J. Am. Chem. Soc.* **2012**, *134*, 5448-5451.
47. Benito-Hernández, A.; Pandey, U. K.; Cavero, E.; Termine, R.; García-Frutos, E. M.; Serrano, J. L.; Golemmé, A.; Gómez-Lor, B. *Chem. Mater.* **2013**, *25*, 117-121.

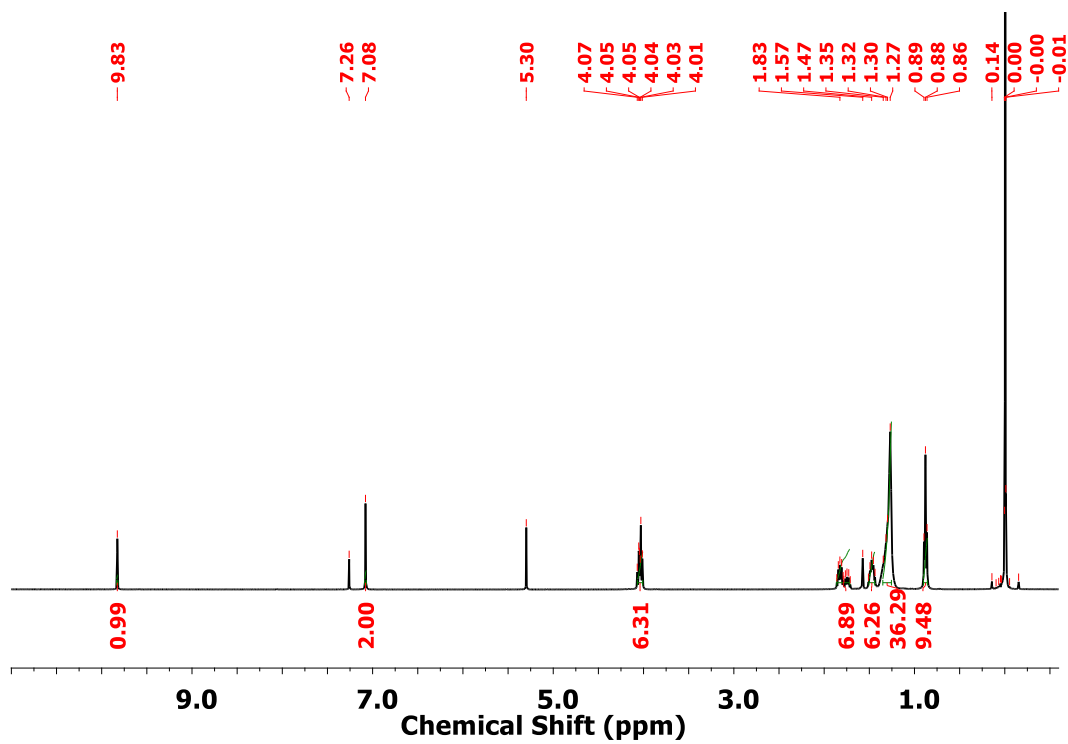
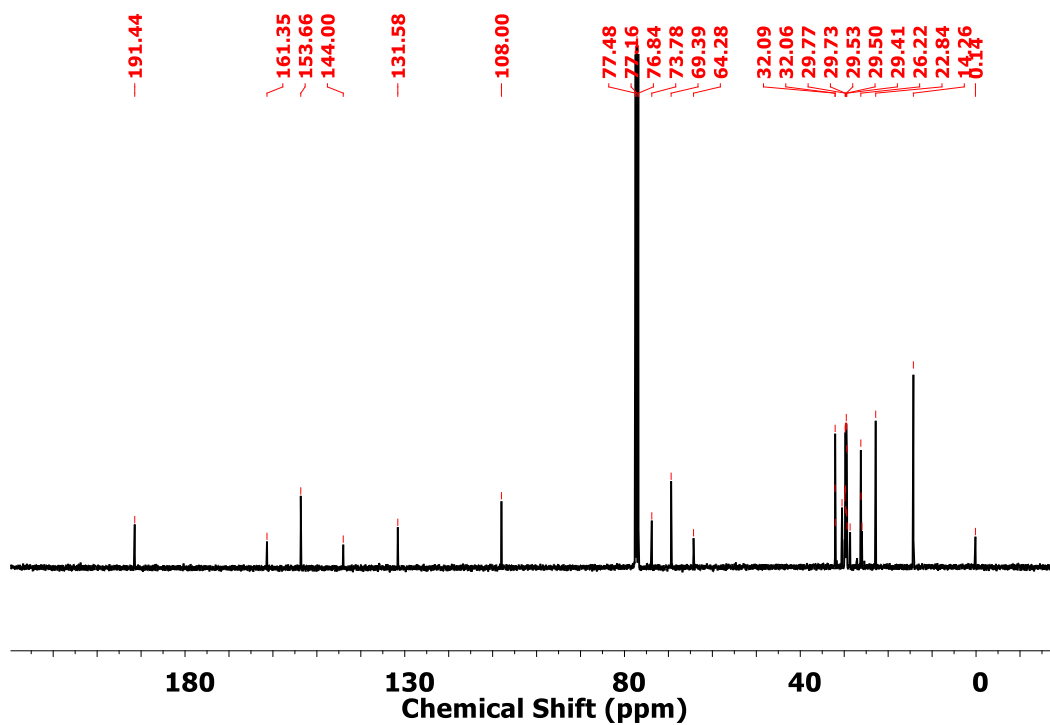
48. Talarico, M.; Termine, R.; García-Frutos, E. M.; Omenat, A.; Serrano, J. L.; Gómez-Lor, B.; Golemme, *Chem. Mater.* **2008**, *20*, 6589-6591.
49. García-Frutos, E. M.; Omenat, A.; Barberá, J.; Serrano, J. L.; Gómez-Lor, B. *J. Mater. Chem. C* **2011**, *21*, 6831-6836.
50. Mott, N. F.; Gurney, D. *Electronic Processes in Ionic Crystals*; Academic Press: New York, **1970**; p 45.
51. Hayashi, H.; Nihashi, W.; Umeyama, T.; Matano, Y.; Seki, S.; Shimizu, Y.; Imahori, H. *J. Am. Chem. Soc.* **2011**, *133*, 10736-10739.
52. Xiao, Q.; Sakurai, T.; Fukino, T.; Akaike, K.; Honsho, Y.; Saeki, A.; Seki, S.; Kato, K.; Takata, M.; Aida, T. *J. Am. Chem. Soc.* **2013**, *135*, 18268-18271.
53. Ruiz, C.; Pandey, U. K.; Termine, R.; García-Frutos, E. M.; López-Espejo, G.; Ortiz, R. P.; Huang, W.; Marks, T. J.; Facchetti, A.; Ruiz Delgado, M. C.; Golemme, A. *ACS Appl. Mater. Interfaces* **2016**, *8*, 26964-26971.
54. De, J.; Bala, I.; Gupta, S. P.; Pandey, U. K.; Pal, S. K. *J. Am. Chem. Soc.* **2019**, *141*, 18799-18805.
55. Chico, R.; de Domingo, E.; Domínguez, C.; Donnio, B.; Heinrich, B.; Termine, R.; Golemme, A.; Coco, S.; Espinet, P. *Chem. Mater.* **2017**, *29*, 7587-7595.
56. Iino, H.; Hanna, J. I.; Bushby, R. J.; Movaghar, B.; Whitaker, B. J.; Cook, M. J. *Appl. Phys. Lett.* **2005**, *87*, 132102.
57. Liu, X.; Usui, T.; Hanna, J. *Chem. Mater.* **2014**, *26*, 5437-5440.
58. Talarico, M.; Termine, R.; García-Frutos, E. M.; Omenat, A.; Serrano, J. L.; Gómez-Lor, B.; Golemme, *Chem. Mater.* **2008**, *20*, 6589-6591.

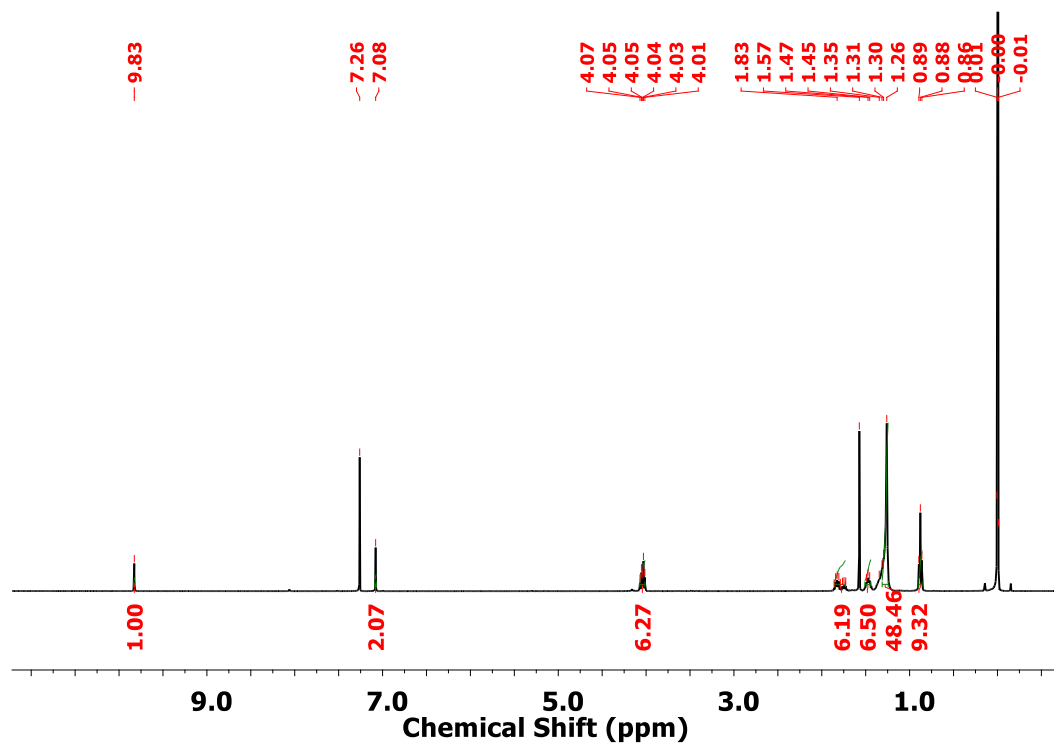
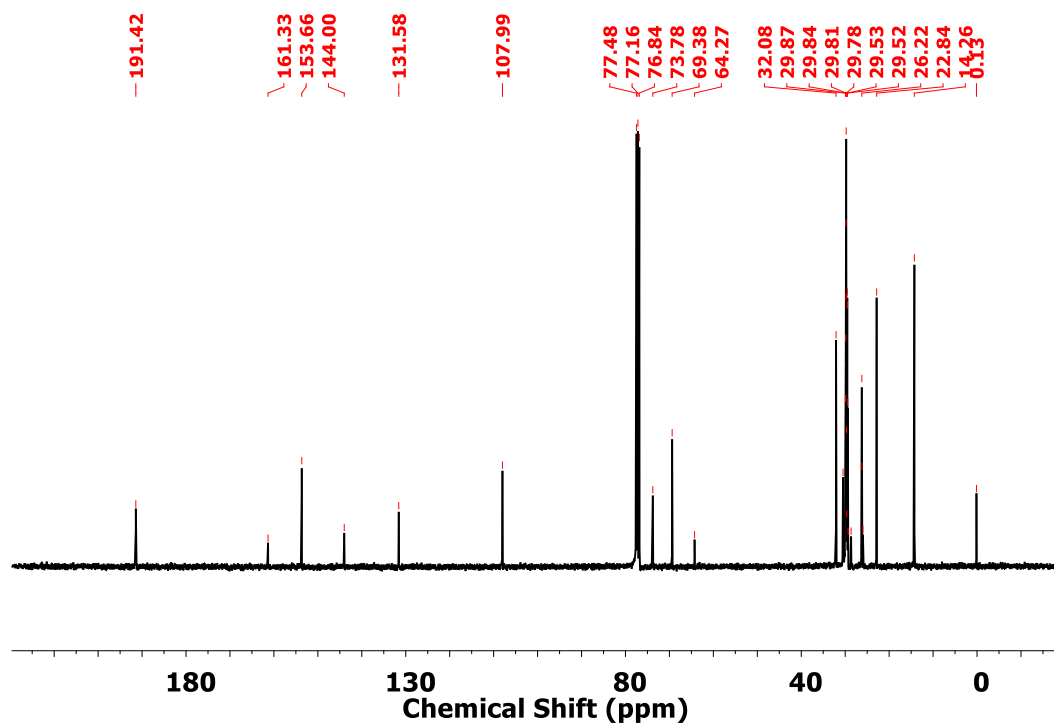


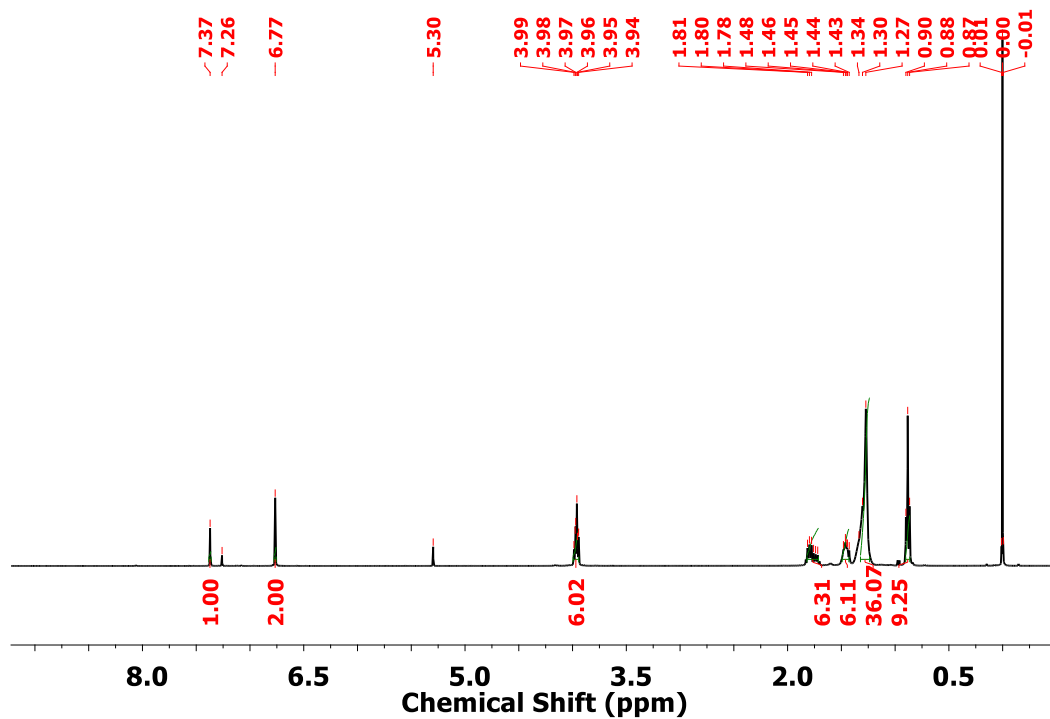
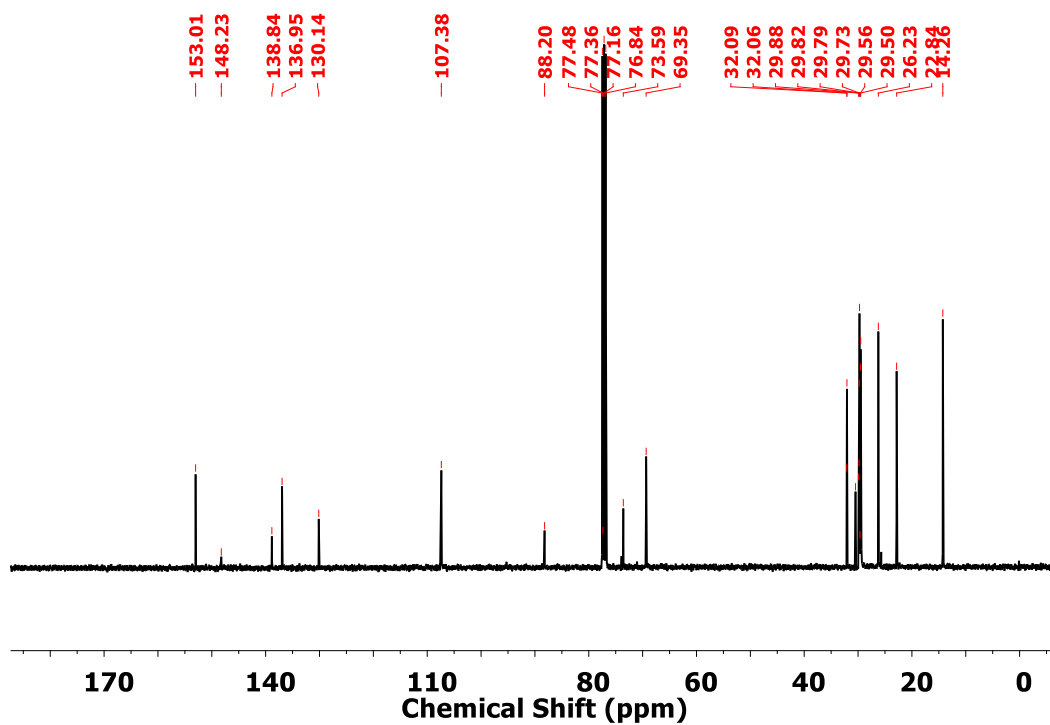
## Appendix IV

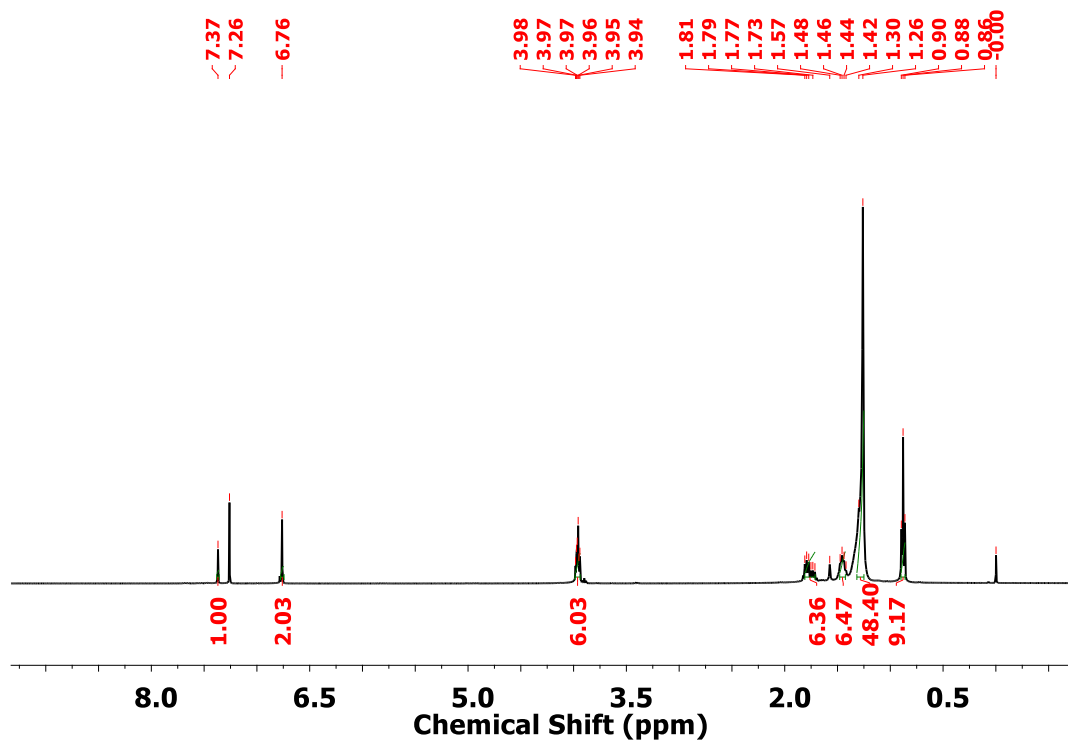
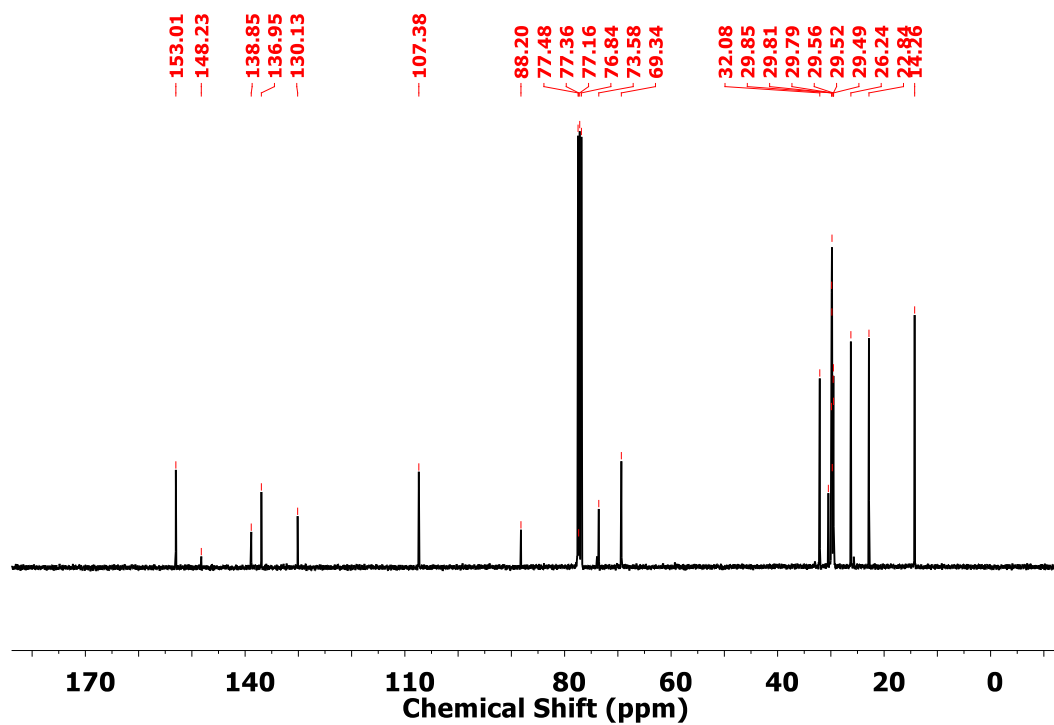
Figure A1.  $^1\text{H}$  NMR spectrum of 9.Figure A2.  $^{13}\text{C}$  NMR spectrum of 9.

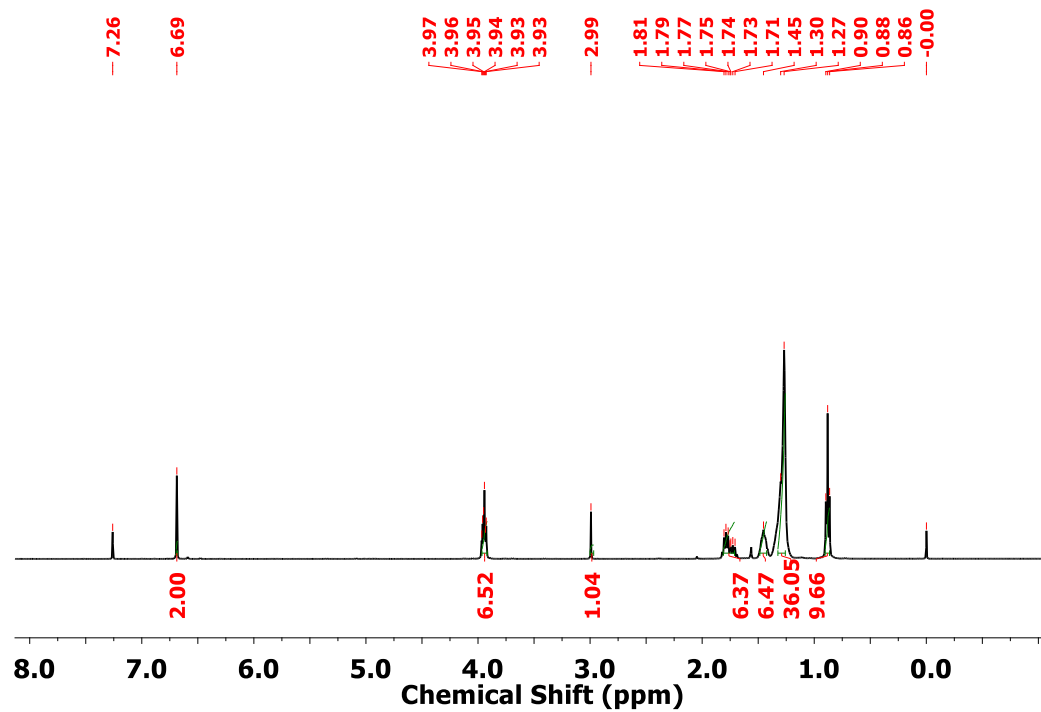
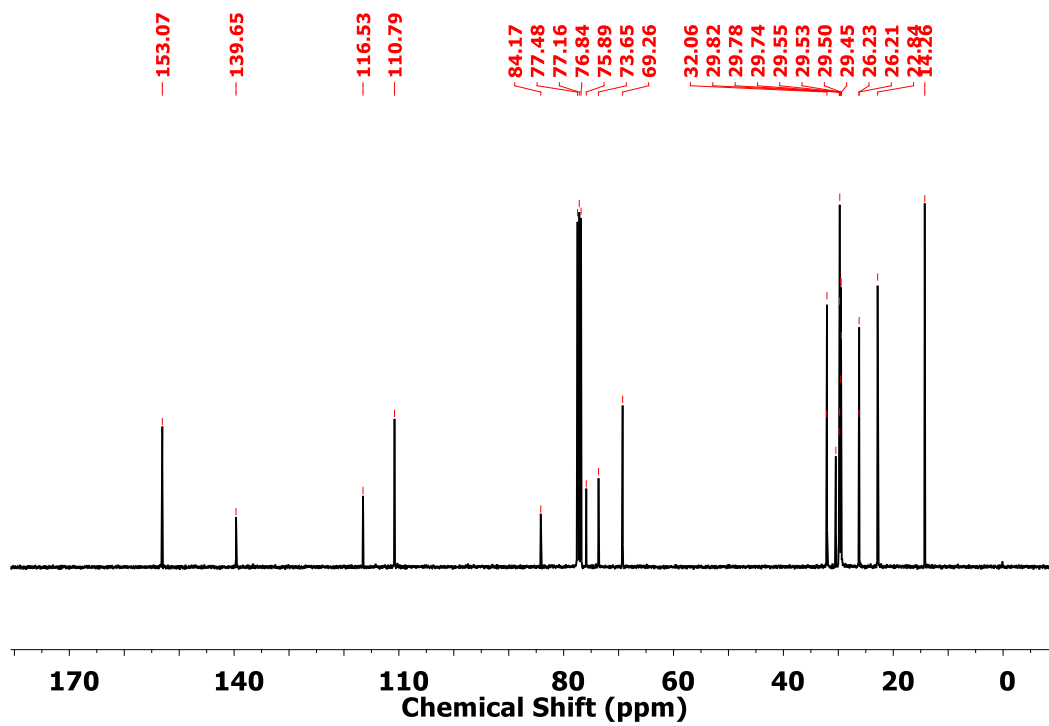
Figure A3. <sup>1</sup>H NMR spectrum of 10.Figure A4. <sup>13</sup>C NMR spectrum of 10.

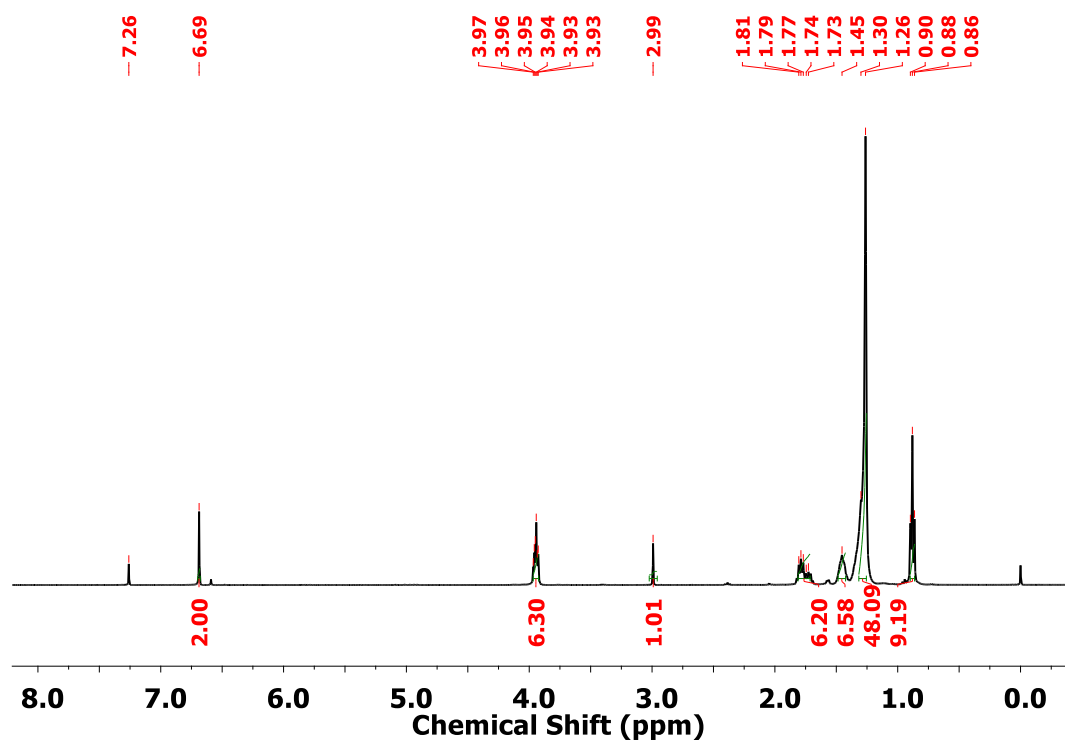
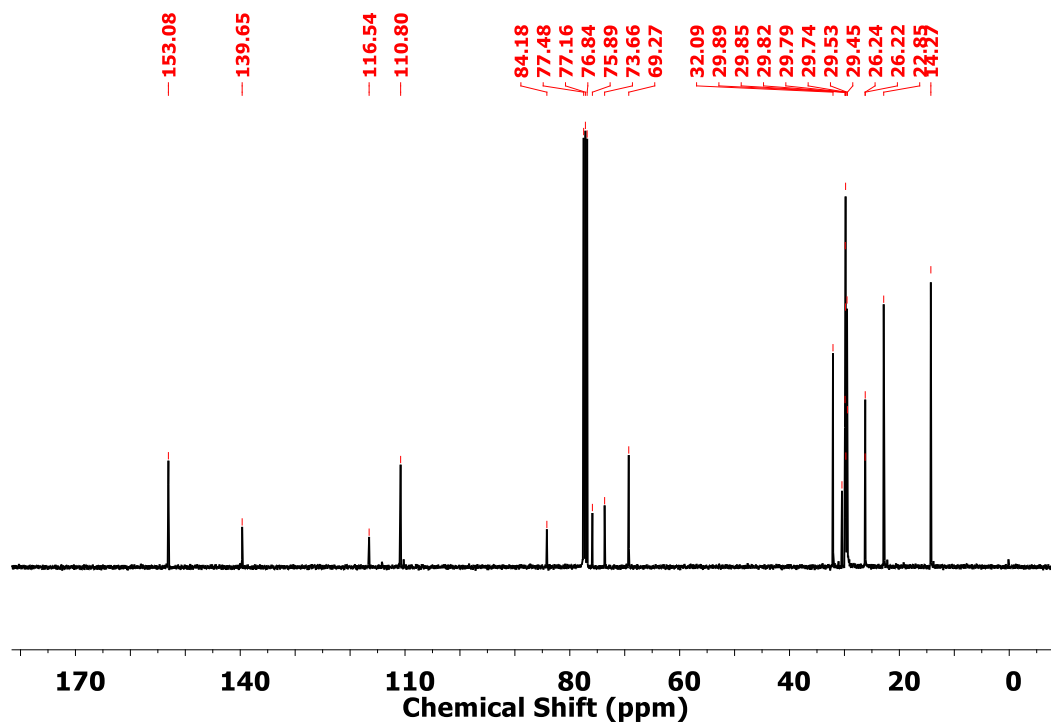
Figure A5. <sup>1</sup>H NMR spectrum of 12a.Figure A6. <sup>13</sup>C NMR spectrum of 12a.

Figure A7. <sup>1</sup>H NMR spectrum of 12b.Figure A8. <sup>13</sup>C NMR spectrum of 12b.

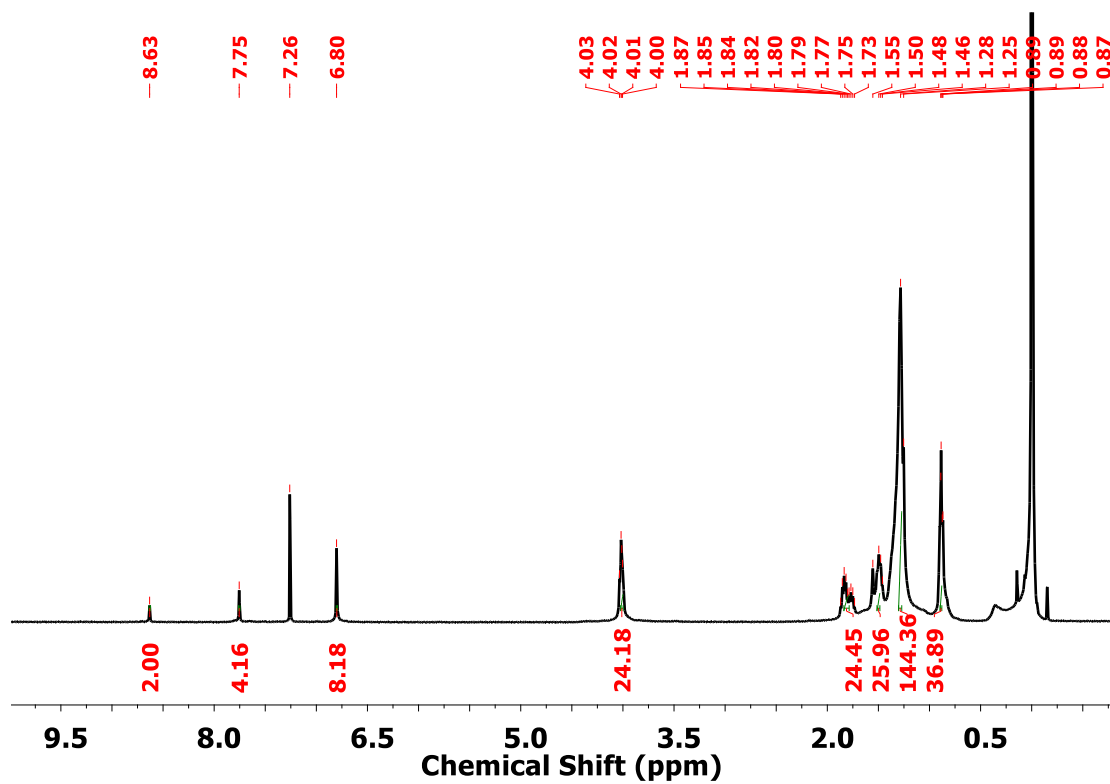
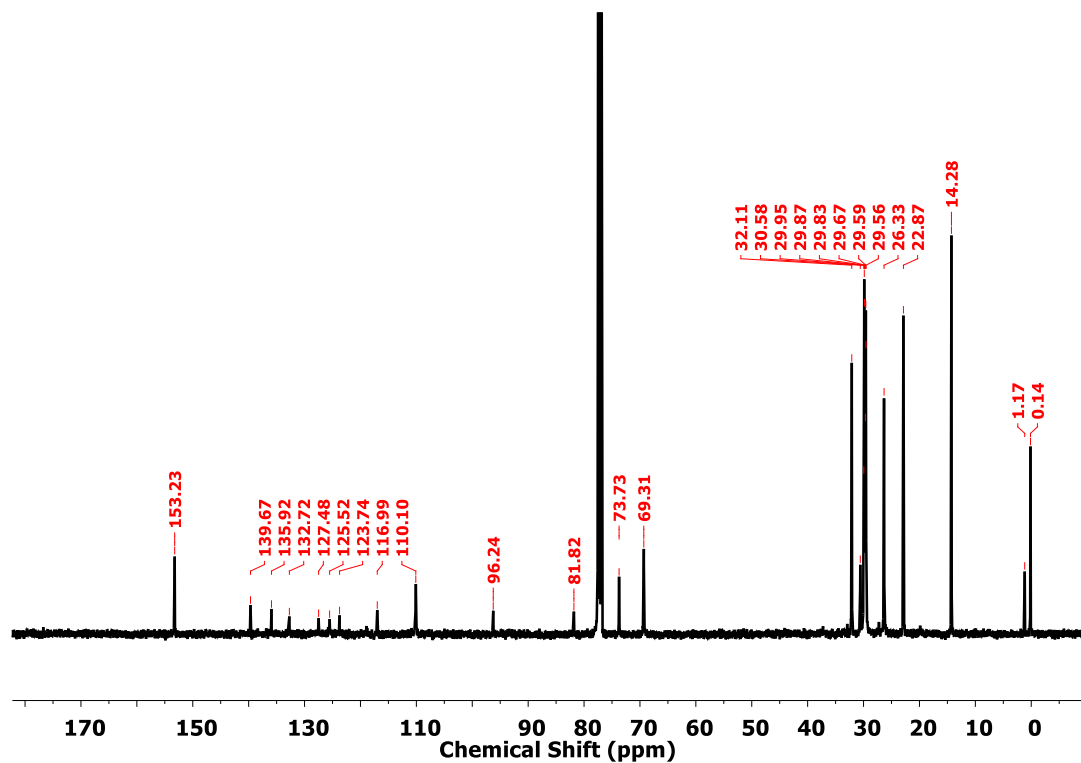
Figure A9. <sup>1</sup>H NMR spectrum of 13a.Figure A10. <sup>13</sup>C NMR spectrum of 13a.

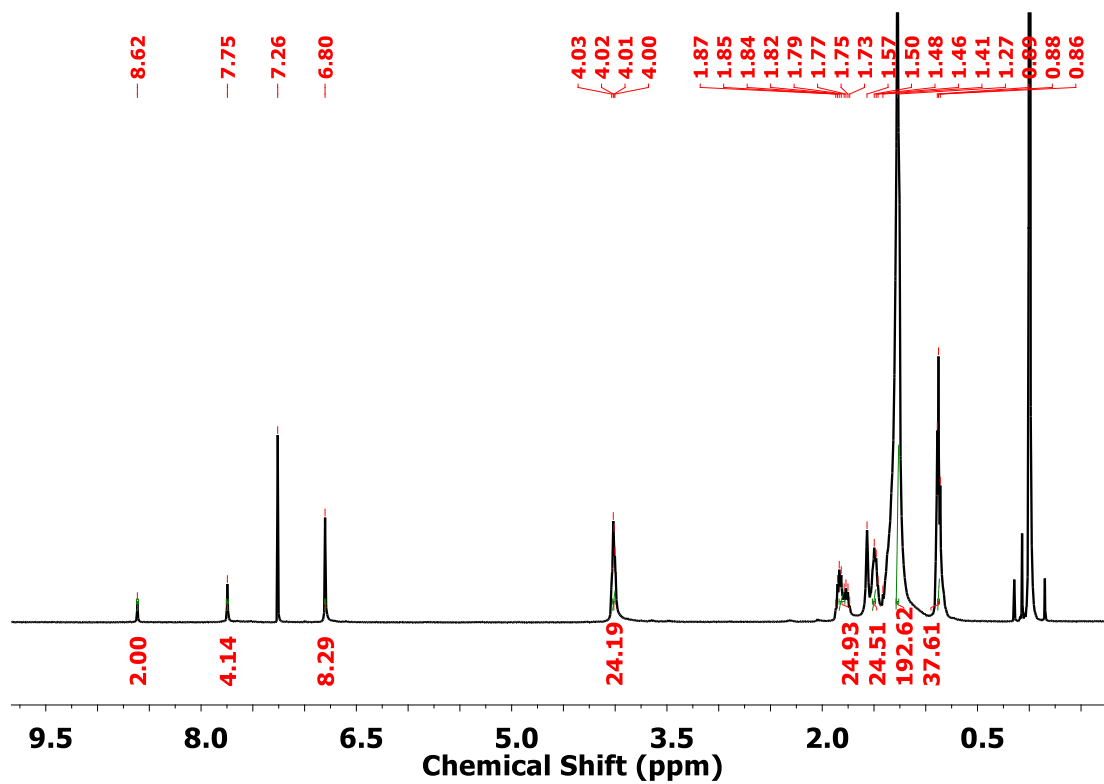
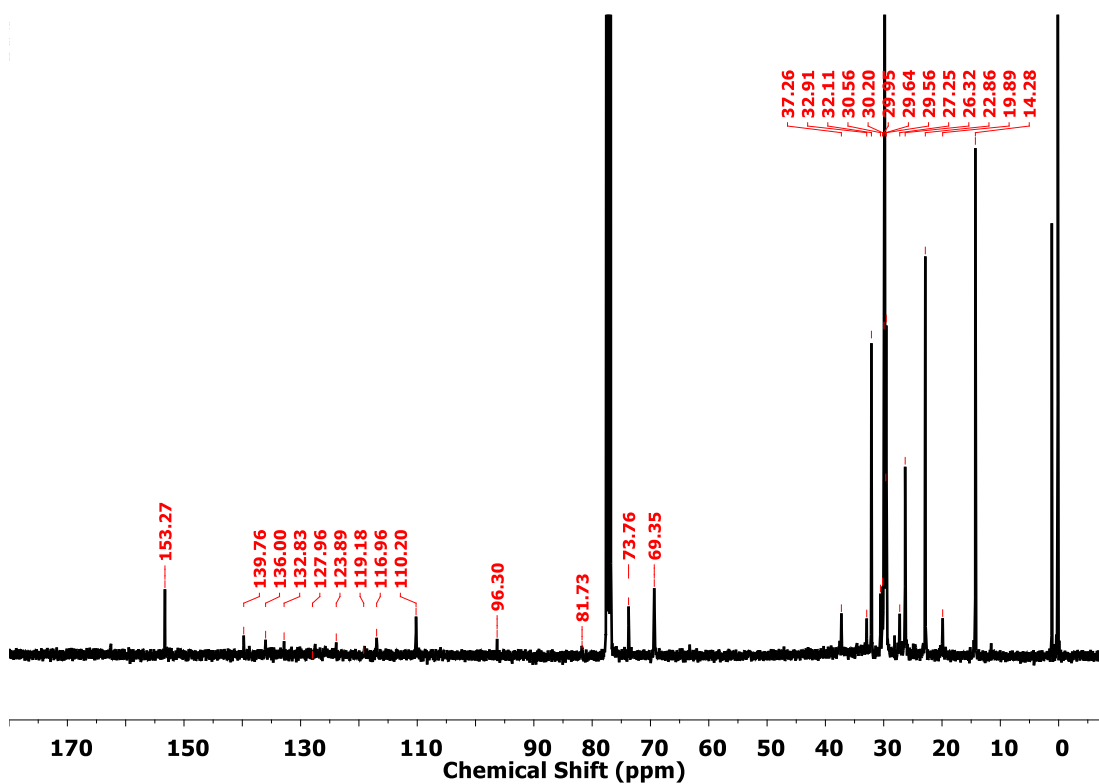
Figure A11. <sup>1</sup>H NMR spectrum of 13b.Figure A12. <sup>13</sup>C NMR spectrum of 13b.

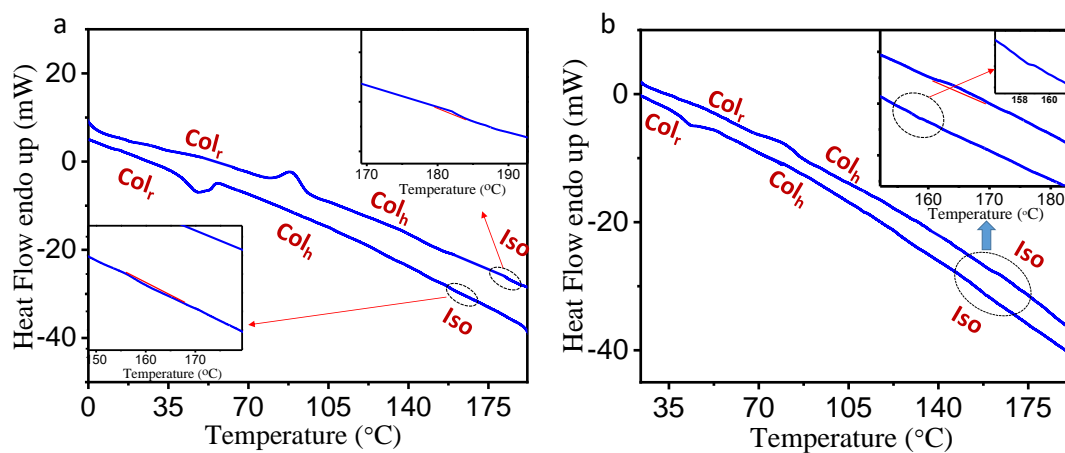
Figure A13. <sup>1</sup>H NMR spectrum of 14a.Figure A14. <sup>13</sup>C NMR spectrum of 14a.

Figure A15. <sup>1</sup>H NMR spectrum of 14b.Figure A16. <sup>13</sup>C NMR spectrum of 14b.



Figure A17. <sup>1</sup>H NMR spectrum of 1.Figure A18. <sup>13</sup>C NMR spectrum of 1.

Figure A19. <sup>1</sup>H NMR spectrum of 2.Figure A20. <sup>13</sup>C NMR spectrum of 2.



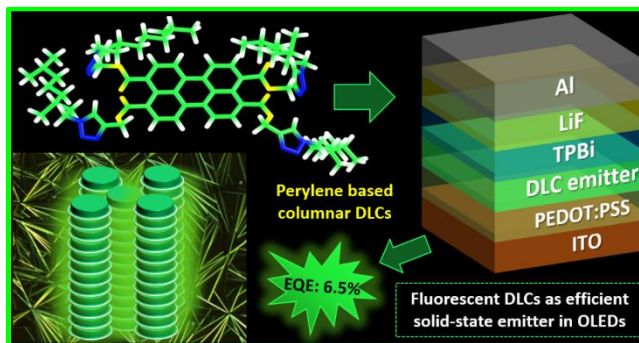
**Figure A21.** DSC thermogram of compound (a) **1** and (b) **2** recorded with the scan rate of 10 °C/min.



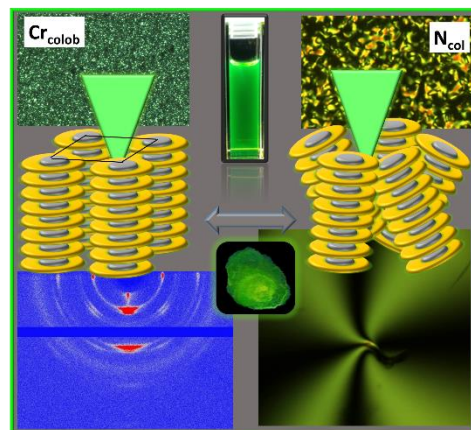
## Chapter 5

### Luminescent Perylene Tetraesters based Columnar Assemblies for Optoelectronic Applications

**Part A:** PTE-based room temperature DLCs, consisting of PTE core modified with triazole groups at the periphery in order to achieve efficient charge transport and luminescent behaviour of discogens were reported in this work. Charge transport behaviour in LC state as well as in neat state was investigated. Solution-processed OLED devices resulted in green-colored electroluminescence with a maximum EQE of 6.5%.



**Part B:** Oligomeric perylene tetraester (PTE) derivatives, consisting of PTE core attached to which four pentakynylbenzene units through flexible alkyl spacers, are reported in this work. Compounds with shorter alkyl spacers ( $n = 6$  and  $8$ ) were found to self-organize into soft crystalline columnar assemblies, those with longer spacers ( $n = 10$ ) exhibited a liquid-crystalline columnar nematic mesophase. All compounds exhibited excellent fluorescence emission properties with a very good quantum yield and large bandgap. Electrical characterization of columnar assemblies showed the potential of the derivatives to act as ion conductors.





## 5.1 Part A: Perylene-triazine Based Columnar Liquid Crystals as Solid-State Fluorescent Emitters in Solution-Processable Organic Light-Emitting Diodes

### 5.1.1 Introduction

The advancement of *n*-type (electron-deficient) semiconductor materials with high electron mobility and good emission properties is rare in comparison to comprehensively studied *p*-type systems known so far.<sup>1</sup> In this respect, perylene-based columnar (Col) liquid crystals (LCs) are the ideal candidates to be explored as emitters in organic light-emitting diodes (OLEDs). Perylene derivatives have gained expedient space in the field of optoelectronics due to their excellent luminescent behaviour, high charge carrier mobility, and remarkable thermal stability.<sup>2,3</sup> In literature, two types of perylene derivatives *viz.* perylene tetraesters (PTE)<sup>3</sup> and perylene bisimides<sup>2,3</sup> are known. However, perylene bisimides are well explored in the field of LCs,<sup>2-12</sup> OLEDs,<sup>13,14</sup> and in photovoltaic devices<sup>15</sup> in comparison to PTE. PTE being substantial electron-deficient (due to the presence of four carboxylate groups) can act as electron transport (*n*-type) materials in OLEDs as well as in organic semiconductors. The electron transport behaviour of PTE can be further improved by aligning the molecules in columnar fashion.<sup>16,17</sup> Col discotic liquid crystals (DLCs) are proved to be promising candidates for their application in OLEDs,<sup>18-22</sup> organic field-effect transistors (OFETs),<sup>23</sup> and organic photovoltaics (OPVs)<sup>18</sup>. However, most of the Col DLCs are luminescent in nature but have not much explored as emitter materials in OLEDs. Their usability in devices offers many advantages. For example, unlike crystalline materials, LCs form a defect-free film on a macroscopic level due to their self-healing ability.<sup>20-22,24</sup> Over crystalline and polymeric materials, DLCs can be achieved in high purity which is extremely important for their usability in device fabrication.<sup>20</sup> In addition to that, solution-processable devices can be accomplished due to the presence of alkyl chains in DLCs which renders huge device fabrication costs for mass production.

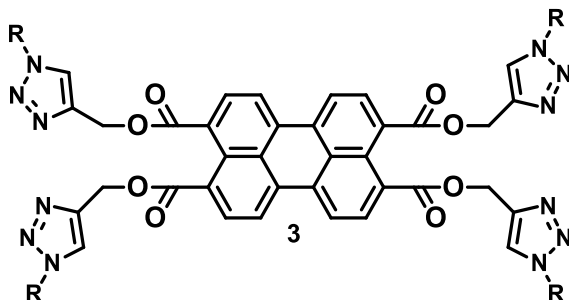
---

Reproduced/Adapted from (Bala, I.; Singh, N.; Yadav, R. A. K.; De, J.; Gupta, S. P.; Singh, D. P.; Dubey, D. K.; Jou, J. H.; Douali, R.; Pal, S. K. *J. Mater. Chem. C* **2020**, *8*, 12485-12494) with permission from The Royal Society of Chemistry. Some part of this work has been included in Master thesis of Ms. Nitya Singh (MS13093) at IISER Mohali and is greatly acknowledged and respected.

PTE derivatives have good electron-transporting ability in addition to their intense luminescent nature. For efficient OLEDs, if the emitter material possesses both solid-state emission behaviour and high charge carrier mobility, the device efficiency improves further.<sup>25</sup> The high charge carrier ability of the emitter moves charge carriers *via* the hopping process faster within the emitter layer. This process leads to better recombination of holes and electrons that give rise to better device efficiency.<sup>26</sup> Therefore, the efforts toward efficient fluorescent emitters based on DLC systems are essential which can break the efficiency limit of fluorescent OLEDs, ease the fabrication process by solution-processable technique, and avoid expensive and toxic metal-based light-emitting diodes.

### 5.1.2 Objectives

The present work involves an effort to achieve highly efficient, solution-processed fluorescent OLEDs based on purely organic DLC materials. To construct efficient fluorescent emitter materials, this work demonstrated a new molecular design of DLC systems based on PTE core. The motivation for the designing of these materials is twofold: First, to achieve the room temperature columnar LCs based on triazole-modified perylene tetraesters to study their structure-mesophase property relationship, in general, as a function of alkyl chains; Second, to employ these materials as solid-state emitters in OLEDs by taking the benefit of triazole modified-peryene fluorophore and the presence of alkyl chains in solution processability.



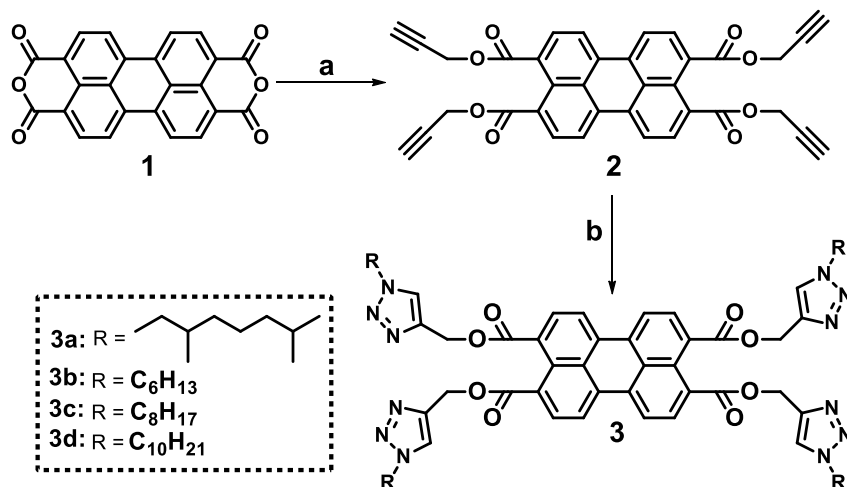
The strategic design of the PTE derivatives involves the introduction of electron-deficient and luminescent triazole groups at the periphery of PTE core that can improve the electron transport and luminescent behaviour of the resulting mesogens. In addition, the repulsive dipolar-dipolar interaction among triazole groups can suppress the intermolecular interactions helpful in lowering the mesophase temperature and preserve the solid-state efficiency simultaneously.



### 5.1.3 Results and discussions

#### 5.1.3.1 Synthesis and characterization

The convergent methodology was used to achieve PTE based target compounds (**3a-d**) in which four triazole groups were attached at the peripheral positions *via* microwave (MW) aided



**Scheme 5.1** Synthesis of compounds **3a-d**: (a) i. KOH, H<sub>2</sub>O, 80 °C, 2 h; ii. propargyl bromide, TOAB, reflux, overnight, yield: 50%; (b) R-N<sub>3</sub>, CuSO<sub>4</sub>, sodium ascorbate, CHCl<sub>3</sub>/EtOH/H<sub>2</sub>O (2:1:1), microwave (MW), yield: 60-72%.

Cu-catalyzed click chemistry. The synthetic steps are depicted in Scheme 5.1. The first step includes the conversion of perylene-3,4,9,10-tetracarboxylic acid dianhydride **1** to its corresponding potassium salt by treating **1** with an aqueous solution of potassium hydroxide.<sup>27</sup> After getting the clear green fluorescent solution of the potassium salt of perylene tetracarboxylic acid, its pH was adjusted to 8-9 by adding dilute HCl solution. Then the propargyl bromide and phase transfer catalyst tetraoctylammonium bromide (TOAB) was added *in-situ* and the solution was refluxed overnight. The colorless solution obtained with red-colored product floats on the surface indicates the completion of the reaction. After column chromatographic purification bright red-colored product **2** was obtained in moderate yield. The alkyl azides prepared from their corresponding 1-Bromo derivatives<sup>28</sup> were treated with **2** in a mixture of solvents chloroform/ethanol/water in the ratio 2:1:1. The mixture was heated at 65 °C in presence of sodium ascorbate and copper sulfate (CuSO<sub>4</sub>) for 2h in MW reactor, resulting **3a-d** in 60-72% yield (after chromatographic purification). The intermediate and target

compounds were structurally and analytically characterized by  $^1\text{H}$  NMR,  $^{13}\text{C}$  NMR, HRMS (Figure A1-A13, Appendix V, Page 313) and FT-IR techniques.

### 5.1.3.2 Thermal behaviour (POM and DSC)

To check the thermal stability of the PTE derivatives thermal gravimetric analysis (TGA) was carried out under a nitrogen atmosphere. Compounds **3a**, **3b**, **3c** and **3d** showed 5% weight loss at 221.1 °C, 205.0 °C, 201.3 °C and 251.0 °C, respectively (Figure 5.1). The decomposition temperatures of all the derivatives were well above the isotropic temperatures (Table 5.1) of the respective compounds. These results ensure the stability of the materials in the respective mesophase temperature range.

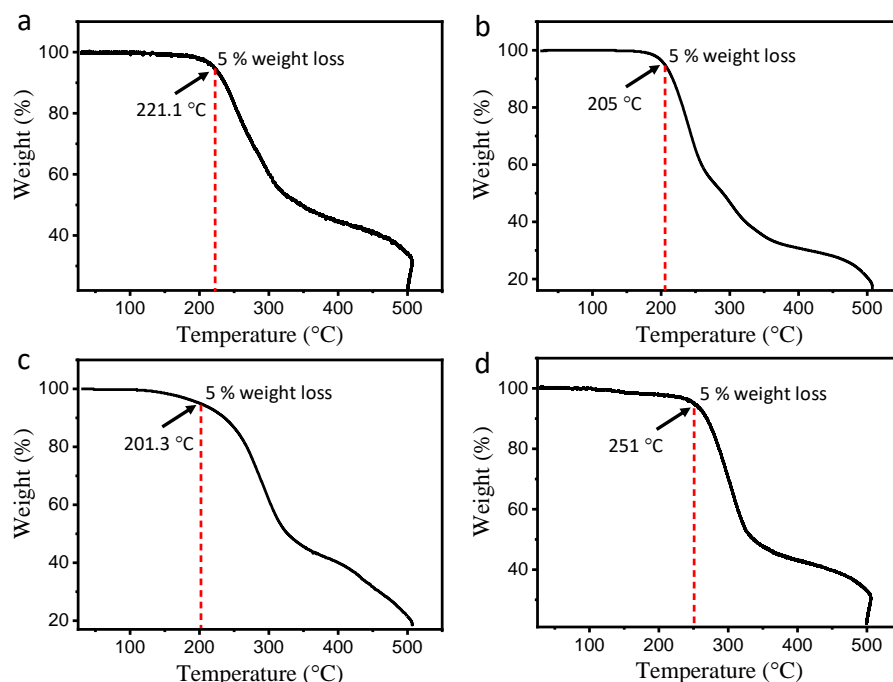


**Figure 5.1** TGA curves of PTE derivatives: (a) **3a** showing stability till 221.1 °C; (b) **3b** showing stability till 205 °C; (c) **3c** showing stability till 201.3 °C; (d) **3d** showing stability up to 251 °C. **Note:** The shown temperature is when the compounds undergo 5% weight loss.

In order to determine the mesomorphic behaviour, compounds were observed under polarized optical microscopy (POM). All compounds exhibited room temperature mesophase and enantiotropic LC behaviour (Table 5.1 and Table A1, Appendix V, Page 320). Under POM, compound **3a** with branched alkyl chain exhibited needle-like fan-shaped textures<sup>29</sup> (Figure 5.2a) on cooling from the isotropic liquid. The texture was easily shearable upon pressing the glass slide and hence indicates the presence of LC phase. The sheared texture corresponding

to compound **3a** is shown in Figure 5.2b. The DSC thermograms (Figure A14a, Appendix V, Page 319) were recorded to know the exact phase transition temperatures. In DSC, **3a** showed a peak at 115.5 °C (0.5 kJ/mol) which corresponds to mesophase to isotropic transition.

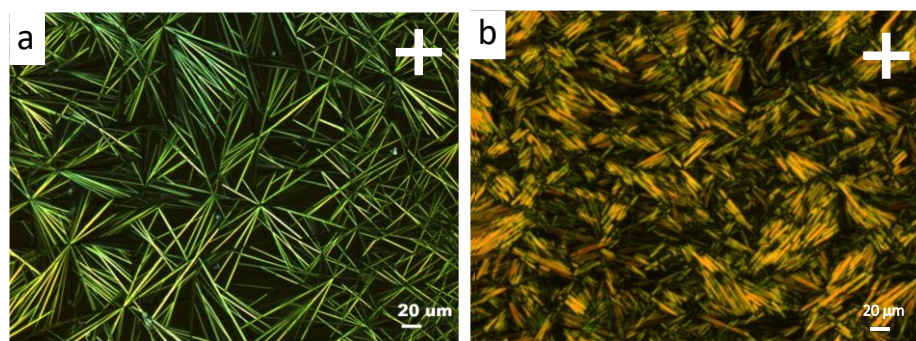


**Figure 5.2** Polarized microscopic images of compound **3a** (a) at 88.1 °C and (b) obtained on shearing the textures at 88.1 °C.

**Table 5.1** Phase transition temperatures of **3a-d**.<sup>a</sup>

Compound	Heating	Cooling	T <sub>d</sub> (°C) <sup>d</sup>
<b>3a</b>	Col <sub>ro</sub> 115.5 <sup>b</sup> (0.51) Iso	Iso 104.2 <sup>b</sup> (1.24) Col <sub>ro</sub>	221.1
<b>3b</b>	Col <sub>ro</sub> 175 <sup>c</sup> Iso	Iso 169 <sup>c</sup> Col <sub>ro</sub>	205.0
<b>3c</b>	Col <sub>ro</sub> 138.5 <sup>b</sup> (11.88) Iso	Iso 124 <sup>c</sup> Col <sub>ro</sub>	201.3
<b>3d</b>	Col <sub>ro</sub> 162.2 <sup>b</sup> (23.92) Iso	Iso 151 <sup>c</sup> Col <sub>ro</sub>	251.0

<sup>a</sup>Enthalpy values in parentheses in kJ/mol and temperatures in °C. <sup>b</sup>Phase transition temperatures observed by DSC technique. <sup>c</sup>Phase transition temperatures determined by POM. <sup>d</sup>Decomposition temperature corresponding to 5% weight loss. Abbreviation: C = compound; Col<sub>ro</sub> = ordered columnar rectangular; Iso = Isotropic.

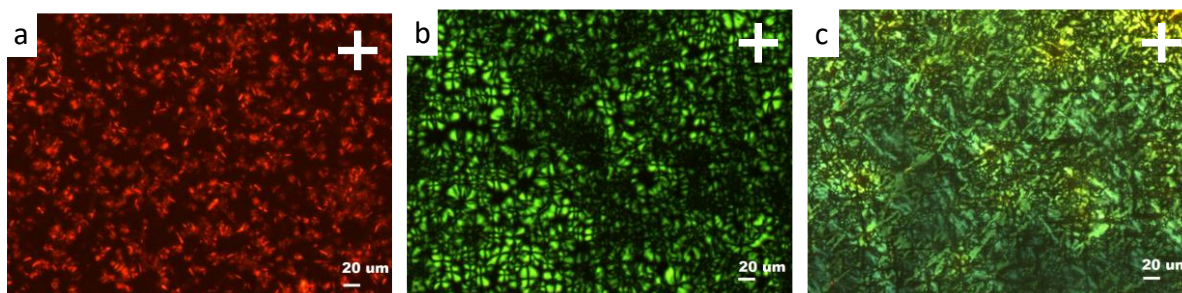


**Figure 5.3** POM textures of perylene derivatives (a) **3b** at 118.8 °C, (b) **3c** obtained at 50.3 °C, (c) **3d** at 103.1 °C, observed on cooling with the rate of 5 °C/min (×200).

On cooling, the mesophase appeared at 104.2 °C (1.2 kJ/mol) which was stable down to room temperature. The compound **3b** (with the peripheral alkyl chain length six) displayed broken-fan-shaped textures (Figure 5.3a) upon observation under POM, typical for Col LCs as reported earlier.<sup>29</sup> However, the transitions were not perceived in DSC, possibly due to insignificant enthalpy changes. Compound **3c** with peripheral chain length eight showed the growth of four-brush textures (Figure 5.3b) characteristic of Col phases. In the heating cycle, the DSC thermogram exhibited a peak at 138.5 °C (with enthalpy 11.88 kJ/mol) which corresponds to mesophase to isotropic phase transition (Figure A14b, Appendix V, Page 319). Although on cooling no observable peak reappeared, the POM observation clearly revealed the appearance of mesophase at 124 °C. On the other hand, compound **3d** possessed dendritic textures (Figure 5.3c) which suggests an indication of Col ordering. In DSC, **3d** displayed one peak at 162.2 °C (23.92 kJ/mol) in the heating cycle which can be correlated to mesophase to isotropic phase transition (Figure A14c, Appendix V, Page 319). However, on cooling the phase transition was observed by POM at 151 °C.

#### 5.1.3.3 X-Ray diffraction studies

In order to determine the columnar lattice in which molecules self-assembled in the mesophase, we have performed X-ray diffraction (XRD) for all the perylene derivatives. For compound **3a**, XRD study revealed two types of columnar assemblies at lower and higher temperatures. The transition temperatures corresponding to each columnar assembly are shown in Table 5.1. Both the assemblies can be indexed to a rectangular lattice i.e., Col<sub>ro1</sub> and Col<sub>ro2</sub>, at lower and higher temperatures, respectively. The Col<sub>ro1</sub> phase observed at lower temperatures, 25 °C (on cooling from isotropic liquid, Figure 5.4a), showed two intense peaks (along with many less intense peaks) in the small-angle region at 42.68 Å and 26.87 Å. These peaks correspond to the diffractions from (20) and (02) planes, respectively, with the lattice parameters  $a = 85.36$  Å,  $b = 53.74$  Å and  $h_c = 3.87$  Å (Table 5.2). The higher temperature rectangular phase (Col<sub>ro2</sub>) (at 80 °C, on cooling from the isotropic melt) exhibited three intense peaks at 41.56 Å, 27.36 Å and 24.71 Å which can be assigned to (20), (02) and (31) planes of rectangular lattice, respectively (Figure 5.4b). The lattice parameters for Col<sub>ro2</sub> phase are  $a = 83.09$  Å,  $b = 54.73$  Å and  $h_c = 3.89$  Å (Table 5.2). The wide-angle region of both the phases consists of a well-

defined strong and broad peak,  $h_c$  which is coming due to perylene core-core  $\pi$ -stacks. Hence, the phases are described to be columnar rectangular ordered ( $\text{Col}_{\text{ro}}$ ) mesophases. In addition,

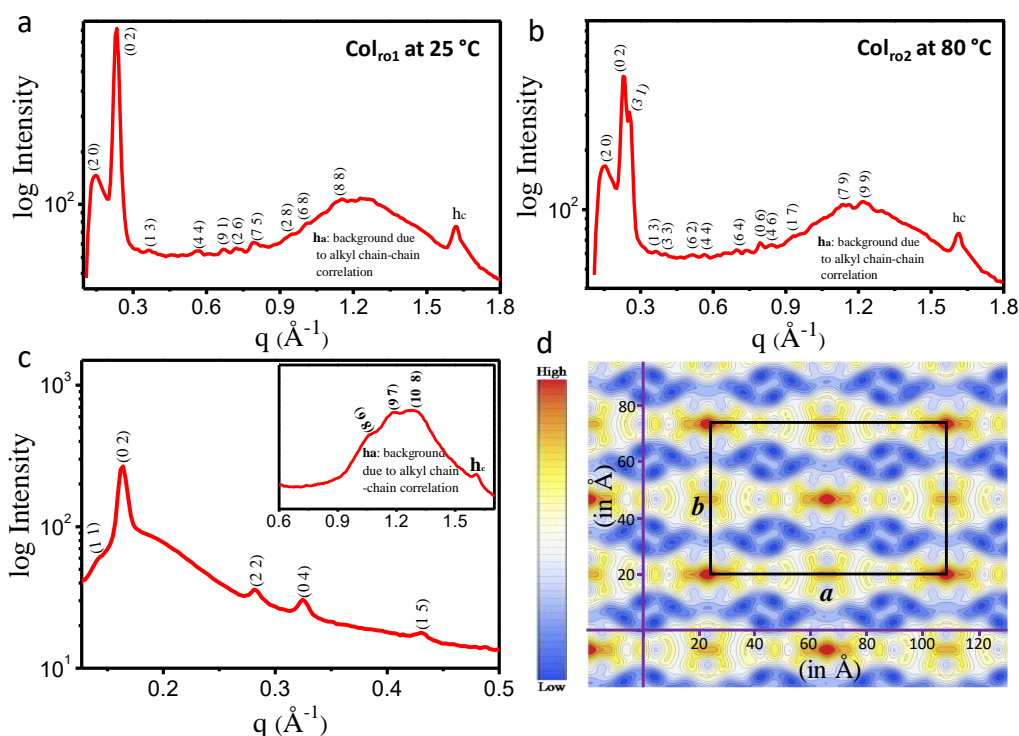


**Figure 5.4** X-ray diffraction (XRD) pattern of PTE derivatives: (a) **3a**:  $\text{Col}_{\text{ro1}}$  phase at 25 °C, (b) **3a**:  $\text{Col}_{\text{ro2}}$  phase at 80 °C, (c) **3c**:  $\text{Col}_{\text{r}}$  phase at 60 °C obtained on cooling the isotropic melt (cooling rate 10 °C/min). (d) Electron density maps shown for **3a** at 25 °C in centered columnar rectangular ( $\text{Col}_{\text{ro}}$ ) phase. Red color represents the high electron density region and deep blue is the lowest. Rectangle represents the unit cell of  $\text{Col}_{\text{ro}}$  phase with lattice parameter  $a$  &  $b$ .

all the peaks are well-fitted with  $hk$  values where  $h+k=2n$ ,  $n$  is an integer, therefore, indicating the phases belong to centred  $\text{Col}_{\text{ro}}$  with  $\text{C2}/m$  space group. Similar to compound **3a**, **3b** and **3d** also exhibited two types of  $\text{Col}$  rectangular mesophases ( $\text{Col}_{\text{ro1}}$  and  $\text{Col}_{\text{ro2}}$ ) (Figure 5.5). The observed lattice parameters, Miller indices are mentioned in Table 5.2 for **3b** and **3d**, respectively.

On the other hand, **3c** showed only one type of mesophase throughout the temperature range as shown in Figure 5.4c. The phase can be indexed on a centred 2D  $\text{Col}_{\text{r}}$  lattice with the lattice parameters and miller indices as mentioned in Table 5.2. Electron density map (EDM) was reconstructed by using the information of peak indexes and intensities corresponding to **3a** at

25 °C as reported earlier.<sup>20,21</sup> The EDM also correspond to the arrangement of molecules in the rectangular lattice as can be seen in Figure 5.4d.

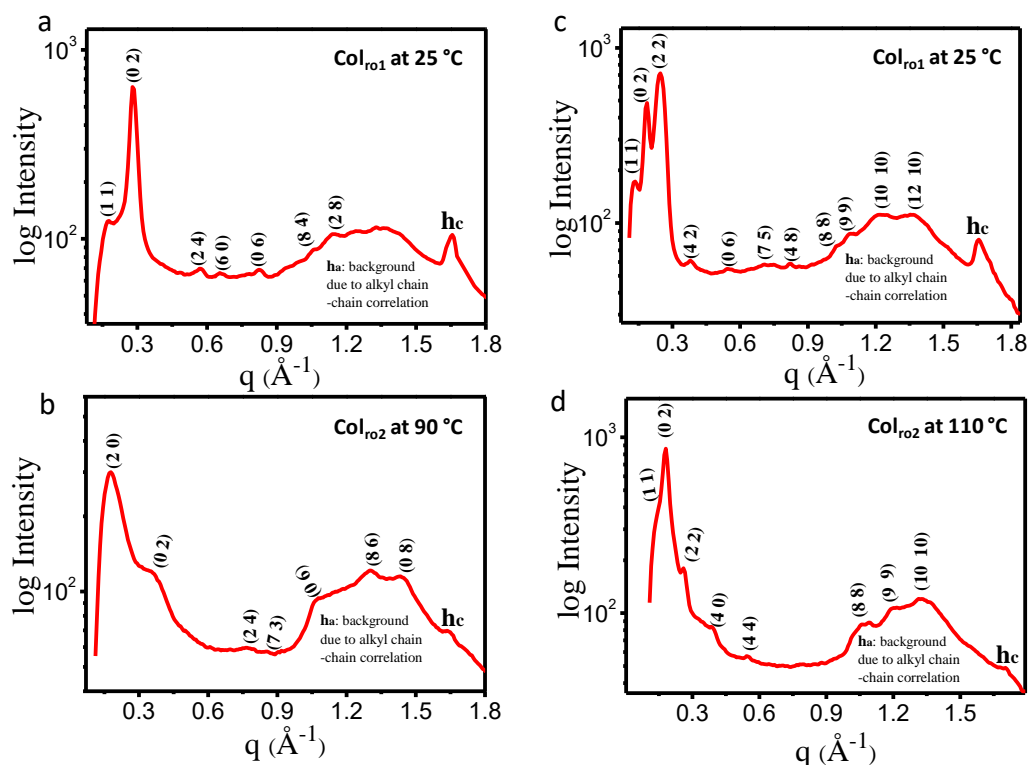


**Figure 5.5** XRD pattern of **3b**: (a) Col<sub>ro1</sub> phase at 25 °C and (b) Col<sub>ro2</sub> phase at 90 °C obtained on cooling the isotropic melt (cooling rate 10 °C/min). XRD pattern of **3d**: (c) Col<sub>ro1</sub> phase at 25 °C and (d) Col<sub>ro2</sub> phase at 110 °C obtained on cooling the isotropic melt (cooling rate 10 °C/min).

**Table 5.2** Phase behaviour, Miller Indices, lattice constants and  $d$ -spacing observed from the XRD studies for compound **3a-d**.

Compound	Mesophase	Lattice constants ( $\text{\AA}$ )	$d_{\text{obs}}^a$ ( $\text{\AA}$ )	$d_{\text{cal}}^b$ ( $\text{\AA}$ )	MI <sup>c</sup> ( $h k$ )
<b>3a</b>	Col <sub>ro1</sub> at 25 °C	$a = 85.36$	42.68	42.68	2 0
		$b = 53.74$	26.87	26.87	0 2
			17.20	17.53	1 3
			11.16	11.37	4 4
			9.40	9.34	9 1
			8.71	8.77	2 6
			7.92	8.06	7 5

			6.67	6.64	2 8
			6.25	6.07	6 8
			5.46	5.68	8 8
			3.87	3.87	<b>h<sub>c</sub></b>
	Col <sub>ro2</sub> at 80 °C	<i>a</i> = 83.09	41.56	41.45	2 0
		<i>b</i> = 54.73	27.36	27.37	0 2
			24.71	24.71	3 1
			17.45	17.82	1 3
			15.49	15.24	3 3
			12.20	12.36	6 2
			11.20	11.43	4 4
			9.59	9.73	6 4
			9.04	9.12	0 6
			8.56	8.35	4 6
			7.92	7.78	1 7
			5.51	5.41	7 9
			5.13	5.08	9 9
			3.89	3.89	<b>h<sub>c</sub></b>
<b>3b</b>	Col <sub>ro1</sub> at 25 °C	<i>a</i> = 58.50	35.70	35.70	1 1
		<i>b</i> = 45.06	22.53	22.53	0 2
			10.79	10.51	2 4
			9.60	9.75	6 0
			7.57	7.51	0 6
			5.94	6.13	8 4
			5.53	5.53	2 8
			3.80	3.80	<b>h<sub>c</sub></b>
	Col <sub>ro2</sub> at 90 °C	<i>a</i> = 70.60	35.30	35.30	2 0
		<i>b</i> = 34.32	17.16	17.16	0 2
			8.10	8.34	3 1
			7.33	7.57	1 3
			5.86	5.72	3 3
			4.83	4.80	6 2
			4.38	4.29	4 4
			3.80	3.80	6 4
<b>3c</b>	Col <sub>ro</sub> at 60 °C	<i>a</i> = 54.70	44.59	44.60	1 1
		<i>b</i> = 77.04	38.52	38.52	0 2
			22.26	22.30	2 2
			19.35	19.26	0 4
			14.56	14.83	1 5

			5.94	6.04	8 6
			5.34	5.32	9 7
			4.97	4.76	10 8
			3.90	3.90	<b>h<sub>c</sub></b>
<b>3d</b>	Col <sub>ro1</sub> at 25 °C	<i>a</i> = 78.10	50.83	50.84	1 1
		<i>b</i> = 66.98	33.49	33.49	0 2
			25.45	25.42	2 2
			16.73	16.87	4 2
			11.39	11.16	0 6
			8.71	8.57	7 5
			7.66	7.69	4 8
			6.14	6.36	8 8
			5.80	5.65	9 9
			5.17	5.08	10 10
			4.60	4.67	12 10
			3.80	3.80	<b>h<sub>c</sub></b>
	Col <sub>ro1</sub> at 110 °C	<i>a</i> = 56.80	47.14	47.14	1 1
		<i>b</i> = 45.08	34.69	34.70	0 2
			23.57	23.57	2 2
			16.05	16.06	4 0
			11.57	11.78	4 4
			5.84	5.89	8 8
			5.23	5.24	9 9
			4.71	4.71	10 10
			3.68	3.68	<b>h<sub>c</sub></b>

<sup>a</sup>*d*<sub>obs</sub>: *d*-spacing obtained from XRD experiments; <sup>b</sup>*d*<sub>cal</sub>: *d*-spacing calculated by equation:  $\frac{1}{d^2} = \left(\frac{h^2}{a^2} + \frac{k^2}{b^2}\right)$  with  $h+k = 2n$ , *n* is integer; *h*, *k* are the miller indices belongs to the reflections of centred columnar rectangular (Col<sub>r</sub>) phases; *a* and *b* are the unit cell parameters, **h<sub>c</sub>** attributes to *d*-spacing arising from core-core correlation.

#### 5.1.3.4 Photophysical electrochemical and theoretical studies

In order to investigate the photophysical behaviour of perylene derivatives **3a-d**, the absorption and emission studies in solution as well as in solid-state were performed (Table 5.3). The solution state studies were carried out in micromolar THF solutions. All the compounds showed similar peaks in absorption as well as in emission spectra irrespective of the chain length. The solution-state and solid-state spectra for compound **3a** have been shown in Figure



5.6a and Figure 5.6b, respectively. In solution state, the compounds exhibited six peaks in the absorption spectra. The three absorption peaks at 291, 265 and 245 nm were aroused due to the vibration speculation from triazole moiety while the peaks at 475, 446, 419 nm associated with the  $0 \rightarrow 0$ ,  $0 \rightarrow 1$  and  $0 \rightarrow 2$  vibrational modes of the perylene ring.<sup>30</sup>

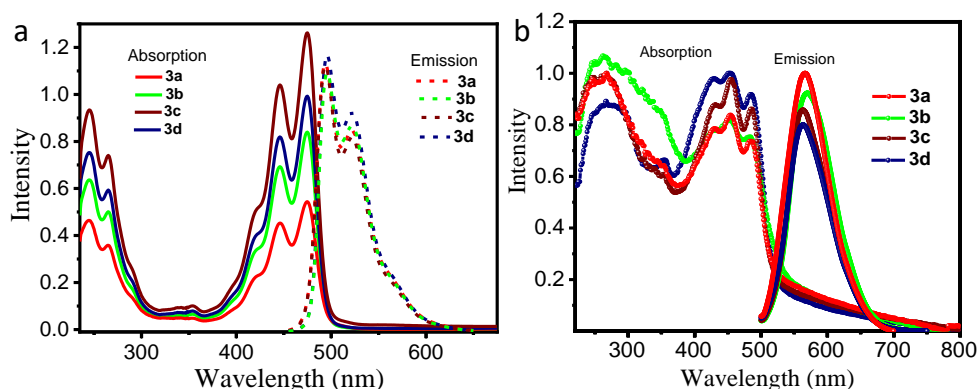


**Figure 5.6** Absorption and emission spectra of perylene derivative **3a-d**: (a) in micromolar THF solution and (b) in thin-film state.

**Table 5.3** Photophysical data of the PTE derivatives.

C	A <sub>solution</sub> <sup>a</sup> Peaks (nm)	E <sub>solution</sub> <sup>a,c</sup> Peaks (nm)	A <sub>solid</sub> Peaks (nm) <sup>b</sup>	E <sub>solid</sub> <sup>c</sup> Peaks (nm)	τ <sup>e</sup> (ns)	φ <sub>FL</sub> <sup>f</sup>	Steady State Anisotropy
<b>3a</b>	245, 265, 291, 419, 446, <sup>b</sup> 475	493, 522, 567 <sup>d</sup>	244, 265, 352, 429, 453, <sup>b</sup> 485	566	3.77	0.40	$4.05 \times 10^{-2}$
<b>3b</b>	245, 265, 291, 419, 446, <sup>b</sup> 475	493, 522, 567 <sup>d</sup>	243, 262, 351, 426, 451, <sup>b</sup> 482	570	3.56	0.56	$2.96 \times 10^{-2}$
<b>3c</b>	245, 265, 291, 419, 446, <sup>b</sup> 475	493, 522, 567 <sup>d</sup>	243, 268, 354, 430, 454, <sup>b</sup> 485	563	3.62	0.50	$3.72 \times 10^{-2}$
<b>3d</b>	245, 265, 291, 419, 446, <sup>b</sup> 475	493, 522, 567 <sup>d</sup>	247, 267, 354, 426, 453, <sup>b</sup> 485	564	3.52	0.24	$3.82 \times 10^{-2}$

<sup>a</sup>in micromolar THF solution. <sup>b</sup>Excitation wavelength, λ<sub>exc</sub>. <sup>c</sup>obtained after exciting at respective λ<sub>exc</sub>. <sup>d</sup>Peak visible upon zooming the corresponding region. <sup>e</sup>τ = fluorescence decay lifetime in CHCl<sub>3</sub>. <sup>f</sup>φ<sub>FL</sub> = Fluorescence quantum yield measured with respect to fluorescein (φ<sub>FL</sub> = 0.79) in 0.1M NaOH. Abbreviation: C- Compound, A<sub>solution</sub>: Solution state absorbance, E<sub>solution</sub>: Solution state emission. A<sub>solid</sub>: Thin-film absorbance, E<sub>solid</sub>: Thin-film emission.

The comparable intensity of triazole peaks to the perylene moiety peaks indicated the additional stacking benefitted from triazole groups. The mirror image emission spectra consisted of three peaks at 493, 522 and 567 nm was appeared due to perylene moiety which indicated that the emission properties of the compounds were primarily dominated by the central perylene core. The absorption peaks in the thin-film due to triazole and perylene moiety becomes more broadened with the slight bathochromic shift due to the increased intermolecular interactions. On the other hand, one emission peak was appeared in a thin-film state with peak maxima shifted to a higher wavelength in comparison to the solution state.

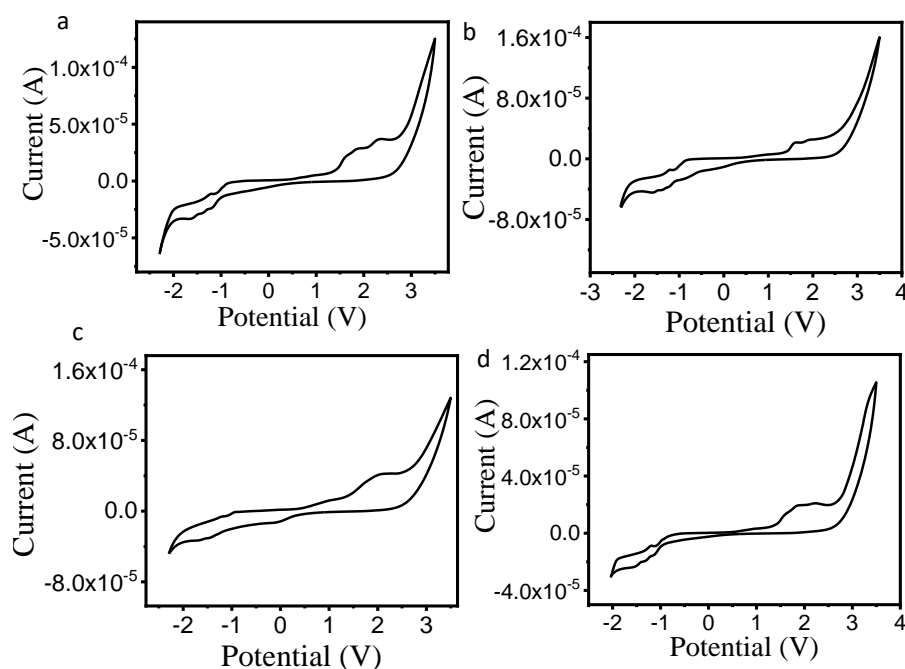


**Figure 5.7** Cyclic Voltammogram of compound (a) **3a**, (b) **3b**, (c) **3c** and (d) **3d** in 0.1 M tetrabutylammonium hexafluorophosphate solution in dichloromethane solvent recorded with scan rate 50 mV/s.

To get more insight into the luminescence efficacy of the materials, relative quantum yield measurements were performed in THF for all the PTE derivatives. The fluorescein was chosen as a standard as it absorbs around the same wavelength as that of the PTE derivatives.<sup>31</sup> The quantum yield values with respect to fluorescein (0.79 in 0.1 M NaOH) varied from 0.24 to 0.56 for **3a-d** (Table 5.3). In addition, to probe the efficiency of the compounds to decay through the fluorescence pathway, lifetime decay measurements were carried out in  $\text{CHCl}_3$ . The fluorescence lifetime was found to be mono-exponential and values lie in the range 3.52-

3.77 ns (Table 5.3). Moreover, the molecular environment such as viscosity, molecular size, etc. affects the fluorescence anisotropy of the molecules. In the present case, the fluorescence anisotropy values were found to be increased with an increase in molecular size (from **3b** to **3d**) and highest for **3a** derivative with branched alkyl chains. This implies that mobility decreases with an increase in size, and hence, anisotropy values increases. The suitable electronic energy levels of the materials are required to employ them in active layers of the optoelectronic and semiconductor devices. Hence the energy levels of the perylene derivatives were determined from the cyclic voltammetry (CV)<sup>31</sup> (Figure 5.7) as well as the ultraviolet photoelectron spectroscopy (UPS) technique (Figure 5.8).

All the compounds exhibited quasi-reversible characteristics in CV carried out in millimolar solutions of the compounds (**3a-d**) in dichloromethane and 0.1 M tetrabutylammonium hexafluorophosphate. The HOMO and LUMO energy levels obtained from CV are listed in Table 5.4 and were used to calculate the electrochemical bandgap ( $\Delta E_{g, cv}$ ).

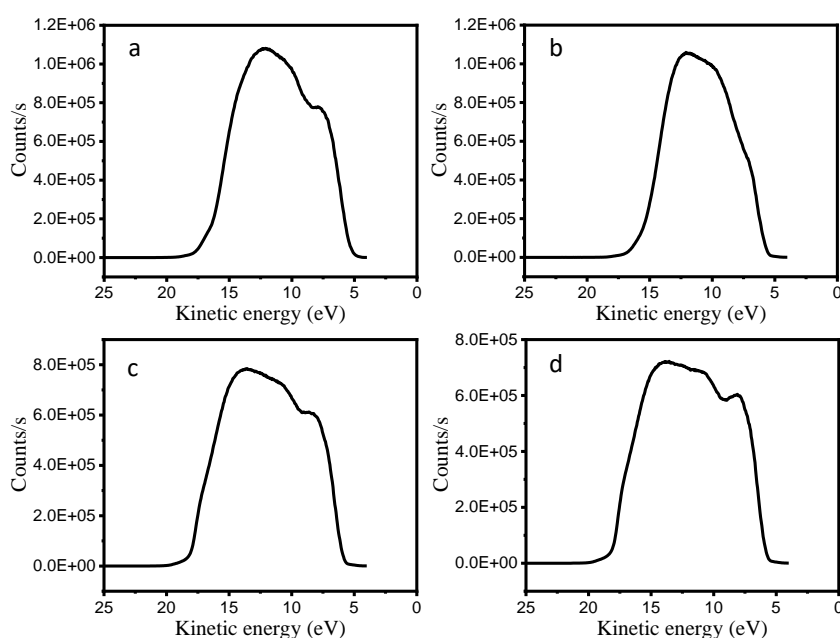


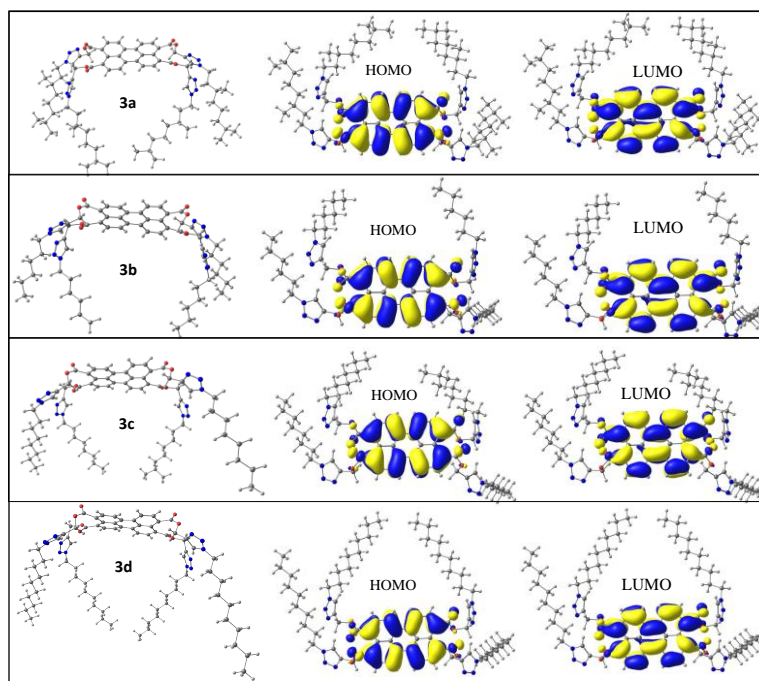
**Figure 5.8** UPS spectra obtained in spin-coated thin-film of compound (a) **3a**; (b) **3b**; (c) **3c**; (d) **3d** on ITO substrates.

The energy levels obtained from UPS technique are lower than as obtained from CV studies. These differences can be attributed to the fact that there are interactions in thin-film as compared to a solution, similar to the well-known changes in the optical bandgap when going from solution to film state.

**Table 5.4** Electrochemical data of the PTE derivatives.

C	$\lambda_{UVonset}$ (nm) <sup>b</sup>	$E_{1red}$ (V) <sup>c</sup>	$E_{1oxd}$ (V) <sup>d</sup>	$E_{HOMO, CV}$ ( $E_{HOMO, UPS}$ ) (eV) <sup>e</sup>	$E_{LUMO, CV}$ ( $E_{LUMO, UPS}$ ) (eV) <sup>f</sup>	$\Delta E_{g, CV}$ (eV) <sup>g</sup>	$\Delta E_{opt}^h$ (eV)	$\Delta E_{DFT}^i$ (eV)
<b>3a</b>	525	-0.92	+1.32	-5.57 (-5.82)	-3.33 (-3.46)	2.24	2.36	2.27
<b>3b</b>	539	-1.05	+1.30	-5.55 (-5.94)	-3.20 (-3.64)	2.35	2.30	2.27
<b>3c</b>	532	-1.11	+1.31	-5.56 (-5.75)	-3.13 (-3.42)	2.42	2.33	2.28
<b>3d</b>	539	-0.94	+1.33	-5.58 (-5.70)	-3.31 (-3.40)	2.27	2.30	2.27

<sup>a</sup>recorded in THF solution ( $\mu$ M). <sup>b</sup>Onset wavelength in thin-film absorption spectra. <sup>c</sup>onset reduction potential. <sup>d</sup>onset oxidation potential. <sup>e</sup>Estimated as:  $E_{HOMO, CV} = -[4.8 - E_{1/2, Fc/Fc^+} + E_{1oxd}]$  eV, where  $E_{1/2, Fc/Fc^+} = 0.55$  V;  $E_{HOMO, UPS} = 21.2 - (E_{cut-off} - E_{Fermi})$ . <sup>f</sup>Estimated as:  $E_{LUMO, CV} = -[4.8 - E_{1/2, Fc/Fc^+} + E_{1red}]$  eV;  $E_{LUMO, UPS} = \Delta E_{opt} + E_{HOMO}$ . <sup>g</sup>Calculated as:  $\Delta E_{g, CV} = E_{LUMO} - E_{HOMO}$ . <sup>h</sup>Calculated as:  $\Delta E_{opt} = 1240/\lambda_{UVonset}$ . <sup>i</sup>Calculated from DFT. Abbreviation: C- Compound,  $\Delta E$  = Bandgap.

**Figure 5.9** Energy minimized geometry and frontier molecular orbitals of **3a-d** at B3LYP/6-31G (d,p) level.

For further estimation of energy levels, DFT calculations were carried out using Gaussian 09 software at the B3LYP/6-31G (d,p) level (Figure 5.9). Both the HOMO and LUMO of the

materials are predominantly distributed on the  $\pi$ -conjugated bonding and anti-bonding orbitals of the perylene core. The bandgap values obtained from DFT are in close agreement with the values obtained from UV and CV studies. Apart from these, the HOMO levels were also deduced from the UPS (Figure 5.8 and Table 5.4) performed on thin-films on an ITO substrate while the LUMOs were extracted from the optical bandgap (measured from the red absorption edge of the thin-film UV-Vis spectra).

### 5.1.3.5 Charge carrier mobility measurements

Perylene tetraesters based liquid crystalline materials can show good electron transport behaviour due to its electron-deficient nature. Thereby, the electron mobility of a representative compound **3a** was investigated in liquid crystalline state by the time of flight (TOF) technique. In this technique, a laser pulse of 355 nm having 5 ns pulse width was made to an incident on the material by using Nd:YAG laser with a laser spot of 8 mm in diameter. The induced charge displacement can be observed *via* a transient photocurrent curve that was measured by a digital oscilloscope coupled to a current amplifier. The charge carrier mobility was obtained by the output transient photocurrent curve.

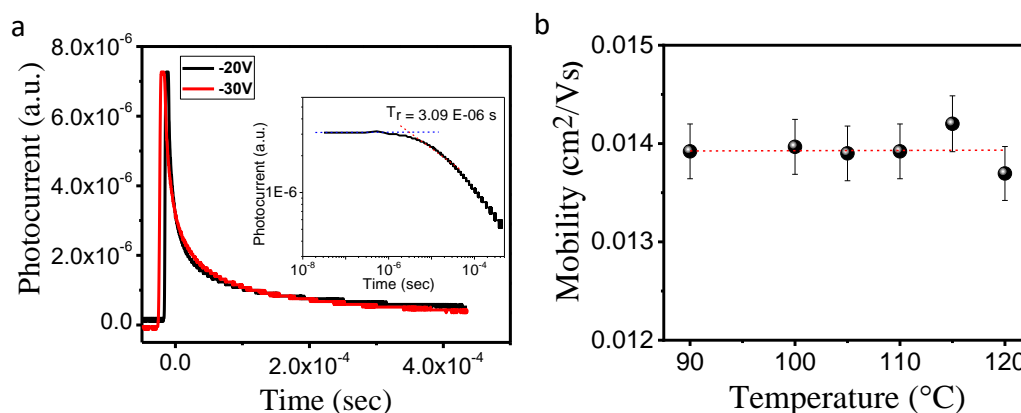


**Figure 5.10** (a) Dispersive transient photocurrent curves of compound **3a** at two different applied voltages, i.e. -20 and -30 V (inset represents the log-log scale curve of dispersive transient photocurrent at -20 V in order to estimate the transient time). (b) Electron mobility versus temperature curve of compound **3a** (red dotted line depicts the linear fit of mobility versus temperature curve).

To execute TOF measurement, compound **3a** was filled in a homeotropic cell thickness of 9.2  $\mu\text{m}$ . Under the application of external voltage (-20 V to -30 V), we obtained a dispersive transient photocurrent curve as shown in Figure 5.10a. The transit time ( $T_r$ ) of charge carriers (electrons) was obtained by the transient photocurrent curve (see inset of Figure 5.10a) and the mobility ( $\mu$ ) was calculated by  $\mu = d^2/Tr.V$ , where  $T_r$  is the transient time obtained by photocurrent curves,  $V$  is the applied voltage and  $d$  is the ITO cell thickness. The charge carrier mobility for electrons was plotted as a function of temperature in Figure 5.10b and temperature-independent electron mobility of  $0.014 \text{ cm}^2 \text{ V}^{-1} \text{ s}^{-1}$  was perceived for **3a**.

### 5.1.3.6 Electroluminescent behaviour

Inspired by excellent photophysical properties, appropriate molecular orbital energy level, high electron mobility, it is expected to attain a high utilization of singlet excitons, hence outstanding device performance in OLED devices consisting of compound **3a** as an emitter.

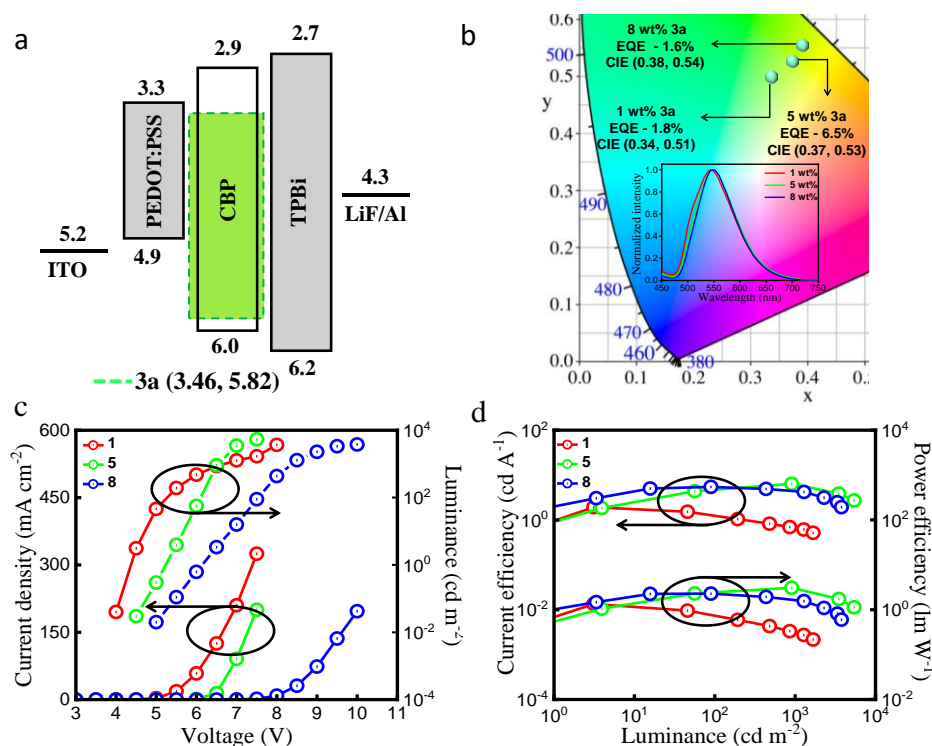


**Figure 5.11** (a) Energy level diagram showing different layers fabricated in solution-processed OLED device and (b) chromaticity plot showing CIE coordinates and EQE Inset: Normalized EL spectra of the devices, (c) current density-voltage-luminance ( $J$ - $V$ - $L$ ) characteristics and (d)

current efficiency-luminance-power efficiency characteristics corresponding to 1.0, 5.0, and 8.0 wt% doped devices.

To investigate the EL property of the emitter, solution-processed multi-layered OLED devices were fabricated with commonly used device structure: ITO (125 nm)/ poly(3,4-ethylenedioxythiophene) polystyrene sulfonate (PEDOT:PSS) (35 nm)/ 4,4'-Bis(N-carbazolyl)-1,1'-biphenyl (CBP):  $x$  wt% of **3a** ( $x = 1, 5, 8$ , and 100) (20 nm)/ 2,2'2''-(1,3,5-benzinetriyl)tris(1-phenyl-1-H-benzimidazole) (TPBi) (35 nm)/ LiF (1 nm)/ Al (150 nm) shown in Figure 5.11a, where PEDOT:PSS works as the hole-injection layer; CBP serves as the host matrix; TPBi functions as the electron-transport layer; and LiF acts as the electron-injection layer. Besides CBP, another host molecule Bis[3,5-di(9H-carbazol-9-yl)phenyl]diphenylsilane (SimCP2) was studied for the EL performance comparison (Figure 5.12). The non-doped device showed very poor performance with a maximum luminance of only 7 cd/m<sup>2</sup> may be due to the existence of strong exciton interactions. Doping of emitter in an appropriate matrix is one of the preeminent ways to segregate the luminogens and modulate substrate polarity, which can be favourable to block detrimental exciton interactions and realizing a well-proportioned HLCT excited state.<sup>32-35</sup> First, CBP was employed as a host for designing the device structure because its HOMO/LUMO levels (6.00/2.90 eV) are well

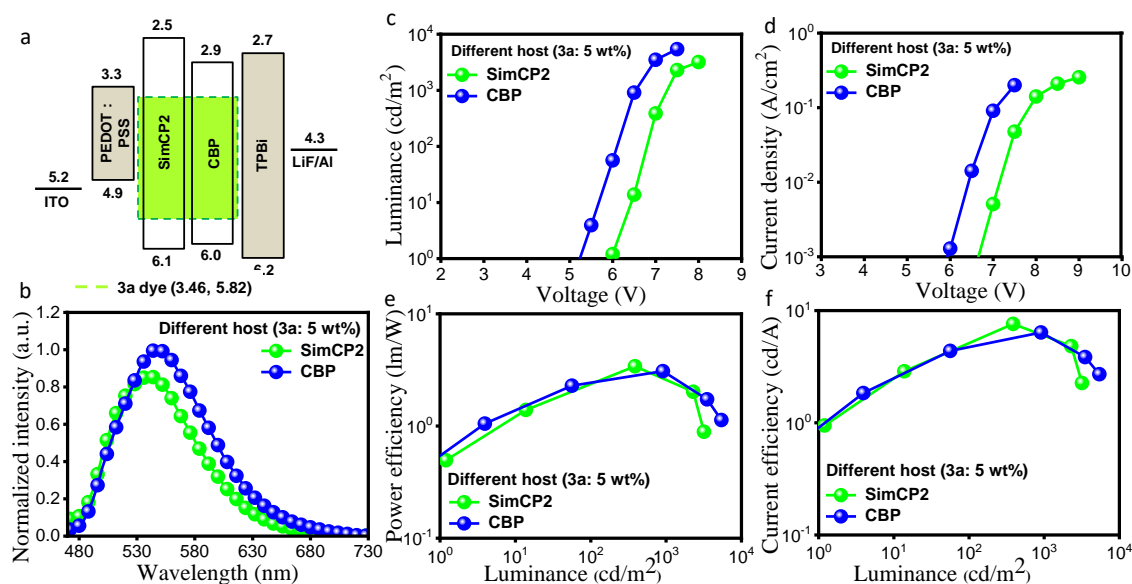


**Figure 5.12** (a) Energy level schematic diagram, (b) electroluminescent spectra (EL), (c) Luminance-voltage, (d) current density-voltage, (e) power efficiency-luminance and (f)

current efficiency-luminance plots of the solution-processed OLED device with 5 wt% of **3a** emitter in SimCP2 and CBP host.

**Table 5.5** Doping concentration effects on the power efficiency (PE), current efficiency (CE), external quantum efficiency (EQE), and maximum brightness ( $L_{\max}$ ) of solution-processed **3a** based OLED devices with different hosts.

Host	Emitter conc. (wt%)	Turn-on voltage (V)	PE <sub>max</sub> / CE <sub>max</sub> / EQE <sub>max</sub> <sup>a</sup> (lm W <sup>-1</sup> / cd A <sup>-1</sup> / %)	PE <sub>1000</sub> / CE <sub>1000</sub> / EQE <sub>1000</sub> <sup>b</sup> (lm W <sup>-1</sup> / cd A <sup>-1</sup> / %)	CIE coordinates	L <sub>max</sub> (cd/m <sup>2</sup> )
<b>CBP</b>	1	4.2	1.3/1.9/ 1.8	0.3/ 0.7/ 1.4	(0.34, 0.51)	3710
	5	5.2	3.1/6.8/ 6.5	3.0/ 6.3/ 6.4	(0.37, 0.53)	5520
	8	6.1	2.4/5.4/ 1.6	1.7/ 4.4/ 1.4	(0.38, 0.54)	3773
	100	6.0	-/-/-	-/ -/ -	-	7
<b>SimCP2</b>	5	5.9	3.0/6.7/4.4	2.7/ 6.0/ 4.4	(0.31, 0.47)	3180

<sup>a</sup>Maximum PE, CE, and EQE. <sup>b</sup>PE, CE, and EQE at 1000 cd/m<sup>2</sup>.

immersed in energy levels of emitter **3a** (5.82/3.46 eV: calculated energy levels from UPS technique measured in thin-film are more reliable for the optoelectronic application, especially the OLED), enabling effective charge/energy transfer between various layers as well as host-guest molecules and hence blocking exciton quenching. As anticipated, outstanding performances were obtained for a device based on 5 wt% of compound **3a** doped in CBP host, achieving maximum brightness ( $L_{\max}$ ) of 5,520 cd/m<sup>2</sup>, current efficiency (CE<sub>max</sub>) of 6.8 cd/A, power efficiency (PE<sub>max</sub>) of 3.1 lm/W, and external quantum efficiency (EQE<sub>max</sub>) of 6.5% as displayed in Figure 5.11 and Table 5.5. Furthermore, OLED devices consisting of 1.0 wt% **3a** exhibited an EQE<sub>max</sub> of 1.8%, PE<sub>max</sub> of 1.3 lm W<sup>-1</sup>, and CE<sub>max</sub> of 1.9 cd m<sup>-2</sup>, and  $L_{\max}$  of 3710 cd m<sup>-2</sup> with CIE coordinates of (0.34, 0.51). The device fabricated with 8.0 wt% showed a relative drop in EL performance with an EQE<sub>max</sub>, PE<sub>max</sub>, and CE<sub>max</sub> of 1.6%, 2.4 lm W<sup>-1</sup>, and 5.4 cd A<sup>-1</sup>, respectively. All OLED devices show yellowish-green EL emissions at 544, 548, and 548 nm for 1.0, 5.0, and 8.0 wt%, respectively, which quite in order to the PL emissions indicating that the EL emissions originate from their excited states. The current-density versus voltage curves of the hole-only (HOD) and electron-only devices (EOD) with device



configuration-HOD: ITO/PEDOT:PSS/**3a**/LiF/Al and EOD: ITO/**3a**/TPBi/LiF/Al, show balanced hole and electron mobilities in their respective fabricated devices (Figure 5.13). This can contribute to the charge balance in the emissive recombination zone and might be considered as one of the factors for the observed EL performance. Interestingly, doping concentration of **3a** highly influences the device EL performance as shown in Figure 5.11. For example, on decreasing the concentration from 8.0 wt% to 5.0 wt%, the EQE increases

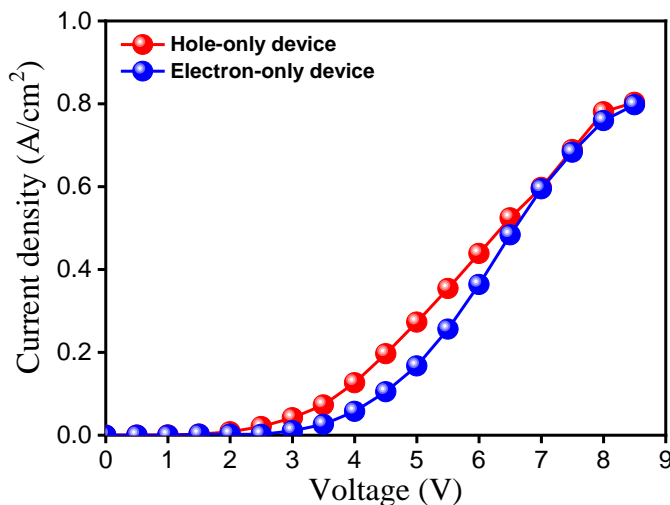


**Figure 5.13** Current density versus Voltage plot of hole-only and electron-only devices of the emitter material **3a** with device configuration-HOD: ITO/PEDOT:PSS/**3a**/LiF/Al and EOD: ITO/**3a**/TPBi/LiF/Al, respectively.

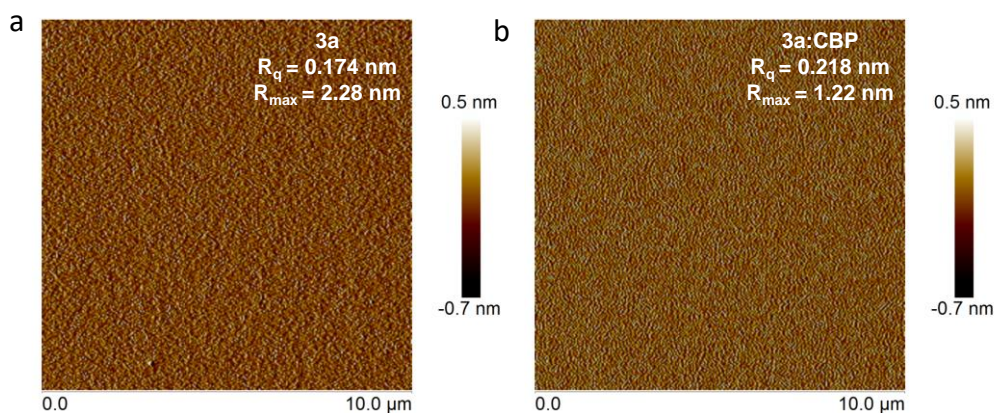


**Figure 5.14** AFM images of (a) **3a** and (b) **3a:CBP** (5 wt% **3a** dopant concentration) spin-coated and cured on ITO glass recorded in tapping mode.

consequently from 1.8% to 6.5%, which can be ascribed to the dilution effect emerging from the dopant uniform dispersion in the host at 5.0 wt%, which prevent the compound from the

crystallization in the solid-state devices and satisfy the surface morphology of the emissive layer, as also confirmed by AFM analysis (Figure 5.14).<sup>34</sup> The mean square roughness of the neat film and CBP-based film (5 wt%) was recorded as 2.28 nm and 1.22 nm, respectively. However, the EQE drops on further decreasing the concentration to 1.0 wt%. The same phenomenon occurs for a non-doped emissive layer-based device.<sup>35</sup> Furthermore, by altering the host matrix from CBP to SimCP2 (Figure 5.12), the EQE<sub>max</sub> of the device slightly decreased to 4.4% and displays a CIE coordinates to (0.31, 0.47) with L<sub>max</sub> of 3180 cd m<sup>-2</sup>.

The EL quantum efficiency in OLED device obeys the following equation:<sup>36-38</sup>

$$\eta_{\text{EL}} = \eta_{\text{rec}} \cdot \eta_{\text{s}} \cdot \eta_{\text{PL}} \cdot \eta_{\text{out}}$$

Where  $\eta_{\text{EL}}$  and  $\eta_{\text{PL}}$  are the EL external quantum efficiency and intrinsic photoluminescent quantum efficiency of an emitter, respectively;  $\eta_{\text{rec}}$  is the recombination efficiency of injected holes and electrons, which could be supposed to be 100% in a well-designed device;  $\eta_{\text{out}}$  is the light out-putting efficiency, assuming  $\eta_{\text{out}} \approx 1/(2n^2) \approx 20\%$  for a glass substrate with a refraction index  $n = 1.5$ , and  $\eta_{\text{s}}$  is the exciton utilization efficiency in OLED device.<sup>36-38</sup> Furthermore, the EL internal quantum efficiency ( $I_{\text{EQE}}$ ) of the molecules was estimated by  $\eta_{\text{EL}}/\eta_{\text{out}}$ .<sup>36-38</sup> The  $\eta_{\text{PL}}$  of the 5 wt% **3a** doped in the CBP host thin-film was determined by following the reference<sup>39</sup> i.e.  $\sim 85 \pm 2\%$ . The  $\eta_{\text{s}}$  in the resultant OLED device were estimated to be  $\sim 37 \pm 1\%$ , assuming the full electron-hole recombination ( $\eta_{\text{rec}} = 100\%$ ). Remarkably, it sufficiently exceeds the spin-statistics limit of the radiative exciton ratio of 25% for conventional

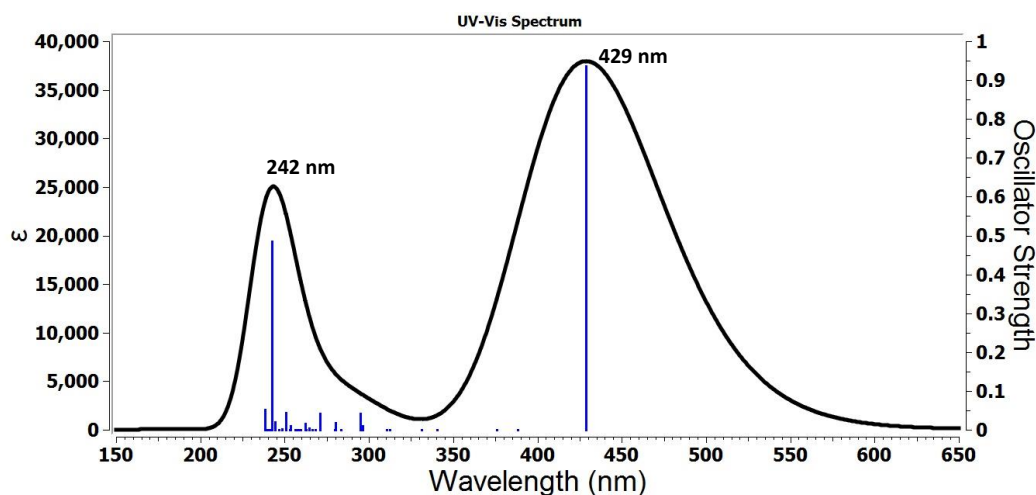


**Figure 5.15** TD-DFT simulated UV-vis absorption spectra of compound **3a** (no. of states considered = 40).

fluorescent OLED devices and indicating that singlet/triplet ratios from hole-electron recombination were larger than 1/3 in these devices. This suggests that the triplet excitons must be used in the present case by employing one of the various possible ways as described in detail below.

In fluorescent OLEDs, a maximum EQE value of 5% is possible with the use of singlet excitons. Several mechanisms such as TADF,<sup>40-42</sup> TTA<sup>43</sup> and followed organic molecules to harvest the triplet excitons in order to break the intrinsic EQE limit of 5% in fluorescent OLEDs.

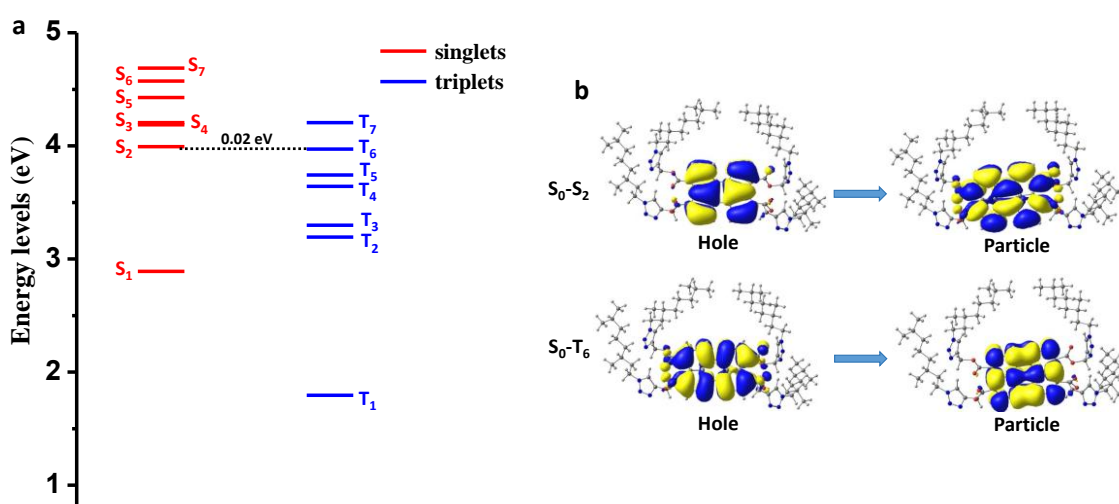


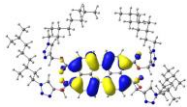
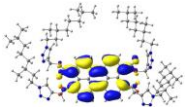
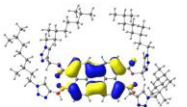
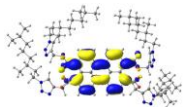
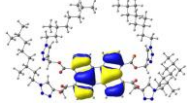
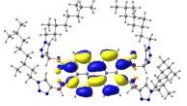
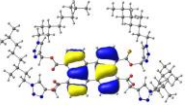
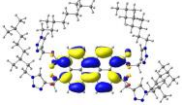
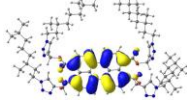
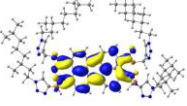
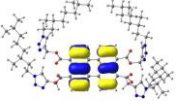
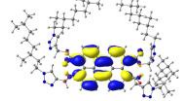
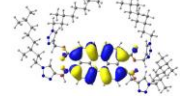
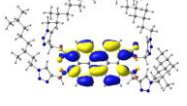
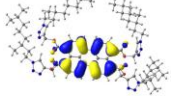
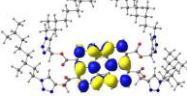
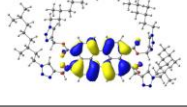
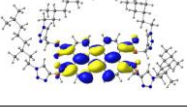
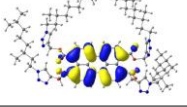
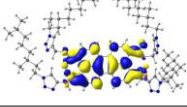
**Figure 5.16** (a) Energy level diagram of theoretically calculated singlet and triplet energy states. (b) Natural transition orbitals of the S<sub>2</sub> and T<sub>6</sub> excited states for compound **3a**.

In the present case, to examine the nature of excited states the natural transition orbitals were calculated and analyzed on the basis of time-dependent DFT (TD-DFT) results using M06-2X/6-31G(d,p) (Figure 5.15). The excited states including seven singlets (S<sub>0</sub> to S<sub>7</sub>) and seven triplet excited states (T<sub>1</sub> to T<sub>7</sub>) were calculated (Table 5.6). The energy gap between the high lying singlet S<sub>2</sub> and triplet T<sub>6</sub> was found to be 0.02 eV (Figure 5.16). Therefore, the “hole” and “particle” NTO’s of S<sub>2</sub> and T<sub>6</sub> were carefully examined. The hole and particle of S<sub>2</sub> and T<sub>6</sub> are spread over the perylene core which indicates the dominant LE particle distributions and demonstrates a LE states.

The LE states impart the fluorescent emitter a high value of photoluminescence quantum yield (PLQY). It can be noted that the charge transfer was also observed from the perylene core to

the four tetra ester groups or *vice versa* which contributes to the charge transfer (CT) excited states. Therefore,  $S_2$  and  $T_6$  excited states exhibited HLCT consists of dominant LE and less CT character. Moreover, only the NTO analysis cannot determine the character and quantitative transition composition of excited-states, particularly, when the wave functions are symmetrically distributed.<sup>44</sup> But after plotting the wave function of electron-hole pair as per transition density matrix (TDM) (using Multiwfn software), the nature of excited states can be known (Figure A15, Appendix V, Page 320). In TDM, the brightness of each point signifies the

**Table 5.6** Calculated natural transition orbitals (NTO) of singlet and triplet excited states.

Excited states (Energies)	Hole	Particle	Excited states (Energies)	Hole	Particle
$S_1$ (2.89 eV)			$T_3$ (3.30 eV)		
$S_2$ (3.99 eV)			$T_4$ (3.64 eV)		
$S_3$ (4.18 eV)			$T_5$ (3.74 eV)		
$T_1$ (1.79 eV)			$T_6$ (3.97 eV)		
$T_2$ (3.19 eV)			$T_7$ (4.20 eV)		

probability of finding electron and hole. The diagonal of the matrix represents the locally excited states while the off-diagonal section indicating the charge transfer character of the excited states. In the TDMs as shown in Figure A15 (Appendix V, Page 320) the brightest zone is localized along the diagonal of 2D color-filled map, which indicates that both electron and hole are localized on a single PE unit, and also there are less bright regions in the off-diagonal matrix suggesting the weak charge-transfer nature, thus, the electronic transition has a dominant LE character in HLCT (as mentioned above). There has been already a report where

HLCT nature of perylene cored emitter material were evaluated by using theoretical investigation.<sup>44</sup>

To further support the HLCT phenomena in PTE derivatives, fluorescence lifetime decay experiments were performed in different solvents (Figure A16, Appendix V, Page 321). Time-resolved fluorescence studies of compound **3a** in different solvents revealed single exponential decay with a lifetime in nanosecond time scale indicating the absence of delayed component (TADF) in emission. However, it displayed a relatively longer lifetime ( $\sim 3.77$  ns) than that of conventional fluorescent emitters, suggesting the presence of hybridized LE and CT components into a single emissive HLCT state,<sup>45-47</sup> hence responsible for the EQE exceeding the upper limit of traditional fluorescent emitters in the present case.

#### 5.1.4 Conclusions

This work demonstrates the design, synthesis, and characterization of new series of perylene tetraesters based columnar liquid crystals. The target materials were achieved *via* microwave method. The derivative **3a** consists of a branched-chain while other derivatives **3b-d** differ in the length of alkyl chains. As a function of alkyl chains, the variation in thermal, photophysical and electrochemical behaviour was well studied. The derivatives showed ordered centered columnar rectangular phases at ambient temperature as determined by X-ray diffraction studies. The systematic variable temperature-dependent studies revealed two types of rectangular phases in case of **3a**, **3b** and **3d** while **3c** showed only one type of mesophase. Due to the excellent physical properties of perylene columnar LCs and high charge transport properties as measured by TOF for **3a**, it was employed as an emitter material in OLEDs. The OLED devices using fluorescent emitter **3a** as a dopant was fabricated with two different hosts: CBP and SimCP2 by varying dopant concentration. The maximum EQE of 6.5% is obtained with CBP host at 5 wt% dopant concentration with CIE coordinates (0.37, 0.53). The breakthrough of efficiency limit of DLCs based fluorescent OLEDs or the conversion of triplet excitons into singlet excitons was explained through HLCT phenomenon by the combination of fluorescence lifetime decay, TDM, TD-DFT and NTO calculations. The calculation of singlet and triplet energies revealed that the  $T_6$  to  $S_2$  excitons conversion is highly possible owing to the almost zero gap between the two levels in addition to their HLCT nature of the natural transition orbitals obtained.

**Acknowledgements.** *Some part of this work has been included in Master thesis of Ms. Nitya Singh (MS13093) at IISER Mohali. The OLED device studies and TOF measurements carried out in collaboration with Prof. J. H Jou's group (at National Tsing Hua University, Taiwan) and Dr. Dharmendra Pratap Singh (at Université du Littoral Côte d'Opale, France) are greatly acknowledged and respected. Dr. Santosh Prasad Gupta (at Patna University) is duly acknowledged for the analysis of XRD data.*

### 5.1.5 Experimental section

**5.1.5.1 Synthesis of precursor 2.** Perylene-3,4,9,10-tetracarboxylic dianhydride (170 mg, 1 equiv.) was taken in a 250 ml round bottom flask. 170 ml of 0.1 M KOH solution is added and heated at 70 °C for about 2 hours. The clear green fluorescent solution of reaction mixture appears due to the formation of tetra potassium carboxylate anion. The solution was allowed to cool down to room temperature, filtered and acidified with dilute hydrochloric acid to get a solution with pH value of 8-9. To this solution, was then added propargyl bromide (412 mg, 8 equiv.) and tetraoctyl ammonium bromide (TOAB, 190 mg, 0.8 equiv.). The reaction mixture was refluxed under vigorous stirring for overnight. The solution became almost colorless and red or brown colored insoluble material floats on the surface. The crude reaction mixture was extracted using chloroform. The reaction mixture was purified through column chromatography by using 1:1 hexane/ethyl acetate (EtOAc) as eluent. After column chromatography the obtained compound was washed several times with methanol and hexane to get pure product. Yield – 40%. **<sup>1</sup>H NMR** (400 MHz, CDCl<sub>3</sub>,  $\delta$  in ppm):  $\delta$  8.23-8.22 (d, 4H,  $J$  = 4.00 Hz),  $\delta$  8.10-8.08 (d, 4H,  $J$  = 8.00 Hz),  $\delta$  4.98 (s, 8H),  $\delta$  2.59 (s, 4H). **<sup>13</sup>C NMR** (100 MHz, CDCl<sub>3</sub>,  $\delta$  in ppm): Due to the limited solubility of compound in the CDCl<sub>3</sub> and insolubility in other solvents, we were unable to record the <sup>13</sup>C spectra of precursor 2. **HRMS-ESI** (m/z): M<sup>+</sup> 581.1286 (calculated for C<sub>36</sub>H<sub>20</sub>O<sub>8</sub> = M<sup>+</sup> 581.1236).

**5.1.5.2 Synthesis of alkyl azides.** 0.5 M stock solution of NaN<sub>3</sub> (0.69 g) in DMSO (21 ml) was prepared by stirring the solution for 24 hours at room temperature. After obtaining the clear solution, to 0.5 M solution of NaN<sub>3</sub> (1.1 equiv.), bromoalkane (1 equiv.) was added. After stirring for 24 hours at room temperature, the reaction mixture was extracted with diethyl ether. After evaporation of the solvent, the resulting mixture was evaporated to dryness. Yield of azides ~ 99%. The formation of the azides was first checked with IR. The appearance of peak

at 2096  $\text{cm}^{-1}$  in IR corresponds to asymmetric stretching frequency for C-N<sub>3</sub>. It also indicates the conversion of bromoalkane to azidoalkane.

**5.1.5.3 Synthesis of final PTE derivatives, 3a-d.** Compound **2** (50 mg, 1 equiv.), corresponding alkyl azide (8 equiv.), CuSO<sub>4</sub>·5H<sub>2</sub>O (1 equiv.) and sodium ascorbate (0.6 equiv.) were solubilized using the following solvent mixture in a microwave reaction vial (G-10). The solvent mixture is CHCl<sub>3</sub> (2 ml)/EtOH (1 ml)/H<sub>2</sub>O (1 ml). The reaction mixture was kept at 65 °C for 1 hour with constant stirring under microwave irradiation. The reaction mixture turned out to be brownish-red and the completion of the reaction was determined by the disappearance of the reactant spot on TLC. After that, the crude mixture was extracted with CHCl<sub>3</sub>/ H<sub>2</sub>O. The crude red solid obtained was purified on neutral alumina by using hexane/EtOAc as eluent. Yield: 60% for **3a**; 63% for **3b**; 68% for **3c**; 72% for **3d**.

Compound **3a**: **FT-IR** ( $\text{cm}^{-1}$ ): 3427, 3143, 2962, 2930, 2855, 1729, 1591, 1463, 139, 1262, 1158, 1095, 1020, 803, 752, 617. **<sup>1</sup>H NMR** (400 MHz, CDCl<sub>3</sub>,  $\delta$  in ppm):  $\delta$  8.26-8.24 (d, 4H,  $J$  = 8.00 Hz),  $\delta$  8.06-8.04 (d, 4H,  $J$  = 8.00 Hz),  $\delta$  7.80 (s, 4H),  $\delta$  5.44 (s, 8H),  $\delta$  4.40-4.34 (m, 8H),  $\delta$  1.95-1.91 (m, 4H),  $\delta$  1.74-1.68 (m, 4H),  $\delta$  1.50-1.45 (m, 8H),  $\delta$  1.29-1.09 (m, 24H), 0.95-0.93 (d, 12 H), 0.84-0.82 (d, 24H). **<sup>13</sup>C NMR** (100 MHz, CDCl<sub>3</sub>,  $\delta$  in ppm): 168.15, 142.37, 131.08, 124.04, 121.63, 114.09, 58.86, 48.74, 39.11, 37.35, 36.88, 31.95, 30.40, 29.72, 29.39, 27.92, 24.53, 22.67, 22.57, 19.27, 14.16. **HRMS-ESI** ( $m/z$ ): M<sup>+</sup> 1313.8132 (calculated for C<sub>76</sub>H<sub>104</sub>N<sub>12</sub>O<sub>8</sub> = M<sup>+</sup> 1313.8178).

Compound **3b**: **FT-IR** ( $\text{cm}^{-1}$ ): 3396, 2925, 2861, 1721, 1587, 1469, 1374, 1275, 1162, 1093, 806, 751, 615. **<sup>1</sup>H NMR** (400 MHz, CDCl<sub>3</sub>,  $\delta$  in ppm):  $\delta$  8.07-8.05 (d, 4H,  $J$  = 8.00 Hz),  $\delta$  7.94-7.92 (d, 4H,  $J$  = 8.00 Hz),  $\delta$  7.83 (s, 4H),  $\delta$  5.45 (s, 8H),  $\delta$  4.38-4.34 (t, 8H,  $J$  = 7.32 Hz),  $\delta$  1.92-1.87 (m, 8H),  $\delta$  1.34-1.27 (m, 24H), 0.86-0.83 (t, 12H,  $J$  = 6.60 Hz). **<sup>13</sup>C NMR** (100 MHz, CDCl<sub>3</sub>,  $\delta$  in ppm): 168.13, 142.35, 133.04, 130.98, 129.43, 128.87, 128.56, 124.14, 121.54, 58.83, 50.51, 31.13, 30.25, 26.17, 22.42, 13.96. **HRMS-ESI** ( $m/z$ ): M<sup>+</sup> 1089.5621 (calculated for C<sub>60</sub>H<sub>72</sub>N<sub>12</sub>O<sub>8</sub> = M<sup>+</sup> 1089.5674).

Compound **3c**: **FT-IR** ( $\text{cm}^{-1}$ ): 3392, 2956, 2925, 2850, 1711, 1465, 1277, 1170, 1093, 840, 791, 750, 589. **<sup>1</sup>H NMR** (400 MHz, CDCl<sub>3</sub>,  $\delta$  in ppm):  $\delta$  8.19-8.17 (d, 4H,  $J$  = 8.00 Hz),  $\delta$  8.02-8.00 (d, 4H,  $J$  = 8.00 Hz),  $\delta$  7.80 (s, 4H),  $\delta$  5.44 (s, 8H),  $\delta$  4.37-4.33 (t, 8H,  $J$  = 7.26 Hz),  $\delta$  1.92-1.88 (m, 8H),  $\delta$  1.41-1.00 (m, 40H), 0.87-0.82 (m, 12H). **<sup>13</sup>C NMR** (100 MHz, CDCl<sub>3</sub>,

$\delta$  in ppm): 168.13, 142.35, 133.17, 131.05, 129.51, 128.97, 124.11, 121.60, 58.86, 53.46, 50.51, 31.86, 30.29, 29.48, 29.40, 29.27, 29.01, 26.52, 22.67, 14.12. **HRMS-ESI** (m/z):  $M^+$  1201.6976 (calculated for  $C_{68}H_{88}N_{12}O_8 = M^+$  1201.6926).

Compound **3d**: **FT-IR** ( $cm^{-1}$ ): 3136, 2958, 2924, 2854, 1724, 1589, 1514, 1466, 1376, 1271, 1158, 1052, 974, 845, 747, 581, 611.  **$^1H$  NMR** (400 MHz,  $CDCl_3$ ,  $\delta$  in ppm):  $\delta$  8.22-8.20 (d, 4H,  $J = 8.00$  Hz),  $\delta$  8.04-8.02 (d, 4H,  $J = 8.00$  Hz),  $\delta$  7.80 (s, 4H),  $\delta$  5.44 (s, 8H),  $\delta$  4.36-4.33 (t, 8H,  $J = 7.26$  Hz),  $\delta$  1.90-1.88 (m, 8H),  $\delta$  1.31-1.22 (m, 56H), 0.86-0.83 (t, 12H,  $J = 6.70$  Hz).  **$^{13}C$  NMR** (100 MHz,  $CDCl_3$ ,  $\delta$  in ppm): 168.13, 142.35, 133.17, 131.05, 129.51, 128.97, 124.11, 121.60, 58.86, 53.46, 50.51, 31.86, 30.29, 29.48, 29.40, 29.27, 29.01, 26.52, 22.67, 14.12. **HRMS-ESI** (m/z):  $M^+$  1313.8115 (calculated for  $C_{76}H_{104}N_{12}O_8 = M^+$  1313.8178).

**5.1.5.4 Ultraviolet photoelectron spectroscopy (UPS).** For UPS measurement, a 2 mg/ml solution of compounds (**3a-d**) in anhydrous chloroform was stirred at 60 °C for 1h. The solution was subsequently spin-coated on cleaned indium tin oxide (ITO) substrates at 2000 rpm for 60 s. The HOMO levels are derived from the formula:  $E_{HOMO,UPS} = 21.2 - (E_{cut-off} - E_{Fermi})$  where  $E_{cut-off}$  and  $E_{Fermi}$  are the kinetic energy obtained at the cut-off (higher energy side) and Fermi edge (lower energy side) of the UPS spectra.



## 5.2 Part B: Perylene-pentaalkynylbenzene based disc tetramers stabilizing columnar nematic and soft crystalline columnar assemblies

### 5.2.1 Introduction

Perylene derivatives have gained particular attention due to their unique features such as high thermal and chemical stability, easy functionalization, large bandgap, near-unity fluorescence quantum yields in the molecular state, *n*-type semiconductor properties and so on.<sup>48</sup> Due to these properties, they are ideal candidates for fabricating organic devices such as organic solar cells,<sup>49</sup> organic field-effect transistors (OFETs),<sup>50</sup> fluorescent sensors,<sup>51</sup> organic light-emitting diodes (OLEDs)<sup>52</sup> *etc.* For example, fluorescent perylene LCs are useful as luminescent electron transport material in OLEDs.<sup>52</sup> Perylene imides (mono- and di-) have been used in bulk-heterojunction solar cells as well as orbital and color tuning.<sup>53</sup> In general, the optical and electronic properties of these derivatives are due to local  $\pi$ - $\pi$  interactions of the perylene chromophore that lead to molecular aggregation and these aggregations further provide means for efficient electron conduction within the aggregates.<sup>8,54,55</sup> Besides, perylene derivatives (bisimides and tetraesters) are found to show crystalline as well as LC phases considering their flexibility of the core as an important parameter for the supramolecular self-assembly. Room temperature columnar mesophase with a wide temperature range is suitable for practical applications in electronic devices. Given that perylene has several positions available for structural modification with a variety of substituents in the core, their mesomorphic, optical and electronic properties can be tuned and tested easily for such types of applications.<sup>15</sup> Therefore, properly substituted room temperature LC perylene derivatives with good self-assembly properties are highly desired from a practical point of view.

Literature survey reveals a wide range of perylene LCs based on perylene bisimides.<sup>5,7,27,56-73</sup> But, there are very few reports for perylene tetraesters (PTE) exhibiting LC behaviour.<sup>27,74-77</sup> Unfortunately, most of the reported PTE compounds show 1) LC mesophase at higher temperature<sup>77</sup> [only a few of them show room temperature (RT) LC behaviour] and 2) self-assemble into either a columnar hexagonal or a columnar rectangular mesophase.<sup>27,74-77</sup> In contrary, implementation of discogens in devices necessitates Col phase at room temperature

along with the formation of highly ordered phase over a wide temperature range.<sup>78</sup> To attain such kind of mesophases at RT and improve their usability in devices certain structural modifications and further understanding of packing in the mesophases are required.

### 5.2.2 Objectives

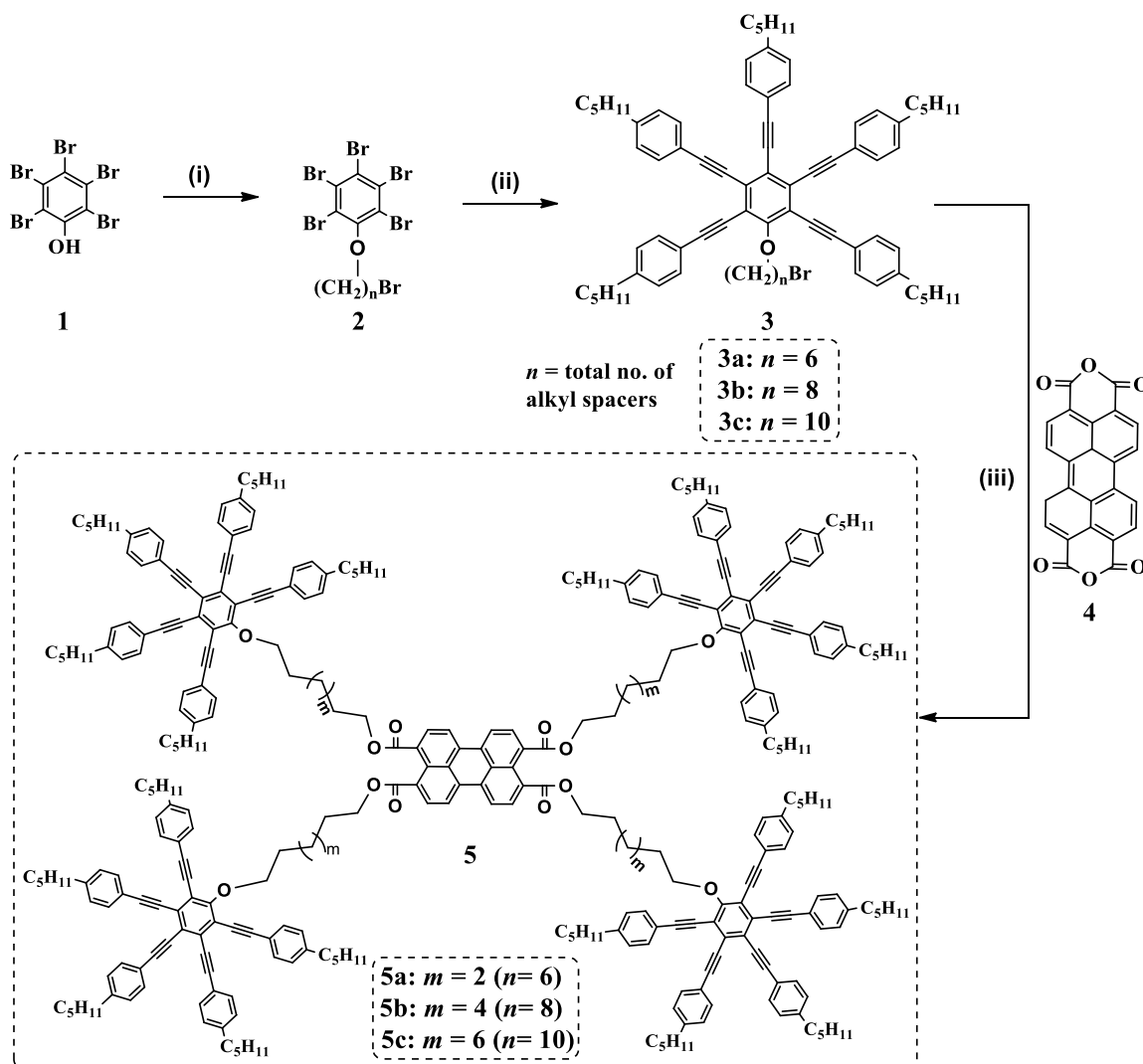
There are only a few reports of perylene tetraesters LCs exhibiting room temperature mesophase which limits their widespread use in applications. With this idea keeping in mind, we sought to explore new strategies to functionalize the PTE that bring down the mesophase behaviour down to room temperature over a wide range. In literature, the major practice to lower down the temperature is to introduce branched chains. The use of the branched chains often reduces melting and isotropic temperatures because of increased disorder and stereoheterogeneity but, do not affect the type of mesophase in many cases. Alternatively, the attachment of multiynes to a discotic core leads to room temperature discotic phases.<sup>79,80</sup> For example, we have reported that linking a pentaalkynylbenzene unit with a triphenylene core through flexible alkyl spacer containing a short rigid ester group in centre leads to columnar mesophase at ambient temperature.<sup>81</sup> Room-temperature columnar structures over a long-range have been reported using multialkynylbenzene-bridged triphenylene-based dyad systems.<sup>82</sup> In this work, an oligomeric approach has been employed by connecting four pentaalkynylbenzene units to the perylene core for the realization of room temperature mesophase and their packing behaviour. Our findings perceived that compounds with shorter alkyl spacers ( $n = 6$  and  $8$ ) (Scheme 5.2) connecting PTE and pentaalkynylbenzene units arranged exclusively in soft, condisc crystals, which are defined as conformationally disordered mesophases.<sup>83-86</sup> Compound with longer alkyl spacer ( $n = 10$ ) exhibited room temperature columnar nematic phase. In addition, they exhibit high quantum yield and exhibit green emission that might be useful for OLEDs applications.

### 5.2.3 Results and discussions

#### 5.2.3.1 Synthesis and characterization

The synthetic strategy to obtain target compounds **5** is illustrated in Scheme 5.2. The synthesis of intermediate compounds **2** and **3** have been reported earlier.<sup>80-82</sup> Compounds **5** were prepared by reacting the pentaalkynylbenzene **3** with perylene-3,4,9,10-tetracarboxylic

dianhydride **4** as follows. The step involves the hydrolysis of **4** (1 equiv.) by refluxing it in aqueous potassium hydroxide followed by acidification to pH 8-9 with dilute HCl to provide perylene-3,4,9,10-tetracarboxylic acid. This was followed by *in situ* addition of **3** (8 equiv.) and tetraoctylammonium bromide (TOAB) (0.8 equiv.) as phase transfer catalyst and refluxing it overnight. The structures of all target molecules were characterized by  $^1\text{H}$  NMR,  $^{13}\text{C}$  NMR, FT-IR (Figure A17-A23, Appendix V, Page 321) and elemental analysis.



**Scheme 5.2** Synthesis of the target compounds **5**. Reagents and conditions: (i)  $\text{K}_2\text{CO}_3$ , KI,  $\text{Br}(\text{CH}_2)_n\text{Br}$ , acetone, reflux, 12 hrs, 80%; (ii)  $\text{Pd}(\text{PPh}_3)_2\text{Cl}_2$ , 4-pentylphenylacetylene, CuI,  $\text{Et}_3\text{N}$ , 100 °C, 80%; (iii) hydrolysis of **4** with KOH,  $\text{H}_2\text{O}$ , 70 °C, 2h, dilute HCl followed by **3**, TOAB, reflux, overnight, 78%.

### 5.2.3.2 Thermal behaviour (POM and DSC)

The thermal behaviour of the perylene derivatives was investigated by polarized optical microscopy (POM) and differential scanning calorimetric (DSC) technique. Compound **5a** with the shortest alkyl spacer ( $n = 6$ ) was highly viscous (Figure 5.17a) and is still shearable showing their soft behaviour. The shearability of the textures in one direction has been shown at room temperature (Figure 5.19a,b). Compound **5a** displayed an unspecific texture with the growth of smaller domains<sup>29,82</sup> (Figure 5.18a). The phase remained stable over a wide temperature range and was cleared at 106 °C with an enthalpy change ( $\Delta H$ ) of 6.2 kJ/mol (Table 5.7). On cooling, texture appeared at 103 °C (bright birefringent textures observed under POM) which remained stable down to room temperature.

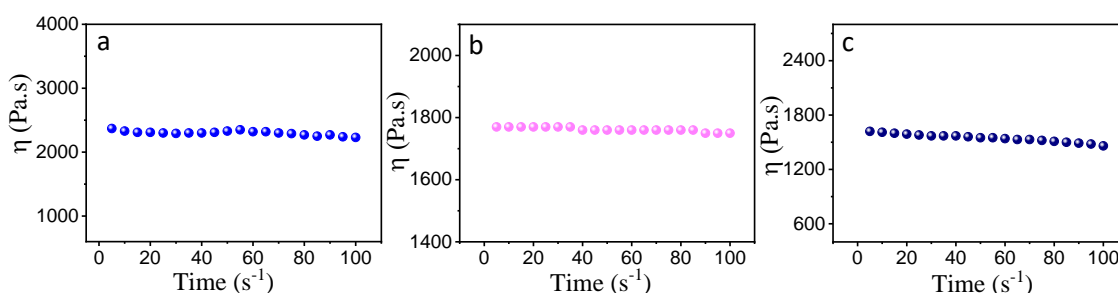


**Figure 5.17** Viscosity measurements of perylene derivatives **5a-c** by rheology: (a) compound **5a**,  $\eta = 2302$  pa.s; (b) compound **5b**,  $\eta = 1762$  pa.s; (c) compound **5c**,  $\eta = 1547$  pa.s, at room temperature and at a shear rate  $10 \text{ s}^{-1}$  indicating viscosities decrease with increasing the alkyl chain spacer.

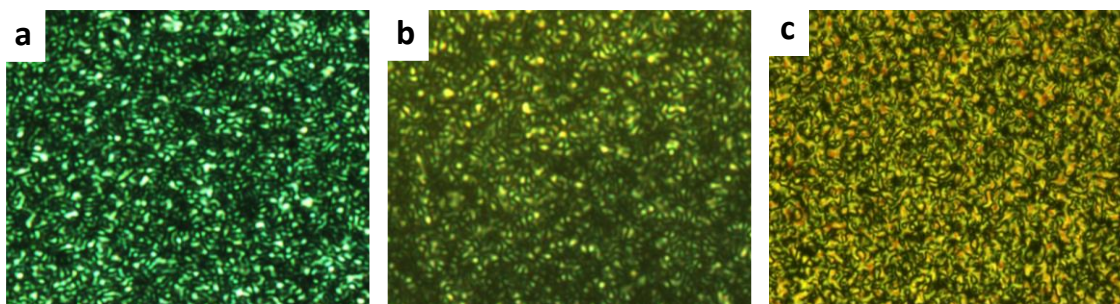


**Figure 5.18** Polarizing optical micrographs of compounds (a) **5a** and (b) **5b** at 67 °C and 25 °C, respectively, showing unspecific growth of textures. (c) The texture of compound **5c** at 49.6 °C under POM. All these textures were observed on cooling from the isotropic phase (scan rate  $5 \text{ °C/min}$ , crossed polarizers, magnification  $\times 500$ ).

Compound **5b** ( $n = 8$ ) also exhibited similar soft crystal behaviour as that of compound **5a**. Under POM, an unidentified texture was appeared (Figure 5.18b) which cleared at about 85 °C and are shearable at room temperature (Figure 5.19c,d). The viscosity of the phase was measured at room temperature (Figure 5.17b). On cooling, the phase appeared at 78 °C that remained stable down to room temperature (up to -50 °C). Interestingly, increasing the spacer length further ( $n = 10$ ), destabilized the order in the mesophase of the hybrid. For instance, compound **5c** ( $n = 10$ ) showed the appearance of columnar textures<sup>29</sup> at room temperature (Figure 5.18c). In DSC, it showed mesophase to isotropic transition at 66 °C with heat of transition of 0.4 kJ mol<sup>-1</sup>. On cooling, the mesophase appeared at 65 °C ( $\Delta H = 0.4$  kJ/mol). The DSC traces obtained on heating and cooling of compound **5c** are shown in Figure A24 (Appendix V, Page 325).

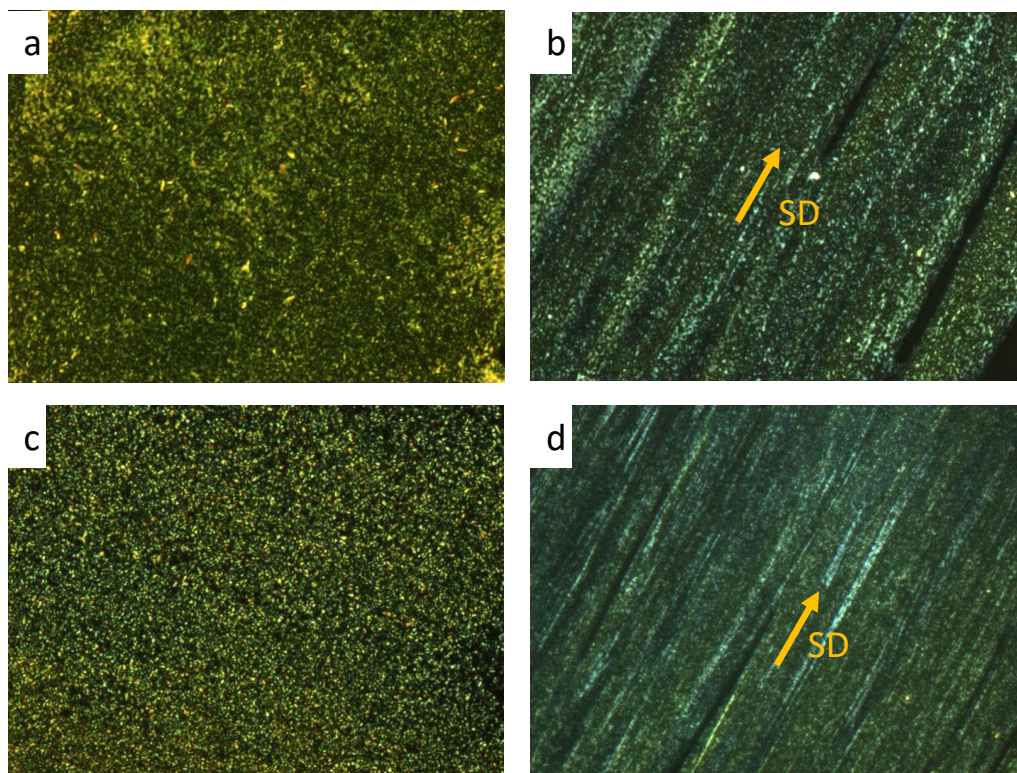


**Figure 5.19** Textures of compound **5a** (a) before shearing; (b) after shearing, and for compound **5b** (c) before shearing; (d) after shearing at room temperature (crossed polarizers, magnification  $\times 500$ ). SD represents shearing direction, indicated by the yellow arrow.

**Table 5.7** Phase transition temperatures of **5a-c**.<sup>a</sup>

Compound	Heating	Cooling
<b>5a</b>	Cr <sub>colob</sub> 106 (6.2) Iso <sup>a</sup>	Iso 103 Cr <sub>colob</sub> <sup>b</sup>
<b>5b</b>	Cr <sub>colob</sub> 85 Iso <sup>b</sup>	Iso 78 Cr <sub>colob</sub> <sup>b</sup>
<b>5c</b>	N <sub>col</sub> 66 (0.4) Iso <sup>a</sup>	Iso 65 (0.4) N <sub>col</sub> <sup>a</sup>

<sup>a</sup>Transition temperature obtained from DSC measurements. <sup>b</sup>Obtained from POM measurements. Abbreviations: Cr<sub>colob</sub> = soft crystal columnar oblique, N<sub>col</sub> = columnar nematic, Iso = isotropic liquid.

### 5.2.3.3 X-Ray diffraction (XRD) studies

The exact nature of the columnar phases formed by these compounds could be deduced only from detailed XRD studies. We performed detailed XRD analysis to examine the exact nature of the mesophases and their corresponding electron density maps (EDMs) were derived from the intensities of the peaks observed in the diffraction patterns. The small-angle X-ray scattering (SAXS) profile of compound **5a** in the isotropic phase (at 110 °C) shows two broad peaks in the small-angle region and one broad peak in the wide-angle regime (Figure 5.20b).

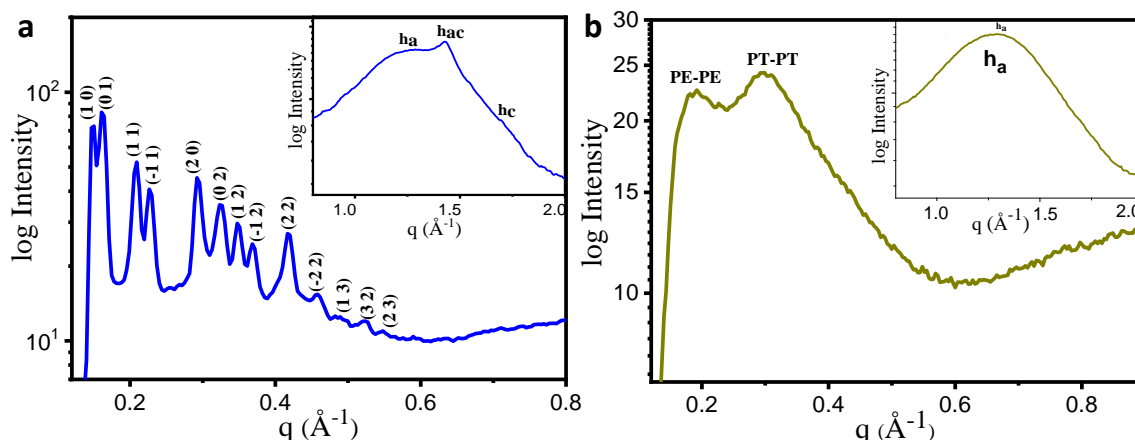


**Figure 5.20** Powder XRD pattern for compound **5a** with indexing for small-angle and wide-angle (inset) peaks (a) at 67 °C and (b) in the isotropic phase at 110 °C; h<sub>a</sub> - fluid chain-chain correlations, h<sub>ac</sub>-partially crystallize chain-chain correlations and h<sub>c</sub>-perylene core-core (face to face) correlations, PE-PE corresponds to side to side perylene correlations and PT-PT corresponds to side to side pentaalkynylbenzene correlations in the mesophase. Indexing in the

red color corresponds to 2D square lattice and deep yellow corresponds to 2D rectangular lattice.

**Table 5.8** Variation of  $d$ -spacing in the phases of compound **5a-b**.

Phase		Small-angle peak (Å)		Wide-angle peak (Å)
<b>C</b>		1 <sup>st</sup> peak	2 <sup>nd</sup> peak	
<b>5a</b>	Iso	32.74	21.16	4.87
	(110 °C)	PE-PE	PT-PT	<b>h<sub>a</sub></b>
<b>5b</b>	Iso	38.50	20.78	4.99
	(85 °C)	PE-PE	PT-PT	<b>h<sub>a</sub></b>

Abbreviations: C-compound; Iso: isotropic phase; PE-PE: perylene core to core interaction; PT-PT: pentaalkynylbenzene core to core interaction. **h<sub>a</sub>** peak appears due to fluid chain-chain correlation.

As the compound consists of a perylene unit connected with four pentaalkynylbenzene units *via* flexible spacers, so, the first and second peak in the small-angle with observed  $d$ -spacing of 32.74 Å and 21.16 Å correspond to side to side PE-PE (PE-perylene) correlations and side to side PT-PT (PT-pentaalkynylbenzene) correlations, respectively (Table 5.8). However, side to side PE-PE correlations  $d$ -spacing is smaller than expected ( $\sim 40$  Å), which indicates interdigitations of the pentaalkynylbenzene discs up-to some extent in the isotropic phase. Further, the wide-angle peak of  $d$ -spacing of 4.87 Å corresponds to the fluid chain-chain correlations. However, in the temperature range from 20 °C to 106 °C the diffraction patterns are found to be unchanged. The un-oriented SAXS pattern showed many sharp Bragg peaks (at 67 °C) (Figure 5.20a). In order to resolve overlapping reflections and facilitate their indexing, GISAXS experiments were carried out on oriented thin films on an ITO-coated glass substrate. For this purpose, a thin film was melt-cast on an ITO-coated glass substrate and annealed for 1 day at 70 °C. The same diffraction peaks were observed both in the GISAXS of thin-film (Figure 5.21a) and in the SAXS pattern of the un-oriented sample (Figure 5.18a). If the reciprocal lattice vectors,  $a^*$  and  $b^*$  are assigned along the equator and meridian, respectively, it could lead to the assembly of the compound having two different kinds of domains. However,



in the present case, there is no clear-cut explanation for the compound to form two distinct domains, both in the unoriented and thin films sample.

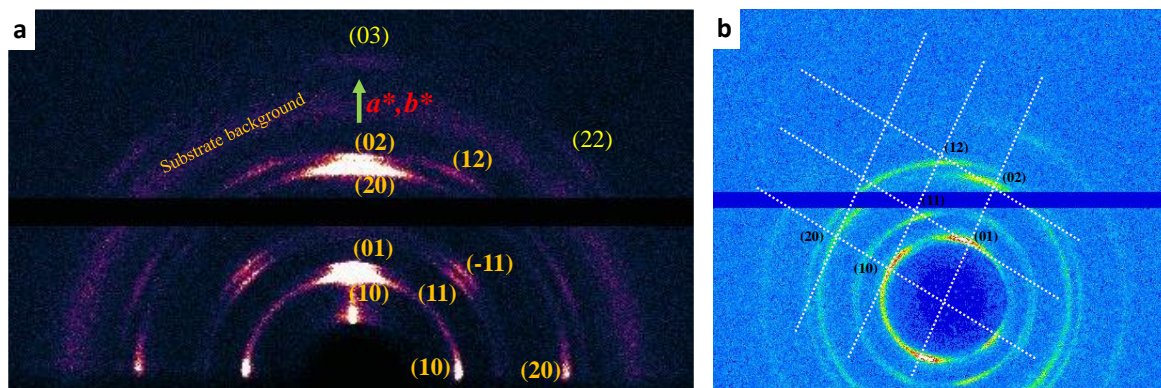


**Figure 5.21** (a) GISAXS pattern of thin-film of compound **5a** on an ITO coated glass substrate recorded at 67 °C obtained after annealing the sample for one day at 70 °C. (b) Partially aligned 2D SAXS diffraction pattern of compound **5a** at 67 °C obtained by shining the X-ray onto the sample near to the wall of the glass capillary.

We further did XRD experiment with a sample filled in the glass capillary and shine the X-ray which exposes the sample near the wall of glass capillary at 67 °C. In result, we found a partially aligned pattern that could be indexed on an oblique lattice (Figure 5.21b). Therefore, for the thin-film pattern  $a^*$  and  $b^*$  are more likely along the meridian and  $c^*$  along the equator and hence indexing of the unoriented pattern was done accordingly. The Bragg's reflections for the compound **5a** at 67 °C were indexed on 2D oblique lattice and space group is determined to be  $P2/m$ . The cell parameter,  $c$ , is determined from the reflection,  $h_c$ , due to perylene core to core (face by face) correlations in the wide-angle region (Figure 5.20a inset). The observed and calculated  $d$ -spacing values are listed in Table 5.9. The calculated cell parameters are  $a = 42.67 \text{ \AA}$ ,  $b = 38.99 \text{ \AA}$ ,  $c = 3.70 \text{ \AA}$ , and  $\alpha = 84.15^\circ$ . In-addition to  $h_c$ , there are  $h_a$  and  $h_{ac}$  reflections in the wide-angle region of spacing  $4.99 \text{ \AA}$  and  $4.39 \text{ \AA}$ , respectively. These reflections are attributing to the fluid chain-chain and partially crystallize chain-chain correlations. The observed phase is soft crystal columnar oblique ( $\text{Cr}_{\text{colob}}$ ). In grazing-incidence small-angle X-ray scattering (GISAXS), the strong Bragg peaks have a maximum intensity on the meridian confirming the presence of planar alignment (Figure 5.21a). Further, no wide-angle peaks were perceived, indicating inadequate diffraction contrast from long-range ordered



columnar  $\pi$ - $\pi$  stacking of the molecules in any orientation.<sup>87</sup> Based on indexing and because the compound was highly viscous, shearable and exhibits sharp reflections confirming the occurrence of soft crystal columnar oblique (Cr<sub>colob</sub>) phase.

**Table 5.9** Phase behaviour, Miller Indices, lattice constants and  $d$ -spacing observed from the XRD studies for compounds **5a** and **5b**. The space group is  $P2/m$ .

Compound	Mesophase	Lattice constants (Å)	$d_{\text{obs}}^a$ (Å)	$d_{\text{cal}}^b$ (Å)	MI <sup>c</sup> (hk)	RI ( $\Phi$ )(M) <sup>c</sup>
<b>5a</b>	Cr <sub>colob</sub> at 67 °C	$a = 42.67$	42.45	42.45	10	87.95(0)(2)
		$b = 38.99$	38.79	38.79	01	100.00(0)(2)
		$c = 3.70$	30.21	30.21	11	62.65(0)(2)
		$\alpha = 84.15^\circ$	27.32	27.28	-11	48.19(0)(2)
			21.30	21.22	20	54.22( $\pi$ )(2)
			19.39	19.39	02	42.17( $\pi$ )(2)
			18.21	18.36	12	38.55(0)(2)
			17.03	17.00	-12	30.12(0)(2)
			15.07	15.10	22	32.53(0)(2)
			13.69	13.64	-22	18.07(0)(2)
			12.80	12.73	13	6.02(0)(2)
			12.01	12.03	32	3.61(-)(2)
			11.49	11.59	23	2.41(-)(6)
			4.99		<b>h<sub>a</sub></b>	
			4.39		<b>h<sub>ac</sub></b>	
			3.70		<b>h<sub>c</sub></b>	
<b>5b</b>	Cr <sub>colob</sub> at 25 °C	$a = 48.90$	19.84	19.70	20	38.82 (0)(2)
		$b = 34.13$	18.10	18.08	11	100.00(0)(2)
		$c = 3.60$	14.70	14.86	-32	15.02(0)(2)
		$\alpha = 126.3^\circ$	12.71	12.82	21	16.10(0)(2)
			11.43	11.28	-33	18.57(0)(2)
			10.30	10.49	-43	14.49(0)(2)
			9.58	9.85	40	14.86( $\pi$ )(2)
			8.3	8.46	-44	17.14( $\pi$ )(2)
			7.40	7.53	32	19.13(0)(2)
			6.22	6.41	42	
			5.60	5.63	70	

4.96	5.00	34
4.59	4.58	06
4.45	4.42	81
4.19		<b>h<sub>ac</sub></b>
3.60		<b>h<sub>c</sub></b>
3.19	3.20	84

$d_{obs}$  : experimental  $d$ -spacing.  $d_{cal}$  : calculated  $d$ -spacing by using the relation:  $\frac{1}{d^2} = \frac{1}{\sin^2 \alpha} \left[ \frac{h^2}{a^2} + \frac{k^2}{b^2} - \frac{2hk \cos \alpha}{ab} \right]$ ;  $h, k$  are the indices of the reflections corresponding to the oblique lattice;  $a, b$  &  $c$  are the unit cell parameters,  $\alpha$  is the angle between  $\vec{a}$  and  $\vec{b}$  where  $|\vec{a}| = a$  and  $|\vec{b}| = b$ .  $h_a$ ,  $h_{ac}$  and  $h_c$  spacings appear due to fluid chain-chain, partially crystallize chain-chain, and perylene core-core (face to face) correlations, respectively.  
<sup>c</sup>Abbreviations: MI- Miller Indices; RI ( $\Phi$ )(M)- Relative Intensity (Phase value) (Multiplicity).

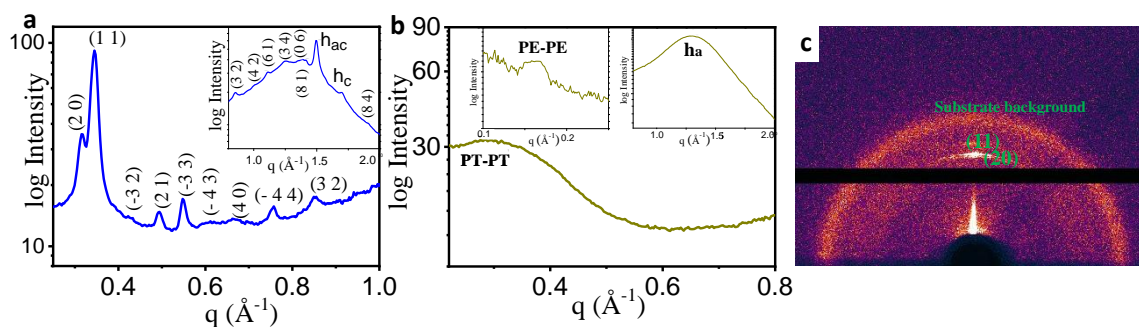


**Figure 5.22** Powder XRD pattern for compound **5b** with indexing for small-angle and wide-angle (inset) peaks (a) at 25 °C. (b) XRD pattern for **5b** in the isotropic phase at 85 °C. (c) GISAXS pattern of thin film of compound **5b** on an ITO-coated glass substrate recorded at 25 °C;  $h_a$  - fluid chain-chain correlations,  $h_{ac}$  - crystallize chain-chain correlations and  $h_c$  – perylene core-core (face to face) correlations, PE-PE corresponds to side to side perylene correlations and PT-PT corresponds to side to side pentaalkynylbenzene correlations in the mesophase.

The powder XRD pattern of compound **5b** at 25 °C (Figure 5.22a) shows reflections in the small and wide-angle region and was remained the same above or below room temperature and to the isotropic phase. These peaks could be indexed on an oblique lattice and the calculated lattice parameters are found to be  $a = 48.90 \text{ \AA}$ ,  $b = 34.13 \text{ \AA}$ ,  $\alpha = 126.3^\circ$  and  $c = 3.60$

Å (Table 5.9). In order to facilitate their indexing GISAXS/GIWAXS experiments were carried out on oriented thin films on an ITO-coated glass substrate. However, in GISAXS pattern only the most intense two peaks (20 and 11) were observed with the same  $d$ -spacing as that of the powder diffraction pattern, while other less intense peaks were not appeared possibly because of their insufficient diffraction contrast or inappropriate alignment (Figure 5.22c). Further in GIWAXS studies, no peaks were observed in the wide-angle region. Therefore, the nature of the lattice could not be deduced from the aligned pattern. Hence the structure of the assembly has been concluded according to the indexing of un-oriented pattern (mentioned above).

Based on indexing of the un-oriented pattern and because the compound **5b** exhibits many reflections in the wide-angle along with the peak observed at 3.6 Å (which is due to disc to disc separation in a column) and less shearable confirmed the occurrence of soft crystal columnar oblique ( $Cr_{colobl}$ ) phase. The XRD pattern in the isotropic phase (85 °C) (Figure 5.22b) is similar as seen in compound **5a** and can be explained similarly. However, spacing due to PE-PE correlations is higher than **5a** which is expected due to higher spacer length (Table 5.8). In order to understand the details of the arrangement of the columns on the 2D oblique lattice, their corresponding EDM is constructed from the diffraction pattern. Here, perylene core stack on top of each other and form columns and these columns arranged on 2D oblique lattice (Figure 5.23).

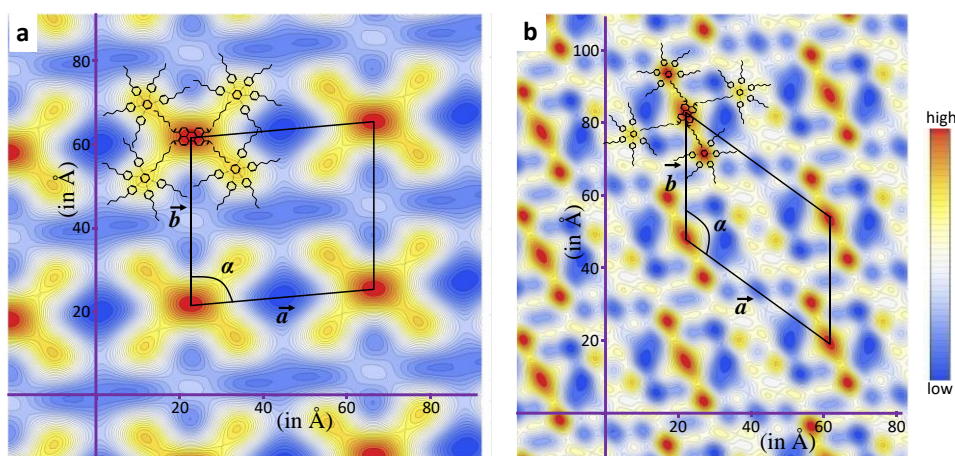


**Figure 5.23.** Reconstructed electron density maps of compounds (a) **5a** and (b) **5b**, showing the arrangement of the column on the 2D oblique lattice. Red represents the highest electron density and deep blue is the lowest. The parallelogram on the map shows the respective 2D unit cell.

The XRD pattern of compound **5c** in the isotropic phase is very similar as observed for compounds **5a** and **5b** and can be explained in a similar manner (Figure 5.24a,c). However, at a temperature below 65 °C, the PE-PE correlation is becoming narrower and PT-PT correlation peak is more or less the same as in the isotropic phase. The XRD pattern of compound **5c** at 25 °C is shown in Figure 5.24b,d. In addition to PE-PE and PT-PT correlation peak, two other peaks ( $h_{ac}$  and  $h_c$ ) appear in the wide-angle region (Figure 5.24b, Table 5.10). Moreover, these two peaks are not seen in the isotropic phase. Further, the sharp  $h_c$  peak appears due to strong perylene core to core correlations which reveal its columnar nature and confirmed the occurrence of columnar nematic ( $N_{col}$ ) phase (schematic is shown in Figure 5.24e). The  $d$ -spacing corresponding to  $h_c$  is found to be 4.09 Å. Because the reported face-to-face distance between two  $\pi$ -conjugated molecules is about 3.51 Å, perylene cores are packed with a tilting angle of 30.88° with respect to the axis of the perylene columns.<sup>88,89</sup>

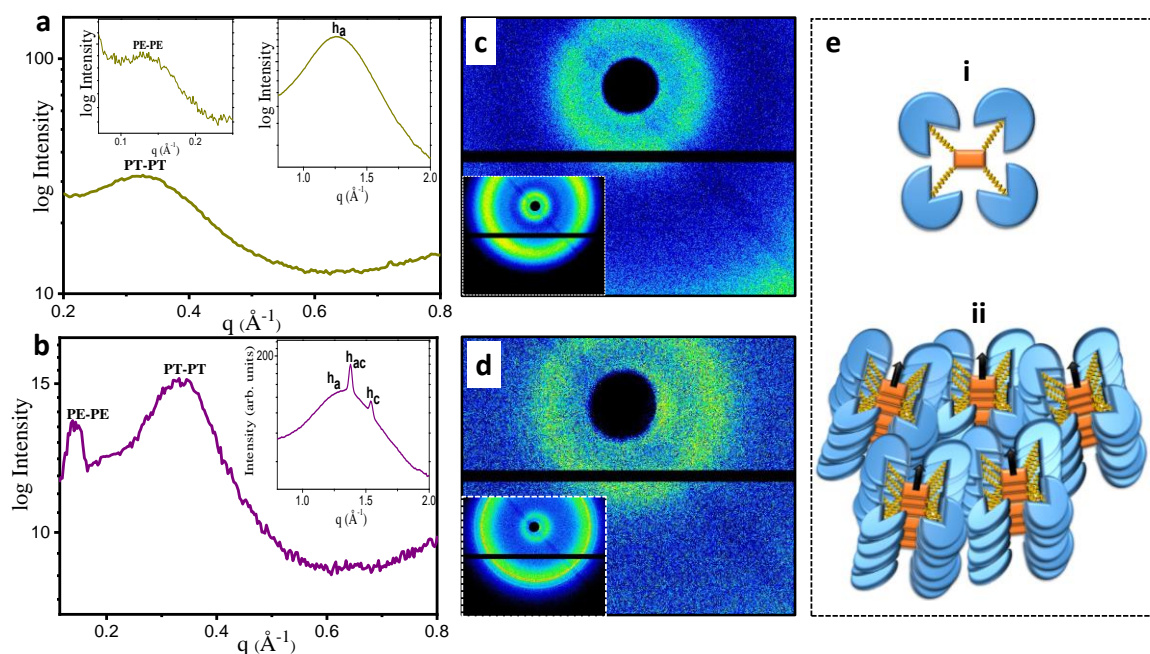


**Figure 5.24** Smaller angle (left inset) and small- and wide-angle (right inset) XRD patterns for compound **5c**, showing (a) isotropic phase and (b)  $N_{col}$  phase at 70 °C and 25 °C, respectively. Corresponding 2D small- and wide-angle (inset) XRD patterns at (c) 70 °C and (d) 25 °C, respectively. (e) Schematic illustrations of (i) compound **5c** and (ii) arrangement of the compound **5c** in the  $N_{col}$  phase.

**Table 5.10** Variation of *d*-spacing in the phases of compound **5c**.

Phase		Small-angle peak (Å)		Wide-angle peak (Å)		
<b>C</b>		1 <sup>st</sup> peak	2 <sup>nd</sup> peak	1 <sup>st</sup> peak	2 <sup>nd</sup> peak	3 <sup>rd</sup> peak
<b>5c</b>	N <sub>col</sub>	42.92	18.34	4.91	4.56	4.09
		PE-PE	PT-PT	(h <sub>a</sub> )	(h <sub>ac</sub> )	(h <sub>c</sub> )
	Iso	45.83	19.05	5.00	-	-
		PE-PE	PT-PT	(h <sub>a</sub> )		

Abbreviations: N<sub>col</sub>: columnar nematic; Iso: isotropic phase; PE-PE: perylene core to core interaction; PT-PT: pentaalkynylbenzene core to core interaction. h<sub>a</sub>, h<sub>ac</sub> and h<sub>c</sub> spacings appear due to fluid chain-chain, partially crystallize chain-chain and perylene (PE) core-core (face to face) correlations, respectively.

The transition from the Cr<sub>colob</sub> phase to the N<sub>col</sub> phase, which happens with increasing spacer length, is due to symmetry breaking. The Cr<sub>colob</sub> phase exhibits long-range positional order, bond orientational order and orientational order, whereas the N<sub>col</sub> phase shows only quasi-long-range orientational order. Moreover, this transition could be explained in terms of the flexibility-induced orientational freedom of the pentaalkynylbenzene discs. As the spacer chain length increases, flexibility increases in same way, which permits more orientational freedom to pentaalkynylbenzene discs and leads to the Cr<sub>colob</sub> to N<sub>col</sub> transition.

#### 5.2.3.4 Photophysical and electrochemical properties

All the perylene derivatives exhibited good luminescence properties as evident from their absorption and emission studies in solution as well as in the solid-state. In solution state, they showed similar absorption and emission spectra indicating that varying spacer length between perylene and pentaalkynylbenzene moieties does not affect their spectral behaviour in solution. The absorption spectra recorded in μM THF solution of compound **5a** showed peaks at 240, 261, 337, 416, 441 and 471 nm with a shoulder peak at 380 nm (Figure 5.25a, Table 5.11) due to perylene<sup>27</sup> and pentaalkynylbenzene moiety.<sup>81,82</sup> Other homologues of the series displayed peaks more or less at the same wavelength (Table 5.11). All the compounds showed green light emission even under daylight conditions (Figure 5.25a inset). Emission spectra exhibited two

strong peaks at 487 and 517 nm characteristic of perylene core<sup>27</sup> with a Stokes' shift of 150 nm (Figure 5.25a). The solid-state absorption and emission spectra were obtained for compounds **5a** and **5b** (Figure 5.25b) and green emission was preserved in solid-state (Figure 5.25b inset). The absorption bands became broader and red-shifted as clearly observed in the spectrum (Figure A25, Appendix V, Page 325). The fluorescence bands in the solid-state (Figure 5.25b) were significantly red-shifted and merged as compared to those in solution state (in  $\mu\text{M}$  THF solution) (Figure 5.25a) which mainly correlate the arrangement of the  $\pi$ -conjugated molecules in solid-state.

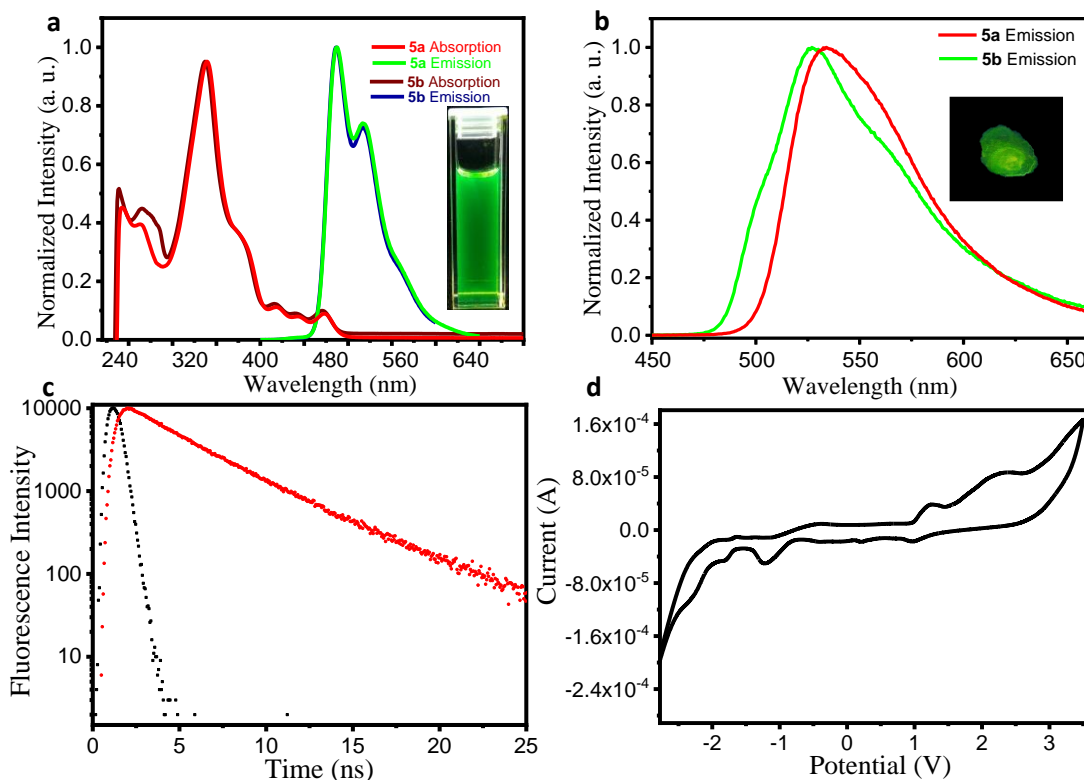


**Figure 5.25** (a) Absorption and emission spectra of compounds **5a** and **5b** in micromolar THF solutions. Inset shows green fluorescence for **5b** in micromolar THF solution under daylight condition. (b) Emission spectra for the spin-coated thin films of compounds **5a** and **5b**. Inset shows green fluorescence of **5b** in the solid-state. (c) Fluorescence decay spectra of compound **5a** ( $\lambda_{\text{exc}} = 337$  nm &  $\lambda_{\text{ems}} = 487$  nm) in micromolar THF solution ( $\chi^2$  value = 1.01). (d) Cyclic voltammogram of compound **5a** in HPLC DCM solution of TBAH (0.1 M) at a scanning rate of 100 mV/s.

**Table 5.11** Photophysical properties of compounds **5a-c**.<sup>a</sup>

	Absorption (nm)	Emission (nm)	$\tau_1(\alpha_1)$ (ns)	$\tau_2(\alpha_2)$ (ns)	$\tau_{av}$ (ns) <sup>c</sup>	$\phi_{FL}$ <sup>d</sup>	Steady State Anisotropy
<b>5a</b>	240, 261, 337, 380, 416, 441, 471	487, 517, 558	2.91 (0.66)	5.40 (0.34)	3.74	0.89	$2.23 \times 10^{-3}$
<b>5b</b>	238, 265, 337, 380, 417, 441, 471	487, 518, 558	2.82 (0.52)	4.72 (0.48)	3.73	0.84	$3.17 \times 10^{-3}$
<b>5c</b>	239, 262, 337, 380, 416, 441, 471	487, 517, 558	2.79 (0.53)	4.66 (0.47)	3.67	0.81	$3.30 \times 10^{-3}$

<sup>a</sup>in micromolar solutions in THF. <sup>b</sup>Corresponding to excitation wavelength 337 nm for all compounds. <sup>c</sup>Average fluorescence lifetime. Fluorescence quantum yield ( $\phi_{FL}$ ) relative to quinine sulphate in 0.1 M H<sub>2</sub>SO<sub>4</sub> ( $\phi_{FL} = 0.54$ ).

In order to know the reorientational dynamics of molecules in solution, fluorescence lifetime (Figure 5.25c and Figure A26, Appendix V, Page 326) and steady-state anisotropy measurements were performed in dilute solutions (10  $\mu$ M in THF). Interestingly, the fluorescence lifetime in all the hybrid oligomers is close to 4 ns (Table 5.11) whereas, the measured lifetime for perylene is 5.2 ns in ethanol solution.<sup>41,76</sup> The observed decrease in lifetime with increasing spacer chain length could be due to higher non-radiative rate involved in the processes (competing for the relaxation of the excited state) because of the change in shape and size of the hybrid oligomers and thus the molecular interactions as reported earlier.<sup>90</sup> Steady-state anisotropy values of the compounds **5a-c** were found to be increased with an increasing number of alkyl spacers. In general, anisotropy values are affected by molecular motion which mainly depends on local environmental factors such as viscosity, molecular confinement and the size of the hybrid molecule. In our case, the increased value of fluorescence anisotropy with increasing the molecular size (from **5a** to **5c**) implies that mobility decreased and hence anisotropy values have increased (Table 5.11). Apart from these, quantum yields calculations were carried out using quinine sulphate in 0.1 M H<sub>2</sub>SO<sub>4</sub> solution (Figure A27, Table 5.11 and

Table A2, Appendix V, Page 327) as a standard as it absorbs at around the same wavelength (347 nm) as that of **5a-c** compounds (337 nm). Quantum yield is affected by how quickly energy leaves the system through alternative processes (non-radiative processes & intersystem crossing). In all the compounds, the quantum yield value is close to 0.9, which means that alternative processes occur at significantly lower rates compared to fluorescence.

In order to find out the electronic energy level that determines the energy and electron transfer processes, cyclic voltammetry (CV) was carried out. CV studies were performed in millimolar (mM) solutions of compounds **5a-c** in oxygen-free dichloromethane solvent, as shown in Figure 5.25d and Figure A28 (Appendix V, Page 328). The optical bandgap ( $\Delta E_{UV}$ ) was obtained from the absorption maxima of compounds **5a-5c** by using the formula  $E = 1240/\lambda$ .<sup>91</sup> The electronic properties of all the compounds were found to be almost similar. In general, the redox processes are ground-state properties associated with the absorption spectra which resulted in similar electrochemical behaviour irrespective of spacer length. HOMO-LUMO energy levels ( $E_{LUMO}$  &  $E_{HOMO}$ ) and electrochemical bandgap ( $\Delta E_{g,CV} = E_{LUMO} - E_{HOMO}$ ) are summarised in Table A3 (Appendix V, Page 327). Both the UV-vis spectra and CV results have shown that different spacer lengths ( $n = 6, 8, 10$  for **5a**, **5b** and **5c**, respectively) had little influence on the electrochemical properties.

#### **5.2.3.5 Conductivity measurements in the soft crystal columnar phase**

The electrical characterization of columnar assemblies is important for finding their application as charge or ion conductors. The ac impedance spectroscopy is an important technique for measuring conductivity by applying fixed alternate voltage with a varying frequency that ranges from megahertz to millihertz. The impedance measurements performed in their LC state were interpreted in terms of equivalent circuits consisting of electrical components like capacitors, resistors and inductors. The samples were heated to their isotropic temperature and were filled through capillary action in an ITO (Indium-Tin oxide) cell separated by a 20  $\mu\text{m}$  spacer and then allowed to cool slowly until the mesophase temperature reached for measurement. This procedure is usually done to align the sample homeotropically so that conductivity can be measured in the direction of column organization. After several attempts, the sample was not aligned properly for both the compounds (**5a** and **5b**) as observed by their POM images (not shown).



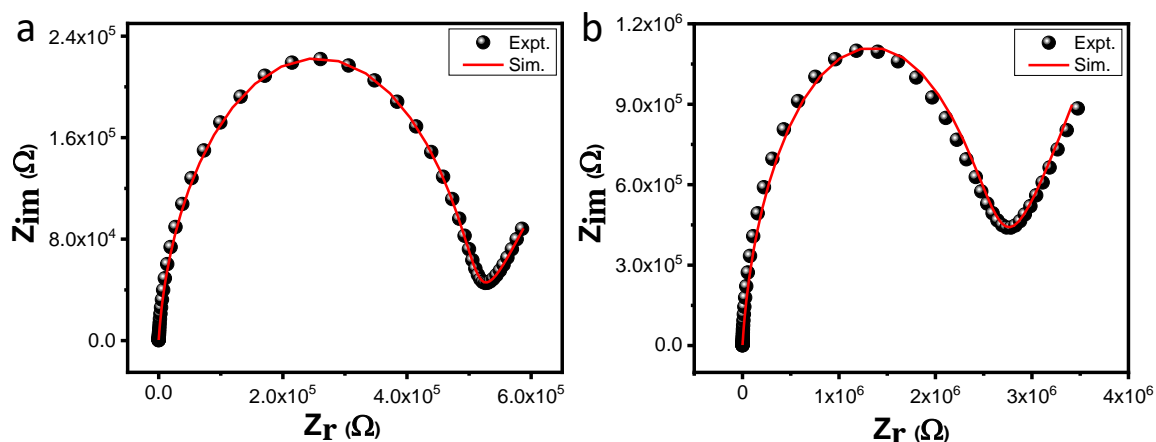


**Figure 5.26** Impedance  $Z_{im}$  vs  $Z_r$  of compounds **5a** and **5b** in their  $Cr_{colob}$  phase and their corresponding circuit. Expt. represents plot obtained from measurement, Sim. represents plot obtained after fitting through software (Nano-electronic Measurement Systems (NeMS), India).

Figure 5.26 shows the complex Impedance graphs ( $Z_{im}$  vs  $Z_r$ ) for compound **5a** and **5b** showing well-defined semicircle fitted by using a software (Nano-electronic Measurement Systems (NeMS), India) which results into a circuit having constant phase element (CPE) in parallel with resistance (R) and wurburg impedance (W), where R is defined as a bulk resistance. Through proper fitting of the plot, R value was obtained. After substituting R values, the conductivity could be obtained by using the formula:  $\sigma = d/(R.A)$ , where  $d$  represents the thickness of the cell (20  $\mu m$ ) and A is the area of the cell. The conductivity values obtained for compounds **5a** and **5b** in the soft columnar crystal phase are  $5.07 \times 10^{-7}$  and  $1.25 \times 10^{-7} S m^{-1}$ , respectively. The conductivity values can be further improved by proper alignment and the mixing of some ions and then these derivatives may find application for further device investigation.

### 5.2.4 Conclusions

The main conclusions of the study reported in this paper are threefold. First, we have synthesized a new series of novel perylene tetraesters derivatives showing soft crystal columnar and nematic columnar mesophases at room temperature over a wide temperature range. Specifically, we observed that compounds **5a** and **5b** with shorter alkyl spacer ( $n = 6, 8$ ) connecting to PE and pentaalkynylbenzene units show soft crystal columnar behaviour.

Interestingly, compound (**5c**) with longer spacer ( $n = 10$ ) is found to self-organize into a room temperature columnar nematic phase. Second, compound **5a** showed two different kinds of lattices as demonstrated by GISAXS/GIWAXS studies. Third, all the molecules showed a green emission in the solution and in the solid-state visible to the naked eye with a very good quantum yield and large bandgap. The length of the peripheral alkyl spacers did not have much effect on the photo-physical properties. This new class of perylene discotics with easy synthesis, room temperature nematic columnar and soft crystal columnar behaviour over a wide temperature range, near unity quantum yield, highly emissive nature and large bandgap make them potential candidates for their use in solid-state displays. In addition, this new class of materials may open up a new field to explore the structure-property relationships for various oligomers based on PE tetraesters.

**Acknowledgement.** *Dr. Santosh Prasad Gupta (at Patna University) is duly acknowledged for the analysis of XRD data.*

### 5.2.5 Experimental section

**5.2.5.1 Synthesis of 5a.** Eluent for purification (hexane/ethyl acetate 9:1). Yield: 68%, yellow solid.  $R_f$ : 0.71 (hexane/ethyl acetate 5:2); m.p: see Table 5.7;  $^1\text{H}$  NMR (400 MHz,  $\text{CDCl}_3$ ,  $\delta$  in ppm):  $\delta$  8.31 (d, 4H,  $J = 8.16$  Hz), 8.05 (d, 4H,  $J = 7.84$  Hz), 7.56-7.52 (m, 40H), 7.16-7.14 (m, 40H), 4.37 (t, 8H,  $J = 5.92, 6.04$  Hz), 4.29 (t, 8H,  $J = 6.56, 6.44$  Hz), 2.66-2.54 (m, 40H), 1.96 (m, 8H), 1.80-1.73 (m, 8H), 1.67-1.56 (m, 40H), 1.36-1.25 (m, 96H), 0.95-0.84 (m, 60H);  $^{13}\text{C}$  NMR (100 MHz,  $\text{CDCl}_3$ ,  $\delta$  in ppm):  $\delta$  168.43, 143.96, 143.91, 131.78, 131.54, 128.54, 128.51, 128.49, 120.73, 120.46, 120.08, 99.38, 87.11, 84.09, 36.00, 31.52, 31.49, 30.97, 26.50, 23.02, 22.57, 22.53, 14.17, 14.08, 14.06; FT-IR ( $\text{cm}^{-1}$ ):  $\nu$  3027.15, 2958.26, 2927.31, 2856.55, 2209.10, 1906.00, 1723.24, 1591.72, 1513.60, 1465.68, 1425.91, 1378.57, 1347.58, 1264.10, 1164.05, 1085.24, 1020.16, 836.63, 805.97, 750.12, 551.40, 530.10; elemental analysis calculated (%) for  $\text{C}_{332}\text{H}_{356}\text{O}_{12}$ : C 87.86, H 7.91; found: C 87.85, H 8.07.

**5.2.5.2 Synthesis of 5b.** Eluent for purification (hexane/ethyl acetate 10:1). Yield: 72 %, yellow solid.  $R_f$ : 0.73 (hexane/ethyl acetate 5:2); m.p: see Table 5.7;  $^1\text{H}$  NMR (400 MHz,  $\text{CDCl}_3$ ,  $\delta$  in ppm):  $\delta$ - 8.31 (d, 4H,  $J = 8.2$  Hz), 8.05 (d, 4H,  $J = 7.8$  Hz), 7.56-7.48 (m, 40H), 7.18-7.13 (m, 40H), 4.37 (t, 8H,  $J = 6.16, 6.2$  Hz), 4.29 (t, 8H,  $J = 6.68, 6.8$  Hz), 2.69-2.54 (m,

40H), 1.96 (m, 8H), 1.80-1.73 (m, 8H), 1.67-1.56 (m, 40H), 1.36-1.25 (m, 112H), 0.95-0.84 (m, 60H);  $^{13}\text{C}$  NMR (100 MHz,  $\text{CDCl}_3$ ,  $\delta$  in ppm):  $\delta$  -168.47, 143.91, 131.77, 131.56, 128.53, 120.49, 120.09, 99.55, 84.09, 74.69, 36.00, 31.48, 30.97, 26.39, 23.02, 22.57, 14.07; FT-IR ( $\text{cm}^{-1}$ ):  $\nu$ - 3026.40, 2956.48, 2927.26, 2855.62, 2210.6, 1902.00, 1716.40, 1513.52, 1466.17, 1425.53, 1348.80, 1272.96, 1162.98, 1086.30, 1019.00, 962.17, 838.27, 813.20, 749.36, 724.53, 554.29, 532.10; elemental analysis calculated (%) for  $-\text{C}_{340}\text{H}_{372}\text{O}_{12}$ : C 87.81, H 8.06; found: C 87.65, H 8.02.

**5.2.5.3 Synthesis of 5c.** Eluent for purification (hexane/ethyl acetate 12.5:1). Yield: 69 %, yellow solid.  $R_f$ : 0.76 (hexane/ethyl acetate 5:2); m.p: see Table 5.7;  $^1\text{H}$  NMR (400 MHz,  $\text{CDCl}_3$ ,  $\delta$  in ppm):  $\delta$  8.35 (d, 4H,  $J = 8.2$  Hz), 8.07 (d, 4H,  $J = 7.84$  Hz), 7.56-7.51 (m, 40H), 7.19-7.17 (m, 40H), 4.36 (t, 8H,  $J = 6.28$ , 6.28 Hz), 4.31 (t, 8H,  $J = 6.76$ , 6.84 Hz), 2.66-2.61 (m, 40H), 1.93 (m, 8H), 1.78 (m, 8H), 1.66-1.61 (m, 40H), 1.36-1.32 (m, 128H), 0.94-0.85 (m, 60H);  $^{13}\text{C}$  NMR (100 MHz,  $\text{CDCl}_3$ ,  $\delta$  in ppm):  $\delta$  168.48, 160.23, 144.00, 143.89, 143.69, 131.78, 128.53, 128.51, 124.09, 120.53, 120.49, 120.11, 99.54, 99.37, 99.31, 87.11, 86.64, 84.11, 74.76, 65.66, 36.00, 31.62, 31.51, 30.97, 29.68, 29.40, 26.44, 22.73, 22.57, 14.07; FT-IR ( $\text{cm}^{-1}$ ):  $\nu$ -3021.90, 2958.62, 2924.68, 2854.05, 2208.90, 1903.60, 1719.00, 1513.30, 1464.62, 1427.80, 1378.10, 1349.70, 1262.06, 1162.75, 1087.77, 1020.25, 802.19, 753.25, 721.30, 554.44, 533.14; elemental analysis calculated (%) for  $-\text{C}_{348}\text{H}_{388}\text{O}_{12}$ : C 87.76, H 8.21; found: C 87.87 H 8.32.

**5.2.5.4 Quantum yield calculation.** Quantum yield was measured according to established procedure by using 0.1 M  $\text{H}_2\text{SO}_4$  solution as the standard. Absolute values were calculated according to the following equation:  $Q_S = Q_R \times (m_S/m_R) \times (n_S/n_R)^2$ , where Q is Quantum yield, m represents slope of the plot of integrated fluorescence intensity vs absorbance, n = refractive index (1.407 for THF and 1.33 for distilled water). The subscript R refers to the reference fluorophore i.e. quinine sulfate in 0.1 M  $\text{H}_2\text{SO}_4$  and subscript S refers to the sample under investigation. In order to minimize the re-absorption effects, absorbance value was kept below 0.15 at the excitation wavelength of 337 nm. Quantum yield of quinine sulfate in 0.1M  $\text{H}_2\text{SO}_4$  solution is 0.54. After substituting the appropriate values, the simplified equation is  $Q_S = 0.54 \times (m_S/m_R) \times (1.407/1.33)^2 = 0.60434 \times (m_S/m_R)$ .

**5.2.5.5 Energy levels calculation from cyclic voltammetry.** The experimental setup for CV measurements consists of a single compartment cell equipped with Ag/AgNO<sub>3</sub> as a reference electrode, a platinum wire as counter electrode and glassy carbon as a working electrode. Millimolar solutions of all the compounds were used for CV measurements. A 0.1 M solution of tetrabutylammoniumhexafluorophosphate was used as a supporting electrolyte. The half-wave potential of the ferrocene/ferrocenium (Fc/Fc<sup>+</sup>) was calculated as  $E_{1/2, \text{Fc/Fc}^+} = (E_{\text{anodic peak potential}} + E_{\text{cathodic peak potential}})/2 = 0.553 + 0.442 = 0.4975 \text{ V}$ . The LUMO energy levels were obtained by the formula  $E_{\text{LUMO}} = - (4.8 - E_{1/2, \text{Fc/Fc}^+} + E_{\text{red, onset}}) \text{ eV}$ , while the HOMO energy levels by  $E_{\text{HOMO}} = - (4.8 - E_{1/2, \text{Fc/Fc}^+} + E_{\text{ox, onset}}) \text{ eV}$ .

**5.2..5.6 Conductivity measurements by ac impedance spectroscopy.** The conductivity values was calculated by using formula:  $\sigma = d/(R.A)$ , where  $\sigma$  = Conductivity in S m<sup>-1</sup>,  $d$  = thickness of the cell,  $A$  = area of the cell,  $R$  = bulk resistance.

## References

1. Nie, H.; Huang, J.; Zhao, Z.; Tang, B. Z. *ACS Symposium Series; American Chemical Society*: Washington, DC, 2016, Volume **2**.
2. Gupta, R. K.; Sudhakar, A. A. *Langmuir* **2019**, *35*, 2455-2479.
3. Gupta, R. K.; Shankar Rao, D. S.; Prasad, S. K.; Achalkumar, A. S. *Chem. Eur. J.* **2018**, *24*, 3566-3575.
4. Cormier, R. A.; Gregg, B. A. *J. Phy. Chem. B* **1997**, *101*, 11004-11006.
5. Cormier, R. A.; Gregg, B. A. *Chem. Mater.* **1998**, *10*, 1309-1319.
6. Struijk, C. W.; Sieval, A. B.; Dakhorst, J. E.; van Dijk, M.; Kimkes, P.; Koehorst, R. B.; Donker, H.; Schaafsma, T. J.; Picken, S. J.; van de Craats, A. M.; Warman, J. M. *J. Am. Chem. Soc.* **2000**, *122*, 11057-11066.
7. Würthner, F.; Thalacker, C.; Diele, S.; Tschierske, C. *Chem. Eur. J.* **2001**, *7*, 2245-2253.
8. Würthner, F. *Chem. Commun.* **2004**, 1564-1579.
9. Jancy, B.; Asha, S. K. *J. Phy. Chem. B* **2006**, *110*, 20937-20947.
10. Dehm, V.; Chen, Z.; Baumeister, U.; Prins, P.; Siebbeles, L. D.; Würthner, F. *Org. lett.* **2007**, *9*, 1085-1088.
11. Jancy, B.; Asha, S. K. *Chem. Mater.* **2007**, *20*, 169-181.
12. Bhavsar, G. A.; Asha, S. K. *Chem. Eur. J.* **2011**, *17*, 12646-12658.
13. Kozma, E.; Mróz, W.; Villafiorita-Monteleone, F.; Galeotti, F.; Andicsová-Eckstein, A.; Catellani, M.; Botta, C. *RSC Adv.* **2016**, *6*, 61175-61179.
14. Vollbrecht, J.; Blazy, S.; Dierks, P.; Peurifoy, S.; Bock, H.; Kitzerow, H. *ChemPhysChem* **2017**, *18*, 2024-2032.
15. Li, C.; Wonneberger, H. *Adv. Mater.* **2012**, *24*, 613-636.
16. Ranke, P.; Bleyl, I.; Simmerer, J.; Haarer, D.; Bacher, A.; Schmidt, H. W. *Appl. Phys. Lett.* **1997**, *71*, 1332-1334.
17. Seguy, I.; Destruel, P.; Bock, H. *Synth. met.* **2000**, *111*, 15-18.
18. Kaafarani, B. R. *Chem. Mater.* **2010**, *23*, 378-396.
19. Setia, S.; Sidiq, S.; De, J.; Pani, I.; Pal, S. K. *Liq. Cryst.* **2016**, *43*, 2009-2050.

20. De, J.; Yang, W. Y.; Bala, I.; Gupta, S. P.; Yadav, R. A. K.; Dubey, D. K.; Chowdhury, A.; Jou, J. H.; Pal, S. K. *ACS Appl. Mater. Interfaces* **2019**, *11*, 8291-8300.
21. Bala, I.; Yang, W. Y.; Gupta, S. P.; De, J.; Yadav, R. A. K.; Singh, D. P.; Dubey, D. K.; Jou, J. H.; Douali, R.; Pal, S. K. *J. Mater. Chem. C* **2019**, *7*, 5724-5738.
22. Bala, I.; Ming, L.; Yadav, R. A. K.; De, J.; Dubey, D. K.; Kumar, S.; Singh, H.; Jou, J. H.; Kailasam, K.; Pal, S. K. *ChemistrySelect* **2018**, *3*, 7771-7777.
23. Gupta, R. K.; Dey, A.; Singh, A.; Iyer, P. K.; Sudhakar, A. A. *ACS Appl. Electron. Mater.* **2019**, *1*, 1378-1386.
24. Eccher, J.; Faria, G. C.; Bock, H.; von Seggern, H.; Bechtold, I. H. *ACS Appl. Mater. Interfaces* **2013**, *5*, 11935-11943.
25. Chen, L.; Jiang, Y.; Nie, H.; Lu, P.; Sung, H. H.; Williams, I. D.; Kwok, H. S.; Huang, F.; Qin, A.; Zhao, Z.; Tang, B. Z. *Adv. Funct. Mater.* **2014**, *24*, 3621-3630.
26. Meerheim, R.; Scholz, S.; Olthof, S.; Schwartz, G.; Reineke, S.; Walzer, K.; Leo, K. *J. Appl. Phys.* **2008**, *104*, 014510.
27. Gupta, S. K.; Setia, S.; Sidiq, S.; Gupta, M.; Kumar, S.; Pal, S. K. *RSC Adv.* **2013**, *3*, 12060-12065.
28. Alvarez, S. G.; Alvarez, M. T. A. *Synthesis* **1997**, *4*, 413-414.
29. Setia, S.; Pal, S. K. *ChemistrySelect* **2016**, *1*, 880-885.
30. Wang, G.; Wang, W.; Miao, R.; Shang, C.; He, M.; Peng, H.; He, G.; Fang, Y. *Phys. Chem. Chem. Phys.* **2016**, *18*, 12221-12230.
31. Bala, I.; Gupta, S. P.; De, J.; Pal, S. K. *Chem. Eur. J.* **2017**, *23*, 12767-12778.
32. Konidena, R. K.; Thomas, K. J.; Pathak, A.; Dubey, D. K.; Sahoo, S.; Jou, J. H. *ACS Appl. Mater. Interfaces* **2018**, *10*, 24013-24027.
33. Yuan, W. Z.; Bin, X.; Chen, G.; He, Z.; Liu, J.; Ma, H.; Peng, Q.; Wei, B.; Gong, Y.; Lu Y.; He, G. *Adv. Opt. Mater.* **2017**, *5*, 1700466.
34. Konidena, R. K.; Thomas, K. J.; Sahoo, S.; Dubey, D. K.; Jou, J. H. *J. Mater. Chem. C* **2017**, *5*, 709-726.
35. Jou, J. H.; Li, J. L.; Sahoo, S.; Dubey, D. K.; Kumar Yadav, R. A.; Joseph, V.; Thomas, K. J.; Wang, C. W.; Jayakumar, J.; Cheng, C. H. *J. Phys. Chem. C* **2018**, *122*, 24295-24303.

36. Wang, C.; Li, X.; Pan, Y.; Zhang, S.; Yao, L.; Bai, Q.; Li, W.; Lu, P.; Yang, B.; Su, S.; Ma, Y. *ACS Appl. Mater. Interfaces* **2016**, *8*, 3041-3049.
37. Li, W.; Pan, Y.; Yao, L.; Liu, H.; Zhang, S.; Wang, C.; Shen, F.; Lu, P.; Yang, B.; Ma, Y. *Adv. Opt. Mater.* **2014**, *2*, 892-901.
38. Yuan, W. Z.; Bin, X.; Chen, G.; He, Z.; Liu, J.; Ma, H.; Peng, Q.; Wei, B.; Gong, Y.; Lu Y.; He, G. *Adv. Opt. Mater.* **2017**, *5*, 1700466.
39. Dai, S. W.; Hsu, B. W.; Chen, C. Y.; Lee, C. A.; Liu, H. Y.; Wang, H. F.; Huang, Y. C.; Wu, T. L.; Manikandan, A.; Ho, R. M.; Tsao, C. S. *Adv. Mater.* **2018**, *30*, 1705532.
40. Wong, M. Y.; Zysman-Colman, E. *Adv. Mater.* **2017**, *29*, 1605444.
41. Liu, Y.; Li, C.; Ren, Z.; Yan, S.; Bryce, M. R. *Nat. Rev. Mater.* **2018**, *3*, 18020.
42. Olivier, Y.; Moral, M.; Muccioli, L.; Sancho-García, J. C. *J. Mater. Chem. C* **2017**, *5*, 5718-5729.
43. Luo, Y.; Aziz, H. *Adv. Funct. Mater.* **2010**, *20*, 1285-1293.
44. Shen, Y.; Zhang, Z.; Liu, H.; Yan, Y.; Zhang, S.; Yang, B.; Ma, Y. *J. Phys. Chem. C* **2019**, *123*, 13047-13056.
45. Tang, X.; Bai, Q.; Peng, Q.; Gao, Y.; Li, J.; Liu, Y.; Yao, L.; Lu, P.; Yang, B.; Ma, Y. *Chem. Mater.* **2015**, *27*, 7050-7057.
46. Konidena, R. K.; Thomas, K. J.; Dubey, D. K.; Sahoo, S.; Jou, J. H. *Chem. Commun.* **2017**, *53*, 11802-11805.
47. Shan, T.; Liu, Y.; Tang, X.; Bai, Q.; Gao, Y.; Gao, Z.; Li, J.; Deng, J.; Yang, B.; Lu, P.; Ma, Y. *ACS Appl. Mater. Interfaces* **2016**, *8*, 28771-28779.
48. Chen, S.; Slattum, P.; Wang, C.; Zang, L. *Chem. Rev.* **2015**, *115*, 11967-11998.
49. Zhan, X. W.; Facchetti, A.; Barlow, S.; Marks, T. J.; Ratner, M. A.; Wasielewski, M. R.; Marder, S. R. *Adv. Mater.* **2011**, *23*, 268-284.
50. Dimitrakopoulos, C. D.; Malenfant, P. R. L. *Adv. Mater.* **2002**, *14*, 99-117.
51. Zhang, X.; Rehm, S.; Safont-Sempere, Marina M.; Würthner, F. *Nat. Chem.* **2009**, *1*, 623-629.
52. Chu, X.; Guan, M.; Zhang, Y.; Li, Y.; Liu, X.; Zeng, Y. *RSC Adv.* **2013**, *3*, 9509-9513.
53. Breeze, A. J.; Salomon, A.; Ginley, D. S.; Gregg, B. A.; Tillmann, H.; Hörhold, H. H. *Appl. Phys. Lett.* **2002**, *81*, 3085-3087.

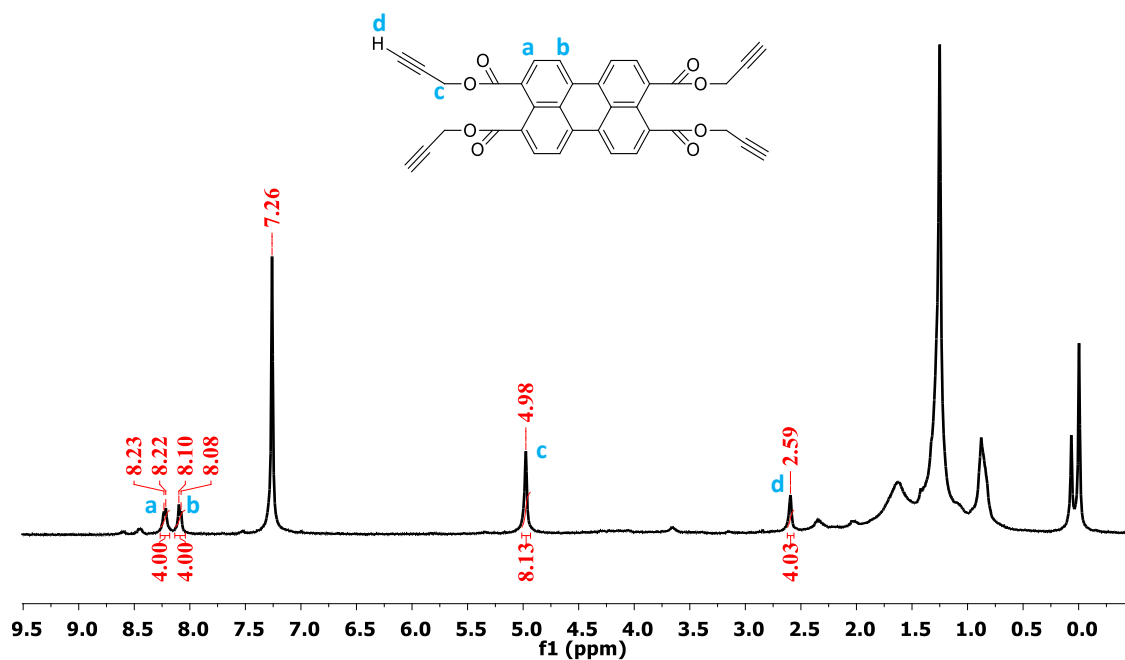
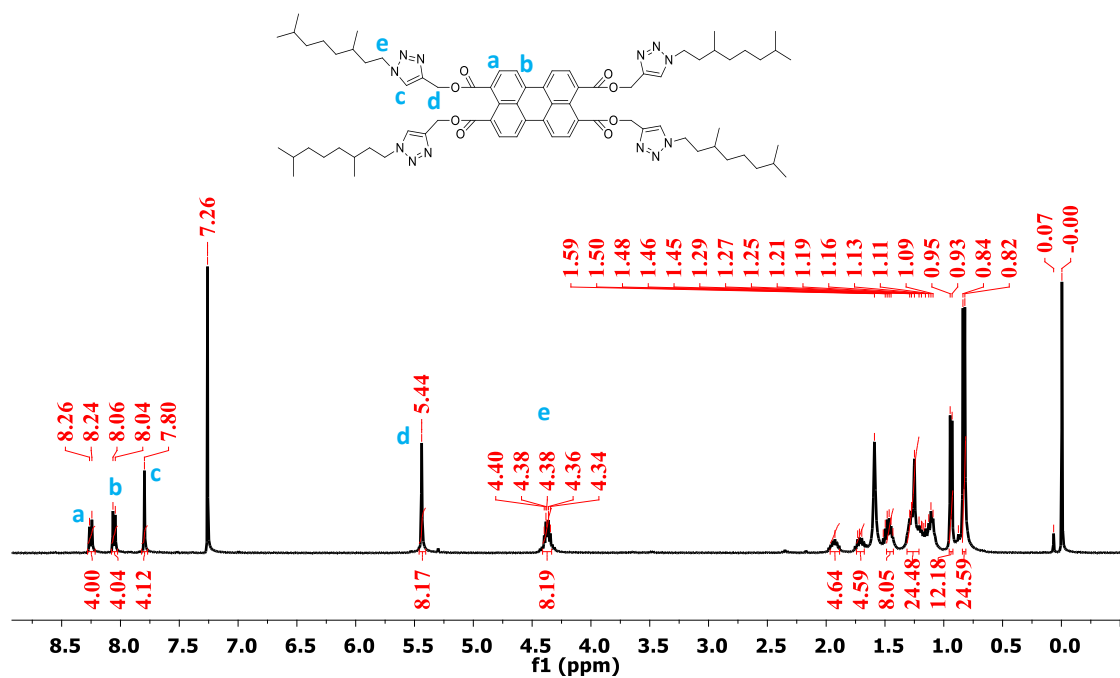
54. Gupta, R. K.; Das, D.; Gupta, M.; Pal, S. K.; Iyer, P. K.; Achalkumar, A. S. *J. Mater. Chem. C* **2017**, *5*, 1767-1781.
55. Görl, D.; Zhang, X.; Würthner, F. *Angew. Chem. Int. Ed.* **2012**, *51*, 6328-6348.
56. Funahashi, M.; Sonoda, A. *J. Mater. Chem.* **2012**, *22*, 25190-25197.
57. Prajitha, K. P.; Chithiravel, S.; Krishnamoorthy, K.; Asha, S. K. *J. Mater. Chem. C* **2014**, *2*, 9882-9891.
58. Muth, M. A.; Gupta, G.; Wicklein, A.; Carrasco-Orozco, M.; Thurn-Albrecht, T.; Thelakkat, M. *J. Phys. Chem. C* **2014**, *118*, 92-102.
59. Kelber, J.; Achard, M. F.; Garreau-de Bonneval, B.; Bock, H. *Chem. Eur. J.* **2011**, *17*, 8145-8155.
60. Zhu, M.; Guo, H.; Yang, F.; Wang, Z. *Dyes Pigm.* **2016**, *133*, 387-394.
61. Wicklein, A.; Lang, A.; Muth, M.; Thelakkat, M. *J. Am. Chem. Soc.* **2009**, *131*, 14442-14453,
62. Kelber, J.; Bock, H.; Thiebaut, O.; Grelet, E.; Langhals, H. *Eur. J. Org. Chem.* **2011**, *4*, 707-712.
63. Hansen, M. R.; Schnitzler, T.; Pisula, W.; Graf, R.; Müllen, K.; Spiess, H. W. *Angew. Chem. Int. Ed.* **2009**, *48*, 4621-4624.
64. Quintana, J. A.; Villalvilla, J. M.; de la Peña, A.; Segura, J. L.; Díaz-García, M. A. *J. Phys. Chem. C* **2014**, *118*, 26577-26583.
65. Mizoshita, N.; Tani, T.; Inagaki, S. *Adv. Funct. Mater.* **2011**, *21*, 3291-3296.
66. Zhang, T.; Sun, D.; Ren, X.; Liu, L.; Wen, G.; Ren, Z.; Li, H.; Yan, S. *Soft Matter* **2013**, *9*, 10739-10745.
67. Gao, B.; Xia, D.; Zhang, L.; Bai, Q.; Bai, L.; Yang, T.; Ba, X. *J. Mater. Chem.* **2011**, *21*, 15975-15980.
68. Funahashi, M.; Yamaoka, M.; Takenami, K.; Sonoda, A. *J. Mater. Chem. C* **2013**, *1*, 7872-7878.
69. Funahashi, M.; Sonoda, A. *Dalton Trans.* **2013**, *42*, 15987-15994.
70. Meng, L.; Wu, Q.; Yang, F.; Guo, H. *New J. Chem.* **2015**, *39*, 72-76.
71. Wicklein, A.; Kohn, P.; Ghazaryan, L.; Thurn-Albrecht, T.; Thelakkat, M. *Chem. Commun.* **2010**, *46*, 2328-2330.

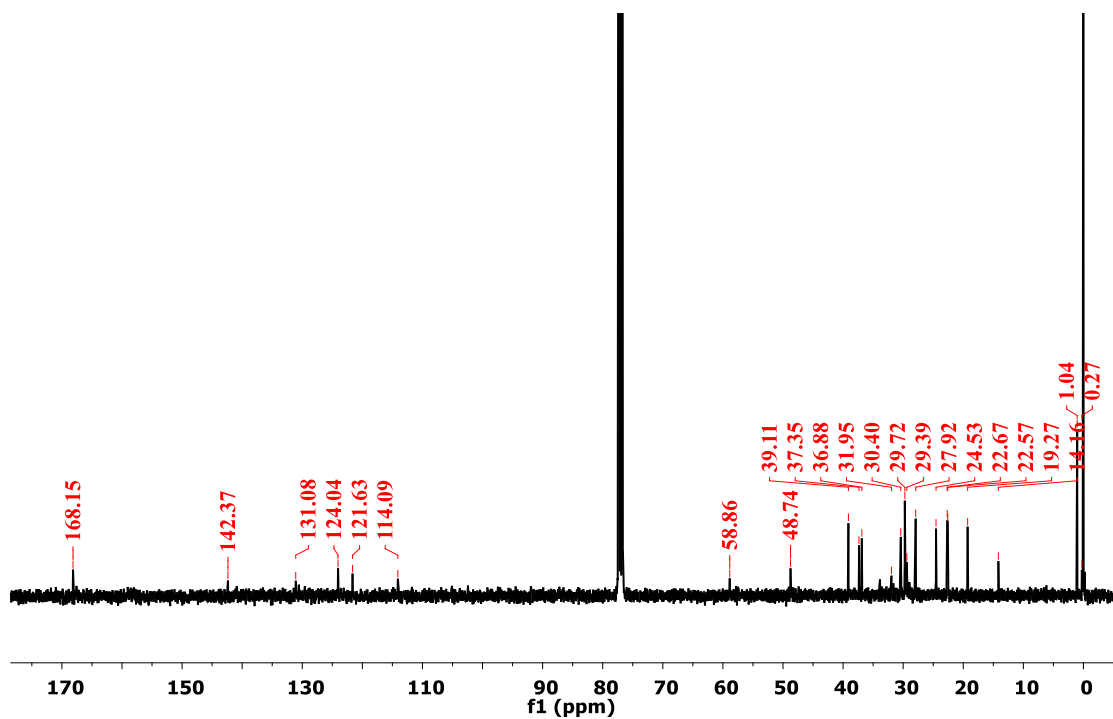
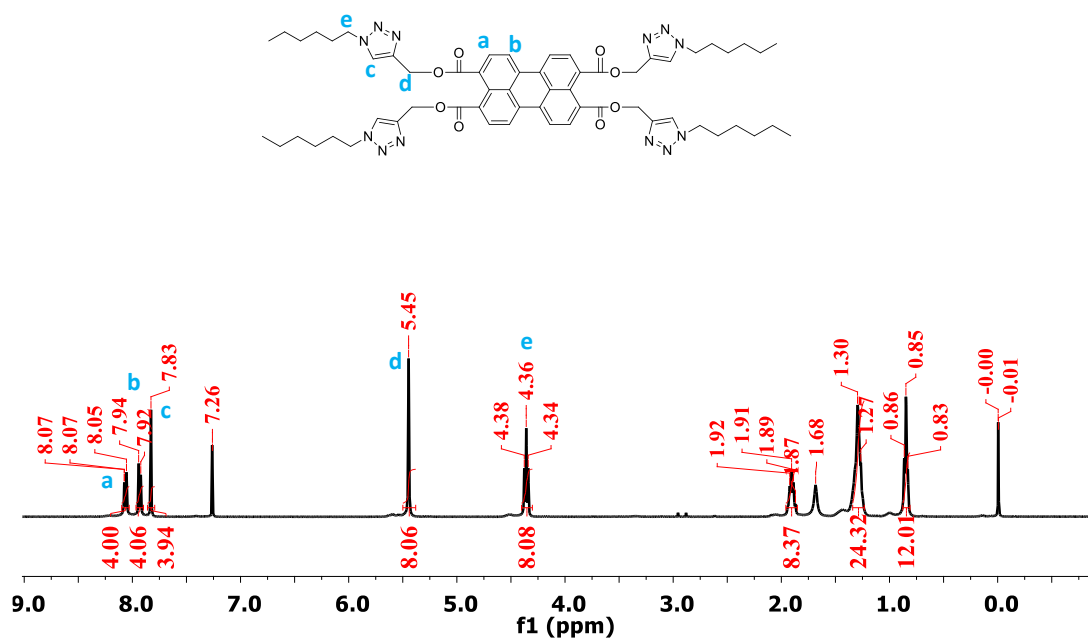


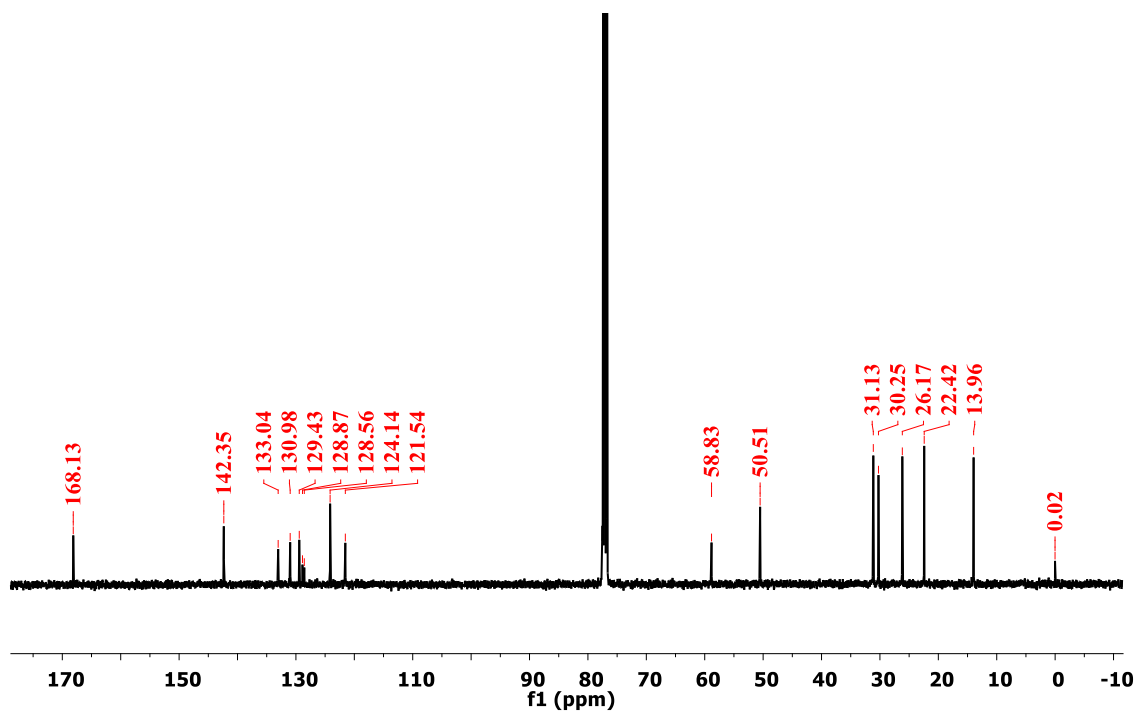
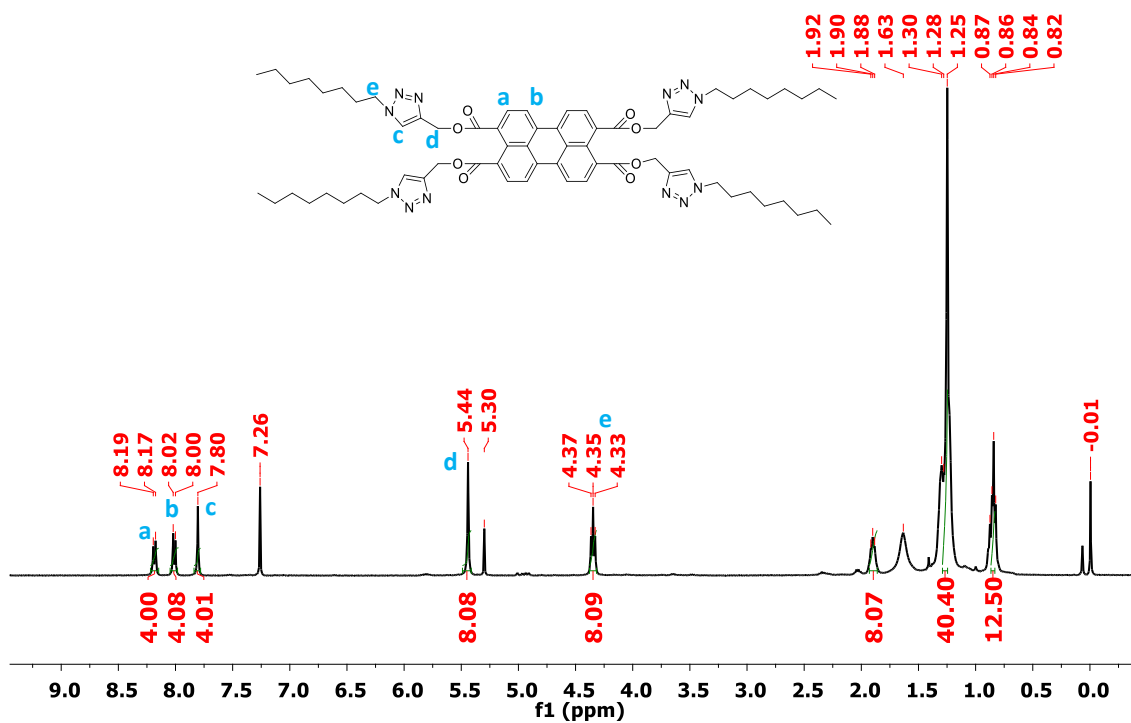
72. Kong, X.; He, Z.; Zhang, Y.; Mu, L.; Liang, C.; Chen, B.; Jing, X.; Cammidge, A. N. *Org. Lett.* **2011**, *13*, 764-767.
73. Wicklein, A.; Muth, M. A.; Thelakkat, M. *J. Mater. Chem.* **2010**, *20*, 8646-8652.
74. Gupta, R. K.; Pathak, S. K.; Pradhan, B.; Gupta, M.; Pal, S. K.; Sudhakar, A. A. *Chem Phys Chem* **2016**, *17*, 859-872.
75. Gupta, R. K.; Pathak, S. K.; Pradhan, B.; Rao, D. S.; Prasad, S. K.; Achalkumar, A. S. *Soft Matter* **2015**, *11*, 3629-3636.
76. Benning, S.; Kitzerow, H. S.; Bock, H. S.; Achard, M. F. *Liquid Crystals* **2000**, *27*, 901-906.
77. Thiebaut, O.; Bock, H.; Grelet, E. *J. Am. Chem. Soc.* **2010**, *132*, 6886-6887.
78. Wang, Y.; Zhang, C.; Wu, H.; Pu, J. *J. Mater. Chem. C* **2014**, *2*, 1667-1674.
79. Bisoyi, H. K.; Kumar, S.; *Chem. Soc. Rev.* **2010**, *39*, 264-285.
80. Gupta, M.; Gupta, S. P.; Rasna, M. V.; Adhikari, D.; Dhara, S.; Pal, S. K. *Chem. Commun.* **2017**, *53*, 3014-3017.
81. Gupta, M.; Bala, I.; Pal, S. K. *Tetrahedron Lett.* **2014**, *55*, 5836-5840.
82. Gupta, M.; Pal, S. K. *Langmuir* **2016**, *32*, 1120-1126.
83. Lehmann, M.; Gloza, S.; Roth, S. *Chem. Mater.* **2015**, *27*, 8181-8184.
84. Lehmann, M.; Maier, P.; Grüne, M.; Hügel, M. *Chem. Eur. J.* **2017**, *23*, 1060-1068.
85. Lehmann, M.; Jahr, M.; Grozema, F. C.; Abellon, R. D.; Siebbeles, L. D.; Müller, M. *Adv. Mater.* **2008**, *20*, 4414-4418.
86. Lehmann, M.; Köhn, C.; Meier, H.; Renker, S.; Oehlhof, A. *J. Mater. Chem.*, **2006**, *16*, 441-451.
87. Jurow, M. J.; Hageman, B. A.; DiMasi, E.; Nam, C. Y.; Pabon, C.; Black, C. T.; Drain, C. M. *J. Mater. Chem. A*, **2013**, *1*, 1557-1565.
88. Goddard, R.; Haenel, M. W.; Herndon, W. C.; Krueger, C.; Zander, M. *J. Am. Chem. Soc.* **1995**, *117*, 30-41.
89. Feng, X.; Pisula, W.; Kudernac, T.; Wu, D.; Zhi, L.; De Feyter, S.; Müllen, K. *J. Am. Chem. Soc.* **2009**, *131*, 4439-4448.
90. Johansson, L. B.-Å. *Spectrochimica Acta A* **1991**, *47*, 857-861.
91. Chang, C. W.; Tsai, H. Y.; Chen, K. Y. *Materials* **2014**, *7*, 5488-5506.

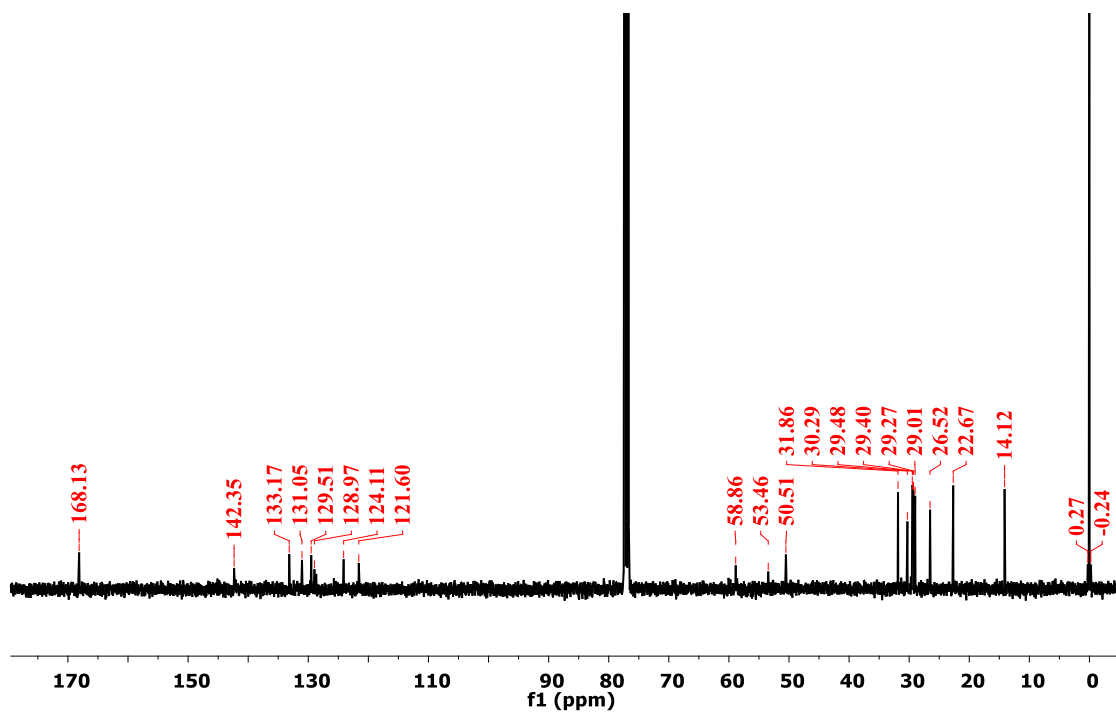
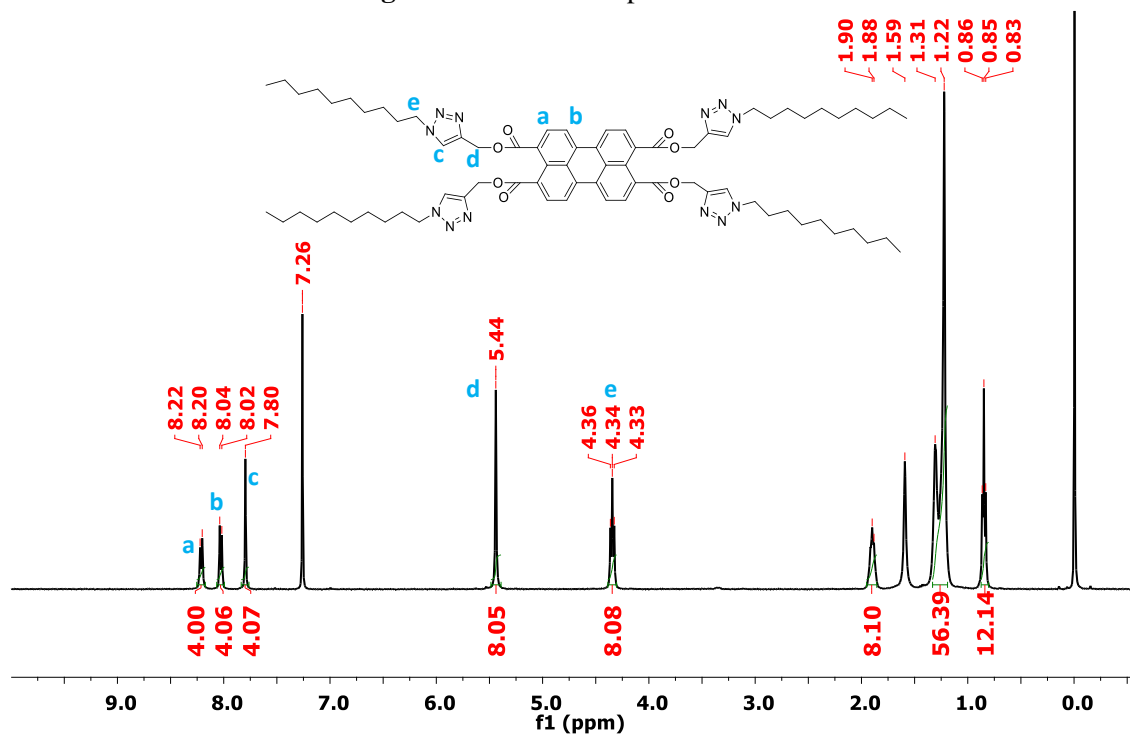


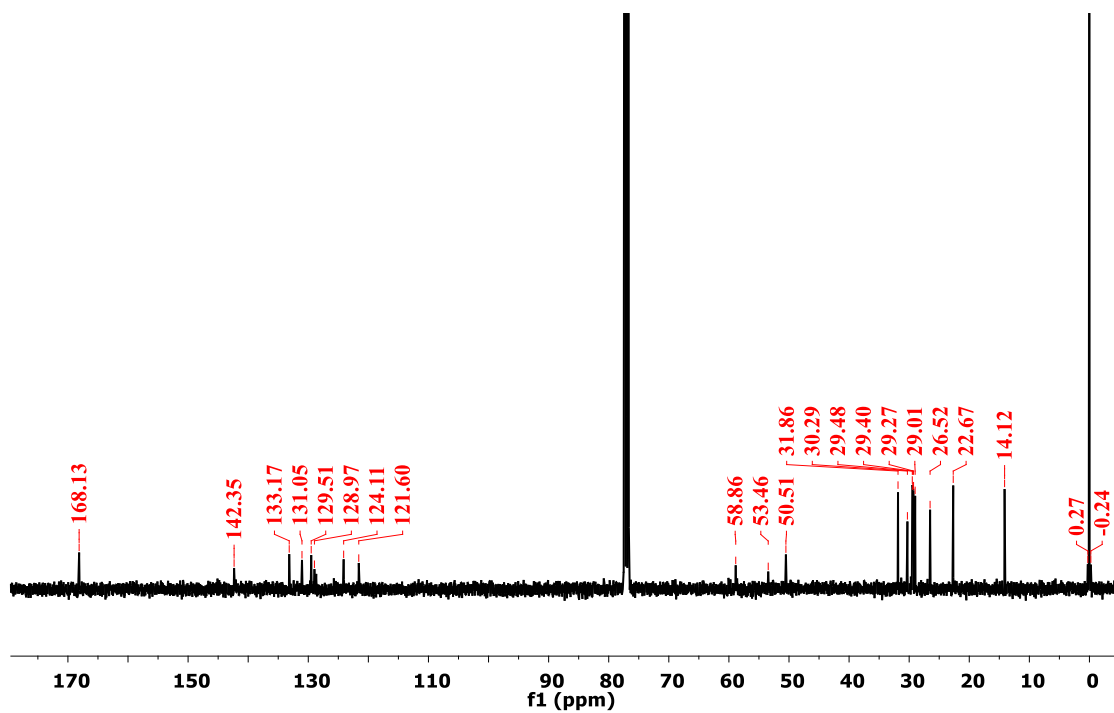
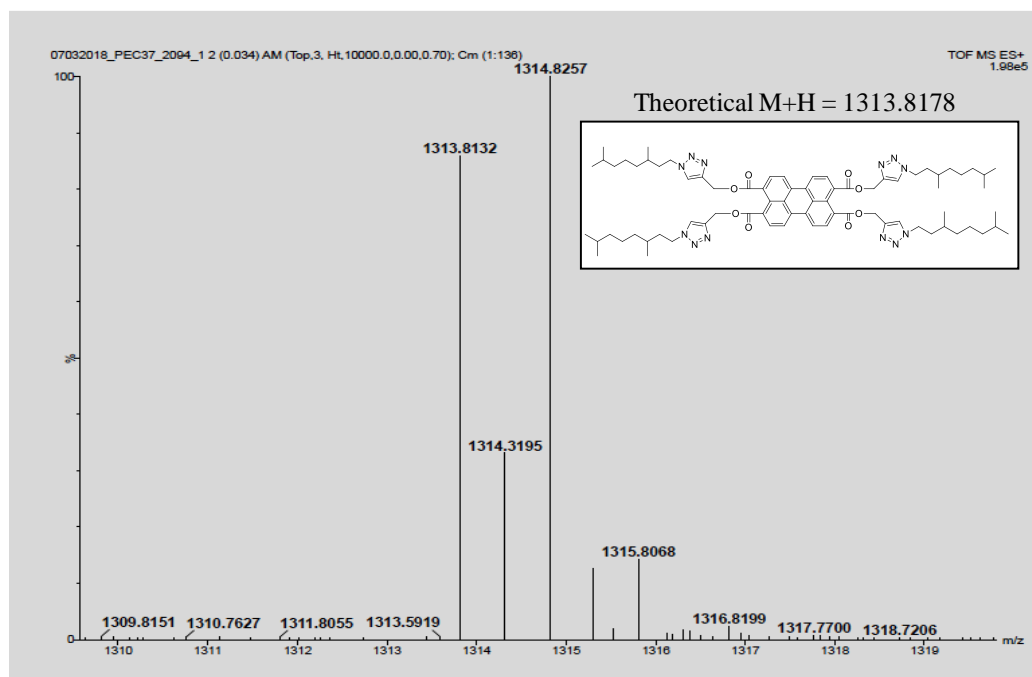
## Appendix V

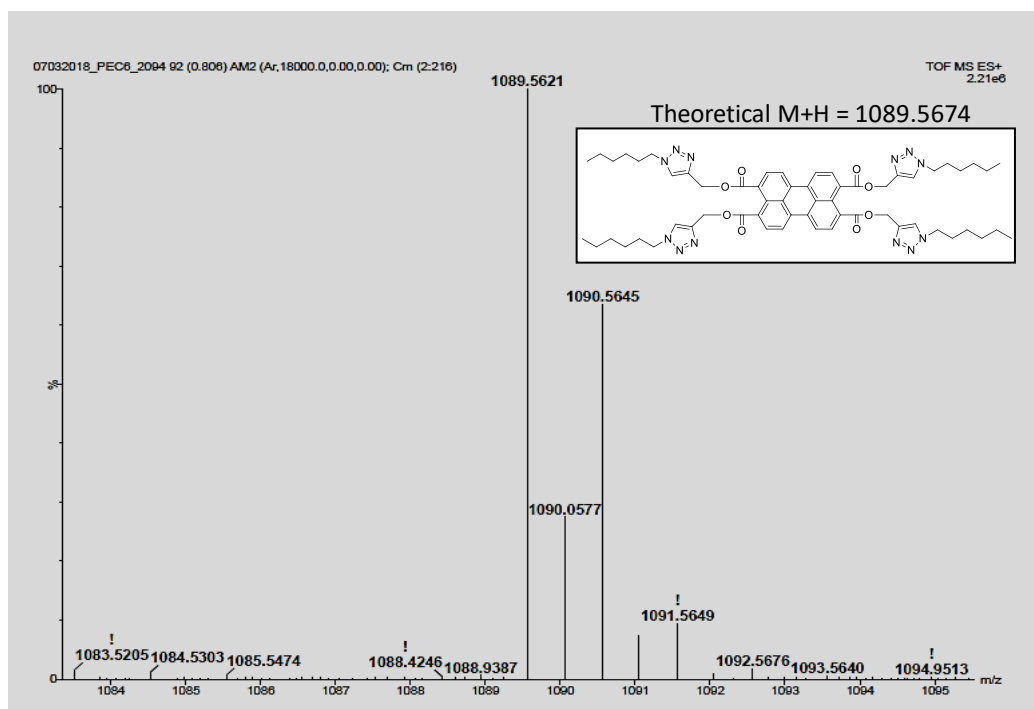
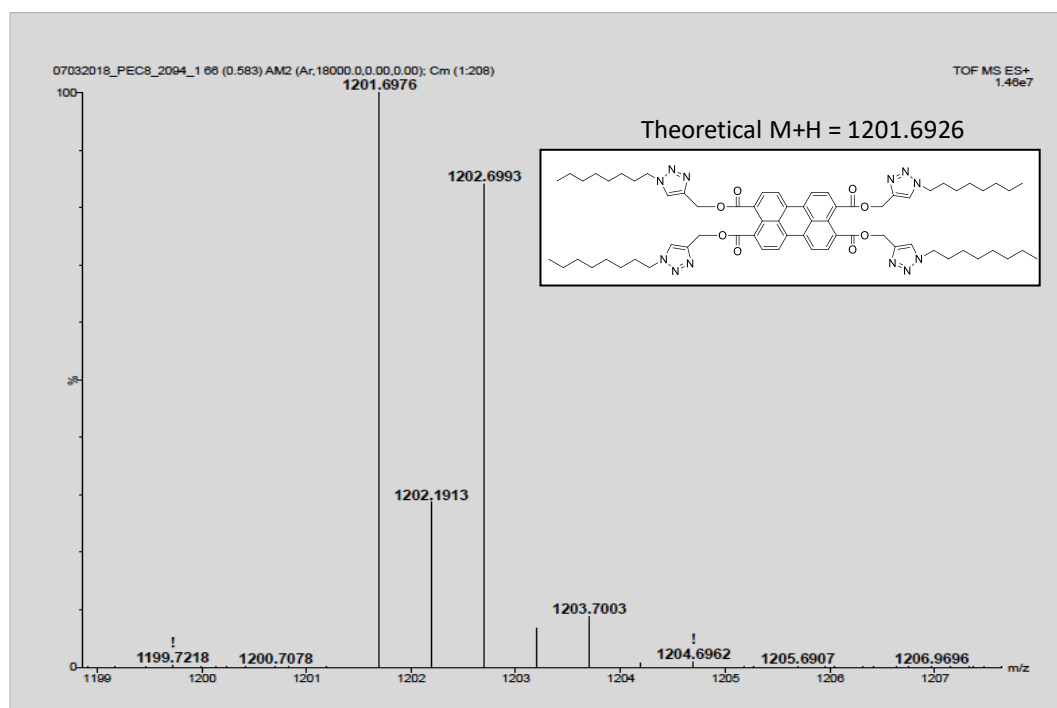
Figure A1. <sup>1</sup>H NMR spectrum of precursor 2.Figure A2. <sup>1</sup>H NMR spectrum of 3a.

Figure A3. <sup>13</sup>C NMR spectrum of 3a.Figure A4. <sup>1</sup>H NMR spectrum of 3b.

Figure A5.  $^{13}\text{C}$  NMR spectrum of **3b**.Figure A6.  $^1\text{H}$  NMR spectrum of **3c**.

Figure A7.  $^{13}\text{C}$  NMR spectrum of **3c**.Figure A8.  $^1\text{H}$  NMR spectrum of **3d**.

Figure A9. <sup>13</sup>C NMR spectrum of **3d**.Figure A10. HRMS spectrum of **3a**.

Figure A11. HRMS spectrum of **3b**.Figure A12. HRMS spectrum of **3c**.



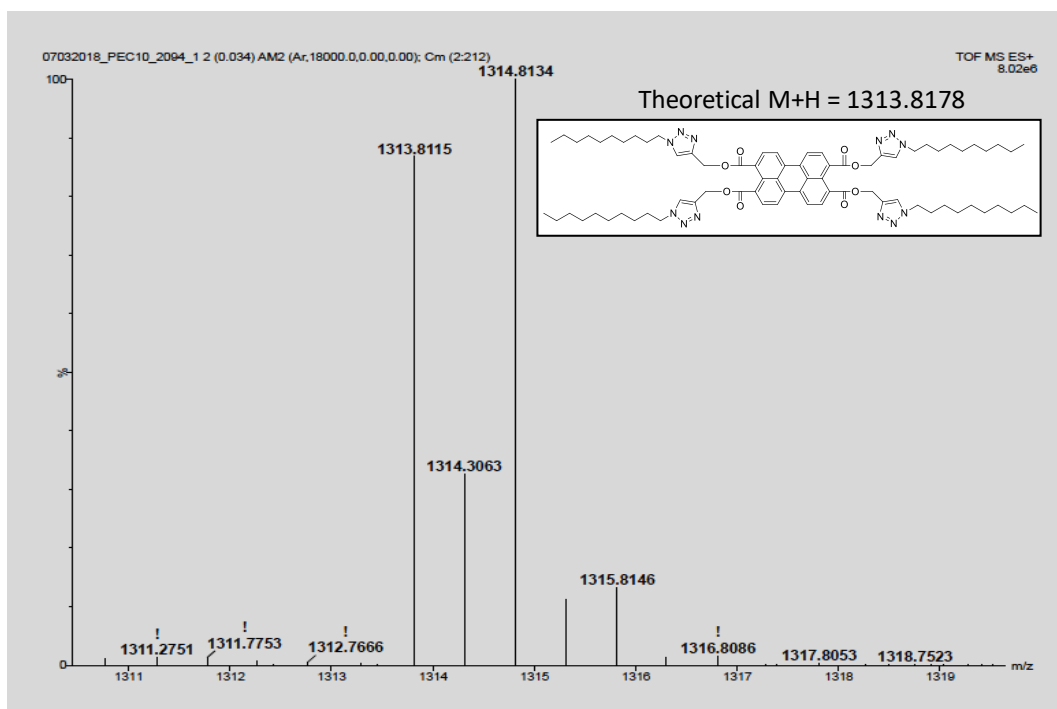


Figure A13. HRMS spectrum of **3d**.

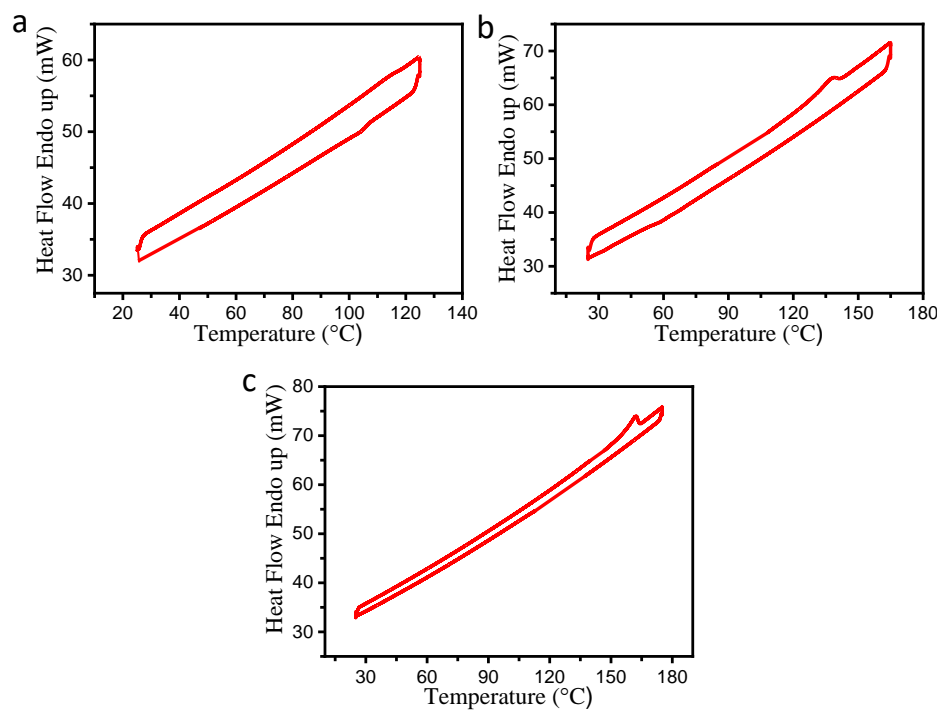
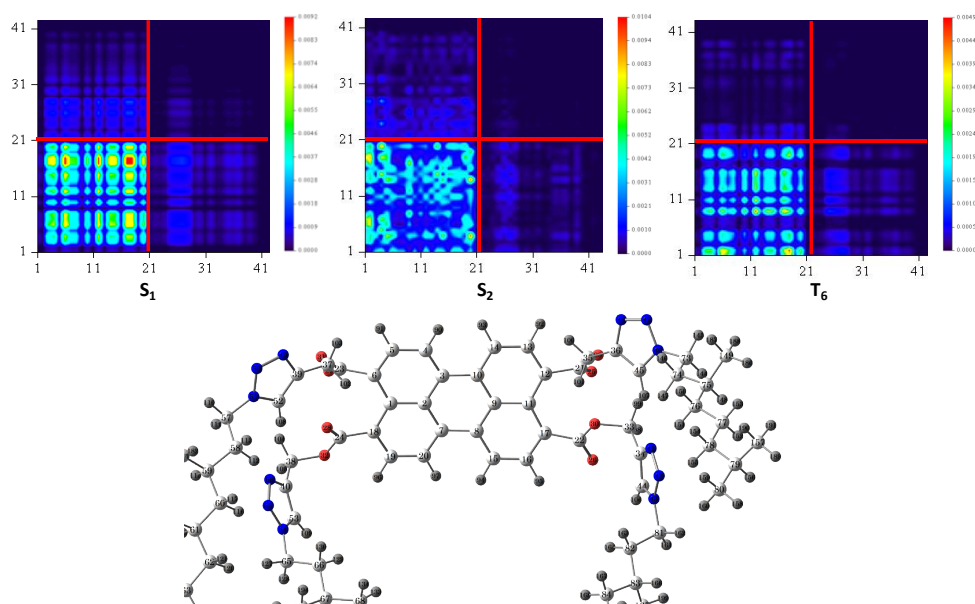


Figure A14. DSC thermogram of PTE derivatives: (a) **3a**; (b) **3c**; (d) **3d**, recorded with the scan rate of 10 °C/min.

**Table A1.** Thermal behaviour of PTE derivatives<sup>a</sup>.

Compound	Heating	Cooling
<b>3a</b>	Col <sub>ro</sub> 115.5 <sup>b</sup> (0.51) Iso	Iso 104.2 <sup>b</sup> (1.24) Col <sub>ro</sub> <sup>d</sup>
<b>3b</b>	Col <sub>ro</sub> 175 <sup>c</sup> Iso	Iso 169 <sup>c</sup> Col <sub>ro</sub> <sup>d</sup>
<b>3d</b>	Col <sub>ro</sub> 162.2 <sup>b</sup> (23.92) Iso	Iso 151 <sup>c</sup> Col <sub>ro</sub> <sup>d</sup>

<sup>a</sup>Enthalpy values in parentheses in kJ/mol. <sup>b</sup>Phase transition through DSC. <sup>c</sup>Phase transition through POM. <sup>d</sup>Columnar rectangular structure (Col<sub>ro</sub>): columnar rectangular morphology at lower temperatures (Col<sub>ro1</sub>) is different from that at higher temperatures (Col<sub>ro2</sub>) as observed from temperature-dependent XRD studies on cooling from the isotropic, however in DSC thermograms, no such transition (Col<sub>ro1</sub> to Col<sub>ro2</sub>) observed, might be due to small structural changes within the same lattice.



**Figure A15.** Transition density matrix (TDM) maps of S<sub>1</sub>, S<sub>2</sub> and T<sub>6</sub> states of compound **3a** along with chemical structure with atom numbers labeled on it. (Note: We did not show here the complete alkyl part as alkyl chains do not contribute to the TDM calculations).

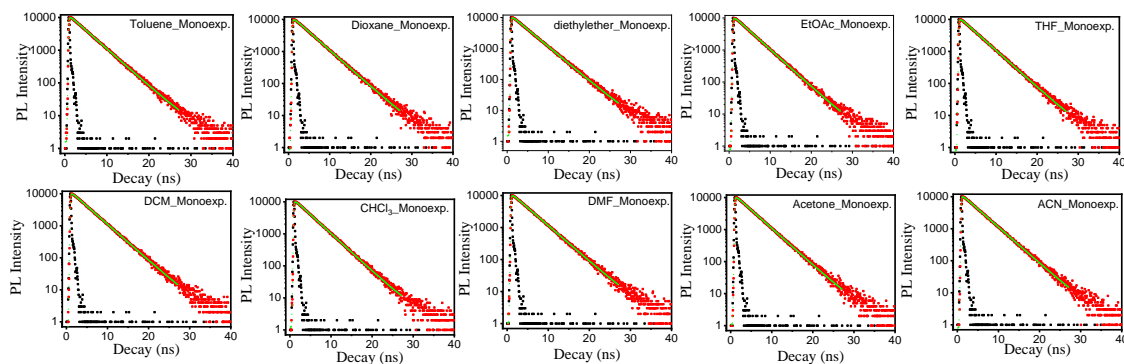


**Figure A16.** Fluorescence lifetime decay spectra of emitter **3a** in various organic solvents. Prompt IRF shown in Black colored squares; Experimental decay in Red-colored squares; Mono-exponential fit in green colored line.

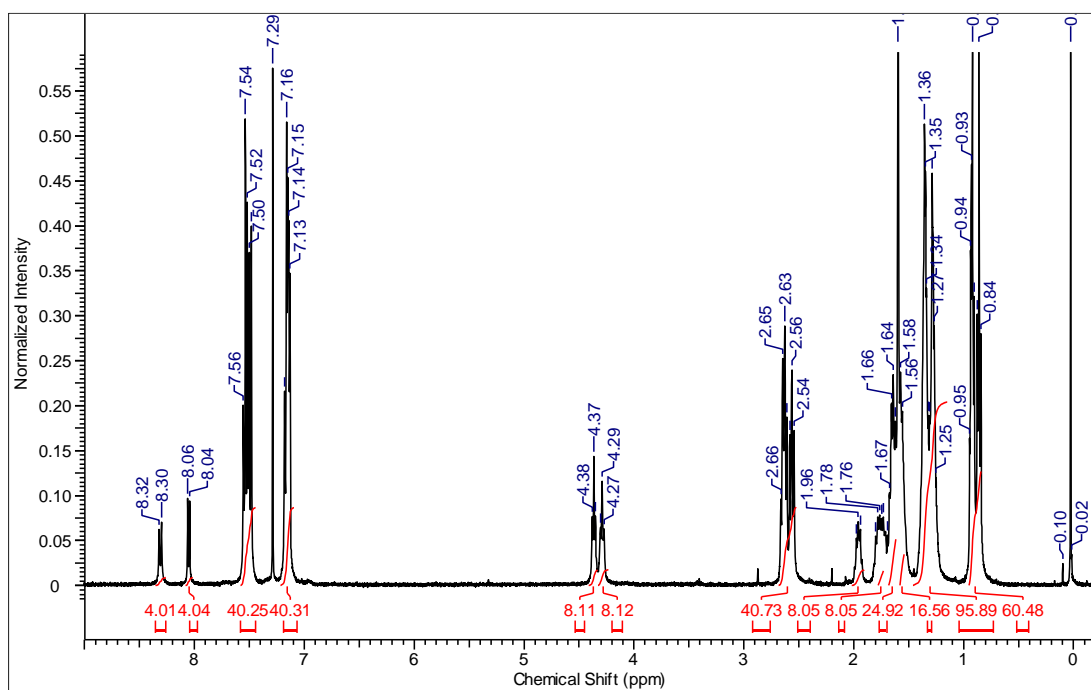


**Figure A17.**  $^1\text{H}$  NMR spectrum of compound **5a**.

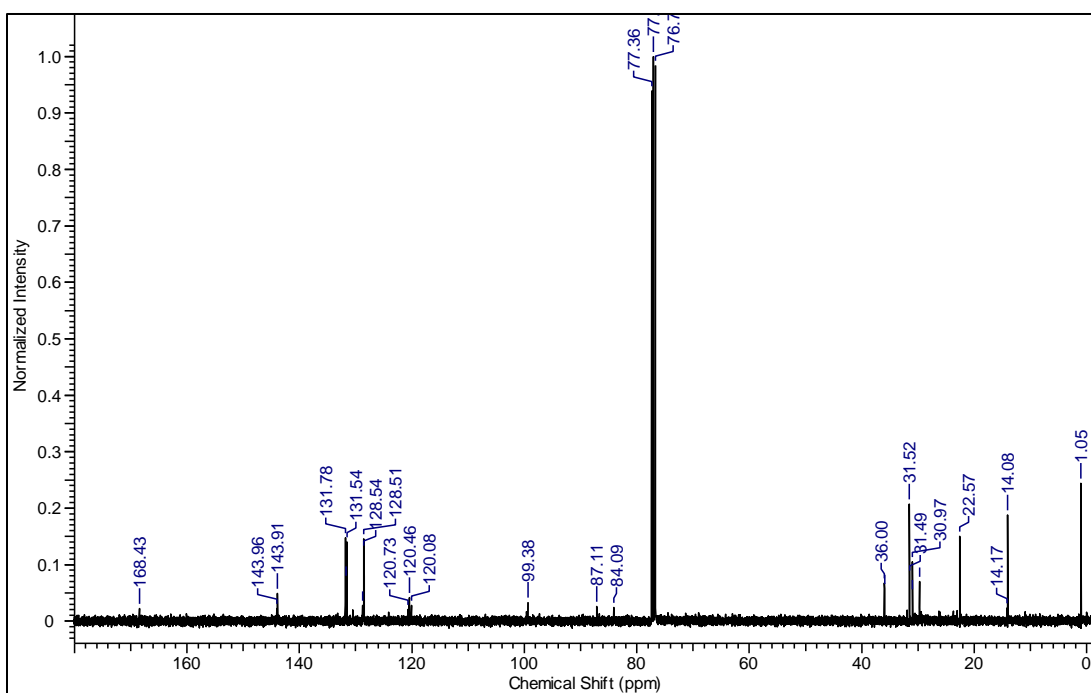


Figure A18. <sup>13</sup>C NMR spectrum of compound **5a**.

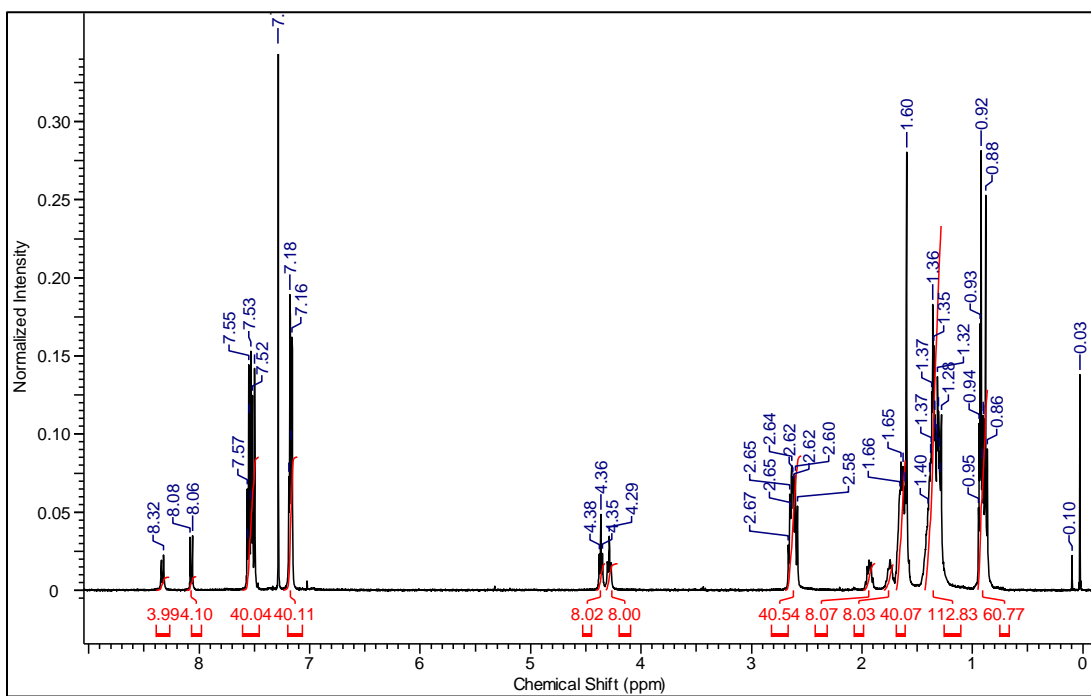


Figure A19. <sup>1</sup>H NMR spectrum of compound **5b**.

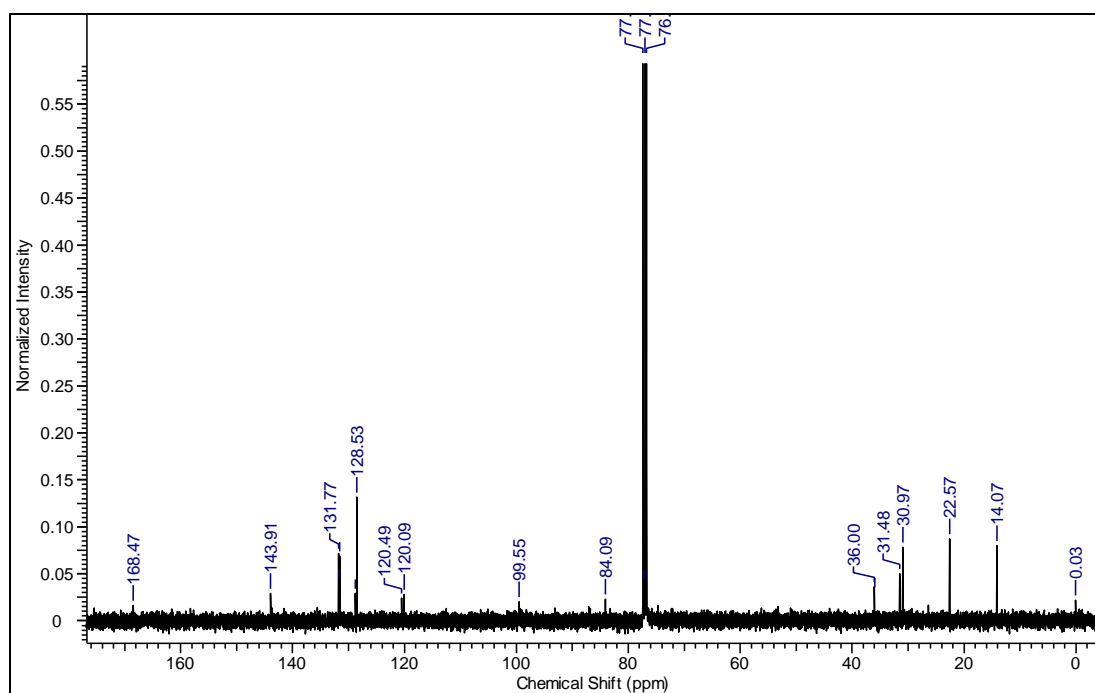


Figure A20. <sup>13</sup>C NMR spectrum of compound **5b**.

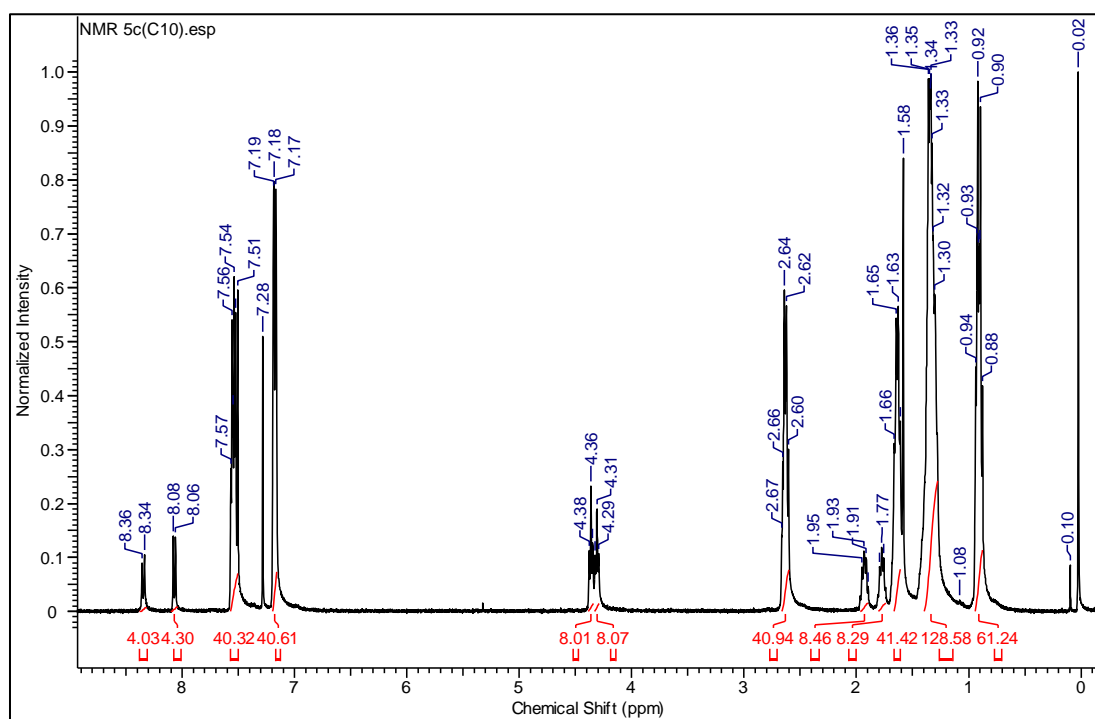
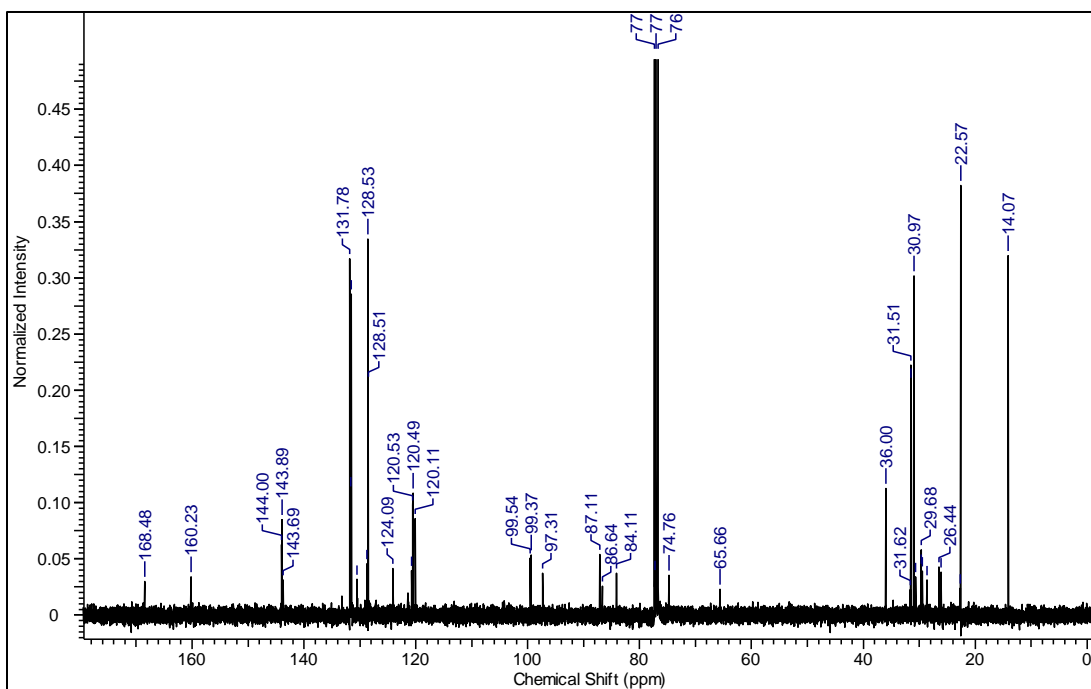
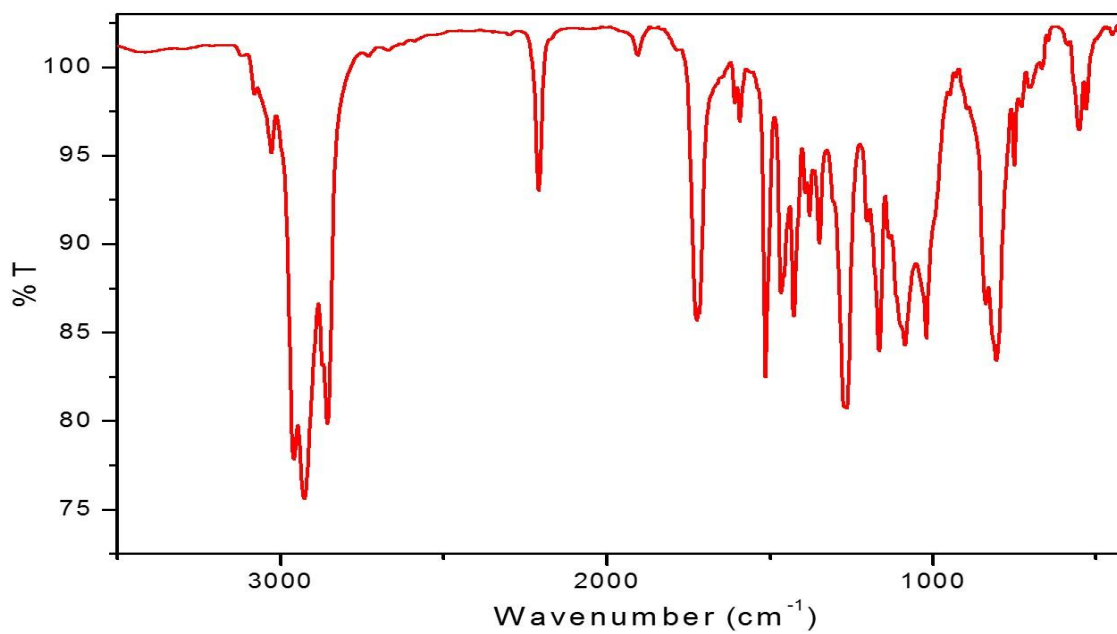


Figure A21. <sup>1</sup>H NMR spectrum of compound **5c**.



**Figure A22.** <sup>13</sup>C NMR spectrum of compound **5c**.



**Figure A23.** Representative FT-IR spectrum of compound **5a**.

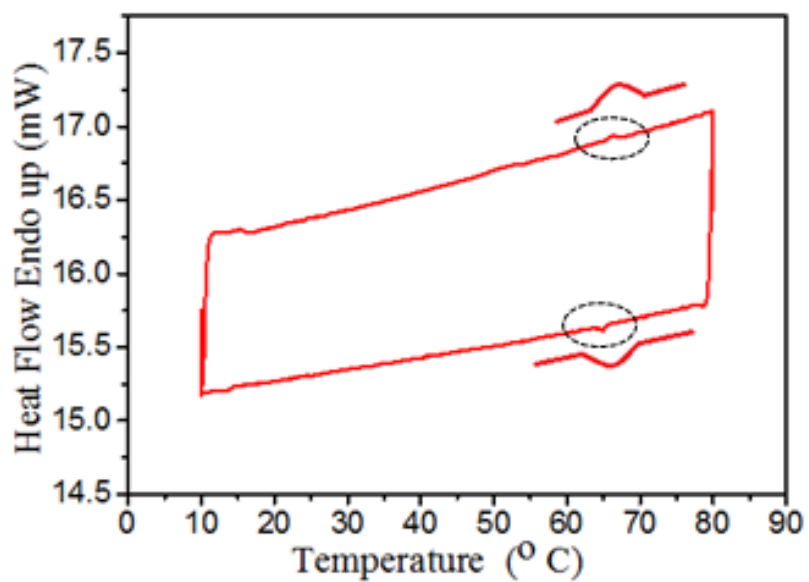


**Figure A24.** DSC curve of compound **5c** on heating and cooling (scan rate 10 °C/min).

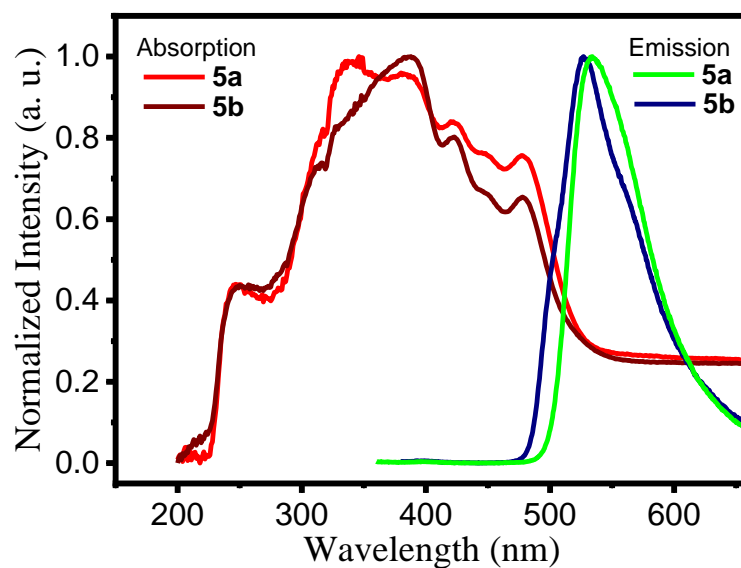


**Figure A25.** Solid-state absorption and emission spectra of compounds **5a** and **5b** in neat film prepared by the drop-cast method.

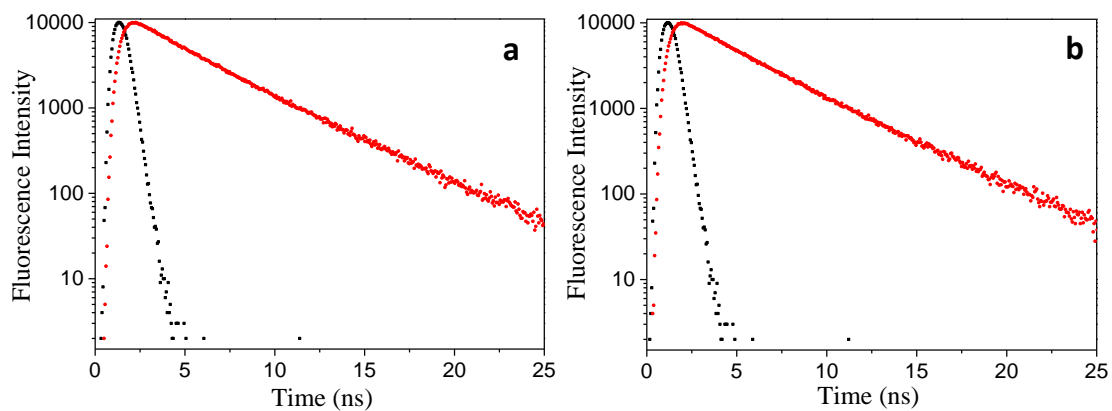


**Figure A26.** Fluorescence decay spectra of compounds (a) **5b** ( $\lambda_{\text{exc}} = 337 \text{ nm}$  &  $\lambda_{\text{ems}} = 487 \text{ nm}$ ); (b) **5c** ( $\lambda_{\text{exc}} = 337 \text{ nm}$  &  $\lambda_{\text{ems}} = 487 \text{ nm}$ ) in micromolar THF solution,  $\chi^2$  value = 1.01 for all the three decay spectra.

**Table A2** Quantum yield values of compound **5a-c**.<sup>a-c</sup>

	ms	mr	$Q_s^{a,b,c}$
<b>5a</b>	$20.4748 \times 10^7$	$13.937 \times 10^7$	0.89
<b>5b</b>	$19.420 \times 10^7$	$13.937 \times 10^7$	0.84
<b>5c</b>	$18.5944 \times 10^7$	$13.937 \times 10^7$	0.81

<sup>a</sup>Measured in THF. <sup>b</sup>Excited at absorption maxima. <sup>c</sup>Standard Quinine sulphate ( $Q_f = 0.54$ ) in 0.1 M  $\text{H}_2\text{SO}_4$ .



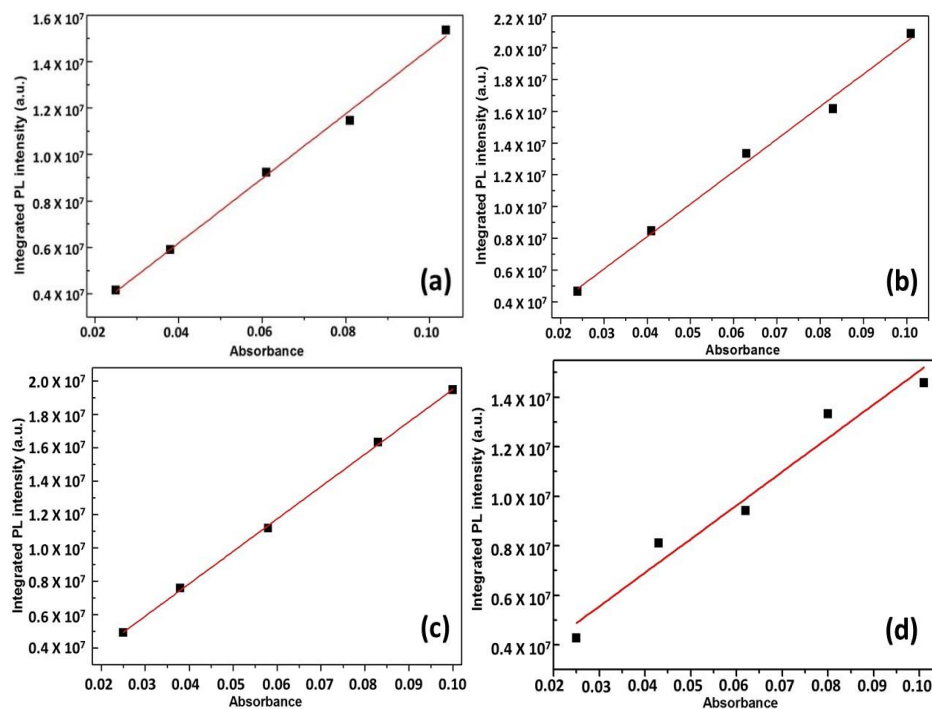


**Figure A27.** Plots of integrated photoluminescence intensity vs absorbance of quinone sulfate (0.1 M H<sub>2</sub>SO<sub>4</sub> solution) excited at 347 nm (a) **5a**; (b) **5b**; (c) **5c**; (d) **5d** excited at 337 nm.

**Table A3.** Electrochemical data for compounds **5a-c**.<sup>a</sup>

	$\lambda_{\text{max}}$ (nm)	$\Delta E_{\text{UV}}^{b,c}$	$E_{1\text{red}}^b$	$E_{1\text{oxd}}^d$	$E_{\text{HOMO}}^{b,e}$	$E_{\text{LUMO}}^{b,f}$	$\Delta E_{\text{g,CV}}^{b,c,g}$
<b>5a</b>	337	3.68	-1.65	0.97	-5.63	-2.50	3.13
<b>5b</b>	337	3.68	-1.65	1.02	-5.93	-2.45	3.48
<b>5c</b>	337	3.68	-1.65	0.94	-5.58	-2.51	3.07

<sup>a</sup>Experimental conditions: Ag/AgNO<sub>3</sub> as reference electrode, glassy carbon working electrode, platinum wire counter electrode, TBAH (0.1M) as a supporting electrolyte.

<sup>b</sup>Electron volts (eV). <sup>c</sup>Bandgap calculated from the absorption maxima ( $\Delta E_{\text{UV}} = 1240/\lambda_{\text{max}}$ ). <sup>d</sup>in volts (V). <sup>e</sup>Calculated by using formula  $E_{\text{HOMO}} = -(4.8 - E_{1/2, \text{Fc}/\text{Fc}^+} + E_{\text{oxd, onset}})$  eV. <sup>f</sup>Calculated by using formula  $E_{\text{LUMO}} = -(4.8 - E_{1/2, \text{Fc}/\text{Fc}^+} + E_{\text{red, onset}})$  eV. <sup>g</sup>Calculated by formula  $\Delta E_{\text{g,CV}} = E_{\text{LUMO}} - E_{\text{HOMO}}$ .

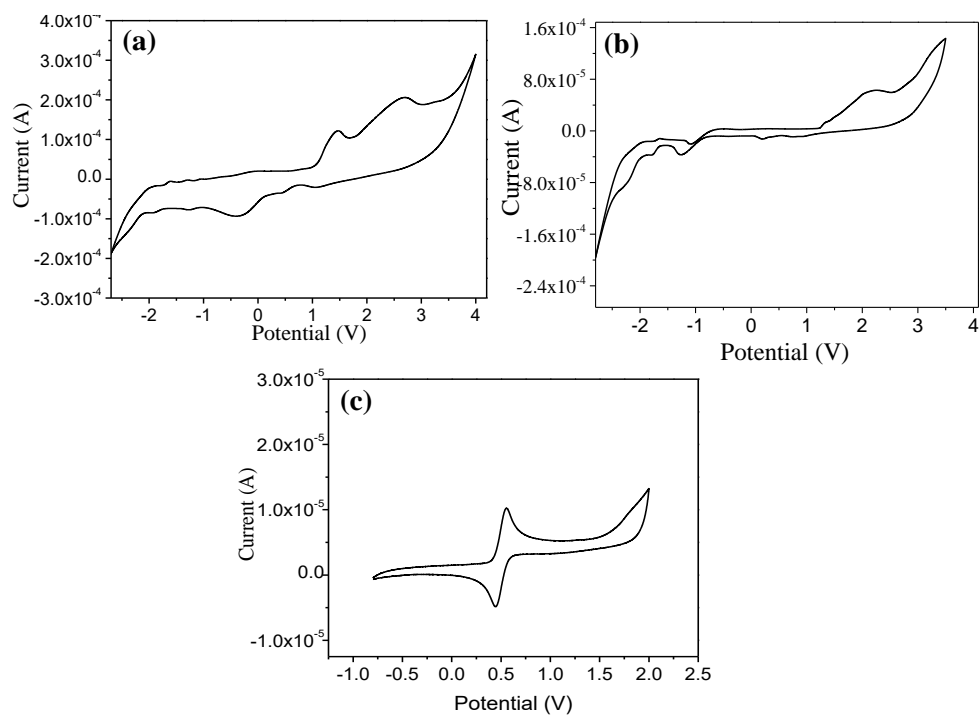


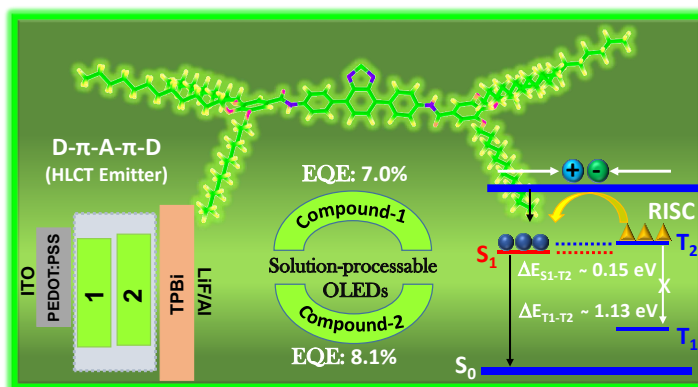
**Figure A28.** Cyclic Voltammograms of all compounds (a) **5b**; (b) **5c**; (c) ferrocene; in anhydrous dichloromethane solution of tetrabutylammoniumhexafluorophosphate (0.1 M) at a scanning rate of 100 mV/s.

## Chapter 6

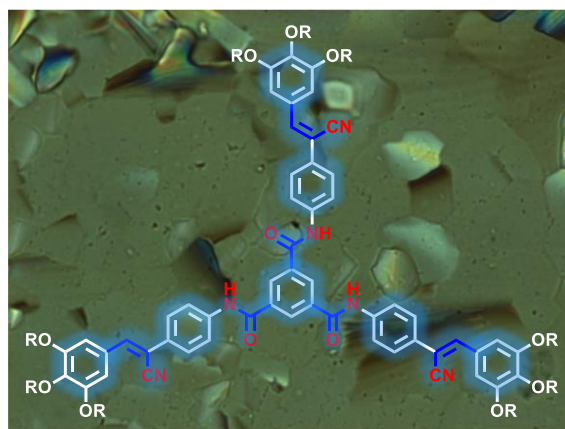
### Linear and Star-Shaped Donor-Acceptor Bridged Structures for (Opto)-Electronic Applications

**Part A:** Benzothiadiazole based donor-acceptor  $\pi$ -conjugated fluorescent molecules were employed in solution-processed green OLED devices that exquisite high external quantum efficiency. The observed high photoluminescence quantum yields corroborate the high exciton utilization efficiency values exceeding its traditional limit (25%), hence

suggesting the utilization of triplet excitons. Apart from the impressive electroluminescence properties of the emitters, the fluorophore was also studied as a chemosensor that showed the selective sensing of the metal cation ( $\text{Fe}^{2+}$ ) and anion ( $\text{I}^-$ ) along with the staining agent of *Hibiscus rosa-sinensis* pollen grains which could find potential applications in diagnostics.



**Part B:** Tricarboxamide-cyanostilbene based star-shaped discogens were synthesized for the realization of efficient semiconducting and emissive properties in the same molecule. The intramolecular H-bonding contributes to the formation of the columnar assembly that is likely to act as charge transport entity too. On the other hand, the promesogenic trialkoxy cyanostilbene fragment imparts the molecular structure with emissive as well as liquid crystalline behaviour. Synthesized derivatives exhibited room temperature columnar hexagonal behaviour over a wide mesomorphic range. When employed as emissive materials in OLEDs, sky-blue colored emission was observed and SCLC measurements revealed ambipolar charge transport with balanced hole and electron mobilities.





## 6.1 Part A: High performing D- $\pi$ -A- $\pi$ -D benzothiadiazole based hybrid local and charge transfer emitters in solution-processed OLEDs

### 6.1.1 Introduction

Organic metal complexes and polymeric systems are successful to surpass the exciton utilization efficiency (EUE) limit, however, high metal cost and batch-wise variations in polymers demand suitable alternatives for mass production. In metal-free fluorescent OLEDs, two well-studied mechanisms *viz.* thermally activated delayed fluorescence (TADF)<sup>1-9</sup> and hybrid local and charge transfer (HLCT) phenomena<sup>10-17</sup> are responsible for achieving greater than 25% EUE. Both processes involve the use of triplet excitons by way of reverse intersystem crossing (RISC) from T<sub>1</sub> to S<sub>1</sub> in case of TADF and T<sub>n</sub> (n > 1) to S<sub>n</sub> (n  $\geq$  1) in HLCT phenomena. Recently, donor-acceptor small  $\pi$ -conjugated organic molecules with HLCT characteristics have garnered significant attention as such type of molecules tactfully integrates the two complementary properties: high photoluminescence quantum yield ( $\eta_{PL}$ ) due to low-lying locally excited (LE) state and high EUE owing to high-lying charge transfer (CT) state and results into high external quantum efficiency (EQE) of the device.<sup>10,13,18</sup> In this context, benzothiadiazole (BTD) derivatives are the most suitable candidates with excellent fluorescence behaviour in solution and solid-state as well.<sup>19</sup> Besides, BTD framework act as a strong acceptor unit and is actively used to tune the energy levels for achieving low band-gap molecules suitable for various optoelectronic devices.<sup>20</sup> Furthermore, the structural modification with electron-donating groups results into a donor-acceptor system. Also, the donor-acceptor fluorophores composed of small organic molecules have a high degree of control on their optical and electronic features due to ease in structural variation.<sup>12,17,21-29</sup> As a result, luminescent BTD derivatives have found their potential use in a variety of applications e.g. as an emitter material in OLEDs,<sup>12,17,23-29</sup> chemosensors,<sup>30</sup> biological imaging,<sup>31</sup> liquid crystals<sup>32-34</sup>, and organic solar cells<sup>35</sup>. Majority of BTD derivatives are employed in photovoltaic applications<sup>35</sup> and emitter materials<sup>12,17,23-29</sup> in OLEDs. For example, Thomas and coworkers reported BTD based red<sup>26</sup> and green<sup>25</sup> emitters showing decent EQE values of 2.1% and 4.6% in OLED devices, respectively. Ma group reported several BTD based donor-

acceptor emitters with color varied from green<sup>12</sup> to orange<sup>17</sup> to deep red<sup>17</sup> in non-doped OLEDs which showed maximum EQEs of 6.95% to 3.80% to 2.80%, respectively. Despite such advancements, low-cost solution-processed BTD based highly efficient emitters are in high scarcity and need further developments. In this context, the present manuscript describes the utilization of BTD derivatives **1** and **2** (Figure 6.1, Scheme 6.1) as highly efficient fluorescent green emitter materials in solution-processable OLEDs with a high EQE of 7.0% in case of **1** and 8.1% for **2** in doped OLEDs. The breakthrough of the traditional EQE limit of fluorescent OLEDs (i.e. 5%) has been explained by the HLCT mechanism. High  $\eta_{\text{PL}}$  and high EUE obtained in the reported BTD emitters are contributing to the high EQE values of the OLED devices. RISC from  $T_2$  to  $S_1$  state *via* “hot exciton” channel is believed to be responsible for the large fraction of the radiative singlet excitons. In addition, the selective chemosensing of ions and staining of pollen grains ability of BTD derivative **1** is also investigated.

### 6.1.2 Objectives

The formation of BTD based D- $\pi$ -A- $\pi$ -D fluorescent molecules was motivated by three goals. Firstly, the BTD electron-acceptor core can be easily substituted at 4,7 positions and can be tuned towards the development of low-cost solution-processed BTD based highly efficient emitters. For that, donor 3,4,5 trialkoxy phenyl groups were substituted at the terminal positions on both sides giving rise to D- $\pi$ -A- $\pi$ -D molecular architecture beneficial to high luminescence efficiency. Secondly, the amide functionality has been used to connect the donor

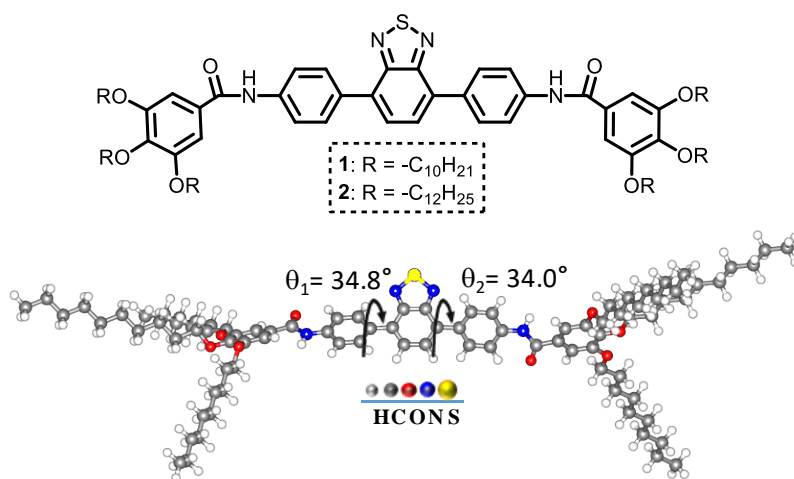


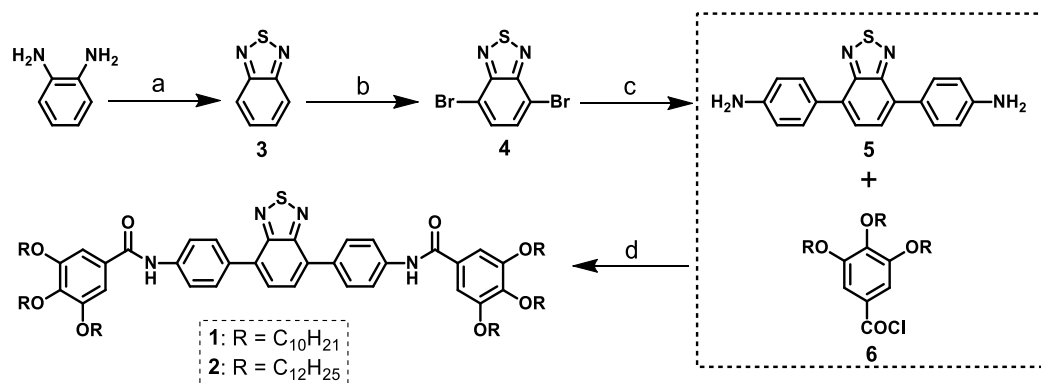
**Figure 6.1** Molecular design and energy minimized structure (for **1**) of BTD derivatives.

and acceptor groups that can coordinate to various metal cations and anions, resulting in the functioning as chemosensor. Thirdly, in continuation to these, the highly luminescent BTD derivatives can be also be used for the staining of various bio-molecules. With these diverse applications, BTD based luminescent molecules are multifunctional and provide an important step forward to expand the applications of small  $\pi$ -conjugated luminescent molecules.

## 6.1.3 Results and discussions

### 6.1.3.1 Synthesis and characterization

The synthesis of BTD derivatives is shown in Scheme 6.1. 4,7-bis[4-(diphenylamino)phenyl]-2,1,3-benzothiadiazole **5** was obtained in three steps as per the reported procedure.<sup>36,37</sup> The first step involves the formation of benzo[c][1,2,5]thiadiazole **3** by treating benzene-1,2-diamine with  $\text{NEt}_3$  and  $\text{SOCl}_2$  in dichloromethane.<sup>37</sup> In the second step, the bromination of **3** gives rise to the synthesis of 4,7-dibromo substituted thiadiazole compound **4**.<sup>37</sup> The Suzuki coupling of **4** with 4-(N-Boc-amino)phenylboronic acid leads to the formation of Boc-protected aminophenyl-substituted BTD derivative which on deprotection in acidic medium forms aminophenyl-BTD derivative **5**.<sup>36</sup> On the other hand, tri-alkoxy benzoyl chloride **6** was synthesized by following the earlier reported procedures.<sup>36,37</sup> Finally, the target compounds **1** & **2** were simply afforded by condensation of trialkoxy benzoyl chloride **6** (1 equiv.) with 4,7-bis[4-(diphenylamino)phenyl]-2,1,3-benzothiadiazole **5** (2 equiv.) in dry THF using  $\text{Et}_3\text{N}$  as



**Scheme 6.1** (a)  $\text{SOCl}_2$ ,  $\text{Et}_3\text{N}$ , DCM, RT; (b)  $\text{Br}_2$ ,  $\text{HBr}$ , 12h, 120 °C; (c) i. 4-(N-Boc-amino)phenylboronic acid,  $\text{Pd}(\text{PPh}_3)_4$ ,  $\text{Na}_2\text{CO}_3$ , aq. DME ii.  $\text{CF}_3\text{COOH}$ ,  $\text{CH}_2\text{Cl}_2$ ; (d)  $\text{Et}_3\text{N}$ , THF, RT, 12h. Yield: **1**: 62%; **2**: 73%.

a base to form amide linked BTD derivatives **1** ( $R = -C_{10}H_{21}$ ) and **2** ( $R = -C_{12}H_{25}$ ). Both the derivatives differ only in the length of alkoxy chains and are characterized by  $^1H$  NMR,  $^{13}C$  NMR (Figure A1-A6, Appendix VI, Page 379), FT-IR and mass spectroscopy.

### 6.1.3.2 Photophysical studies

The absorption and emission behaviour of the derivatives were checked in solution state (in THF,  $10^{-5}$  M) and in neat films obtained by drop-casting the  $\mu M$  solutions onto the quartz plates (Figure 6.2a,b, Table 6.1 and Figure A7, Appendix VI, Page 382). Both the derivatives exhibited similar behaviour in the solution state due to the presence of a similar chromophoric BTD unit. Mainly two peaks were observed in the absorption spectra which were at 307 nm and 410 nm for **1** while at 307 nm and 421 nm for **2**. The peaks at lower wavelength 307 nm arise due to  $\pi-\pi^*$  transition while the band at longer wavelength 410/421 nm (for **1/2**) is likely to be occurred because of CT transition from electron-donating moiety to the electron-deficient chromophore. In the simulated/experimental UV-vis spectrum, the observed intense band at 265/307 nm corresponds to the  $S_0-S_4$  excited states (Figure 6.2c) and related to  $\pi-\pi^*$  transition, as can be predicted from the corresponding natural transition orbitals (NTOs) (Table 6.3). On the other hand, the band at 388/421 nm appeared due to the  $S_0-S_1$  transition and consists of a CT component. Emission peaks at 549 nm for **1** and 547 nm for **2** were observed in the solution state, suggesting a green-colored emission, as can be seen from the insets of Figure A7a (Appendix VI, page 382) and Figure 6.2a, respectively.

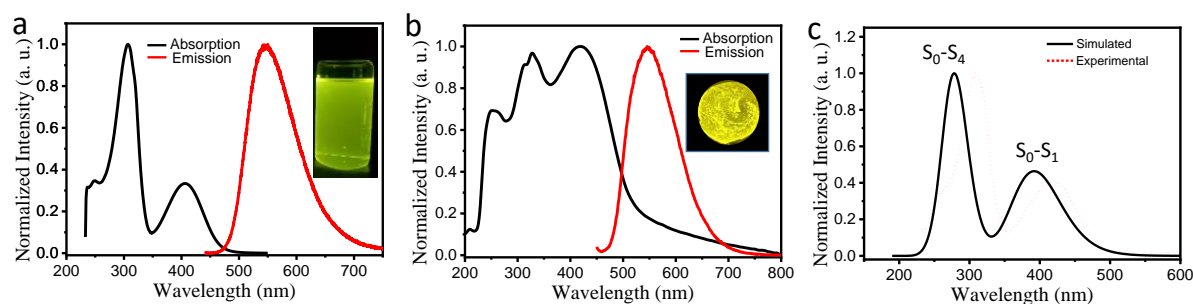


**Figure 6.2** Absorption and Emission spectra of compound **2**: (a) in solution state (THF,  $10^{-5}$  M); (b) thin-film state. Inset images presented the green and yellow colored luminescence showed by **2** under 365 nm UV light. (c) TD-DFT simulated (black solid line) (no. of states considered = 40) and experimental (red dotted line) UV-vis absorption spectra of compound **2** in THF solvent.



**Table 6.1** Photophysical and electrochemical data of the BTB derivatives **1** and **2**.

C	$\lambda_{\text{abs}}$ (nm) <sup>a</sup>	$\lambda_{\text{ems}}$ (nm) <sup>b</sup>	$\lambda_{\text{abs}}$ (nm) <sup>c</sup>	$\lambda_{\text{ems}}$ (nm) <sup>d</sup>	E <sub>HOMO</sub> (eV) <sup>e</sup>	E <sub>LUMO</sub> (eV) <sup>e</sup>	$\Delta E_{\text{CV}}$ (eV) <sup>f</sup>
<b>1</b>	249, 307, 410	549	261, 351, 431	561	-5.39	-3.56	1.83
<b>2</b>	249, 307, 421	547	256, 313, 327, 419	546	-5.38	-3.44	1.94

<sup>a</sup>Absorption peaks in solution state; <sup>b</sup>Emission peaks in solution state; <sup>c</sup>Absorption peaks in thin-film state; <sup>d</sup>Emission peaks in the thin-film state; <sup>e</sup>energy levels calculated from cyclic voltammetry (see experimental section); <sup>f</sup>band-gap calculated by using  $\Delta E_{\text{CV}} = E_{\text{LUMO}} - E_{\text{HOMO}}$ . Abbreviation: C-compound.

In case of compound **1** in the thin-film state, the shift was not prominent (only 12 nm) and the emission peak was slightly redshifted to 561 nm. On the other hand, in the case of **2**, the emission peak almost remained unchanged from the solution state (547 nm) to the thin-film state (546 nm). The insignificant red-shift in the case of **1** and negligible shift in **2** indicate the twisted structure of the molecules, as can also be seen from the optimized geometry of the representative compound **1**, where the two phenyl rings surrounded the BTB moiety are twisted by an angle of 34.81 and 34.01 with respect to the BTB unit (Figure 6.1).

For a better understanding of the intramolecular CT features of the BTB derivatives, solvatochromic experiments were carried out for compound **2**. The absorption (Figure 6.3a) and emission (Figure 6.3b) spectra were recorded in different solvents (0.08 mM) varying from nonpolar to polar solvents. From the non-polar hexane to polar DMF, a red-shift of 46 nm was observed in the emission peaks (Table 6.2). The red-shifts in the emission peaks indicate the CT behaviour of the excited states.<sup>23</sup> Furthermore, the quantification of the impact of solvent polarity on the nature of the excited states was carried out using the Lippert–Mataga relationship (Figure 6.3d).<sup>38</sup> The Lippert–Mataga plot provides information about the change in the dipole moment of the emissive state, S<sub>1</sub>, by relating the Stokes shift ( $\nu_a - \nu_f$ ) to the solvent polarity. The plot of Stokes shift versus orientational polarizability showed two slopes having a linear correlation in the low- and high-polarity regimes, indicating the change in the dipole moment of the S<sub>1</sub> state. We inferred that the increase in the CT character on increasing the solvent polarity suggests the presence of LE in low-polarity solvents and CT states in higher-

polarity solvents. Also, the fluorescence intensity was observed to be the highest in nonpolar solvents demonstrating the presence of LE states, while the decline in higher polar solvents is due to the predominant CT character (Figure 6.3c). The ground state dipole moment was estimated to be 1.81 D with the help of DFT at the B3LYP/6-31G(d,p) level.

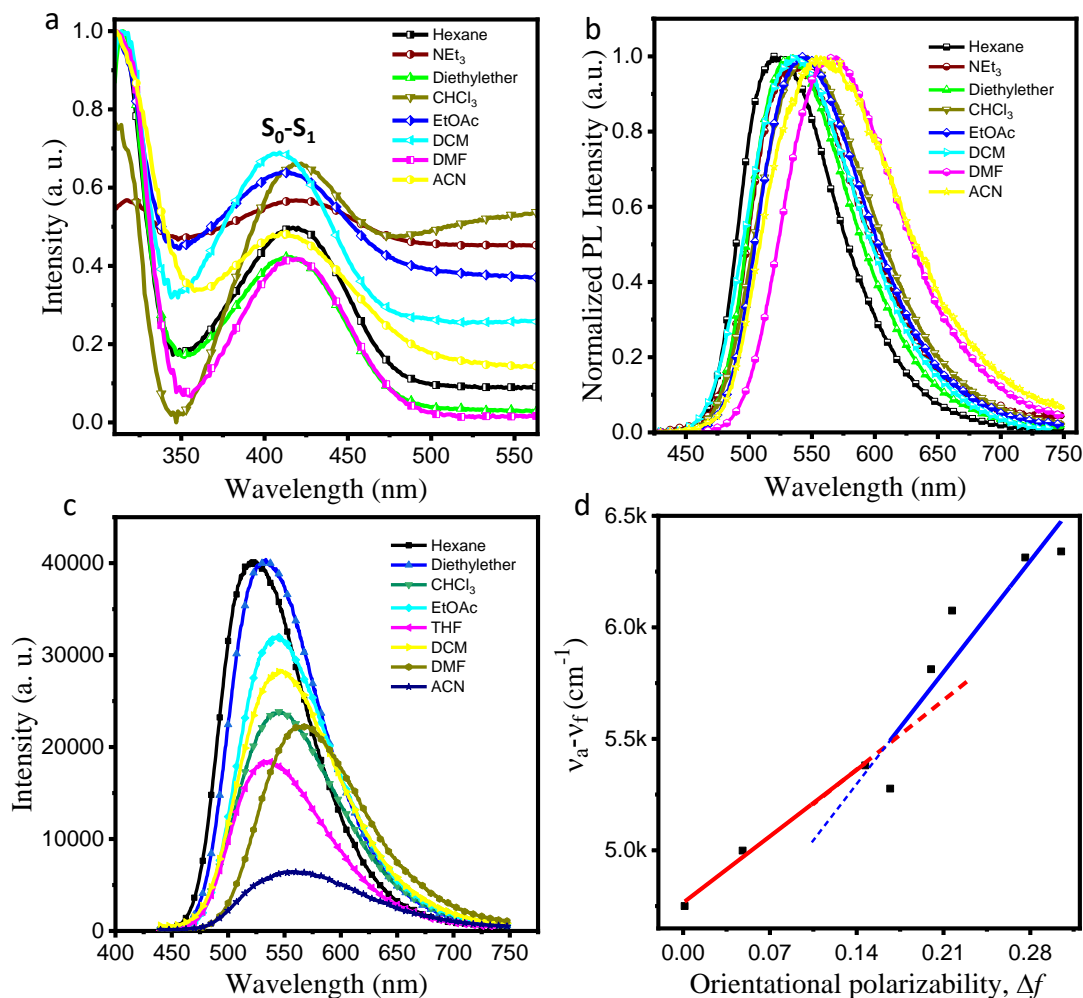


**Figure 6.3** Solvent-dependent (a) absorption and (b) emission studies of compound **2** (0.08 mM). (c) Solvent-dependent fluorescence spectra of compound **2** in different solvents. (d) Linear correlation of orientational polarization,  $\Delta f$  of solvent medium with the Stokes' shift ( $\nu_a - \nu_f$ ) for compound **2**.

Further, the calculated excited state dipole moment was found to be 14.34 D in low-polarity solvents and 18.90 D in high-polarity solvents, also supporting the coexistence of two types of states, i.e. weak CT (i.e. LE) and strong CT states. In the solvents of intermediate polarity, one

‘hybridized state’ is expected, known as the HLCT state, which is favourable for the good emission properties of the fluorophore.

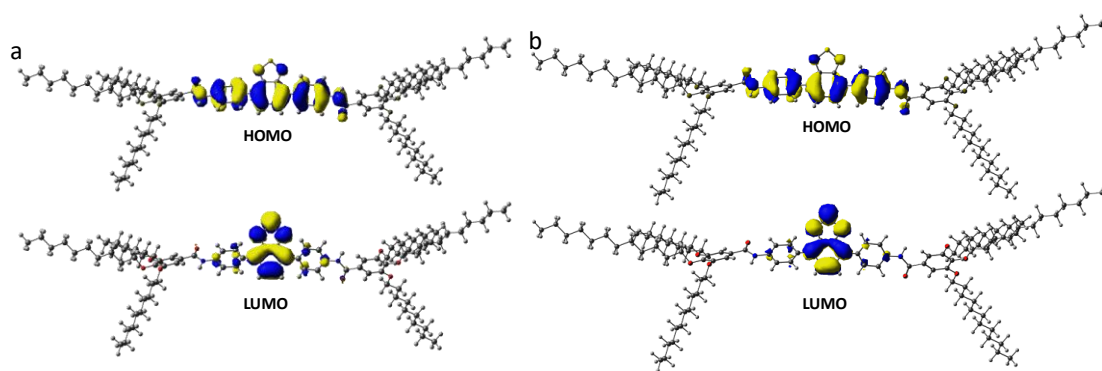
**Table 6.2** Solvatochromic absorption and emission data for Lippert-Mataga model.<sup>38</sup>

Compound <b>1</b>				
Solvents	$\Delta f^a$	$\lambda_{\text{abs}}$ (nm) <sup>b</sup>	$\lambda_{\text{em}}$ (nm) <sup>c</sup>	$\nu_a-\nu_f$ (cm <sup>-1</sup> ) <sup>d</sup>
Hexane	0.0012	417	520	4750
Triethylamine (NEt <sub>3</sub> )	0.048	419	530	4999
Chloroform (CHCl <sub>3</sub> )	0.147	422	546	5381
Diethyl ether	0.167	416	542	5277
Ethyl acetate (EtOAc)	0.200	411	540	5812
Dichloromethane (DCM)	0.217	410	536	6075
Dimethylformamide (DMF)	0.276	417	566	6313
Acetonitrile (ACN)	0.305	410	554	6340

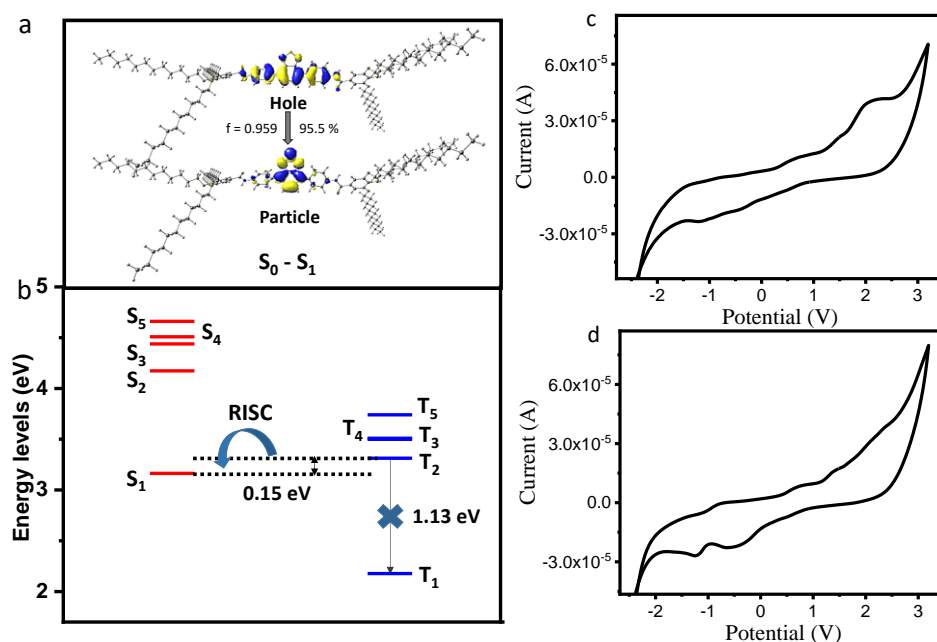
<sup>a</sup>Oriental polarizability of the solvent. <sup>b</sup> $\lambda_{\text{abs}}$  = absorption maximum. <sup>c</sup> $\lambda_{\text{em}}$  = emission maximum. <sup>d</sup> $\nu_a-\nu_f$  = the Stokes shift.

### 6.1.3.3 Theoretical and electrochemical studies

To further explore the electronic properties of the compounds, geometry optimization in the ground state and frontier molecular orbital calculations were done by DFT using B3LYP/6-31G (d,p) basis set. As displayed in Figure 6.4 for both the compounds, the HOMOs of the BTD derivatives are localized on the electron-donor horizontal backbone (composed of three benzene rings) of the molecules. The LUMOs are located on the central electron-deficient BTD moiety and slightly extended to the neighboring benzene rings. Such type of orbital features including spatial separation in conjunction with slight overlap generally results in the orbital coupling and charge transfer features in the molecule. This adequate bipolar nature is beneficial to the better charge transport and high photoluminescence (PL) efficiency of the materials when employed as an emitter component in an OLED device.<sup>12,25</sup> The DFT analysis revealed that the phenyl rings adjacent to the BTD moiety are at an angle of 34.8° and 34.0° (Figure 6.1). This intramolecular twist in the molecular orbitals is favourable for the occurrence of LE



**Figure 6.4** Frontier molecular orbitals of compounds (a) **1** and (b) **2** as obtained by DFT method at B3LYP/6-31G (d,p) level.

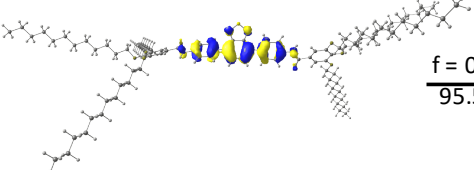
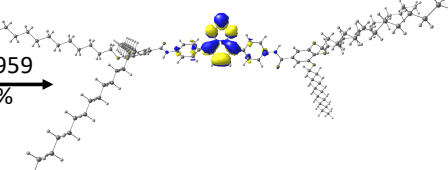
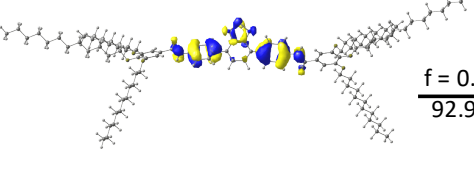
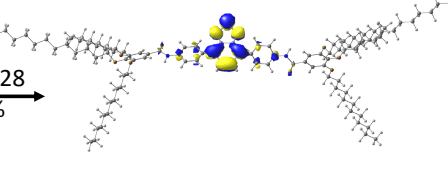
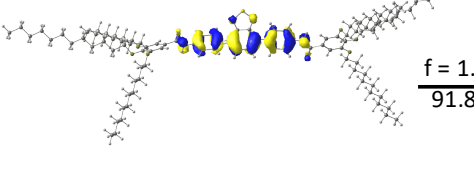
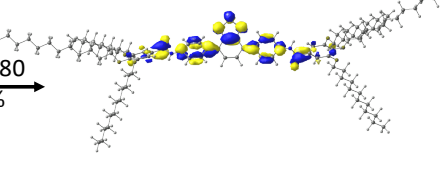
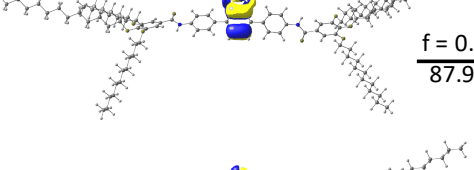
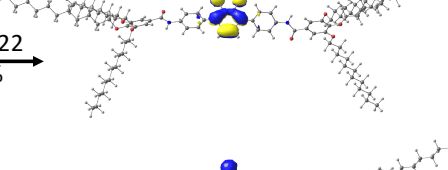
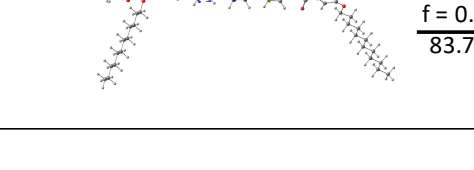
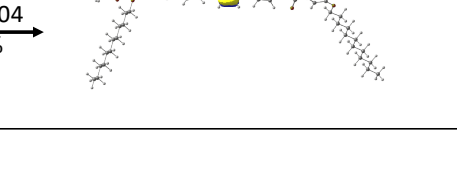


**Figure 6.5** (a) Natural transition orbitals (isosurface 0.02 a. u.) for  $S_0 \rightarrow S_1$  excitation calculated for compound **2** (' $f$ ' represents oscillator strength). (b) Singlet and triplet excited energy states demonstrating reverse intersystem crossing (RISC) from  $T_2$  to  $S_1$  state. Cyclic voltammogram of compounds (c) **1** and (d) **2** in HPLC dichloromethane solution of tetrabutylammonium hexafluorophosphate (0.1 M) performed at a scanning rate  $50 \text{ mVs}^{-1}$ .

and CT states in the molecules.<sup>10-17</sup> Additionally, twisted molecular geometry in combination with the rigid chromophores overcome the detrimental  $\pi$ - $\pi$  stacking interactions in the solid-state, which usually leads to aggregation-caused fluorescence quenching, while simultaneously allowing the adequate  $\pi$ -interaction necessary for the better charge hopping when used in devices.<sup>25,39</sup>

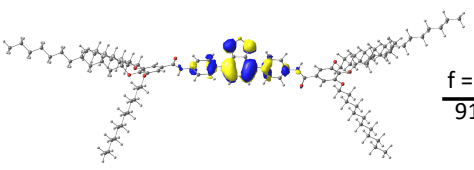
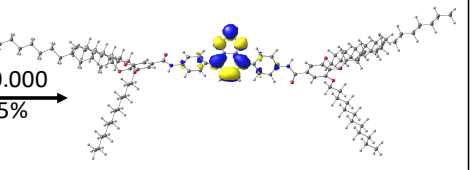
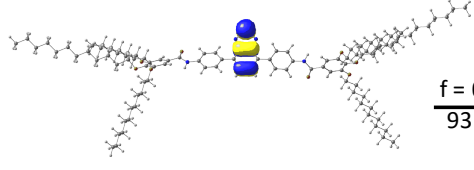
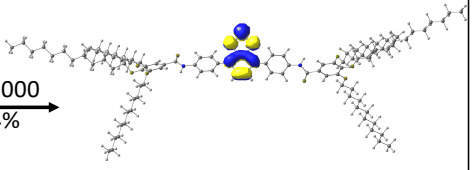
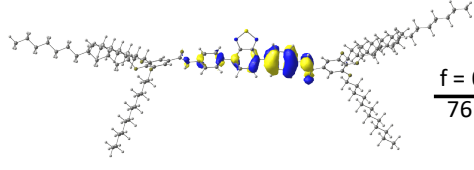
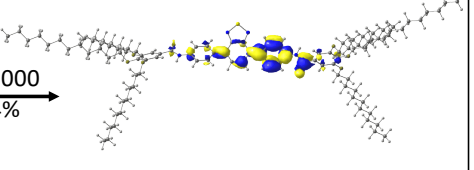
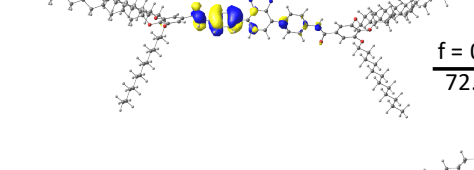
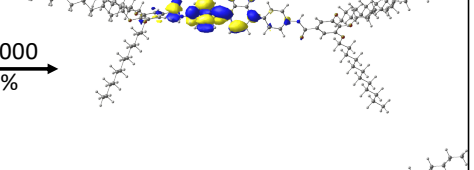
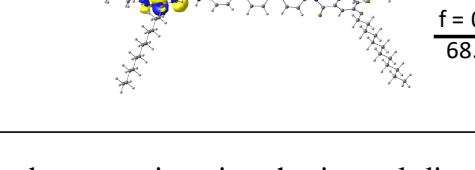
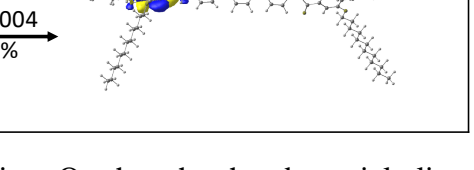
In order to understand the properties of excited states, TD-DFT and natural transition orbitals (NTO) in case of **2** were evaluated (Figure 6.5, Table 6.3 and 6.4).<sup>10-17</sup>

**Table 6.3** Calculated natural transition orbitals (NTO) of first five singlet excited states.

Excited states (energies)	"Hole"	"Particle"
$S_1$ (3.16 eV)		 $f = 0.959$ 95.5%
$S_2$ (4.17 eV)		 $f = 0.028$ 92.9%
$S_3$ (4.44 eV)		 $f = 1.780$ 91.8%
$S_4$ (4.51 eV)		 $f = 0.222$ 87.9%
$S_5$ (4.66 eV)		 $f = 0.004$ 83.7%

The calculated energy levels of the first five singlet and triplet states are plotted in Figure 6.5b. The small energy gap of 0.15 eV was found between singlet  $S_1$  and triplet  $T_2$  state ( $\Delta E_{S_1/T_2}$ ) while the  $T_2$  to  $T_1$  energy gap ( $\Delta E_{T_2/T_1}$ ) of ca. 1.13 eV was large enough which will not allow triplet excitons to decay to  $T_1$  state. Therefore, the triplet excitons in  $T_2$  state can easily undergo a spin-flip transition to singlet  $S_1$  state. The 'hole' of the singlet state is mainly located on the

**Table 6.4** Calculated natural transition orbitals (NTO) of first five triplet excited states.

Excited states (energies)	"Hole"	"Particle"
T <sub>1</sub> (2.18 eV)		
	$f = 0.000$ 91.5%	
T <sub>2</sub> (3.31 eV)		
	$f = 0.000$ 93.4%	
T <sub>3</sub> (3.50 eV)		
	$f = 0.000$ 76.4%	
T <sub>4</sub> (3.51 eV)		
	$f = 0.000$ 72.5%	
T <sub>5</sub> (3.74 eV)		
	$f = 0.004$ 68.4%	

three consecutive benzene rings in a horizontal direction. On the other hand, particle lies on the electron-deficient 2,1,3 BTB group and slightly on the adjacent phenyl rings. This spatial distribution of hole and particle along with the partial overlap indicates the HLCT nature of S<sub>1</sub> excited state. As a result of small  $\Delta E_{S_1/T_2}$  and large  $\Delta E_{T_2/T_1}$  gap along with the HLCT nature of the S<sub>1</sub> state makes the RISC process highly favourable *via* hot exciton channel. Therefore, the use of triplet excitons in addition to singlet excitons in these BTB based emitters becomes highly favourable by HLCT phenomena when used in OLED devices. The electrochemical characterization of the BTB derivatives provided insight into the redox behaviour of the electroactive compounds. The oxidation and reduction onsets in the cyclic voltammogram were employed to calculate the HOMO and LUMO energy levels (Figure 6.5c,d). For **1/2**

calculated HOMO levels are -5.39/-5.38 eV and LUMO levels are -3.56/-3.44 eV (Table 6.1). The low-lying LUMO and high-lying HOMO of the molecules indicate the ambipolar charge transport nature<sup>40</sup> of the BTD derivatives.

#### 6.1.3.4 Sensing and bio-imaging studies

The highly emissive green colored luminescence of BTD derivative **1** was checked for its sensing ability towards metal cations and anions. The BTD derivatives upon excitation at 407 nm showed an emission band at 537 nm (in THF:H<sub>2</sub>O, 90:10 (v/v), H<sub>2</sub>O: 1mM tris-buffered saline (TBS), pH = 7.4) and displayed green fluorescence in the solution state. Thereby, the sensing ability of **1** towards various metal ions and anions was investigated by monitoring the change in fluorescence intensity upon the addition of various ions in  $5 \times 10^{-6}$  M parent solution (THF:H<sub>2</sub>O, 90:10 (v/v), H<sub>2</sub>O: 1mM tris-buffered saline (TBS), pH = 7.4). No change in the fluorescence intensity was observed on the addition of various metal ions tested (Co<sup>2+</sup>, Zn<sup>2+</sup>, Al<sup>3+</sup>, Pb<sup>2+</sup>, Mn<sup>2+</sup>, Cd<sup>2+</sup>, Cu<sup>2+</sup>, Fe<sup>2+</sup> and Ni<sup>2+</sup>) except Fe<sup>2+</sup> (Figure 6.6a). On the addition of 78  $\mu$ M of Fe<sup>2+</sup> into the parent solution of **1**, fluorescence intensity gets quenched (Figure 6.6b). Quenching of fluorescence intensity in the presence of Fe<sup>2+</sup> is may be due to the complex formation of **1** with Fe<sup>2+</sup>. As shown in the inset of Figure 6.6b, fluorescence intensity decreased linearly on increasing the concentration of Fe<sup>2+</sup> up to 72  $\mu$ M and the detection limit was calculated as low as 41 ppb (Figure A8a, Appendix VI, Page 382). Quenching constant was calculated using a Stern-Volmer plot as  $2.23 \times 10^3$  M<sup>-1</sup> (Figure A8b, Appendix VI, Page 382). Non-linear fitting of Stern-Volmer plot shows that fluorescence quenching is due to the combination of both dynamic and static mechanisms.<sup>8</sup> Using Benesi-Hildebrand plot, the binding constant was calculated as  $4.53 \times 10^4$  M<sup>-1</sup> (Figure A8c, Appendix VI, Page 382). Further to confirm the binding of **1** with Fe<sup>2+</sup>, we have performed the <sup>1</sup>H NMR titration in CDCl<sub>3</sub> (Figure 6.6c). It was observed that protons correspond to the amide hydrogen of **1** at 8.04 ppm get shifted to 8.77 ppm without deprotonating. It means Fe<sup>2+</sup> binds to -NH of **1**. It is evident from Figure 6.6d, **1** is highly selective and sensitive for the detection of Fe<sup>2+</sup> and the competitive experiment showed that there is no interference of other ions for the detection of Fe<sup>2+</sup>.

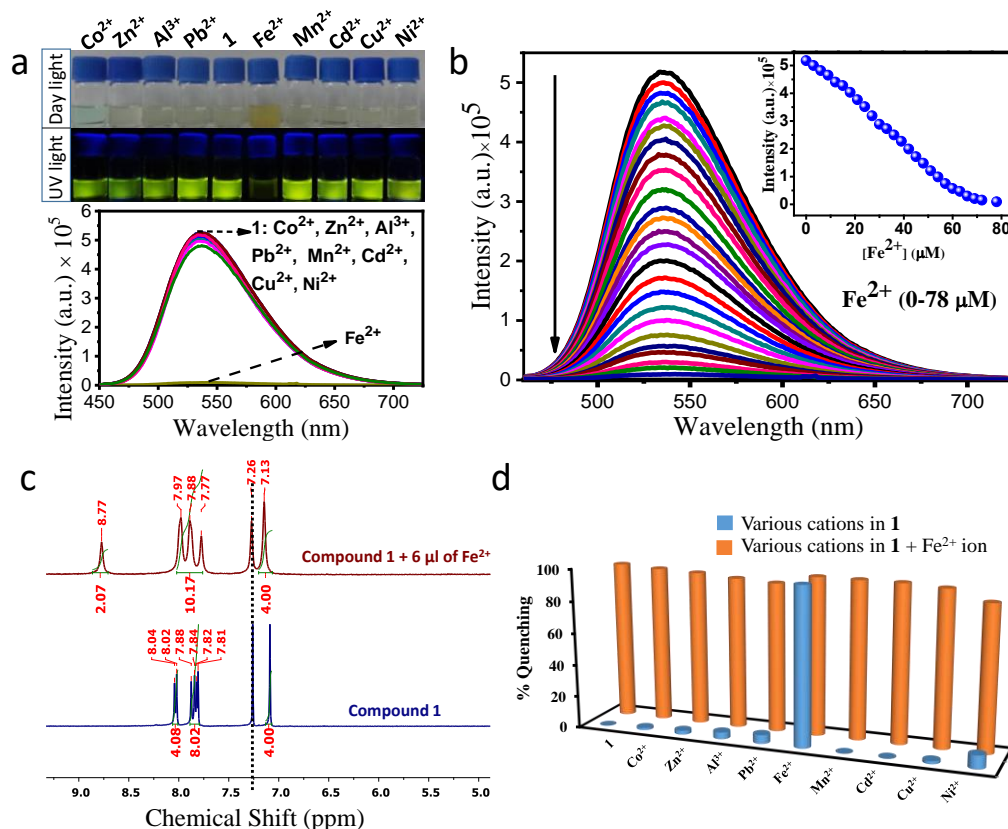


**Figure 6.6** (a) Fluorescence spectra of **1** on the addition of various metal ions. Inset (top) consists of photographs of **1** on the addition of different metal ions under normal and UV (365 nm) light. (b) Fluorescence titration spectra of **1** (5 μM) with Fe<sup>2+</sup> ions (0-78 μM) in THF:H<sub>2</sub>O (90:10, v/v, H<sub>2</sub>O: 1mM tris-buffered saline (TBS), pH = 7.4). Inset shows the change in fluorescence intensity on the addition of various concentrations of Fe<sup>2+</sup> ions;  $\lambda_{\text{ex}} = 407$  nm and  $\lambda_{\text{em}} = 537$  nm for THF:H<sub>2</sub>O (90:10, v/v, H<sub>2</sub>O: 1mM tris-buffered saline (TBS), pH = 7.4) parent solution of compound **1**. (c) Comparative <sup>1</sup>H NMR spectra of compound **1** (10<sup>-2</sup> M) upon addition of 6 μl of Fe<sup>2+</sup> ion (10<sup>-3</sup> M). (d) The blue bars represent the fluorescence intensity of **1** in presence of different cations (78 μM), the orange bars represent the fluorescence intensity of **1** in presence of different cations (78 μM) followed by the addition of 78 μM of Fe<sup>2+</sup>.

In addition, we have tested the sensing ability of **1** towards the anions under similar conditions (Figure 6.7 and Figure A9, Appendix VI, Page 383). Among the various anions tested here (F<sup>-</sup>, Cl<sup>-</sup>, Br<sup>-</sup>, I<sup>-</sup>, NO<sub>3</sub><sup>-</sup>, CH<sub>3</sub>COO<sup>-</sup>, SO<sub>4</sub><sup>2-</sup>, and CO<sub>3</sub><sup>2-</sup>), only I<sup>-</sup> showed the fluorescence quenching. Figure 6.7 revealed the high selectivity and sensitivity towards the I<sup>-</sup> anion. Detection limit was calculated as 32 ppb (Figure A9a, Appendix VI, Page 383) and from the Stern-Volmer plot, quenching constant was obtained as  $5.85 \times 10^3 \text{ M}^{-1}$  (Figure A9b, Appendix VI, Page 383).



Using Benesi-Hildebrand method binding constant was calculated as  $1.85 \times 10^4 \text{ M}^{-1}$  (Figure A9c, Appendix VI, Page 383).

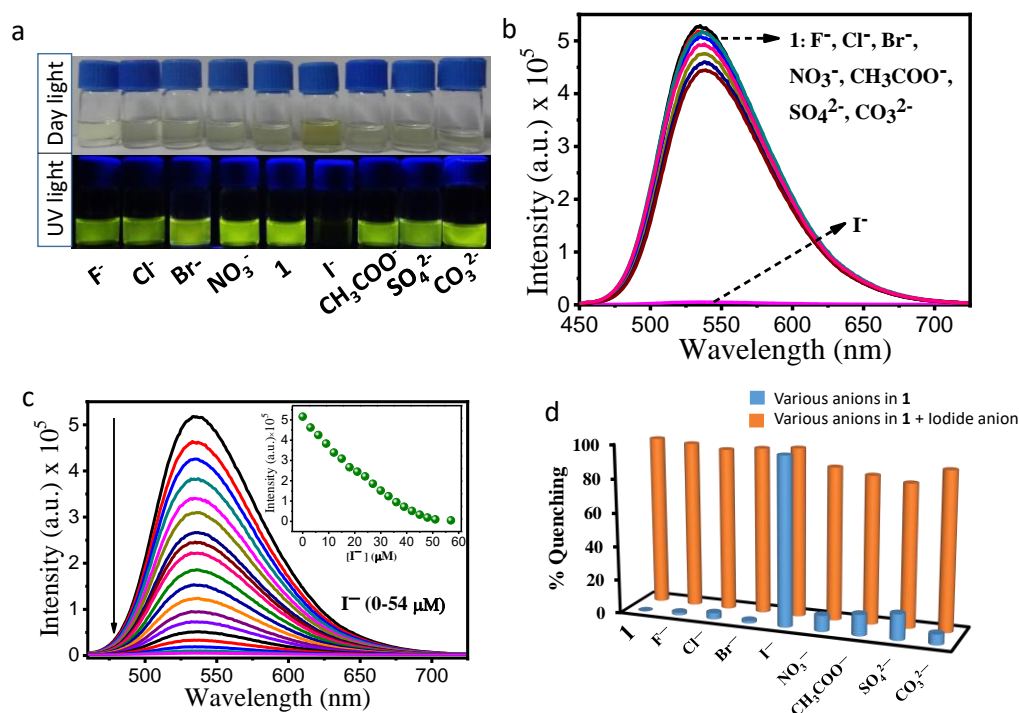


**Figure 6.7** (a) Photographs of **1** on addition of different anions under normal and UV (365 nm) light. (b) Fluorescence spectra of **1** on addition of various anions. (c) Fluorescence titration spectra of **1** (5 μM) with I<sup>-</sup> ions (0-54 μM) in THF:H<sub>2</sub>O (90:10, v/v, H<sub>2</sub>O: 1mM tris-buffered saline (TBS), pH = 7.4). Inset: change in fluorescence intensity on addition of various concentrations of I<sup>-</sup> ions.  $\lambda_{\text{ex}} = 407 \text{ nm}$  and  $\lambda_{\text{em}} = 537 \text{ nm}$  for THF:H<sub>2</sub>O (90:10, v/v, H<sub>2</sub>O: 1mM tris-buffered saline (TBS), pH = 7.4) parent solution of compound **1**. (d) The blue bars represent the fluorescence intensity of **1** in presence of different anions (54 μM), the orange bars represent the fluorescence intensity of the above solution upon further addition of 54 μM of I<sup>-</sup>.

Further, compound **1** showed potential application as a staining agent. Pollen grains of *Hibiscus rosa-sinensis* was treated with compound **1** for 15 min at ambient temperature, which showed green fluorescence in the intracellular area. This suggests that compound **1** is cell-permeable and successfully stained the pollen grains (Figure 6.8).

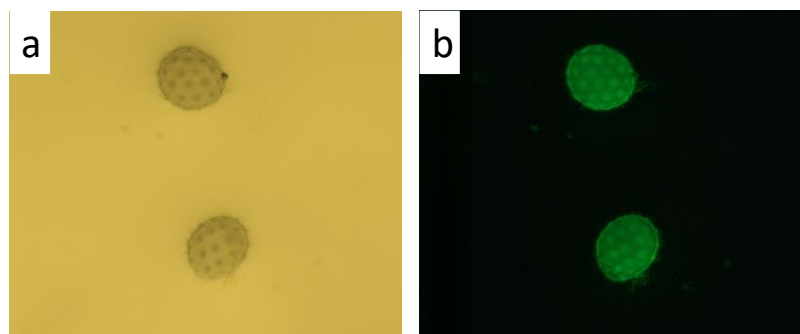


**Figure 6.8** Fluorescence microscopic photographs of pollen grains of *Hibiscus rosa-sinensis* in presence of compound **1** (a) bright field and (b) dark field.

#### 6.1.3.5 Electroluminescence behaviour

The BTD derivatives **1** & **2** display excellent photophysical behaviour (with well-proportioned HLCT excited state) and electrochemical behaviour that inspired us to investigate the electroluminescent (EL) properties *via* utilizing these compounds in OLED device fabrication. To evaluate the EL characteristics of these BTD based small molecules, solution-processed doped devices were fabricated. A bipolar host 4,4'-Bis(9-carbazolyl)-biphenyl (CBP) was employed to fabricate devices using emitter **1** and **2** with device configurations of ITO/PEDOT:PSS (35 nm)/CBP: x wt% of emitter (dopant) **1** or **2** (x = 1.0, 3.0, and 5.0) (22 nm)/TPBi (40 nm)/ LiF (1.5 nm)/ Al (150 nm) as displayed in Figure 6.9a. As the triplet energy of CBP host (2.60 eV) is greater than the triplet energy of the emitter molecules **1** (2.31 eV) and **2** (2.44 eV), thereby ensures the exciton confinement in the emitter layer and hence expected higher device efficiency.<sup>41</sup> The presence of long side-chains in compounds **1** and **2** renders its excellent solubility in organic solvents and allowed the devices to be solution-processable along with the good miscibility within CBP host matrix to form the homogeneous emissive layer.<sup>42</sup> The topography images of CBP:**1** and CBP:**2** films (at 1 wt% of dopant concentration) measured by AFM in tapping mode are well in homogeneity as seen in Figure 6.10. The root mean square (RMS) roughness of pure CBP:**1** and CBP:**2** film was recorded as 5.21 nm ( $R_q = 1.85$  nm,  $R_a = 1.12$  nm) and 4.78 nm ( $R_q = 1.26$  nm,  $R_a = 0.95$  nm), respectively, indicating the good miscibility between compound and CBP host.

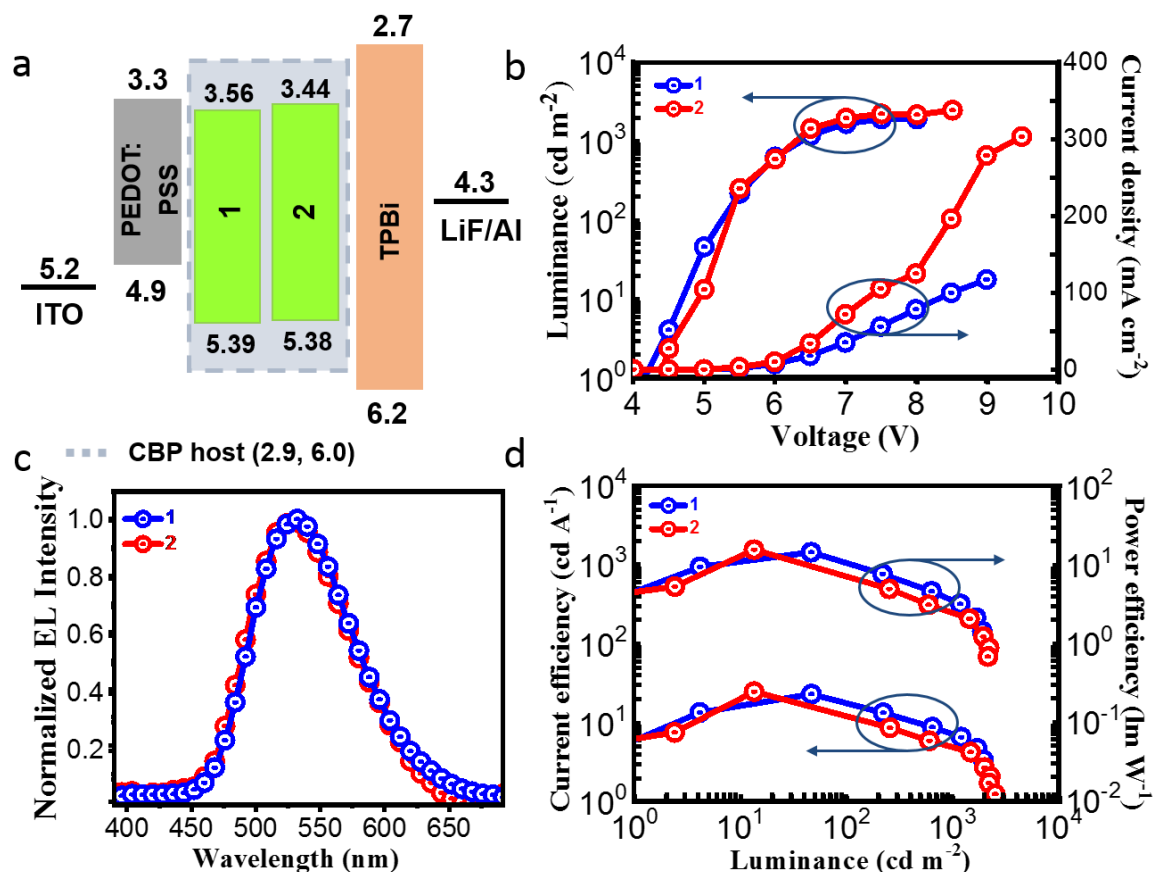


**Figure 6.9** (a) Schematic energy level diagram of the solution-processed OLED devices with emitter **1** and **2**, (b) Luminance-voltage-current density curve, (c) Normalized EL spectra, (d) Current efficiency-luminance-power efficiency curves for compound **1** and **2** based devices. Note: All the measurements are for solution-processed devices in CBP with 1.0 wt% of dopant concentration.

The devices were fabricated by employing the emitters **1** and **2** doped at three different concentrations 1, 3 and 5 wt% in CBP host matrix. The doping concentration of the emitter materials has a strong influence on the EL behaviour of the devices. For example, on decreasing the doping concentration from 5 wt% to 3 wt% to 1 wt%, the EQE increases subsequently from 1.7% to 4.7 % to 7.0% in case of **1** and from 2.1% to 5.1% to 8.1% for emitter **2** (Table 6.5). The increase in EQE on decreasing the doping concentration can be attributed to the dilution effect originating from the uniform dispersion of dopant with CBP host as confirmed by AFM (Figure 6.10), resulting in the suppression of aggregates that minimized the concentration-quenching of fluorophores in the solid-state.<sup>42</sup>

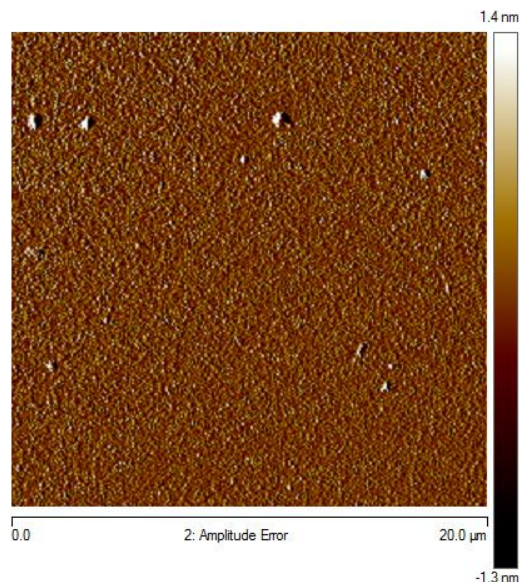


**Figure 6.10** The topography image of thin-film of compound **2** (1.0 wt%) doped with CBP host, measured by AFM in tapping mode.

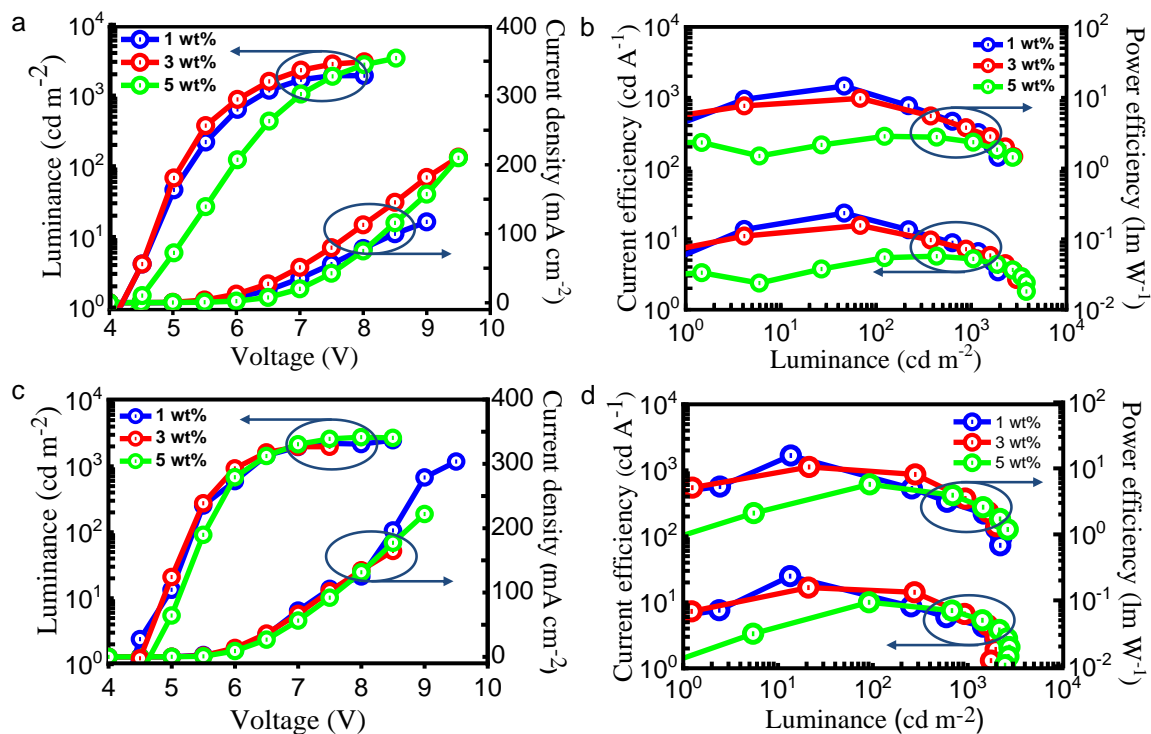


**Figure 6.11** (a) & (c) Luminance-voltage-current density curve, (b) & (d) current efficiency-luminance-power efficiency curves for compounds **1** (a and b) and **2** (c and d) based solution-processed OLED devices using CBP host with 1, 3 and 5 wt% of emitter concentration.

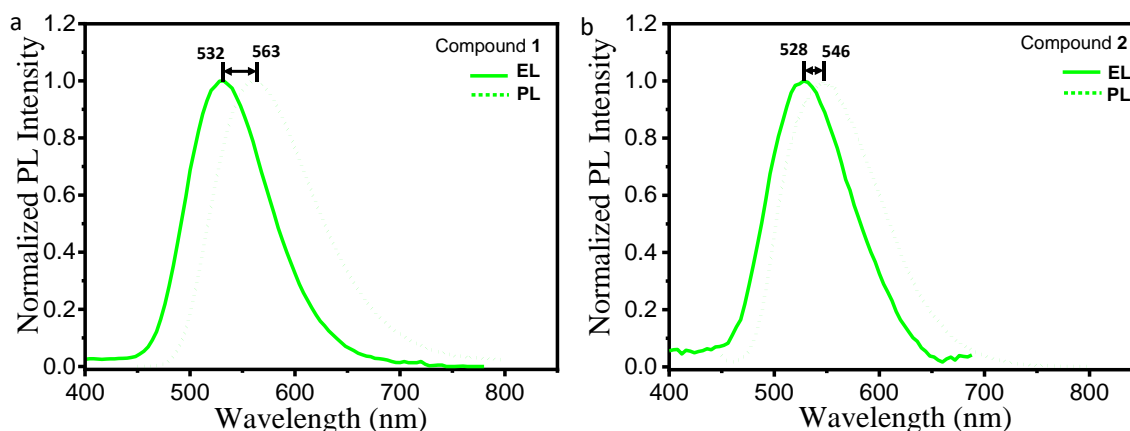


**Figure 6.12** Electroluminescence (EL) and photoluminescence (PL) spectrum of compounds (a) **1** and (b) **2** in the thin-film state. EL spectra were recorded for compounds **1** and **2** at 1 wt% doping concentration of emitters with CBP host.

The current density, luminance vs. voltage, current efficiency (CE), power efficiency (PE) vs. luminance curves, and EL characteristics of best devices (1 wt%) for **1** and **2**, and with 3 wt% and 5 wt% doped devices are displayed in Figure 6.9b-d and Figure 6.11, respectively. For best devices, both the emitters exhibit green-colored luminescence as observed from EL spectra that displayed a peak at 532 nm for **1** and 546 nm for **2** (Figure 6.9c). It can be noted that for both the compounds EL spectra of doped devices (Figure 6.12) become narrow and blue shifted (31 nm for **1** and 18 nm for **2**) in comparison to its PL spectra which indicates the suppression of aggregates upon doping with the CBP host. Such type of blue shifts and narrowing of peaks has been reported earlier when the emitter materials doped with the CBP host.<sup>43</sup> However, the emission lies in the green region, indicating that the electroluminescence is originating indeed from the emissive layers with no excimer or exciplex emission.

For compound **2**, the device exhibited better performance, with a maximum current efficiency of 24.9 cd A<sup>-1</sup>, power efficiency of 15.6 lm W<sup>-1</sup> and EQE of 8.1% with maximum brightness of 2476 cd m<sup>-2</sup>. Furthermore, device displays better power efficiency PE<sub>max.~PE100</sub> (24.3%) and current efficiency CE<sub>max.~CE100</sub> (23.3%) roll-off than the compound **1** based devices (Table A1, Appendix VI, Page 383). Figure 6.14 illustrates the EQE versus voltage plots of the devices displaying an efficiency roll-off profile. It is noteworthy that the triplet energy of compound **2** (2.44 eV) is sufficiently higher than compound **1** (2.31 eV) (Figure 6.13) and well in order with CBP (2.60 eV) host that enables favourable host-guest energy transfer, hence

**Table 6.5** Electroluminescent data of the BTD derivatives **1** and **2**.

Emitter	Emitter conc. (wt%)	PE <sub>max</sub> / CE <sub>max</sub> / EQE <sub>max</sub> <sup>a</sup> (lm W <sup>-1</sup> / cd A <sup>-1</sup> / %)	PE <sub>100</sub> / CE <sub>100</sub> / EQE <sub>100</sub> <sup>b</sup> (lm W <sup>-1</sup> / cd A <sup>-1</sup> / %)	CIE <sub>xy</sub> <sup>c</sup>	L <sub>max</sub> <sup>d</sup> (cd m <sup>-2</sup> )
<b>1</b>	<b>1</b>	14.5/ 23.1/ 7.0	10.0/ 16.0/ 6.1	(0.31, 0.55)	1910
	3	9.7/ 15.5/ 4.7	9.3/ 14.9/ 4.5	(0.31, 0.55)	2995
	5	2.8/ 5.7/ 1.7	2.7/ 5.0/ 1.5	(0.35, 0.57)	3798
<b>2</b>	1	15.6/ 24.9/ 8.1	11.8/ 19.1/ 6.2	(0.29, 0.51)	2476
	3	10.5/ 16.7/ 5.1	7.2/ 11.5/ 4.8	(0.32, 0.56)	1978
	5	5.7/ 10.0/ 2.1	5.7/ 10.0/ 1.8	(0.31, 0.50)	2758

<sup>a</sup>Maximum power efficiency (PE<sub>max</sub>), current efficiency (CE<sub>max</sub>) and external quantum efficiency (EQE<sub>max</sub>). <sup>b</sup>Power efficiency (PE<sub>100</sub>), current efficiency (CE<sub>100</sub>) and external quantum efficiency (EQE<sub>100</sub>) at 100 cd m<sup>-2</sup>. <sup>c</sup>CIE coordinates at 100 cd m<sup>-2</sup>. <sup>d</sup>Maximum measured luminance (L<sub>max</sub>) of the device.

demonstrating an effective charge balance and exciton confinement state in the emissive layer of compound **2** based devices. Compound **1** performed comparably less well, exhibiting a maximum current efficiency of 23.1 cd A<sup>-1</sup>, power efficiency of 14.5 lm W<sup>-1</sup> and EQE of 7.0% with brightness of 1910 cd m<sup>-2</sup>.

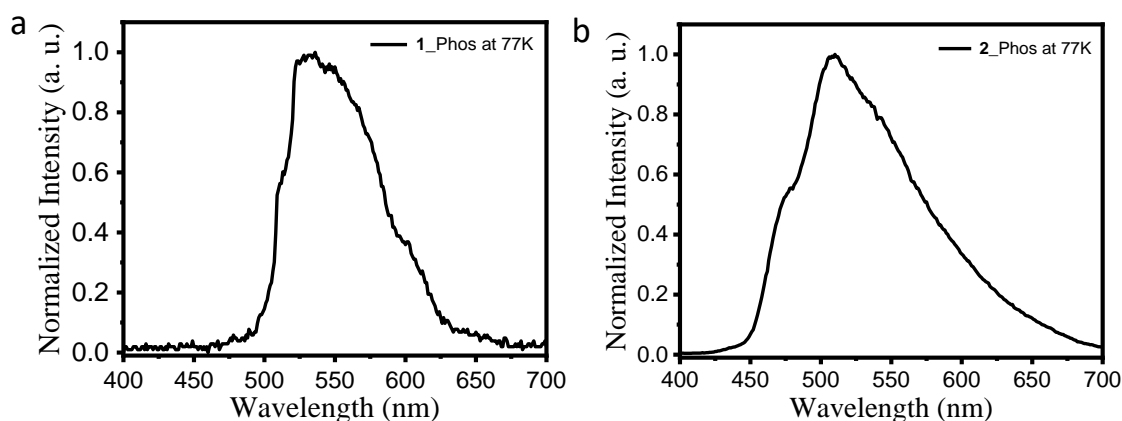


**Figure 6.13** Low-temperature (at 77 K) phosphorescence (Phos) spectra of compounds (a) **1** ( $\lambda = 537$  nm; triplet energy ( $E_T$ ) = 2.31 eV) and (b) **2** ( $\lambda = 508$  nm;  $E_T$  = 2.44 eV) in THF.

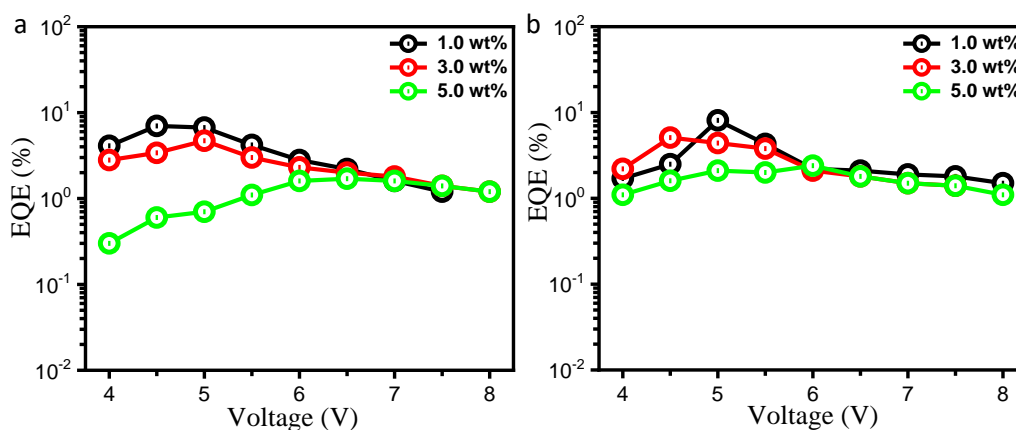


**Figure 6.14** EQE (%) versus voltage (V) plots of the devices displaying an efficiency roll-off profile for compounds (a) **1** and (b) **2** based solution-processed OLED devices using CBP host with 1, 3 and 5 wt% of emitter (**1** and **2**) concentration.

The devices exhibiting high EQE values (Table 6.5) than the traditional limit by surpassing its EUE beyond 25% suggesting the use of both singlet as well as triplet excitons. The EUE of the devices can be calculated by using the following equation:<sup>12,17</sup>

$$\eta_{\text{EQE}} = \eta_{\text{rec}} \cdot \eta_{\text{S}} \cdot \eta_{\text{PL}} \cdot \eta_{\text{out}}$$

In the above equation,  $\eta_{\text{EQE}}$  is the EQE of an OLED device,  $\eta_{\text{S}}$  represents the EUE.  $\eta_{\text{PL}}$  is the photoluminescence quantum yield,  $\eta_{\text{rec}}$  denotes the proportion of electron-hole recombination which is usually assumed to be unity in an ideal case.  $\eta_{\text{out}}$  is the light out-coupling efficiency, which is ~20% for ITO-based flat thin-film OLEDs.<sup>12</sup> Once the  $\eta_{\text{EQE}}$  and  $\eta_{\text{PL}}$  are known,  $\eta_{\text{S}}$  can be calculated. The  $\eta_{\text{PL}}$  of the neat films was measured and found to be 81% and 85% for compounds **1** and **2**, respectively. The corresponding  $\eta_{\text{S}}$  in the resultant OLED devices were estimated (using above equation) to be ~43% and ~48%, assuming the full electron-hole recombination i.e.  $\eta_{\text{rec}}$  is considered to be unity. Remarkably, EUE sufficiently surpasses the spin-statistics limit of the radiative exciton ratio of 25% for conventional fluorescent OLEDs. This indicates the utilization of triplet excitons by spin-flip mechanism is happening by one of the various possible mechanistic pathways *viz.* HLCT, TADF and TTA. As probed in the above sections, the Lippert-Mataga plots and nature of excited states for the representative compound **2** revealed the HLCT nature of the excited states, thereby the conversion of triplet excitons to singlet excitons takes place by RISC phenomena using ‘hot exciton’ channel.

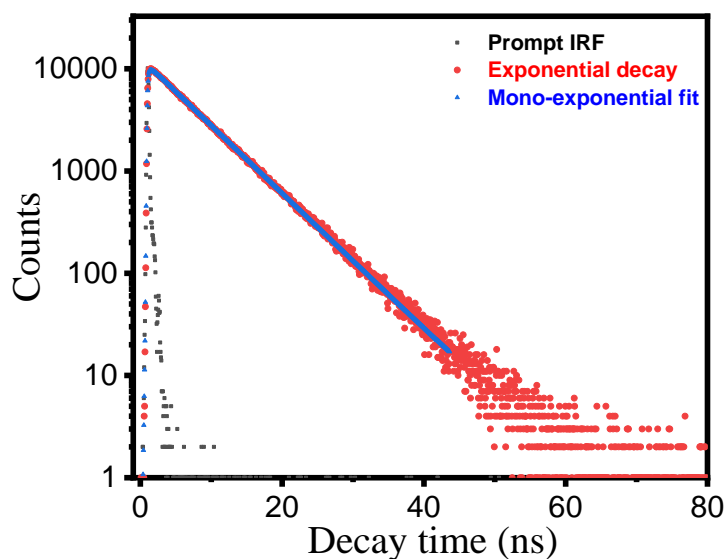


**Figure 6.15** Fluorescence decay spectra of compound **2** in diethylether (solvent of moderate polarity),  $\chi^2$  value = 1.27;  $\tau$  = 6.53 ns.

The mono-exponential PL decay of compound **2** also supports the presence of a hybridized state (Figure 6.15). Moreover, the existence of a shorter lifetime and the absence of any delayed component in the PL decay excludes the possibility of the TADF mechanism.

#### 6.1.4 Conclusions

This work explored the application of luminescent benzothiadiazole derivatives (**1** and **2**) as efficient emitter materials in solution-processable OLED devices. The emitter materials exhibited green-colored electroluminescence in the fabricated devices with the breakthrough of the traditional EQE limit of fluorescent OLEDs. The obtained maximum EQE value of 7.0% for compound **1** and 8.1% for compound **2** surpassing the traditional limit was explained with the aid of systematic photophysical studies and quantum chemical calculations. The conclusive studies revealed the occurrence of the HLCT phenomena where the triplet excitons from  $T_2$  triplet state to  $S_1$  singlet state take place through the RISC process *via* ‘hot-exciton’ channel. On the other hand, compound **1** showed the sensitive and selective sensing towards Fe(II) ions among various cations and I<sup>-</sup> anion among several anions with a detection limit as low as 41 ppb and 32 ppb, respectively. It was also successfully applied in bio-imaging using pollen grains which could find potential applications in diagnostics. Therefore, we believe that the present findings will certainly offer an important guideline for multifunctional molecular



design and provide an important step forward to expand the applications of small  $\pi$ -conjugated luminescent molecules.

**Acknowledgements.** *The OLED device studies have been carried out in collaboration with Prof. J. H Jou's group at National Tsing Hua University, Taiwan and is greatly acknowledged and respected. Dr. Manisha Devi (at IISER Mohali) is duly acknowledged for the fluorescence sensing. We are highly thankful to Dr. Kamalakannan Kailasam from INST Mohali for helping us in this project.*

## 6.1.5 Experimental section

**6.1.5.1 Characterization data of Intermediate 4,7-bis[4-(diphenylamino)phenyl]-2,1,3-benzothiadiazole 5.** FT-IR ( $\text{cm}^{-1}$ ): 3468, 3365, 1620, 1602, 1544, 1519, 1475, 1346, 1327, 1301, 1273, 1186, 1132, 1114, 855, 823.  $^1\text{H}$  NMR (500 MHz\*,  $\text{CDCl}_3$ ,  $\delta$  in ppm):  $\delta$  7.82-7.81 (d, 4H,  $J = 8.65$  Hz), 7.68 (s, 2H), 6.86-6.84 (d, 4H,  $J = 8.55$  Hz), 3.83 (s, 4H). \*Note: This NMR spectrum has been recorded on a 500 MHz NMR spectrometer.  $^{13}\text{C}$  NMR (125 MHz $^\dagger$ ,  $\text{CDCl}_3$ ,  $\delta$  in ppm):  $\delta$  154.45, 146.76, 132.39, 130.39, 128.04, 127.04, 115.23.  $^\dagger$ Note: This NMR spectrum has been recorded on a 125 MHz NMR spectrometer.

**6.1.5.2 Characterization data of BTD derivative 1.** FT-IR ( $\text{cm}^{-1}$ ): 3300, 2951, 2923, 2853, 1645, 1582, 1520, 1495, 1468, 1426, 1336, 1238, 1215, 892, 827.  $^1\text{H}$  NMR (400 MHz,  $\text{CDCl}_3$ ,  $\delta$  in ppm):  $\delta$  8.05-8.03 (d, 4H,  $J = 8.28$  Hz), 7.85-7.81 (dd, 8H), 7.09 (s, 4H), 4.08-4.02 (m, 12H), 1.86-1.75 (m, 12H), 1.51-1.46 (m, 12H), 1.32-1.28 (m, 72H), 0.90-0.87 (t, 18H,  $J = 6.36$  Hz).  $^{13}\text{C}$  NMR (100 MHz,  $\text{CDCl}_3$ ,  $\delta$  in ppm):  $\delta$  165.90, 154.19, 153.38, 141.67, 138.35, 133.51, 132.49, 130.04, 129.91, 127.88, 120.27, 105.96, 73.72, 69.58, 32.09, 32.07, 29.90, 29.84, 29.80, 29.75, 29.57, 29.51, 26.24, 22.84, 14.28. HRMS-MALDI ( $\text{M}+\text{H}$ ) $^+$  for  $\text{C}_{92}\text{H}_{142}\text{N}_4\text{O}_8\text{S}$ : calculated – 1464.0627, observed – 1464.0251

**6.1.5.3 Characterization data of BTD derivative 2.** FT-IR ( $\text{cm}^{-1}$ ): 3267, 2954, 2921, 2850, 1738, 1645, 1582, 1524, 1495, 1467, 1426, 1378, 1339, 1241, 1188, 1120, 1081, 969, 894, 824.  $^1\text{H}$  NMR (400 MHz,  $\text{CDCl}_3$ ,  $\delta$  in ppm):  $\delta$  8.04-8.02 (d, 4H,  $J = 8.68$  Hz), 7.88-7.81 (m, 8H), 7.09 (s, 4H), 4.07-4.01 (m, 12H), 1.85-1.74 (m, 12H), 1.49-1.45 (m, 12H), 1.26 (s, 96H), 0.89-0.86 (t, 18H,  $J = 6.44$  Hz).  $^{13}\text{C}$  NMR (100 MHz,  $\text{CDCl}_3$ ,  $\delta$  in ppm):  $\delta$  165.85, 154.22, 153.43, 141.75, 139.44, 138.34, 132.53, 130.08, 127.91, 120.22, 114.21, 106.01, 73.74, 69.64,

32.09, 30.49, 29.86, 29.82, 29.67, 29.58, 29.53, 29.32, 26.25, 22.86, 14.29. HRMS-MALDI (M+H)<sup>+</sup> for C<sub>104</sub>H<sub>166</sub>N<sub>4</sub>O<sub>8</sub>S: calculated – 1633.2538, observed – 1633.2627

**6.1.5.4 Calculation of dipole moment.** The dipole moment in the excited states was calculated by using Lippert-Mataga equation given by:

$$\Delta\nu = \frac{2\Delta f}{4\pi\epsilon_0\hbar ca^3}(\mu_e - \mu_g)^2 + b$$

$$\Delta f = \frac{\epsilon - 1}{2\epsilon + 1} - \frac{n^2 - 1}{2n^2 + 1}$$

where  $\Delta\nu = \nu_a - \nu_f$  represents the Stokes shift,  $\nu_a$  and  $\nu_f$  stands for absorption and emission frequency (cm<sup>-1</sup>),  $\Delta f$  is the orientation polarizability of the solvent,  $\epsilon_0$  is the permittivity of the vacuum,  $\hbar = h/2\pi$ , where  $h$  is the Planck's constant,  $c$  is the velocity of light in vacuum,  $a$  is the Onsager radius and  $b$  is a constant,  $\epsilon$  is the solvent dielectric,  $n$  is the solvent refractive index,  $\mu_e$  and  $\mu_g$  are the dipole moments of the excited and ground states, respectively, and  $(\mu_e - \mu_g)^2$  is proportional to the slope of the Lippert-Mataga plot.

**6.1.5.5 Calculations of quenching constant, detection limit and binding constant.** The quenching constant of compound **1** for Fe<sup>2+</sup>/I<sup>-</sup> ion was determined from the non-linear Stern-Volmer curve. The exponential quenching equation given below was used to fit the non-linear Stern-Volmer curve<sup>10</sup>:

$$\frac{I_o}{I} = Ae^{Kx} + B$$

Where A, B, and K are constants. Quenching constant can be calculated as  $A \times K$ .

The detection limit (DL) of compound **1** towards Fe<sup>2+</sup>/I<sup>-</sup> ions was determined from the following equation:

$$DL = \frac{3 \times SD}{S}$$

Where SD is the standard deviation of the blank solution detected 5 times; S is the slope of the calibration curve.

The binding constant,  $K_a$ , for compound **1** towards Fe<sup>2+</sup>/I<sup>-</sup> ions was determined using the Benesi-Hildebrand equation 1 for Fe<sup>2+</sup> and 2 for I<sup>-</sup> respectively:

$$\log\left(\frac{I-I_o}{I_f-I_o}\right) = \log[M^{x-}] + \log K_a \quad \text{-----(1)}$$

$$\frac{1}{(I-I_o)} = \frac{1}{[K_a(I_{max}-I_o)[M^{x+}]n]} + \frac{1}{I_{max}-I_o} \quad \text{----- (2)}$$

where  $I_o$  is the emission intensity of the host in the absence of guest,  $I$  represent the emission intensity of the host recorded in the presence of an added guest,  $I_f$  or  $I_{max}$  is the emission intensity in the presence of added analyte ( $[M^{x+/-}]_{max}$ ) and  $K_a$  represents the binding/association constant.

**6.1.5.6 Theoretical studies.** The geometrical optimization of compounds **1** & **2** was carried out by DFT calculations using B3LYP functional with 6-31G(d,p) basis set. Excited states were calculated by time-dependent DFT (TD-DFT) calculations within the Tamm–Dancoff approximation (TDA) using the ground state optimized geometries.

**6.1.5.7 OLED device fabrication and testing.** The solution-processed OLEDs were fabricated with a simple structure of ITO/PEDOT:PSS (35 nm)/ emissive layer (22 nm)/ TPBi (40 nm)/ LiF (1.5 nm)/ Al (150 nm). The patterned indium tin oxide (ITO) substrates were pre-cleaned with the routine procedure; acetone (30 min, 50 °C), isopropyl alcohol (30 min, 60 °C) and deionized water (15 min, RT) under sonication and further treated by UV-ozone for 30 min. A 30 nm layer of PEDOT:PSS (4000 rpm) was deposited on the ITO substrate *via* spin-coating to form a hole injection layer (HIL). The PEDOT:PSS coated substrates were baked in an oven at 120 °C for 15 min. The emissive layer (EML) consisting of CBP host matrix doped with **1** and **2** (1, 3, 5, or 100 wt%) was spin-coated (2500 rpm) from a fresh THF solution. A device structure of TPBi (40 nm)/ LiF (1.5 nm)/ Al (150 nm) was thermally deposited in sequence in a vacuum chamber at a base pressure of less than  $4 \times 10^{-6}$  Pa. The current density-luminance-voltage characteristics were measured by a Keithley source measurement unit (Keithley 2400). The EL spectra of the devices were measured by SpectraScan PR650 spectrophotometer. All measurements were carried out at room temperature under ambient conditions.



## **6.2 Part B: Electroluminescent and ambipolar charge transport behaviour of AIE-active discotic liquid crystals based on alkoxy cyanostilbenes connected benzenetricarboxamide**

### **6.2.1 Introduction**

Molecular materials with both semiconducting and emissive properties are rare<sup>44</sup> although crucial for the advancement of integrated optoelectronic devices such as organic light-emitting transistors,<sup>45</sup> organic pumped lasers<sup>46</sup> and so on. It is rather challenging to design the molecules with complementary properties because the molecules with compact and strong packing, however, give rise to excellent charge transport properties but quench terribly the solid-state luminescence. Particularly, crystalline  $\pi$ -conjugated molecules exhibit strong molecular packing, thereby act as good charge transport systems but at the same time detrimental to solid-state emission properties due to the formation of excimers and exciplexes.<sup>44,47,48</sup> On the other hand, in amorphous materials, the intermolecular interactions get weak, resulting in highly emissive systems but disadvantageous to semiconducting property.<sup>44</sup> To solve this problem, dynamic materials manifesting optimum amount of  $\pi$ - $\pi$  interactions are potential candidates for the realization of efficient semiconducting and emissive properties in the same molecule. Discotic liquid crystal<sup>49-52</sup> (DLC) is an ideal class of dynamic  $\pi$ -conjugated materials that forms an interface between the crystalline and amorphous materials. In DLCs, disc-shaped molecules form columnar architectures and substantiate one-dimensional conduction. In addition, utilization of either luminescent central discotic cores or emissive peripheral flexible side groups can impart the emissive behaviour to DLC semiconductor materials. Consequently, DLC materials with rational design can efficiently tune the two complementary properties in the same molecular system. In this work, we have developed such systems that behaved as emitter materials in organic light-emitting diodes (OLEDs) with efficient ambipolar charge transport behaviour.

Among the diverse molecular systems, cyanostilbenes,<sup>53-56</sup> known as highly luminescent and

---

Bala, I.; Kaur, H.; Yadav, R. A. K.; De, J.; Gupta, S. P.; Jou, J. H.; Pandey, U. K. P.; Pal, S. K. Electroluminescent AIE-active discotic liquid crystals based on alkoxy cyanostilbenes functionalized benzenetricarboxamide with ambipolar charge transport. *Submitted*. Some part of this work has been included in Master thesis of Ms. Harpreet Kaur (MS15179) at IISER Mohali and is greatly acknowledged and respected.

aggregation-induced emissive materials. Apart from their emissive nature, they can also serve as electron-acceptor fragment in the molecular structure and can contribute to electron transport.<sup>57</sup> To realize ambipolar materials, various approaches such as bridged electron donor-acceptor (D-A) moieties,<sup>58</sup> blendings of donor and acceptor molecules<sup>43</sup> have been employed. OLED materials do not require a mobility value more than  $10^{-4}$ - $10^{-2}$   $\text{cm}^2 \text{V}^{-1} \text{s}^{-1}$  due to short electrical channel length but a balanced ambipolar charge transport is preferred for efficient functioning.<sup>59</sup>

## 6.2.2 Objectives

With the aim of achieving dynamic materials for the realization of efficient semiconducting and emissive properties in the same molecule, we have designed the tricarboxamide based DLC materials (**1a-c**) (Figure 6.16) where the  $C_3$ -symmetric tricarboxamide core is substituted with cyanostilbene based flexible luminophoric groups. In  $C_3$  symmetric tricarboxamide derivatives, it is well established that intramolecular H-bonding contributes to the formation of the columnar assembly that is likely to act as a charge transport entity. On the other hand, the promesogenic trialkoxy cyanostilbene fragment imparts the molecular structure with emissive as well as liquid crystalline behaviour. All three derivatives exhibited room temperature columnar hexagonal behaviour over a wide mesomorphic range. When employed as emissive materials in OLEDs, sky-blue colored emission was observed and SCLC measurements revealed ambipolar charge transport with balanced hole and electron mobilities for all three compounds.

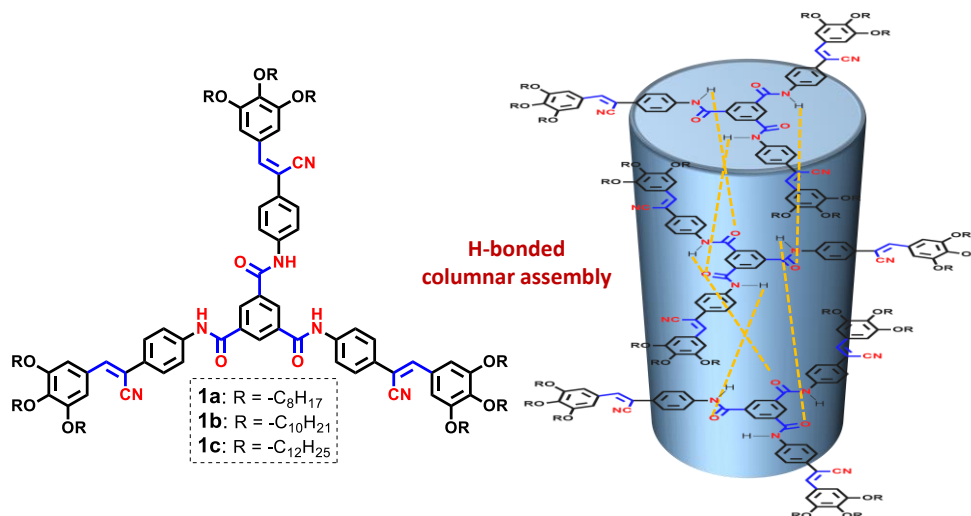
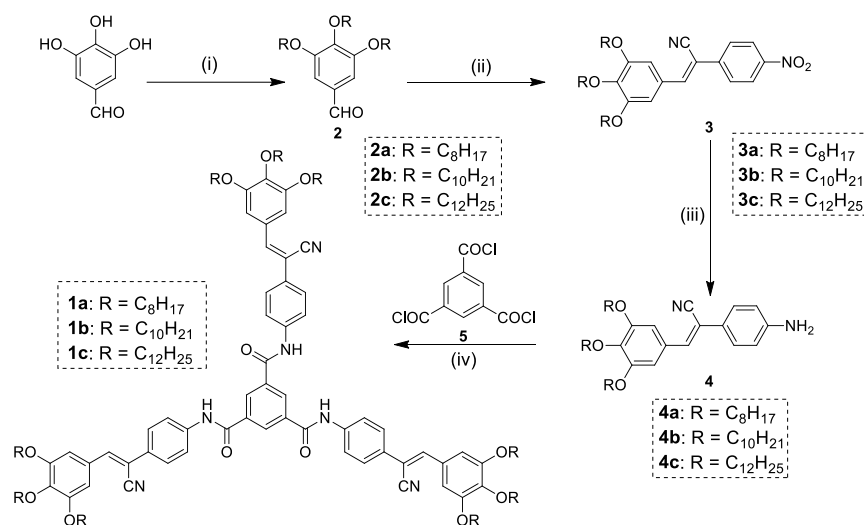


**Figure 6.16** Molecular structure of tricarboxamide-cyanostilbene based derivatives.

## 6.2.3 Results and discussions

### 6.2.3.1 Synthesis and Characterization

The target materials **1a-c** were synthesized by following Scheme 6.2. The key intermediate, trimesoyl chloride was synthesized from the commercially available trimesic acid.<sup>60</sup> On the other hand, the synthesis of amine derivatives **4a-c** were commenced from the Williamson etherification of 3,4,5-trihydroxy benzaldehyde with different alkyl bromides (RBr: R = -C<sub>8</sub>H<sub>17</sub>, -C<sub>10</sub>H<sub>21</sub>, -C<sub>12</sub>H<sub>25</sub>) using potassium carbonate (K<sub>2</sub>CO<sub>3</sub>) as a base in the presence of catalytic amount of potassium iodide (KI).<sup>61</sup>



**Scheme 6.2** Reagents & Conditions: (i) K<sub>2</sub>CO<sub>3</sub>, RBr, dry DMF, 90 °C, 12h; (ii) 4-Nitrophenylacetonitrile, ethanol, piperidine; (iii) SnCl<sub>2</sub>·2H<sub>2</sub>O, ethanol/THF (3:2 (v/v)); (iv) pyridine, THF, 90 °C, 18h. Yield of **1a-c**: 76-84%.

After the formation of alkylated 3,4,5-trialkyloxy benzaldehyde derivatives **2a-c**, they were condensed with 4-Nitrophenylacetonitrile with the use of piperidine as a base to give nitro derivatives **3a-c**.<sup>56</sup> Further, the selective reduction of the nitro group in the presence of cyano functionality was performed with stannous chloride dihydrate as a reducing agent to give the reduced amino derivatives **4a-c**.<sup>53</sup> Finally, the obtained amines were condensed with trimesoyl chloride to achieve the target tricarboxamide derivatives **1a-c** in good yields.<sup>60</sup> All the final derivatives were characterized by NMR (<sup>1</sup>H and <sup>13</sup>C) (Figure A10-A15, Appendix VI, Page 384), HRMS (MALDI) (Figure A16-A18, Appendix VI, Page 387) and FT-IR studies. The mass spectra of **1a-c** were recorded to further confirm their structures.

### 6.2.3.2 Thermal behaviour

The thermal properties of TCA derivatives **1a-c** were thoroughly investigated with the use of various techniques. For instance, the thermal stability was examined by employing thermogravimetric analysis (TGA) technique (Figure 6.17). The TCA derivatives **1a-c** exhibited good stability ( $>300$  °C) with the decomposition temperatures corresponding to 5% weight loss lie at 344 °C for **1a**, 311 °C for **1b** and 331 °C for **1c**.

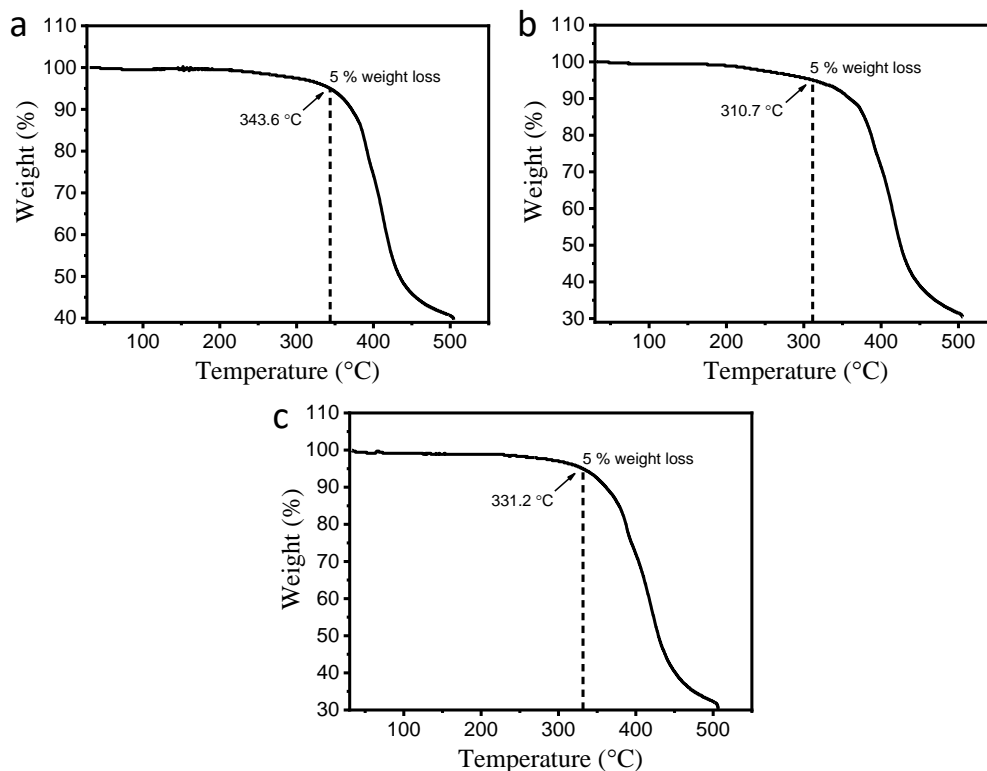


**Figure 6.17** TGA curves recorded under nitrogen atmosphere (scan rate: 10 °C/min) compounds **1a-c** displaying the decomposition temperatures corresponding to the 5% weight loss.

On the other hand, the mesogenic thermal behaviour was studied with the combination of polarized optical microscopy (POM), differential scanning calorimetry (DSC), and X-ray diffraction (XRD) technique. The optical textures of the LC phases were recorded on cooling the sample (rate 10 °C/min) from the isotropic melt. All the compounds showed typical textures of columnar phases formed by discotic LCs (Figure 6.18a,c,e). In DSC, compound **1a** showed one peak on heating at 278.6 °C associated with enthalpy change ( $\Delta H$ ) of 4.5 kJ/mol which corresponds to mesophase to isotropic transition (Figure A19a, Page 388).



**Table 6.6** Thermal behaviour of the tricarboxamide (TCA) DLC materials.<sup>a</sup>

Compound	Heating (°C)	Cooling (°C)	T <sub>c</sub> (°C) <sup>b</sup>
<b>1a</b>	Col <sub>h</sub> 278.64 (4.49) Iso	Iso 252.80 (3.05) Col <sub>h</sub>	344
<b>1b</b>	Col <sub>h</sub> 250.55 (8.01) Iso	Iso 230.68 (1.55) Col <sub>h</sub>	311
<b>1c</b>	Cr -12.5 (3.1) G 54.03 (3.14) Col <sub>h</sub> 210.94 (1.97) Iso	Iso 201.84 (1.71) Col <sub>h</sub> 41.38 (2.40) G -19.1 (2.4) Cr	331

<sup>a</sup>enthalpy in brackets in kJ/mol. <sup>b</sup>decomposition temperatures (T<sub>c</sub>) corresponding to 5% weight loss.

The peak appears reversibly on the cooling cycle at 252.8 °C ( $\Delta H = 3.0$  kJ/mol) indicating the isotropic phase transforms to columnar LC phase which persists beyond room temperature. Upon heating, compound **1b** underwent isotropization at 250.6 °C ( $\Delta H = 8.0$  kJ/mol) and the reappearance of isotropic to mesophase transition peak on cooling was perceived at 230.7 °C ( $\Delta H = 1.6$  kJ/mol) and after that, no other peak observed till a very low temperature. In contrary to compounds **1a** and **1b**, **1c** exhibited one lower temperature peak at 54.03 °C ( $\Delta H = 3.1$  kJ/mol) on the heating scan. The same peak recurred at 41.38 °C ( $\Delta H = 2.4$  kJ/mol) in cooling trace and can be assigned to columnar phase to glassy state transition (as no changes observed in XRD pattern). It is worthy to mention that all the compounds **1a-c** spanned a wide mesomorphic range in the heating as well as in the cooling cycle. The existence of broad enantiotropic mesophases can be attributed to the fact that the presence of electron-withdrawing groups such as cyano creates a local dipole that stabilizes mesophases, increasing the interval of LC phase. The phase transition temperatures with their associated enthalpies are listed in Table 6.6.

The X-ray diffraction pattern of compound **1a** in the mesophase temperature range exhibits three peaks in the small-angle region with  $d$ -spacing in the ratio  $\frac{1}{1} : \frac{1}{\sqrt{4}} : \frac{1}{\sqrt{7}}$  corresponding to reflection from the planes (10), (20), and (21) of the hexagonal lattice (Figure 6.18b,d,f). Moreover, there is one broad peak,  $h_a$ , in wide-angle region of spacing 4.96 Å, which appears due to fluid alkyl chain-chain correlation. And one broad hump  $h_c$ , with spacing 3.85 Å, indicative of the  $\pi$ - $\pi$  interactions between cores. The calculated value of the lattice parameter

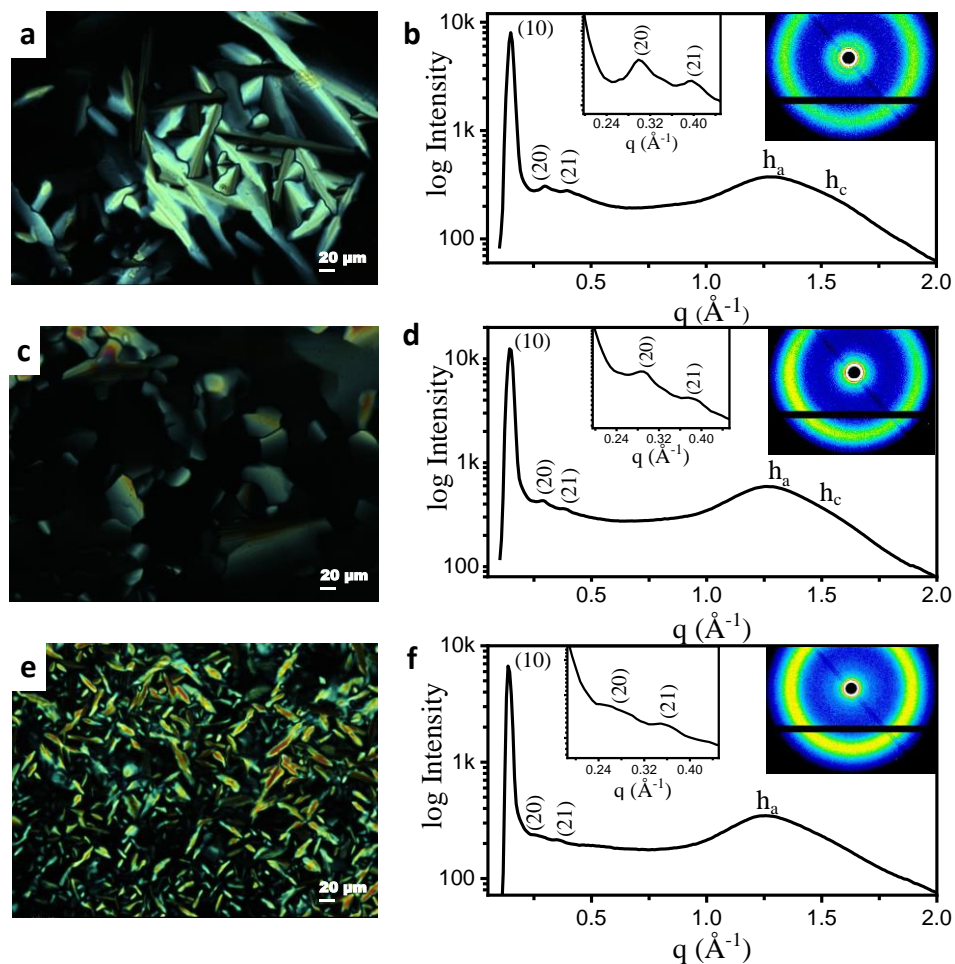


**Figure 6.18** Polarized optical images (POM) for compound (a) **1a**, (c) **1b** and (e) **1c**. 1D and 2D (inset) X-ray diffraction patterns for compound (b) **1a**, (d) **1b** and (f) **1c**.

at temperature 70 °C is found to be to  $a = 48.38 \text{ \AA}$  (Figure 6.18b, Table 6.7). The structure remains columnar hexagonal in the mesophase regime and the lattice parameter is found to be more or less constant with temperature. Similarly, compounds **1b** (Figure 6.18d) and **1c** (Figure 6.18f) were found to exhibit a columnar hexagonal ( $\text{Col}_h$ ) phase throughout the mesophase regime. Moreover, the calculated value of lattice parameter at temperature 60 °C for **1b** and 70 °C for **1c** was found to be  $49.63 \text{ \AA}$  and  $52.58 \text{ \AA}$  (Table 6.7), respectively. The structure remains  $\text{Col}_h$  in the mesophase regime and lattice parameter is found to be more or less constant. Interestingly, the number of correlated columns along the column plane of hexagonal lattice is found to be about six for compounds **1a** and **1b** and about seven for compound **1c**.

Further, to have a better understanding of the arrangement of molecule in hexagonal phase, electron density maps (EDMs) have been constructed by using the information of the

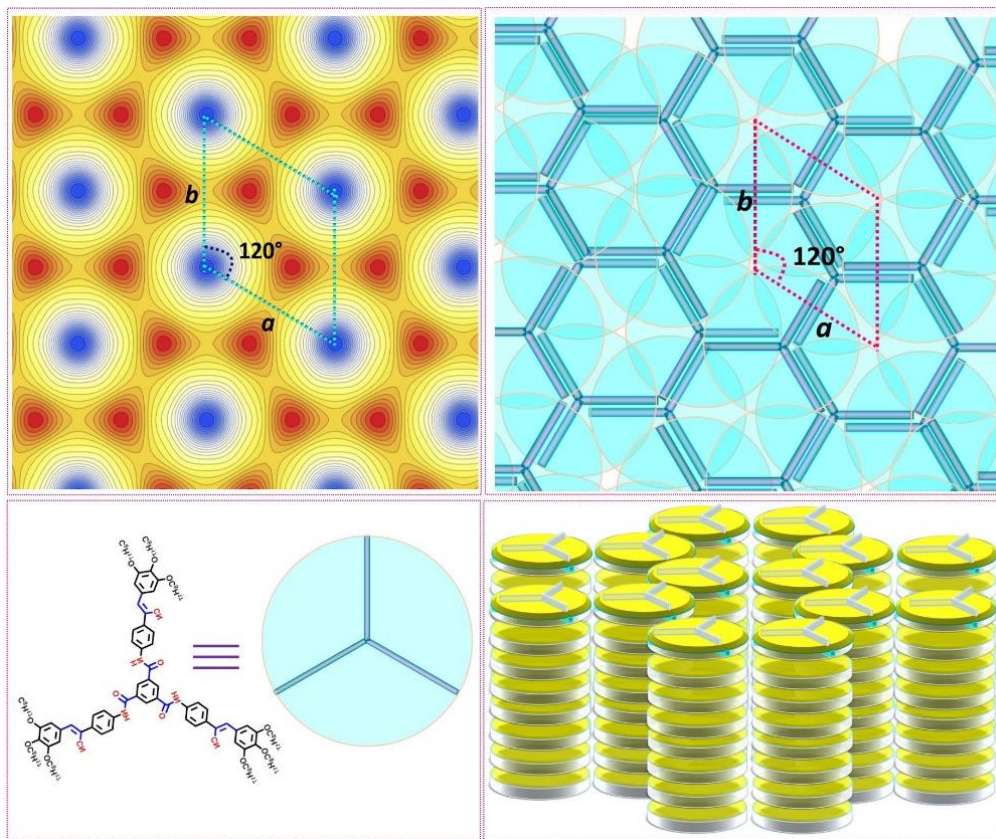


**Figure 6.19** (Top left) Electron density map in the columnar hexagonal phase. (Bottom left) Molecular can be assumed as star-shaped. (Top right) The molecule arranges on a 2D lattice such that the high density i.e. rigid part of the molecule forms the honey-comb structure and the low density i.e. fluid chain part arranged on a 2D hexagonal lattice. The rhombus shows the unit cell which effectively contains two molecules. (Bottom right) Exhibit the three-dimensional arrangement of the molecule.

peaks indexes and intensities.<sup>43,60,62</sup> The representative EDM for compound **1a**, is shown in Figure 6.19. It is clear from the EDM that higher electron density regions exhibit honey-comb structure and the low electron density region forms a regular hexagonal lattice. Thus the proposed model must exhibit a honey-comb structure. Further, we know that the molecular weights of the compounds **1a**, **1b**, and **1c** are 1970.81 g/mol, 2223.29 g/mol, and 2475.77g/mol, respectively and the density of compounds is about 1g/cm<sup>3</sup>. Further, the

calculated lattice parameters of the hexagonal lattice,  $a$  for the compounds **1a**, **1b**, and **1c** are 48.38 Å, 49.63 Å, and 52.58 Å, respectively. The  $c$  parameter can be taken as equal to  $h_c$  which is 3.65 Å. Hence, the volume of the unit cell for the compounds **1a**, **1b**, and **1c** are  $7.3987 \times 10^{-21} \text{ cm}^3$ ,  $7.78596 \times 10^{-21} \text{ cm}^3$ , and  $8.73906 \times 10^{-21} \text{ cm}^3$ , respectively. In order to have a density of about  $1 \text{ g/cm}^3$ , there must be two compounds in each unit cell. If we take two compounds in each unit cell then the calculated value of density for compounds **1a**, **1b**, and **1c** are  $0.88 \text{ g/cm}^3$ ,  $0.95 \text{ g/cm}^3$ , and  $0.94 \text{ g/cm}^3$ , respectively. Thus, it is clear that the arrangement of the molecules is such that they form a honey-comb structure and same time there are two molecules in each unit-cell. Now, the compound can be assumed as star-shaped, and their arrangement on 2D and 3D are shown in Figure 6.19 which is best matching with electron density map and the requirement of two molecules per unit cell for the mass density of about  $1 \text{ g/cm}^3$ .

**Table 6.7** The Miller indices, observed and calculated  $d$ -spacing corresponding to planes of the diffraction peaks of the 2D hexagonal lattice.

Compound	Phase	MI <sup>a</sup> ( $hk$ )	$d_{\text{obs}}^b$ (Å)	$d_{\text{cal}}^c$ (Å)	RI <sup>d</sup> I( $hk$ )	M <sup>e</sup>	$\Phi(hk)^f$
<b>1a</b>	Col <sub>h</sub> (70 °C) $a = 48.38 \text{ Å}$	10	41.90	41.90	100	6	$\pi$
		20	20.93	20.95	3.84	6	$\pi$
		21	15.84	15.84	3.49	12	$\pi$
		$h_a$	4.96		1.00	12	0
		$h_c$	3.65		0.68	6	0
<b>1b</b>	Col <sub>h</sub> (60 °C) $a = 49.63 \text{ Å}$	10	42.98	42.98	100.00	6	$\pi$
		20	21.57	21.49	3.46	6	$\pi$
		21	16.27	16.24	2.89	6	$\pi$
		$h_a$	4.98				
		$h_c$	3.65				
<b>1c</b>	Col <sub>h</sub> (70 °C) $a = 52.58 \text{ Å}$	10	45.54	45.54	100.00	6	$\pi$
		20	22.73	22.77	3.46	6	$\pi$
		21	17.44	17.21	3.19	12	$\pi$
		$h_a$	4.99				

<sup>a</sup>Miller Indices (MI) ( $hk$ ) observed in columnar hexagonal (Col<sub>h</sub>) phase,  $a$  represent unit cell parameters,  $h_a$  &  $h_c$  correspond to chain-chain and core-core correlation, respectively.  
<sup>b</sup> $d_{\text{obs}}$ : experimental  $d$ -spacing. <sup>c</sup> $d_{\text{cal}}$ : calculated  $d$ -spacing using equation:  $\frac{1}{d^2} = \left[ \frac{4}{3} \left( \frac{h^2 + hk + k^2}{a^2} \right) + \frac{l^2}{c^2} \right]$ . <sup>d</sup>Relative intensity (RI). <sup>e</sup>Multiplicity (M). <sup>f</sup>Phase ( $\Phi(hk)$ ).

### 6.2.3.3 Photophysical, electrochemical and theoretical studies

The photophysical behaviour of tricarboxamide derivatives **1a-c** was studied. In thin-film, the absorption and emission maxima for compounds **1a-c** lied in the range of 371-402 nm and 495-502 nm, respectively (Figure 6.20a,b and Figure A20, Appendix VI, Page 389). This indicated that qualitatively, all the derivatives exhibited cyan color emission in a thin-film state.

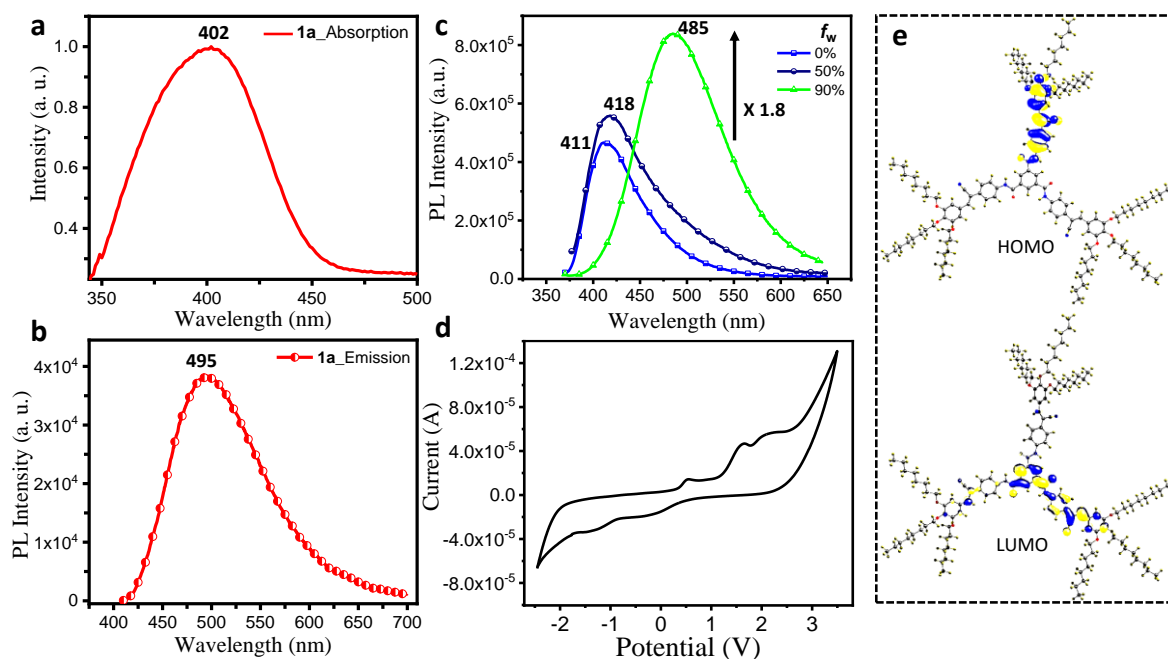


**Figure 6.20** (a) Absorption and (b) emission studies of **1a** in thin-film state prepared by the drop-cast method. (c) Variation of photoluminescence (PL) intensity on adding the different fractions of water into the solution of compound **1a** in THF ( $10^{-6}$  M). (d) Cyclic Voltammogram of **1a** in HPLC dichloromethane solution of tetrabutylammoniumhexafluorophosphate (0.1 M) performed at a scanning rate  $50 \text{ mVs}^{-1}$ . (e) Frontier molecular orbitals of compound **1a** as obtained by the DFT method at B3LYP/6-31G (d,p) level.

The aggregation behaviour of representative compound **1a** was studied for which its emission spectrum was assessed under aggregated conditions. This was done by using various volume ratios of THF/water, ranging from neat THF to water/THF 9:1 (v/v) (Figure 6.20c). It was observed that the intensity of emission was enhanced almost doubled upon increasing the water

fraction from 0 to 90% (v/v). It was also noticed that together with the enhancement in the emission intensity from pure THF to maximum water content, the emission maximum also gets red-shifted from 411 to 485 nm. This clearly indicates the occurrence of aggregation-induced emission enhancement (AIEE) phenomena in the tricarboxamide substituted cyanostilbene derivatives. Due to the presence of mixed electron-donor and acceptor fragments in the molecular structure of the tricarboxamide derivatives, both the oxidation and reduction processes were expected to occur. In cyclic voltammograms of **1a-c** derivatives, the two peaks were observed in the oxidation cycle while one peak in the reduction cycle (Figure 6.20d and Figure A21, Appendix VI, Page 389). The highest and lowest occupied molecular orbitals, i.e. HOMO and LUMO for **1a/1b/1c** were estimated to be -5.36/-5.47/-5.38 eV and -3.49/-3.44/-3.47 eV. The observation of low-lying HOMO and LUMO energy levels clearly indicates the ambipolar nature of the tricarboxamide derivatives. This can be further supported by the spatially separated HOMO and LUMO of **1a** derivative shown in Figure 6.20e.

#### 6.2.3.4 Charge transport properties

The electronic properties of the tricarboxamide-cynaostilbene DLC derivatives were investigated by SCLC technique in solution-processable thin-films. Most of the charge transport studies of DLC derivatives, especially by SCLC technique were performed in the melt-processable samples<sup>61,40, 63-67</sup> and not much explored in solution-processable thin-films<sup>68-70</sup>. For hole and electron mobility measurements, diode device configuration of ITO-PEDOT-PSS (25 nm)-**1a/1b/1c**-(100 nm)-MoO<sub>3</sub> (5nm)/Ag (120nm) for hole-only and ITO-ZnO (30 nm)-**1a/1b/1c** (100 nm)-Ag (120 nm) for electron-only devices were fabricated by spin-coating the solution of **1a-c**. The detailed methods for device fabrication are shown in experimental section 6.2.5. ITO-PEDOT-PSS and ITO-ZnO electrodes were chosen as hole and electron injecting electrodes (Ohmic) based on their work function alignment with the HOMO and LUMO of **1a-c**, respectively. In SCLC technique, when the current density passing through the material under the effect of applied voltage ( $V$ ) varies directly proportional to the square of voltage ( $J \propto V^2$ ) and inversely proportional to the sample thickness  $d$  ( $J \propto 1/d^3$ ), then the mobility can be extracted from the trap-free Mott-Gurney law as:<sup>71</sup>

$$J = \frac{9}{8} \epsilon_r \epsilon_0 \mu \frac{V^2}{d^3} \quad (1)$$

where  $\epsilon_r$  is the relative dielectric constant of the material (3.10 for **1a-c**) and  $\epsilon_0$  is the permittivity of free space,  $J$  is the current per unit area ( $6.6 \text{ mm}^2$ ),  $V$  is the applied voltage and  $d$  is the thickness of the active layer of material (**1a-c**). However, in case shallow traps (related to thermal energy)<sup>72</sup> are present in the material, usually, a higher-order dependence of voltage is observed and the data can be modeled with the modified Mott-Gurney equation (2)<sup>73</sup> where field-dependent charge mobility correction is introduced.

$$J = \frac{9}{8} \epsilon_r \epsilon_0 \mu \frac{V^2}{d^3} \exp(0.891\gamma \sqrt{\frac{V}{d}}) \quad (2)$$

here,  $\gamma$  is the fitting parameter representing the strength of the field dependence of mobility.

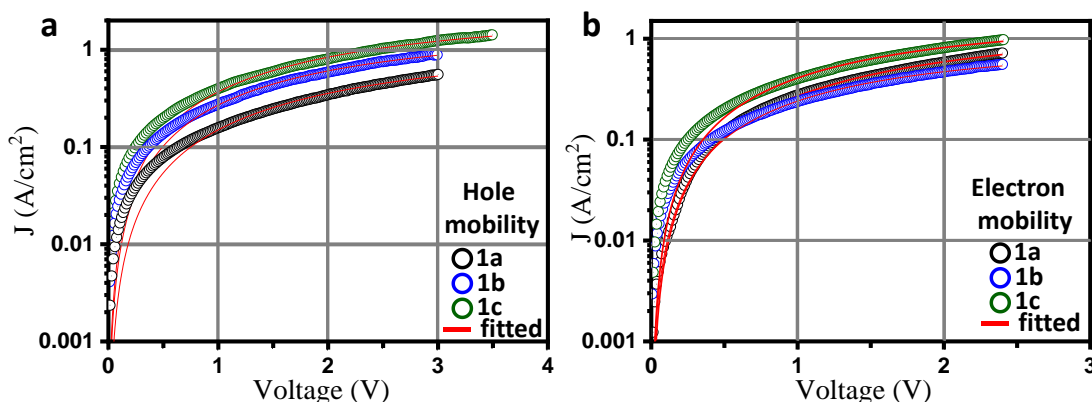


**Figure 6.21**  $J$ - $V$  curves obtained for compounds **1a-c** for (a) hole and (b) electron mobilities extracted from space charge limited current devices.

The hole and electron mobility values for compounds **1a-c** were extracted using the modified Mott-Gurney equation (2) by fitting the measured  $J$ - $V$  curves obtained for hole (Figure 6.21a) and electron (Figure 6.21b) charge carriers. The balanced hole and electron mobilities of order  $10^{-3}$  were observed in all the compounds as listed in Table 6.8. Taking consideration of electron affinity of the central tricarboxamide and side electron-withdrawing cyanovinylene groups, the electron transport can be assumed to originate from these segments.

**Table 6.8** Hole and electron mobility values of compounds **1a-c**.<sup>a</sup>

Compounds	Hole mobility ( $\times 10^{-3} \text{ cm}^2 \text{ V}^{-1} \text{ s}^{-1}$ )	Electron mobility ( $\times 10^{-3} \text{ cm}^2 \text{ V}^{-1} \text{ s}^{-1}$ )
<b>1a</b>	$3.72 \pm 0.50$	$2.34 \pm 1.49$
<b>1b</b>	$3.76 \pm 0.44$	$3.04 \pm 1.23$



<b>1c</b>	$5.30 \pm 0.92$	$2.63 \pm 1.15$
<sup>a</sup> Average mobility values of best five samples (see Table A2 and A3, Appendix VI, Page 390).		

On the other hand, trialkoxy-phenyl units substituted at the peripheral positions are assumed to serve as electron-donating groups that can contribute to the hole mobility.

### 6.2.3.5 Electroluminescent properties

The high thermal, photo-physical, electrochemical, and ambipolar characteristics of novel fluorescent-AIE materials encouraged us to further explore their plausible applications in OLED devices. To further evaluate the overall electroluminescence (EL) performance, solution-processed multilayer doped and non-doped OLED devices were fabricated with an optimized device structure and the energy level diagram of the studied/respective devices were illustrated in Figure 6.22a. Non-doped devices: ITO (125 nm)/ PEDOT:PSS (40 nm)/ **1a** (25 nm)/ TPBi (35 nm)/ LiF (0.5 nm)/ Al (150 nm). Doped devices: ITO (125 nm)/ PEDOT:PSS (40 nm)/ 1.0, 3.0, and 5.0 wt% of **1a** doped in CBP host (25 nm)/ TPBi (35 nm)/ LiF (0.5 nm)/ Al (150 nm). Non-doped devices display poor EL performance and brightness when compared with doped devices. Charge leakage and unbalanced carrier transport across the emissive layer may be a possible reason for unfavourable EL performance. It is well known that the OLED device performance of any fluorescent-AIE emitter highly influences by the doping concentration and host matrix. Table 6.9 summarizes the effect of dopant concentration on the OLED device EL characteristics, including turn-on voltage ( $V_{on}$ ), power efficiency (PE), current efficiency (CE), and external quantum efficiency (EQE). In case of **1a**, the best performing 3.0 wt% based OLED device shows a sky blue emission with a peak at 472 nm in its EL spectra (Figure 6.22b inset) with a maximum luminance ( $L_{max}$ ) of 1255 cd/m<sup>2</sup>, a power efficiency (PE<sub>max</sub>) of 2.0 lm/W, a current efficiency (CE<sub>max</sub>) of 1.9 cd/A, and external quantum efficiency (EQE<sub>max</sub>) of 1.0%. As the dopant concentration increased from 3.0 wt% to 5.0 wt%,



the device EL performance starts to decline, which might be due to the concentration-quenching effect.

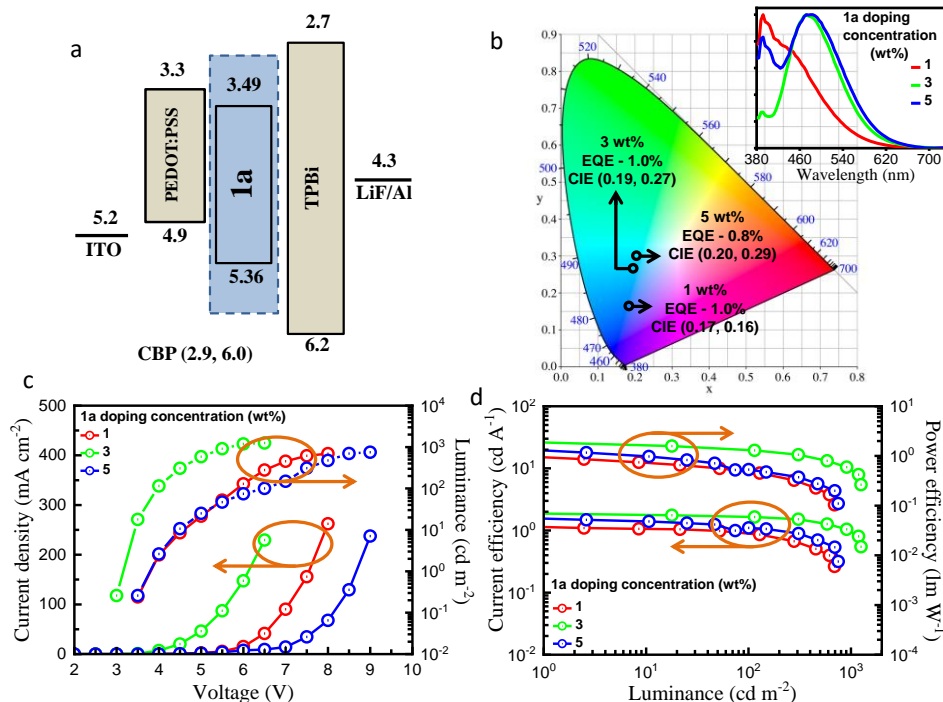


**Figure 6.22.** (a) Schematic illustration of energy level diagram. (b) CIE chromatogram and inset show the EL plots. (c) Current density and luminance versus voltage plots. (d) Current efficiency and power efficiency versus luminance plots for the solution-processed OLED devices using 1, 3 and 5wt% **1a** emitter doped in CBP host.

Furthermore, OLED devices consisting of 1.0 wt% **1a** exhibited an EQE<sub>max</sub> of 1.0%, PE<sub>max</sub> of 1.0 lm/W, and CE<sub>max</sub> of 1.2 cd/m<sup>2</sup>, and L<sub>max</sub> of 693 cd/m<sup>2</sup> with CIE coordinates of (0.17, 0.16). The device fabricated with 5.0 wt% **1a** doped in CBP host showed a relatively low performance with an EQE<sub>max</sub>, PE<sub>max</sub>, and CE<sub>max</sub> of 0.8%, 1.4 lm/W, and 1.6 cd/A, respectively. It can be clearly observed that the current density in the OLED devices is gradually decreased with increasing dopant concentration from 3.0 wt% to 5.0 wt%, inferring that the charge-trapping effect is possibly involved for the EL emission in addition to the energy-transfer process from the host-guest. Since, both HOMO and LUMO energy levels of **1a** are submerged within the HOMO of 6.0 eV and LUMO of 2.9 eV of CBP host and possess a small hole injection barrier of 0.64 eV reasonable for a low V<sub>on</sub> of 3.0 V and high current density device. It indicates the proper dispersion of dopant into the host matrix with the annihilation of aggregation in thin-films and source of emission from the emissive layer. Figure 6.22 shows the EL characteristics

of **1a** based fabricated OLED devices, including *J-V-L* curves, EL spectra, and CIE plot spectrogram. It is interesting to observe a high PE and low  $V_{on}$  for the 3.0 wt% based device.

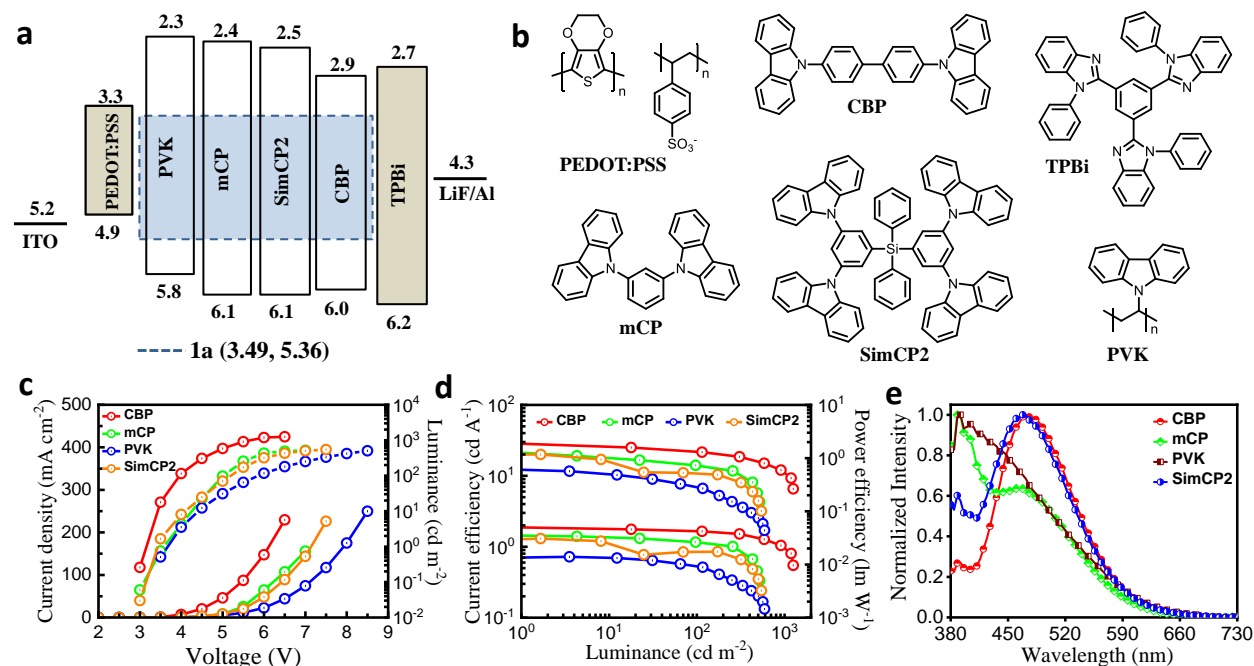


**Figure 6.23** (a) Schematic illustration of Energy-level diagram. (b) Chemical structures of transporting layer materials and various hosts used in fabricating the devices. (c) Current density and luminance versus voltage plots. (d) Current efficiency and power efficiency versus luminance plots. (e) EL plots for the solution-processed OLED devices using 3 wt% **1a** emitter doped in different hosts CBP, mCP, SimCP2 and PVK.

**Table 6.9** Electroluminescent data of **1a** emitter at different dopant concentrations with CBP host and best 3.0 wt% based device with different hosts.

Host	Dopant (wt%)	Turn-on Voltage ( $V_{on}$ )	$PE_{max}/CE_{max}/EQE_{max}$ ( $lm\ W^{-1}/cd\ A^{-1}/\%$ ) <sup>a</sup>	$PE_{100}/CE_{100}/EQE_{100}$ ( $lm\ W^{-1}/cd\ A^{-1}/\%$ ) <sup>b</sup>	CIE coordinates	Max. Lum. ( $cd\ m^{-2}$ ) <sup>c</sup>	
1a	CBP	1	3.7	1.0/ 1.2/ 1.0	0.5/ 0.9/ 1.0	(0.17, 0.16)	693
		3	3.0	2.0/ 1.9/ 1.0	1.3/ 1.7/ 0.9	(0.19, 0.27)	1255
		5	3.7	1.4/ 1.6/ 0.8	0.5/ 1.1/ 0.6	(0.20, 0.29)	751
		100	5.2	-/ -/ -	-/ -/ -	-	2
	mCP	3	3.5	1.3/ 1.4/ 0.9	0.7/ 1.2/ 0.9	(0.19, 0.23)	521
	SimCP2	3	3.3	1.2/ 1.2/ 0.6	0.5/ 0.8/ 0.5	(0.18, 0.24)	545
	PVK	3	3.6	0.6/ 0.7/ 0.4	0.3/ 0.5/ 0.4	(0.20, 0.22)	591

Power efficiency, current efficiency and external quantum efficiency at maximum luminance<sup>a</sup> and at 100  $cd\ m^{-2}$  luminance<sup>b</sup>. <sup>c</sup>Maximum luminance.

Additionally, the EL performance of **1a** is further optimized through employing different hosts, mCP, PVK, and SimCP2 (Figure 6.23a,b). Figure 6.23a illustrates the schematic energy level diagram of the studied OLED devices with different hosts. The CBP-based device exhibited an EQE<sub>max</sub> of 1.0%, which was declined to 0.9%, 0.6%, and 0.4% as the host altered to mCP, SimCP2, and PVK, respectively. The employed host displays a significant impact on the overall device EL performance. For example, the optimized doping concentration 3.0 wt% of **1a**, the CBP containing device achieved a PE<sub>max</sub> of 2.0 lm/W, CE<sub>max</sub> of 1.9 cd/A, and EQE<sub>max</sub> of 1.0%, as shown in Table 6.9. The expected reasons why the CBP-based devices displayed better EL performance compared to other counterparts, may be attributed to the following key factors.<sup>74</sup> The CBP host possesses a LUMO (-2.90 eV) lower than that of the TPBi (-2.70 eV), leading to a favourable electron injection alleyway, i.e. a well-shaped structure with -0.20 eV electron trap, whereas other host materials possess a higher electron migration barrier of 0.20-0.40 eV. The overlapping region for the CBP-based devices is significantly higher than that of the counter hosts. It reveals that CBP-based devices enable effective energy transfer mechanisms. Furthermore, CBP possesses higher charge carrier mobilities than the other host materials, this characteristic may lead to a much effective exciton recombination generation. Figure 6.23c-e displays the EL characteristics of the 3.0 wt% of **1a** based devices employed within different host materials.

## 6.2.4 Conclusions

In conclusion, we have reported C<sub>3</sub>-symmetric tricarboxamide core substituted cyanostilbene based luminophoric liquid crystalline derivatives. All three derivatives exhibited room temperature columnar hexagonal behaviour over a wide mesomorphic range. When employed as emissive materials in OLEDs, sky-blue colored emission was observed and SCLC measurements revealed ambipolar charge transport with balanced hole and electron mobilities for all three compounds.

**Acknowledgements.** *Some part of this work has been included in Master thesis of Ms. Harpreet Kaur (MS15179) at IISER Mohali. The OLED device studies and SCLC measurements carried out in collaboration with Prof. J. H Jou's group (at National Tsing Hua University, Taiwan) and Dr. Upendra Kumar Pandey (at Shiv Nadar University) are greatly acknowledged and*

respected. Dr. Santosh Prasad Gupta (at Patna University) is duly acknowledged for the analysis of XRD data.

### 6.2.5 Experimental section

All other precursor materials **2a-c**,<sup>75</sup> **3a-c**<sup>76</sup>, and **4a-c**<sup>77</sup> are synthesized as per the cited references.

**6.2.5.1 Synthesis of target materials 1a-c.** Trimesoyl chloride (0.24 g, 1 equiv.) in dry DCM (4 ml) was slowly added to a solution of **4a** (2 g, 2.90 mmol) in dry DCM (10 ml). After 5 minutes, trimethylamine (3.2 equiv.) was added. The mixture was left for stirring at room temperature for 20 hours and then purified by column chromatography in silica gel (60-120 mesh).

Compound **1a**: **<sup>1</sup>H NMR (400 MHz, CDCl<sub>3</sub>,  $\delta$  ppm)**: 9.07 (s, 3H), 8.45 (s, 3H), 7.74-7.73 (d, 6H), 7.54-7.52 (d, 6H), 7.30 (s, 3H), 7.04 (s, 6H), 3.98-3.94 (m, 18H), 1.82-1.73 (m, 18H), 1.43-1.42 (m, 18H), 1.27 (broad s, 72H), 0.87-0.85 (m, 27H). **<sup>13</sup>C NMR (100 MHz, CDCl<sub>3</sub>,  $\delta$  ppm)**: 164.50, 153.15, 153.06, 141.89, 140.2, 138.42, 130.87, 128.57, 126.34, 120.86, 118.69, 108.63, 107.75, 73.77, 69.19, 32.05, 31.99, 30.49, 29.83, 29.70, 29.59, 29.53, 29.46, 26.28, 26.19, 22.81. **MALDI-MS**:  $m/z$  calcd for C<sub>126</sub>H<sub>180</sub>N<sub>6</sub>O<sub>12</sub> (M+Na): 1992.3557. Found: 1992.3573

Compound **1b**: **<sup>1</sup>H NMR (400 MHz, CDCl<sub>3</sub>,  $\delta$  ppm)**: 8.96 (s, 3H), 8.47 (s, 3H), 7.77-7.75 (d, 6H,  $J = 6.12$  Hz), 7.57-7.55 (d, 6H,  $J = 6.80$  Hz), 7.33 (s, 3H), 7.06 (s, 6H), 3.99-3.97 (m, 18H), 1.75-1.70 (m, 18H), 1.44-1.43 (m, 18H), 1.25 (broad s, 108H), 0.87-0.84 (t, 27H,  $J = 5.52$  Hz). **<sup>13</sup>C NMR (100 MHz, CDCl<sub>3</sub>,  $\delta$  ppm)**: 164.56, 153.16, 153.06, 141.92, 140.19, 138.44, 130.86, 128.56, 126.36, 120.83, 118.72, 108.53, 107.75, 73.76, 69.18, 32.07, 30.50, 29.92, 29.84, 29.79, 29.67, 29.56, 29.53, 26.31, 26.22, 22.83. **MALDI-MS**:  $m/z$  calcd for C<sub>144</sub>H<sub>216</sub>N<sub>6</sub>O<sub>12</sub> (M+Na): 2244.6374. Found: 2244.6482.

Compound **1c**: **<sup>1</sup>H NMR (400 MHz, CDCl<sub>3</sub>,  $\delta$  ppm)**: 8.81 (s, 3H), 8.52 (s, 3H), 7.77-7.76 (d, 6H,  $J = 6.28$  Hz), 7.60-7.58 (d, 6H,  $J = 7.08$  Hz), 7.34 (s, 3H), 7.08 (s, 6H), 4.00-3.98 (m, 18H), 1.77 (m, 18H), 1.44 (m, 18H), 1.25 (broad s, 144H), 0.87-0.84 (m, 27H). **<sup>13</sup>C NMR (100 MHz, CDCl<sub>3</sub>,  $\delta$  ppm)**: 153.05, 152.99, 140.14, 138.28, 130.88, 128.45, 126.32, 120.77, 118.58, 108.49, 107.67, 73.67, 69.18, 59.52, 38.15, 31.96, 31.26, 30.39, 29.82, 29.78,

29.55, 29.43, 26.20, 26.11, 22.73, 14.15. **MALDI-MS:**  $m/z$  calcd for  $C_{144}H_{216}N_6O_{12}$  (M+Na): 2496.9191. Found: 2496.9070.

**6.2.5.2. SCLC device fabrication.** The charge transport properties of **1a-c** were investigated by SCLC technique. The device configurations of ITO-PEDOT-PSS-**1a/1b/1c**-MoO<sub>3</sub>/Ag for hole-only and ITO-ZnO-**1a/1b/1c**-Ag for electron-only devices were employed. For that, pre-patterned indium tin oxide (ITO) (Xinyan Technologies, Taiwan, 15  $\Omega/\text{cm}^2$ ) were first cleaned using 5% soap solution (Hellmanex<sup>TM</sup> III, Sigma Aldrich), deionized water, acetone and isopropyl alcohol (IPA) in an ultrasonicator in a sequential manner. Cleaned substrates were then dried using a gentle blow of nitrogen gas followed by 20 min of UV ozone (Nova Scan PSD- Pro Series) treatment at 50 °C in order to remove residues. The electron-only devices were fabricated as follows, the prepared Zinc oxide (ZnO) sol-gel solution was first filtrated through a 0.45  $\mu\text{m}$  nylon filter and then spin-coated with a spin speed of 4500 rpm for 60 sec to form a thin layer of around 28 nm thickness. The spin-coated substrates were then baked at 180 °C for 1 hr at ambient conditions. The active layer of **1a/1b/1c** was prepared by spin-coating the solution of compounds (**1a/1b/1c**) (10 mg/ml) in anhydrous chloroform on top of ZnO coated substrates at 1000 rpm for 60 sec forming ~ 90 nm thick layer. Thickness of all the layers was measured using Dektak surface profiler. Finally, the space charge limited current (SCLC) devices were completed by evaporating 120 nm of Ag at  $1 \times 10^{-6}$  mbar pressure using thermal evaporator. The active area of the fabricated devices was 6.6 mm<sup>2</sup>. Similarly, the preparation of hole-only devices was commenced from the deposition of PEDOT-PSS layer by spin-coating its filtered solution onto pre-cleaned and UV-ozone treated ITO substrates with a spin speed of 4500 rpm for 60 sec, fetching the layer thickness of 25 nm. PEDOT-PSS coated substrates were then baked at 140 C on hot plate for 15 min. The active layer of **1a/1b/1c** was spin-coated with layer thickness of 100 nm. After the complete drying of the active layer, a 5 nm layer of MoO<sub>3</sub> and 120 nm layer of Al was evaporated on top of active layer.

Current-voltage ( $J$ - $V$ ) characteristics were performed immediately on the completed sample using Keithley 2436 B dual-channel source meter. The dielectric constant of materials **1a-c** was extracted from capacitance-voltage characteristics ( $\epsilon_r \sim 3.10$ ) using high-frequency LCR meter ZM2376 (NF Corporation) with an applied oscillation level voltage of 1 V and frequency sweep from 20 Hz to 2 MHz.

**6.2.5.3. OLED device fabrication.** All the solution-processed OLED devices were fabricated on indium-tin-oxide (ITO) coated glass substrates were employed as anode, which was sequentially cleaned in an ultrasonication bath with the detergent solution, deionized water (10 min), acetone (30 min, 50 °C), and isopropanol (30 min, 60 °C). Subsequently, the as-cleaned substrates were treated by ultraviolet (UV) ozone for 15 min and then poly(3,4-ethylenedioxythiophene)/polystyrenesulfonate (PEDOT:PSS) was spin-coated (4000 rpm, 20 sec) onto the substrates from an aqueous solution, which was then baked at 120 °C for 15 min inside the nitrogen maintained glove box. Afterward, the emissive layer (CBP: x wt% emitter; x = 1.0, 3.0, 5.0, and 100) was spin-coated onto the PEDOT:PSS layer. Finally, TPBi (35 nm), LiF (0.5 nm), and Al (150 nm) layers were constructively deposited via a thermal evaporation process and the effective device area is 0.9 cm<sup>2</sup>. PEDOT:PSS acted as the hole transporting material (HTM), 2,2',2''-(1,3,5-benzinetriyl)-tris(1-phenyl-1-H-benzimidazole) (TPBi) was employed as electron transporting material (ETM), and 4,4'-Bis(N-carbazolyl)-1,1'-biphenyl (CBP) as the host matrix. The device characterizations and measurements were carried out at room temperature (RT) under ambient conditions without any encapsulation. The EL spectra were recovered through an optical analyzer, Photo Research PR745. The current-density and luminance versus applied voltage characteristics were measured by Keithley 2400 and Konica Minolta Chromameter CS200, respectively.

## References

1. Uoyama, H.; Goushi, K.; Shizu, K.; Nomura, H.; Adachi, C. *Nature* **2012**, *492*, 234-238.
2. Zhang, Q.; Li, B.; Huang, S.; Nomura, H.; Tanaka, H.; Adachi, C. *Nat. Photonics* **2014**, *8*, 326-332.
3. Zhang, Q.; Li, J.; Shizu, K.; Huang, S.; Hirata, S.; Miyazaki, H.; Adachi, C. *J. Am. Chem. Soc.* **2012**, *134*, 14706-14709.
4. Luo, J.; Xie, G.; Gong, S.; Chen, T.; Yang, C. *Chem. Commun.* **2016**, *52*, 2292-2295.
5. Li, Y.; Xie, G.; Gong, S.; Wu, K.; Yang, C. *Chem. Sci.* **2016**, *7*, 5441-5447.
6. Tao, Y.; Yuan, K.; Chen, T.; Xu, P.; Li, H.; Chen, R.; Zheng, C.; Zhang, L.; Huan, W. *Adv. Mat.* **2014**, *26*, 7931-7958.
7. Wang, H.; Xie, L.; Peng, Q.; Meng, L.; Wang, Y.; Yi, Y.; Wang, P. *Adv. Mater.* **2014**, *26*, 5198-5204.
8. Wang, S.; Yan, X.; Cheng, Z.; Zhang, H.; Liu, Y.; Wang, Y. *Angew. Chem. Int. Ed.* **2015**, *54*, 13068-13072.
9. Luo, J.; Gong, S.; Gu, Y.; Chen, T.; Li, Y.; Zhong, C.; Xie, G.; Yang, C. *J. Mater. Chem. C* **2016**, *4*, 2442-2446.
10. Li, W.; Liu, D.; Shen, F.; Ma, D.; Wang, Z.; Feng, T.; Xu, Y.; Yang, B.; Ma, Y. *Adv. Funct. Mater.* **2012**, *22*, 2797-2803.
11. Zhang, H.; Zeng, J.; Luo, W.; Wu, H.; Zeng, C.; Zhang, K.; Feng, W.; Wang, Z.; Zhao, Z.; Tang, B. Z. *J. Mater. Chem. C* **2019**, *7*, 6359-6368.
12. Wang, C.; Li, X.; Pan, Y.; Zhang, S.; Yao, L.; Bai, Q.; Li, W.; Lu, P.; Yang, B.; Su, S.; Ma, Y. *ACS Appl. Mater. Interfaces* **2016**, *8*, 3041-3049.
13. Zhang, S.; Li, W.; Yao, L.; Pan, Y.; Shen, F.; Xiao, R.; Yang, B.; Ma, Y. *Chem. Commun.* **2013**, *49*, 11302-11304.
14. Zhang, S.; Yao, L.; Peng, Q.; Li, W.; Pan, Y.; Xiao, R.; Gao, Y.; Gu, C.; Wang, Z.; Lu, P.; Li, F. *Adv. Funct. Mater.* **2015**, *25*, 1755-1762.
15. Tang, X.; Bai, Q.; Peng, Q.; Gao, Y.; Li, J.; Liu, Y.; Yao, L.; Lu, P.; Yang, B.; Ma, Y. *Chem. Mater.* **2015**, *27*, 7050-7057.

16. Konidena, R. K.; Thomas, K. J.; Dubey, D. K.; Sahoo, S.; Jou, J. H. *Chem. Commun.* **2017**, 53, 11802-11805.
17. Li, W.; Pan, Y.; Yao, L.; Liu, H.; Zhang, S.; Wang, C.; Shen, F.; Lu, P.; Yang, B.; Ma, Y. *Adv. Opt. Mater.* **2014**, 2, 892-901.
18. Yao, L.; Zhang, S. T.; Wang, R.; Li, W. J.; Shen, F. Z.; Yang, B.; Ma, Y. *Angew. Chem.* **2014**, 126, 2151-2155.
19. Zhang, X.; Gorohmaru, H.; Kadowaki, M.; Kobayashi, T.; Ishi-i, T.; Thiemann, T.; Mataka, S. *J. Mater. Chem.* **2004**, 14, 1901-1904.
20. Wang, J. L.; Xiao, Q.; Pei, J. *Org. lett.* **2010**, 12, 4164-4167.
21. da Cunha, M. P.; Do, T. T.; Yambem, S. D.; Pham, H. D.; Chang, S.; Manzhos, S.; Katoh, R.; Sonar, P. *Mater. Chem. Phys.* **2018**, 206, 56-63.
22. Sonar, P.; Singh, S. P.; Leclere, P.; Surin, M.; Lazzaroni, R.; Lin, T. T.; Dodabalapur, A.; Sellinger, A. *J. Mater. Chem.* **2009**, 19, 3228-3237.
23. Wan, Q.; Tong, J.; Zhang, B.; Li, Y.; Wang, Z.; Tang, B. Z. *Adv. Opt. Mat.* **2020**, 8, 1901520.
24. Findlay, N. J.; Breig, B.; Forbes, C.; Inigo, A. R.; Kanibolotsky, A. L.; Skabara, P. *J. J. Mater. Chem. C* **2016**, 4, 3774-3780.
25. Pathak, A.; Justin Thomas, K. R.; Singh, M.; Jou, J. H. *J. Org. Chem.* **2018**, 82, 11512-11523.
26. Justin Thomas, K. R.; Lin, J. T.; Velusamy, M.; Tao, Y. T.; Chuen, C. H. *Adv. Funct. Mater.* **2004**, 14, 83-90.
27. Huang, J.; Qiao, X.; Xia, Y.; Zhu, X.; Ma, D.; Cao, Y.; Roncali, J. *Adv. Mater.* **2008**, 20, 4172.
28. Huang, J.; Li, C.; Xia, Y. -J.; Zhu, X. -H.; Peng, J.; Cao, Y. *J. Org. Chem.* **2007**, 72, 8580.
29. Zhou, Y.; He, Q.; Yang, Y.; Zhong, H.; He, C.; Sang, G.; Liu, W.; Yang, C.; Bai, F.; Li, Y. *Adv. Funct. Mater.* **2008**, 18, 3299.
30. Bryant, J. J.; Lindner, B. D.; Bunz, U. H. *J. Org. Chem.* **2013**, 78, 1038-1044.
31. Shi, E.; Gao, Z.; Yuan, M.; Wang, X.; Wang, F. *Polym. Chem* **2015**, 6, 5575-5579.
32. Huang, D.; Prehm, M.; Gao, H.; Cheng, X.; Liu, Y.; Tschierske, C. *RSC adv.* **2016**, 6, 21387-21395.



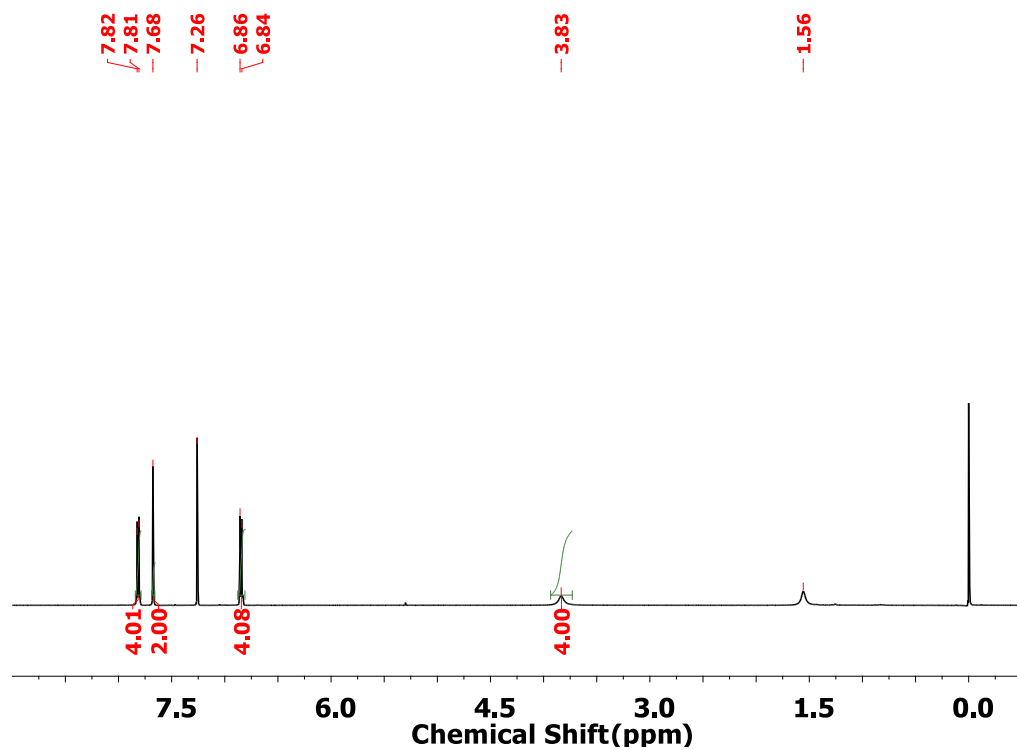
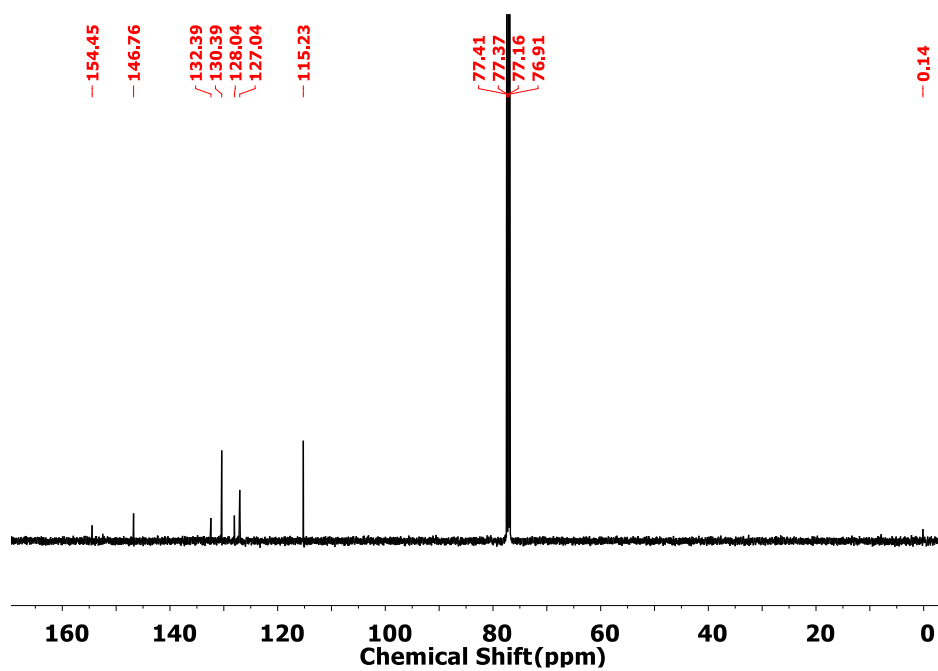
33. Echeverri, M.; Martín, I.; Concellón, A.; Ruiz, C.; Anselmo, M. S.; Gutiérrez-Puebla, E.; Serrano, J. L.; Gómez-Lor, B. *ACS Omega* **2018**, *3*, 11857–11864.
34. Hu, J.; Xiao, Y.; Chang, Q.; Gao, H.; Cheng, X. *J. Mol. Liq.* **2019**, *286*, 110844.
35. Du, J.; Biewer, M. C.; Stefan, M. C. *J. Mater. Chem. A* **2016**, *4*, 15771.
36. Ishi-i, T.; Nakamura, N.; Mine, T.; Imamura, S.; Shigeiwa, M.; Gorohmaru, H.; Maeda, S. *Chem. Lett.* **2009**, *38*, 1042-1043.
37. Wu, J.; Lai, G.; Li, Z.; Lu, Y.; Leng, T.; Shen, Y.; Wang, C. *Dyes Pigm.* **2016**, *124*, 268-276.
38. Grabowski, Z. R.; Rotkiewicz, K.; Rettig, W. *Chem. Rev.* **2003**, *103*, 3899-4032.
39. Pham, H. D.; Hu, H.; Wong, F. L.; Lee, C. S.; Chen, W. C.; Feron, K.; Manzhos, S.; Wang, H.; Motta, N.; Lam, Y. M.; Sonar, P. *J. Mater. Chem. C* **2018**, *6*, 9017-9029.
40. De, J.; Bala, I.; Gupta, S. P.; Pandey, U. K.; Pal, S. K. *J. Am. Chem. Soc.* **2019**, *141*, 18799.
41. Dubey, D. K.; Krucaite, G.; Swayamprabha, S. S.; Yadav, R. A. K.; Blazeivicius, D.; Tagare, J.; Chavhan, S.; Hsueh, T. C.; Vaidyanathan, S.; Grigalevicius, S.; Jou, J. H. *Org. Electron* **2020**, *79*, 105633.
42. Bala, I.; Singh, N.; Yadav, R. A. K.; De, J.; Gupta, S. P.; Singh, D. P.; Dubey, D. K.; Jou, J. H.; Douali, R.; Pal, S. K. *J. Mater. Chem. C* **2020**, *8*, 12485-12494.
43. Bala, I.; Yang, W. Y.; Gupta, S. P.; De, J.; Yadav, R. A. K.; Singh, D. P.; Dubey, D. K.; Jou, J. H.; Douali, R.; Pal, S. K. *J. Mater. Chem. C* **2019**, *7*, 5724-5738.
44. Liu, Z.; Zhang, G.; Zhang, D., *Chem. Eur. J.* **2016**, *22*, 462-471.
45. Zhang, C.; Chen, P.; Hu, W. *Small* **2016**, *12*, 1252-1294.
46. Zhang, W.; Yao, J.; Zhao, Y. S. *Acc. Chem. Res.* **2016**, *49*, 1691-1700.
47. Hoebe, F. J. M.; Jonkheijm, P.; Meijer, E. W.; Schenning, A. P.H. *Chem. Rev.* **2005**, *105*, 1491-1546.
48. Thomas, S. W.; Joly, G. D.; Swager, T. M. *Chem. Rev.* **2007**, *107*, 1339-1386.
49. Kumar, S. *Chem. Soc. Rev.* **2006**, *35*, 83-109.
50. Wo'hrle, T.; Wurzbach, I.; Kirres, J.; Kostidou, A.; Kapernaum, N.; Litterscheidt, J.; Haenle, J. C.; Staffeld, P.; Baro, A.; Giesselmann, F.; Laschat, S. *Chem. Rev.* **2015**, *116*, 1139-1241.

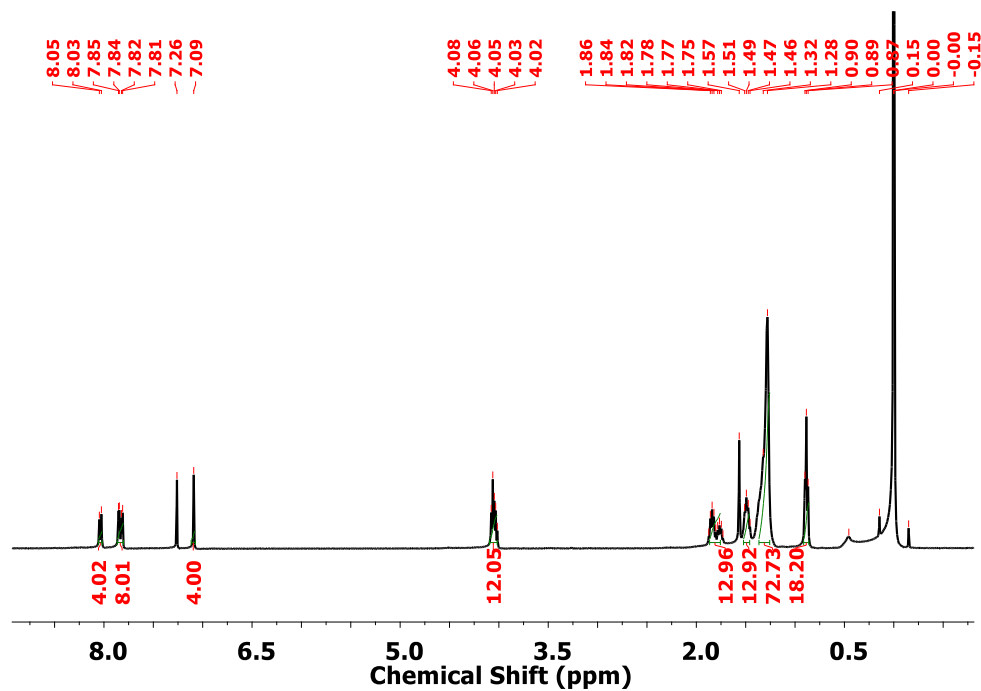
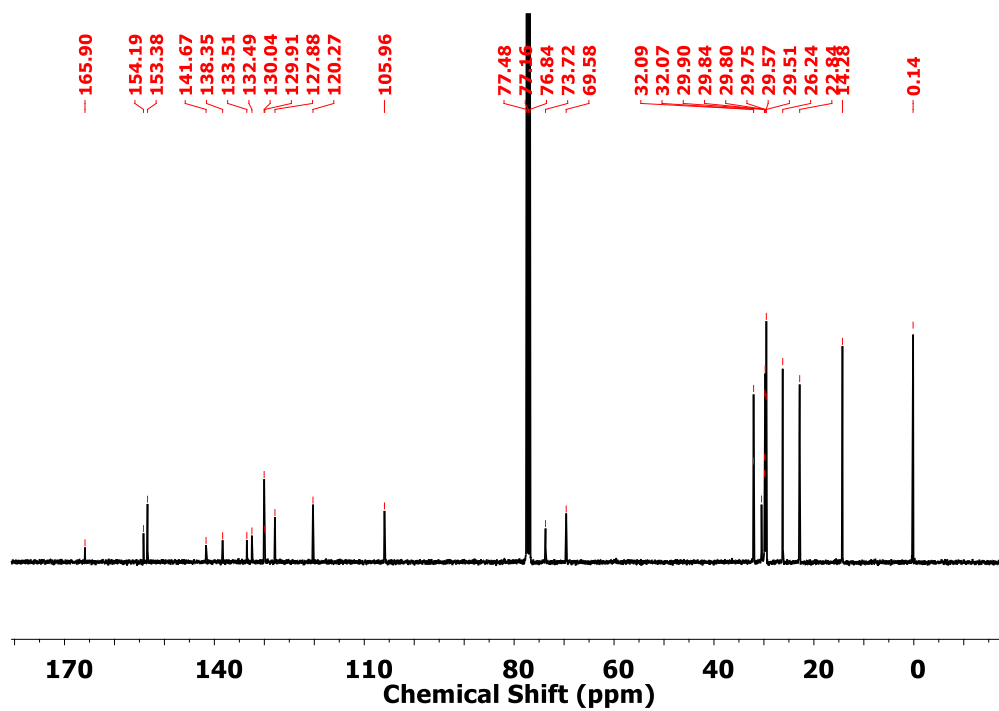
51. Kaafarani, B. R. *Chem. Mater.* **2010**, *23*, 378-396.
52. Setia, S.; Sidiq, S.; De, J.; Pani, I.; Pal, S. K. *Liq. Cryst.* **2016**, *43*, 2009-2050.
53. Ding, Z.; Ma, Y.; Shang, H.; Zhang, H.; Jiang, S. *Chem. Eur. J.* **2019**, *25*, 315-322.
54. Gopinath, A.; Ramamurthy, K.; Subaraja, M.; Selvaraju, C.; Nasar, A. S. *New J. Chem.* **2018**, *42*, 10243-10253.
55. Lu, H.; Qiu, L.; Zhang, G.; Ding, A.; Xu, W.; Zhang, G.; Wang, X.; Kong, L.; Tian, Y.; Yang, J. *J. Mater. Chem. C* **2014**, *2*, 1386-1389.
56. Gupta, R. K.; Pathak, S. K.; De, J.; Pal, S. K.; Achalkumar, A. S. *J. Mater. Chem. C* **2018**, *6*, 1844-1852.
57. Cho, H. H.; Kim, S.; Kim, T.; Sree, V. G.; Jin, S. H.; Kim, F. S.; Kim, B. J. *Adv. Energy Mater.* **2018**, *8*, 1701436.
58. Mativetsky, J. M.; Kastler, M.; Savage, R. C.; Gentilini, D.; Palma, M.; Pisula, W.; Müllen, K.; Samorì, P. *Adv. Funct. Mater.* **2009**, *19*, 2486-2494.
59. Dadvand, A.; Moiseev, A. G.; Sawabe, K.; Sun, W. H.; Djukic, B.; Chung, I.; Takenobu, T.; Rosei, F.; Perepichka, D. F. *Angew. Chem. Int. Ed.* **2012**, *51*, 3837-3841.
60. Devi, S.; Bala, I.; Gupta, S. P.; Kumar, P.; Pal, S. K.; Venkataramani, S. *Org. Bio. Chem.* **2020**, *17*, 1947-1954.
61. Bala, I.; De, J.; Gupta, S. P.; Singh, H.; Pandey, U. K.; Pal, S. K. *Chem. Commun.* **2020**, *56*, 5629-5632.
62. Gupta, S. P.; Gupta, M.; Pal, S. K. *ChemistrySelect* **2017**, *2*, 6070-6077.
63. An, Z.; Yu, J.; Jones, S. C.; Barlow, S.; Yoo, S.; Domercq, B.; Prins, P.; Siebbeles, L. D.; Kippelen, B.; Marder, S. R. *Adv. Mater.* **2005**, *17*, 2580-2583.
64. Demenev, A.; Eichhorn, S. H.; Taerum, T.; Perepichka, D. F.; Patwardhan, S.; Grozema, F. C.; Siebbeles, L. D.; Klenkler, R. *Chem. Mater.* **2010**, *22*, 1420-1428.
65. Domercq, B.; Yu, J.; Kaafarani, B. R.; Kondo, T.; Yoo, S.; Haddock, J. N.; Barlow, S.; Marder, S. R.; Kippelen, B. *Mol. Cryst. Liq. Cryst.* **2008**, *481*, 80-93.
66. Gracia, I.; Feringán, B.; Serrano, J. L.; Termine, R.; Golemme, A.; Omenat, A.; Barberá, J. *Chem. Eur. J.* **2015**, *21*, 1359-1369.
67. Muth, M. A.; Gupta, G.; Wicklein, A.; Carrasco-Orozco, M.; Thurn-Albrecht, T.; Thelakkat, M. *J. Phys. Chem. C* **2014**, *118*, 92-102.

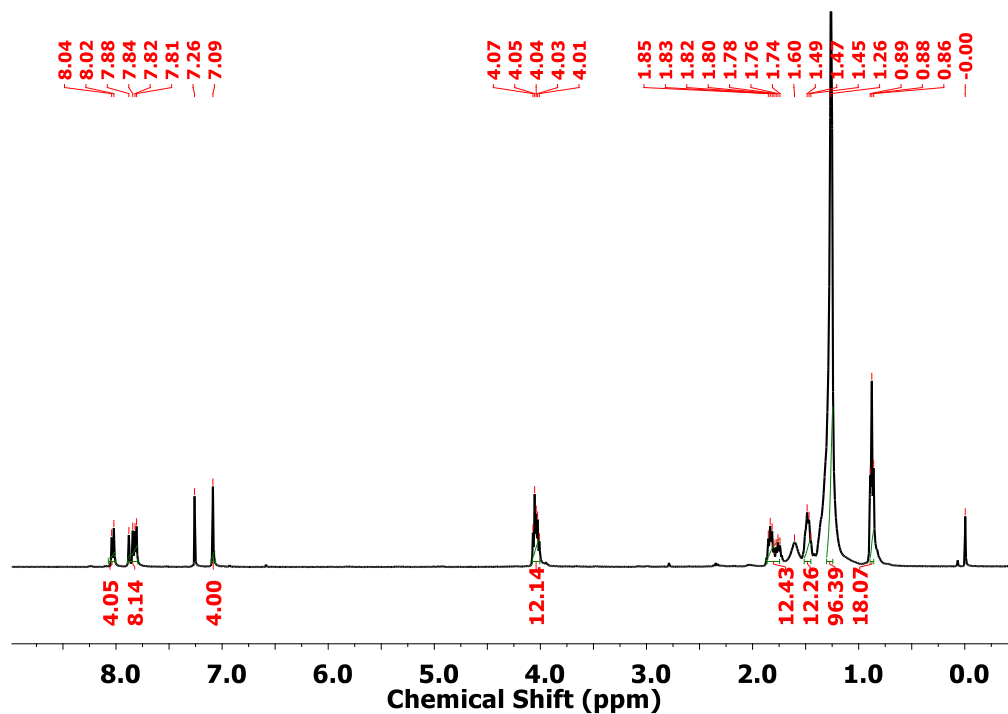
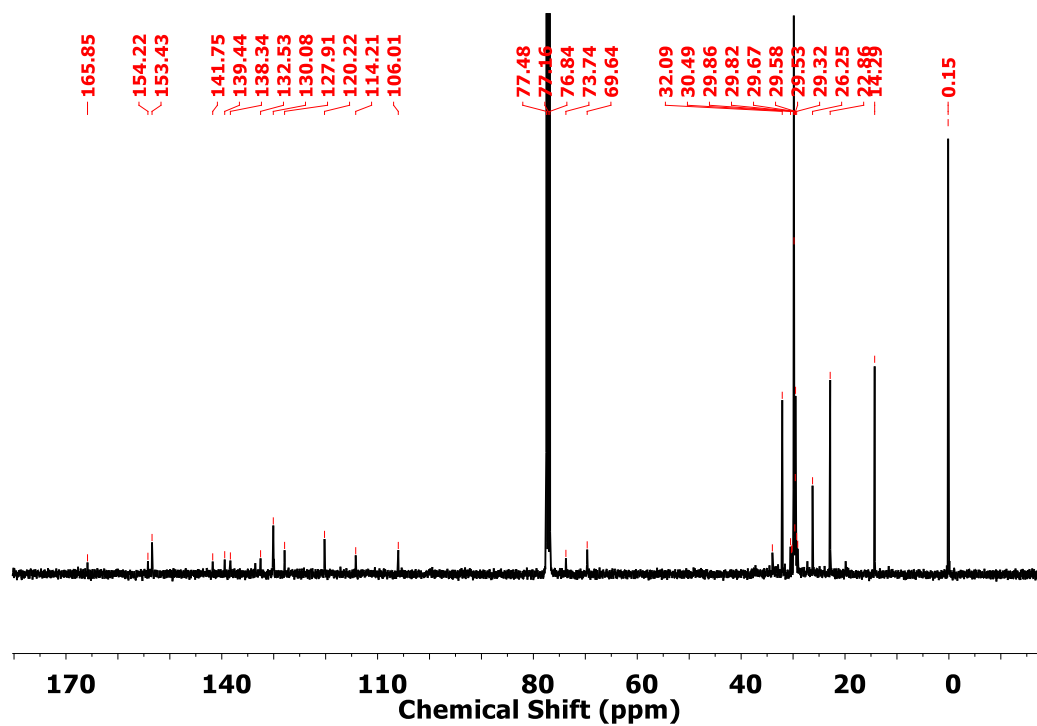
68. Shao, J.; Chang, J.; Chi, C. *Org. Bio. Chem.* **2012**, *10*, 7045-7052.
69. Khan, A. A.; Rughoobur, G.; Kamarudin, M. A.; Sepe, A.; Dolan, J. A.; Flewitt, A. J.; Qasim, M. M.; Wilkinson, T. D. *Org. Electron.* **2016**, *36*, 35-44.
70. Zhao, L.; Yang, B.; Zeng, L.; Luo, K.; Wang, H.; Ni, H.; Yang, C.; Li, Q. *Dyes Pigm.* **2019**, *164*, 398-406.
71. Mott, N. F., RW Gurney *Electronic Processes in Ionic Crystals* Oxford University Press. *New York*, **1940**.
72. Moiz, S. A.; Khan, I. A.; Younis, W. A.; Karimov, K. S. *Conducting Polymers* **2016**, 91.
73. Murgatroyd, P. N. *J. Phys. D* **1970**, *3*, 151.
74. Bala, I.; Ming, L.; Yadav, R. A. K.; De, J.; Dubey, D. K.; Kumar, S.; Singh, H.; Jou, J. H.; Kailasam, K.; Pal, S. K. *ChemistrySelect* **2018**, *3*, 7771-7777.
75. Bala, I.; De, J.; Gupta, S. P.; Singh, H.; Pandey, U. K.; Pal, S. K. *Chem. Commun.* **2020**, *56*, 5629-5632.
76. Gupta, R. K.; Pathak, S. K.; De, J.; Pal, S. K.; Achalkumar, A. S. *J. Mater. Chem. C* **2018**, *6*, 1844-1852.
77. Ding, Z.; Ma, Y.; Shang, H.; Zhang, H.; Jiang, S. *Chem. Eur. J.* **2019**, *25*, 315-322.

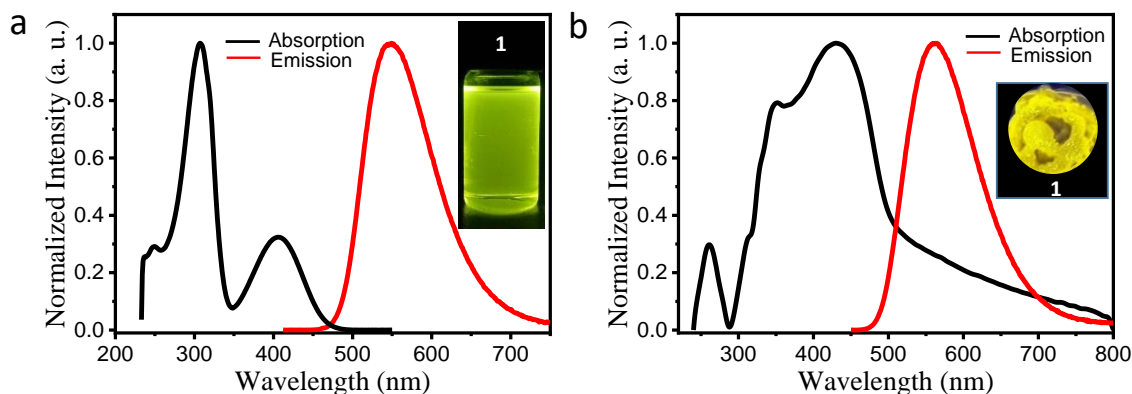


## Appendix VI

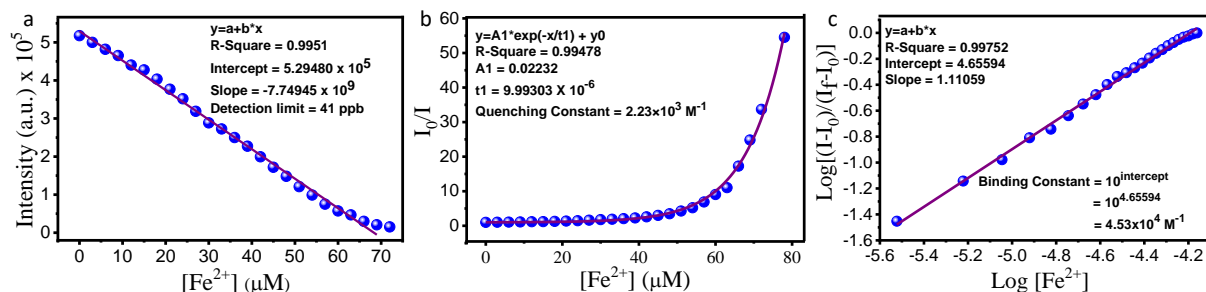
Figure A1. <sup>1</sup>H NMR of compound 5.Figure A2. <sup>13</sup>C NMR of compound 5.

Figure A3. <sup>1</sup>H NMR of compound 1.Figure A4. <sup>13</sup>C NMR of compound 1.

Figure A5. <sup>1</sup>H NMR of compound 2.Figure A6. <sup>13</sup>C NMR of compound 2.

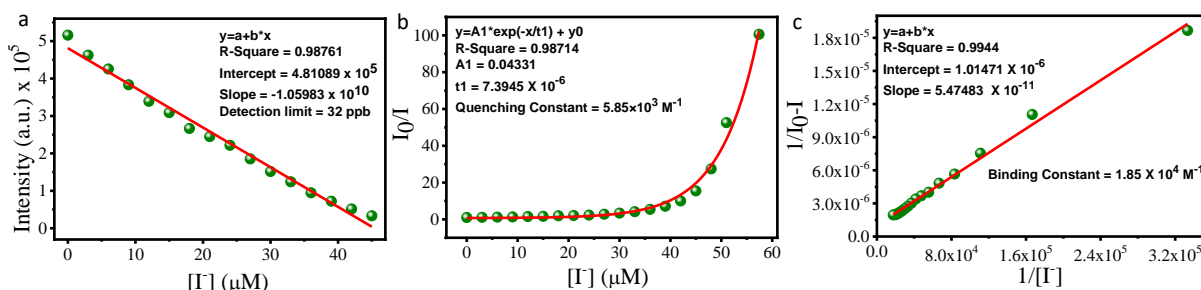


**Figure A7.** Absorption and emission spectra of compound **1**: (a) in solution state (THF,  $10^{-5}$  M) and (b) in the thin-film state (prepared by drop-casting the millimolar solution of compound **1** in DCM). Inset images presented the green and yellow colored luminescence showed by **1** under 365 nm UV light in solution and thin-film state, respectively.



**Figure A8.** (a) Plot between fluorescence intensity vs concentration of  $\text{Fe}^{2+}$  for the calculation of detection limit. (b) Stern-Volmer plot of **1** on addition of  $\text{Fe}^{2+}$  at  $\lambda_{\text{em}}^* = 537$  nm for calculating quenching constant. (c) Benesi-Hildebrand plot of **1**. $\text{Fe}^{2+}$  association at  $\lambda_{\text{em}} = 537$  nm for calculating binding constant. \*Note:  $\lambda_{\text{em}} = 537$  nm is for THF:H<sub>2</sub>O (90:10, v/v, H<sub>2</sub>O: 1mM tris-buffered saline (TBS), pH = 7.4) parent solution of compound **1**.



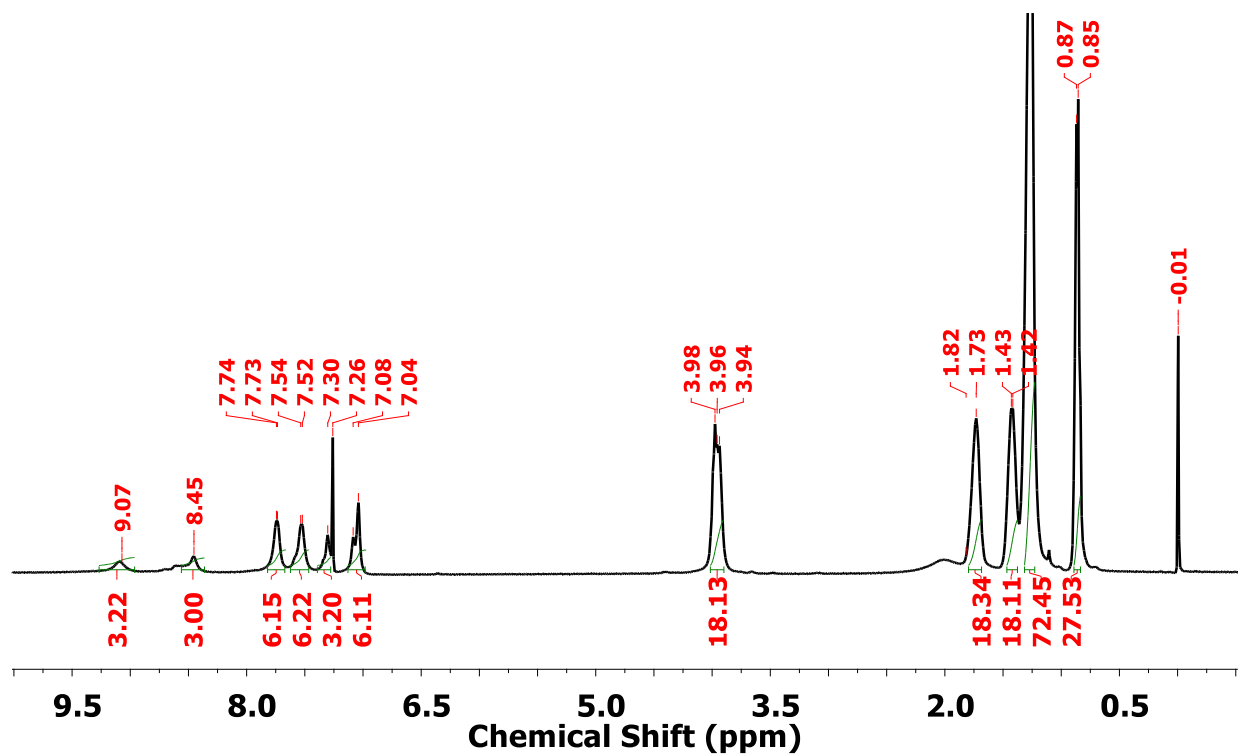
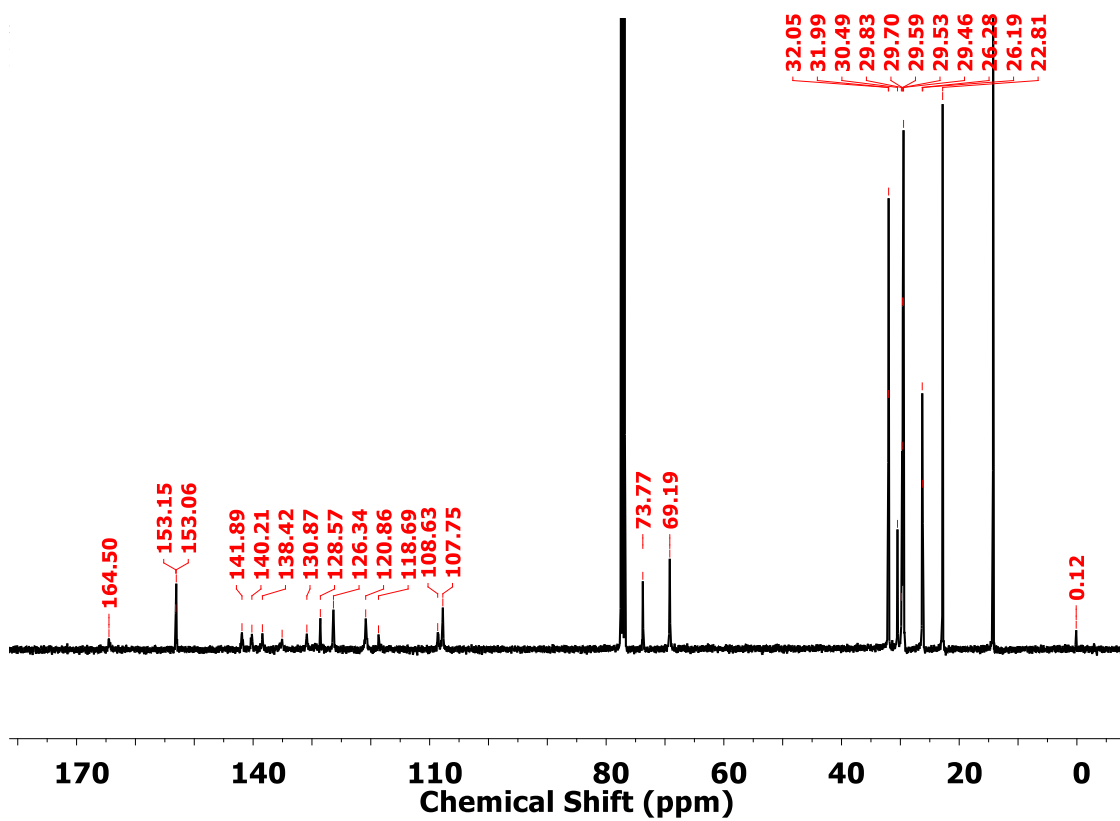


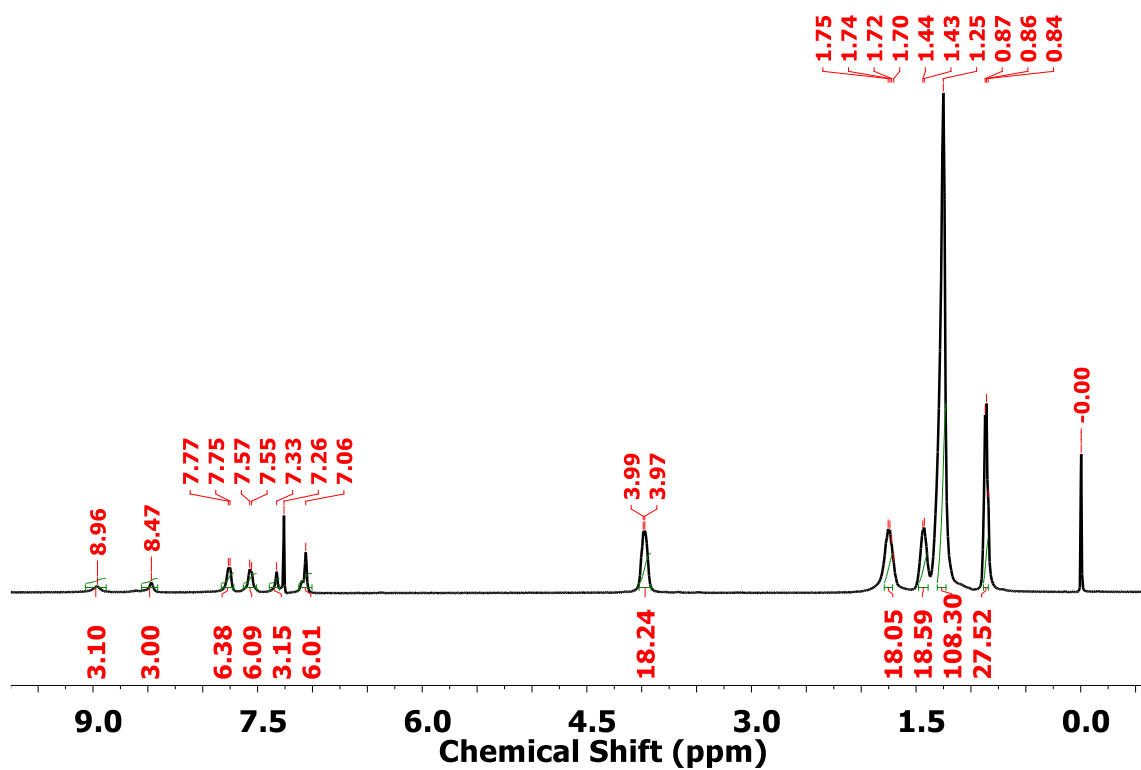
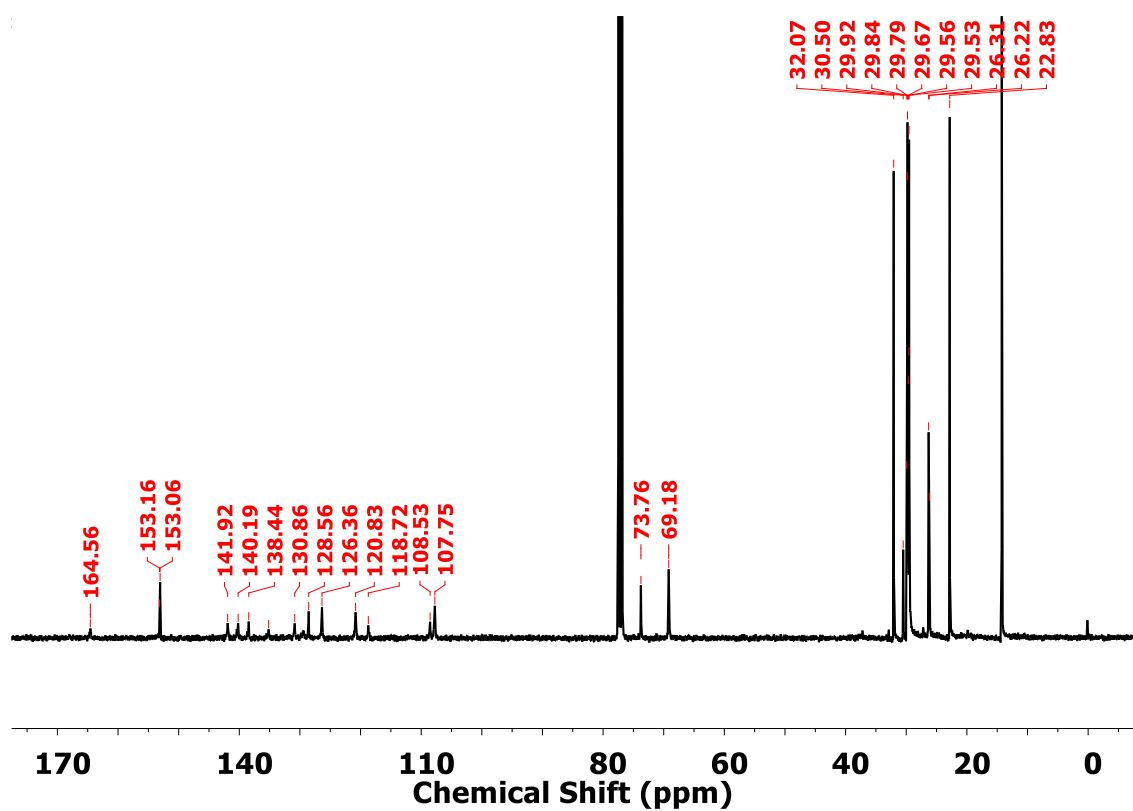
**Figure A9.** (a) Plot between fluorescence intensity at  $\lambda_{\text{em}}^* = 537 \text{ nm}$  vs concentration of  $I^-$  for the calculation of detection limit. (b) Stern-Volmer plot of **1** on addition of  $I^-$  at  $\lambda_{\text{em}} = 537 \text{ nm}$  for calculating quenching constant. (c) Benesi-Hildebrand plot of ligand **1**. $I^-$  association at  $\lambda_{\text{em}} = 537 \text{ nm}$  for calculating binding constant. \*Note:  $\lambda_{\text{em}} = 537 \text{ nm}$  is for THF:H<sub>2</sub>O (90:10, v/v, H<sub>2</sub>O: 1mM tris-buffered saline (TBS), pH = 7.4) parent solution of compound **1**.

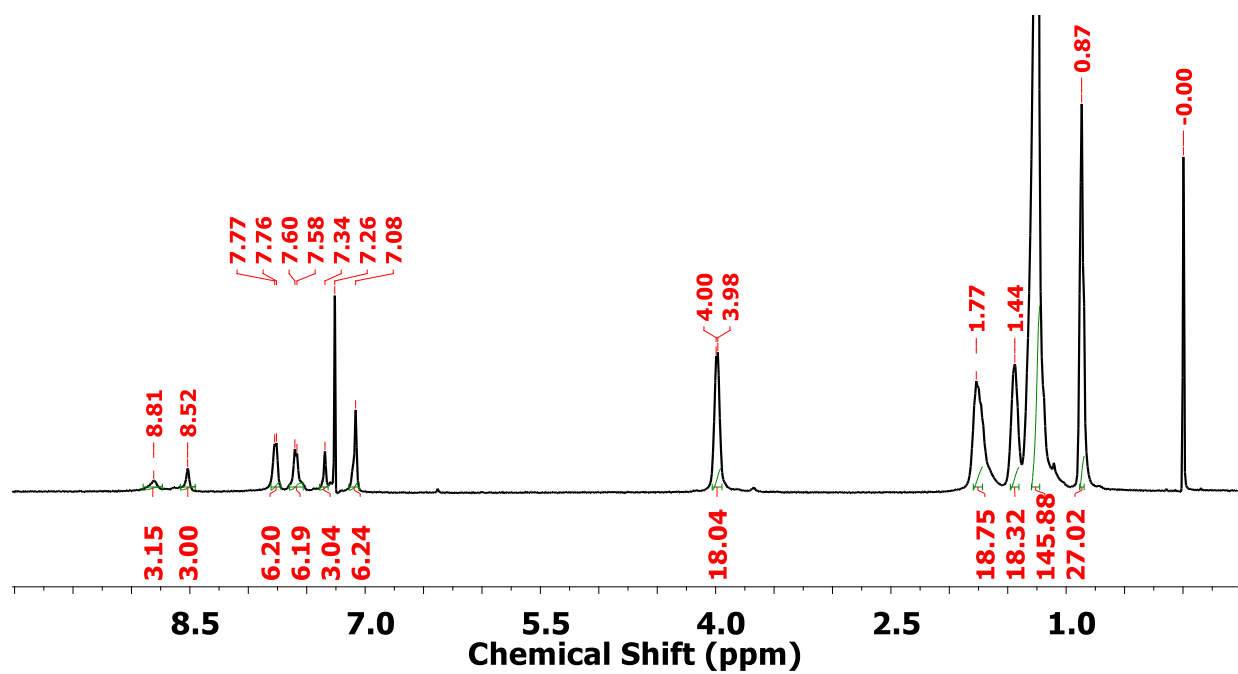
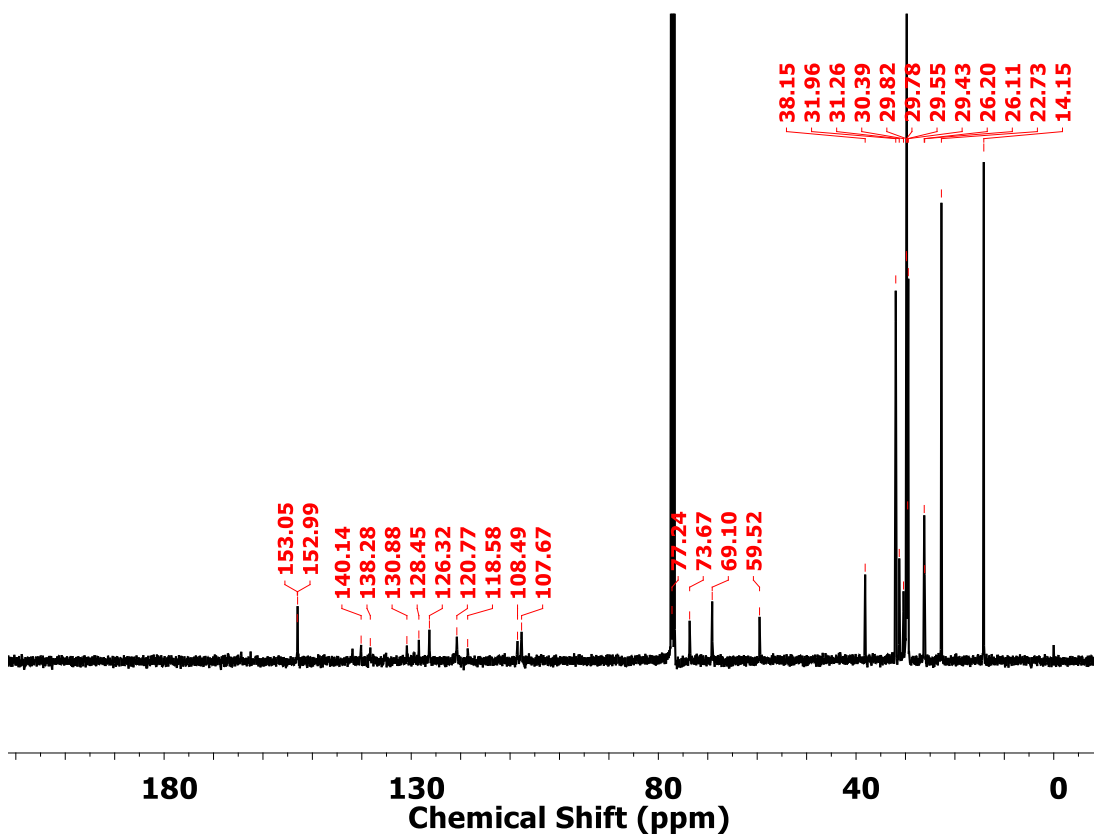
**Table A1.** Summary of EL performance and roll-off ratio of the best OLED devices.

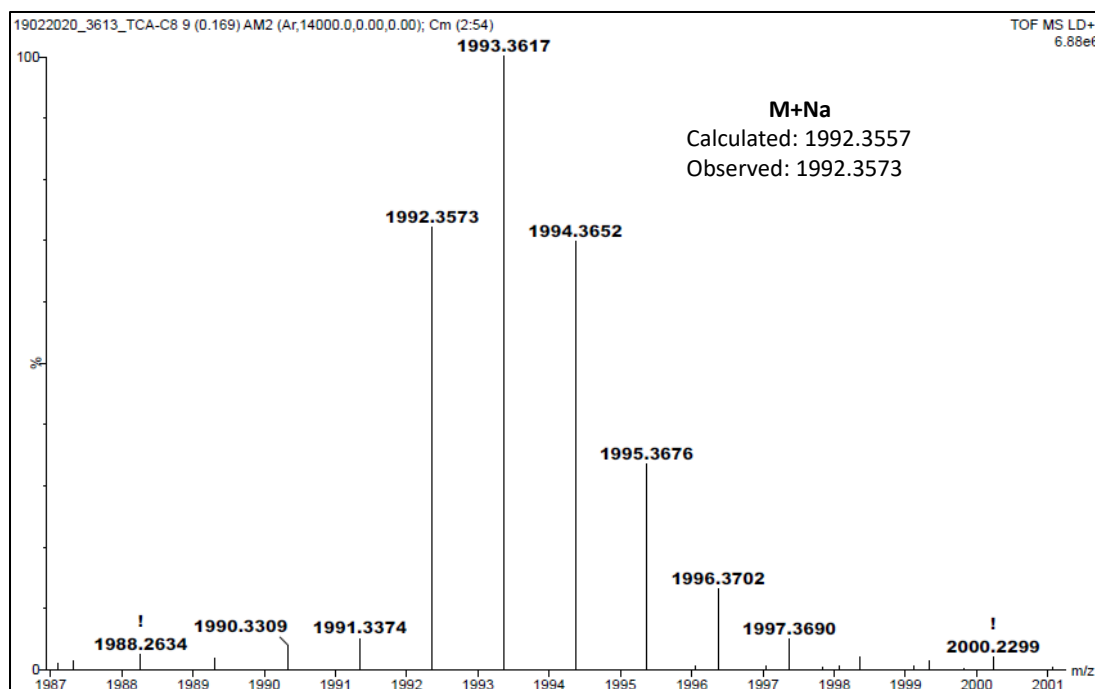
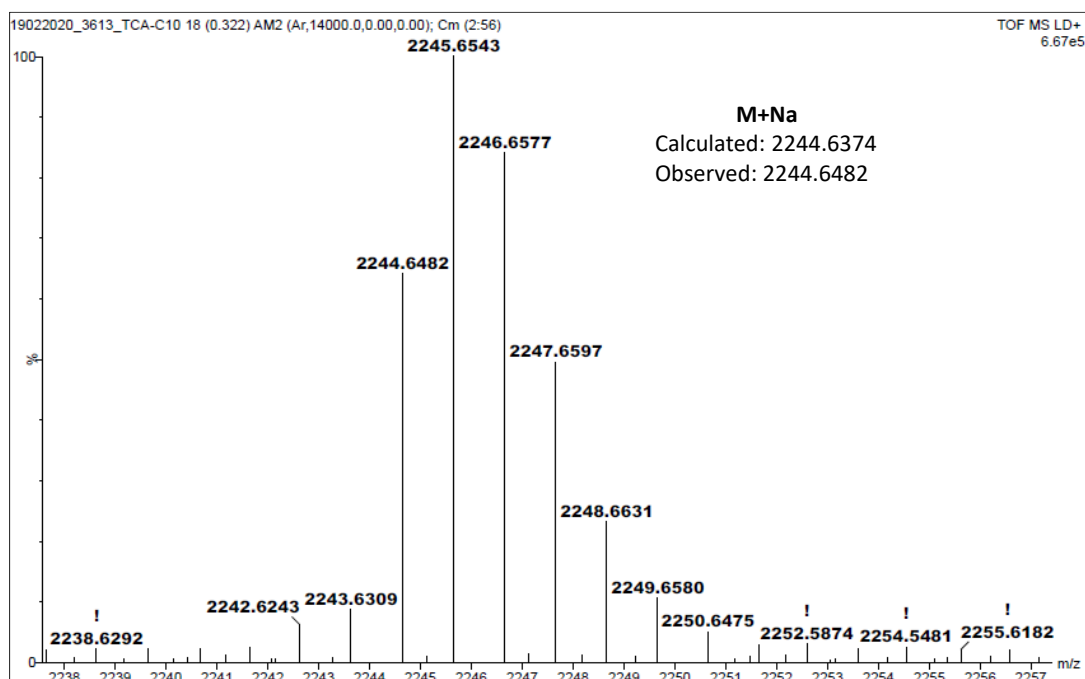
	PE <sub>max</sub> / CE <sub>max</sub> / EQE <sub>max</sub> (lm W <sup>-1</sup> / cd A <sup>-1</sup> / %)	PE <sub>100</sub> / CE <sub>100</sub> / EQE <sub>100</sub> (lm W <sup>-1</sup> / cd A <sup>-1</sup> / %)	PE <sub>max</sub> ~PE <sub>100</sub> <sup>a</sup> (%)	CE <sub>max</sub> ~CE <sub>100</sub> <sup>b</sup> (%)	EQE <sub>max</sub> ~EQE <sub>100</sub> <sup>c</sup> (%)
<b>1</b>	14.5/ 23.1/ 7.0	10.0/ 16.0/ 6.1	31.0	30.7	12.8
<b>2</b>	15.6/ 24.9/ 8.1	11.8/ 19.1/ 6.2	24.3	23.3	23.4

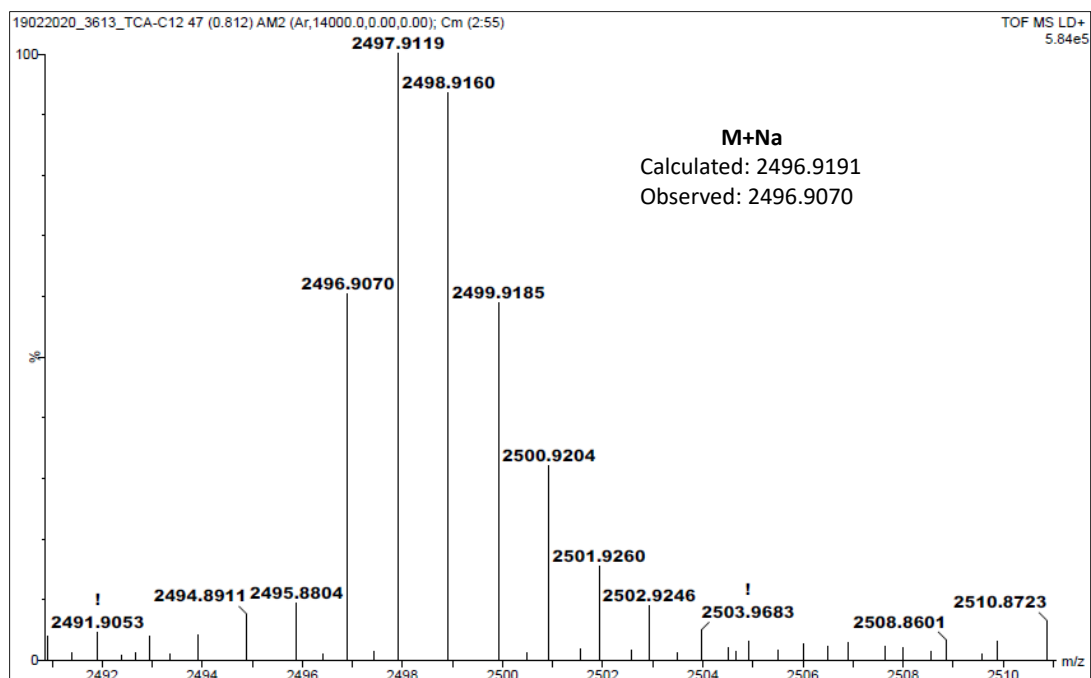
<sup>a</sup>Power efficiency roll-off (PE<sub>max</sub>~PE<sub>100</sub>). <sup>b</sup>Current efficiency roll-off (CE<sub>max</sub>~CE<sub>100</sub>).  
<sup>c</sup>External quantum efficiency roll-off (EQE<sub>max</sub>~EQE<sub>100</sub>).

Figure A10. <sup>1</sup>H NMR spectrum of compound 1a.Figure A11. <sup>13</sup>C NMR spectrum of compound 1a.

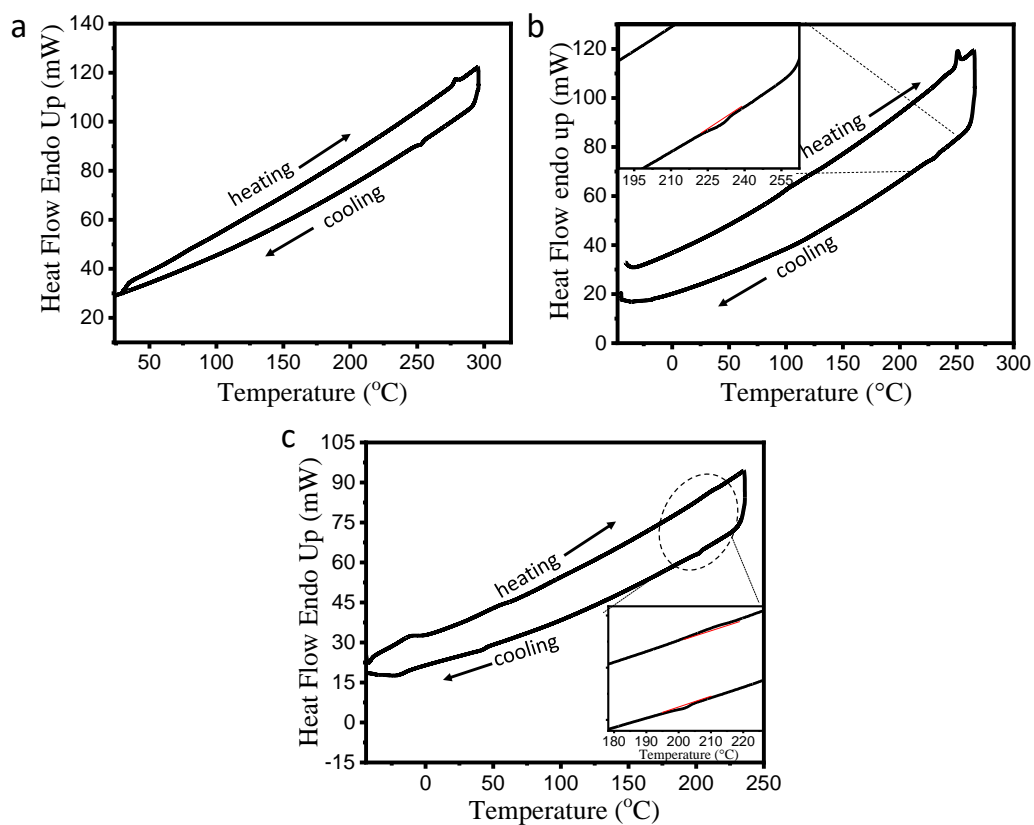
Figure A12. <sup>1</sup>H NMR spectrum of compound **1b**.Figure A13. <sup>13</sup>C NMR spectrum of compound **1b**.

Figure A14. <sup>1</sup>H NMR spectrum of compound 1c.Figure A15. <sup>13</sup>C NMR spectrum of compound 1c.

Figure A16. HRMS spectrum of compound **1a**.Figure A17. HRMS spectrum of compound **1b**.



**Figure A18.** HRMS spectrum of compound **1b**.



**Figure A19.** DSC traces of compounds **1a-c**: (a) **1a**; (b) **1b** and (c) **1c** recorded with the scan rate of 10 °C/min under nitrogen atmosphere.

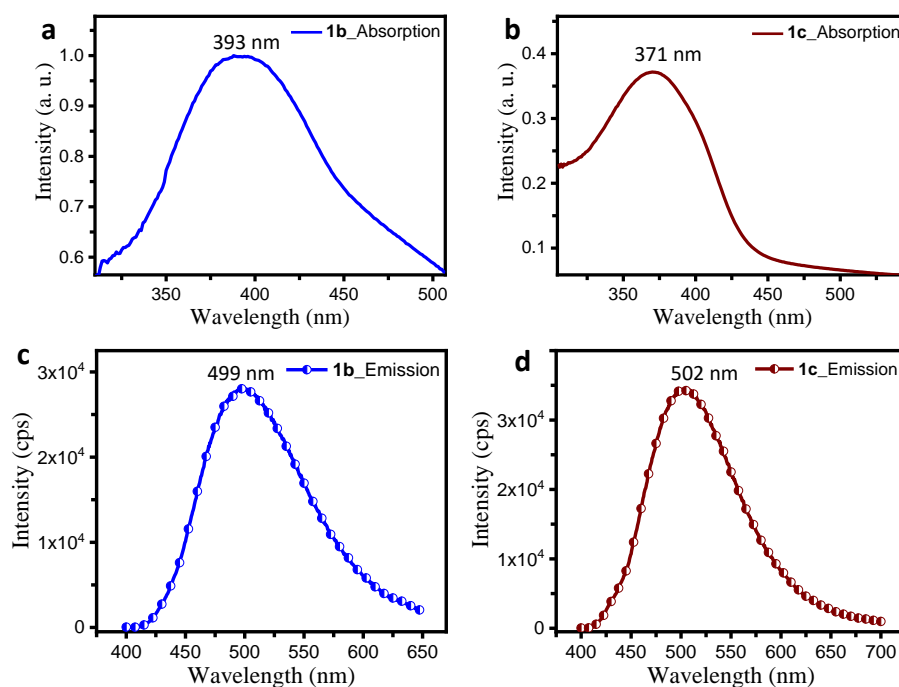


**Figure A20.** Absorption (a & c) and emission (b & d) studies of **1a-c** in thin-film state prepared by the drop-cast method.

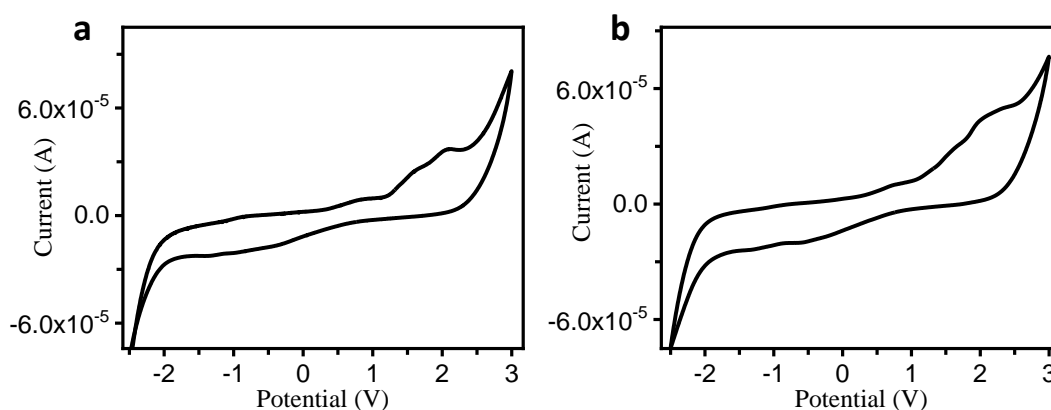


**Figure A21.** Cyclic Voltammogram of (a) **1b** and (b) **1c** in HPLC dichloromethane solution of tetrabutylammonium hexafluorophosphate (0.1 M) performed at a scanning rate  $50 \text{ mVs}^{-1}$ .

**Table A2.** Statistic table of all the hole mobility values for compounds **1a-c**.

No of Samples	<b>1a</b> Hole mobility ( $\times 10^{-3} \text{ cm}^2 \text{ V}^{-1} \text{ s}^{-1}$ )	<b>1b</b> Hole mobility ( $\times 10^{-3} \text{ cm}^2 \text{ V}^{-1} \text{ s}^{-1}$ )	<b>1c</b> Hole mobility ( $\times 10^{-3} \text{ cm}^2 \text{ V}^{-1} \text{ s}^{-1}$ )
<b>1</b>	4.00	4.08	6.81
<b>2</b>	4.45	4.36	5.37
<b>3</b>	3.21	3.57	5.02
<b>4</b>	3.50	3.50	4.91
<b>5</b>	3.46	3.30	4.38
<b>Average</b>	3.72	3.76	5.30
<b>Std. Dev.</b>	0.50	0.44	0.92
Final hole mobility values ( $\text{cm}^2 \text{ V}^{-1} \text{ s}^{-1}$ )	$(3.72 \pm 0.50) \times 10^{-3}$	$(3.76 \pm 0.44) \times 10^{-3}$	$(5.30 \pm 0.92) \times 10^{-3}$

**Table A3.** Statistic table of all the electron mobility values for compounds **1a-c**.

No of Samples	<b>1a</b> Electron mobility ( $\times 10^{-3} \text{ cm}^2 \text{ V}^{-1} \text{ s}^{-1}$ )	<b>1b</b> Electron mobility ( $\times 10^{-3} \text{ cm}^2 \text{ V}^{-1} \text{ s}^{-1}$ )	<b>1c</b> Electron mobility ( $\times 10^{-3} \text{ cm}^2 \text{ V}^{-1} \text{ s}^{-1}$ )
<b>1</b>	3.20	1.08	4.55
<b>2</b>	1.14	4.12	2.04
<b>3</b>	4.53	3.84	2.88
<b>4</b>	1.71	3.54	1.85
<b>5</b>	1.11	2.60	1.84
<b>Average</b>	2.34	3.04	2.63
<b>Std. Dev.</b>	1.49	1.23	1.15
Final electron mobility values ( $\text{cm}^2 \text{ V}^{-1} \text{ s}^{-1}$ )	$(2.34 \pm 1.49) \times 10^{-3}$	$(3.04 \pm 1.23) \times 10^{-3}$	$(2.63 \pm 1.15) \times 10^{-3}$



## Chapter 7

### Conclusions

This thesis presents the work which was carried out to develop new design strategies towards the achievement of discotic liquid crystalline materials for their usability in emissive and charge transport devices. Covalent as well as non-covalent synthetic methodologies were adopted to obtain these materials. The work described in the thesis can be concluded as follows:

(1) Formation of room temperature DLC materials utilizing conventional synthetic methodology to achieve columnar architectures based on heptazine core which was formerly, unfamiliar to discotic mesomorphic materials before this report. In this work,  $C_3$ -symmetric heptazine core is attached to three tri-alkoxy (Alkyl chain:  $R = -CH_3$ ,  $-C_8H_{17}$  and  $-C_{12}H_{25}$ ) substituted benzene derivatives *via* amino linkage (Figure 7.1).

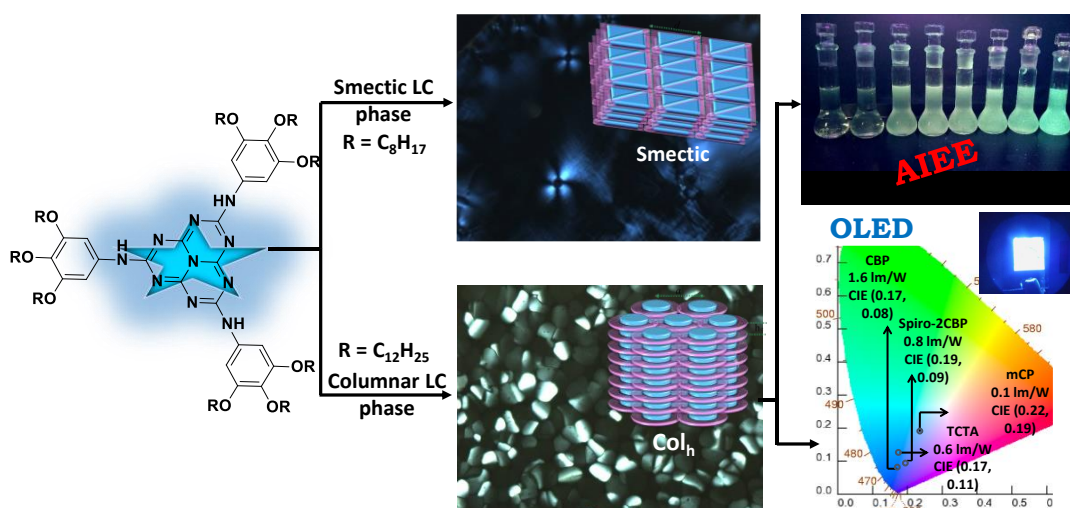


**Figure 7.1** Molecular structure of synthesized heptazine based DLCs showing smectic and columnar assemblies with AIE behaviour and deep blue emission in OLEDs.

Compounds with long peripheral alkyl chain lengths  $R = -C_8H_{17}$  and  $-C_{12}H_{25}$  were found to be mesomorphic. LC self-assembly behaviour was quite dependent on alkyl chain length. For instance, a derivative with a shorter alkyl chain length exhibits smectic (Sm) phase while with longer chain length shows columnar hexagonal mesophase ( $Col_h$ ) due to effective space-filling. The formation of the Sm and  $Col_h$  phase is attributed to the formation of hydrogen-bonded ribbon and disc-like (with no hydrogen bonding) self-assembled structures, respectively. The formation of these structures is well supported by their polarized optical microscopy (POM)

and X-ray diffraction (XRD) studies. The derivative with Col<sub>h</sub> self-assembly has been investigated for the conductivity measurements by AC impedance spectroscopy and showed a conductivity value of  $1.12 \times 10^{-7} \text{ S m}^{-1}$ . Heptazine based DLCs manifest a unique balance of  $\pi$ - $\pi$  interaction to form columnar materials and simultaneously retain luminescence efficiency in the solid-state together with aggregation-induced emission (AIE) behaviour. In this chapter, AIE and electroluminescence (EL) behaviour of columnar LC material was investigated. The deep-blue emission was observed in fabricated OLED devices using host-guest configuration.

(2) Synthesis and characterization of a new class of H-bonded fluorescent LCs based on heptazine fluorophore discotic core by adopting non-covalent H-bonded synthetic approach (Figure 7.2). Interestingly, the pure heptazine derivatives (non-mesomorphic) on complexation with tri-alkoxy benzoic acids exhibit enantiotropic columnar mesomorphism over a wide range of temperatures including room temperature. Such systems have self-assembled into columnar mesophases, though both the H-bonded components were not mesogenic on their own. Inherently fluorescent nature of the heptazine derivative results in the formation of fluorescent H-bonded complexes that showed sky-blue emission in the solution as well as in the solid-state.

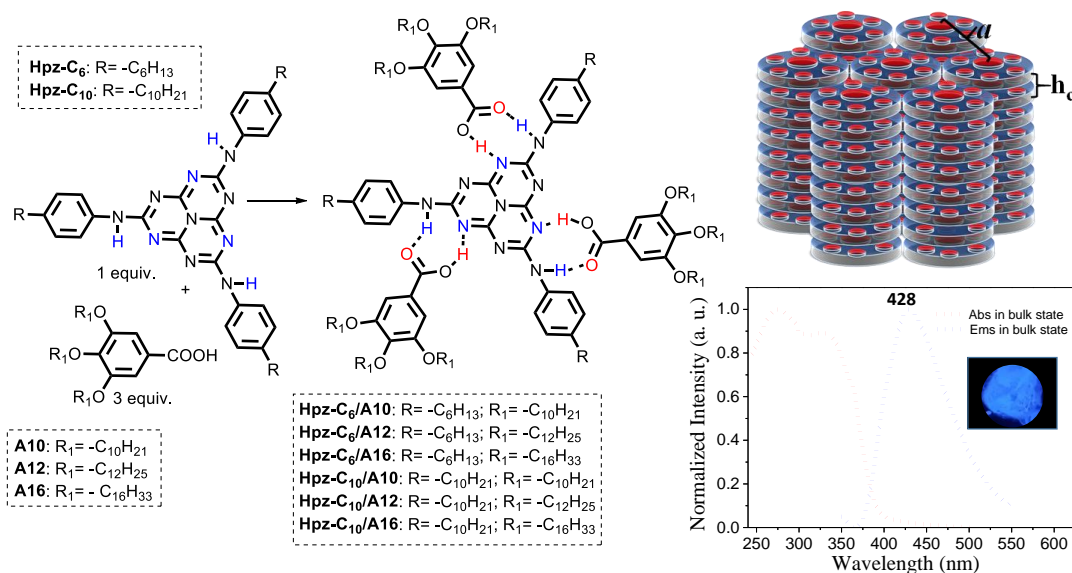


**Figure 7.2** Formation of H-bonded fluorescent discotic liquid crystals forming columnar assemblies.

(3) Synthesis, characterization and application of H-bonded DLCs forming segregated donor (D) (triphenylene) and acceptor (A) (heptazine) columnar assemblies linked through complementary H-bonding *via* flexible methylene spacers  $[-(\text{CH}_2)_n; n = 6, 8, 9]$  (Figure 7.3). Among the three synthesized complexes, only eight and nine spacer length containing complexes showed ambipolar charge transport with the former demonstrating maximum hole mobility of  $1.60 \text{ cm}^2 \text{ V}^{-1} \text{ s}^{-1}$  and later showing maximum electron mobility of  $2.90 \times 10^{-3} \text{ cm}^2 \text{ V}^{-1} \text{ s}^{-1}$ , measured through space charge limited current (SCLC) technique. Effect of alignment was studied on bulk mobility that led to the differences in the observed mobility values.

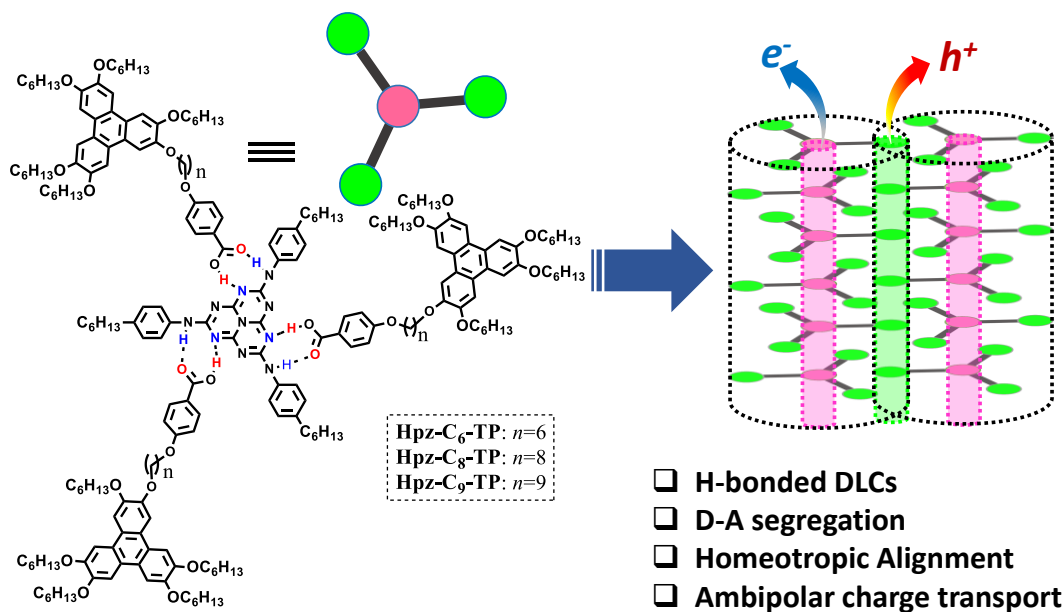


**Figure 7.3** Formation of supramolecular H-bonded complexes exhibiting segregated donor (triphenylene)-acceptor (heptazine) complexes beneficial for efficient ambipolar charge transport.

(4) Oligomeric disc-disc approach was adopted towards the achievement of novel functional DLC materials that has combined the properties of both the entities into a single compound. Triphenylene (TP) and pentaalkynylbenzene (PA) based discotic dimers connected by using the CuI-Et<sub>3</sub>N catalyzed click reaction between terminal TP alkyne and PA azide were synthesized (Figure 7.4). TP derivatives favour columnar organisation due to their rigid conjugated core whereas multialkynyl benzenes are the most investigated blue-light emitting discotic nematogens. The resulting dimers formed columnar rectangular and smectic mesophases at ambient temperature with emissive properties. Further, the induction of stable

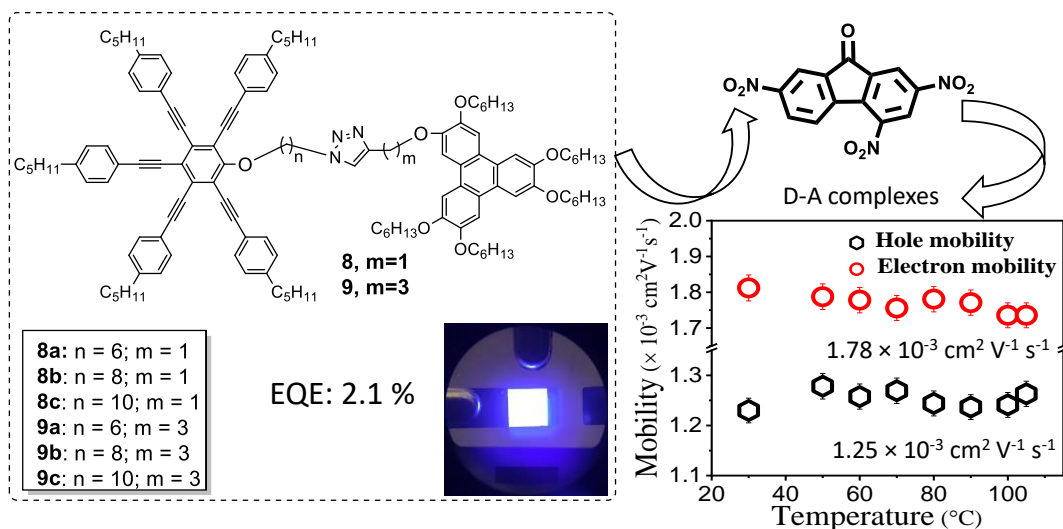


**Figure 7.4** Molecular design of triphenylene (TP) and pentaalkynylbenzene (PA) based discotic dimers for luminescence and charge transport application.

$\text{Col}_h$  mesomorphism is driven through charge-transfer interactions of electron-rich PA and TP moieties with electron-acceptor 2,4,7-trinitrofluorenone (TNF) molecules. The synthesis, thermal behaviour, and the mesomorphic properties of neat compounds and their binary systems (attained after doping with TNF) are discussed in detail. The doped devices have been fabricated by using neat compounds as emitter materials in OLED devices that result in the deep blue emission. Additionally, the electronic properties of one of the charge transfer complex are investigated *via* TOF method which revealed its ambipolar nature. The donor-acceptor molecular interactions among discogens (electron donor) and TNF (electron acceptor) stabilizes the mesophase and contributes towards the ambipolar nature of the resulting complexes.

(5) A new rod-disc oligomeric DLC system containing six cyanobiphenyl based rod-like moieties attached radially to a central truxene (TX) discotic core *via* flexible alkyl spacers (Figure 7.5). TX core was chosen because it is known as a promising scaffold for potential construction of large molecular architectures, easy functionalization, high thermal stability, good fluorescence capacity,  $C_3$  symmetrical structure, *etc.* Thus, TX derivatives can act as an attractive building block for many applications in the field of optoelectronics. In this work, we have shown that how the discotic columnar phase transformed to discotic nematic phase upon the introduction of 4-cyanobiphenyl units as confirmed by POM and XRD studies.

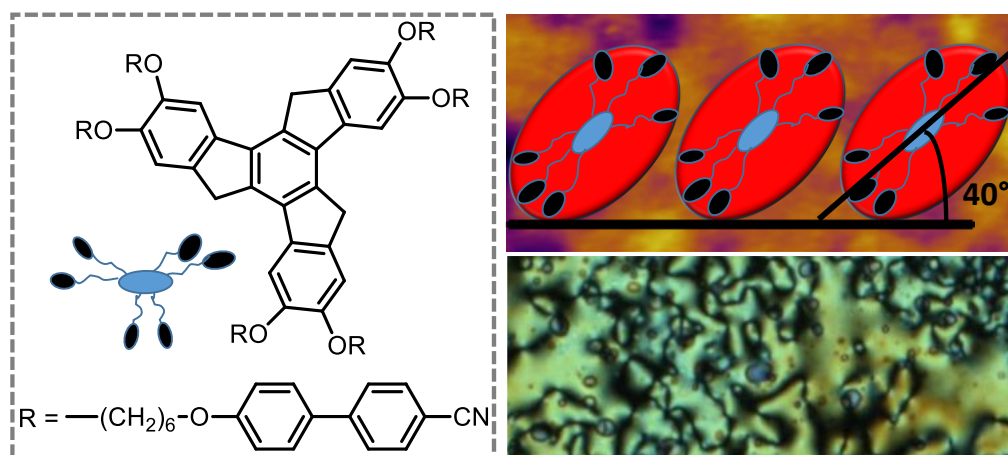


**Figure 7.5** Molecular design of truxene-cyanobiphenylene based rod-disc oligomeric DLC system displaying discotic nematic phase and tilted molecular orientation at air-solid interface.

Due to the presence of strong polar groups and long alkyl chains, these molecules showed the formation of good monolayer properties. The ultrathin monolayer of TX derivative was studied at air-water and air-solid interface. Air-water interface studies by Brewster angle microscopy, showed a very uniform grey-colored region in the monolayer state which gradually transformed to 3D crystals at the collapsed state. Air-solid interface studies *via* atomic force microscopy by transferring the monolayer on the hydrophilic glass substrates showed an edge-on configuration with a tilted orientation of the molecule at an angle of  $40^\circ$ .

(6) A new design system employing a new core fragment for DLCs namely, tetrathienoanthracene (TTA) attached to which are four tri-alkoxybenzene units *via* alkyne spacers was developed (Figure 7.6). The derivatives result in the formation of room temperature columnar phases. The design was motivated by the following two goals. First, the inclusion of multiple  $\text{S}\cdots\text{S}$  interactions coupled with  $\pi$ - $\pi$  stacking in TTA derivatives provide an effective spatial overlap of the electronic wave functions of the molecules in discs and lead to excellent hole-carrier mobilities. Second, the presence of triple bond spacers provides extended conjugation over the whole molecule and at the same time can reduce the stacking distances, favourable for high charge transport. The materials showed homeotropic columnar ordering at room temperature over a macroscopic area and effect of alignment on bulk mobility was measured *via* SCLC method. A high hole mobility of  $4.22 \text{ cm}^2 \text{ V}^{-1} \text{ s}^{-1}$  was observed at ambient temperature in the largely aligned sample.

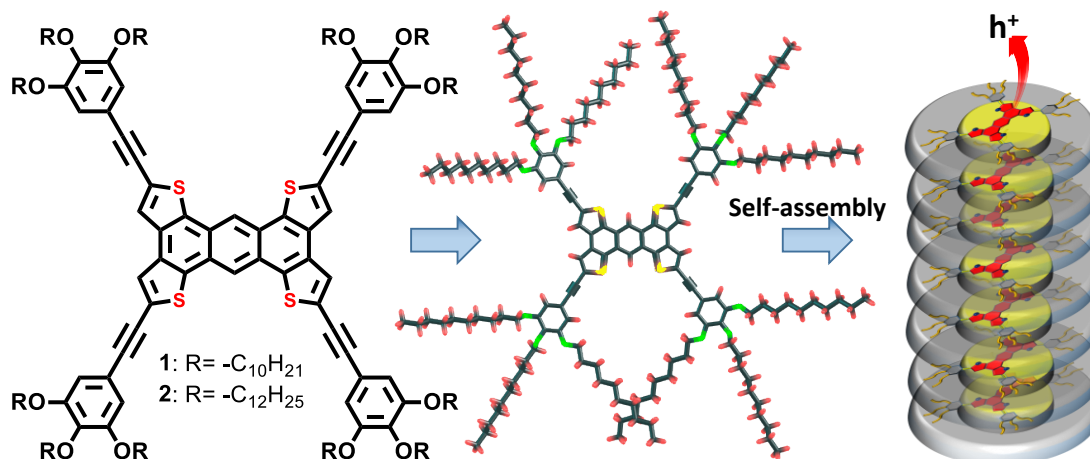


**Figure 7.6** Molecular design of tetrathienoanthracene (TTA) based DLCs attached to which are four tri-alkoxybenzene units *via* alkynyl spacers.

(7) Design strategy for the achievement of a new series of PTE based DLCs that exhibit the room temperature columnar mesophase and act as efficient fluorescent emitter materials in OLEDs. The molecular design involves the attachment of triazole moieties with the PTE discotic core *via* click chemistry (Figure 7.7). Triazole groups were chosen as they can improve

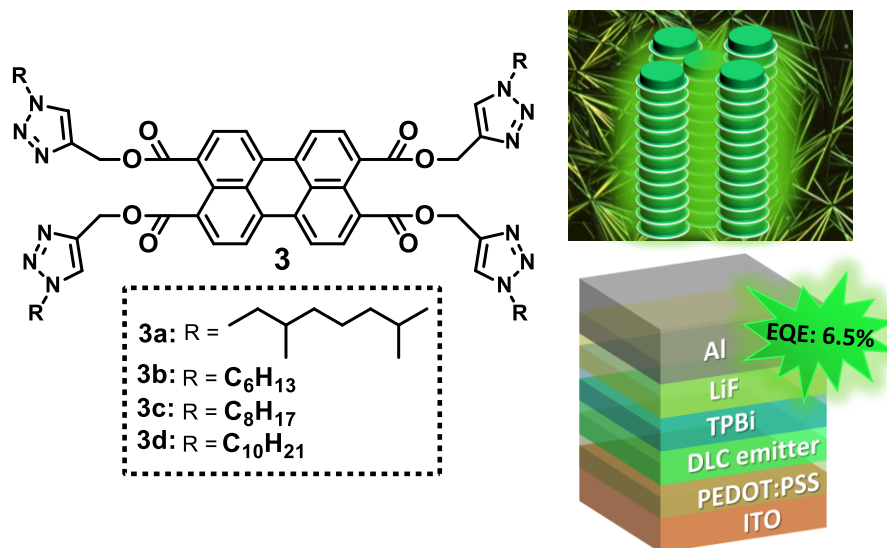


**Figure 7.7** Perylene tetraesters based luminescent DLCs substituted with four triazole groups *via* click chemistry.

the electron transport as well as tune the luminescence behaviour of discogens. All the PTE derivatives exhibited ordered columnar rectangular mesophases at ambient temperatures



suitable for various device applications. The electron mobility of triazole modified PTE derivative was measured in the mesophase by time of flight (TOF) technique and found to be  $0.014 \text{ cm}^2 \text{ V}^{-1} \text{ s}^{-1}$ . However, the balanced hole and electron charge transport behaviour was observed in fabricated hole-only and electron-only devices. Taking advantage of both charge transport and the luminescence nature of the PTE derivative in OLEDs, a series of devices were fabricated by utilizing PTE derivative as a sole emitter and in the dispersed form at 1, 5 and 8 wt% with the (carbazolyl)-1,10-biphenyl (CBP) host and at 5 wt% in the bis[3,5-di(9H-carbazol-9-yl)phenyl]diphenylsilane (SimCP2) host. A significantly high value of the external quantum efficiency (EQE) of 6.5% is obtained in doped devices with the CBP host at 5 wt% dopant concentration with CIE coordinates of (0.37,0.53) that corresponds to green color.

(7) Synthesis and characterization of perylene tetraesters (PTE) based luminescent DLCs consisting of PTE core attached to which four bulky pentalkynylbenzene units through flexible methylene spacers  $[-(\text{CH}_2)_n]$  (Figure 7.8). Here, the motive is to induce room temperature LC behaviour and high luminescence efficiency by minimizing the core-core interactions. Also, we sought to gain an additional insight into the packing of the hybrids in the mesophase through simple variation in the number of alkyl spacers  $[-(\text{CH}_2)_n; n = 6, 8, 10]$  connecting the PTE core and multiyne units. Compounds with shorter alkyl spacers ( $n = 6$  and  $8$ ) were found to self-organize into soft crystalline columnar assemblies, and those with longer spacer ( $n = 10$ )

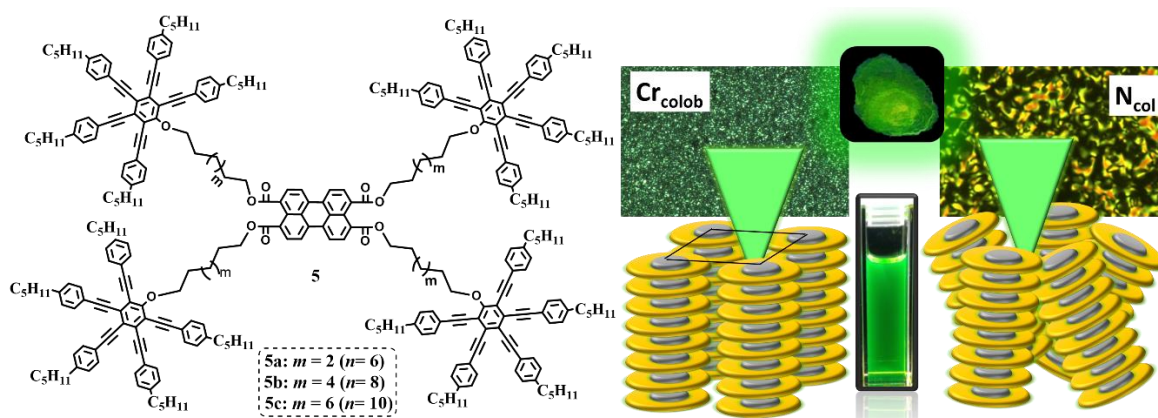


**Figure 7.8** Perylene tetraesters based luminescent DLCs substituted with four bulky pentalkynylbenzene units through flexible methylene spacers.

exhibited a liquid-crystalline columnar nematic mesophase. All compounds exhibited excellent fluorescence emission properties with a very good quantum yield and large bandgap. Electrical

characterization of columnar assemblies showed the potential of the derivatives to act as ion conductors.

(9) Synthesized benzothiadiazole (BTD) based donor-acceptor  $\pi$ -conjugated fluorescent molecules for their application in solution-processed green OLED devices that exquiste high EQE as high as 8.1% (Figure 7.9). The observed high photoluminescence (PL) quantum yield corroborates the high EUE which exceeded its traditional limit (25%), hence, suggested the utilization of triplet excitons. The reported emitters combine two parameters, i.e. high PL efficiency and high EUE, which are of key importance to harvest maximum EL in OLED devices. Based on the photophysical (solvatochromic experiment) and quantum chemical calculations, the impacts of the D- $\pi$ -A- $\pi$ -D molecular design on the regulation of the locally excited and charge transfer components were revealed, which explained the observed high EQE and EUE values for the BTD-based emitters. The development of emitters with a hybrid local and charge-transfer state in combination with the ‘hot exciton’ mechanism is an important strategy to produce highly efficient fluorescent-emitter materials. Besides the impressive EL properties of the emitters, the material was investigated as a chemosensor that showed the selective sensing of metal cation ( $\text{Fe}^{2+}$ ) and anion ( $\text{I}^-$ ).

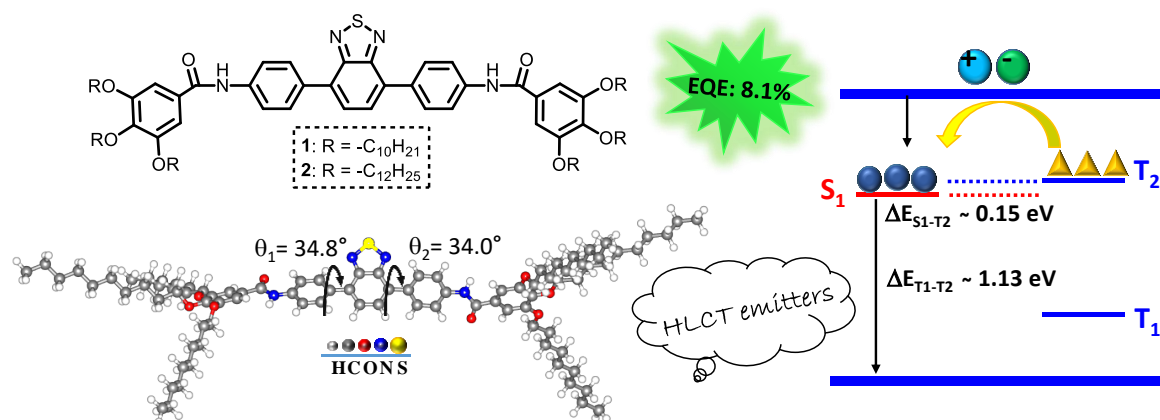


**Figure 7.9** Benzothiadiazole based hybrid localized and charge transfer (HLCT) donor-acceptor  $\pi$ -conjugated fluorescent molecules for their application in solution-processed green OLED devices

(10 Synthesized tricarboxamide based DLC materials where the  $C_3$ -symmetric triamide core is substituted with cyanostilbene based flexible luminophoric groups (Figure 7.10). In triamide



derivatives, intramolecular H-bonding contributes to the formation of the columnar assembly that is likely to act as a charge transport entity. On the other hand, the promesogenic trialkoxy cyanostilbene fragment is responsible for the emissive as well as LC behaviour of the derivatives. All the derivatives exhibited room temperature  $\text{Col}_h$  behaviour over a wide mesomorphic range. EL performance of the materials was studied in solution-processed multilayer doped and non-doped OLED devices. Non-doped devices display poor EL performance and brightness when compared with doped devices. The electronic properties of the triamide-cyanostilbene DLC derivatives were investigated by the SCLC technique in solution-processable thin-films which showed the ambipolar charge transport in all the derivatives.

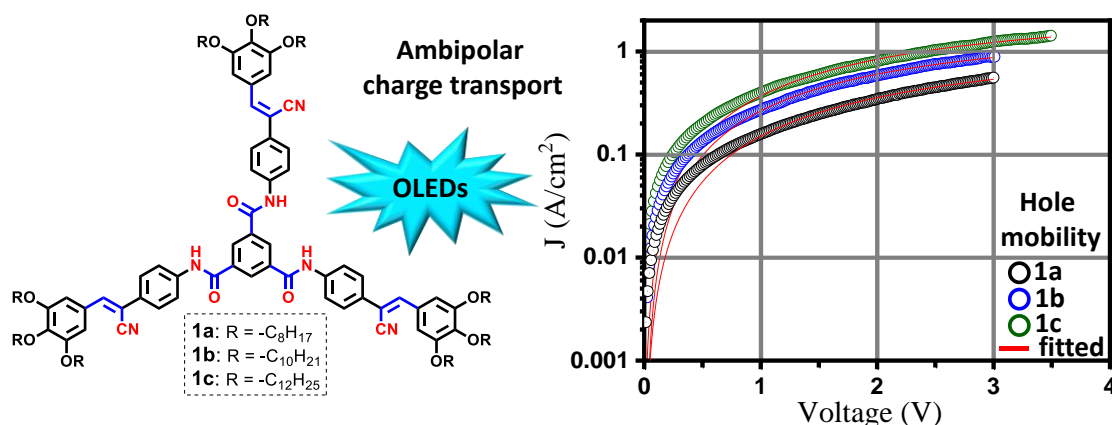


**Figure 7.10** Tricarboxamide based DLC materials substituted with cyanostilbene based flexible luminophoric groups to achieve luminescent and efficient charge transport DLCs.



## List of Publications

1. **Bala, I.**; De, J.; Gupta, S. P.; Singh, H.; Pandey, U. K.; Pal, S. K. High Hole Mobility in Room Temperature Discotic Liquid Crystalline Tetrathienoanthracenes. *Chem. Commun.* **2020**, *56*, 5629-5632.
2. **Bala, I.**; De, J.; Gupta, S. P.; Pandey, U. K.; Pal, S. K. *J. Mater. Chem. C*, **2021**, DOI: 10.1039/D1TC01898A.
3. De, J.; **Bala, I.**; Gupta, S. P.; Pandey, U. K.; Pal, S. K. High Hole Mobility and Efficient Ambipolar Charge Transport in Heterocoronene-based Ordered Columnar Discotics. *J. Am. Chem. Soc.* **2019**, *141*, 18799-18805.
4. **Bala, I.**; Yadav, R. A. K.; Devi, M.; De, J.; Singh, N.; Kailasam, K.; Jayakumar, J.; Jou, J. H.; Cheng, C. H.; Pal, S. K. High-performing D- $\pi$ -A- $\pi$ -D Benzothiadiazole-based Hybrid Local and Charge-transfer Emitters in Solution-processed OLEDs. *J. Mater. Chem. C* **2020**, *8*, 17009-17015.
5. **Bala, I.**; Singh, N.; Yadav, R. A. K.; De, J.; Gupta, S. P.; Singh, D. P.; Dubey, D. K.; Jou, J. H.; Douali, R.; Pal, S. K. Room Temperature Perylene Based Columnar Liquid Crystals as Solid-state Fluorescent Emitters in Solution-processable Organic Light-Emitting Diodes. *J. Mater. Chem. C* **2020**, *8*, 12485-12494.
6. **Bala, I.**; Yang, W. Y.; Gupta, S. P.; De, J.; Yadav, R. A. K.; Singh, D. P.; Dubey, D. K.; Jou, J. H.; Douali, R.; Pal, S. K. Room Temperature Discotic Liquid Crystalline Triphenylene-Pentaalkynylbenzene Dyads as An Emitter in Blue OLEDs and Their Charge Transfer Complexes with Ambipolar Charge Transport Behaviour. *J. Mater. Chem. C* **2019**, *7*, 5724-5738.
7. **Bala, I.**; Singh, H.; Battula, V. R.; Gupta, S. P.; De, J.; Kumar, S.; Kailasam, K.; Pal, S. K. Heptazine: an Electron-Deficient Fluorescent Core for Discotic Liquid Crystals. *Chem. Eur. J.* **2017**, *23*, 14718-14722.
8. **Bala, I.**; Gupta, S. P.; De, J.; Pal, S. K. Room-Temperature Columnar Nematic and Soft Crystalline Columnar Assemblies of a New Series of Perylene-Centred Disc Tetramers. *Chem. Eur. J.* **2017**, *23*, 12767-12778.
9. **Bala, I.**; Gupta, S. P.; Kumar, S.; Singh, H.; De, J.; Sharma, N.; Kailasam, K.; Pal, S. K. Hydrogen-Bond Mediated Columnar Liquid Crystalline Assemblies of C<sub>3</sub>-Symmetric Heptazine Derivatives at Ambient Temperature. *Soft Matter* **2018**, *14*, 6342-6352.
10. **Bala, I.**; Ming, L.; Yadav, R. A. K.; De, J.; Dubey, D. K.; Kumar, S.; Singh, H.; Jou, J. H.; Kailasam, K.; Pal, S. K.; Deep-Blue OLED Fabrication from Heptazine Columnar Liquid Crystal Based AIE-Active Sky-Blue Emitter. *ChemistrySelect* **2018**, *3*, 7771-7777.
11. **Bala I.**; Pal, S. K. Rod-Disc Oligomeric Liquid Crystal Based on 4-Cyanobiphenyl and Truxene Core. *Liq. Cryst.* **2016**, *43*, 963-971.

12. **Bala, I.**; Kaur, H.; Yadav, R. A. K.; De, J.; Gupta, S. P.; Jou, J. H.; Pandey, U. K. P.; Pal, S. K. Electroluminescent AIE-active discotic liquid crystals based on alkoxy cyanostilbenes functionalized benzenetricarboxamide with ambipolar charge transport. *Submitted*.
13. Devi, S.<sup>§</sup>; **Bala, I.**<sup>§</sup>; Gupta, S. P.; Kumar, P.; Pal, S. K.; Venkataramani, S. Reversibly Photoswitchable Alkoxy Azobenzenes Connected Benzenetricarboxamide Discotic Liquid Crystals With Perpetual Long Range Columnar Assembly. *Org. Biomol. Chem.* **2019**, *17*, 1947-1954. (<sup>§</sup>authors contributed equally)
14. Dhingra, S.; **Bala, I.**; De, J.; Gupta, S. P.; Pandey, U. K.; Pal, S. K. An electron-deficient tris (triazole)-based discotic liquid crystal that exhibits fast electron transport. *J. Mater. Chem. C*, **2021**, *9*, 5628-5632.
15. De, J.; Yang, W. Y.; **Bala, I.**; Gupta, S. P.; Yadav, R. A. K.; Dubey, D. K.; Chowdhury, A.; Jou, J. H.; Pal, S. K. Room-Temperature Columnar Liquid Crystals as Efficient Pure Deep-Blue Emitters in Organic Light-Emitting Diodes with an External Quantum Efficiency of 4.0%. *ACS Appl. Mater. Interfaces* **2019**, *11*, 8291-8300.
16. De, J.; Devi, M.; Shah, A.; Gupta, S. P.; **Bala, I.**; Singh, D. P.; Douali, R.; Pal, S. K. Luminescent Conductive Columnar  $\pi$ -Gelators for Fe (II) Sensing and Bio-Imaging Applications. *J. Phys. Chem. B* **2020**, *124*, 10257-10265.
17. De, J.; Gupta, S. P.; Swayamprabha, S. S.; Dubey, D. K.; **Bala, I.**; Sarkar, I.; Dey, G.; Jou, J. H.; Ghosh, S.; Pal, S. K.; Blue Luminescent Organic Light Emitting Diode Devices of a New Class of Star-Shaped Columnar Mesogens Exhibiting  $\pi$ - $\pi$  Driven Supergelation. *J. Phys. Chem. C* **2018**, *122*, 23659-23674.
18. De, J.; Gupta, S. P.; **Bala, I.**; Kumar, S.; Pal, S. K. Phase Behavior of a New Class of Anthraquinone-Based Discotic Liquid Crystals. *Langmuir* **2017**, *33*, 13849-13860.
19. De, J.; M. M., A. H.; Yadav, R. A. K.; Gupta, S. P.; **Bala, I.**; Chawla, P.; Kesavan, K. K.; Jou, J. H.; Pal, S. K. AIE-active Mechanoluminescent Discotic Liquid Crystals for Applications in OLEDs and Bio-imaging. *Chem. Commun.* **2020**, *56*, 14279-14282.
20. Battula, V. R.; Singh, H.; Kumar, S.; **Bala, I.**; Pal, S. K.; Kailasam, K. Natural Sunlight Driven Oxidative Homocoupling of Amines by a Truxene-Based Conjugated Microporous Polymer. *ACS Catal.* **2018**, *8*, 6751-6759.
21. Singh, H.; Tomer, V. K.; Jena, N.; **Bala, I.**; Sharma, N.; Nepak, D.; De Sarkar, A.; Kailasam, K.; Pal, S. K. A Porous, Crystalline Truxene-based Covalent Organic Framework and its Application in Humidity Sensing. *J. Mater. Chem. A* **2017**, *5*, 21820-21827.
22. Gupta, M.; **Bala, I.**; Pal, S. K. A Room Temperature Discotic Mesogenic Dyad Based-on Triphenylene and Pentaalkynylbenzene. *Tetrahedron Lett.* **2014**, *55*, 5836-5840.

## Honors, Awards and Recognitions

1. *Japan Society for the Promotion of Science (JSPS)* postdoctoral fellowship (FY2021).
2. Selected and funded by UGC-NRC to attend 7-days workshop “*Soft and Active Matter*” at University of Hyderabad, India.
3. “*Room-Temperature Columnar Nematic and Soft Crystalline Columnar Assemblies of a New Series of Perylene-Centred Disc Tetramers*” research work was featured as frontispiece in *Chemistry-A European Journal*.
4. “*Rod-Disc Oligomeric Liquid Crystal Based on 4-Cyanobiphenyl and Truxene Core*” research work was featured as cover picture in *Liquid Crystals*.
5. *Excellence of Merit Certificate* in the Integrated PhD (Chemistry) for best academic position (2015) at Indian Institute of Science Education and Research (IISER) Mohali.
6. Funding from *Council of Scientific and Industrial Research (CSIR)* fellowship for pursuing PhD.

## Conferences

1. “*Influence of Horizontal Alignment in Efficient Charge Transport of Discotic Liquid Crystals*” Invited Talk in International Conference on Liquid Crystals, Liquid Crystalline Polymers and Nanosystems (**ICLCPN 2019**), 13-15 December 2019, at Mahatma Gandhi University, Kottayam, Kerala, India.
2. “*Room Temperature Columnar Liquid Crystals as An Efficient Pure Deep-Blue Emitter in OLEDs*” Oral Presentation in 26<sup>th</sup> National Conference on Liquid Crystals (**NCLC-2019**), October 21-23, 2019 at Chitkara University, Punjab, India.
3. “*Heptazine Based Columnar Mesogens as Blue Emitter in OLEDs*” Poster Presentation in Frontiers in Chemical Sciences (**FICS-2018**) December 6-8, 2018, at Indian Institute of Technology (IIT) Guwahati, India.
4. “*Novel electron-deficient Columnar Mesogens as Blue Emitter in OLEDs*” Poster Presentation in 27<sup>th</sup> International Liquid Crystal Conference (**ILCC 2018**) on July 22-27, 2018 at International Conference Centre, Kyoto, Japan.
5. “*Discotic Liquid Crystals as Efficient Blue Emitter in OLEDs*” Poster Presentation in **ACS ON CAMPUS**, February 9, 2018 at IISER Mohali, India.

6. “*Mesomorphism in a New Class of Heptazine-Based Discotic Liquid Crystals*” Poster Presentation in 24<sup>th</sup> National Conference on Liquid Crystals (**NCLC-2017**), October 11-13, 2017 at IISER Mohali, India.
7. “*Development of Perylene Based Luminescent Discotic Liquid Crystals*” Oral Presentation in 23<sup>rd</sup> National Conference on Liquid Crystals (**NCLC-2016**), December 7- 9, 2016 at Indian School of Mines (ISM) Dhanbad, India.
8. “*Mesomorphism in truxene based liquid crystals*” Poster Presentation in 22<sup>rd</sup> National Conference on Liquid Crystals (**NCLC-2015**), December 21-23, 2015 at DIT University, Dehradun, India.
9. Participated at the **Royal Society of Chemistry Roadshows 2017** held at IISER Mohali on 14<sup>th</sup> November 2017.
10. Volunteered actively in the organization of **24<sup>th</sup> National Conference on Liquid Crystals (NCLC-2017)**, October 11-13, 2017 at IISER Mohali, India.
11. Participated at **2<sup>nd</sup> CRIKC Nanoscience Day**, August 8, 2016 at INST Mohali, India.
12. Participated at workshop on **Solid State and Material Chemistry**, February 8, 2016 at INST Mohali, India.
13. Participated at **Inside Raman**, December 10-11, 2015 at IISER Mohali, India.

# VITA

## Indu Bala

Indu Bala was born and raised in Una, Himachal Pradesh where she did her schooling. She did her bachelors in chemistry honors from Panjab University, Chandigarh in 2013. In the same year, she joined IISER Mohali as an Integrated PhD (chemistry) student. She was awarded two-year fellowship during her MS (chemistry) by Ministry of Human Resource Development (MHRD), Government of India. She was awarded “Certificate of Merit” in her MS for best academic performance. She had successfully qualified CSIR-JRF (chemistry) in 2014. She started her doctoral research in august 2015 under the supervision of Dr. Santanu Kumar Pal. Her research work includes the design, synthesis and characterization of discotic liquid crystalline polycyclic aromatic hydrocarbons with a strong interest on their application in electronic devices. During her PhD, Indu attended several national and international conferences where she presented her work as poster/oral presentations. She has authored and co-authored 21 publications in reputed peer-reviewed international journals. In 2020, she was awarded prestigious JSPS postdoctoral fellowship.

